

Basins and related tectonics

Edited by

Guiting Hou, Wenlong Ding, Shuping Chen, Yuan Neng
Jianwei Feng and Wei Ju

Published in

Frontiers in Earth Science



FRONTIERS EBOOK COPYRIGHT STATEMENT

The copyright in the text of individual articles in this ebook is the property of their respective authors or their respective institutions or funders. The copyright in graphics and images within each article may be subject to copyright of other parties. In both cases this is subject to a license granted to Frontiers.

The compilation of articles constituting this ebook is the property of Frontiers.

Each article within this ebook, and the ebook itself, are published under the most recent version of the Creative Commons CC-BY licence. The version current at the date of publication of this ebook is CC-BY 4.0. If the CC-BY licence is updated, the licence granted by Frontiers is automatically updated to the new version.

When exercising any right under the CC-BY licence, Frontiers must be attributed as the original publisher of the article or ebook, as applicable.

Authors have the responsibility of ensuring that any graphics or other materials which are the property of others may be included in the CC-BY licence, but this should be checked before relying on the CC-BY licence to reproduce those materials. Any copyright notices relating to those materials must be complied with.

Copyright and source acknowledgement notices may not be removed and must be displayed in any copy, derivative work or partial copy which includes the elements in question.

All copyright, and all rights therein, are protected by national and international copyright laws. The above represents a summary only. For further information please read Frontiers' Conditions for Website Use and Copyright Statement, and the applicable CC-BY licence.

ISSN 1664-8714
ISBN 978-2-8325-3246-1
DOI 10.3389/978-2-8325-3246-1

About Frontiers

Frontiers is more than just an open access publisher of scholarly articles: it is a pioneering approach to the world of academia, radically improving the way scholarly research is managed. The grand vision of Frontiers is a world where all people have an equal opportunity to seek, share and generate knowledge. Frontiers provides immediate and permanent online open access to all its publications, but this alone is not enough to realize our grand goals.

Frontiers journal series

The Frontiers journal series is a multi-tier and interdisciplinary set of open-access, online journals, promising a paradigm shift from the current review, selection and dissemination processes in academic publishing. All Frontiers journals are driven by researchers for researchers; therefore, they constitute a service to the scholarly community. At the same time, the *Frontiers journal series* operates on a revolutionary invention, the tiered publishing system, initially addressing specific communities of scholars, and gradually climbing up to broader public understanding, thus serving the interests of the lay society, too.

Dedication to quality

Each Frontiers article is a landmark of the highest quality, thanks to genuinely collaborative interactions between authors and review editors, who include some of the world's best academicians. Research must be certified by peers before entering a stream of knowledge that may eventually reach the public - and shape society; therefore, Frontiers only applies the most rigorous and unbiased reviews. Frontiers revolutionizes research publishing by freely delivering the most outstanding research, evaluated with no bias from both the academic and social point of view. By applying the most advanced information technologies, Frontiers is catapulting scholarly publishing into a new generation.

What are Frontiers Research Topics?

Frontiers Research Topics are very popular trademarks of the *Frontiers journals series*: they are collections of at least ten articles, all centered on a particular subject. With their unique mix of varied contributions from Original Research to Review Articles, Frontiers Research Topics unify the most influential researchers, the latest key findings and historical advances in a hot research area.

Find out more on how to host your own Frontiers Research Topic or contribute to one as an author by contacting the Frontiers editorial office: frontiersin.org/about/contact

Basins and related tectonics

Topic editors

Guiting Hou — Peking University, China

Wenlong Ding — China University of Geosciences, China

Shuping Chen — China University of Petroleum, Beijing, China

Yuan Neng — China University of Petroleum Beijing, Karamay Campus, China

Jianwei Feng — China University of Petroleum (East China), China

Wei Ju — China University of Mining and Technology, China

Citation

Hou, G., Ding, W., Chen, S., Neng, Y., Feng, J., Ju, W., eds. (2023). *Basins and related tectonics*. Lausanne: Frontiers Media SA. doi: 10.3389/978-2-8325-3246-1

Table of contents

04	Editorial: Basins and related tectonics Guiting Hou
06	Determining effective faults for hydrocarbon accumulation in slope areas of petroliferous basins: Methods and applications Fan Zili, Fu Guang, Fan Xiaodong, Wang Shuli, Xiao Hongwei, Fu Hongjun and Guo Xiaobo
17	Fission-track thermochronological evidence for the Yanshanian tectonic evolution of the northern Junggar Basin, northwest China Zenhua Li, Zhanjun Chen, Yuhai Fan, Lan Yu, Suyu Zhang and Xiangyang Li
30	The proto-type basin and tectono-paleogeographic evolution of the Tarim basin in the Late Paleozoic Jinkai Xia, Ziqi Zhong, Shaoying Huang, Caiming Luo, Hong Lou, Haining Chang, Xiang Li and Lunyan Wei
47	Reconstruction of proto-type basin and tectono-paleogeography of Tarim block in early Paleozoic Ziqi Zhong, Jinkai Xia, Shaoying Huang, Caiming Luo, Haining Chang, Xiang Li, Lunyan Wei and Hao Zhang
64	Structural evolution characteristics and genesis of buried hill faults in the Chengdao–Zhuanghai area Zhiwei Wang, Kai Zhang, Qunhu Wu, Hongke Zhou, Shina Yu and Yang Li
79	Reconstruction of the proto-type basin and tectono-paleogeographical evolution of Tarim in the Cenozoic Lunyan Wei, Shaoying Huang, Caiming Luo, Yunjiang Duan, Jinkai Xia, Ziqi Zhong, Xiang Li and Haining Chang
96	Structural evolution and mechanism of multi-phase rift basins: A case study of the Panyu 4 Sag in the Zhu I Depression, Pearl River Mouth Basin, South China Sea Bowe Guo, Fusheng Yu and Hui Li
122	Reconstruction of the proto-type basin and tectono-paleogeography of Tarim Block in the Mesozoic Xiang Li, Haining Chang, Shaoying Huang, Caiming Luo, Yunjiang Duan, Hao Zhang, Jinkai Xia, Ziqi Zhong and Lunyan Wei
137	A new superimposed model of the Tongnanba anticline in northeastern Sichuan and its exploration implications Yonghe Zhai, Zhuxin Chen, Yuqing Zhang, Nan Su, Lining Wang, Rong Ren and Geng Yang
152	Study on the structural characteristics of the Yangdachengzi oil layer in the Quantou Formation, ZY block, central depression, Songliao Basin Chunyu He, Yan Lin, Tianze Zhang, Jisheng Ma, Yunfei Li, Jiaju Cheng and Yinde Zhang



OPEN ACCESS

EDITED AND REVIEWED BY

Derek Keir,
University of Southampton,
United Kingdom

*CORRESPONDENCE

Guiting Hou,
✉ gthou@pku.edu.cn

RECEIVED 18 July 2023

ACCEPTED 25 July 2023

PUBLISHED 01 August 2023

CITATION

Hou G (2023), Editorial: Basins and related tectonics.
Front. Earth Sci. 11:1260508.
doi: 10.3389/feart.2023.1260508

COPYRIGHT

© 2023 Hou. This is an open-access article distributed under the terms of the [Creative Commons Attribution License \(CC BY\)](https://creativecommons.org/licenses/by/4.0/). The use, distribution or reproduction in other forums is permitted, provided the original author(s) and the copyright owner(s) are credited and that the original publication in this journal is cited, in accordance with accepted academic practice. No use, distribution or reproduction is permitted which does not comply with these terms.

Editorial: Basins and related tectonics

Guiting Hou*

School of Earth and Space Sciences, Peking University, Beijing, China

KEYWORDS

basin, tectonics, evolution, prototype basin, tectono-paleogeography, seismic exploration, structures, methods

Editorial on the Research Topic Basins and related tectonics

Sedimentary basins are the largest potential stores of captured carbon dioxide and serve as important environments for other resources such as hydrogen and hydrocarbon fuels. Better understanding the stratigraphy, structural geology, and related tectonics of basins is critical to recognize the evolution history of basins and utilize them for societal and environmental needs. Since the year 2000, new methods have been applied in basin-related research, motivating global data and detailed basin data concerning their tectonics, structures, sedimentary facies, exploration, and utilization. We believe that a Research Topic focused on basins and their tectonics is necessary to resolve the needs of the open access-based science community.

This Research Topic presents the state of the basin-related research, including new methods and ideas applied in the interpretation of seismic reflection data, salt tectonics, fractures, structure and tectonics of a basin, the prototype basin, tectono-paleogeography, evolution of basins, and coupling between basins and orogens. The methods include the seismic profile explanation, balanced section technique, sedimentary facies analysis, and numerical and physical modeling approaches, along with research from basins including paleomagnetism, zircon dating ages, sedimentary data, and lithological facies. These papers contribute to promote research on basins and related tectonics.

The Research Topic Basins and related tectonics concludes 10 papers, including eight research articles, one method article, and one review article. The Research Topic focused on the Tarim Basin, Junggar Basin, Sichuan Basin, Songliao Basin, Bohai Bay Basin, and South China Sea Basin, which are important hydrocarbon basins in China.

The Tarim Basin is a large superimposed basin rich in petroleum resources in northwestern China, which has experienced five stages of complex tectonic-sedimentary evolution. The reconstruction of the prototype basin and its surrounding background is of great significance for understanding the distribution of petroleum reservoirs in the superimposed basin, and provides a tectonic background and theoretical guidance for petroleum exploration in the Tarim Basin.

The Tarim Basin is a prospective hydrocarbon basin in northwestern China. Based on high-confidence paleomagnetic data and peripheral background analysis, the global plate tectonic patterns of the Tarim Block in different periods of the early Paleozoic, the late Paleozoic, the Mesozoic, and the Cenozoic are reconstructed by [Zhong et al.](#), [Xia et al.](#), [Li et al.](#), and [Wei et al.](#) According to the distribution of sedimentary facies and the pattern of uplift and depression, the boundaries of the three stages of the prototype basin are determined by marginal sedimentary facies, and the denudation areas are supplemented

by the thickness trend method and restored by decreasing amounts based on 81 large sections of the whole Tarim Basin. The prototype basin and tectono-paleogeographic maps of the Tarim Basin in the different stages of the early Paleozoic, late Paleozoic, Mesozoic, and Cenozoic are reconstructed by [Zhong et al.](#), [Xia et al.](#), [Li et al.](#), and [Wei et al.](#) based on the aforementioned basic research. The Tarim Basin underwent important tectonic evolution in the early Paleozoic, the late Paleozoic, the Mesozoic, and the Cenozoic. The prototype basin and tectono-paleogeography of the Tarim Basin are related to the tectonic environment surrounding the basin.

The Junggar Basin is another important hydrocarbon basin in northwestern China. [Li et al.](#) analyzed 15 apatite samples of fission-track dating and eight zircon samples obtained from the northern Junggar Basin. Apatite FT ages ranged from 131 to 42 Ma, and zircon FT ages ranged between 205 and 132 Ma. The northern Junggar Basin underwent three tectono-thermal events during 165–161, 93–81, and 72–66 Ma. The thermal events of 165–161 Ma may suggest magmatic activity during the Yanshanian stage, while the 93–86 and 72–66 Ma events show Late Cretaceous uplift and cooling. These results suggest that the Yanshanian tectono-thermal events involve the evolution of the Junggar Basin in the Mesozoic.

The Sichuan Basin is one of the important basins in southwestern China. The deep reservoirs are explored and developed for these years. The Tongnanba anticline in the northeastern Sichuan Basin was subjected to the compression of the Micangshan and Dabashan thrust belts, forming a complex superimposed structure with three deformation structure layers controlled by three detachment layers in three stages. [Zhai et al.](#) proposed that these deformation layers extended in the NW-SE direction and formed the long-distance detachment thrust structure controlled by the Micangshan thrust belt in the late stage.

The Songliao Basin is a large Mesozoic–Cenozoic basin discovered earlier in China. [He et al.](#) proposed that the hydrocarbon accumulation in the upper member of the Quantou Formation is controlled by folds and faults in the central Songliao Basin. The faults in the area are classified into three stages. The three-dimensional structure of the third member of the Quantou Formation is explained by the integration of well logging and seismic data; then, the fracture characteristic and the tectonic history of the Yangdachengzi oil layer are analyzed in the Research Topic.

The Bohai Bay Basin is a well-developed hydrocarbon basin in eastern China. Based on the most recent progress of exploration and development, [Wang et al.](#) quantitatively analyzed the structural characteristics and fault activity of the buried hill using the balanced section technique in the Research Topic. The structural evolution of the area was simulated by a tectonophysics modeling experiment. The NNE-trending fault is a left-handed fault that formed in the background of the left-handed strike-slip activity of the Tanlu fault zone. The EW-trending fault is closely related to the near-SN extension in the Late Cretaceous.

The South China Sea Basin is an important prospective sea basin with rich hydrocarbon resources. Using 2D and 3D seismic data and modeling, [Guo et al.](#) proposed that the Zhu I Depression in the basin, as a series of half-grabens bounded by NE-NEE-trending normal faults, has undergone two phases of extension during the Paleogene. Two phases of structural-sedimentary evolution suggest that the Panyu 4 Sag was formed in the multi-stage extension. Since

the Paleogene, the structural evolution of the Panyu 4 Sag has been controlled by coupling among the Pacific, Eurasian, and Indian plates, related to the orientation of subduction of the Pacific plate transferring from NNW to NWW.

[Zili et al.](#) proposed two methods that are proposed in the Research Topic to identify effective faults for hydrocarbon accumulation in slope areas. The first method focuses on the location of the sand bodies and paleotectonic ridges, controlling the lateral migration path of hydrocarbons in slope areas. The second method resolves the lateral sealing parts of faults that are oriented perpendicular or oblique to the channel sand bodies.

These papers on the Research Topic Basin and related tectonics suggest that the structures, sedimentary facies, and evolution of these basins are related to the tectonics surrounding these basins. The tectonics control the structures, facies, configuration of depressions and uplifts, and stress field, along with the reservoirs, migration, and accumulation of petroleum in these basins.

Author contributions

GH: writing-original draft, review, and editing, and conceptualization.

Acknowledgments

GH, Wenlong Ding, Shuping Chen, Yuan Neng, Jianwei Feng, and Wei Ju edited the Research Topic “Basin and related tectonics,” who have made a substantial direct and intellectual contribution to the work and approved it for publication. The author thanks the other authors for their contributions, and the reviewers and editorial staff for their efforts to pull together this article Research Topic. The author also thanks the Editorial Office of Frontiers in Earth Science for the kind invitation to edit this Research Topic and the editor-in-chief VA for their support.

Conflict of interest

The author declares that the research was conducted in the absence of any commercial or financial relationships that could be construed as a potential conflict of interest.

The author declared that they were an editorial board member of Frontiers, at the time of submission. This had no impact on the peer review process and the final decision.

Publisher's note

All claims expressed in this article are solely those of the authors and do not necessarily represent those of their affiliated organizations, or those of the publisher, the editors, and the reviewers. Any product that may be evaluated in this article, or claim that may be made by its manufacturer, is not guaranteed or endorsed by the publisher.



OPEN ACCESS

EDITED BY

Wenlong Ding,
China University of Geosciences, China

REVIEWED BY

Quanzhong Guan,
Chengdu University of Technology,
China
Qingqiang Meng,
SINOPEC Petroleum Exploration and
Production Research Institute, China
Kun Zhang,
Southwest Petroleum University, China

*CORRESPONDENCE

Fan Xiaodong,
fanxddq@petrochina.com.cn
Fu Hongjun,
63970597@qq.com

SPECIALTY SECTION

This article was submitted to Structural
Geology and Tectonics,
a section of the journal
Frontiers in Earth Science

RECEIVED 24 September 2022

ACCEPTED 10 November 2022

PUBLISHED 10 January 2023

CITATION

Zili F, Guang F, Xiaodong F, Shuli W,
Hongwei X, Hongjun F and Xiaobo G
(2023), Determining effective faults for
hydrocarbon accumulation in slope
areas of petroliferous basins: Methods
and applications.
Front. Earth Sci. 10:1052611.
doi: 10.3389/feart.2022.1052611

COPYRIGHT

© 2023 Zili, Guang, Xiaodong, Shuli,
Hongwei, Hongjun and Xiaobo. This is
an open-access article distributed
under the terms of the [Creative
Commons Attribution License \(CC BY\)](#).
The use, distribution or reproduction in
other forums is permitted, provided the
original author(s) and the copyright
owner(s) are credited and that the
original publication in this journal is
cited, in accordance with accepted
academic practice. No use, distribution
or reproduction is permitted which does
not comply with these terms.

Determining effective faults for hydrocarbon accumulation in slope areas of petroliferous basins: Methods and applications

Fan Zili^{1,2}, Fu Guang¹, Fan Xiaodong^{2*}, Wang Shuli²,
Xiao Hongwei², Fu Hongjun^{3*} and Guo Xiaobo²

¹School of Earth Sciences, Northeast Petroleum University, Daqing, China, ²Exploration and Development Research Institute of Daqing Oilfield Co Ltd, Daqing, China, ³Petrochina Daqing Tamsag, LLC, Daqing, China

From accumulation mechanisms and the identification of effective faults, hydrocarbon distribution in slope areas of petroliferous basins is assessed. In this study, we superimpose two methods to develop a set of key methods, which can identify effective faults for hydrocarbon accumulation in slope areas. The first of this set of methods includes locating the distribution area of the connected sand bodies and paleotectonic ridges overlying the formation where the sand bodies are located, which aids determining the lateral migration path of hydrocarbons in slope areas. The second set of methods includes identifying the lateral sealing parts of faults that are oriented perpendicular or oblique to the channel sand bodies, thereby determining the faults that are effective for hydrocarbon accumulation. By applying these methods, we identify the effective faults in the first member of the Nantun Formation (K_1n_1) on the Wunan slope of the Wuerxun Depression in the Hailar Basin. The results show that the effective faults in K_1n_1 are located mainly in its middle and northern parts, with a few distributed in the south-central part. This is conducive to reservoir development, since hydrocarbons which were generated in the western trough source rocks of K_1n_1 , accumulated in the nearby trap formed from a suitable configuration of the fault and sand body of K_1n_1 . This is consistent with previous exploration data, and the observation that hydrocarbons discovered in K_1n_1 on the Wunan slope are mainly distributed in the middle and northern parts of the region, and a small amount occur in the south-central part. The results show that this set of methods is feasible for determining effective faults for hydrocarbon accumulation in slope areas.

KEYWORDS

slope area, hydrocarbon accumulation, effective faults, determination method, wunan slope area, the 1 st member of the nantun formation (K_1n_1)

Introduction

Research on hydrocarbon exploration in the slope areas of petroliferous basins has expanded considerably in recent years. The results suggest that in slope areas, the distribution of hydrocarbons is influenced by its lateral migration path and controlled by whether or not faults are sealed, the relationship between these faults and the spread of the river channel sand bodies, as well as the relationship between the faults and the lateral migration path of the hydrocarbons. Sealed faults along hydrocarbon migration pathways that are oriented perpendicular or oblique to the channel sand bodies are effective in reservoir formation; other faults are not considered as effective for hydrocarbon accumulation.

Recently, multiple studies have attempted the identification of effective faults for hydrocarbon accumulation in slope areas; these studies adopted a similar methodology. For example, Jin (2012), Henares et al. (2014), Zhu et al. (2015), Li et al. (2017),

Meng et al. (2020a) and Yang et al. (2020b), made predictions of the argillaceous content of fault rocks by assessing fault distance in the target formation, as well as the thickness of the faulted rock formation and their argillaceous content. Studies also assessed the lateral sealing of faults according to the predicted relative value of the argillaceous content of the fault rocks (Lyu et al., 2016; Fu et al., 2012; Fu and Zhan, 2016; Wang et al., 2017). Other studies focused on two aspects—the distribution of the sand body connection area and oil–gas potential field at the top of the formation, which were then combined to predict the lateral migration path of hydrocarbons in the slope area (Zhou et al., 2006; Wang et al., 2009; Fu and Wang, 2018a; Wang et al., 2018b; Fu and Wang, 2019); the relationship between the lateral migration path of the hydrocarbons and the distribution of faults were used to identify the effective faults for hydrocarbon accumulation. A common observation from these studies is that faults located only along the lateral migration path of hydrocarbons are effective for hydrocarbon

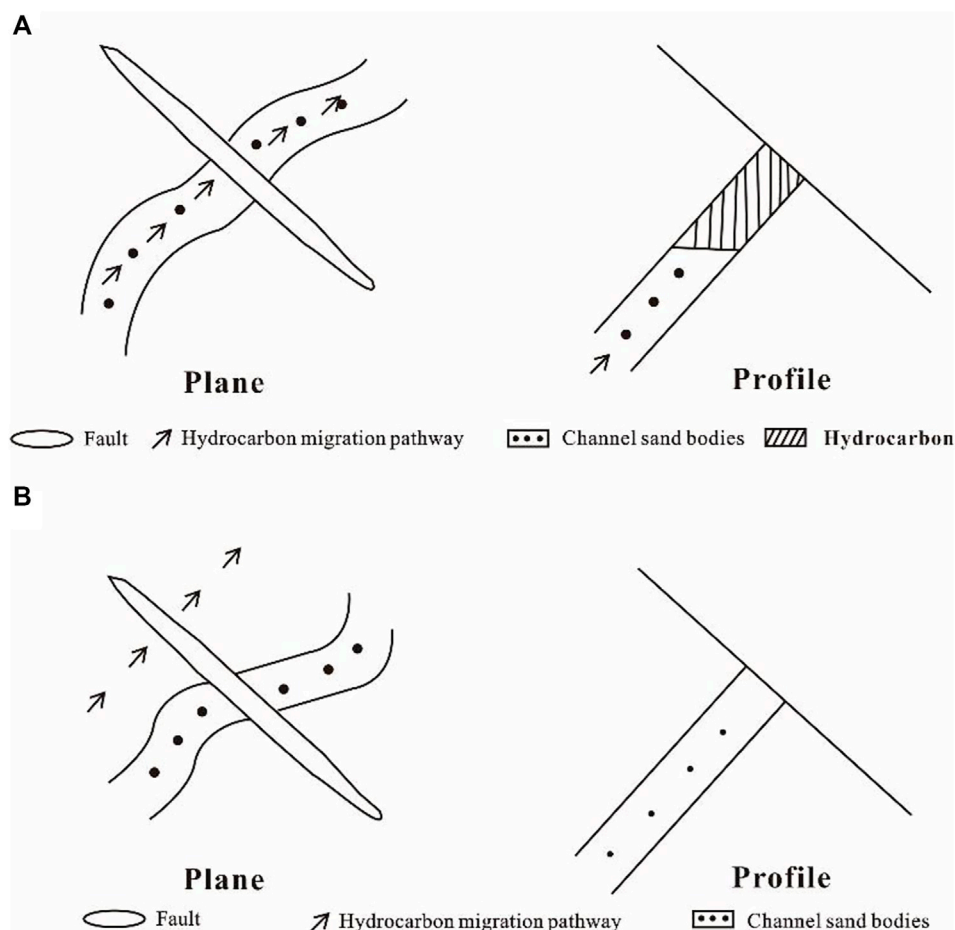


FIGURE 1

Schematic of typical faults for hydrocarbon accumulation in a slope area; (A) Effective faults for hydrocarbon accumulation; (B) Non-effective faults for hydrocarbon accumulation.

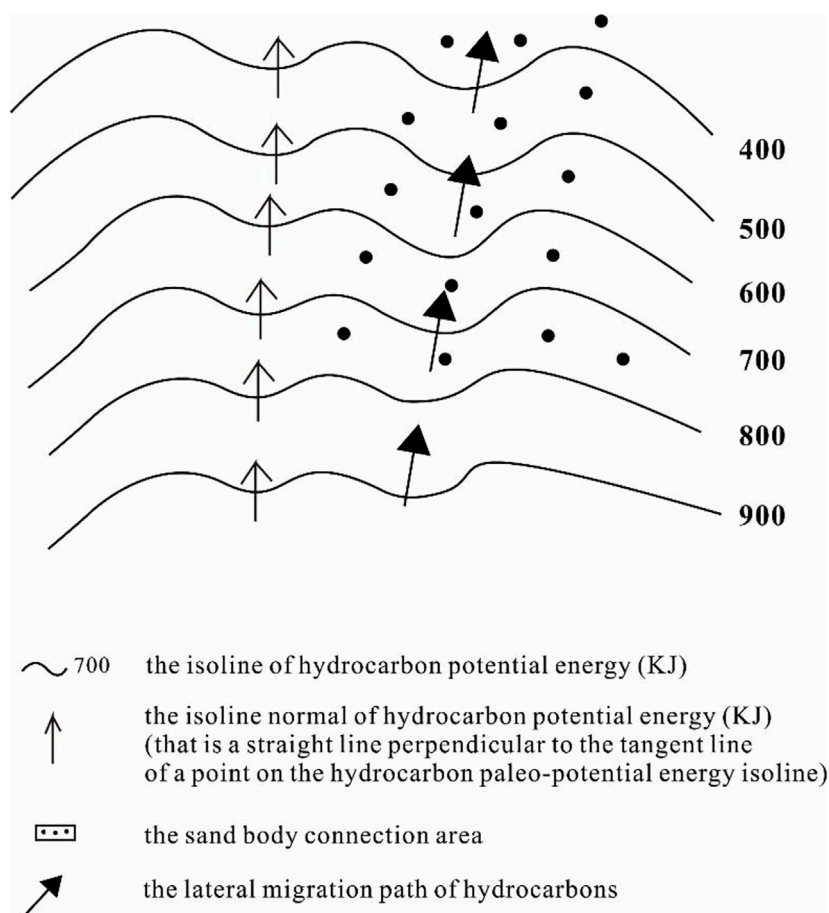


FIGURE 2

Schematic determining the lateral migration path of hydrocarbons in a slope area.

accumulation. This has contributed to an improved understanding of the regularity of hydrocarbon distributions in slope areas of petroliferous basins and improved hydrocarbon exploration practices.

However, the distribution of hydrocarbons in slope areas is affected not only by fault sealing and lateral migration path distribution, but also by their spatial configuration, in addition to the spatial configuration of the fault orientations and the orientation of the channel sand bodies. Relatively few field-based studies of effective faults for hydrocarbon accumulation in slope areas combine these influences in their assessments. Most studies are limited to the spatial configuration between sealed faults and the lateral migration path of hydrocarbons (Fu et al., 2014; Wu et al., 2015; Hu et al., 2018) and do not consider the configuration between sealed faults and the orientation of channel sand bodies. Thus, these results do not accurately reflect the hydrocarbon distribution in slope areas; this makes hydrocarbon exploration practices uncertain and risky. Effective fault determination methods for hydrocarbon

accumulation in slope areas is important for correct understanding of the hydrocarbon distribution in slope areas and for guiding the exploration.

Identifying effective faults for hydrocarbon accumulation in slope areas

Exploration studies show how hydrocarbon generated from source rocks in sag areas move along a lateral migration path in a sand body to slope areas under the effect of buoyancy. Hydrocarbons accumulate in traps formed by a suitable configuration of the lateral migration path of hydrocarbons with the fault and sand body; no hydrocarbons accumulate if the configuration of the trap consists of just the fault and sand body. Most fault and sand body traps form as a result of the perpendicular or oblique intersection of sealed faults and channel sand bodies. Therefore, only sealed faults that are perpendicular

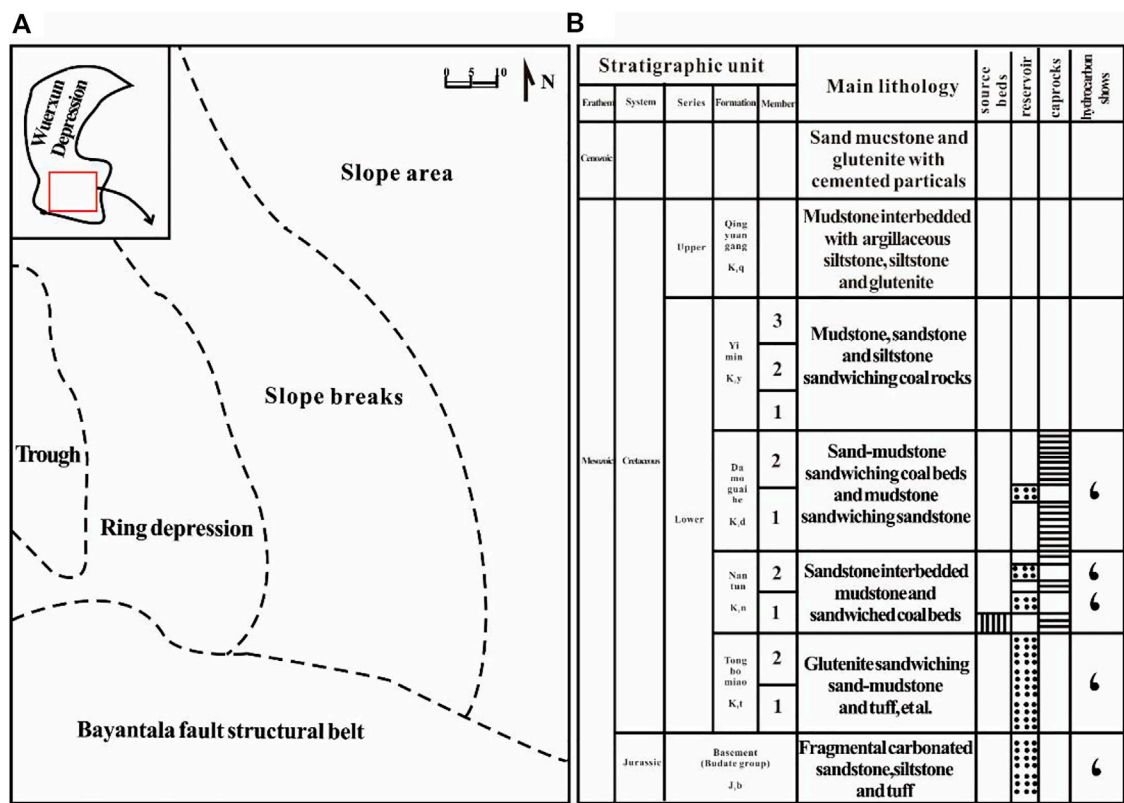


FIGURE 3 (A) Structural and (B) stratigraphic characteristics of the Wunan slope area.

or oblique to the channel sand bodies and located in the lateral migration path of the hydrocarbons could stop their lateral migration. This would allow the hydrocarbons to accumulate in traps formed by suitable configurations of the fault and sand body (Figure 1A). If sealed faults, perpendicular or oblique to the channel sand bodies, are not located along the lateral migration path of the hydrocarbons, they would not accumulate in the fault—sand body configuration (Figure 1B). This analysis demonstrates that only sealed faults located in the lateral migration path of hydrocarbons, and oriented perpendicular or oblique to channel sand bodies, are effective faults for hydrocarbon accumulation in slope areas. If any these three conditions are not met, the fault is not considered effective for hydrocarbon accumulation in slope areas.

Method of determining effective faults for hydrocarbon accumulation in slope areas

To determine the effective faults for hydrocarbon accumulation in slope areas, the lateral migration path of

hydrocarbons in the slope areas and the distribution of the sealed faults are identified. Configuring them could help determine the effective faults for hydrocarbon accumulation.

To determine the lateral migration path of hydrocarbons in slope areas, the areal distribution of the connected sand body in the target layer and the distribution of paleotectonic ridges overlying the sand body are confirmed first. When superimposed, they demarcate the lateral migration path of hydrocarbons in the slope area. A distribution map of sand ratio of the formation in the target formation is made from drilling data—specifically, the sand ratio of the formation at known wells and the characteristics of the hydrocarbon in the sand body. From this, the minimum sand ratio of the formation in which the sand bodies are located in the hydrocarbon distribution area is taken as the minimum sand ratio of the formation required for sand body connection (Zhang et al., 2018). Encircling the area where the sand ratio of the formation is larger than the minimum sand ratio of the formation required for sand body connection, gives us the sand body connection area (Figure 2). The paleo-burial depth of the formation top where the sand body occurs is reconstructed by the paleo-burial depth reconstruction method (Fu et al., 2021)

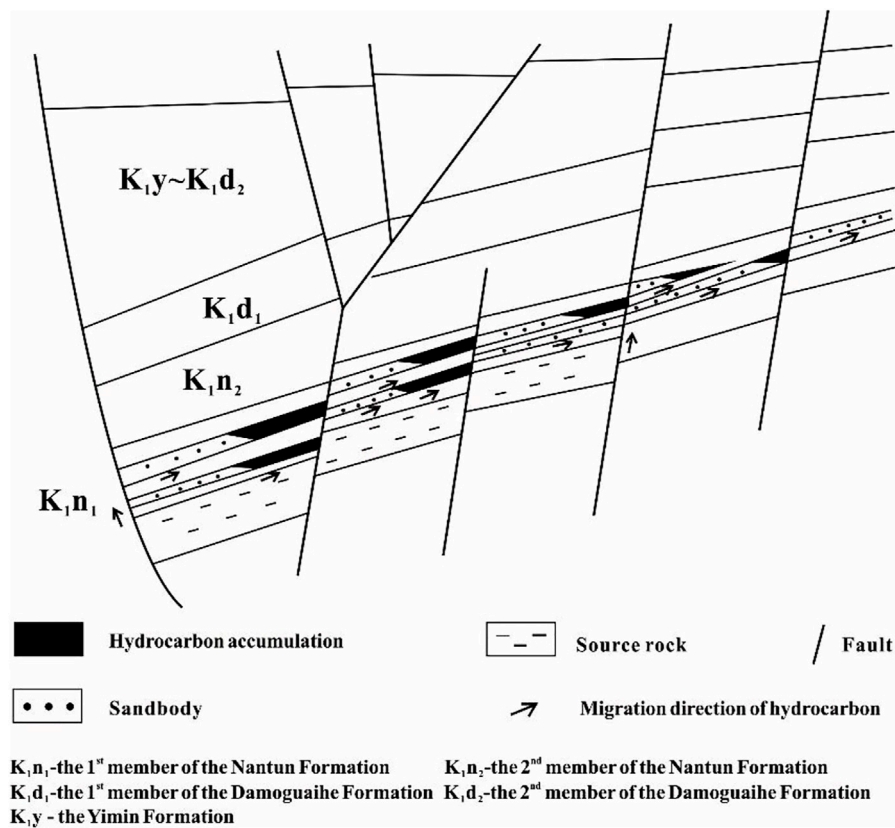


FIGURE 4

Schematic of the hydrocarbon accumulation model for the first member of the Nantun Formation (K_{1n1}) in the Wunan slope area.

to estimate the paleo-burial depth during hydrocarbon accumulation. The hydrocarbon paleo-potential energy is calculated from Eq. 1 to create a paleo-potential energy distribution map (Figure 2). The distribution of paleotectonic ridges overlying the formation where the sand body is located can be obtained by the hydrocarbon paleo-potential energy isoline method (Figure 2). The lateral migration path of hydrocarbons in the slope area is obtained by superimposing the above-mentioned sand body connection area with the distribution of paleotectonic ridges overlying the formation where the sand body is located (Figure 2).

$$\varnothing = gz + \frac{p}{\rho} \quad (1)$$

where: \varnothing is the paleo hydrocarbon potential energy value of the fault plane (KJ); g is the gravitational acceleration (m/s^2); z is the ancient burial depth of the fault plane (m); p is the fluid pressure of the fault plane (MPa), obtained from $p_w z$, where p_w is the formation water density (g/cm^3); ρ is the hydrocarbon density (g/cm^3).

To determine the distribution of sealed effective faults, it is necessary to determine the distribution of the sections of the

faults that are laterally sealed and the distribution of faults that are oriented perpendicular or oblique to the channel sand bodies. For this, the distribution of faults developed in the target formation of the slope area is interpreted from 3D seismic data, the fault distance in the target formation, and the thickness and argillaceous content of the rock formation being faulted. The argillaceous content of faults at different sites is calculated from Eq. 2; thus, the argillaceous content of the fault rocks at all known wells in the study area is estimated, as well as the displaying features of the hydrocarbon in nearby target formations. The minimum argillaceous content of fault rocks in the hydrocarbon distribution area is taken as the minimum argillaceous content of fault rocks required for hydrocarbon accumulation through faults (Fu and Hu, 2016). Sealed fault sites typically have greater fault rock argillaceous content than the minimum argillaceous content of fault rocks required to trap hydrocarbons.

$$R_f = \frac{\sum_{i=1}^n H_i R_i}{L} \quad (2)$$

Where R_f is the fault rock shale content (%); H_i is the i^{th} faulted strata thickness (m); R_i is the i^{th} faulted strata shale content (%); n

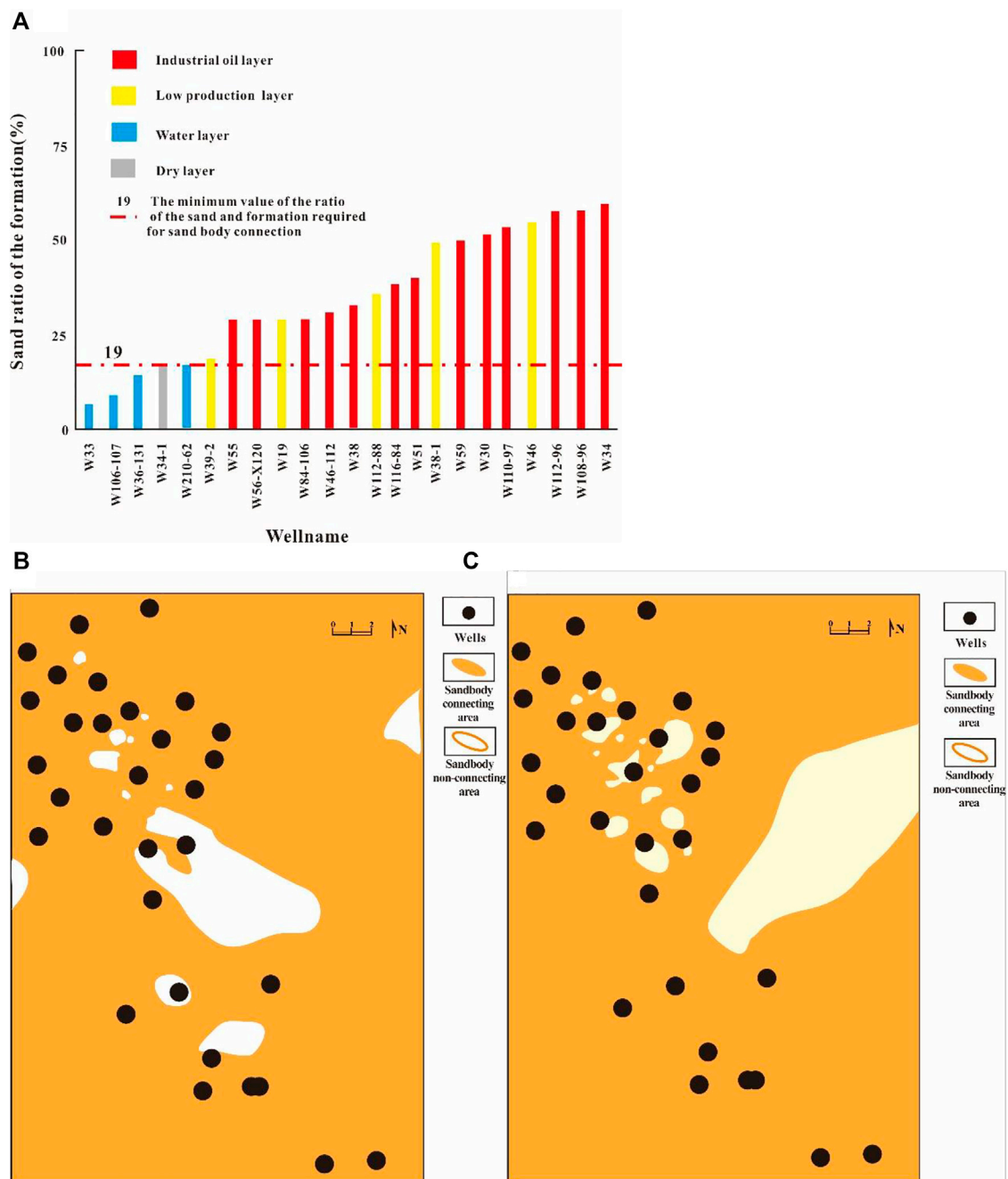


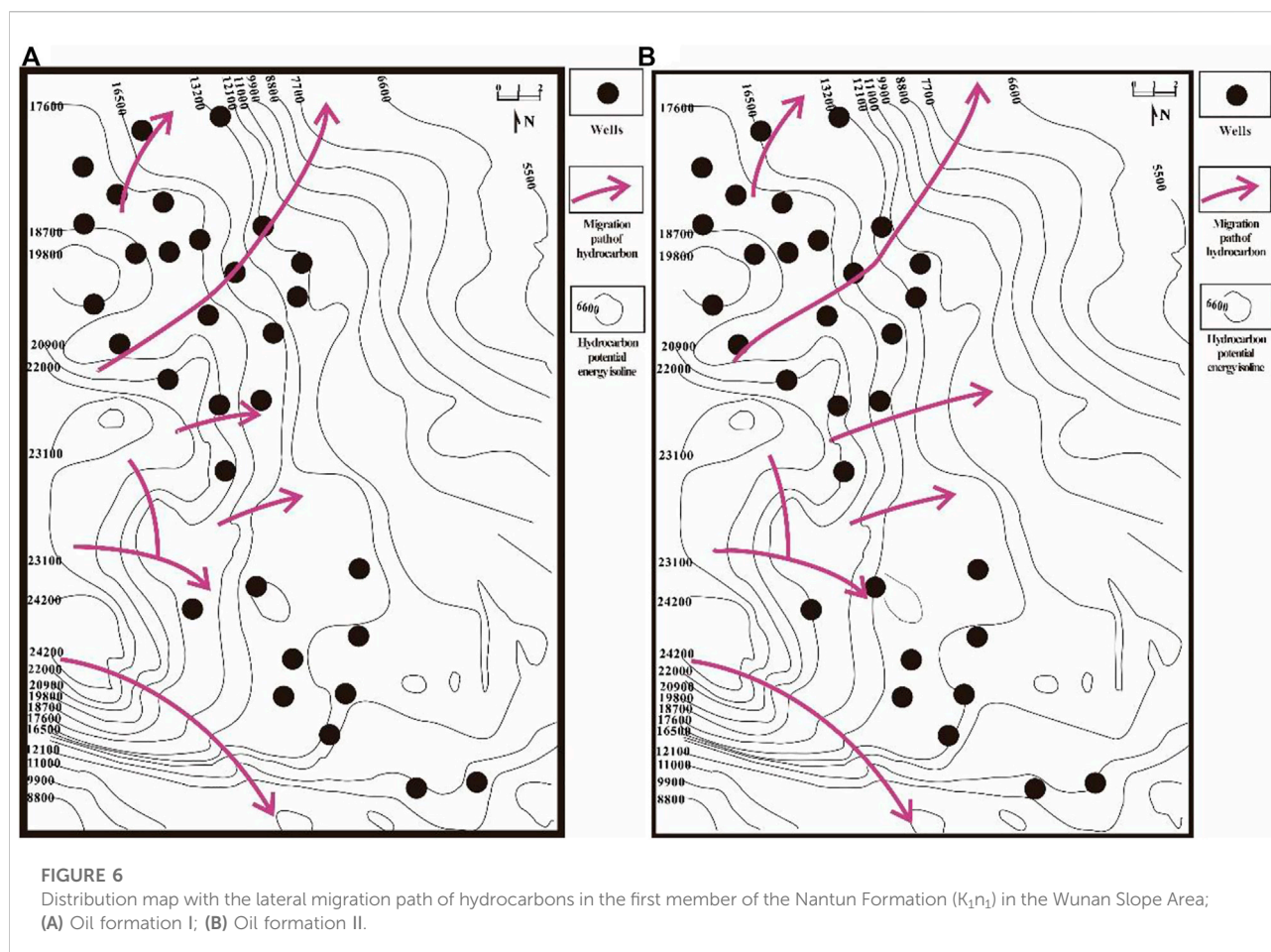
FIGURE 5

Determination of sand body connection distribution area for the first member of the Nantun Formation (K_1n_1) in the Wunan slope area; (A) The determination chart of the minimum value of the ratio of the sand and formation required for sand body connecting distribution in the Nantun Formation; (B) The sand body connecting distribution in oil formation I of K_1n_1 ; (C) The sand body connecting distribution in oil formation II of K_1n_1 .

is the number of layers of the faulted strata; L is fault displacement (m).

Research on sedimentary microfacies in the study area help determine the direction of the spread of channel sand bodies. The orientation of fault extensions developed within the target

formation are acquired by interpreting the above-mentioned 3D seismic data. The distribution of faults that are perpendicular or oblique to the channel sand bodies are obtained by combining the direction of the spread of channel sand bodies with the orientation of fault extensions. When the



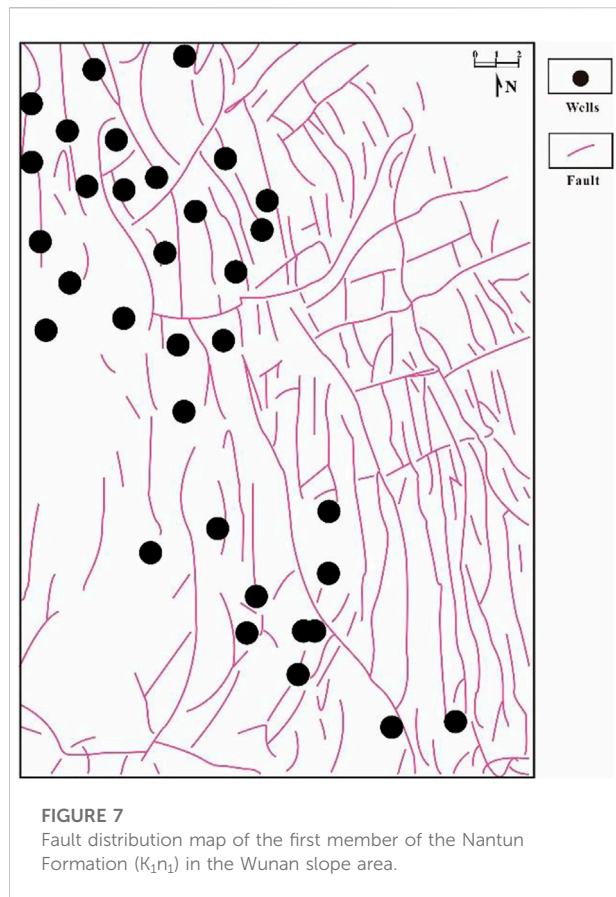
distribution of the sealed part of the faults are superimposed over faults that are perpendicular or oblique with the channel sand bodies, the parts that overlap mark the distribution area of the effective faults that seal-in the hydrocarbons (Figure 1). Superimposing the distribution of the lateral migration path of the hydrocarbons in the slope area and the distribution of effective faults which seal them in, the sealed faults that are located both on the lateral migration path of the hydrocarbons, and are perpendicular or oblique to the channel sand bodies are the effective faults for the accumulation of hydrocarbons (Figure 1).

Feasibility study from the Wunan slope

The methods discussed in this paper were applied to the first member of the Nantun Formation (K_1n_1) on the Wunan slope of the Wuerxun Depression in the Hailar Basin. We examined the potential of this method in determining the effective faults for hydrocarbon accumulation in the Wunan slope area by

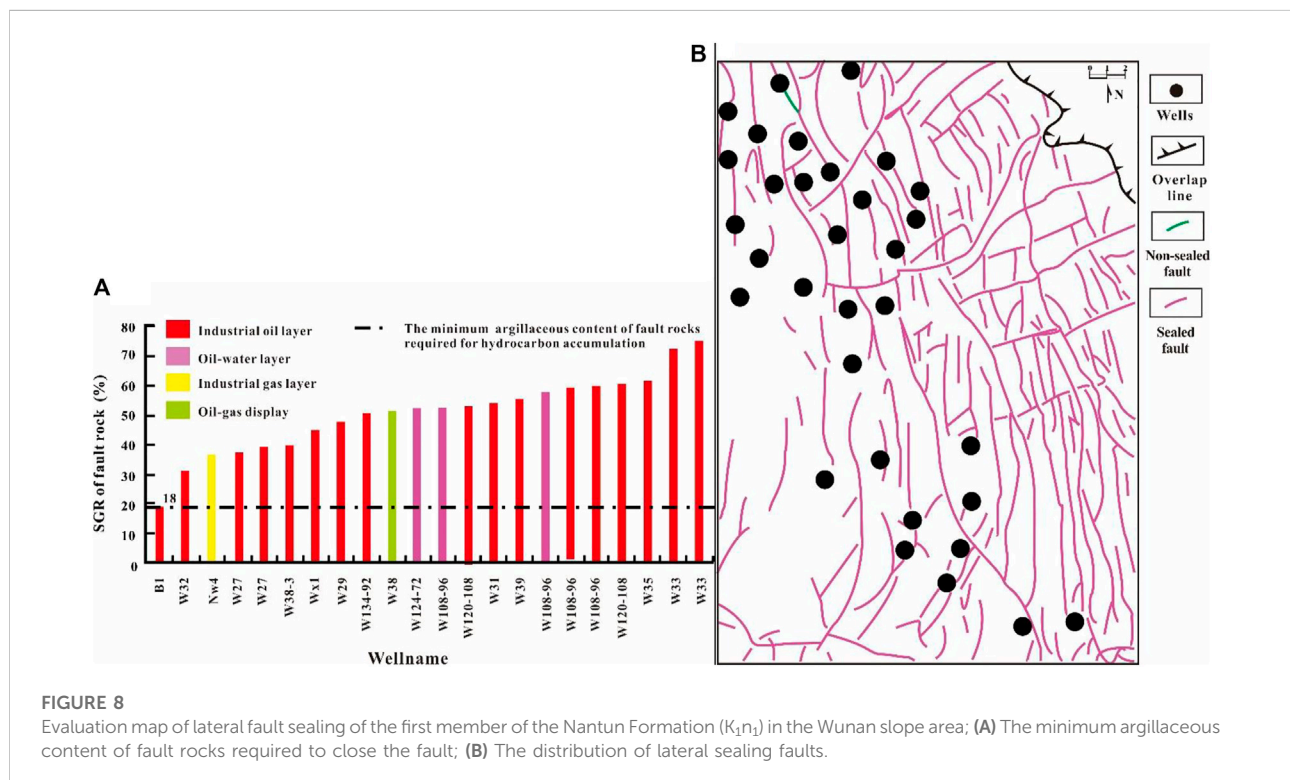
correlating the results from this sample study with the currently known distribution of hydrocarbons in the area.

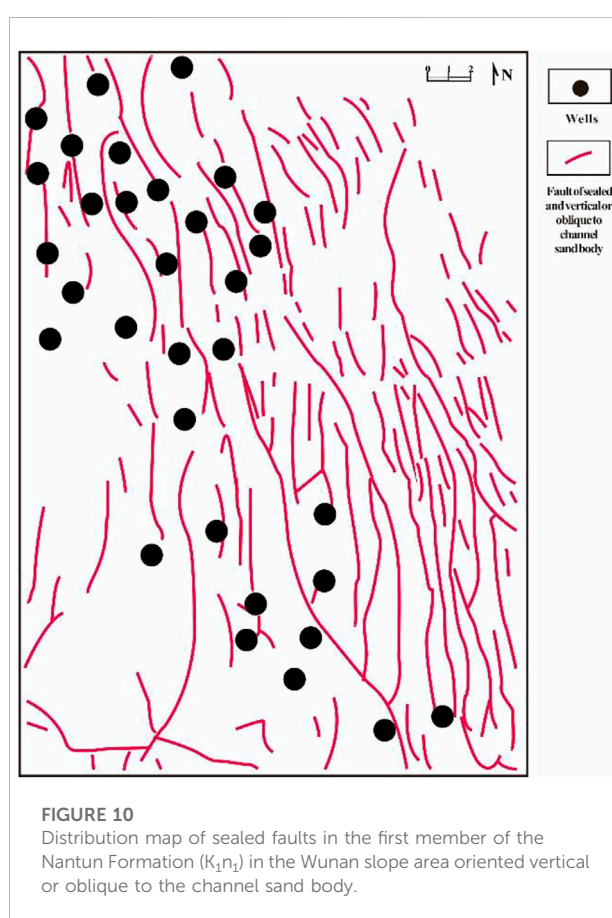
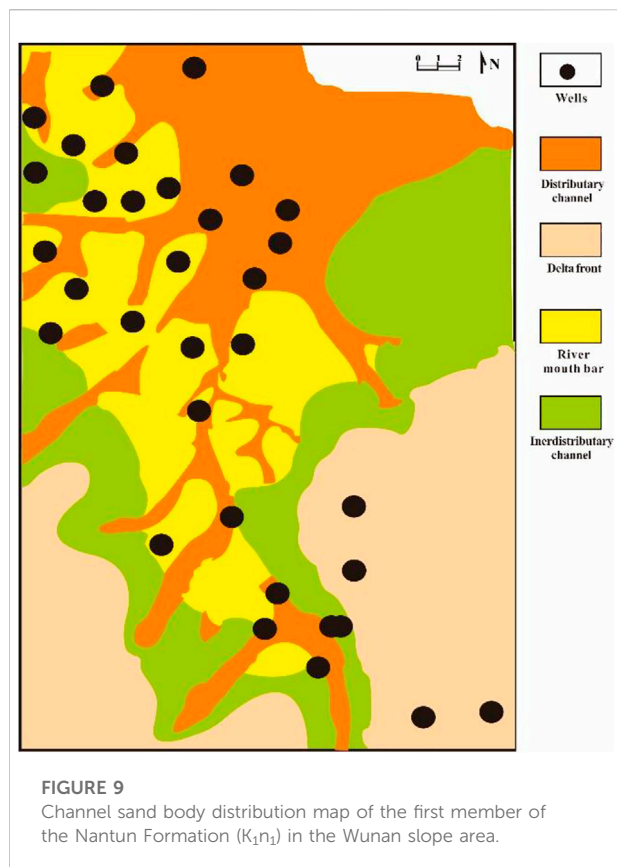
The Wunan slope area is located to the east of the troughs in the southern part of the Wuerxun Depression. It includes three tectonic units—ring depressions, slope breaks, and slope areas (Figure 3). Currently, the Wuerxun Depression is the focus area for hydrocarbon exploration. The stratigraphy of this area includes, from bottom to top, the Lower Cretaceous Tongbomiao Formation, the Nantun Formation, the Damoguaihe Formation and the Yimin Formation, the Upper Cretaceous Qingyuangang Formation, with thin Cenozoic strata (Figure 3). A large volume of the hydrocarbons occur in K_1n_1 ; they originate from the lower source rocks in K_1n_1 of the western trough. In planar view, the hydrocarbons are mainly distributed near the faults in the slope area of the ring depressions and slope breaks, but not all faults in the slope area host hydrocarbons. This is mainly controlled by the distribution of the effective faults for the hydrocarbon accumulation. To guide the hydrocarbon exploration in K_1n_1 in the Wunan slope area requires accurate identification of the effective faults for hydrocarbon accumulation.



The typical structure of hydrocarbon reservoirs corresponds well with the accumulation model for hydrocarbons trapped in K_1n_1 along the Wunan slope. Here, the hydrocarbons generated from the source rocks in the lower part of K_1n_1 in the western trough migrate upward through the oil source faults. These faults not only connect the source rocks in the lower part of K_1n_1 with the K_1n_1 reservoir, they were active at the end of the sedimentation period of the Yimin Formation which marks the hydrocarbon accumulation period. Since they are blocked by the regional mudstone caprock of the first Member of the Damoguaihe Formation (K_1d_1), the hydrocarbons laterally migrate to the K_1n_1 reservoir and laterally, to its slope area. They accumulate, finally, in the trap formed by a suitable configuration of the fault and sand body, and form a reservoir (Figure 4).

The sand ratio of the formation for the two oil formations in K_1n_1 are obtained from the drilling data. When combined with the hydrocarbon distribution for the Nantun Formation in this area (Figure 5A), the minimum value of sand ratio of the formation required for sand body connection is estimated to be about 19%. The distribution of the sand body connection area for these two oil formations in the Wunan slope area is also obtained (Figure 5B, Figure 5C). Except for a part of the central area, Figure 5B clearly shows that sand bodies of oil formation I of K_1n_1 in the Wunan slope area are all connected. The sand bodies of oil formation II of K_1n_1 are also connected, except for parts of the central and northeastern area (Figure 5C). The





burial depth of the top of the K_1n_1 formation is obtained from the paleo-burial depth reconstruction method (Fu et al., 2021) and corresponds to the paleo-burial depth of formation during the hydrocarbon accumulation period, i.e. the late sedimentary period of the Yimin Formation (Fu et al., 2013). The hydrocarbon paleo-potential energy value is calculated from Eq. 1. The distribution of the paleotectonic ridges that overlie the formation where the sand bodies are located is obtained from the hydrocarbon paleo-potential energy field. The distribution of the lateral migration paths of the hydrocarbons in K_1n_1 is obtained by superimposing the distribution of the sand body connection areas of K_1n_1 in Wunan slope area with the distribution of the paleotectonic ridges overlying the formation where the sand bodies are located (Figure 6). This figure suggests that there are seven lateral migration paths, from west to east, in the Wunan slope area. The three lateral migration paths of the hydrocarbon extend northward, and the four lateral migration paths of the hydrocarbon extend southward.

The faults developed within K_1n_1 in the Wunan slope area are interpreted from 3D seismic data (Figure 7); the data suggests that a majority of the faults are oriented NW, a few are oriented NEE, and a small number are oriented in the N–S direction. Apart from in the western area, the faults are well-developed and

widely distributed; the average density of faults is 0.4–0.5 per km. The fault distance in K_1n_1 , the thickness of the rock formation and the argillaceous content (SGR) of the faulted formations are estimated from this 3D seismic data. Eq. 2 is used to calculate the argillaceous content of the faults in K_1n_1 ; the minimum argillaceous content of fault rocks required for hydrocarbon accumulation is estimated to be about 18%—from the relationship between the argillaceous content of the fault rocks at all known wells and the distribution of hydrocarbons in the area (Figure 8A). The fault lateral sealing of K_1n_1 in the Wunan slope area is evaluated accordingly (Figure 8B); it can be seen that almost all the faults are laterally sealed except for a few in the north.

Sedimentary microfacies studies in the region suggest that the orientation of the channel sand body spread in the Wunan slope area is NNE (Figure 9). This is compared with the fault distributions that are perpendicular or oblique to channel sand bodies in the Wunan area (Figure 7 and Figure 9). The results show that the faults in K_1n_1 that are perpendicular or oblique to the river channel are mainly oriented NW and near-N–S; a few are oriented in the NE direction (Figure 10). Faults perpendicular or oblique to the channel sand bodies in the region

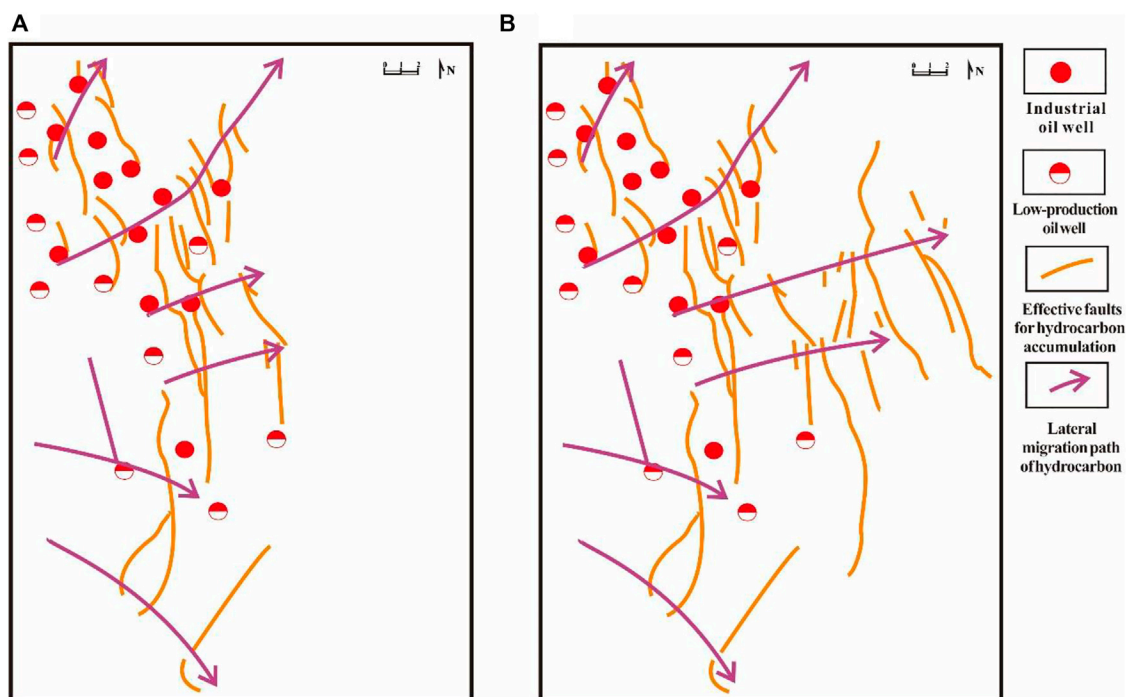


FIGURE 11

Relationship between hydrocarbon accumulating effective faults and hydrocarbon distribution in the first member of the Nantun Formation (K_1n_1) in the Wunan slope area; (A) Oil formation I of K_1n_1 ; (B) Oil formation II of K_1n_1 .

are widely distributed, except for in the southwestern region—where they are not developed.

Effective sealing faults that aid hydrocarbon accumulation in K_1n_1 are widely distributed in the study area—except in the southwest, where these faults are not developed (Figure 8, Figure 10). The distribution of effective faults for hydrocarbon accumulation in K_1n_1 in the Wunan slope area are obtained by superimposing the distribution of the hydrocarbon lateral migration paths and the distribution of the effective sealing faults that support hydrocarbon accumulation (Figure 11). It can be seen that the effective faults for hydrocarbon accumulation are mainly distributed in the middle and northern part of K_1n_1 ; a comparatively smaller number of faults are distributed in the south-central part. Thus, oil formation I has fewer effective faults for hydrocarbon accumulation in K_1n_1 than oil formation II.

The hydrocarbons discovered in K_1n_1 are mainly distributed in the middle and northern part of the Wunan slope area, near the effective faults for hydrocarbon accumulation (Figure 11). Here, hydrocarbons that accumulate near effective faults are obtained from the lateral migration of hydrocarbons from the source rocks of K_1n_1 of the western trough. Their accumulation is conditional on the configuration of the trap formed by the fault and sand body; they are found by drilling.

Conclusion

The lateral migration path of the hydrocarbons in the slope area were determined by identifying the sand body connection area, and the paleotectonic ridges overlying the formation where the sand body is located. By determining the lateral sealing part of the faults and faults that are perpendicular or oblique to the channel sand bodies, the effective faults for sealing hydrocarbons can be determined. The superimposition of these two methods creates a set of key methods to determine the effective faults for hydrocarbon accumulation in slope areas.

These methods were applied to effective faults determination in the Wunan slope area of the Wuerxun Depression in the Hailar Basin. The effective faults in K_1n_1 were identified mainly in the middle and northern part, with a smaller number distributed in the south-central part. This is conducive to hydrocarbon accumulation from the source rocks in K_1n_1 in the western trough given the nearby trap formed from fault and sand body configurations. This result is consistent with the discovery of hydrocarbons in K_1n_1 in the Wunan slope area, i.e., hydrocarbons are mainly located in the middle and northern part, and with a smaller volume in the center of the southern part.

These methods could be applied to sandy mudstone petroliferous basins to identify effective faults for hydrocarbon accumulation in slope areas.

Data availability statement

The original contributions presented in the study are included in the article/supplementary material, further inquiries can be directed to the corresponding authors.

Author contributions

FZ, Writing—original draft, editing, Data curation, and Formal analysis. FG, Methodology and Data curation. FX, Methodology and Resources. WS, Methodology. XH, Data curation. FH, Methodology and Resources. GX, Resources.

Acknowledgments

We thank editors and reviewers for insightful comments in improving the manuscript.

References

- Fu, G., and Hu, X. L. (2016). Method of fault vertical sealing ability judged by the mudstone content of fault-rock and its application. *J. Earth Sci. Environ.* 38 (5), 660–667. doi:10.3969/j.issn.1672-6561.2016.05.009
- Fu, G., Shi, J. J., and Lyu, Y. F. (2012). An improvement in quantitatively studying lateral seal of faults. *Acta Pet. Sin.* 33 (3), 414–418. doi:10.7623/syxb201203010
- Fu, G., Shi, J. J., and Lyu, Y. F. (2013). Study of ancient displacement pressure of fault rock recovery and its sealing characteristics. *J. China Univ. Min. Technol.* 42 (6), 996–1001. doi:10.13247/j.cnki.jcmt.2013.06.018
- Fu, G., Sun, T. W., and Lyu, Y. F. (2014). An evaluation method of oil-gas lateral transporting ability of fault-sandstone configuration in Nanpu depression. *J. China Univ. Min. Technol.* 43 (1), 79–87. doi:10.13247/j.cnki.jcmt.000016
- Fu, G., and Wang, H. (2018a). Differences of distribution characteristics of oil and gas by the control of fault-sand transporting system in uplifted area and slope area. *J. China Univ. Petroleum Ed. Nat. Sci.* 42 (3), 22–30. doi:10.3969/j.issn.1673-5005.2018.03.003
- Fu, G., and Wang, H. (2019). Prediction method of favorable position in oil-gas accumulation around oil-source. *Geotect. Metallogenia* 43 (1), 69–76. doi:10.16539/j.ddgzyckx.2019.01.006
- Fu, G., and Zhan, M. W. (2016). Geological conditions for lateral sealing of active faults and relevant research methods. *Nat. Gas. Ind.* 36 (10), 28–34. doi:10.1016/j.ngib.2017.07.008
- Fu, G., Guo, H. Y., and Han, X. (2021). A prediction method of favorable positions of transporting oil and gas capacity configuration in different periods of faults. *Natural Gas Geosci.* 32 (1), 28–37. doi:10.11764/j.issn.1672-1926.2020.10.003
- Henares, S., Caracciolo, L., Cultrone, G., Fernandez, J., and Viseras, C. (2014). The role of diagenesis and depositional facies on pore system evolution in a Triassic outcrop analogue (SE Spain). *Mar. Petroleum Geol.* 51, 136–151. doi:10.1016/j.marpetgeo.2013.12.004
- Hu, C. M., Fu, G., and Zhan, M. W. (2018). Hydrocarbon upward migration condition in different directions and prediction method of distribution area. *Geol. Rev.* 64 (1), 227–236. doi:10.16509/j.georeview.2018.01.017
- Jin, Z. J. (2012). Formation and accumulation of oil and gas in marine carbonate sequences in Chinese sedimentary basins. *Sci. China Earth Sci.* 55, 368–385. doi:10.1007/s11430-011-4264-4
- Li, D., He, D. F., Lian, Y., Lu, Y., and Yi, Z. (2017). Structural evolution and late carboniferous magmatism of the zhongguai arc in the Western junggar basin, northwest China: Implications for tectonic evolution of the junggar ocean. *Int. Geol. Rev.* 59 (10), 1234–1255. doi:10.1080/00206814.2016.1160801
- Lyu, Y. F., Wang, W., Hu, X. L., Fu, G., Shi, Y. F., and Wang, J. J. (2016). Quantitative evaluation method of fault lateral sealing. *Petroleum Explor. Develop.* 43 (2), 310–316. doi:10.11698/PED.2016.02.20
- Meng, Q., Bai, X. F., Zhang, W. J., Fu, L., Xue, T., and Bao, L. (2020a). Accumulation and exploration of petroleum reservoirs in west slope of northern Songliao Basin, China. *Petroleum Explor. Dev.* 47 (2), 254–265. doi:10.1016/S1876-3804(20)60044-1
- Wang, C., Lyu, Y. F., Fu, G., Wang, Y. G., Liu, Z., Sun, T. W., et al. (2017). Ancient lateral sealing evaluation method of fault and its application in hydrocarbon accumulation period. *Earth Sci.* 42 (10), 1787–1801. doi:10.3799/dqkx.2017.549
- Wang, H. R., Fu, G., Su, B., Sun, T. W., and Tang, W. H. (2018b). A method to determine preferential pathways for hydrocarbon migration in “lower source rock and upper reservoir” combination and its application. *Oil Gas Geol.* 39 (6), 1237–1245. doi:10.11743/ogg20180613
- Wang, J. W., Song, G. Q., Song, S. J., Wang, X. Z., and Gao, X. (2009). Controlling factors for petroleum dominant lateral migration along Eocene carrier beds in southern slope of Dongying sag. *J. China Univ. Petroleum Ed. Nat. Sci.* 33 (5), 36–40. doi:10.1016/j.postharvbio.2008.09.010
- Wu, K. J., Liu, L. F., Xiao, F., Zhou, C. X., and Xu, Z. J. (2015). Characteristics of the hydrocarbon pathway system and transport model of the Chepaizi and its surrounding areas in the Junggar basin of China. *J. China Univ. Min. Technol.* 44 (1), 86–96. doi:10.13247/j.cnki.jcmt.000119
- Yang, X., Ji, H. C., Dou, L. R., Du, Y. B., Jia, H. B., Chen, L., et al. (2020b). Tectono-sedimentary characteristics in the area with distributed normal faults: Lower Cretaceous Prosopis Formation in the northern slope of the Bongor Basin, Chad. *J. Petroleum Sci. Eng.* 190, 107081. doi:10.1016/j.petrol.2020.107081
- Zhang, J., Fu, G., and Song, D. L. (2018). Lateral migration hydrocarbon identification in fault-sand configuration. *Oil Geophys. Prospect.* 53 (05), 1041–1048. doi:10.13810/j.cnki.issn.1000-7210.2018.05.018
- Zhou, Q. H., Lyu, Y. F., Fu, G., Zhou, Q. Q., and Jiang, L. (2006). The pool-forming pattern and main control factors in west slope of the north of songliao basin. *Nat. Gas. Geosci.* 6, 765–769. doi:10.11764/j.issn.1672-1926.2006.06.765
- Zhu, G. Y., Zou, C. N., Yang, H. J., Wang, K., Zheng, D. M., Zhu, Y. F., et al. (2015). Hydrocarbon accumulation mechanisms and industrial exploration depth of large-area fracture-cavity carbonates in the Tarim Basin, Western China. *J. Petroleum Sci. Eng.* 133, 889–907. doi:10.1016/j.petrol.2015.03.014

Conflict of interest

The authors FZ, FX, WS, XH, and GX were employed by the Exploration and Development Research Institute of Daqing Oilfield Co Ltd. The author FH was employed by Petrochina Daqing Tamsag, LLC.

The remaining authors declare that the research was conducted in the absence of any commercial or financial relationships that could be construed as a potential conflict of interest.

Publisher's note

All claims expressed in this article are solely those of the authors and do not necessarily represent those of their affiliated organizations, or those of the publisher, the editors and the reviewers. Any product that may be evaluated in this article, or claim that may be made by its manufacturer, is not guaranteed or endorsed by the publisher.



OPEN ACCESS

EDITED BY
Derek Keir,
University of Southampton,
United Kingdom

REVIEWED BY
Liang Qiu,
China University of Geosciences, China
Junling Pei,
Chinese Academy of Geological Sciences
(CAGS), China

*CORRESPONDENCE
Zhenhua Li,
✉ 250759492@qq.com

SPECIALTY SECTION
This article was submitted to Structural
Geology and Tectonics,
a section of the journal
Frontiers in Earth Science

RECEIVED 20 August 2022
ACCEPTED 02 January 2023
PUBLISHED 12 January 2023

CITATION
Li Z, Chen Z, Fan Y, Yu L, Zhang S and Li X
(2023), Fission-track thermochronological
evidence for the Yanshanian tectonic
evolution of the northern Junggar Basin,
northwest China.
Front. Earth Sci. 11:1023655.
doi: 10.3389/feart.2023.1023655

COPYRIGHT
© 2023 Li, Chen, Fan, Yu, Zhang and Li. This
is an open-access article distributed under
the terms of the [Creative Commons
Attribution License \(CC BY\)](https://creativecommons.org/licenses/by/4.0/). The use,
distribution or reproduction in other
forums is permitted, provided the original
author(s) and the copyright owner(s) are
credited and that the original publication in
this journal is cited, in accordance with
accepted academic practice. No use,
distribution or reproduction is permitted
which does not comply with these terms.

Fission-track thermochronological evidence for the Yanshanian tectonic evolution of the northern Junggar Basin, northwest China

Zhenhua Li^{1*}, Zhanjun Chen¹, Yuhai Fan², Lan Yu¹, Suyu Zhang¹ and Xiangyang Li³

¹Energy Engineering Department, Longdong University, Qingyang, China, ²China Coal Technology and Engineering Group, Xi'an, China, ³Gansu Bureau of Coalfield Geology, Qingyang, China

The Junggar Basin is a multicycle intracontinental sedimentary basin developed on the pre-Mesozoic deformed basement. For a long time, the Junggar Basin and its adjacent Altai orogeny have been a focus of debate for geologists studying the opening and closing history of the Paleozoic Asian Ocean and Cenozoic intracontinental deformation. However, there has been no detailed research on the intracontinental tectonic activities of northern Xinjiang since the Mesozoic, particularly the Yanshanian tectonic activities in the northern Junggar Basin. Fission-track (FT) dating was conducted on 15 apatite samples and eight zircon samples obtained from the northern Junggar Basin to better understand the Yanshanian tectonic evolution. The results showed that apatite FT (AFT) ages ranged from 131 to 42 Ma and zircon FT ages ranged from 205 to 132 Ma. Based on the AFT track thermal history modeling and the regional geological data, we proposed that the northern Junggar Basin underwent three tectonic thermal events during 165–161, 93–81, and 72–66 Ma. The thermal events of 165–161 Ma may indicate magmatic activity during the Yanshanian, while the 93–86 and 72–66 Ma events reflect Late Cretaceous uplift and cooling. This study has confirmed the tectonic evolution of the Yanshanian in the northern Junggar Basin from the perspective of thermochronology. It has also revealed that the Yanshanian orogeny, a regional tectonic event, may have also occurred in northwest China.

KEYWORDS

fission-track thermochronology, yanshanian, tectonic evolution, northern junggar basin, magmatism

Introduction

Junggar Basin is an important sedimentary energy basin rich in oil, gas, and coal resources in northwest China (Xiao et al., 1992; Zhao, 1992; Cai et al., 2000). This basin is sandwiched between the Altai and Tianshan Mountains and is part of the Central Asian Orogenic Belt (CAOB). Its Paleozoic tectonic evolution is mainly characterized by a continental margin collision and orogeny. In the Late Paleozoic, the Junggar Basin and its adjacent areas formed a large tectonic collage mainly comprising island arcs, microcontinental blocks, and a paleo-oceanic crust (Zhang et al., 2017; Xiao et al., 2020; Zhu et al., 2020). After the Mesozoic, the Junggar Basin entered a stage of intracontinental evolution, and the tectonic activity of this basin was mainly controlled by the far-field effects of the Indian–Eurasian plate collision (Allen et al., 1994; Jolivet et al., 2001; Zhang et al., 2017). The tectonic thermal evolution and intracontinental deformation of the Junggar Basin and its adjacent areas since the

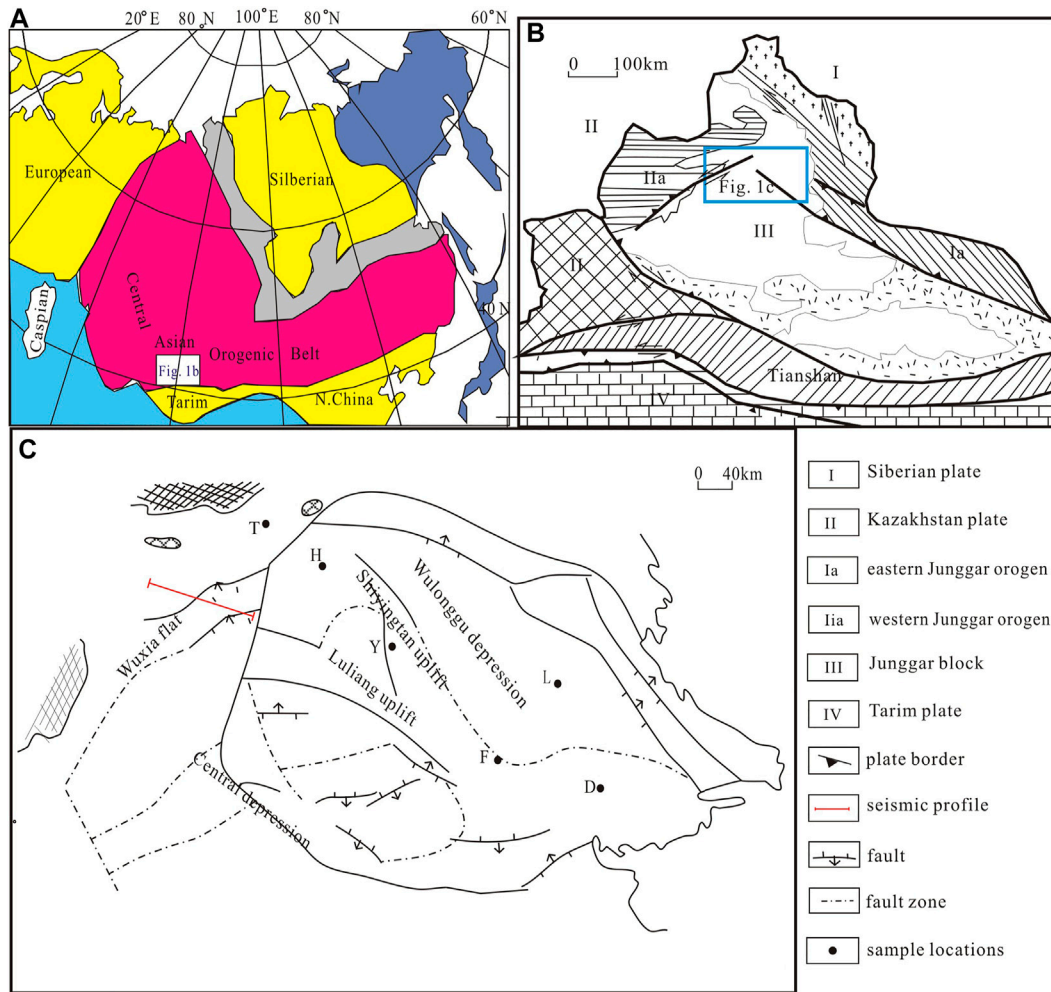


FIGURE 1

(A) Simplified tectonic map of the Central Asian Orogenic Belt. (B) Structural map of Junggar Basin and its adjacent areas (modified from Li et al., 2010). (C) Structural sketch and sample collection points of the study area.

Mesozoic have attracted the interests of many geologists (Zhou and Cai, 1990; Qiu et al., 2002; Jia et al., 2005; Wang and Xu, 2006; Dong et al., 2019; Cao et al., 2020; Hou et al., 2020; He et al., 2021; Wu et al., 2021; He et al., 2022a; Zhang et al., 2022).

Few studies have been conducted on Mesozoic tectonic activities in the Junggar Basin and its adjacent areas compared with those on Paleozoic and Cenozoic activities, and the tectonic processes and patterns during the Mesozoic are not clear. (Li et al., 2010; Yu et al., 2016; Wu et al., 2021; He et al., 2022b; Zhang et al., 2022). East Asia was widely affected by the Mesozoic Yanshanian orogeny, which resulted in complex intracontinental deformation, violent magmatic intrusions, and volcanic eruptions (Qiu et al., 2018; Yan and Qiu, 2020). This further led to substantial changes in the surface structures, landforms, paleoenvironments, and paleoecosystems of East Asia, and it is of considerable importance to the tectonics of eastern China (Dong et al., 2000; Dong et al., 2007; Dong et al., 2015; Dong et al., 2019; Faure et al., 2012; Zhu et al., 2020; Qiu et al., 2022a). Owing to the weak influence of the Yanshanian orogeny in northwest China, particularly the Junggar Basin, the Yanshanian tectonic event has not attracted considerable attention (Qiu et al., 2022b). With studies being conducted on the Yanshanian orogeny and its thermal effects in

western China, researchers have gradually realized the significance of the Yanshanian orogeny for understanding mineralization in the Junggar Basin and Yanshanian tectonic evolution (Zhang et al., 1994; Dong et al., 2000; Fang et al., 2006; Guo et al., 2006; He and Gao, 2008; Yang et al., 2015; Yang et al., 2017; Sun et al., 2018; Dong et al., 2019; Zhu et al., 2020). However, the strength and timing of the Yanshanian tectonic evolution in the northern Junggar Basin are still poorly understood. Therefore, this paper will discuss the Yanshanian tectonic evolution of the northern Junggar Basin in the late Mesozoic from the tectonic thermochronology perspective.

Fission-track (FT) thermochronology was developed on the basis of the closure temperature theory and the concept of cooling age, which effectively records tectonic events in the low-temperature range and recovers corresponding geothermal histories (Gleadow et al., 1986; Gallagher et al., 1998; Ruiz et al., 2004; Ketcham et al., 2018; Tian et al., 2020a). FT thermochronology has been widely used in a variety of studies, including analysis of the thermal history of sedimentary basins, rock uplift rates, constrained stratigraphy ages, and the tectonic evolution of basins (Zhu et al., 2005; Patel et al., 2014; 2015; Ge et al., 2016; Ansberque et al., 2018; Jian et al., 2018; Bernet, 2019; Zattin and Wang, 2019; Peng et al., 2020; Tian et al., 2020b; He

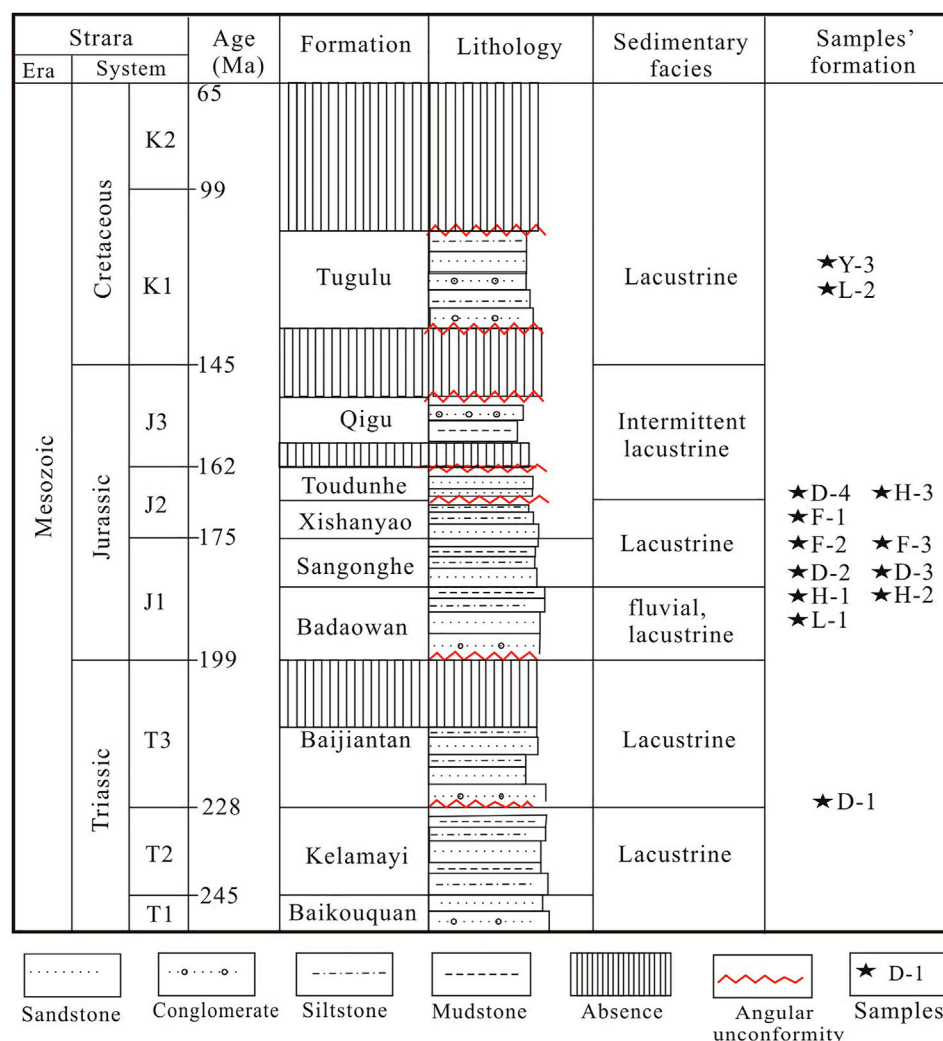


FIGURE 2

Generalized stratigraphic column of the Northern Junggar Basin showing sample locations, lithology and depositional facies.

et al., 2021; He et al., 2022a; He et al., 2022b). We studied the tectonic thermal evolution, including the peak age, of the northern Junggar Basin during the Yanshanian *via* zircon and apatite FT (AFT) dating. We concluded that the northern Junggar Basin experienced magmatism 165–161 Ma and later multiple uplift and denudation events 93–81 Ma and 72–66 Ma, respectively, which may be the response of northwest China to the Yanshanian orogeny.

Geological setting

The Junggar Basin is located in the southwestern CAOB (Figure 1A) at the intersection of the Kazakhstan, Siberia, and Tarim plates (Figure 1B). It is superimposed on the Precambrian crystalline and Hercynian-folded, metamorphic basements (Xiao et al., 1992; Li et al., 2010). Moreover, it is slightly triangular and extends for approximately 130,000 km². The study area, located in the northern part of the Junggar Basin, included the structural units of the Wulonggu depression, the Luliang uplift, the Shiyintan uplift, the Dibeil uplift, and the Wuxia fault-step belt. Further, it is bordered by

the Zaire and Halarat Mountains to the northwest and by the Karamaili and Almantai Mountains to the northeast (Figure 1C). The evolution of the northern Junggar Basin involved five main tectonic stages: residual basin (Early Hercynian), intracontinental rift basin (Late Carboniferous to Early Permian), multicycle intracontinental compressional depression basin (Late Hercynian to Indosinian), multicycle intracontinental basin (Yanshanian to Early Himalayan), and intracontinental orogen (Mid-late Himalayan) (Zhao, 1992; Han et al., 2006; Zhang et al., 2017).

The Paleozoic in the study area is dominated by dark gray pyroclastic rocks. The Paleogene rocks are mainly purplish-red and silty mudstones with a small distribution range. Widely distributed Neogene rocks are mostly sandstones, conglomerates, and mudstones (Figure 2.). The Triassic mainly comprises gray to black mudstones interbedded with sandstones. The Early Jurassic is dominated by fluvial-lacustrine sandstones, glutenites, mudstones, and coal seams with abundant fossils. The Middle Jurassic Xishanyao Formation is dominated by fluvial-lacustrine coal-bearing clastic rocks, whereas the Toudunhe Formation is dominated by intermittent lacustrine

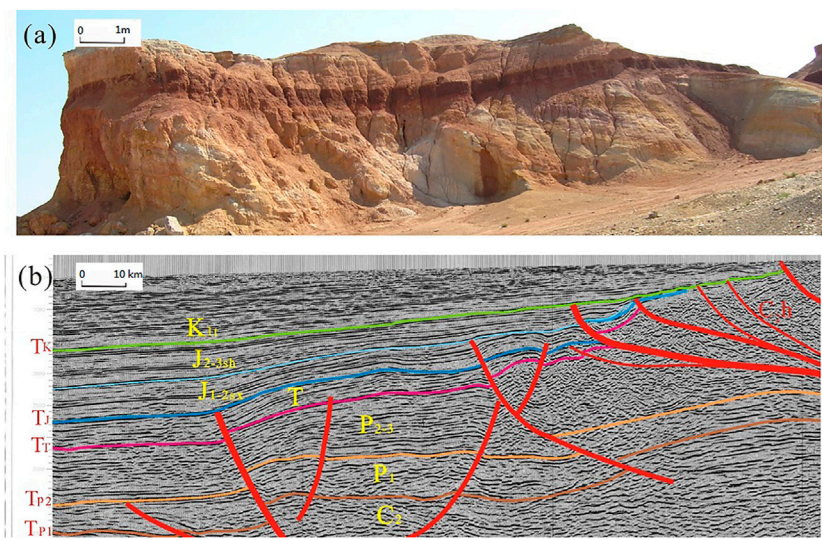


FIGURE 3
Stratigraphic unconformity in northern Junggar Basin. **(A)**The outcrop profile shows the angular unconformity between the lower Cretaceous and the upper Jurassic. **(B)** Unconformity in the study area shown by seismic profile.

TABLE 1 Details of samples used in this study.

Sample	Location	Stratigraphy	Lithology	Rock specimen
D-1	Luliang uplift	T _{2-3sq}	Sandstone	Drilling core
D-2	Luliang uplift	J _{1b}	Sandstone	Outcrop rock
D-3	Luliang uplift	J _{1s}	Sandstone	Outcrop rock
D-4	Luliang uplift	J _{2sh}	Sandstone	Outcrop rock
D1	Luliang uplift	C	Tuff	Drilling core
Y-1	Shiyingtang uplift	C	Tuff	Drilling core
Y-2	Shiyingtang uplift	p	Tuff	Outcrop rock
Y-3	Shiyingtang uplift	K _{1tg}	Sandstone	Outcrop rock
Y1	Shiyingtang uplift	C	Tuff	Drilling core
F-1	Luliang uplift	J _{2sh}	Sandstone	Drilling core
F-2	Luliang uplift	J ₁₋₂	Sandstone	Outcrop rock
F-3	Luliang uplift	J ₁₋₂	Sandstone	Outcrop rock
H-1	Shiyingtang uplift	J _{1b}	Sandstone	Outcrop rock
H-2	Shiyingtang uplift	J _{1s}	Sandstone	Outcrop rock
H-3	Shiyingtang uplift	J _{2x}	Sandstone	Outcrop rock
L-1	Wulonggu depression	J _{1s}	Sandstone	Outcrop rock
L-2	Wulonggu depression	K _{1tg}	Siltstone	Outcrop rock
T-1	Northern orogenic belt	C	Granite	Outcrop rock

brownish-red sandstones and pebbly sandstones. The Late Jurassic Qigu Formation is largely absent. The Early Cretaceous Tugulu Formation mainly comprises shallow lacustrine mudstones interbedded with sandstones, and the Late Cretaceous is mostly absent.

Based on the comprehensive analysis of outcropping rock, seismic profiles, and stratigraphic characteristics, the Yanshanian period stratigraphic unconformities in the north of the Junggar Basin are mainly between the Toutunhe and Xishanyao Formations, the Cretaceous and the Jurassic, and the Paleogene and the Cretaceous

(Figure 3). The unconformities were mostly a result of weak compression–deformation during uplift–exhumation.

Materials and methods

Samples

A total of 23 samples were analyzed, i.e., 15 samples were analyzed *via* AFT dating, and eight samples were analyzed *via* zircon fission-track (ZFT) dating. The samples were collected from surface detrital rocks from Mesozoic strata and three drill cores (wells Y, D, and F) from the study area (Table 1; Figure 1C; Figure 2). Samples D and F were obtained from Luliang uplift, among which D1 was collected from the Carboniferous drilling core, D-1 and F-1 were collected from the Triassic and Jurassic drilling cores respectively, and D-2, D-3, D-4, F-2, and F-3 were collected from the Jurassic outcrop rocks. Samples L-1 and L-2 were collected from the Jurassic and Cretaceous outcrops in the Wulonggu depression, respectively. Samples Y and H were from the Shiyingtian uplift, among which Y1 was from the Carboniferous drilling core, Y-1 was from the Jurassic drilling core, Y-2 and Y-3 were from the Jurassic and Cretaceous outcrop rocks, respectively, and H-1, H-2, H-3 were from the Jurassic outcrop rocks. Sample T-1 was collected from the Carboniferous outcrop rock on the northern edge of the Junggar Basin. The samples were mainly sandstones, siltstones, and Carboniferous to early Cretaceous tuffs. Each sample weighed more than 3 kg.

FT dating

Sedimentary detrital grains exhibit three annealing states: unreset, partial reset, and reset (Bernet and Garver, 2005; Braun et al., 2006). The FT ages of unreset grains have a low test probability ($P[\chi^2] < 5\%$) and the unreset grains are older than the stratigraphic age; this mainly represents the uplift–exhumation cooling age of a source region. Variation in the lag time between the FT age and the sedimentary age of unreset grains reveals the uplift–exhumation history of the source region. The FT ages of reset grains have a high test probability ($P[\chi^2] > 5\%$) and the reset grains are younger than the stratigraphic age; this age mainly represents the cooling age when the grains rise through the closure temperature after high-temperature annealing.

Using reset grain ages, track lengths, and thermal history modeling, we determined the tectonic thermal evolution of the Junggar sedimentary basin. The FT ages of the partial reset grains were generally older than or close to the stratigraphic age, which indicated the FT mixed ages of the partial reset grains in the source area (Braun et al., 2006). Using an appropriate statistical method to analyze these mixed ages, we can obtain the cooling age and tectonic thermal evolution information for the source region and sedimentary basin.

The closure temperature is the temperature of a thermochronological system at the time corresponding to its apparent age; it varies with grain size, chemical composition, and cooling rate (Dodson, 1973). Generally, the effective closure temperatures of apatite and zircon are approximately $120^\circ\text{C} \pm 10^\circ\text{C}$ and $240^\circ\text{C} \pm 50^\circ\text{C}$, respectively (Dodson, 1973; Zaun and Wagner, 1985; Laslett et al., 1987; Hurford, 1991; Braun et al., 2006; Bernet, 2009; Tian et al., 2020a). If the grains rapidly rise through the closure

temperature after high-temperature annealing, the FT age represents the cooling age of the tectonic thermal events. If the grains have been exposed to a long-term and complex thermal history after high-temperature annealing, the FT ages of the grains are mostly mixed ages, which must be analyzed and screened to obtain an effective cooling age. Commonly used methods for analyzing the FT age of a single grain include the radial chart view, $P(\chi^2)$ test, and binomial fitting. FT age groups can be directly obtained using the radial chart view method, whereby grains in the same group undergo the same thermal event. The $P(\chi^2)$ test is used to determine whether the grains belong to the same group depending on whether their ages obey the Poisson distribution. The binomial fitting method requires at least 50 grains, and their peak ages can be directly determined *via* data fitting (Galbraith and Laslett, 1993; Brandon, 1996; Brandon, 2002). Overall, the statistical distribution of FT ages, length characteristics, and peak age analyses can be used to obtain quantitative chronological constraints for tectonic thermal events.

Zircon and apatite grains used for FT analysis were separated from the samples *via* conventional heavy-liquid separation and magnetic separation techniques. FT dating was performed using the external detector method (Galbraith and Laslett, 1997) at the Institute of High Energy Physics, Beijing, China. The separated grains were mounted in epoxy resin and polyfluoroalkoxy fluororubber sheets, and the inner surfaces of the grains were exposed *via* polishing. The zircon grains were etched in a KOH–NaOH eutectic solution at 220°C for 30 h. The apatite grains were etched in a 6.6% HNO_3 solution at 25°C for 30 s to reveal the spontaneous FT. A low-uranium-content muscovite detector was used to determine induced FT density, and CN5 and CN2 uranium dosimeter glasses were used to detect apatite and zircon neutron fluxes, respectively. After irradiation, the muscovite external detector was etched in 40% HF at 25°C for 30 min, and the number of tracks was counted using a microscope (Olympus) under 1,000x magnification. The FT ages were calibrated using the zeta calibration method (Hurford and Green, 1983; Green, 1985), with a zircon zeta value of 124.1 ± 6.4 (1σ) and an apatite zeta value of 357.8 ± 6.9 (1σ).

Results

The results of the FT dating (see Tables 2, 3) showed the AFT central ages ranged from 42 ± 3 to 131 ± 9 Ma and the ZFT ages ranged from 134 ± 9 Ma to 205 ± 17 Ma; the distribution of FT ages was mainly related to tectonic units. The FT ages indicated four main age groups: 165–161, 131–122, 93–86, and 72–66 Ma. This indicates the multistage uplift–exhumation thermal evolution of the northern Junggar Basin during the Middle to Late Yanshanian.

Apatite FT dating

The $P(\chi^2)$ test is usually used to determine whether grains belong to the same group (Galbraith and Green, 1990; Galbraith and Laslett, 1993). $P(\chi^2) > 5\%$ means that the grains belong to the same group and undergo a single cooling process. $P(\chi^2) < 5\%$ means that the grains belong to different groups and represent a mixed age, for example, when the grains come from different source regions and remain in the partial annealing zone for a long period. The AFT dating results (Table 2; Figure 4) indicated that the $P(\chi^2)$ of all the samples was $>5\%$, and the track length of

TABLE 2 Apatite fission track data of the northern Junggar Basin.

Sample	Grains(n)	Stratigraphyage	ρ_s (10^5 /cm) (Ns)	ρ_i (10^5 /cm) (Ni)	ρ_d (10^5 /cm) (N)	P (χ^2) (%)	Central age (Ma) ($\pm 1\sigma$)	Pooled age (Ma) ($\pm 1\sigma$)	L (μ m) (N)
D-1	29	T _{2-3xq}	2.728 (503)	4.581 (852)	8.130 (10,300)	100	93 \pm 6	93 \pm 6	10.9 \pm 2.0 (104)
D-2	27	J _{1b}	3.192 (423)	7.248 (1,454)	97.4 (10,300)	98.1	72 \pm 4	72 \pm 4	11.1 \pm 1.8 (101)
D-3	28	J _{1s}	4.175 (685)	8.422 (1,453)	9.582 (10,300)	91.7	92 \pm 5	92 \pm 5	11.6 \pm 1.7 (106)
D-4	29	J _{2sh}	4.584 (542)	9.702 (1,176)	9.693 (10,300)	100	88 \pm 6	88 \pm 6	11.5 \pm 1.6 (92)
Y-1	28	C	.877 (118)	1.226 (165)	8.911 (10,322)	100	122 \pm 15	122 \pm 15	10.4 \pm 2.0 (105)
Y-2	28	P	2.262 (149)	2.657 (175)	7.906 (10,322)	99.9	128 \pm 15	128 \pm 15	12.2 \pm 2.3 (103)
Y-3	28	K _{1tg}	3.702 (564)	7.029 (1,071)	8.576 (10,300)	98.2	86 \pm 5	86 \pm 5	11.3 \pm 1.7 (104)
F-1	12	J _{2sh}	7.500 (443)	30.467 (1,687)	8.800 (10,300)	55.1	42 \pm 3	42 \pm 3	11.4 \pm 1.6 (54)
F-2	23	J ₁₋₂	3.656 (806)	8.685 (1932)	8.688 (10,300)	7.5	66 \pm 5	70 \pm 4	12.1 \pm 1.9 (108)
F-3	31	J ₁₋₂	5.308 (1,142)	12.262 (2,518)	8.130 (10,300)	59.0	67 \pm 3	67 \pm 3	11.8 \pm 2.0 (102)
H-1	27	J _{1b}	4.350 (860)	6.298 (1,315)	9.805 (10,300)	100	129 \pm 7	129 \pm 7	12.3 \pm 1.7 (92)
H-2	28	J _{1s}	1.094 (492)	1.472 (647)	9.247 (10,300)	100	131 \pm 9	131 \pm 9	13.5 \pm 2.1 (115)
H-3	13	J _{2x}	2.907 (340)	7.557 (525)	8.688 (10,300)	12.5	67 \pm 8	64 \pm 6	12.5 \pm 2.2 (40)
L-1	28	J _{1s}	4.040 (1,232)	6.887 (1890)	9.805 (10,300)	25.2	108 \pm 6	110 \pm 5	12.7 \pm 1.8 (107)
L-2	27	K _{1tg}	3.536 (642)	6.648 (1,248)	9.917 (10,300)	71.2	101 \pm 6	101 \pm 6	12.8 \pm 1.6 (112)

Note: n is the number of grains analyzed; ρ_s is spontaneous fission track density; N_s is the number of spontaneous fission tracks counted; ρ_i is induced fission track density; Ni is the number of induced fission tracks counted; ρ_d is fission track density measured in dosimeter glass CN5; Nd is the number of induced fission tracks counted in dosimeter glass CN5; P (χ^2) is chi-square probability; σ is the error of mean confined track lengths; L is mean confined fission track length; N is the number of tracks.

TABLE 3 Zircon fission track data of the northern Junggar Basin.

Sample	Grains (n)	Stratigraphy age	ρ_s (10^5 /cm) (Ns)	ρ_i (10^5 /cm) (Ni)	ρ_d (10^5 /cm) (N)	P (χ^2) (%)	Central age (Ma) ($\pm 1\sigma$)	Pooled age (Ma) ($\pm 1\sigma$)
D-1	21	T _{2-3xq}	108.264 (2,246)	18.106 (362)	3.353 (5,868)	33.1	134 \pm 9	135 \pm 9
D-2	20	J _{1b}	145.521 (1,649)	22.541 (264)	3.691 (5,868)	0.5	165 \pm 16	165 \pm 14
D1	23	C	132.233 (4,556)	19.154 (644)	3.402 (5,868)	1.3	151 \pm 10	151 \pm 9
Y1	22	C	135.304 (3,405)	17.451 (454)	3.476 (5,868)	24.3	174 \pm 13	176 \pm 12
F-3	19	J ₁₋₂	143.861 (3,013)	24.041 (501)	3.680 (5,868)	59.1	146 \pm 9	146 \pm 9
H-1	25	J _{1b}	135.174 (5,036)	18.440 (684)	3.327 (5,868)	66.2	161 \pm 10	161 \pm 10
L-1	21	J _{1s}	143.134 (4,288)	18.694 (587)	3.252 (5,868)	38.8	163 \pm 10	163 \pm 10
T-1	23	C	98.461 (2,410)	11.889 (291)	3.828 (5,933)	27.6	205 \pm 17	207 \pm 16

Note: n is the number of grains analyzed; ρ_s is spontaneous fission track density; N_s is the number of spontaneous fission tracks counted; ρ_i is induced fission track density; Ni is the number of induced fission tracks counted; ρ_d is fission track density measured in dosimeter glass CN2; Nd is the number of induced fission tracks counted in dosimeter glass CN2; P (χ^2) is chi-square probability; σ is the error of mean confined track lengths.

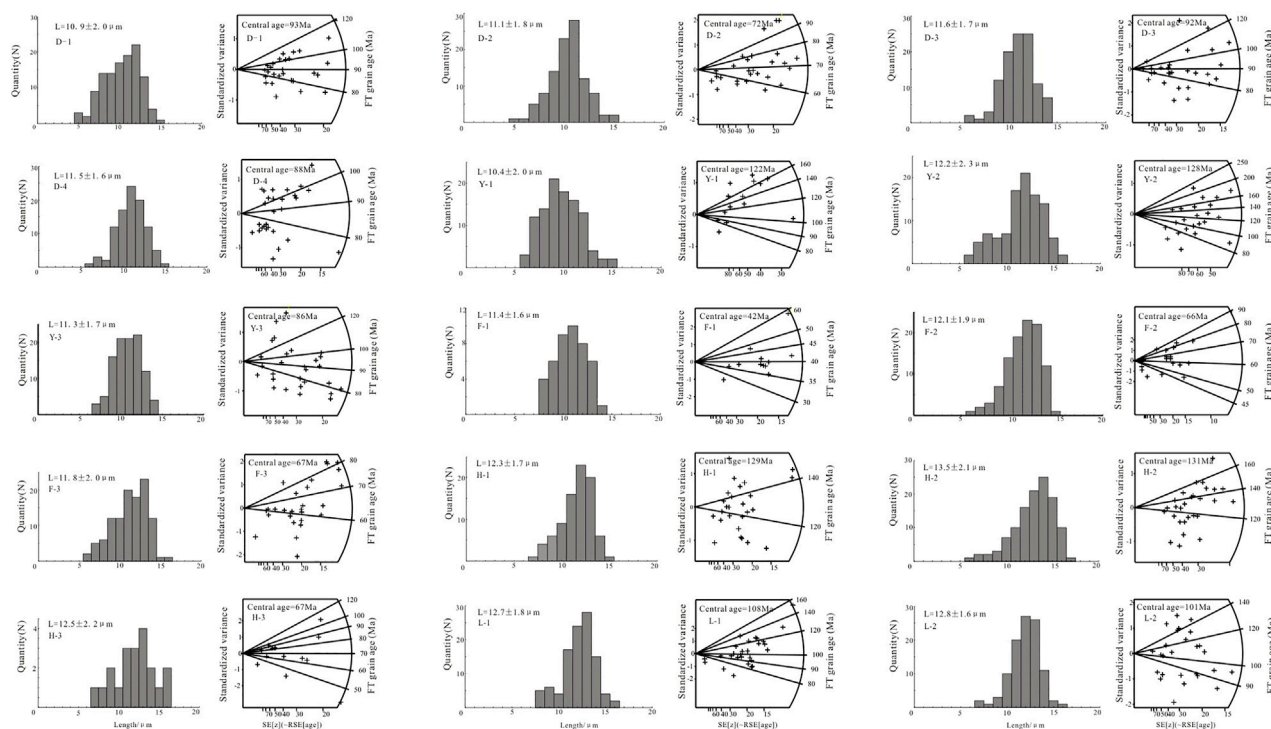


FIGURE 4

Fission track length histograms and radiograms of apatite grains from the northern Junggar Basin. The left panels of each group are fission track length histograms, the right panels are fission track radiograms, in which, X and Y-axes represent the age accuracy and standard deviations of single grains, respectively.

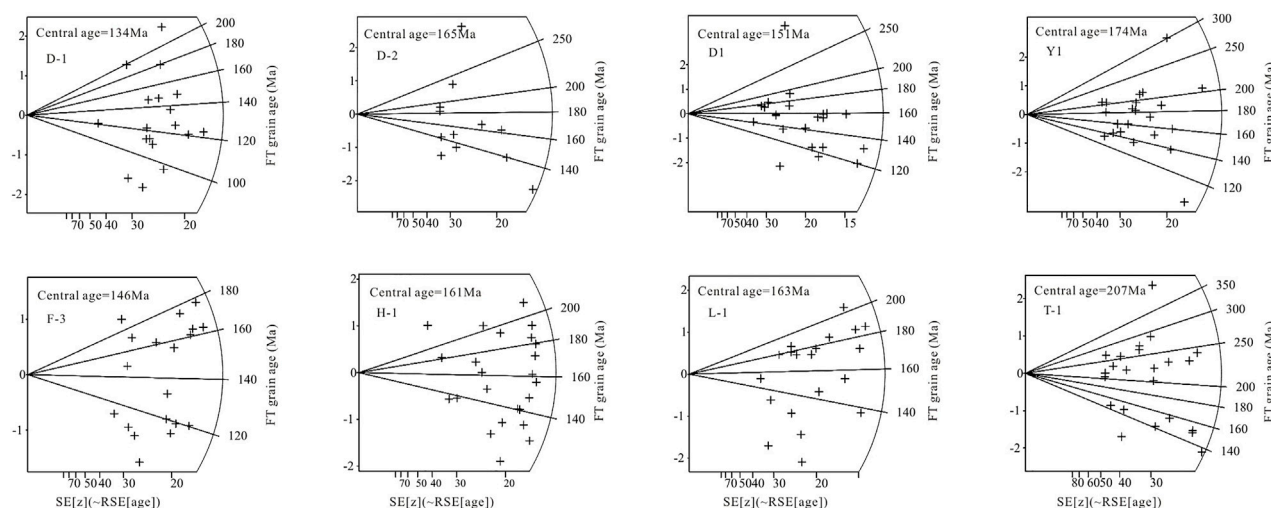


FIGURE 5

Radiograms of ZFT single grain ages from the northern Junggar Basin. X and Y-axes represent the age accuracy and standard deviations of single grains, respectively.

the grains presented a single peak. This indicated that the sampled grains belong to a single age group, which means that all the sampled grains underwent a single cooling process. The AFT central ages ranged from 42 ± 3 to 131 ± 9 Ma, and the peak ages were mainly 131–122, 93–86, and 72–66 Ma.

Zircon FT dating

The ZFT dating results are shown in Table 3 and Figure 5. Six samples showed $P(\chi^2) > 5\%$, indicating that the grains belong to the same group. The D-2 and D1 samples showed $P(\chi^2) < 5\%$, indicating

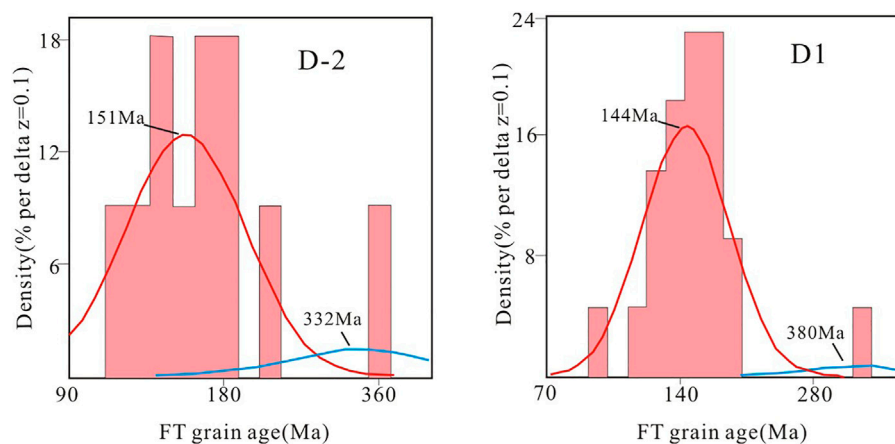


FIGURE 6

Frequency histograms of single grains of ZFT ages and age components calculated by binomial fitting method.

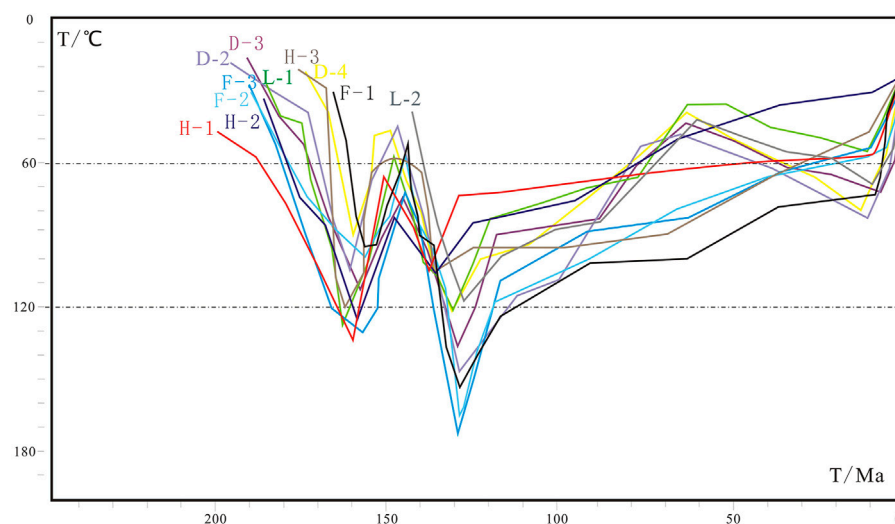


FIGURE 7

Results of thermal history modeling.

mixed ages. These two samples were analyzed using the binomial fitting method (Figure 6). Sample D-2 had peak ages of 144 and 380 Ma, and sample D1 had peak ages of 151 and 332 Ma. Because the ages of 380 and 332 Ma were older than the stratigraphic age of the samples, they reflected the thermal history of the grains in the source regions. Therefore, we determined the peak ages to be 144 and 151 Ma, representing the thermal history of the basin. Overall, the ZFT ages ranged from 134 ± 9 Ma to 205 ± 17 Ma, and the peak ages were mainly 165–161 Ma.

Thermal history modeling

Shortening AFT patterns reflect cooling paths through the apatite partial annealing zone. Important information can be obtained by modeling the thermal history of apatite grains using specific ages and

track lengths, including the timings and temperatures of tectonic thermal events in basins. The partial annealing zone is defined as the temperature range in which FTs can be partially retained on a geological time scale. The track will be completely annealed when the temperature is above that zone, and it will be well preserved when the temperature is below that zone. When the temperature is within this range, the FT length will shorten or become non-existent, and a new fission track will be simultaneously produced. Generally, the partial annealing zone of apatite is 60°C–120 °C (Braun et al., 2006; Tian et al., 2020a).

In this study, the AFTSolve program (Ketcham, 2005) was used to model the time–temperature path based on the grain ages and track lengths of 11 typical samples. The initial Dpar value was 1.5 μm , and the initial track length was calculated based on the Dpar value. The initial modeling temperature is the temperature of the stratum during deposition, generally approximately 20°C; therefore, it was set as

10°C–30°C. The maximum burial time and temperature range were the modeling constraints, and the modeling temperature was less than the maximum burial temperature of the stratum. For each sample, inverse thermal history modeling was run for 100,000 paths to find the best fitting curve. The modeling results (Figure 7) showed that there were two tectonic thermal events in the northern Junggar Basin during the Yanshanian, which resulted in partial or complete annealing of apatite. The first tectonic thermal event (buried heating) occurred between 165 and 161 Ma, and the second tectonic thermal event occurred between 131 and 128 Ma.

Discussion

Yanshanian magmatism

Large-scale magmatic activities mainly occurred in the Junggar Basin and its adjacent areas during the Paleozoic. The intracontinental tectonic thermal evolution started in the Mesozoic (Xiao et al., 1992; Qiu et al., 2002); therefore, magmatic activities were substantially weakened, resulting in reduced volcanic age records. However, based on detrital zircon geochronology, large numbers of late Mesozoic magmatism have been recorded for detrital materials collected from the Junggar Basin. For example, *via* zircon U–Pb dating, Yang et al. (2013) obtained peak ages of 144 and 162 Ma from the Manas section of the Junggar Basin, Fang et al. (2015) obtained a peak age of 153 Ma for the grains obtained from the Toutunhe section, and Zhu et al. (2020) obtained peak ages of 132 and 169 Ma for the grains obtained from the Wangjiagou section and 161 Ma for the grains obtained from the Kelamaili section. Additionally, Liu et al. (2018) used laser ablation inductively coupled plasma mass spectrometry to obtain a zircon U–Pb age of 189 Ma for the grains obtained from the northeastern Junggar Basin, confirming the existence of Early Jurassic magmatism in the northeastern Junggar Basin.

Yanshanian magmatism in orogenic belts adjacent to the Junggar Basin has also been studied, particularly in the Altay and Tianshan areas. Zhang et al. (1994) determined a tectonomagmatic Ar–Ar age of 131 Ma (Middle Yanshanian) for granites in the Altay area. Chen et al. (1999) obtained an Ar–Ar age of 149–135 Ma from tectonic thermochronological records for granites in the Altay area. Zircon U–Pb ages of 154.9 ± 1.9 Ma and 152.7 ± 1.8 Ma were determined for Eastern Tianshan by Liu et al. (2019). These studies have confirmed the existence of Yanshanian magmatism around the Junggar Basin.

In our study, ZFT ages ranged from 205 to 132 Ma, with a peak age of 165–161 Ma. Except for samples D-1 and T-1, the FT ages of other samples were concentrated at approximately 160 Ma, indicating that the study area experienced important tectonic thermal events during this period. Generally, the FT age of the old strata in the same area should be newer than that of the new strata above it. However, the Carboniferous sample T-1 has the oldest FT age of 205 ± 17 Ma. This may be related to the fact that the sample was collected from the orogenic belt on the northern margin of the Junggar basin, which has experienced different tectonic evolution processes. High temperatures are required for annealing and partial annealing of zircon owing to its high closure temperature ($240^\circ\text{C} \pm 50^\circ\text{C}$). Considering the evidence of the existence of Middle Yanshanian magmatism in the Junggar Basin and the two tectonic thermal events that resulted in the partial or complete annealing of apatite, we chose to interpret the tectonic

thermal event that occurred from 165 to 161 Ma to be a result of magmatism. The AFT ages ranged from 131 to 42 Ma, with peak ages of 131–122 Ma, 93–86 Ma, and 72–66 Ma. The FT ages of the four samples, Y-1, Y-2, H-1, and H-2, were distributed between 122 and 131 Ma. These samples were collected from the Shiyintan uplift, and the sampling points were relatively close, which may reflect a tectonic thermal event of 130 Ma. Considering that the closure temperature of zircon is higher than that of apatite, the ZFT (165–161 Ma) and AFT ages (131–122 Ma) probably represent FT age recordings of the same tectonic thermal event, possibly reflecting a nearly continuous Yanshanian tectonic thermal event.

Yanshanian tectonic events are also reflected in the sedimentary characteristics and contact relationships of the strata. The appearance of intermittent brownish-red lacustrine sandstones in the Toutunhe Formation shows that the climate tended toward an arid environment. The angular unconformity at the top of the Toutunhe Formation and the absence of the Upper Jurassic strata (Figure 3) indicate that uplift may have started after the deposition of the Toutunhe Formation in the Middle Jurassic. An unconformity at the base of the Cretaceous is widely developed across the whole region and the whole of western China. This indicates a strong tectonic event that lasted from the Middle to Late Jurassic to the Early Cretaceous. Based on the most recent international stratigraphic age of 163.5 Ma for the Upper Jurassic and our newly obtained 165–161 Ma ZFT ages, we consider the start of the Yanshanian orogeny in the northern Junggar Basin to be approximately 163 Ma.

Uplift and cooling events in the Late Yanshanian

Our new AFT ages show that there were two uplift and cooling events at 93–86 and 72–64 Ma, which correspond to the widespread absence of Upper Cretaceous strata in the study area. Additionally, these uplift and cooling events are also reflected in the sedimentary characteristics and contact relationships of adjacent areas. For example, Upper Cretaceous strata are absent in the eastern Tarim Basin, and Paleogene strata directly overlie Lower Cretaceous strata. There is an angular unconformity between Upper Cretaceous and Lower Cretaceous strata in the Turpan–Hami Basin and between Upper Cretaceous and Lower Jurassic strata in the western Tianshan Mountains (Zhu et al., 2005; 2020; He and Gao, 2008; Yang et al., 2015; 2017). Thermochronology studies have also documented Late Cretaceous uplift–exhumation events in the Junggar Basin and its adjacent areas: AFT ages of 90–25 Ma for an uplifting event in northern Junggar Basin (Li et al., 2010; Li et al., 2014); AFT ages of 120–45 Ma for cooling stages in the southern margin of the Junggar Basin (Zhang et al., 2022); AFT thermochronology and seismic profiles revealed a rapid uplift (ca. 100–60 Ma) in the Late Cretaceous Paleocene in the eastern Junggar Basin (Wu et al., 2021); AFT ages of 120–60 Ma for Cretaceous uplifting events in the Altai region (Yuan et al., 2004; Johan et al., 2006); AFT ages of 110–70 Ma for a rapid uplift–exhumation event in the Tianshan Mountains (Hendrix et al., 1994; Guo et al., 2002; Glorie et al., 2010; Luo et al., 2012; Zhang et al., 2017); and the Eastern Tianshan and southern part of the east Junggar experienced moderate to rapid basement cooling throughout the Cretaceous (He et al., 2022b). These studies indicate that an uplift–exhumation event occurred during the Late Cretaceous that affected the Junggar

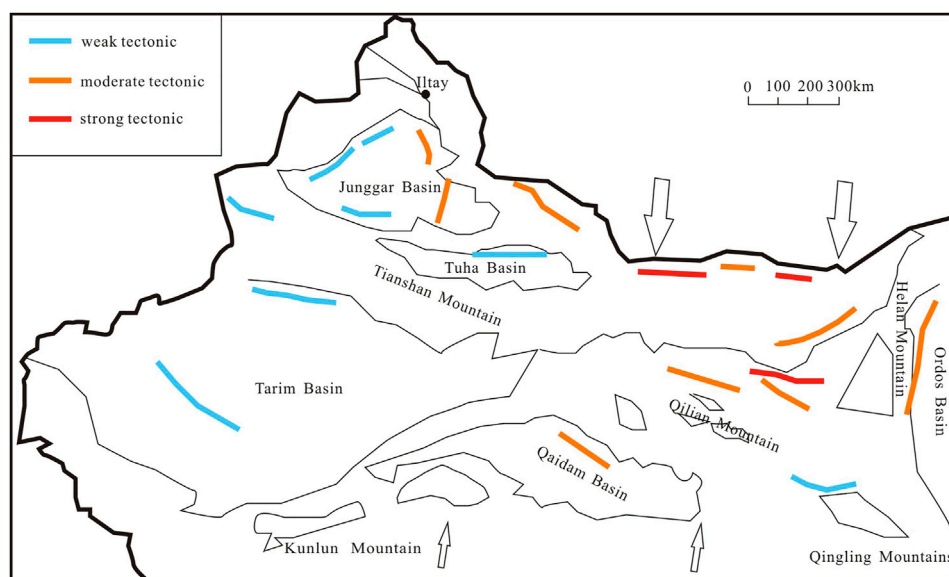


FIGURE 8
Structural strength characteristics of middle Yanshanian in Northwest China (modified from [Chen et al., 2004](#)).

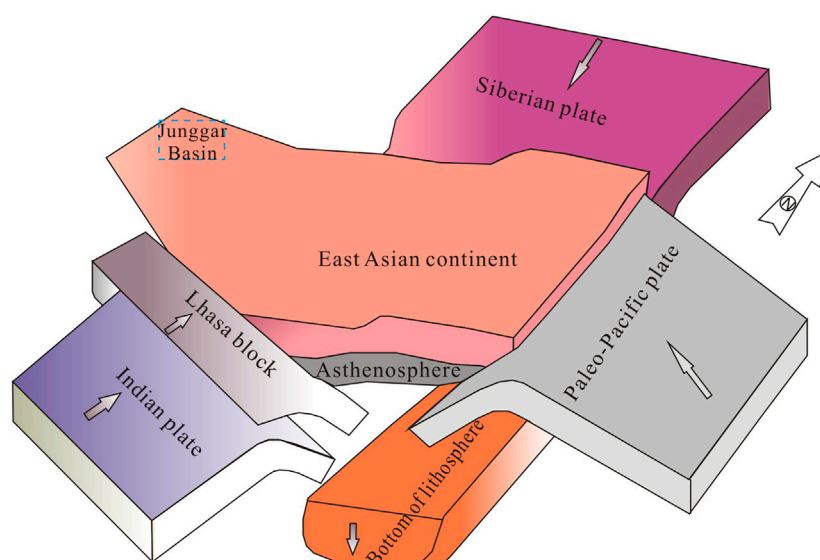


FIGURE 9
Schematic diagram of Mesozoic multi-plate convergence in East Asia continent.

Basin and its adjacent areas, which may have been the result of a distal collision between the Kohistan–Dras island arc and the Lhasa terrane.

Influence of the yanshanian orogeny on the Junggar Basin

The Yanshanian orogeny, a major geological tectonic event, occurred after the formation of the Triassic continent in East Asia. Beginning around 170 Ma in the Middle Jurassic, there were three

main successive tectonic periods: a deformation period (175–136 Ma), an extension period (135–90 Ma), and a weak compression–deformation period (89–80 Ma) ([Dong et al., 2019](#)). The Yanshanian orogeny substantially influenced the tectonic evolution of eastern China; however, in northwest China, the effects of the Yanshanian orogeny seem to be relatively weak ([Figure 8](#)). A regional tectonic uplift event led to the shrinking of a sedimentary basin ([Chen et al., 2004](#); [Jia et al., 2005](#)).

Generally, the effects of the Yanshanian orogeny on the Junggar Basin were relatively minor and mainly manifested *via* the overall

uplift of the basin, the narrowing and discontinuity of Jurassic sedimentation, and the deposition of glutenite in front of the orogenic belt (Jia et al., 2005; Zhang et al., 2006; He and Gao, 2008). Consequently, the Yanshanian orogeny in the Junggar Basin has mostly been ignored. However, widely developed unconformity at the base of Cretaceous strata is found in the Junggar Basin and across western China (Zhou and Cai, 1990; Jia et al., 2005; He and Gao, 2008; Yang et al., 2015; Yang et al., 2017) and stretches as far west as Kazakhstan (Jolivet et al., 2013). Additionally, the Yanshanian orogeny transformed Jurassic and younger strata *via* large-scale uplift and denudation, formation of a thrust system, multiple large-scale uplifts, and reactivation of large-scale faults in western China (Hendrix et al., 1992; He and Gao, 2008; Dong et al., 2019). This indicates that the Yanshanian orogeny was an important regional tectonic event.

Driving force of the yanshanian tectonic events in northwest China

With the disintegration of the united paleocontinent, three giant continental margin convergence orogenic systems (i.e., the Mongolia–Okhotsk orogenic system in the north, the Paleo-Pacific orogenic system in the east, and the Bangonghu–Nujiang orogenic system in the west) were formed around the East Asian continent in the Jurassic. Deformation and propagation of these marginal tectonic belts to the interior of the continent led to a large-scale intracontinental orogeny that formed the Yanshanian multiplate convergence tectonic system (Figure 9). The Mongolia–Okhotsk orogenic system, proximal to the northeast Junggar Basin, is a northeast-trending orogenic belt. The closing of the Mongolia–Okhotsk ocean occurred about 182–174 Ma, and the metamorphic peak of the collision zone occurred about 175–165 Ma (Zorin, 1999; Mo et al., 2005). This tectonic event may have been the driving force for the development of the Middle and Late Jurassic unconformity in the northern Junggar Basin and its adjacent areas. During the Late Jurassic–Early Cretaceous, the Lhasa block collided with the southern edge of Asia and the Bangong–Nujiang Tethys Ocean was completely closed (Allen et al., 1994; Jolivet et al., 2001), which may have exacerbated tectonic deformation in the northern Junggar Basin and its adjacent areas. Additionally, the northeast–southwest directed continental collision between the Kolyma–Omolon block in northeast Russia and the Siberian craton during the Late Jurassic to Early Cretaceous (Oxman, 2003) resulted in compressive stress transfer from the northeast edge of Siberia to Junggar and its adjacent areas through the rigid Siberian craton. In the Late Cretaceous, the Gangdise block collided with the Lhasa block (Hendrix et al., 1992). The combination of these block collisions led to an intracontinental orogeny in Central Asia and a cooling uplift event in the late Mesozoic. The opening and development of the Yanshanian tectonic events were closely related to the plate convergence and collision of the Paleo-Pacific, Tethys, and Mongolia–Okhotsk tectonic domains. The tectonic evolution of the Junggar Basin and its adjacent areas has been affected by these multiplate compression and collision events.

Conclusion

- 1) The central AFT and ZFT ages in the northern Junggar Basin are 131–42 Ma and 205–132 Ma, respectively.
- 2) These new thermochronological data indicate that the tectonic evolution of the northern Junggar Basin mainly occurred in 165–161, 93–81, and 72–66 Ma. We have interpreted the 165–161 Ma tectonic thermal event as the result of magmatism and the 93–81 and 72–66 Ma events as uplift and cooling events, respectively. We prove that the magmatism indicates the opening of the Yanshanian orogeny in the Junggar Basin, and the 93–86 and 72–64 Ma uplift and cooling events are the results of the collision between the Kohistan–Dras island arc and the Lhasa terrane.
- 3) Our new FT data thermochronologically confirm the Yanshanian tectonic evolution in the northern Junggar Basin, which confirms that the Yanshanian orogeny, a regional tectonic event, may have extended to northwest China.

Data availability statement

The datasets presented in this study can be found in online repositories. The names of the repository/repositories and accession number(s) can be found in the article/supplementary material.

Author contributions

ZL was responsible for the methodology and writing of this paper. ZC, YF, XL, and LY conducted the field work and collected the samples. SZ was responsible for language checking, grammar proofreading, and editing.

Funding

This study was funded by the National Natural Science Foundation of China (No. 42162015) and the Youth Science and Technology Foundation of Gansu Province (No. 20JR10RA139).

Conflict of interest

The authors declare that the research was conducted in the absence of any commercial or financial relationships that could be construed as a potential conflict of interest.

Publisher's note

All claims expressed in this article are solely those of the authors and do not necessarily represent those of their affiliated organizations, or those of the publisher, the editors and the reviewers. Any product that may be evaluated in this article, or claim that may be made by its manufacturer, is not guaranteed or endorsed by the publisher.

References

- Allen, M. B., Windley, B. F., and Zhang, C. C. (1994). Cenozoic tectonics in the urumqi-korla region of the Chinese tien Shan. *Geol. Chau* 83, 406–416. doi:10.1007/bf00210554
- Ansberque, C., Godard, V., Olivetti, V., Bellier, O., de Sigoyer, J., Bernet, M., et al. (2018). Differential exhumation across the longriba fault system: Implications for the eastern Tibetan plateau. *Tectonics* 37, 663–679. doi:10.1002/2017tc004816
- Bernet, M. A. (2009). A field-based estimate of the zircon fission-track closure temperature. *Chem. Geol.* 259, 181–189. doi:10.1016/j.chemgeo.2008.10.043
- Bernet, M. (2019). Exhumation studies of mountain belts based on detrital fission track analysis on sand and sandstones. *Fission-Track Thermochronology its Appl. Geol.*, 269–277.
- Bernet, M., and Garver, J. I. (2005). Fission track analysis of detrital zircon. *Rev. Mineralogy Geochem.* 58, 205–237. doi:10.2138/rmg.2005.58.8
- Brandon, M. T. (2002). Decomposition of mixed grain age distributions using binomfit. *Track* 24, 13–18.
- Brandon, M. T. (1996). Probability density plot for fission-track grain-age samples/fission-track grain-age samples. *Radiat. Meas.* 26, 663–676. doi:10.1016/s1350-4487(97)82880-6
- Braun, J., Beek, P. D., and Batt, G. (2006). *Quantitative thermochronology: Numerical methods for the interpretation of thermochronological data*. Cambridge: Cambridge University Press.
- Cai, Z. X., Chen, F. J., and Jia, Z. Y. (2000). Types and tectonic evolution of Junggar Basin. *Geosci. Front.* 7, 431–440.
- Cao, Y., Chen, F., and Zhao, F. (2020). Tectono-magmatic events in Junggar Basin during jurassic period. *Geol. Xinjiang* 38, 341–347.
- Chen, F. J., Zhang, G. Y., and Chen, Z. N. (2004). Fe/Zn double metal cyanide (DMC) catalyzed ring-opening polymerization of propylene oxide. *Geoscience* 18, 269–272. doi:10.1016/j.porgcoat.2004.03.003
- Chen, F. W., Li, H. Q., Gong, D. H., Cai, H., and Chen, W. (1999). New evidence from isotopic geochronology of Yanshanian diagenesis and mineralization in the Altay orogenic belt, China. *Chin. Sci. Bull.* 44, 1142–1148.
- Dodson, M. H. (1973). Closure temperature in cooling geochronological and petrological systems. *Contributions Mineralogy Petrology* 40, 259–274. doi:10.1007/bf00373790
- Dong, S. W., Wu, X. H., Wu, Z. H., Deng, J. F., Gao, R., and Wang, C. S. (2000). On tectonic seesawing of the East Asia continent-Global implication of the Yanshan movement. *Geol. Rev.* 46, 8–13.
- Dong, S. W., Zhang, Y. Q., Li, H. L., Shi, W., Xue, H. M., Li, J. H., et al. (2019). The yanshan orogeny and late mesozoic multi-plate convergence in East asia—commemorating 90th years of the “yanshan orogeny. *Sci. China Earth Sci.* 61, 1888–1909. doi:10.1007/s11430-017-9297-y
- Dong, S. W., Zhang, Y. Q., Long, C. X., Yang, Z. Y., Ji, Q., Wang, T., et al. (2007). Jurassic tectonic revolution in China and New interpretation of the Yanshanian movement. *Acta Geol. Sin.* 81, 1449–1461.
- Dong, S. W., Zhang, Y. Q., Zhang, F. Q., Cui, J. J., Chen, X. H., Zhang, S. H., et al. (2015). LateJurassic-early cretaceous continental convergence and intracontinental orogenesis in East Asia: A synthesis of the yanshan revolution. *Asian Earth Sci.* 114, 750–770. doi:10.1016/j.jseas.2015.08.011
- Fang, S. H., Song, Y., and Jia, C. Z. (2006). Relationship between Cretaceous basal conglomerate and oil/gas reservoiring in the Junggar Basin. *Nat. Gas. Ind.* 26, 13–16.
- Fang, Y. N., Wu, C. D., Guo, Z. J., Hou, K. J., Dong, L., Wang, L. X., et al. (2015). Provenance of the southern Junggar Basin in the Jurassic: Evidence from detrital zircon geochronology and depositional environments. *Sediment. Geol.* 315, 47–63. doi:10.1016/j.sedgeo.2014.10.014
- Faure, M., Lin, W., and Chen, Y. (2012). Is the Jurassic (Yanshanian) intraplate tectonics of North China due to westward indentation of the North China block? *Terra nova.* 24, 456–466. doi:10.1111/ter.12002
- Galbraith, R. F., and Green, P. F. (1990). Estimating the component ages in a finite mixture/finite mixture. *Nucl. Tracks Radiat. Meas.* 17, 197–206. doi:10.1016/1359-0189(90)90035-v
- Galbraith, R. F., and Laslett, G. M. (1997). Statistical modelling of thermal annealing of fission tracks in zircon/fission tracks in zircon. *Chem. Geol.* 140, 123–135. doi:10.1016/s0009-2541(97)00016-8
- Galbraith, R. F., and Laslett, G. M. (1993). Statistical models for mixed fission track ages/fission track ages. *Nucl. Tracks Radiat. Meas.* 21, 459–470. doi:10.1016/1359-0189(93)90185-c
- Gallagher, K., Brown, R. W., and Johnson, C. (1998). Fission track analysis and its applications to geological problems. *Annu. Rev. Earth Planet. Sci.* 26, 519–572. doi:10.1146/annurev.earth.26.1.519
- Ge, X., Shen, C., Selby, D., Deng, D., and Mei, L. (2016). Apatite fission-track and Re-Os geochronology of the xuefeng uplift, China: Temporal implications for dry gas associated hydrocarbon systems/fission-track and Re-osgeochronology of the xuefeng uplift, China: Temporal implications for dry gas associated hydrocarbon systems. *Geology* 44, 491–494. doi:10.1130/g37666.1
- Gleadow, A. J. W., Duddy, I. R., Green, P. F., and Lovering, J. F. (1986). Confined fission track lengths in apatite: A diagnostic tool for thermal history analysis. *Contributions Mineralogy Petrology* 94, 405–415. doi:10.1007/bf00376334
- Glorie, S., Grave, J. D., Buslov, M. M., Elburg, M. A., Stockli, D. F., Gerdes, A., et al. (2010). Multi-method chronometric constraints on the evolution of the northern Kyrgyz tien Shan granitoids (central asian orogenic belt): From emplacement to exhumation. *J. Asian Earth Sci.* 38, 131–146. doi:10.1016/j.jseas.2009.12.009
- Green, P. F. (1985). Comparison of zeta calibration baselines for fission-track dating of apatite, zircon and sphene/fission-track dating of apatite, zircon and sphene. *Chem. Geol.* 58, 1–22. doi:10.1016/0168-9622(85)90023-5
- Guo, Z. J., Zhang, Z. C., and Liao, G. H. (2002). Uplifting process of eastern Tianshan mountains: Evidence from fission track age and its tectonic significance. *Xinjiang Geol.* 20, 331–334.
- Guo, Z. J., Zhang, Z. C., Wu, C. D., Fang, S. H., and Zhang, R. (2006). The mesozoic and cenozoic exhumation history of tianshan and comparative studies to the junggar and Altai mountains. *Acta Geol. Sin.* 80, 1–15.
- Han, B. F., Ji, J. Q., Sun, B., Chen, L. H., and Zhang, L. (2006). Late Paleozoic vertical growth of continental crust around the Junggar Basin, Xinjiang, China (part1): Timing of post-collisional plutonism. *Acta Petrol. Sin.* 22, 1077–1086.
- He, Z. L., and Gao, S. L. (2008). The Yanshanian movement and its control over hydrocarbon accumulation in Western China. *Oil Gas Geol.* 29, 419–427.
- He, Z. Y., Wang, B., Glorie, S., Su, W. B., Ni, X. H., Jepson, G., et al. (2022b). Mesozoic building of the eastern tianshan and east Junggar (NW China) revealed by low-temperature thermochronology. *Gondwana Res.* 103, 37–53. doi:10.1016/j.gr.2021.11.013
- He, Z. Y., Wang, B., Nachtergaele, S., Glorie, S., Ni, X. H., Su, W. B., et al. (2021). Long-term topographic evolution of the Central Tianshan (NW China) constrained by low-temperature thermochronology. *Tectonophysics* 817, 229066. doi:10.1016/j.tecto.2021.229066
- He, Z. Y., Wang, B., Su, W. B., Glorie, S., Ni, X. H., Liu, J. S., et al. (2022a). Meso-Cenozoic thermo-tectonic evolution of the Yili block within the Central Asian Orogenic Belt (NW China): Insights from apatite fission track thermochronology. *Tectonophysics* 823, 229194. doi:10.1016/j.tecto.2021.229194
- Hendrix, M. S., Dumitru, T. A., and Graham, S. A. (1994). Late oligocene early miocene unroofing in the Chinese tianshan: An early effect of the India-Asia collision. *Geology* 22, 487–490. doi:10.1130/0091-7613(1994)022<0487:loemui>2.3.co;2
- Hendrix, M. S., Graham, S. A., Carroll, A. R., Sobel, E. R., Mcknight, C. L., Schulein, B. J., et al. (1992). Sedimentary record and climatic implications of recurrent deformation in the Tian Shan: Evidence from Mesozoic strata of the north Tarim, south Junggar, and Turpan basins, northwest China. *Geol. Soc. Am. Bull.* 104, 53–79. doi:10.1130/0016-7606(1992)104<0053:sracio>2.3.co;2
- Hou, G. F., Zeng, D. L., and Niu, Z. J. (2020). New discovery of sandy debris flow sandbody and its implications for oil and gas exploration in the Junggar Basin. *Nat. Gas. Ind.* 40, 41–49.
- Hurford, A. J., and Green, P. F. (1983). The zeta age calibration of fission track dating. *Chem. Geol.* 41, 285–317. doi:10.1016/s0009-2541(83)80026-6
- Hurford, A. J. (1991). Uplift and cooling pathways derived from fission track analysis and mica dating: A review. *Geol. Rundsch.* 80, 349–368. doi:10.1007/bf01829371
- Jia, C. Z., Wei, G. Q., and Li, B. L. (2005). Yanshanian tectonic features in West-central China and their petroleum geological significance. *Oil Gas Geol.* 26, 9–15.
- Jian, X., Guan, P., Zhang, W., Liang, H., Feng, F., and Fu, L. (2018). Late cretaceous to early eocene deformation in the northern Tibetan plateau: Detrital apatite fission track evidence from northern qaidam basin. *Gondwana Res.* 60, 94–104. doi:10.1016/j.gr.2018.04.007
- Johan, D. G., Michael, M. B., and Peter, V. H. (2006). Distant effects of India Eurasia convergence and Mesozoic intracontinental deformation in Central Asia: Constraints from apatite fission-track thermo-chronology. *J. Asian Earth Sci.* 3, 1–17.
- Jolivet, M., Brunel, M., Seward, D., Xu, Z., Yang, J., Roger, F., et al. (2001). Mesozoic and cenozoic tectonics of the northern edge of the Tibetan plateau: Fission-track constraints. *Tectonophysics* 343, 111–134. doi:10.1016/s0040-1951(01)00196-2
- Jolivet, M., Heilbronn, G., Robin, C., Barrier, L., Bourquin, S., Guo, Z., et al. (2013). Reconstructing the Late Palaeozoic-Mesozoic topographic evolution of the Chinese Tianshan: Available data and remaining uncertainties. *Adv. Geosciences* 37, 7–18. doi:10.5194/adgeo-37-7-2013
- Ketcham, R. A. (2005). Forward and inverse modeling of low-temperature thermochronometry data. *Rev. Mineralogy Geochem.* 58, 275–314. doi:10.2138/rmg.2005.58.11
- Ketcham, R. A., vander, B. P., Barbarand, J., Bernet, M., and Gautheron, C. (2018). Reproducibility of thermal history reconstruction from apatite fission-track and (U-Th)/He data/fission-track and (U-Th)/He data. *Geochim. Geophys. Geosystems* 19, 2411–2436. doi:10.1029/2018gc007555
- Laslett, G. M., Green, P. F., Duddy, I. R., and Gleadow, A. J. W. (1987). Thermal annealing of fission tracks in apatite: A quantitative analysis. *Chem. Geology: Isotope Geosci. Sect.* 65, 1–13. doi:10.1016/0168-9622(87)90057-1

- Li, W., Hu, J. M., and Qu, H. J. (2010). Fission track analysis of Junggar Basin peripheral orogen and its geological significance. *Acta Geol. Sin.* 84, 171–182.
- Li, Z. H., Chen, G., Cui, J. B., Chen, Z. J., H. J. Y., Ding, C., et al. (2014). Fission track age of yanshanian tectonic-thermal events in the northern Junggar Basin. *Geol. Sci. Technol. Inf.* 33, 9–14.
- Liu, S. B., Dou, H., Li, H. B., and Wen, Z. G. (2019). Geological significance of the discovery of Late Jurassic intermediate-acidic intrusive rock in Bogeda area of East Tianshan, Xinjiang, and its U-Pb zircon age. *Geol. Bull. China* 38, 288–294.
- Liu, S. B., Dou, H., Zhang, W. M., Peng, Z. J., Zhang, L., and Zhang, W. R. (2018). Discovery of Jurassic trachyandesite and its geological significance in the northwestern of Junggar Basin. *Geol. Rev.* 64, 1519–1529.
- Luo, M., Zhu, W. B., Zheng, B. H., and Zhu, X. Q. (2012). Mesozoic-Cenozoic tectonic evolution of the Kuqa Basin: Evidence from apatite fission track data. *Earth Sci.* 37, 893–902.
- Mo, S. G., Han, M. L., and Li, J. Z. (2005). Composition and orogeny of Mongolia Okhotsk orogenic belt Process. *J. Shandong Univ. Sci. Technol.* 24, 50–52.
- Oxman, V. S. (2003). Tectonic evolution of the mesozoic verkhoysansk-kolyima belt (NE Asia). *Tectonophysics* 365, 45–76. doi:10.1016/s0040-1951(03)00064-7
- Patel, R. C., Singh, P., and Lal, N. (2015). Thrusting and back-thrusting as post-emplacement kinematics of the AlmoraKlippe: Insights from low-temperature thermochronology. *Tectonophysics* 653, 41–51. doi:10.1016/j.tecto.2015.03.025
- Patel, R. C., Sinha, H. N., Kumar, B. A., and Singh, P. (2014). Basin provenance and post-depositional thermal history along the continental P/T boundary of the Raniganj basin, eastern India: Constraints from apatite fission track dating/fission track dating. *J. Geol. Soc. India.* 83, 403–413. doi:10.1007/s12594-014-0057-7
- Qiu, L., Kong, R. Y., Yan, D. P., Mu, H. X., Sun, W. H., Sun, S., et al. (2022a). Paleo-Pacific plate subduction on the eastern Asian margin: Insights from the Jurassic foreland system of the overriding plate. *GSA Bull.* 134, 2305–2320. doi:10.1130/b36118.1
- Qiu, L., Kong, R. Y., Yan, D. P., Wells, M. L., Wang, A., Sun, W., et al. (2018). The Zhayao tectonic window of the Jurassic Yantai thrust system in Liaodong Peninsula, NE China: Geometry, kinematics and tectonic implications. *J. Asian Earth Sci.* 06, 58–71. doi:10.1016/j.jseas.2018.06.012
- Qiu, L., Yan, D. P., Ma, H. B., Sun, S. H., Deng, H. L., Zhou, Z. C., et al. (2022b). Late Cretaceous geodynamics of the Palaeo-Pacific plate inferred from basin inversion structures in the Songliao Basin (NE China). *Terra nova.* 34, 465–473. doi:10.1111/ter.12612
- Qiu, N. S., Yang, H. B., and Wang, X. L. (2002). Tectonic thermal evolution of Junggar Basin. *Geol. Sci.* 37, 423–429.
- Ruiz, G. M. H., Seward, D., and Winkler, W. (2004). Detrital thermochronology-a new perspective on hinterland tectonics, an example from the Andean Amazon Basin, Ecuador. *Basin Res.* 16, 413–430. doi:10.1111/j.1365-2117.2004.00239.x
- Sun, W. J., Zhao, S. J., Li, S. Z., and Li, T. (2018). Mesozoic tectonic migration in eastern Junggar Basin. *Geotect. Metallogenia* 38, 52–61.
- Tian, P. F., Yuan, W. M., and Yang, X. Y. (2020a). Basic principles, important concepts and geological applications of thermochronology. *Geol. Rev.* 66, 975–1003.
- Tian, P. F., Yuan, W. M., Yang, X. Y., Feng, Z. R., Chen, X., and Yuan, E. J. (2020b). Multi-stage tectonic events of the Eastern Kunlun Mountains, Northern Tibetan Plateau constrained by fission track thermochronology. *J. Asian Earth Sci.* 198, 104428. doi:10.1016/j.jseas.2020.104428
- Wang, J. B., and Xu, X. (2006). Post collisional tectonic evolution and mineralization in Northern Xinjiang. *Acta Geol. Sin.* 80, 23–31.
- Wu, Z. J., Han, X. Z., Ji, H., Cai, Y. F., Xue, L., and Sun, S. J. (2021). Mesozoic-Cenozoic tectonic events of eastern Junggar Basin, NW China and their significance for uranium mineralization: Insights from seismic profiling and AFT dating analysis. *Ore Geol. Rev.* 139, 104488. doi:10.1016/j.oregeorev.2021.104488
- Xiao, W. J., Song, D. F., Windley, B. F., Li, J. L., Han, C. M., Wan, B., et al. (2020). Accretionary processes and metallogenesis of the Central Asian Orogenic Belt: Advances and perspectives. *Sci. China Earth Sci.* 63 (3), 33.
- Xiao, X. C., Tang, Y. Q., and Feng, Y. M. (1992). *Geotectonics of northern Xinjiang and its adjacent areas*. Beijing: Geology Press, 16–42.
- Yan, D. P., and Qiu, L. (2020). Geology of China and adjacent regions: An introduction. *J. Asian Earth Sci.* 203, 104533. doi:10.1016/j.jseas.2020.104533
- Yang, P., Wu, G. H., Ren, Z. L., Zhou, R. J., Zhao, J. X., and Zhang, L. P. (2020). Tectono-thermal evolution of Cambrian–Ordovician source rocks and implications for hydrocarbon generation in the eastern Tarim Basin, NW China. *J. Asian Earth Sci.* 194, 104267. doi:10.1016/j.jseas.2020.104267
- Yang, W., Jolivet, M., Guo, Z. J., Zhang, Z. C., and Wu, C. D. (2013). Source to sink relations between the tianshan and Junggar Basin (northwest China) from late palaeozoic to quaternary: Evidence from detrital U-Pb zircon geochronology. *Basin Res.* 22, 219–240. doi:10.1111/j.1365-2117.2012.00558.x
- Yang, Y. T., Guo, Z. X., and Luo, Y. J. (2017). Middle-late jurassic tectonostratigraphic evolution of central Asia, implications for the collision of the karakoram-lhasa block with Asia. *Earth Sci. Rev.* 166, 83–110. doi:10.1016/j.earscirev.2017.01.005
- Yang, Y. T., Song, C. C., and He, S. (2015). Jurassic tectonostratigraphic evolution of the Junggar Basin, NW China: A record of mesozoic intraplate deformation in central Asia. *Tectonics* 34, 86–115. doi:10.1002/2014tc003640
- Yuan, W. M., Dong, J. Q., Tang, Y. H., and Bao, Z. K. (2004). Thermal history of the Tereketi batholith in Altay Mountains, northern Xinjiang: Evidence from apatite fission track analysis. *Acta Geosci. Sin.* 25, 199–204.
- Zattin, M., and Wang, X. X. (2019). Exhumation of the Western Qinling mountain range and the building of the northeastern margin of the Tibetan Plateau. *J. Asian Earth Sci.* 177, 307–313. doi:10.1016/j.jseas.2019.04.002
- Zaun, P. E., and Wagner, G. A. (1985). Fission-track stability in zircons under geological conditions. *Nucl. Tracks Radiat. Meas.* 10, 303–307. doi:10.1016/0735-245x(85)90119-x
- Zhang, C. J., He, D. F., and Shi, X. (2006). Formation and evolution of multi-cycle superimposed Basin in junggar. *Pet. Geol.* 1, 47–58.
- Zhang, H. H., Zhang, Z. C., Tang, W. H., Li, K., Li, J. F., Wang, Q., et al. (2022). Burial and exhumation history of Jurassic sedimentary rocks in the southern margin of the Junggar Basin Implications for the growth of the northern Tianshan Mountains. *J. Asian Earth Sci.* 236, 105339.
- Zhang, Q. F., Hu, A. Q., and Zhang, G. X. (1994). Isotopic age evidence of Mesozoic Cenozoic magmatism in Altay area. *Geochemistry* 23, 269–280.
- Zhang, W. G., Chen, Z. L., and Cai, L. B. (2017). Fission track evidence of Cretaceous uplift exhumation in Western Tianshan. *Acta Geol. Sin.* 91, 510–522.
- Zhao, B. (1992). Formation and evolution of Junggar Basin. *Petroleum Geol. Xinjiang* 13, 191–196.
- Zhou, L. R., and Cai, H. W. (1990). Yanshan movement in Northwest China northwest geosciences. *Northwest Geosci.* 30, 64–78.
- Zhu, W. B., Wan, J. L., and Shu, L. S. (2005). Application of fission track technology in structural evolution. *Acta Geol. Sin.* 11, 593–600.
- Zhu, W. B., Wang, F. J., Cao, Y. Y., and Wang, S. L. (2020). Tectono-magmatic events in tianshan mountains and adjacent areas during yanshanian movement period. *Acta Geol. Sin.* 94, 1331–1346.
- Zorin, Y. A. (1999). Geodynamics of the Western part of the Mongolia-Okhotsk collisional belt, trans-Baikar region (Russia) and Mongolia. *Tectonophysics* 306, 33–56. doi:10.1016/s0040-1951(99)00042-6



OPEN ACCESS

EDITED BY

Wei Ju,
China University of Mining and
Technology, China

REVIEWED BY

Yuan Neng,
China University of Petroleum Beijing,
China
Guangyou Zhu,
Research Institute of Petroleum
Exploration and Development (RIPE),
China

*CORRESPONDENCE

Jinkai Xia,
✉ 1901110591@pku.edu.cn

SPECIALTY SECTION

This article was submitted to Structural
Geology and Tectonics,
a section of the journal
Frontiers in Earth Science

RECEIVED 13 November 2022

ACCEPTED 18 January 2023

PUBLISHED 02 February 2023

CITATION

Xia J, Zhong Z, Huang S, Luo C, Lou H,
Chang H, Li X and Wei L (2023), The proto-
type basin and tectono-paleogeographic
evolution of the Tarim basin in the
Late Paleozoic.
Front. Earth Sci. 11:1097101.
doi: 10.3389/feart.2023.1097101

COPYRIGHT

© 2023 Xia, Zhong, Huang, Luo, Lou,
Chang, Li and Wei. This is an open-access
article distributed under the terms of the
[Creative Commons Attribution License
\(CC BY\)](https://creativecommons.org/licenses/by/4.0/). The use, distribution or
reproduction in other forums is permitted,
provided the original author(s) and the
copyright owner(s) are credited and that
the original publication in this journal is
cited, in accordance with accepted
academic practice. No use, distribution or
reproduction is permitted which does not
comply with these terms.

The proto-type basin and tectono-paleogeographic evolution of the Tarim basin in the Late Paleozoic

Jinkai Xia^{1*}, Ziqi Zhong¹, Shaoying Huang², Caiming Luo²,
Hong Lou², Haining Chang¹, Xiang Li¹ and Lunyan Wei¹

¹The Key Laboratory of Orogenic Belts and Crustal Evolution, Ministry of Education, School of Earth and Space Sciences, Peking University, Beijing, China, ²Institute of Petroleum Exploration and Development, Tarim Oilfield Company, Korla, China

The Tarim basin is a large composite and superimposed sedimentary basin that has undergone complex multi-period and polycyclic tectonic movements. Understanding the proto-type basin and tectono-paleogeographic evolution of this complex superimposed basin is important for understanding the basin-mountain coupling and dynamical mechanisms of the Paleo-Asian and Tethys tectonic systems as well as hydrocarbon exploration and development. Based on previous works, together with the recent exploration, and geological evidences, three global plate tectonic pattern maps, four Tarim proto-type basin maps (in present-day geographic coordinates) and four regional tectono-paleogeography maps (in paleogeographic coordinates) during the Late Paleozoic are provided in this paper. Based on these maps, the proto-type basin and tectono-paleogeographic features of the Tarim basin during the Late Paleozoic are illustrated. The Devonian to Permian is an important period of terranes/island-arcs accretion and oceanic closure along the periphery of the Tarim block, and a critical period when the polarity of Tarim basin (orientation of basin long-axis) rotated at the maximum angle clockwise. During the Late Paleozoic, the periphery of the Tarim block was first collisional orogeny on its northern margin, followed by continuous collisional accretion of island arcs on its southern margin: on the Northern margin, the North and South Tianshan Oceans closed from East to West; on the South-Western margin, the Tianshuihai Island Arc gradually collided and accreted. These tectonic events reduced the extent of the seawater channel of the passive continental margin in the Western part of the basin until its complete closure at the end of the Permian. The Tarim basin was thus completely transformed into an inland basin. This is a process of regression and uplift. The Southwest of the Tarim basin changed from a passive to an active continental margin, through back-arc downwarping and eventually complete closure to foreland setting. The intra-basin lithofacies range from shelf-littoral to platform-tidal flat to alluvial plain-lacustrine facies. The tectonic-sedimentary evolution of the Tarim basin is strongly controlled by peripheral geotectonic setting.

KEYWORDS

Tarim basin, proto-type basin, tectono-paleogeography, Late Paleozoic, evolution

1 Introduction

As the largest interior basin in the world, Tarim basin is an outstanding natural laboratory to study proto-type basin and tectono-paleogeography. A clear determination of the proto-type basin of Tarim basin and its peripheral tectono-paleogeography can be useful to understand tectonic evolution of Paleo-Asian and Tethyan tectonic systems, to evaluate its resource potentials, and even to deduce the paleoclimate.

For these reasons, many studies have been performed to understand the dynamic evolution of basins and their relationship to paleogeography (Allen and Allen, 1990; Jia et al., 2004; Woodcock, 2004; Lin et al., 2012b; Ingersoll, 2012; Liu J. D. et al., 2014; Ingersoll, 2019). Numerous studies on tectono-paleogeography have also been performed in different areas and periods of the Tarim basin with different focuses: some focus on the development process of the Craton (Wang et al., 2017; Wang et al., 2019), some on the spatial and temporal spreading of the sedimentary facies' belts (Carroll et al., 1995; Zhang J. et al., 2007; Zhang J. et al., 2008; Wu et al., 2013; Li S. Z. et al., 2014; He et al., 2015) and some on the division of the stratigraphic sequence (Lin et al., 2009; 2012a; Zhao et al., 2009; Zhao et al., 2011). These studies have all made progress to varying degrees, and have provided guidance for hydrocarbon source rock evaluation and hydrocarbon exploration. However, due to the limited data or low accuracy, the maps compiled by different scholars in different periods have certain differences, mainly in the study area, sedimentary boundary, and microfacies distribution (Zheng et al., 2022). Moreover, with the progress of oil and gas exploration and development, there may still be some problems with these previous studies: 1) The previous paleo-plate tectonic patterns do not highlight the position of Tarim block. 2) The previous proto-type basin is only limited in the Tarim basin, lacking of overall analysis, and basin-mountain coupling processes. 3) The previous tectono-paleogeographic maps are still compiled in "fixed theory" (Feng et al., 2004; Hou et al., 2014). Therefore, it is necessary to carry out a new round of research on proto-type basin and tectono-paleogeography.

Based on numerous previous research results, the Tarim proto-type basins for each period of the Late Paleozoic were recovered using the latest field sections, drilling logs and seismic sections in this paper. In addition, the tectono-paleogeographic maps in each period were also given in conjunction with the investigation of peripheral plates of the Tarim basin to show the role of surrounding tectonic setting in controlling the basin interior. It is hoped that these maps will provide a basis for the interaction between the Tarim basin and the Paleo-Asian and Tethys tectonic systems, and provide fundamental supports for assessment of hydrocarbon exploration prospect in the Tarim basin.

2 Geological setting and plate tectonic configuration

The Tarim basin, a large-scale superimposed basin (Jia et al., 1997; He et al., 2007; Gao et al., 2017), is located in Central Asia, in the Xinjiang Province in China. It covers an area of $560 \times 10^3 \text{ km}^2$ and is the largest inland basin in China. It can be divided by seven first-order tectonic units: the Kuqa Depression, the Tabei Uplift, the Northern Depression, the Central Uplift, the Southwest Depression, the Southeast Faulted Uplift, and the Southeast Depression (He et al.,

2016). These seven first-order tectonic units are subdivided into 17 Secondary structural units (Figure 1A).

2.1 Tectonics and stratigraphy

Tectonically, the periphery of the Tarim basin underwent oceanic opening, subduction, oceanic closure, island arcs accretion, and collision processes during the Phanerozoic (Tapponnier et al., 2001; Xiao and Santosh, 2014). The processes reflect several phases of tectonism, magmatism, and metamorphism. Therefore, the tectonic environment around Tarim basin is quite complex (Figure 1A). The Tarim basin is separated from the Kazakhstan-Junggar block by the Tianshan Orogenic Belt to the North (Gao et al., 2013). The Tianshan Orogenic Belt is part of the Central Asian Orogenic Belt and is divided by two Paleozoic sutures (Windley et al., 1990; Allen et al., 1991; Ma et al., 2014) into three parts: the Northern Tianshan, Central Tianshan and Southern Tianshan. The Central Tianshan is also commonly referred to as the Yili-Central Tianshan Terrane together with the Yili block in the West (Allen et al., 1993). To the Southwest of the Tarim basin is the West Kunlun Orogenic Belt, which includes the North Kunlun, the Central, and South Kunlun, and the Tianshuihai Terrane (Zhang C. L. et al., 2019); to the Southeast are the Altyn-Qilian Island Arc, the Qaidam block, and Bayankala block. To the South are the North Qiangtang block, South Qiangtang block, Lhasa block and Himalayan Orogeny (Sobel and Dumitru, 1997; Pan et al., 2002).

Stratigraphically, the Tarim basin contains a pre-Sinian cratonic crystallized basement, above which a complete sedimentary sequence of the Sinian and Palaeozoic accumulated (Liu et al., 2016). During the Sinian and Paleozoic, marine calcareous, and terrigenous deposits were dominant until the Carboniferous (Laborde et al., 2019). A carbonate platform surrounded by passive continental margins and a deep shelf developed widely in the Cambrian and Ordovician, respectively. The Lower Silurian to Middle Devonian was dominated by sandstones of littoral deposits. A strong uplift event occurred in the late Middle Devonian, forming a regional unconformity (Figure 2) between the Middle and Upper Devonian. Shallow marine clastic rocks and limestone with biogenic limestone as interbeds occurred in the Carboniferous units (Li et al., 2015). The Permian sediments transition from bottom to top mainly from marine carbonates and sandstones to lacustrine or fluvial clastic rocks (Deledaer, 1996), with intervening volcanic rocks. After the Permian, marine deposition ceased in the Tarim basin with a change from calcareous to terrigenous deposits characterizing most of the Mesozoic sediments.

2.2 Plate tectonic configuration

The basis for recovering the proto-type basin and tectono-paleogeography is to understand the plate tectonic framework. Plate tectonic framework involves large-scale basin-mountain coupling and controls the formation and evolution of ocean-continent configuration, orogenic belts, and basins. Therefore, it can be used to reveal the process of ocean closure and orogenic uplift (Huang et al., 2023).

At present, most of the global plate tectonic evolution maps are reconstructed by Gplate software based on the global paleomagnetic database (Müller et al., 2018). However, large foreign plates are the

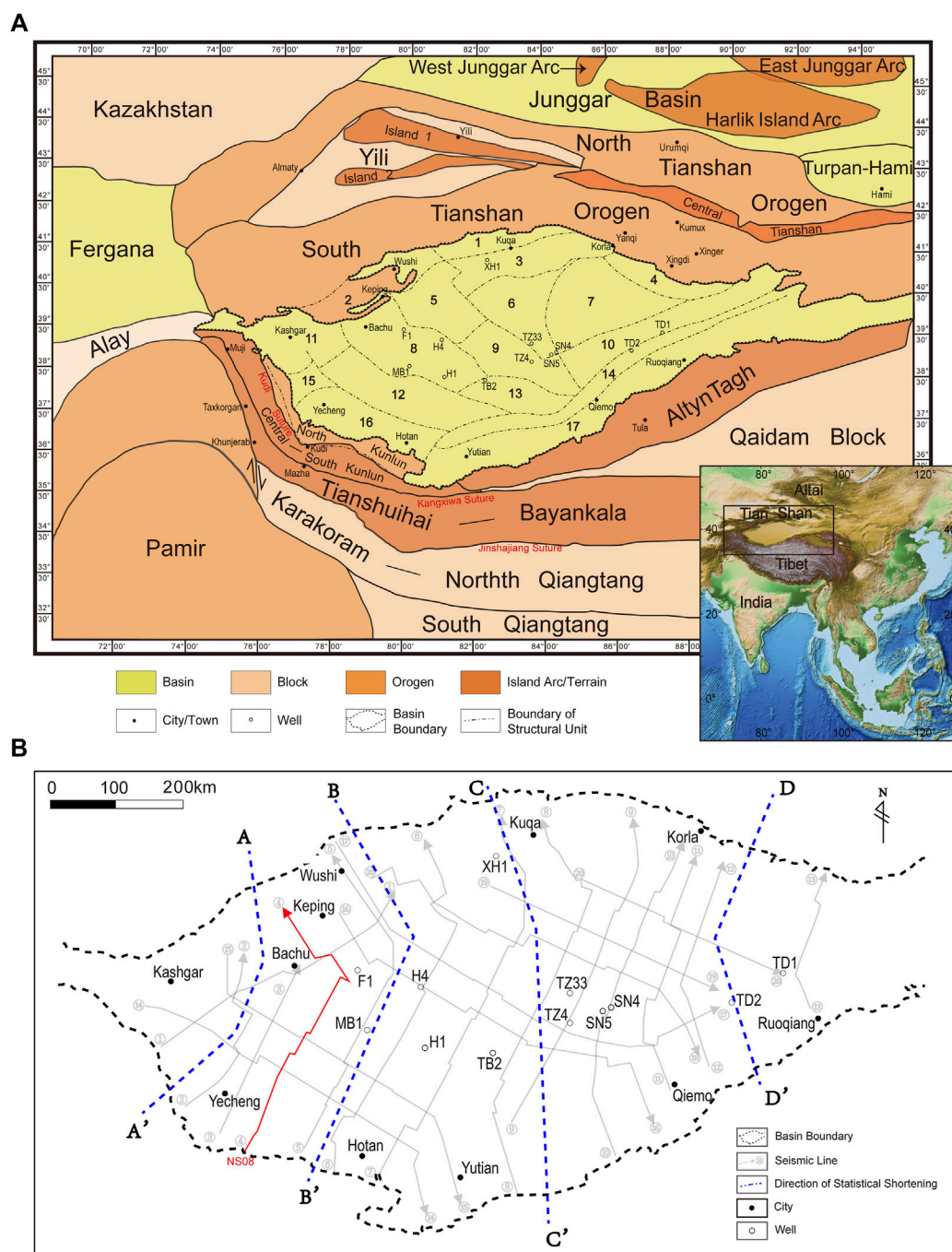


FIGURE 1

Schematic structural maps of the Tarim basin and adjacent areas, and location of the study area. **(A)** Schematic structural map of the Tarim basin and adjacent areas (modified after He et al., 2016); Structural units of Tarim basin: 1-Kuqa Depression; 2-Kalpin Faulted Uplift; 3-Tabei Uplift; 4-Kongque River Slope; 5-Awati Depression; 6-Shuntuguole Uplift; 7-Manjiaer Depression; 8-Bachu Uplift; 9-Tazhong Uplift; 10-Guchengxu Uplift; 11-Kashi Depression; 12-Maigaiti Slope; 13-Tangguzibas Depression; 14-Tanan Uplift; 15-Shache Bulge; 16-Yecheng Depression; 17-Southeast Depression. **(B)** Location of 20 basin-scale seismic sections used to calculate shortening. These shortening data are integrated on four representative lines (AA', BB', CC', and DD') (cf. Laborde et al., 2019). The seismic section NS08 and the balanced cross-section recovered from it are shown in Figure 5.

priority core plates, and the three plates in China (Tarim block, North China block and South China block) are not paid enough attention.

The three plates in China should be constrained by high-confidence paleomagnetic data (Huang et al., 2008; 2018) and tectonic comparison in geological affiliation. The positions of the three plates in China can be appropriately adjusted on the same latitude, but they cannot be adjusted

arbitrarily, and the spatial constraints between plates should be considered. The new global tectonic configuration in the Late Paleozoic is reconstructed by GPlate software based on the high-confidence paleomagnetic data (Huang et al., 2023).

In Devonian, the Tarim block, the North China Plate and the South China Plate were separated from the Gondwana continent and

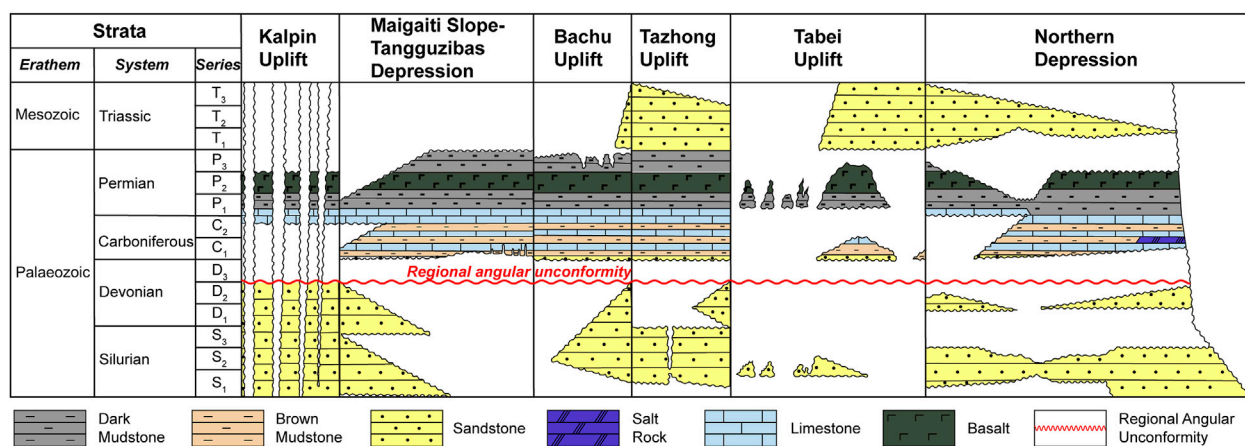


FIGURE 2
Silurian-Triassic tectonic-sedimentary evolution in the Tarim basin.

the Laurentia-Baltica-Siberia continent. The Tarim block was at around 15°N and formed a “ T_N^S ” pattern with the North China Plate and South China Plate. The Tarim block was generally in a “Western compression, eastern extension” tectonic setting: the Paleo-Asian Ocean (Paleo-Tianshan Ocean) westward subducted under the Siberian-Kazakh continent, the Paleo-Asian Ocean domain was contracting, and the Southern Kunlun/Southern Altyn Ocean to the east was expanding (Figure 3A).

In Carboniferous, Gondwana, and Laurasia merged to form the main body of Pangaea, laying the foundation for the basic pattern of global plate tectonics (Figure 3B). The Tarim block drifted northwards to about 25°N and the Paleo-ocean (North and South Tianshan Ocean) on the northern edge of the Tarim block entered a period of major closure (Han et al., 2006; Wang et al., 2007; Charvet et al., 2011; Han and Zhao, 2018; Alexeev et al., 2019). In the Late Carboniferous, Tarim block collided with Kazakh-Yili (Gao et al., 2009; Su et al., 2010; Han et al., 2011; Liu D. et al., 2014; Zhang et al., 2014a; Wang et al., 2022). By rotating clockwise, Tarim block gradually collided with Kazakhstan from east to west, forming the Kazakh Horseshoe Orocline (Abrajevitch et al., 2007; Götz and Hielscher, 2010; Li J. et al., 2014; Yi et al., 2015). At this time, the Tarim block ended its history of independent drift and became the southern edge of the Eurasian continent (Zhao et al., 2003; Xiao et al., 2008; Wilhem et al., 2012; Xiao et al., 2013). Tarim block regulated its position in relation to the other blocks in the Laurasia by rotating clockwise (Li et al., 2015).

During the Early-Middle Permian, the Western and middle segments of the Paleo-Asian Ocean had been closed, leaving only its Eastern segment unclosed. Tarim block joined the main body of Pangaea (Zhao et al., 2018). As a result of the crustal uplift caused by the late Hercynian tectonic movement, the seawater in the remnant bay of the Southwestern Tianshan area was gradually retreating Westward. The sedimentary environment within the basin also changed from marine to terrestrial (Chen et al., 2006; Luo et al., 2012; Zou et al., 2014). At the same time, the Tarim block produced intense volcanic activity, with large igneous provinces developing from 251 to 272 Ma. In the Late Permian (c. 270 Ma), Pangaea reached its largest scale, and was surrounded by the Panthalassa (Figure 3C). A series of orogenic belts, including the Central Asian Orogenic Belt and the Uralian Orogenic Belt, on the Laurasia and its periphery, resulting

in the final assembly of Pangaea (Li and Jiang, 2013). At the end of the Permian, the Paleo-Asian Ocean closed completely (Eizenhöfer et al., 2014; 2015a; 2015b), the Paleo-Tethys Ocean subducted northwards and the Neo-Tethys Ocean began to spread. Tarim block was located to the north of the Paleo-Tethys Ocean and had been collaged with the Eurasian plate to the North. After the assemblage of Pangaea, the positions between the plates were adjusted by strike-slip faults. The Tarim block was adjusted by a large left-lateral strike-slip fault.

3 Methodology and database

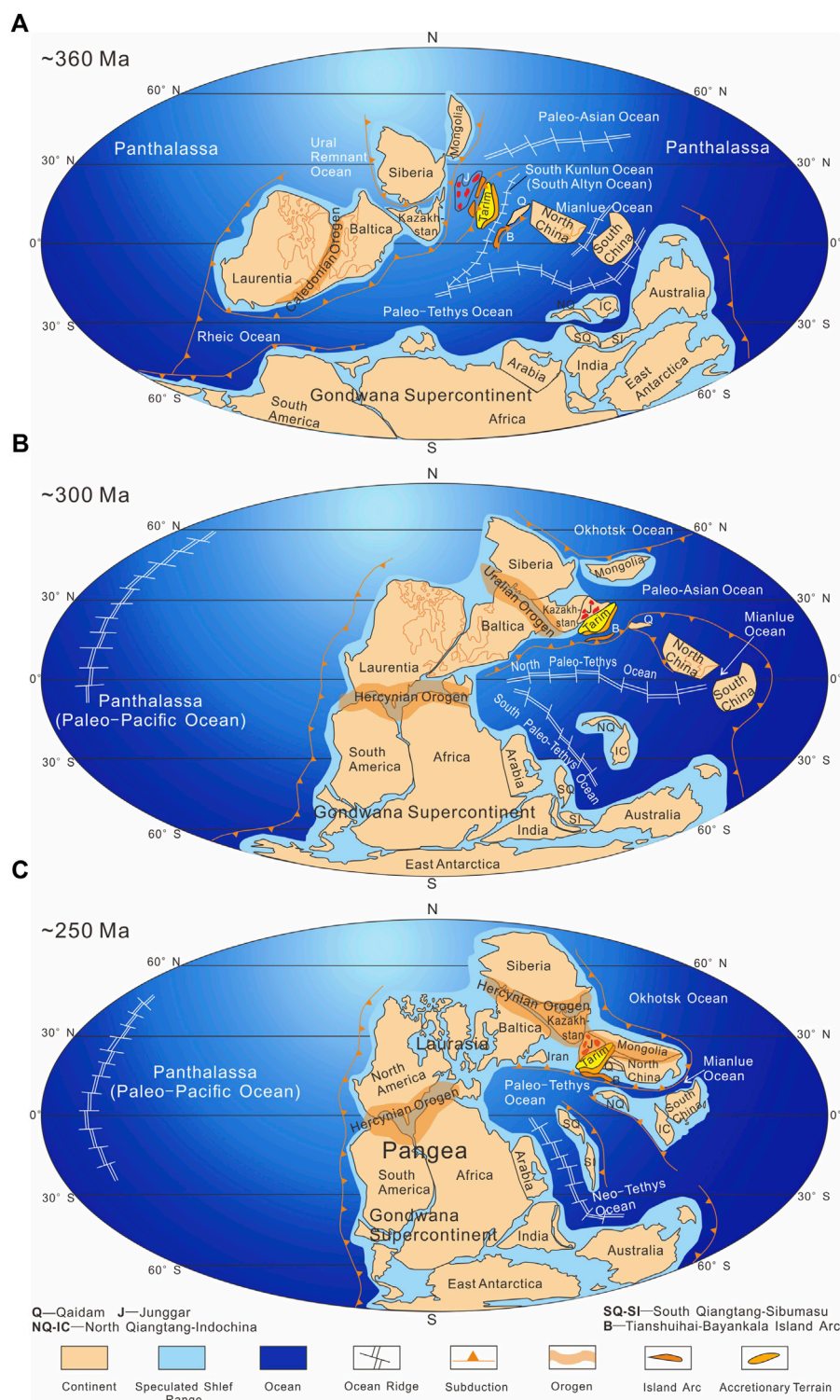
The proto-type basin analysis based on the thought of “mobile tectono-paleogeography”, which includes basin resetting, restoration, and reshaping (Hou et al., 2019; He et al., 2020), is the core of this study. Basin resetting is to restore the geotectonic position of the proto-type basin in its development period. Basin restoration is to restore the initial status of the proto-type basin, including its scope and sedimentary facies distribution. Basin reshaping is to restore the superposition and modification processes, mainly the restoration of the amount of elongation/shortening of the basin.

Specifically, there are four steps in creating proto-type basin maps with tectonic background.

Firstly, replenishing the erosion thickness and restoring the intact isopach maps of the Tarim basin, which is mainly based on the residual strata thickness (Figure 4) from Bureau of Geophysical Prospecting, China, according to the characteristics of the sedimentary thickness trends in the different basins. The thickness trend method can find the boundary of the proto-type basin with the help of the trend of the isopach in the isopach map, and it can also be analyzed by the trend surface of a certain thickness layer in the seismic profile (Zhang X. B. et al., 2007; Yu et al., 2016).

Secondly, extending the intact isopach maps outwards based on the amount of shortening (Table 1) counted by 81 balanced cross-sections (Lou et al., 2016; Laborde et al., 2019) to restore the pre-deformation deposition extent and proto-type basin boundary.

Thirdly, restoring the distribution of lithofacies (intra-basin and marginal facies) according to lithofacies-paleogeographic maps and isopach maps. When the lithofacies-paleogeographic maps contradict

**FIGURE 3**

Reconstructing of global plates distribution in Devonian Period (A), Carboniferous Period (B), and Permian (C).

the isopach maps, take the former as more credible due to the compilation of lithofacies-paleogeographic maps based on analysis of wells and outcrops in the whole basin.

Finally, completing the peripheral tectonic background of the Tarim basin according to the previous literatures and then obtaining the Tarim proto-type basin maps in the fourth chapter.

The maps compiled in this paper include two aspects: 1) The Tarim proto-type basin maps with peripheral tectonic setting under the current geographical coordinates in Late Paleozoic in the fourth chapter; 2) Tectono-paleogeographic maps of Tarim block and its peripheral areas under paleogeographic coordinates in Late Paleozoic in the fifth chapter.

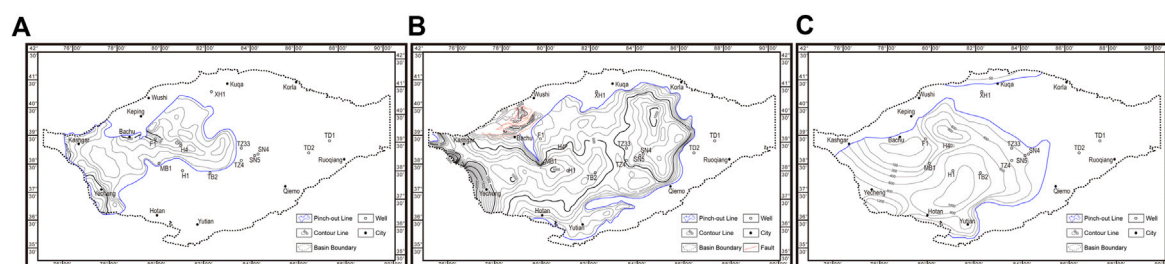


FIGURE 4

Residual strata thickness of Tarim Basin in Devonian Period (A), Carboniferous Period (B), and Permian (C).

The data used in this study include: the residual strata thickness of Tarim basin from Devonian to Permian (Bureau of Geophysical Prospecting, China), lithofacies distribution maps of Tarim basin in different periods of Late Paleozoic, 81 seismic sections and their balanced cross-sections, and some information on drillings and outcrops. These basic data are mainly provided by the Tarim Oilfield Company.

3.1 The residual thickness of the Tarim basin

Bureau of Geophysical Prospecting INC. has completed a set of residual thickness maps (Figure 4) based on the fine interpretation of basic seismic horizons in the Tarim basin, combined with information from drilling and geological outcrops. These residual thickness maps are the basis for recovering the original thickness distribution of the basin prior to deformation.

Based on the residual strata thickness in Figure 4, according to the characteristics of different type basins, restore the intact isopach map. For a marginal basin, the isopach should be open, outward, and asymmetric. While for an intracratonic basin, the isopach should be concentric and closed. If encountering a platform or a surficial sea, then the isopach should be symmetrical but with openings connected to the shelf or marginal sea. For other kinds, their isopach maps should also be restored in accordance with their characteristics and locations in the Tarim block.

3.2 The amount of shortening of the basin

It is key work to calculate the shortening amount according to the balanced cross-sections in reconstruction of proto-type basin. The balanced cross-sections can provide information on the elongation/shortening of the strata (Lin et al., 2015; Wang et al., 2020a; Wang et al., 2020b). The restoration process for balanced cross-sections, where the mass conservation principle is the basic criterion, is usually inverse, i.e., starting from a current interpreted structural cross section to its pre-deformed morphology (Dahlstrom, 1969; Zhang and Chen, 1998). The stratum length balance restoration method and the area balance restoration method (Jiang et al., 2018) are used in this study. And the restoration process is carried out in 3D-MOVE software, including three steps: compaction correction, fault displacement restoration and layer leveling. The stratigraphic lengths and the amount of shortening in each period can be obtain after restoring the balanced cross-sections.

Figure 1B shows the positions of 20 basin-scale sections used in this study for the statistics of basin shortening data. Among them, 10 balanced cross-sections are restored by us. Here, the NS08 section is taken as an example to show the shortening process of the basin (Figure 5).

Because the deformation mainly exists along the margin of Tarim basin, the total shortening of each section is distributed to its two ends according to the ratio of deformation at both ends (Figure 6). These shortening data are integrated on four representative lines (AA', BB', CC', and DD') (Figure 1B; Table 1). The extension or shortening amount measured in this paper is from Devonian, Carboniferous, and Permian to Cenozoic. Data since the Cenozoic are referenced from Laborde et al. (2019).

The foreland (mountain front) zone is the main deformed part of the proto-type Tarim basin, with the largest proportion of Cenozoic shortening accounting for 70–90%. Overall, the distribution of shortening in the marginal segments of the Tarim basin shows a certain regularity: the shortening decreases from west to east, which is probably due to the increasing distance from the Pamir tectonic syntax.

4 Reconstruction of Tarim proto-type basin in the Late Paleozoic

4.1 Late devonian: A back-arc extensional basin in the southwestern Tarim basin

In the Early-Middle Devonian, Tarim basin basically inherited its Silurian sedimentary framework (Li et al., 2015). By the end of the Middle Devonian, the Early Hercynian Movement made the Tarim basin strongly uplifted and subjected to denudation and planation, forming a regional angular unconformity (Liu et al., 2008) (Figure 2) between the Middle and Upper Devonian. The tectonic framework of the Tarim basin undergone important changes as a result of the Early Hercynian movement (Huang, 1986; He et al., 2005; Li et al., 2015; Wu et al., 2016), which made the basin present a tectonic environment of “compression in the northeast and southeast, extension in the southwest” (Figure 7A). The northeast and southeast of Tarim basin uplifted strongly, forming the denudation areas in these regions (Figure 7A). The compression from these two directions caused the basin to tilt uplift from East to West, showing a pattern of “Eastern uplift, Western depression” (Lin et al., 2012b), and seawater mainly invaded the basin from the West (Hu et al., 2010; Ma et al., 2019). The

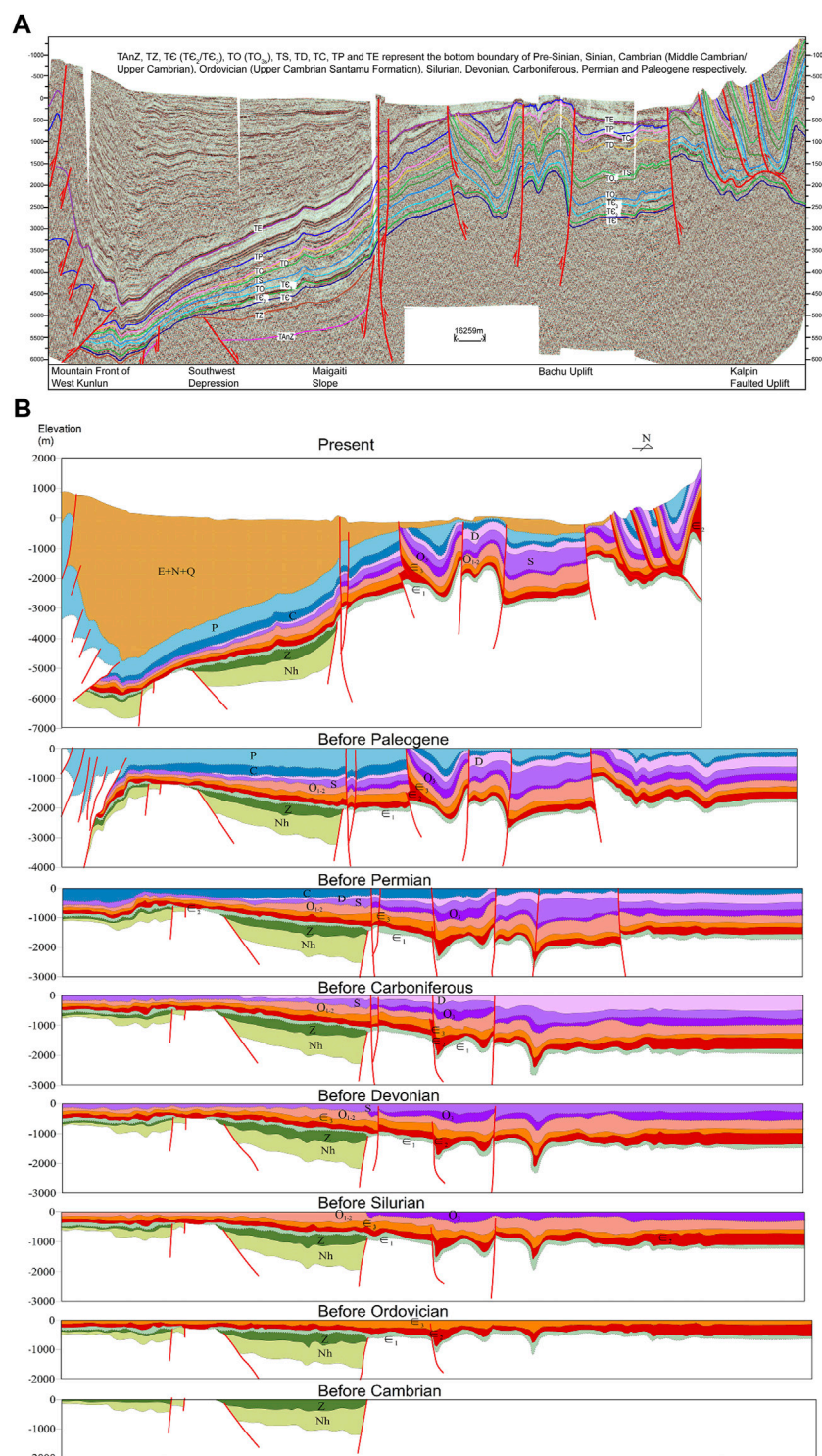


FIGURE 5

Geological interpretation of seismic section NS08 (A) and its recovered balanced cross-section (B). The location of seismic section NS08 is shown in Figure 1.

Southwest of Tarim basin changed from passive continental margin to back-arc extensional environment (Figure 7A).

There were several inherited paleo-uplifts in the basin, including Shaya Uplift in the North, Tadong Uplift in the East and Tanan Uplift in the South (Chen, 2000). The basin formed an open-sea basin with

Westward opening and a tectonic depressive bay basin centered on the Awati Depression (Ma et al., 2019) (Figure 7A).

It is controlled by the paleo-geomorphic background that the shelf-shore facies (Liu et al., 2016) were mainly developed in the basin from West to East (Figure 7A). Tarim basin was surrounded by shallow

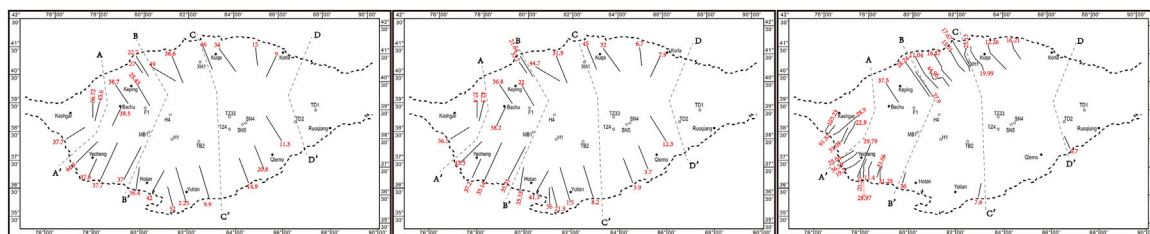


FIGURE 6
Distribution of shortening at the basin margin calculated from each seismic section.

continental shelf, the Western part of which was relatively open with huge thickness turbidite clastic rocks (Lin et al., 2011). From west to east, the sedimentary environment showed a changing trend from shelf-shore to backshore-delta around the paleo-uplift (Figure 7A). Shelf facies mainly developed gray-green mudstone intercalated with thin siltstone, shore facies mainly developed tabular cross bedding and low angle cross bedding quartz sandstone (Zhang H. et al., 2009). Delta facies developed in well TB2 and estuarine facies developed in well TZ4 (Xu, 2009; Jia et al., 2017) (Figure 7A). Marginal facies such as deltas (Figure 7A) indicated the boundaries of proto-type basin and the major provenance areas. The quartz sandstone of the lower sandstone section of the Donghetang Formation was deposited in the Bachu-Maigaiti area. The Kalpin paleo-uplift in the North and the Madong paleo-uplift in the South provided sufficient clastic materials, forming a shelf-shore sedimentary system, and the sand body sedimentation gradually migrated Eastward (Su, 2019). The H1 well area received provenance from the southern paleo-uplift in the basin (Figure 7A), and developed gravelly shore facies (Zhu et al., 2016). The Kuqa area received the provenance from the Tabei paleo-uplift and the Xingdi area (Su, 2019).

It is the tectonic background around the basin that controlled the above phenomena in the basin. On the periphery of the basin, the eastern segment of the South Tianshan Ocean began to shrink and the western segment was still expanding (Figure 7A). The Central-South Kunlun Island Arc, which was collaged to the southwestern margin of the Tarim basin at the end of the Early Paleozoic (Matte et al., 1996; Zhang Y. et al., 2019), was a low underwater uplift (Figure 7A). The

Southern Kunlun Ocean lied between the continental margin of the Southwest margin of Tarim basin and the Tianshuihai Island Arc, which began to move to the southwest of the Tarim basin. The Altyn-Qilian Island Arc, which was collaged to the Southeast edge of Tarim basin at the end of the Early Palaeozoic (Xu et al., 2011), had become a part of the Southeast Uplift. The Southern Altyn Ocean, which existed between the Altyn—Qilian Island Arc and Qaidam block, subducted northward, causing the Southeastern Tarim basin to continuously uplift (Figure 7A).

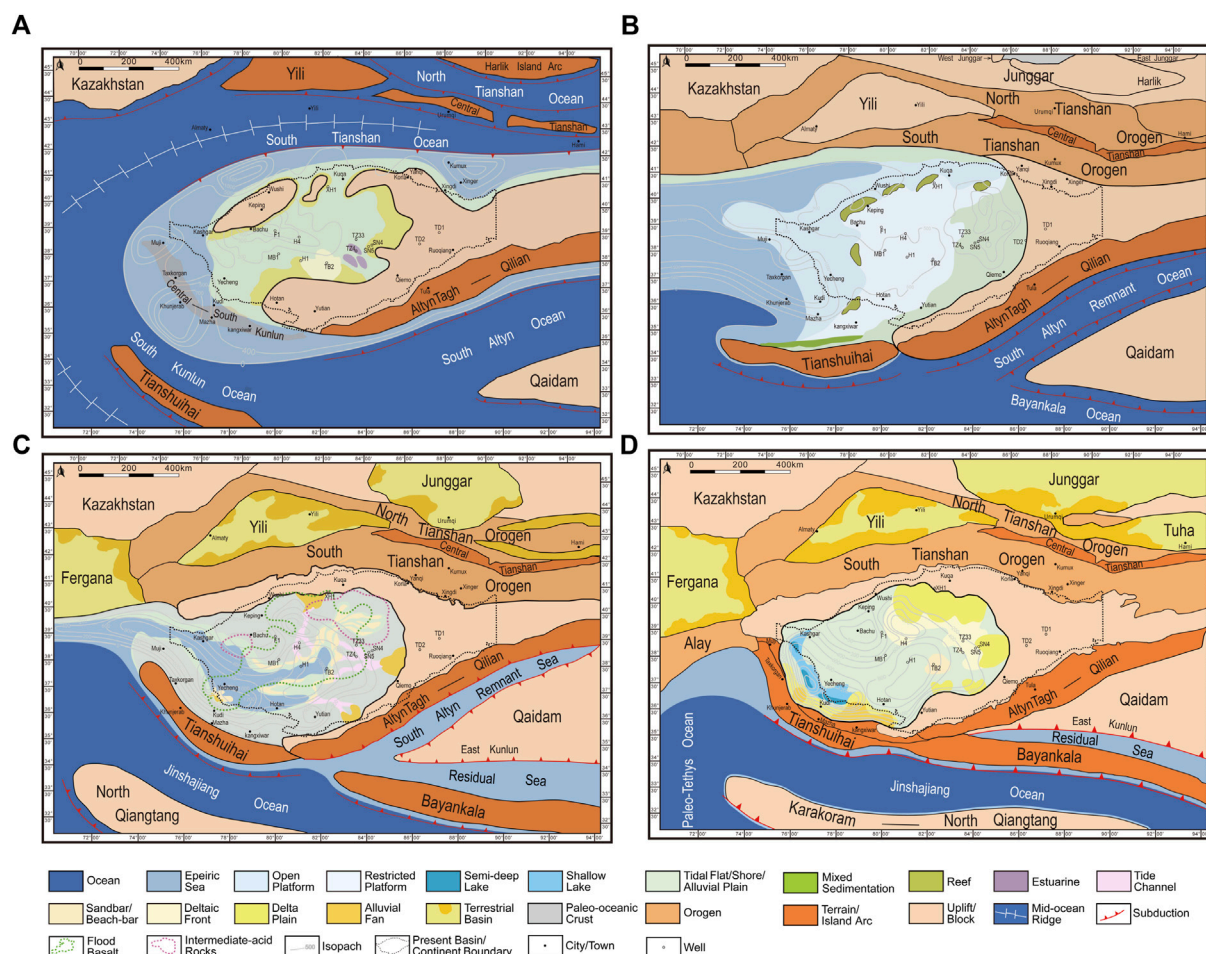
4.2 Late carboniferous: Transition from a back-arc extensional basin to a back-arc downwarping basin in the southwestern Tarim basin

From the beginning of Carboniferous, the Tarim block generally subsided and undergone extensive marine transgression (Zhuang et al., 2002; Ma et al., 2019). There were marked differences in the paleogeography and the width of the sedimentary facies expressed due to their location (Figure 7B).

The range of the proto-type basin changed significantly (Figure 7B). The boundary of the proto-type basin in the East starting from the Westernmost part of the Kongque River Slopes, passing through the Manjiaer Depression to the south and reaching the Guchengxu Uplift. At the junction of the south side of Guchengxu Uplift and the Southeastern Fault-Uplift, the boundary turned

TABLE 1 Shortening amount of Tarim Basin between Devonian, Carboniferous, Permian Periods and present (/km).

Distribution of the shortening amount	Cenozoic	Devonian	Carboniferous	Permian
	Period	Period	Period	Period
North margin of AA'	36.00	39.88	38.68	37.50
South margin of AA'	32.00	41.30	41.00	36.68
North margin of BB'	21.00	31.03	30.51	25.80
South margin of BB'	35.00	40.43	40.05	36.00
North margin of CC'	22.00	38.87	36.30	17.80
South margin of CC'	0.90	9.02	8.88	7.60
North margin of DD'	~0	12.00	7.30	~0
South margin of DD'	0.30	16.05	8.00	6.70



southwest and basically extended parallel to the Southeastern Fault-Uplift to the southern Tarim basin.

In terms of the Uplift-Depression Framework, the entire Tarim basin still maintained the overall geomorphology of high in the East and low in the West (Xie et al., 1997; Zhang G. et al., 2007) (Figure 7B), specifically manifested as ring uplifts in the North, East, and southeast (Li et al., 2015), and depressions in the central and Western regions (Figure 7B). The Northeast of the basin was the main denudation area. The middle part was an intracraton depression (Zhang G. et al., 2007), with stable sedimentation.

Within the Tarim proto-type basin, the large areas (such as Kuqa Depression, Shaya Uplift, and Kalpin Uplift) West of the Kongque River Slopes in the Northern part of the basin were submerged due to the transgression from Southwest to Northeast (Xie et al., 1997) (Figure 7B). The area with larger relative water depth was in the west of Kuqa Depression. The water depth of Shaya Uplift to the South was relatively shallow. In general, the basin developed interactive marine and terrestrial deposits and marine carbonate rocks deposits (Carroll et al., 1995) (Figure 7B). The Carboniferous System was generally 500–1000 m thick, and its loss in Eastern and Southeastern Tarim basin was caused by uplift and denudation in the late stage (He et al., 2005; Wu et al., 2020).

From East to West, tidal flat facies, restricted platform facies, the open platform facies, and shallow marine shelf facies developed in

sequence (Ye et al., 1997; Pu et al., 2014) (Figure 7B). The tidal flat facies developed in the Eastern part of the basin were in the form of NE-SW trending strips, the width of which was greater within the Guchengxu Uplift and the Manjiaer Depression (Figure 7B). The tidal flat facies mainly developed mudstone and limestone during the sedimentary period of Xiaohaizi Formation (Gu et al., 2003). For example, the Xiaohaizi Formation of well TZ33 drilled limestone with a single layer thickness of more than 5 m and mudstone with a relatively thin layer thickness. The restricted platform facies had the largest distribution range, occupying most of the central Tarim basin (Figure 7B). The lithology of restricted platform facies was mainly gray thin-layer mudstone and medium-thick layered limestone, with argillaceous limestone developed locally. On the outside of the restricted platform, there was the band-shaped high-energy facies (Xu, 2009) with unstable width between the restricted platform and the open platform (Figure 7B). The high-energy facies band in the platform had an S-shaped trend, which might be related to the two finger-shaped residual bays left in the west and southwest of the Tarim basin (Figure 7B). In the high-energy zone, the platform margin reef was mainly developed along the S-shaped platform margin (Guo et al., 2018), and its lithology was mainly bioclastic limestone. The outside of the high-energy zone was open platform facies, which

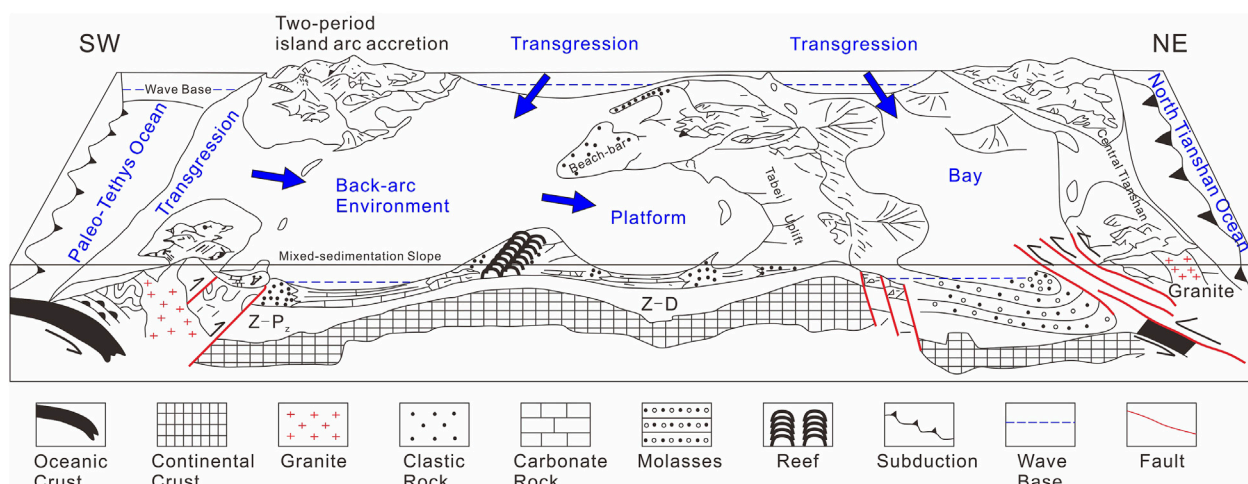


FIGURE 8

Carboniferous-Permian proto-type basin configuration in Tarim basin (modified according to He et al., 1992; Gong, 2010; Zhou et al., 2014).

was mainly composed of continuously deposited thick layers of limestone (dolomite), but generally mud rocks were not developed (Qi et al., 2020). There was a mixed sedimentation zone (Figure 7B) in Southwest of the Tarim basin, which was similar to the foreland basin on the Eastern side of the Andes.

The Tianshuihai Island Arc began to collapse and approach, but it had not completely closed the Tarim basin (Figure 7B). The South Kunlun Ocean shrunk further and was close to almost closure. The Southwestern Tarim basin changed from a back-arc extensional basin to a compressive downwarping basin. Currently, the Southwestern margin of the Tarim basin was the active continental margin (Li et al., 2015) (Figure 8). The residual ocean of the South Altyn lied between the Qaidam and Tarim block. The subduction zones in the north and south of Qaidam block were both subducted towards it (Figure 7B).

4.3 Late Middle Permian: Transition from back-arc flexural basin to foreland basin

Since Permian, large-scale regression occurred in the western Tarim basin (Liu et al., 1994; Liu X. et al., 2014), and the eastern Tarim basin became the uplift erosion area. During the Middle Permian, the Paleo-Tethys Ocean south of the Kangxiwar Fault continued to subduct to the Tarim block (Hofmann et al., 2011; Yang et al., 2011; Liu K. et al., 2014; Zhang Y. et al., 2019) (Figure 7C), which further developed the southwest back-arc flexural basin. Increased orogenic activity in the northern Tarim block uplifted the eastern and northern parts of the basin, accompanied by large-scale intermediate-acid volcanic magmatism (Liu et al., 2016) (Figure 7C).

The range of the proto-type basin changed greatly (Figure 7C). From the north side of the Kalpin Fault-Uplift to the east, including most of the Kuqa Depression and the eastern Shaya Uplift were uplifted and exposed to erosion. East of the central part of the Manjiaer Depression, the central part of the Guchengxu Uplift and

most areas east of Southeastern Fault-Uplift were uplifted and eroded (Qi et al., 2020). Overall, the Tarim basin was surrounded by a semi-enclosed uplift in the northwest, north, east, and southeast, along with an island arc belt developed in the southwest, as a residual epeiric sea that might open only in the west (Zhu et al., 2007) (Figure 7C).

The central and eastern Tarim basin in the Middle Permian was a westward sloping intra-cratonic depression basin (Chen X. et al., 2013). The paleo-geomorphological features were generally shallow in the southeast and deep in the northwest, with the greater water depth in the NE-E direction.

A set of residual shallow sea and tidal flat deposits were developed in the western basin (Ye et al., 1997) (Figure 7C). The residual shallow sea was mainly developed in the southwest of the basin, extending eastward into two branches (Figure 7C). The northern branch extended northeast to the eastern part of the Madong Thrust Belt, and the southern branch extended eastward to the western part of the Southeastern Fault-Uplift. Alluvial fans of varying sizes developed within the mud flat deposits. Typical wells drilled in mixed flat deposits, such as well SN5, were dominated by mudstones and silty mudstones, interbedded with thin to medium bedded fine sandstones and gravel-bearing fine sandstones (Qi et al., 2020). Banded mixed-flat deposits were developed between residual shallow sea and mud flat. At the same time, beach sandbars were more developed in the mixed flat, especially in the frontal area of the braided river (Figure 7C). The emergence of the thousand-meter continental molasse (He et al., 2005) in the Duwa Formation in southwestern Tarim basin indicated that a back-arc foreland basin was formed in southwestern Tarim basin (Zou et al., 2014; He, 2022).

Besides sedimentary rocks, plenty of magmatic rocks were developed in the western part of Tabei Uplift, Bachu Uplift, Tazhong Uplift, Southwest Depression, Awati Depression and western Manjiaer Depression, and their rock types mainly included basic basalt, diabase, gabbro and alkaline syenites (Liu et al., 1994; Chen et al., 2006).

4.4 Late Permian: A closed terrestrial intra-cratonic basin in whole

At the end of Permian, the Southern Tianshan area was completely orogenic uplift with the shrinkage of the residual sea in the southwest Tianshan area (Carroll et al., 1995). Alay area uplifted and transformed into an orogenic belt (Figure 7D). At the same time, Tarim basin was fully integrated into the Paleo-Eurasia continent (Zhao et al., 1990), and only the Paleo-Tethys Ocean existed on its South side. The continuous Northward subduction of the Paleo-Tethys Ocean (Xiao et al., 2003; Schwab et al., 2004; Robinson et al., 2007; Zhang Y. et al., 2019; Zhang et al., 2020) resulted in the complete collage and collision of the Tianshuihai Island Arc with the Tarim block (Li H. et al., 2014), which eventually closed the opening of the Western Tarim block (Figure 7D). Therefore, the main characteristics of the paleogeographic pattern of Tarim block and its surrounding areas in the Late Permian were that the sea water had completely retreated, and Tarim basin became a closed terrestrial intra-cratonic basin in whole (He et al., 2013; Ma et al., 2019) (Figure 7D).

Compared with the Late Carboniferous and Middle Permian, the proto-type basin at the end of the Permian was narrowed in the southwest (Figures 7C, D). In the Southern part of the basin, the proto-basin marginal uplift extended Westward. The proto-type basin in the east is basically bounded by the large uplift area.

The continuous uplift in the southeastern Tarim basin resulted in great changes in the uplift-depression framework of the Late Permian. Specifically, the paleogeomorphology changed from the former marine facies and residual marine facies of “high in the east and low in the west” into the closed lacustrine facies (Qi et al., 2020). Geomorphologic features also showed the typical lake-basin landscape of “high at the edge and low in the middle”. The area with the greatest water depth was distributed in NW-SE direction.

At the end of Permian, lacustrine facies—lacustrine delta facies—coastal plain facies deposits were mainly developed in the Tarim basin (Zhu et al., 2007) (Figure 7D). There were narrow lacustrine deposits only in the southwest of the basin (He et al., 2013). There were deltas/fan deltas deposits on the inner edge of the basin, and the rest of the basin was alluvial plain. Three provenance systems were mainly developed in the North, East, and Southwest of the basin (Chen S. et al., 2013). The delta in the Northern part of the basin was a large delta system composed of overlapping delta lobe bodies. The delta front could be pushed southward to the Southern part of Awati Depression and the central part of Shuntuoguole lower uplift. In the Eastern part of the basin, a nearly EW-trending delta system was developed (Figure 7D), and the deltaic front could move westward to the central region of the Katak Uplift. Typical well drilled in this delta deposit was SN4 well. In addition, a relatively large deltaic front beach bar sand body (Figure 7D) was also developed outside the delta front (central area of Tanggubasi Depression). There were three semi-deep lake areas in Southwestern Tarim basin, which might be potential source-rock development areas.

In summary, the Tarim basin was in the regional tectonic background of plate convergence during the Carboniferous-Permian, a transitional stage from plate spreading regime to plate collision regime. The Northern Tarim basin became a foreland basin (Carroll et al., 1995) due to the closure of the Southern Tianshan Ocean. In contrast, the Southwestern Tarim basin entered a period of

transition from a back-arc extensional basin to a foreland basin through a downwarp basin, and was by no means an open passive continental margin (Figure 8), as supported by the mixed coastal-clastic shore facies deposited here. Only the extensive sea shelf existed as a seawater channel in the western part of the Tarim basin. The Carboniferous-Permian basin genesis of the Southwestern Tarim basin was relatively similar to the Cenozoic Western Pacific trench, arc and basin system.

5 Reconstruction of tectono-paleogeography around the Tarim basin

Tectono-paleogeography is an important part of the research in multicycle superimposed sedimentary basins. Evolution of sedimentary basins is closely related to surrounding tectonic setting (Zhang et al., 2016; Wu et al., 2020). In reverse, the study of tectono-paleogeography can provide feedback for the proto-type basin analysis above to see if there are any improprieties. Sorting out the late Paleozoic tectono-paleogeography evolution of Tarim basin can offer an intuitive picture of how Tarim basin and its surrounding areas evolved and the tectonic factors driving these evolutions.

The tectono-paleogeographic maps in paleo-latitudinal coordinates have a range between the global plate tectonic maps and the proto-type basin maps and are integrations of the two.

Firstly, the proto-type basin maps are rotated in accordance with the paleolatitude and long axis direction of the Tarim block in the global plate maps. Then, the range of the span of about 30° latitude and 40° longitude is selected in this paper. According to the paleogeographic spatial pattern of the Tarim block and its surrounding plates, the proto-type basin maps are extended outwards to the periphery of the basin under the paleolatitude geographical coordinates. Finally, the paleogeographic information of the peripheral plates is supplemented to compile the tectono-paleogeographic maps of the Tarim block for each period.

5.1 Devonian tectono-paleogeography

In Devonian, the Tarim block was independently dissociated between the Gondwana continent and Siberia-Kazakhstan continent (Figure 9A). Siberia and Kazakhstan were separated by the ocean and were not yet united as a continent (Windley et al., 2007). The southeastern edge of Siberia and the eastern edge of Kazakhstan were shallow-sea continental shelf (Golonka et al., 2006; Zhang G. et al., 2019) (Figure 9A). Siberia and Kazakhstan were approaching Tarim block due to subduction of the Paleo-Asian Ocean, while Junggar Island Arcs were between the Siberia-Kazakhstan and Tarim blocks (Xiao et al., 2009; Carmichael et al., 2019). The North and South Tianshan Oceans were both subducted bidirectionally (Charvet et al., 2011; Ge et al., 2012; Guo et al., 2013; Han and Zhao, 2018).

The Western side of the North Tianshan Ocean subducted beneath the Harlik Island Arc (part of the Chinese North Tianshan Arc system) (Carmichael et al., 2019; Zhang et al., 2021), while the Eastern side subducted eastwards beneath the Yili-Central Tianshan Island Arc (Ren et al., 2017). In addition, the Southern Tianshan Ocean also subducted westwards (Figure 9A), resulting in the both

sides of the Yili-Central Tianshan Island Arc were clipped under the subduction zone and continued to develop (Han and Zhao, 2018; Huang et al., 2020).

The South Tianshan Ocean tended to close in the north, but it was still expanding in the South. It was shaped like a “bell-mouth” with the opening facing South (Figure 9A). In the eastern part of the Tarim block, the Central-South Kunlun and Altyn Island Arcs collided with the Tarim block as early as the end of the Ordovician due to the Late Caledonian Movement (He et al., 2011; Zhang et al., 2015; Dong et al., 2018). The Central-South Kunlun Island Arc was already submerged, with a wide passive margin to its southeast, across the South Kunlun Ocean from the Tianshuihai Island Arc (Dong et al., 2021) (Figure 9A). The South Altyn ocean subducted to the west, contracting the oceanic domain and causing continued uplift to the southeast of the Tarim block. The Tianshuihai Island Arc and Qaidam block were in a “Western extension, Eastern compression” tectonic environment, with the north-western side of the Paleo-Tethys Ocean subducting beneath the Tianshuihai Island Arc and Qaidam block (Figure 9A). In terms of land-sea framework, the Southern and Southeastern edges of Qaidam block and the Southwestern edge of North China plate were shallow-sea continental shelf (Figure 9A), and there was an ocean between Qaidam block and North China plate (Golonka et al., 2006; Li et al., 2018).

5.2 Carboniferous tectono-paleogeography

The tectono-paleogeographic map (Figure 9B) of the Tarim block at the end of Carboniferous showed that with the clockwise rotation of Mongolia, the middle part of the Paleo-Asian Ocean in southern Mongolia contracted, and the Southern edge of Mongolia was shallow marine environment (Hou et al., 2014; Liu et al., 2017). The Ural Ocean closed and formed orogenic belt (He et al., 2013). The Kazakh and Siberian plates collided, with the Siberian Sea remaining between them (Figure 9B). The southern part of Kazakhstan was shallow-sea continental shelf, and the gulf extended to the central part of Kazakhstan (Wan and Zhu, 2007), with lake basins developed on the continent (Ma et al., 2020). Affected by the closure of the North and South Tianshan Ocean (Charvet et al., 2011; Alexeiev et al., 2019) and the collision between Tarim block and Yili-Central Tianshan Island Arc (Han et al., 2011; Liu D. et al., 2014; Zhao et al., 2018; Wang et al., 2020), the oceanic crust of the Junggar arc system disappeared and the new continental crust was formed, but shallow sea remained overlying (Figure 9B). In Southwestern Tarim block, the demise of the South Kunlun Ocean caused the Tianshuihai Island Arc to begin colliding with the Tarim block. The Northern, Eastern, and Southern parts of Tarim block were raised in a half-ring shape, forming a sea basin that opened to the West. As the Southwest Tianshan did not completely close (Liu et al., 1994; He et al., 2005), the remaining remnant bay connected with the shallow sea in the Southern Kazakhstan through the Western opening of Tarim block (Figure 9B). To the South of the Tianshuihai Island Arc, the Paleo-Tethys Ocean subducted towards Tarim block (Zhang et al., 2022), resulting in the Southern Tarim block being an active continental margin (Figure 9B). Between Qaidam and Tarim block was the South Altyn Remnant Ocean, and the subduction belts existed on both the north and south sides of the Qaidam block (Figure 9B).

5.3 Late Middle Permian tectono-paleogeography

The Middle Permian tectono-paleogeographic map (Figure 9C) of the Tarim block showed that the Kazakhstan inherited its late Carboniferous pattern (Van der Voo et al., 2006). On the one hand, the southward subduction of the Okhotsk Ocean closed the middle part of the Paleo-Asian Ocean in the south of the Mongolia plate to form the residual sea (Figure 9C); on the other hand, due to the convergence and compression, the Junggar and Tianshan Orogenic Belts were integrated into the magnificent Central Asian Orogenic Belt (Figure 9C). The Tarim block continued its clockwise rotational adjustment. The remnant bay in the Southwest Tianshan region disappeared (Carroll et al., 1995) and the Fergana and Yili area developed into terrestrial basins (Clarke, 1984; Moisan et al., 2011). The Paleo-Tethys Ocean continued to subduct northwards (Cocks and Torsvik, 2013; Xiao et al., 2013), resulting in continuous collision between the Tianshuihai Island Arc and the Tarim block (Zhang Z. et al., 2009). The west opening of Tarim block was further closed, and only a narrow channel (Figure 9C) was left as the channel for the withdrawal of seawater. The North and South sides of Qaidam-North Qilian block were both remnant sea, and the Bayankala Island Arc in the South was approaching to the north. North China plate also joined the Pangea supercontinent and was surrounded by shallow-sea continental shelf (Zhao et al., 2018). Central North China and Western Mongolia were lacustrine facies (Figure 9C), and there were shallow marine facies between North China and Mongolia plate (Jolivet, 2015; Niu et al., 2021). The North Qiangtang block was in a shallow marine environment (Hou et al., 2014; Zhang G. et al., 2019) between the Eastern Paleo-Tethys Ocean and Mianlue Ocean.

5.4 Late Permian tectono-paleogeography

As shown in Figure 9D, the Central Asian Orogenic Belt continued to increase in size as the withdrawal of seawater and uplift orogeny in southern Kazakhstan at the end of the Permian (Korobkin and Buslov, 2011; Ma et al., 2020). A remnant marine environment lied between the Iranian plate and the Fergana basin (Figure 9D). The range of uplift of the Mongolia plate also increased, with only a bay remaining to its east. At the same time, the Alay uplift orogeny (Gao et al., 2019) completely withdrew the seawater from the Tarim basin, which was thus transformed into terrestrial deposits (Carroll et al., 1995; Chen et al., 2006; He et al., 2013; Zou et al., 2014; Li et al., 2021). There were lacustrine deposits in the southwest of the Tarim basin (Figure 9D), and the peripheral foreland basin was generally developed. North China plate collided with Mongolia plate (Zhao et al., 1990) and the Qaidam-Qilian block had also been collaged with the Tarim block (Jolivet, 2015) (Figure 9D). Blocks such as Qiangtang in the south pushed northwards (Song et al., 2015; Xu et al., 2015; Hu et al., 2022; Ju et al., 2022), and the Paleo-Tethys Ocean continued to subduct beneath the Eurasian continent to the North (Pullen et al., 2008; Xiao et al., 2013; Yan et al., 2016; Li et al., 2020).

In conclusion, the Tarim block maintained clockwise rotation in the Late Paleozoic (Figures 9A–D), and the rotation angle of the Tarim block in the Late Paleozoic is much more than the other periods.

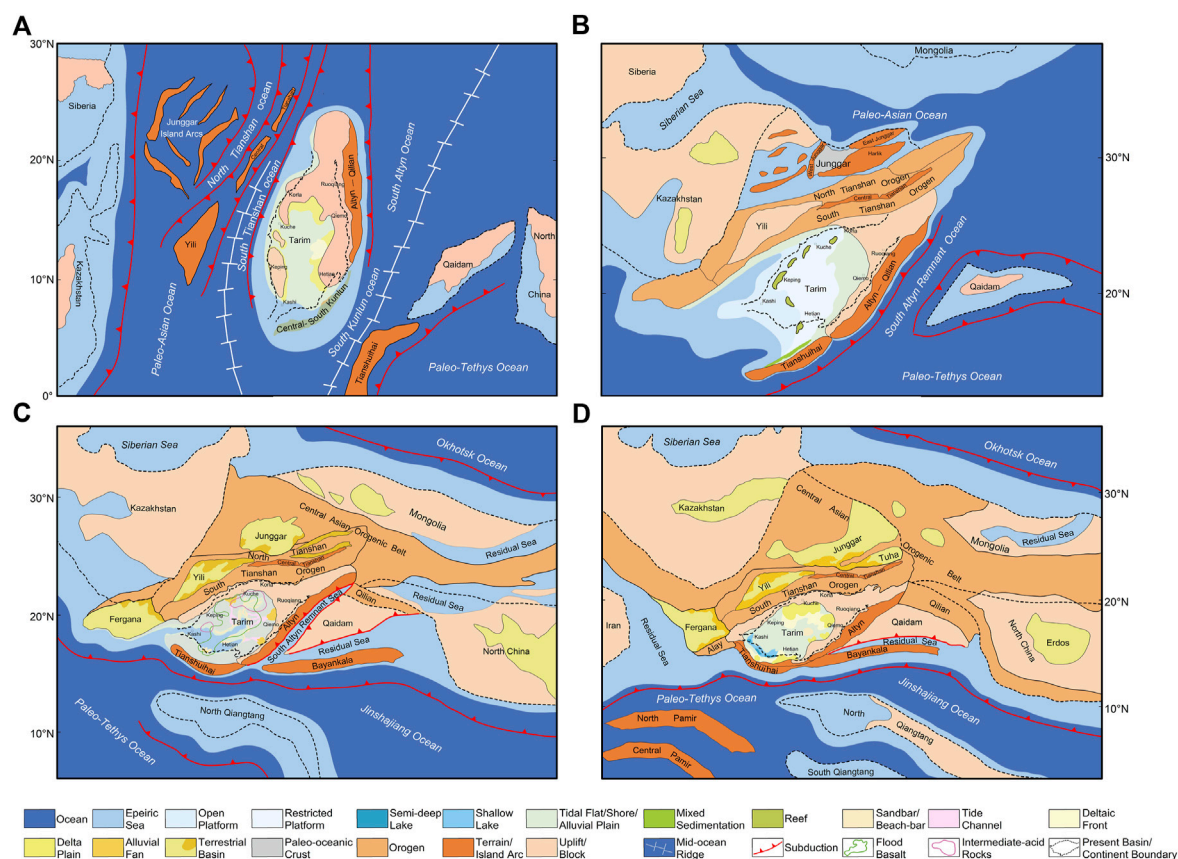


FIGURE 9

Tectono-paleogeography of Tarim and adjacent areas in late Devonian (A), late Carboniferous (B), late Middle Permian (C) and late Permian (D).

6 Conclusion

- 1) The evolution of the proto-type Tarim basin is strongly controlled by the geotectonic setting of the periphery. The transition from shelf-littoral to platform-tidal flat to alluvial plain-lacustrine facies in the basin reflected a process of regression and uplift. This process was controlled by the shift in the peripheral tectonic setting of the basin: the North Tianshan Ocean and South Tianshan Ocean closed from east to west; the Tianshuihai Island Arc gradually collaged to the southwest of the Tarim block, reducing the extent of the opening of the passive margin of the western Tarim basin and closing it completely by the end of the Permian, resulting in the complete transformation of the Tarim Basin from a westward-opening marine basin to a terrestrial intra-cratonic basin.
- 2) The Southwestern Tarim basin was by no means an open, extensive passive margin during the Carboniferous-Permian, but rather transformed from a passive continental margin to an active continental margin through back-arc downwarp and eventually complete closure to uplift.
- 3) The Tarim block was located between 15°–25° N in the global plate tectonic framework in the Late Paleozoic. The Tarim block ended its independent drift to become the southern edge of the Eurasian continent at the end of the Carboniferous. The Tarim block witnessed and participated in the assemblage of the Pangea supercontinent. Meanwhile, its polarity (orientation of basin long-axis) underwent a significant clockwise rotation—from NNE to NE,

which is associated with the closure of the Paleo-Asian Ocean from West to East to form the Central Asian Orogenic Belt.

- 4) As a result of the global Hercynian Orogeny Movement, the Tarim block and its surrounding tectonic setting underwent a major transformation: the Paleo-Asian Ocean and Paleo-Tethys Ocean closed in succession (the South Tianshan ocean completely closed at the end of the Carboniferous, the South Kunlun Ocean and South Allyn Ocean closed at the end of the Permian), followed by arc-continent collision and continental collision. The Tarim basin transitioned from a back-arc extensional basin to a back-arc foreland basin.

Data availability statement

The datasets presented in this study can be found in online repositories. The names of the repository/repositories and accession number(s) can be found in the article/Supplementary Material.

Author contributions

JX undertook most of the main work of this paper, including data collection, analysis, balanced profile restoration, manuscript writing, drawing maps, and so on; ZZ, XL performed some analysis work; SH, CL, and HL provide information and some maps; HC, LW: investigation. All authors contributed to manuscript read, and approved the submitted version.

Conflict of interest

SH, CL, and HL were employed by Institute of Petroleum Exploration and Development, Tarim Oilfield Company.

The remaining authors declare that the research was conducted in the absence of any commercial or financial relationships that could be construed as a potential conflict of interest.

References

- Abrajevitch, A., Van der Voo, R., Levashova, N. M., and Bazhenov, M. L. (2007). Paleomagnetic constraints on the paleogeography and oroclinal bending of the Devonian volcanic arc in Kazakhstan. *Tectonophysics* 441 (1-4), 67–84. doi:10.1016/j.tecto.2007.04.008
- Alexiev, D. V., Biske, Yu. S., Djenchuraeva, A. V., Kröner, A., and Getman, O. F. (2019). Late carboniferous (kasimovian) closure of the South Tianshan Ocean: No triassic subduction. *J. Asian Earth Sci.* 173, 54–60. doi:10.1016/j.jseas.2019.01.001
- Allen, M., Windley, B., Chi, C., Zhong-Yan, Z., and Guang-Rei, G. (1991). Basin evolution within and adjacent to the Tien Shan range, NW China. *Jgs* 148, 369–378. doi:10.1144/gsjgs.148.2.0369
- Allen, M., Windley, B., and Zhang, C. (1993). Palaeozoic collisional tectonics and magmatism of the Chinese Tien Shan, central Asia. *Tectonophysics* 220, 89–115. doi:10.1016/0040-1951(93)90225-9
- Allen, P. A., and Allen, J. R. (1990). *basin analysis: Principles and applications*. London: Blackwell Scientific Publication.
- Carmichael, S. K., Waters, J. A., Königshof, P., Suttner, T. J., and Kido, E. (2019). Paleogeography and paleoenvironments of the late devonian Kellwasser event: A review of its sedimentological and geochemical expression. *Glob. Planet. Change* 183, 102984. doi:10.1016/j.gloplacha.2019.102984
- Carroll, A. R., Graham, S. A., Hendrix, M. S., Ying, D., and Zhou, D. (1995). Late Paleozoic tectonic amalgamation of northwestern China: Sedimentary record of the northern Tarim, northwestern Turpan, and southern Junggar Basins. *Geol. Soc. Am. Bull.* 107, 571–594. doi:10.1130/0016-7606(1995)107<0571:ptao>2.3.co;2
- Charvet, J., Shu, L., Laurent-Charvet, S., Wang, B., Faure, M., Cluzel, D., et al. (2011). Paleozoic tectonic evolution of the Tianshan belt, NW China. *Sci. China Earth Sci.* 54, 166–184. doi:10.1007/s11430-010-4138-1
- Chen, H., Yang, S., Wang, Q., Luo, J., Jia, C., Wei, G., et al. (2006). Sedimentary response to the Early-Mid Permian basaltic magmatism in the Tarim plate. *Geol. China* 33 (3), 545–552. doi:10.3969/j.issn.1000-3657.2006.03.010
- Chen, R. (2000). On forming conditions for non-anticlinal oil and gas pools in the Tarim Basin. *Exp. Pet. Geol.* 22 (3), 215–219. doi:10.11781/sydz200003215
- Chen, S., Zhao, Z., Ji, W., Li, R., Liu, R., and Cha, X. (2013a). The characteristic of tectonic-lithofacies paleogeography during Early-Middle Permian in the west Kunlun and adjacent areas. *Chin. J. Geol.* 48 (4), 1015–1032. doi:10.3969/j.issn.0563-5020.2013.04.005
- Chen, X., Dong, Y., Chen, H., and Wang, J. (2013b). Sequence structures and evolution patterns of the triassic in the platform of Tarim Basin. *Geol. Sci. Technol. Inf.* 32 (4), 50–54.
- Clarke, J. W. (1984). Geology and possible uranium deposits of the Fergana region of soviet central Asia. *U. S. Geol. Surv.* doi:10.3133/ofr84513
- Cocks, L. R. M., and Torsvik, T. H. (2013). The dynamic evolution of the Palaeozoic geography of eastern Asia. *Earth-Science Rev.* 117, 40–79. doi:10.1016/j.earscirev.2012.12.001
- Dahlstrom, C. D. A. (1969). Balanced cross section. *Can. J. Geosciences* 6, 743–757. doi:10.1139/c69-069
- Deledda, C. (1996). Sedimentary system of carboniferous-permian of Western Tarim. *Xinjiang Geol.* 14 (4), 386–393. [in Chinese with English abstract].
- Dong, Y., He, D., Sun, S., Liu, X., Zhou, X., Zhang, F., et al. (2018). Subduction and accretionary tectonics of the East Kunlun Orogen, Western segment of the central China orogenic system. *Earth-Science Rev.* 186, 231–261. doi:10.1016/j.earscirev.2017.12.006
- Dong, Y. P., Sun, S. S., Santosh, M., Zhao, J., Sun, J. P., He, D. F., et al. (2021). Central China orogenic belt and amalgamation of east asian continents. *Gondwana Res.* 100, 131–194. doi:10.1016/j.gr.2021.03.006
- Eizenhöfer, P. R., Zhao, G. C., Sun, M., Zhang, J., Han, Y. G., and Hou, W. Z. (2015a). Geochronological and Hf isotopic variability of detrital zircons in Paleozoic strata across the accretionary collision zone between the North China craton and Mongolian arcs and tectonic implications. *GSA Bull.* 127, 1422–1436. doi:10.1130/B31175.1
- Eizenhöfer, P. R., Zhao, G. C., Zhang, J., Han, Y. G., Hou, W. Z., Liu, D. X., et al. (2015b). Geochemical characteristics of the Permian basins and their provenances across the Solonker Suture Zone: Assessment of net crustal growth during the closure of the Palaeo-Asian Ocean. *Lithos* 224–225, 240–255.
- Eizenhöfer, P. R., Zhao, G. C., Zhang, J., and Sun, M. (2014). Final closure of the paleo-Asian ocean along the solonker suture zone: Constraints from geochronological and geochemical data of permian volcanic and sedimentary rocks. *Tectonics* 33, 441–463. doi:10.1002/2013TC003357
- Feng, Z., Peng, Y., Jin, Z., and Xiaozhang, S. (2004). *Lithofacies paleogeography of the cambrian and ordovician in China*. Beijing: Petroleum Industry Press.
- Gao, H., He, D., Tong, X., Wen, Z., and Wang, Z. (2017). Tectonic-depositional environment and proto-type basin evolution of the cambrian in the Tarim Basin. *Geoscience* 31 (1), 102–118. doi:10.3969/j.issn.1000-8527.2017.01.009
- Gao, J., Long, L., Klemd, R., Qian, Q., Liu, D., Xiong, X., et al. (2009). Tectonic evolution of the South tianshan orogen and adjacent regions, NW China: Geochemical and age constraints of granitoid rocks. *Int. J. Earth Sci.* 98, 1221–1238. doi:10.1007/s00531-008-0370-8
- Gao, J., Zhu, M., and Wang, X. (2019). Large-scale porphyry-type mineralization in the central asian metallogenic domain: Tectonic background, fluid feature and metallogenic deep dynamic mechanism. *Acta Geol. Sin.* 93 (1), 24–71. doi:10.1016/j.jseas.2017.10.002
- Gao, R., Hou, H., Cai, X., Knapp, J., He, R., Liu, J., et al. (2013). Fine crustal structure beneath the junction of the southwest Tian Shan and Tarim Basin, NW China. *Lithosphere* 5 (4), 382–392. doi:10.1130/L248.1
- Ge, R., Zhu, W., Wu, H., Zheng, B., Zhu, X., and He, J. (2012). The paleozoic northern margin of the Tarim craton: Passive or active? *Lithos* 142–143, 1–15. doi:10.1016/j.lithos.2012.02.010
- Golonka, J., Krobicki, M., Paják, J., Van Giang, N., and Zuchiewicz, W. (2006). “Global plate tectonics and paleogeography of Southeast Asia,” in *Faculty of Geology, geophysics and environmental protection* (Arkadia, Kraków: AGH University of Science and Technology).
- Gong, W. (2010). The deformational characteristics of the Tekilik thrust-nappe structures in southwest Tarim basin. *J. Oil Gas Technol.* 32 (5), 46–48. doi:10.3969/j.issn.1000-9752.2010.05.010
- Görz, I., and Hielscher, P. (2010). An explicit plate kinematic model for the orogeny in the southern Uralides. *Tectonophysics* 493, 1–26. doi:10.1016/j.tecto.2010.07.005
- Gu, J., Zhu, X., and Jia, J. (2003). *The deposits and reservoirs in the Tarim Basin*. Beijing: Petroleum Industry Press.
- Guo, C., Gao, J., and Li, Z. (2018). Depositional and provenance records of lower Permian sandstones from Sishichang area, northwestern Tarim Basin: Implications for tectonic evolution. *Earth Sci.* 43 (11), 4149–4168.
- Guo, R., Qin, Q., Muhetaer, Z., Zhao, L., Sun, M., and Wei, Z. (2013). Geological characteristics and tectonic significance of Ordovician granite intrusions in the Western segment of Quruqtagh, Xinjiang. *Earth Sci. Front.* 20 (4), 251–263.
- Han, B. F., He, G. Q., Wang, X. C., and Guo, Z. J. (2011). Late carboniferous collision between the Tarim and Kazakhstan-Yili terranes in the Western segment of the South tian Shan orogen, central Asia, and implications for the northern Xinjiang, Western China. *Earth Sci. Rev.* 109 (3-4), 74–93. doi:10.1016/j.earscirev.2011.09.001
- Han, B. F., Ji, J. Q., Song, B., Chen, L. H., and Zhang, L. (2006). Late Paleozoic vertical growth of continental crust around the Junggar Basin, Xinjiang, China (part I): Timing of post-collisional plutonism. *Acta Petrol. Sin.* 22 (5), 1077–1086. doi:10.3321/j.issn:1000-0569.2006.05.003
- Han, Y., and Zhao, G. (2018). Final amalgamation of the tianshan and junggar orogenic collage in the southwestern central asian orogenic belt: Constraints on the closure of the paleo-Asian ocean. *Earth-Sci. Rev.* 186, 129–152. doi:10.1016/j.earscirev.2017.09.012
- He, B., Jiao, C., Xu, Z., Cai, Z., Liu, S., Zhang, J., et al. (2015). Distribution and migration of the phanerozoic palaeo-uplifts in the Tarim Basin, NW China. *Earth Sci. Front.* 22 (3), 277–289. doi:10.13745/j.esf.2015.03.024
- He, B., Jiao, C., Xu, Z., Cai, Z., Liu, S., and Zhang, Y. (2011). Manifestation of the middle-late caledonian tectonic movement along the altun-West Kunlun orogenic belt in the tangguzibas depression, Tarim basin. *Acta Petrol. Sin.* 27 (11), 3435–3448.
- He, B., Jiao, C., Xu, Z., Cai, Z., and Yu, Z. (2016). The paleotectonic and paleogeography reconstructions of the Tarim Basin and its adjacent areas (NW China) during the late Early and Middle Paleozoic. *Gondwana Res.* 30, 191–206. doi:10.1016/j.gr.2015.09.011
- He, D. F., Jia, C. Z., and Li, D. S. (2005). Formation and evolution of polycyclic superimposed Tarim Basin. *Oil Gas Geol.* 26 (1), 64–77. doi:10.11743/ogg20050109
- He, D., Li, D., He, J., and Wu, X. (2013). Comparison in petroleum geology between Kuqa depression and Southwest depression in Tarim Basin and its exploration significance. *Acta Pet. Sin.* 34 (02), 201–218. doi:10.7623/syxb201302001
- He, D., Li, D., Wang, C., Liu, S., and Chen, J. (2020). Status, thinking, and methodology of studying on the mobile tectono-paleogeography. *J. Palaeogeogr. Chin. Ed.* 22 (1), 1–28. doi:10.7605/gdxb.2020.01.001

Publisher's note

All claims expressed in this article are solely those of the authors and do not necessarily represent those of their affiliated organizations, or those of the publisher, the editors and the reviewers. Any product that may be evaluated in this article, or claim that may be made by its manufacturer, is not guaranteed or endorsed by the publisher.

- He, D. (2022). Multi-cycle superimposed sedimentary basins in China: Formation, evolution, geologic framework and hydrocarbon occurrence. *Earth Sci. Front.* 29 (6), 024–059. doi:10.13745/j.esf.2022.8.1
- He, D., Zhou, X., Zhang, Z., and Yang, X. (2007). Types of Ordovician prototype basins in the Tarim region and their evolution. *Sci. Bull.* 52 (S1), 126–134. doi:10.1007/s11434-007-6010-z
- He, Z. L., Gou, H. W., Li, X. R., and Yan, X. G. (1992). Prototype basin and sedimentary model of permo-carboniferous in Tarim plate. *Oil Gas Geol.* 13 (1), 1–14.
- Hofmann, R., Goudemand, N., Wasmer, M., Bucher, H., and Hautmann, M. (2011). New trace fossil evidence for an early recovery signal in the aftermath of the end-Permian mass extinction. *Palaeogeogr. Palaeoclimatol. Palaeoecol.* 310, 216–226. doi:10.1016/j.palaeo.2011.07.014
- Hou, F., Zhang, X., Wen, Z., Gao, Z., Feng, Y., Sun, J., et al. (2014). Paleogeographic reconstruction and tectonic evolution of major blocks in China since Paleozoic. *Mar. Geol. Quat. Geol.* 34 (6), 9–26. doi:10.3724/SP.J.1140.2014.06009
- Hou, M. C., Chen, A. Q., Ogg, J. G., Ogg, G. M., Huang, K. K., Xing, F. C., et al. (2019). China paleogeography: Current status and future challenges. *Earth Sci. Rev.* 189, 177–193. doi:10.1016/j.earscirev.2018.04.004
- Hu, X. M., Ma, A. L., Xue, W. W., Garzanti, E., Cao, Y., Li, S. M., et al. (2022). Exploring a lost Ocean in the Tibetan plateau: Birth, growth, and demise of the bangong-nujiang ocean. *Earth Sci. Rev.* 229, 104031. doi:10.1016/j.earscirev.2022.104031
- Hu, Y., Zhang, Z., and Wang, E. (2010). Characteristics of different types of slope belt and its oil-control effect in Tarim Basin. *Lithol. Reserv.* 22 (4), 72–79. doi:10.3969/j.issn.1673-8926.2010.04.013
- Huang, B. C., Yan, Y. G., Piper, J. D. A., Zhang, D. H., Yi, Z. Y., Yu, S., et al. (2018). Paleomagnetic constraints on the paleogeography of the East Asian blocks during late Paleozoic and early Mesozoic times. *Earth-Sci. Rev.* 186, 8–36. doi:10.1016/j.earscirev.2018.02.004
- Huang, B., Zhou, Y., and Zhu, R. (2008). Discussions on Phanerozoic evolution and formation of continental China, based on paleomagnetic studies. *Earth Sci. Front.* 15 (3), 348–359. doi:10.3321/j.issn:1005-2321.2008.03.031
- Huang, H., Wang, T., Tong, Y., Qin, Q., Ma, X., and Yin, J. (2020). Rejuvenation of ancient micro-continents during accretionary orogenesis: Insights from the Yili block and adjacent regions of the SW central asian orogenic belt. *Earth-Sci. Rev.* 208, 103255. doi:10.1016/j.earscirev.2020.103255
- Huang, H. Y. (1986). Tectonic cycle characteristics in Xinjiang. *Northwest. Geol.* 1986, 10–18.
- Huang, S., Xie, H., and Hou, G. (2023). The key transition of Chinese plates configuration in the early Paleoproterozoic. *J. Earth Sci.* In press.
- Ingersoll, R. V. (2019). “Subduction-related sedimentary basins of the US cordillera,” in *The sedimentary basins of the United States and Canada*. Editor A. D. Miall (Amsterdam, Netherlands: Elsevier), 477–510. doi:10.1016/B978-0-444-63895-3.00011-5
- Ingersoll, R. V. (2012). “Tectonics of sedimentary basins, with revised nomenclature,” in *Tectonics of sedimentary basins: Recent advances*. Editors B. Cathy (Antonio (Oxford, UK: Blackwell Publishing Ltd.), 1–43.
- Jia, C., Wei, G., and Wang, L. (1997). *The structural characteristics and hydrocarbon of the Tarim Basin in China*. Beijing: Petroleum Industry Press.
- Jia, C. Z., Sun, L. D., Zhou, X. Y., Gu, J. Y., Liang, D. G., Zhang, W., et al. (2004). *plate tectonics and continental dynamics in the Tarim Basin*. Beijing: Petroleum Industry Press.
- Jia, D., Tian, J., Zhang, X., Zhu, H., Lin, X., Su, B., et al. (2017). Sequence stratigraphy and sedimentary evolution of donghe sandstone in Tarim Basin. *Oil Gas Geol.* 38 (6), 1123–1134. doi:10.11743/ogg20170613
- Jiang, Z., Jiang, S., Lan, X., Wang, B., Huang, S., and Zhang, H. (2018). Neotectonic evolution of the Tarim Basin craton from neogene to quaternary. *Int. Geol. Rev.* 60 (10), 1213–1230. doi:10.1080/00206814.2017.1379365
- Jolivet, M. (2015). Mesozoic tectonic and topographic evolution of central Asia and tibet: A preliminary synthesis. *Geol. Soc. Lond. Spec. Publ.* 427 (1), 19–55. doi:10.1144/sp427.2
- Ju, Q., Zhang, Y. C., Yuan, D. X., Qiao, F., Xu, H. P., Zhang, H., et al. (2022). Permian foraminifers from the exotic limestone blocks within the central Qiangtang Metamorphic Belt, Tibet and their geological implications. *J. Asian Earth Sci.* 239, 105426. doi:10.1016/j.jseas.2022.105426
- Korobkin, V. V., and Buslov, M. M. (2011). Tectonics and geodynamics of the Western central Asian fold belt (Kazakhstan paleozooids). *Russ. Geol. Geophys.* 52, 1600–1618. doi:10.1016/j.rgg.2011.11.011
- Laborde, A., Barrier, L., Simoes, M., Li, H., Coudroy, T., Van der Woerd, J., et al. (2019). Cenozoic deformation of the Tarim Basin and surrounding ranges (Xinjiang, China): A regional overview. *Earth-Sci. Rev.* 197, 102891. doi:10.1016/j.earscirev.2019.102891
- Li, H., Wang, J., Wu, G., Shi, L., Wang, B., Hu, X., et al. (2014c). Features and formation mechanism of middle Caledonian faults in west of Tangguzibasi depression, Tarim Basin. *J. Central South Univ. Sci. Technol.* 45 (12), 4331–4341.
- Li, J., and Jiang, H. (2013). *World atlas of Plate Tectonic reconstruction, lithofacies paleogeography and palaeoenvironment*. Beijing: Geological Publishing House.
- Li, J., Wang, H., Li, W., and Zhou, X. (2014a). Discussion on global tectonics evolution from plate reconstruction in Phanerozoic. *Acta Pet. Sin.* 35 (2), 207–218. doi:10.7623/syxb201402001
- Li, J., Zhou, X., Li, W., Wang, H., Liu, Z., Zhang, H., et al. (2015). Preliminary reconstruction of tectonic paleogeography of Tarim Basin and its adjacent areas from cambrian to triassic, NW China. *Geol. Rev.* 61 (6), 1225–1234.
- Li, S., Zhao, S., Liu, X., Cao, H., Yu, S., Li, X., et al. (2018). Closure of the proto-tethys Ocean and early paleozoic amalgamation of microcontinental blocks in east Asia. *Earth-Science Rev.* 186, 37–75. doi:10.1016/j.earscirev.2017.01.011
- Li, S. Z., Kang, Z. H., and Meng, M. M. (2014b). Permian sedimentary environment evolution in southwest Tarim. *Xinjiang Geol.* 32 (4), 451–456. doi:10.3969/j.issn.1000-8845.2014.04.005
- Li, W., Zhang, Z., and Lin, T. (2021). Analysis of the boundary properties of the Tarim block during the main tectonic period. *Chem. Eng. Des. Commun.* 47 (10), 11–12. doi:10.3969/j.issn.1003-6490.2021.10.006
- Li, Y., Robinson, A. C., Gadoev, M., and Oimuhammadzoda, I. (2020). Was the Pamir salient built along a late paleozoic embayment on the southern asian margin? *Earth Planet. Sci. Lett.* 550, 116554. doi:10.1016/j.epsl.2020.116554
- Li, Z., Gao, J., Guo, C., and Xu, J. (2015). Devonian-Carboniferous tectonic evolution of continental margins in northern Tarim block, Northwest China: Constrained by basin-fill sequences and provenance system. *Earth Sci. Frontiers* 2015, 35–52. [in Chinese with English abstract].
- Lin, B., Zhang, X., Xu, X., Yuan, J., Neng, Y., and Zhu, J. (2015). Features and effects of basement faults on deposition in the Tarim Basin. *Earth-Sci. Rev.* 145, 43–55. doi:10.1016/j.earscirev.2015.02.008
- Lin, C., Li, S., Liu, J., Qian, Y., Luo, H., Chen, J., et al. (2011). Tectonic framework and paleogeographic evolution of the Tarim basin during the Paleozoic major evolutionary stages. *Acta Petrol. Sin.* 27 (1), 210–218.
- Lin, C. S., Yang, H. J., Liu, J. Y., Rui, Z. F., Cai, Z. Z., Li, S. T., et al. (2012a). Sequence architecture and depositional evolution of the Ordovician carbonate platform margins in the Tarim Basin and its response to tectonism and sea-level change. *Basin Res.* 24 (5), 559–582. doi:10.1111/j.1365-2117.2011.00536.x
- Lin, C. S., Yang, H. J., Liu, J. Y., Rui, Z. F., Cai, Z. Z., and Zhu, Y. F. (2012b). Distribution and erosion of the Paleozoic tectonic unconformities in the Tarim Basin, Northwest China: Significance for the evolution of paleo-uplifts and tectonic geography during deformation. *J. Asian Earth Sci.* 46, 1–19. doi:10.1016/j.jseas.2011.10.004
- Lin, C., Yang, H., Liu, J., Peng, L., Cai, Z., Yang, X., et al. (2009). Paleostuctural geomorphology of the Paleozoic central uplift belt and its constraint on the development of depositional facies in the Tarim Basin. *Sci. China Ser. D Earth Sci.* 52 (6), 823–834. doi:10.1007/s11430-009-0061-8
- Liu, D., Guo, Z., Jolivet, M., Cheng, F., Song, Y., and Zhang, Z. (2014a). Petrology and geochemistry of early permian volcanic rocks in south tian Shan, NW China: Implications for the tectonic evolution and phanerozoic continental growth. *Int. J. Earth Sci.* 103 (3), 737–756. doi:10.1007/s00531-013-0994-1
- Liu, H., Somerville, I., Lin, C., and Zuo, S. (2016). Distribution of palaeozoic tectonic superimposed unconformities in the Tarim Basin, NW China: Significance for the evolution of palaeogeomorphology and sedimentary response. *Geol. J.* 51, 627–651. doi:10.1002/gj.2664
- Liu, J. D., Qi, L. X., Tian, J. C., Li, Z. J., and Zhang, X. B. (2014b). *Tectonic evolution and sedimentary lattice in the Tarim Basin*. Beijing: Science Press.
- Liu, J., Lin, C., Peng, L., Chen, Q., Zhang, X., and Zhou, X. (2008). Distribution patterns of the end of the Middle Devonian tectonic unconformity and their constrain on the development and distribution of favorable stratigraphic traps in the Tarim Basin. *Oil Gas Geol.* 29 (2), 268–275. doi:10.11743/ogg20080217
- Liu, K., Wang, Y., Jiang, G., Zhang, S., and Zhang, K. (2014c). Evolution of Neoproterozoic-Mesozoic sedimentary basins of west Kunlun area. *Earth Science-Journal China Univ. Geosciences* 39 (8), 987–999. doi:10.3799/dqkx.2014.090
- Liu, X., Graham, S., Chang, E., Wu, S., Fu, D., Yao, J., et al. (1994). Tectonic evolution of Tarim plate and its surrounding area since Late Paleozoic. *Earth Science-Journal China Univ. Geosciences* 19 (6), 715–725.
- Liu, X., Zhang, X., Liu, L., Li, B., Zhang, X., Song, H., et al. (2014d). The new achievements and main progress in regional geological exploration and mineral resources survey of Karaiqi area, Xinjiang. *Geol. Bull. China* 33 (1), 1–8. doi:10.3969/j.issn.1671-2552.2014.01.002
- Liu, Y., Li, W., Feng, Z., Wen, Q., Neubauer, F., and Liang, C. (2017). A review of the paleozoic tectonics in the eastern part of central asian orogenic belt. *Gondwana Res.* 43, 123–148. doi:10.1016/j.jgr.2016.03.013
- Lou, Q. Q., Xiao, A. C., Zhong, N. C., and Wu, L. (2016). A method of proto-type restoration of large depressions with terrestrial sediments: A case study from the cenozoic Qaidam basin. *Acta Petrol. Sin.* 32 (03), 892–902. (in Chinese).
- Luo, J., Che, Z., Zhang, G., Nian, X., and Zhang, X. (2012). Early-Middle Permian basin-mountain coupling features between northwestern margin of the Tarim basin and the South Tianshan orogen. *Acta Petrol. Sin.* 28 (8), 2506–2514.
- Ma, C., Li, J., Cao, Z., Liu, L., and Wang, M. (2020). Lithofacies paleogeographic reconstruction and evolution of the Carboniferous-Permian basin group in Central Asia. *Acta Petrol. Sin.* 36 (11), 3510–3522. doi:10.18654/1000-0569/2020.11.16
- Ma, Q., Ma, T., Yang, H., Zhao, X., and Zhu, Y. (2019). Development characteristics of the third-order sequence of upper devonian-lower carboniferous shore-mixed shelf in Tarim Basin, NW China. *Petroleum Explor. Dev.* 46 (04), 701–710. doi:10.1016/s1876-3804(19)60227-2

- Ma, X., Shu, L., Meert, J., and Li, J. (2014). The paleozoic evolution of central tianshan: Geochemical and geochronological evidence. *Gondwana Res.* 25 (2), 797–819. doi:10.1016/j.gr.2013.05.015
- Matte, Ph., Tapponnier, P., Arnaud, N., Bourjot, L., Avouac, J. P., Vidal, Ph., et al. (1996). Tectonics of western tibet, between the Tarim and the indus. *Earth Planet. Sci. Lett.* 142, 311–330. doi:10.1016/0012-821x(96)00086-6
- Moisan, P., Voigt, S., Pott, C., Buchwitz, M., Schneider, J. W., and Kerp, H. (2011). Cycadalean and bennettitalean foliage from the triassic madygen lagerstätte (SW Kyrgyzstan, central Asia). *Rev. Palaeobot. Palynol.* 164 (1–2), 93–108. doi:10.1016/j.revpalbo.2010.11.008
- Müller, R. D., Cannon, J., Qin, X., Watson, R. J., Gurnis, M., Williams, S., et al. (2018). GPlates: Building a virtual Earth through deep time. *Geochem. Geophys. Geosystems* 19, 2243–2261. doi:10.1029/2018GC007584
- Niu, Y. Z., Shi, G. R., Ji, W. H., Zhou, J. L., Wang, J. Q., Wang, K., et al. (2021). Paleogeographic evolution of a Carboniferous–Permian sea in the southernmost part of the Central Asian Orogenic Belt, NW China: Evidence from microfacies, provenance and paleobiogeography. *Earth-Science Rev.* 220, 103738. doi:10.1016/j.earscirev.2021.103738
- Pan, G., Li, X., Wang, L., Ding, J., and Chen, Z. (2002). Preliminary division of tectonic units of the Qinghai-Tibet Plateau and its adjacent regions. *Geol. Bull. China* 21 (11), 701–707. doi:10.3969/j.issn.1671-2552.2002.11.002
- Pu, R., Yun, L., Su, J., Guo, Q., and Dang, X. (2014). Growth conditions and 3-D seismic delineation of carboniferous barrier reefs in the southwestern Tarim Basin. *J. Earth Sci.* 2014, 315–323. doi:10.1007/s12583-014-0429-3
- Pullen, A., Kapp, P., Gehrels, G. E., Vervoort, J. D., and Ding, L. (2008). Triassic continental subduction in central tibet and mediterranean-style closure of the Paleo-Tethys Ocean. *Geology* 36 (5), 351–354. doi:10.1130/g24435a.1
- Qi, L., Li, Z., and Lü, H. (2020). *Tectonic sedimentary evolution and oil and gas exploration in Tarim superimposed basin*. Beijing: Science Press.
- Ren, R., Guan, S. W., Han, B. F., and Su, L. (2017). Chronological constraints on the tectonic evolution of the Chinese Tianshan Orogen through detrital zircons from modern and palaeo-river sands. *Int. Geol. Rev.* 59, 1657–1676. doi:10.1080/00206814.2017.1292468
- Robinson, A. C., Yin, A., Manning, C. E., Harrison, T. M., Zhang, S.-H., and Wang, X.-F. (2007). Cenozoic evolution of the eastern Pamir: Implications for strain-accommodation mechanisms at the Western end of the Himalayan-Tibetan Orogen. *Geol. Soc. Am. Bull.* 119 (7/8), 882–896. doi:10.1130/b25981.1
- Schwab, M., Ratschbacher, L., Siebel, W., McWilliams, M., Minaev, V., Lutkov, V., et al. (2004). Assembly of the Pamirs: Age and origin of magmatic belts from the southern Tien Shan to the southern Pamirs and their relation to Tibet. *Tectonics* 23, TC4002. doi:10.1029/2003tc001583
- Sobel, E., and Dumitru, T. (1997). Thrusting and exhumation around the margins of the Western Tarim basin during the India-Asia collision. *J. Geophys. Res. Solid Earth* 102, 5043–5063. doi:10.1029/96jb03267
- Song, P. P., Ding, L., Li, Z. Y., Lippert, P., Yang, T. S., Zhao, X. X., et al. (2015). Late triassic paleolatitude of the Qiangtang block: Implications for the closure of the Paleo-Tethys Ocean. *Earth Planet. Sci. Lett.* 424, 69–83. doi:10.1016/j.epsl.2015.05.020
- Su, B. R. (2019). *Sedimentary records, provenance analysis and paleogeography of the Donghetang Formation of late devonian in Tarim basin* ([Chengdu (Sichuan)]: Chengdu University of Technology). [dissertation/Doctoral thesis].
- Su, W., Gao, J., Klemm, R., Li, J., Zhang, X., Li, X., et al. (2010). U-Pb zircon geochronology of tianshan eclogites in NW China: Implication for the collision between the Yili and Tarim blocks of the southwestern altaids. *Eur. J. Mineralogy* 22 (4), 473–478. doi:10.1127/0935-1221/2010/0022-2040
- Tapponnier, P., Xu, Z., Roger, F., Mayer, B., Arnaud, N., Wittlinger, G., et al. (2001). Oblique stepwise rise and growth of the Tibet plateau. *Science* 294, 1671–1677. doi:10.1126/science.105978
- Van der Voo, R., Levashova, N. M., Skrinnik, L. I., Kara, T. V., and Bazhenov, M. L. (2006). Late orogenic, large-scale rotations in the Tien Shan and adjacent mobile belts in Kyrgyzstan and Kazakhstan. *Tectonophysics* 426, 335–360. doi:10.1016/j.tecto.2006.08.008
- Wan, T., and Zhu, H. (2007). Positions and kinematics of Chinese continental blocks in reconstruction of global paleo-continent for Paleozoic and Triassic. *Geoscience* 21 (1), 1–13. doi:10.3969/j.issn.1000-8527.2007.01.001
- Wang, B., Chen, Y., Zhan, S., Shu, L. S., Faure, M., Cluzel, D., et al. (2007). Primary carboniferous and permian paleomagnetic results from the Yili block (NW China) and their implications on the geodynamic evolution of Chinese tianshan belt. *Earth Planet. Sci. Lett.* 263, 288–308. doi:10.1016/j.epsl.2007.08.037
- Wang, C., Tang, H., Zheng, Y., Dong, L., Li, J., and Qu, X. (2019). Early Paleozoic magnetism and metallogeny related to Proto-Tethys subduction: Insights from volcanic rocks in the northeastern Altyn Mountains, NW China. *Gondwana Res.* 75, 134–153. doi:10.1016/j.gr.2019.04.009
- Wang, Q., Li, S., Zhao, S., Mu, D., Guo, R., and Somerville, I. (2017). Early paleozoic Tarim orocline: Insights from paleogeography and tectonic evolution in the Tarim Basin. *Geol. J.* 52 (S1), 436–448. doi:10.1002/gj.2985
- Wang, T., Jin, Z., Li, H., et al. (2020a). Processes and causes of Phanerozoic tectonic evolution of the Western Tarim Basin, northwest China. *Pet. Sci.* 17, 279–291. doi:10.1007/s12182-019-00424-x
- Wang, T., Jin, Z., Shi, Z., Dai, X., and Cheng, R. (2020b). Phanerozoic plate history and structural evolution of the Tarim Basin, northwestern China. *Int. Geol. Rev.* 62 (12), 1555–1569. doi:10.1080/00206814.2019.1661038
- Wang, X., Klemm, R., Li, J., Gao, J., Jiang, T., Zong, K., et al. (2022). Paleozoic subduction-accretion in the southern central asian orogenic belt: Insights from the wuwamen accretionary complex of the Chinese South Tianshan. *Tectonics* 41, e2021TC006965. doi:10.1029/2021tc006965
- Wilhem, C., Windley, B. F., and Stampfli, G. M. (2012). The altaids of central Asia: A tectonic and evolutionary innovative review. *Earth Sci. Rev.* 113, 303–341. doi:10.1016/j.earscirev.2012.04.001
- Windley, B. F., Alexeiev, D., Xiao, W., Kröner, A., and Badarch, G. (2007). Tectonic models for accretion of the central asian orogenic belt. *J. Geol. Soc.* 164, 31–47. doi:10.1144/0016-76492006-022
- Windley, B. F., Allen, M. B., Zhang, C., Zhao, Z. Y., and Wang, G. R. (1990). Paleozoic accretion and cenozoic redeformation of the Chinese tien Shan range, central Asia. *Geology* 18 (2), 128. doi:10.1130/0091-7613(1990)018<0128:paacro>2.3.co;2
- Woodcock, N. H. (2004). Life span and fate of basins. *Geology* 32, 685–688. doi:10.1130/g20598.1
- Wu, G., Deng, W., Huang, S., Zheng, D., and Pan, W. (2020). Tectonic-paleogeographic evolution in the Tarim Basin. *Chin. J. Geol.* 55 (2), 305–321. doi:10.12017/dzxx.2020.020
- Wu, G., Li, Y., Liu, Y., and Zhao, Y. (2013). Paleozoic sediment-tectonic evolution and basin dynamic settings in Wushi-Kalpin-Bachu area, northwest Tarim. *J. Palaeogeogr.* 15 (2), 203–218. doi:10.7605/gdxb.2013.02.018
- Wu, G., Pang, X., and Li, M. (2016). *The structural characteristics of carbonate rocks and their effects on hydrocarbon exploration in craton basin: A case study of the Tarim Basin*. Beijing: Science Press.
- Xiao, W., Han, C., Yuan, C., Sun, M., Lin, S., Chen, H., et al. (2008). Middle cambrian to permian subduction-related accretionary orogenesis of northern Xinjiang, NW China: Implications for the tectonic evolution of central Asia. *J. Asian Earth Sci.* 32, 102–117. doi:10.1016/j.jseas.2007.10.008
- Xiao, W. J., Windley, B. F., Allen, M., and Han, C. M. (2013). Paleozoic multiple accretionary and collisional tectonics of the Chinese Tianshan orogenic collage. *Gondwana Res.* 23, 1316–1341. doi:10.1016/j.gr.2012.01.012
- Xiao, W. J., Windley, B. F., Yuan, C., Sun, M., Han, C. M., Lin, S. F., et al. (2009). Paleozoic multiple subduction-accretion processes of the southern Altaids. *Am. J. Sci.* 309, 221–270. doi:10.2475/03.2009.02
- Xiao, W., and Santosh, M. (2014). Paleozoic multiple accretionary and collisional tectonics of the Chinese Tianshan orogenic collage. *Gondwana Res.* 25, 1429–1444. doi:10.1016/j.gr.2014.01.008
- Xiao, W., Zhou, H., Windley, B. F., Yuan, C., Chen, H., Zhang, G., et al. (2003). Structures and evolution of the multiple accretionary complexes, western Kunlun orogenic belt (China). *Xinjiang Geol.* 21 (1), 31–36.
- Xie, X., Wu, Q., and Lu, H. (1997). Tectonic framework and sedimentary feature of the Tarim Basin in paleozoic. *Acta Sedimentol. Sin.* 15 (1), 153–156.
- Xu, J. (2009). *Sequence stratigraphy of upper devonian-carboniferous in Tarim Basin* ([Changsha (Hunan)]: Central South University). [dissertation/Doctoral thesis].
- Xu, Z., Dilek, Y., Cao, H., Yang, J., Robinson, P., Ma, C., et al. (2015). Paleo-tethyan evolution of tibet as recorded in the east cimmerides and west cathaysides. *J. Asian Earth Sci.* 105, 320–337. doi:10.1016/j.jseas.2015.01.021
- Xu, Z., Li, S., Zhang, J., Yang, J., He, B., Li, H., et al. (2011). Paleo-Asian and Tethyan tectonic systems with docking the Tarim block. *Acta Petrol. Sin.* 27 (1), 1–22.
- Yan, M., Zhang, D., Fang, X., Ren, H., Zhang, W., Zan, J., et al. (2016). Paleomagnetic data bearing on the mesozoic deformation of the Qiangtang block: Implications for the evolution of the paleo- and meso-tethys. *Gondwana Res.* 39, 292–316. doi:10.1016/j.gr.2016.01.012
- Yang, D., Li, S., Wang, S., Wan, Q., Zhao, D., and Xu, J. (2011). Detrital composition of Upper Carboniferous sandstone in northern Tarim basin and its implications for provenance and tectonic attributes. *Acta Petrologica Mineralogica* 30 (4), 645–653. doi:10.3969/j.issn.1000-6524.2011.04.008
- Ye, L., Wang, G., and Zhai, X. (1997). Geology of the Kuqa river and Kalpin, Tarim Basin. *Xinjing Geol.* 15 (2), 174–192.
- Yi, Z. Y., Huang, B. C., Xiao, W. J., Yang, L. K., and Qiao, Q. Q. (2015). Paleomagnetic study of late paleozoic rocks in the tacheng basin of west junggar (NW China): Implications for the tectonic evolution of the Western altaids. *Gondwana Res.* 27, 862–877. doi:10.1016/j.gr.2013.11.006
- Yu, H. B., Qi, J. F., Yang, X. Z., Sun, T., Liu, Q. X., and Cao, S. J. (2016). Analysis of mesozoic proto-type basin in kuga depression, Tarim Basin. *Xinjiang Pet. Geol.* 37 (06), 644–653+666. (in Chinese with English abstract). doi:10.7657/XJPG20160604
- Zhang, B., Chen, W., Yu, S., Yin, J., Li, J., Sun, J., et al. (2014a). Subduction process of South Tianshan ocean during paleozoic. *Acta Petrol. Sin.* 30 (8), 2351–2362. (in Chinese with English abstract).
- Zhang, C. L., Ye, X. T., Zou, H. B., and Chen, X. Y. (2016). Neoproterozoic sedimentary basin evolution in southwestern Tarim, NW China: New evidence from field observations, detrital zircon U-Pb ages and Hf isotope compositions. *Precambrian Res.* 280, 31–45. doi:10.1016/j.precamres.2016.04.011

- Zhang, C. L., Zou, H. B., Ye, X. T., and Chen, X. Y. (2019a). Tectonic evolution of the West Kunlun orogenic belt along the northern margin of the Tibetan plateau: Implications for the assembly of the Tarim terrane to Gondwana. *Geosci. Front.* 10 (3), 973–988. doi:10.1016/j.gsf.2018.05.006
- Zhang, C., Ma, H., and Liu, X. (2022). Architecture and tectonic evolution of the Pamir plateau: A review. *Geol. Rev.* 68 (5), 1653–1673.
- Zhang, G., Liu, W., Zhang, L., Xu, B., Li, H. H., Zhang, B., et al. (2015). Cambrian-Ordovician prototypic basin, paleogeography and petroleum of Tarim Craton. *Earth Sci. Front.* 22 (3), 269–276. doi:10.13745/j.esf.2015.03.023
- Zhang, G., Tong, X., Xin, R., Wen, Z., Ma, F., Huang, T., et al. (2019b). Evolution of lithofacies and paleogeography and hydrocarbon distribution worldwide (I). *Petroleum Explor. Dev.* 46, 664–686. doi:10.1016/s1876-3804(19)60225-9
- Zhang, G., Zhao, W., Wang, H., Li, H., and Liu, L. (2007a). Multicycle tectonic evolution and composite petroleum systems in the Tarim Basin. *Oil Gas Geol.* 28 (5), 653–663. doi:10.11743/ogg20070517
- Zhang, H., Yang, H., Shou, J., Zhang, R., Geng, Z., and Wang, B. (2009a). Sedimentary periods of Donghe sandstone and hydrocarbon exploration in Tarim Basin. *Acta Pet. Sin.* 30 (6), 835–842. doi:10.7623/syxb200906008
- Zhang, J., Luo, J., Qing, Y., Cao, Y., and Fan, J. (2007b). The sedimentary feature and structure significance of turbidite Carboniferous Permian on the northwestern margin of the Tarim Basin. *J. Northwest Univ. Nat. Sci. Ed.* 37 (5), 819–824.
- Zhang, L., Zhang, B., Dong, Z., Xie, Y., Li, W., Peng, Z., et al. (2020). Tectonic setting and metallogenetic conditions of Carboniferous Malkansu giant manganese belt in West Kunlun Orogen. *J. Jilin Univ. (Earth Sci. Ed.)* 50 (5), 1340–1357. doi:10.13278/j.cnki.jjuese.20190294
- Zhang, M., and Chen, F. (1998). Application condition of balanced-section technique and the case analysis. *Oil Geophys. Prospect.* 33 (4), 532–540.
- Zhang, M., Wang, G. C., Zhang, X. H., Liao, Q. A., Wang, W., Guo, R. L., et al. (2021). Reconstruction of the silurian to devonian stratigraphic succession along the northeastern margin of the junggar block, Xinjiang, NW China, and its tectono-paleogeographic implications for the southwestern central asian orogenic belt. *Sediment. Geol.* 411, 105780. doi:10.1016/j.sedgeo.2020.105780
- Zhang, X. B., Zhang, S. N., Zhao, X. K., He, J. J., Li, K., Dai, H. S., et al. (2007c). Calculation of denudation thickness of superimposed basin by seism stratigraphic comprehensive method: A case study from the aekule uplift in Tarim Basin. *Xinjiang Pet. Geol.* 2007, 366–368. (in Chinese). doi:10.3969/j.issn.1001-3873.2007.03.030
- Zhang, X., Tian, J., and Peng, J. (2008). The lithofacies-paleogeography and space-time evolution of Silurian-Devonian in the Tarim Basin. *Acta Sedimentol. Sin.* 26 (5), 762–771.
- Zhang, Y., He, D., and Liu, C. (2019c). Three-dimensional geological structure and genetic mechanism of the Bachu uplift in the Tarim Basin. *Earth Sci. Front.* 26 (1), 134–148. doi:10.13745/j.esf.sf.2019.1.1
- Zhang, Z., Wang, Y., Yun, J., Zhou, B., Zhao, Z., and Zheng, M. (2009b). Control of faults at different evolution stages on hydrocarbon accumulation in Tazhong area, the Tarim Basin. *Oil Gas Geol.* 30 (3), 316–323. doi:10.11743/ogg20090310
- Zhao, G. C., Wang, Y. J., Huang, B. C., Dong, Y. P., Li, S. Z., Zhang, G. W., et al. (2018). Geological reconstructions of the east asian blocks: From the breakup of rodonia to the assembly of Pangea. *Earth Sci. Rev.* 186, 262–286. doi:10.1016/j.earscirev.2018.10.003
- Zhao, J., Liu, G., Lu, Z., Zhang, X., and Zhao, G. (2003). Lithospheric structure and dynamic processes of the Tianshan orogenic belt and the Junggar basin. *Tectonophysics* 376, 199–239. doi:10.1016/j.tecto.2003.07.001
- Zhao, X., Coe, R. S., Zhou, Y. X., Wu, H. R., and Wang, J. (1990). New palaeomagnetic results from northern China: Collision and suturing with Siberia and Kazakhstan. *Tectonophysics* 181, 43–81.
- Zhao, Z., Luo, J., and Zhang, Y. (2011). Lithofacies paleogeography of cambrian sequences in the Tarim Basin. *Acta Pet. Sin.* 32 (6), 937–948.
- Zhao, Z., Wu, X., Pan, W., Zhang, X., Zhang, L., Ma, P., et al. (2009). Sequence lithofacies and paleogeography of ordovician in Tarim Basin. *Acta Sedimentol. Sin.* 27 (5), 939–955. (in Chinese with English abstract).
- Zheng, H., Tian, J., Hu, Z., Zhang, X., Zhao, Y., and Meng, W. (2022). Lithofacies palaeogeographic evolution and sedimentary model of the Ordovician in the Tarim Basin. *Oil Gas Geol.* 43 (4), 733–745. doi:10.11743/ogg20220401
- Zhou, R. Q., Fu, H., Xu, G. S., and Gao, Y. F. (2014). The opening-closing of surrounding ocean Basin in response to tectonic-sedimentation in Tarim Basin. *Sci. Technol. Eng.* 14 (35), 1671–1815. doi:10.3969/j.issn.1671-1815.2014.35.002
- Zhu, H., Su, B., Jia, D., and Li, C. (2016). Sedimentary facies plane distribution characteristics of central uplift belt in different periods in Donghetang Formation. *Coal Technol.* 35 (7), 105–107. doi:10.13301/j.cnki.ct.2016.07.043
- Zhu, R., Xu, H., Deng, S., and Guo, H. (2007). Lithofacies palaeogeography of the Permian in northern China. *J. Palaeogeogr.* 9 (2), 133–142. doi:10.3969/j.issn.1671-1505.2007.02.002
- Zhuang, X., Xiao, L., and Yang, J. (2002). Sedimentary facies in southwestern region of Tarim Basin. *Xinjiang Geol.* 20, 78–82. doi:10.3969/j.issn.1000-8845.2002.z1.014
- Zou, Y., Ta, J., Xing, Z., Xu, Z., Tang, T., and Hao, Y. (2014). Evolution of sedimentary basins in Tarim during neoproterozoic-paleozoic. *Earth Science-Journal China Univ. Geosciences* 39 (8), 1200–1216.



OPEN ACCESS

EDITED BY

Wei Ju,
China University of Mining and
Technology, China

REVIEWED BY

Jin Lai,
China University of Petroleum, China
Hongwei Yin,
Nanjing University, China

*CORRESPONDENCE

Ziqi Zhong,
✉ 2101110667@pku.edu.cn

SPECIALTY SECTION

This article was submitted to Structural
Geology and Tectonics,
a section of the journal
Frontiers in Earth Science

RECEIVED 17 November 2022

ACCEPTED 23 January 2023

PUBLISHED 03 February 2023

CITATION

Zhong Z, Xia J, Huang S, Luo C, Chang H,
Li X, Wei L and Zhang H (2023),
Reconstruction of proto-type basin and
tectono-paleogeography of Tarim block in
early Paleozoic.
Front. Earth Sci. 11:1101360.
doi: 10.3389/feart.2023.1101360

COPYRIGHT

© 2023 Zhong, Xia, Huang, Luo, Chang, Li,
Wei and Zhang. This is an open-access
article distributed under the terms of the
[Creative Commons Attribution License
\(CC BY\)](https://creativecommons.org/licenses/by/4.0/). The use, distribution or
reproduction in other forums is permitted,
provided the original author(s) and the
copyright owner(s) are credited and that
the original publication in this journal is
cited, in accordance with accepted
academic practice. No use, distribution or
reproduction is permitted which does not
comply with these terms.

Reconstruction of proto-type basin and tectono-paleogeography of Tarim block in early Paleozoic

Ziqi Zhong^{1*}, Jinkai Xia¹, Shaoying Huang², Caiming Luo²,
Haining Chang¹, Xiang Li¹, Lunyan Wei¹ and Hao Zhang¹

¹The Key Laboratory of Orogenic Belts and Crustal Evolution, Ministry of Education, School of Earth and Space Sciences, Peking University, Beijing, China, ²Institute of Petroleum Exploration and Development, Tarim Oilfield Company, Korla, China

Tarim Basin is a large, superimposed basin rich in petroleum resources, which has experienced many stages of complex tectonic-sedimentary evolution. As the basic geological study of the Tarim Basin, the proto-type basin and tectono-paleogeographic evolution are of great significance for understanding the distribution of petroleum reservoirs in the superimposed basin and provide tectonic background and theoretical guidance for petroleum exploration. According to the residual thickness map, as well as other lithofacies and seismic data, the scopes of the proto-type basin are determined by the marginal facies method and the thickness trend method, and the shortening amounts are calculated by the balanced cross-section method. Based on these data and previous works, four proto-type basin maps of Tarim Basin in present-day geographic coordinates and four tectono-paleogeographic maps of Tarim Basin in paleogeographic coordinates during the early Paleozoic are reconstructed, which directly show the changes of sedimentary and uplift-depression pattern caused by the transformation of the tectonic environment from extension to compression. In the Cambrian, the Tarim Basin was controlled by the extensional tectonic environment, with the sedimentary framework of "carbonate platform in the west, deep-water basin in the east". At the end of the Ordovician, the Kudi Ocean and the North Altyn Ocean were closed, and the Central and South Kunlun terrane and the Altyn-Qilian terrane were collaged with the Tarim block, which directly led to the transformation of the uplift-depression pattern in the Tarim Basin from east-west differentiation to north-south differentiation, thus changing the sedimentary environment of the Tarim Basin in the late Ordovician to Silurian.

KEYWORDS

Tarim basin, early paleozoic, proto-type basin, tectono-paleogeography, evolution

1 Introduction

Tarim Basin is a large, superimposed basin in northwest China, located between the Qinghai-Tibet Plateau and Tianshan Mountains, covering an area of more than 560,000 square kilometers. It has great potential for petroleum exploration (Li et al., 2019; Tian et al., 2021), and its rich petroleum resources depend on good reservoir-forming conditions, which means that the exploration of petroleum resources needs sufficient basic geological research as a support. The Tarim Basin developed on the Tarim block and underwent multiple stages of complex tectonic-sedimentary evolution (Jia., 1997; He et al., 2005; Lin et al., 2011; Li et al., 2015). The evolutionary history of the Tarim block involves the convergence and disintegration of several supercontinents, including the Rodinia and the Gondwana supercontinent (Xu et al., 2011; Torsvik and Cocks, 2013; Li et al., 2014, 2015; Maruyama et al., 2014; He et al., 2015).

Many achievements have been made in the study of the Tarim proto-type basin and tectono-paleogeography in the early Paleozoic (Chen et al., 2015; Gao et al., 2016, 2017a, 2017b; Tian et al., 2018), but there is a lack of research on the systematic combination of the tectonic background and the proto-type basin. The Tarim Basin has experienced many stages of complex tectonic evolution and the superimposed geological evolution of multiple original basins, which strongly reshaped the original paleogeographic features of the Tarim Basin. The peripheral background of each stage of the Tarim Basin is an intuitive reflection of tectonism, which is closely related to the restoration of the Tarim proto-type basin (Lin et al., 2011; Li et al., 2015; Wu et al., 2020). According to residual thickness maps, rock facies, drilling data, and numerous seismic profiles, the proto-type basin and tectono-paleogeographic maps of Tarim Basin in the early Paleozoic are reconstructed in the paper.

2 Geological setting and plate tectonic configuration

2.1 Regional setting

The Tarim block is located between the Central Asian orogenic belt and the Tethys domain, sandwiched between the West Kunlun, Altyn Tagh, and South Tianshan Mountains (Figure 1A). The Yili terrane, the Central Tianshan terrane, the Altyn-Qilian terrane, and the Central and South Kunlun terrane are distributed clockwise in the periphery of the Tarim block from south to north, bounded by the South Tianshan Ocean, North Altyn Ocean and Kudi Ocean in the early Paleozoic (Figure 1B). The Tarim Basin is composed of Archean-early Neoproterozoic metamorphic crystalline basement and thick Nanhua-Quaternary sedimentary rock series, which can be divided vertically into five structural layers: pre-Nanhua basement, Nanhua-Sinian rift basin, Cambrian-Ordovician marine carbonate platform, Silurian-Cretaceous clastic rock depression and Cenozoic foreland basin (Figure 1C, Jia., 2004; Lin et al., 2011; Wu et al., 2020; Wu et al., 2021). According to the unconformities, the sedimentary tectonic evolution of the Tarim Basin is divided into four major development and evolution stages, with seven tectonic episodes (Lin et al., 2011; Wu et al., 2020; Wu et al., 2021). The Sinian-late Devonian is the first stage, which is controlled by Caledonian movement and experiences a complete tectonic cycle (Figure 1C, Lin et al., 2008, 2011). In the early Paleozoic, the Tarim Basin was essentially in the marine environment and developed extensive marine deposits. During the Sinian to Silurian period, the oceans around the Tarim Basin experienced a process of expansion to closure, which played a decisive role in the internal subsidence and filling evolution model of the basin.

In the late Proterozoic to early Cambrian, the Tarim Basin was in the stage of rapid extensional subsidence, accompanied by the development of a series of rifts (Xu et al., 2008; Yun et al., 2014; Wu et al., 2016; Wu et al., 2018; Wu et al., 2020; Wang T et al., 2021), with the pattern of “uplift in the south and depression in the north”. In the Cambrian to early Ordovician, the Tarim block has been separated from the Rodinia supercontinent (Figure 1C), located on the north shore of the original Tethys Ocean (Li et al., 2008; Li et al., 2010; Dong et al., 2018), developing a large carbonate platform with a thickness of more than 2000 m (Li et al., 2010; Gao and Fan, 2015; Gao et al., 2017a). At the end of the early Ordovician, the South Paleo-Tethys

Ocean began to subduct (Li et al., 2017; Dong et al., 2018), forming the E-W trending paleo-uplift in the basin by the compression from the south, which was finalized at the end of the Ordovician (Wu et al., 2016). In the late Ordovician, with the closure of the Kudi Ocean and the North Altyn Ocean (Figure 1C, Jia., 2004; Li et al., 2017), the Tarim Basin underwent a great transition from extension to extrusion, and a large area of uplift and denudation occurred in the south and east of the basin, forming a widely distributed unconformity. This situation became more and more intense in the late Ordovician, and the north-south differentiation pattern was formed (Gao et al., 2012; Gao et al., 2016; Gao et al., 2017b; Wu et al., 2016). During the Silurian, the southern part of the Tarim Basin was uplifted on a large scale, and deposits were only developed in the north of the Central Uplift Belt (Figure 1C, Lin et al., 2011, 2012; Zheng et al., 2014).

2.2 Tarim block in the global plate tectonics and its evolution

Restoring the position of paleo-continent or block in deep time is an important part in the paleogeographic reconstruction, and paleomagnetism is the only quantitative tool. By reconstructing the paleomagnetic field, the paleo-latitude, direction, and rotation of the block can be obtained (Torsvik and Cocks, 2004; Hou et al., 2008; Hou et al., 2020; Torsvik et al., 2016; Torsvik and Cocks, 2019). However, the paleo-longitude position of the block cannot be determined by paleomagnetism, and the frequent reversal of paleomagnetism makes it impossible to determine whether the calculated paleolatitude is south latitude or north latitude. At this point, other geological evidence, such as paleontology (Cocks and Torsvik, 2002; Cao et al., 2017), sediment facies, orogenic belts, magmatic activity (Steinberger et al., 2004; Torsvik et al., 2016), marine geophysics (Matthews et al., 2016), and so on, are needed.

(1) The paleogeographic location of the Tarim block based on paleomagnetism

For the Tarim block, on the one hand, due to the large-scale magmatic activity in the Paleo-Asian Oceanic tectonic domain at the end of the late Paleozoic (Xiao et al., 2009) and the significant tectonic deformation caused by the collision between India and the Asian continent in the Cenozoic (Johnson., 2002; Huang et al., 2009), most of the magnetic materials in the early Paleozoic experienced heavy magnetization and could not effectively record the paleogeographic location at that time. On the other hand, the early Paleozoic strata in Tarim Basin are mainly marine limestone and marl with weak magnetism, so it is difficult to obtain reliable primary remanence which represents the information of paleomagnetic field in the period of rock formation. So far, the reliable paleomagnetic data accumulated in the early Paleozoic era are very limited.

After Fischer statistics of these paleomagnetic poles with high confidence (Van der Voo., 1990), the paleomagnetic pole positions of the Tarim block in the early Paleozoic are obtained (Table 1, Li et al., 1990; Fang et al., 1996; Huang et al., 2019). Combined with the Apparent Polar Wander Paths (Wen et al., 2017) and peripheral geological background analysis, the global plate tectonic patterns are reconstructed in different periods of the early Paleozoic (Figure 2, late Cambrian, late Ordovician, and late Silurian).

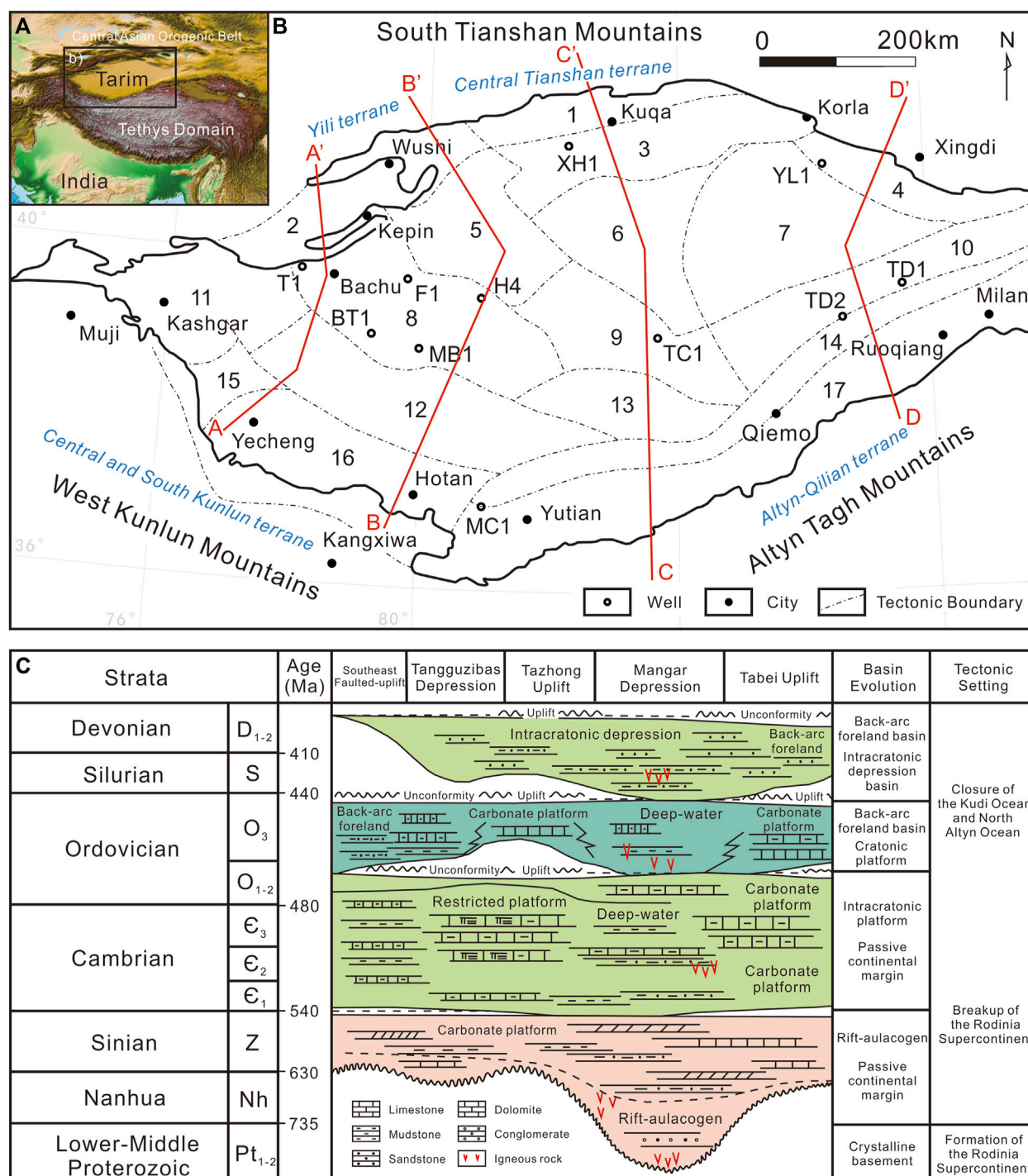


FIGURE 1

(A) Location of the Tarim Basin. (B) Tectonic framework of the Tarim Basin (modified after He et al., 2016). Structural units of the Tarim Basin: 1-Kuqa Depression; 2-Kepingtage Faulted-uplift; 3-Tabei Uplift; 4-Kongquehe Slope; 5-Awati Depression; 6-Shuntuoguole Uplift; 7-Manjiaer Depression; 8-Bachu Uplift; 9-Tazhong Uplift; 10-Guchengxu Uplift; 11-Kashi Depression; 12-Maigaiti Slope; 13-Tangguzibas Depression; 14-Tanan Uplift; 15-Shache Bulge; 16-Yecheng Depression; 17-Southeast Depression. The shortening amount is integrated on four representative lines (AA', BB', CC' and DD' in Table 2), which are red lines. (C) Tectonic-sedimentary evolution sequence of Tarim Basin in the middle-late Proterozoic to Devonian (modified after Lin et al., 2011).

The Tarim block was located in the middle-low latitude of the southern Hemisphere during the late Cambrian period (Table 1, Figure 2A, Huang et al., 2018; Zhao et al., 2018), along with the South China block on the western side of the Gondwana supercontinent. The periphery of the Tarim block is in a passive

continental margin environment, and although the original Tethys Ocean has been formed between the Tarim block and Australia plate, they are still related and similar in many aspects (Figure 2A, Zhao et al., 2018). At this time, the eastern continental groups, such as North China block and Siberia plate, have shifted from the other side of the

TABLE 1 Summary of available Early Paleozoic paleomagnetic poles for the Tarim block. Slat = Sampling locality Latitude; SLong = Sampling locality Longitude; N/n = Number of sites/number of samples; Plat = Pole Latitude; Plong = Pole Longitude; A₉₅ = 95% confidence oval (or dp/dm, semi minor and major axes of 95% confidence ellipsoid). Cam, O, S, and D indicate the Cambrian, Ordovician, Silurian, and Devonian times with 1= Early, 2 = Middle, and 3 = Late.

Age	Lithology	Locality	Slat	Slong	N/n	Plat	Plong	A ₉₅	Reference
S ₃ -D ₂	Sandstones	Kalpin	40.5	78.8	3/-	9.8	152.7	3.6/5.5	Fang et al., 1996
S ₁ -D ₂	Limestones	Tarim	40.6	79.0	-/40	16.5	165.2	2.9/5.3	Li et al., 1990
S ₂	Sandstones	Kalpin	40.6	79.6	4/-	12.1	158.4	4.1/7.2	Fang et al., 1996
S ₁₋₂	Sandstones	Kalpin	40.5	78.7	10/70	19.1	172.9	5.5	Huang et al., 2019
O ₂₋₃	Limestones	Kalpin and Aksu	40.6	78.9	-/99	-33.5	185.3	2.8/4.1	Huang et al., 2019
O ₁	Limestones	Yaerdang Mountains	41.3	83.4	3/-	-20.4	180.6	8.5/15	Fang et al., 1996
Cam ₂ -O ₂	Limestones	Yaerdang Mountains	41.3	83.4	5/15	-46.1	188.9	6.1/8.8	Sinopec Research Report

earth to the Western Hemisphere (Huang et al., 2018), and the three Chinese blocks (North China block, South China block, and Tarim block) show an N-S/T pattern (Figure 2A, Zhao et al., 2018).

After the middle-late Ordovician, the close relationship between the South China block and the Gondwana supercontinent is likely to last until the middle Devonian (Yang et al., 2004), while the Tarim block, located on the outermost margin of the Gondwana supercontinent, separated from it with its rapid clockwise rotation (Van der Voo, 1993) and moved northwestward rapidly from middle-late Ordovician to middle Silurian to cross the ancient equator (Figures 2B, C). The paleomagnetic poles of the middle-late Ordovician and Silurian further confirmed that a large southward apparent polar wander occurred in the Tarim block, which may be related to the significant northwestward movement and rotation of the Tarim block during the early Paleozoic (Sun and Huang, 2009).

By the end of the Silurian, the Tarim block had made a large drift to the northwest and completely broke away from the Gondwana supercontinent (Figure 2C, Huang et al., 2008, 2018; Zhao et al., 2018). This is consistent with the closure of the Kudi Ocean and the North Altyn Ocean on the southern margin of the Tarim block, in the late Ordovician-Silurian, and the collage events of the Central and South Kunlun terrane and the Altyn-Qilian terrane (Li et al., 2017). The late Ordovician to Silurian is the key period for the transition from N-S/T pattern to T-N/S pattern for the three blocks in China (Figure 2C, Zhao et al., 2018).

- (2) The relationship between Tarim block and the surrounding block based on geological affinity

The South China block and Tarim block were at the same latitude in the early Paleozoic, and the changes of magnetic declination recorded by the two blocks were also similar, indicating that the two blocks were closely related in the early Paleozoic. In addition, the affinity between the two blocks and the Gondwana supercontinent, in the early Paleozoic, is supported by a large amount of geological and paleogeographic data (Huang et al., 2000; Sun and Huang, 2009).

The geological study shows that the South China block and the Tarim block are consistent in the spatial distribution of Sinian tillite, and there are strong similarities in Cambrian and Ordovician sediments, biota characteristics, and their temporal and spatial distribution, indicating that South China and Tarim blocks are closely related from Sinian to Ordovician (Zhu et al., 1998). Moreover, the age of basement formation and the early Paleozoic

metalogenic effects of the South China block and Tarim block show clear similarities to those of the Australia plate (Nie, 1991).

During the Ordovician period, the South China block, Tarim block, and Australia plate are very similar in the appearance of chitin and other paleontological groups, which are likely to belong to the “Pacific type” with high disparity (Duan and Ge, 1992; Chen and Wang, 1996; Duan and Ge, 2005; Sun and Huang, 2009). The paleogeographic study of trilobites shows that all of the North China block, South China block, and Australia plate belong to the Asian-Australian biological region, but there are significant differences between the North and South China blocks. In the comparison of the detrital zircon age spectrum, the South China and Tarim blocks have obvious differences with the North China block, which suggests that, even if the paleolatitude of these three blocks are very close (Huang et al., 2018), the North China block may be far away from other blocks in spatial location.

3 Database and methods

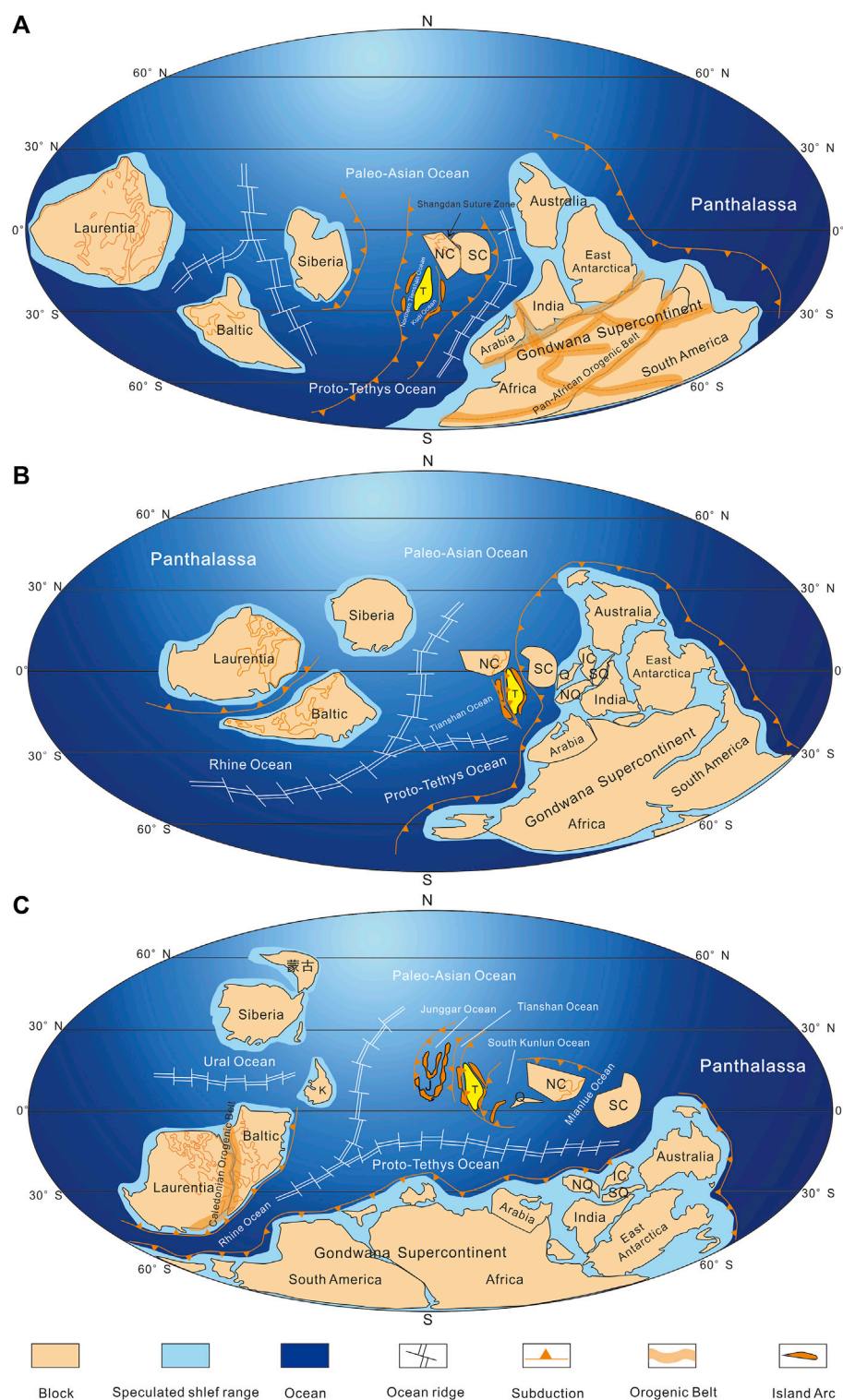
3.1 Database

The Tarim proto-type basin is an important research object. At present, the early Paleozoic maps of the Tarim Basin mainly include the tectonic-sedimentary environment maps compiled by Gao et al., 2016; Gao et al., 2017a; Gao et al., 2017b, the sedimentary model maps compiled by Chen et al., 2015, and the lithofacies paleogeographic maps provided by Tarim Oilfield Company.

The main data used include the residual thickness maps of Tarim Basin (Figure 3), the evolution maps of the equilibrium profile of Tarim Basin, the stratigraphic correlation maps of Tarim Basin, several seismic profiles (Figure 4 for example), and the peripheral margin shortening rate of Tarim Basin in Cenozoic (Jia et al., 2006; He et al., 2013; Chen et al., 2015; Tian et al., 2018; Laborde et al., 2019 and data from Tarim Oilfield Company).

3.2 Principles

The principles of proto-type basin recovery can be simply summarized as the following three aspects: the initial status, the practical process, and the real location (Lou et al., 2016; He et al., 2020; Liu et al., 2020), called P1, P2, and P3 hereafter.

**FIGURE 2**

Reconstructing of global plates distribution in Cambrian Period (A), Ordovician Period (B), and Silurian Period (C). T-Tarim; NC-North China; SC-South China; Q-Qaidam; NQ-North Qiangtang; IC-Indochina; SQ-South Qiangtang; J-Junggar; K-Kazakhstan. (modified after Huang et al., 2018; Zhao et al., 2018).

P1 is to restore the scope and sedimentary facies distribution of the proto-type basin, and then analyze the type of the basin, including the uplift-depression pattern and sedimentary system of the proto-type basin, which needs to be restored on the basis of drilling, outcrop, seismic profile, and other basic data, especially the constraint

condition of the basin boundary and the recovery of denudation area (Tong and He, 2001; Zhang G. Y. et al., 2019; Zheng et al., 2021; Wang, p et al., 2021).

P2 is to restore the superposition transformation process of the proto-type basin, that is, the recovery of extension or shortening.

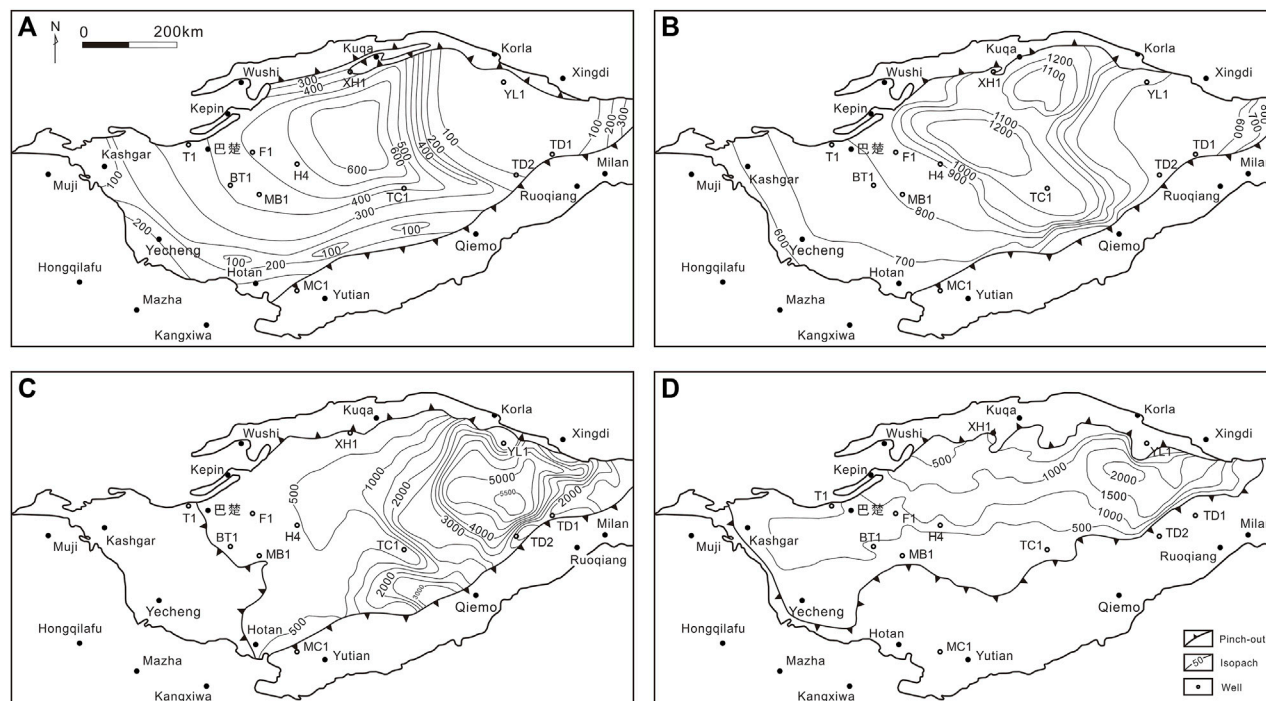


FIGURE 3 Residual thickness maps of Tarim in late middle-Cambrian (A), late Cambrian (B), late Ordovician (C), and late Silurian (D). (modified after [Chen et al., 2015](#) and data comes from Tarim Oilfield Company).

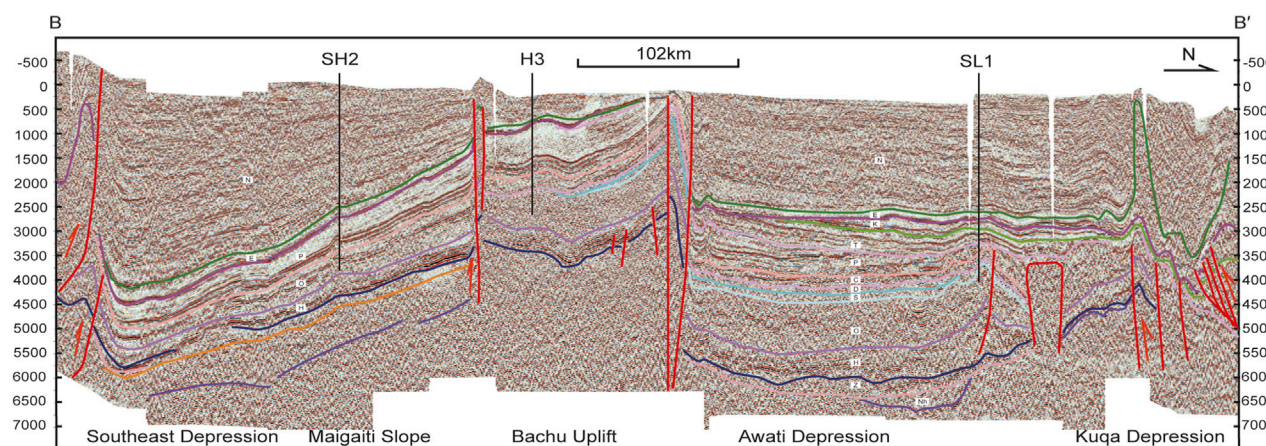


FIGURE 4 Geological interpretation of seismic section BB'. The location of this seismic section is shown in [Figure 1B](#).

Under the transformation of tectonics such as the Caledonian movement and Himalayan movement, there may be a great difference between the observed sedimentary range and the original sedimentary range, and the shortening can be calculated by the restoration of balanced cross sections ([Laborde et al., 2019](#)).

P3 is to restore the tectonic position during the development of the proto-type basin. On the one hand, to determine the paleo-position of the plate, that is, the paleolatitude, which can be measured and calculated by paleomagnetism ([Torsvik and Cocks, 2004](#); [Hou et al., 2020](#)) and analogy through the method of comparative tectonics; on the

other hand, the basin-mountain relationship is established by source-to-sink system analysis and clastic zircon analysis, which is useful for determining the relative position of the plate ([Hou et al., 2019](#); [Shao et al., 2019](#)).

3.3 Methods

The proto-type basin restoration methods for the Tarim Basin are mainly based on P1 and P2, and P3 is used to determine the location of

the Tarim block in the global plate tectonics. Detailed methods are described below.

- (1) The core point of the proto-type basin restoration lies in the scope of the proto-type basin. To determine the scope of the proto-type basin is to determine the boundary of the proto-type basin, which can be determined by the marginal facies method and the thickness trend method. The premise of using the marginal facies method is to clarify the type of the proto-type basin, different basins have different marginal facies, such as the marginal facies of lake basins are fan delta facies (Jiang, 2010; Ji et al., 2020; Wang and Lin, 2021). The thickness trend method can find the boundary of the proto-type basin with the help of the trend of the isopach in the isopach map, and it can also be analyzed by the trend surface of a certain thickness layer in the seismic profile (Zhang C, L et al., 2007; Yu et al., 2016). The residual thickness map is limited to the interior of the present Tarim Basin, so it is necessary to make up the isopach so as to restore the denudation area. The precondition of completing the isopach is to clarify the type of the proto-type basin, which can judge the opening and closing of the isopach. For example, the isopach of a rift basin is generally symmetric, while that of a foreland basin is asymmetric.
- (2) Restoring the original scope of the proto-type basin is indispensable, which means restoration to the state prior to shortening or expansion. The balanced cross-section method is to expand the scope of the proto-type basin after calculating the shortening by the balanced cross-section technique (Lou et al., 2016; Laborde et al., 2019).
- (3) According to the tectonic background analysis of the Tarim Basin, the island arc, terrane and ocean are placed on the peripheral margin of the Tarim Basin to show the oceanic-continental pattern. This step also needs to clarify the type of the peripheral basin of the Tarim block. If the basin is a passive continental margin basin, then the scope of the corresponding basin is relatively wide, and the terrane can be far away from the Tarim block; if the peripheral basin is an active continental margin, then the range of the basin is relatively narrower, and the terrane can be close to the Tarim block.

4 Result

4.1 Shortening amount of Tarim Basin

Laborde et al. (2019) made a detailed analysis of the shortening amount of Tarim Basin caused by various factors in the Cenozoic era (Table 2). Based on the statistical analysis of 81 profiles, in which 10 profiles (BB' for example, Figure 4) are recovered (Figure 5) by this study and 71 profiles provided by Tarim Oilfield Company, the shortening amount (Table 2) of 4 representative lateral lines (AA', BB', CC', DD', which are shown in Figure 1B), from early Paleozoic to pre-Cenozoic, are obtained.

Due to the influence of the Pamir Salient on the west side of the Tarim Basin, the shortening of the Tarim Basin gradually decreases from west to east, and the Cenozoic shortening rate accounts for the largest proportion of the total shortening rate in the western margin of the Tarim Basin, especially in the southwestern margin, up to 70% (southern margin of BB', Table 2). According to the calculated shortening rate of each side, the scope of the proto-type basin can be extended. It should be noted that the shortening amount of the Tarim Basin is mainly reflected in the margin of the Tarim Basin, which is shown visually on the outside of these two red dotted lines in Figure 5, and the impact on the interior of the Tarim Basin can be ignored.

4.2 Reconstruction of early Paleozoic proto-type Tarim Basin

Due to the long-term and complexity of geological evolution, the original proto-type basin will experience many tectonic actions of different properties. During these tectonic processes, the uplifting pattern, basin properties, and distribution of sedimentary facies in the Tarim Basin have undergone great change, which play important roles in hydrocarbon accumulation, migration, and trap (Lin et al., 2008). Through the analysis of residual basin fillings and tectonic background, restoring the proto-type of the basin and analyzing the later transformation is of great significance to understand the distribution of petroleum reservoirs in the superimposed basin (Wang et al., 2010; Chen et al., 2017).

TABLE 2 Shortening amount of Tarim Basin from Cenozoic, Silurian, Ordovician, Cambrian to the present (km).

Distribution of the shortening amount	Cenozoic (Laborde et al., 2019)	Silurian (this study)	Ordovician (this study)	Cambrian (this study)
Northern margin of AA'	36.0	54.0	65.0	64.0
Southern margin of AA'	32.0	46.0	50.0	50.0
Northern margin of BB'	21.0	43.0	50.0	47.0
Southern margin of BB'	35.0	50.0	54.0	50.0
Northern margin of CC'	22.0	39.0	45.0	42.0
Southern margin of CC'	0.9	15.0	20.0	16.0
Northern margin of DD'	0.0	15.0	23.0	23.0
Southern margin of DD'	0.3	24.0	36.0	33.0

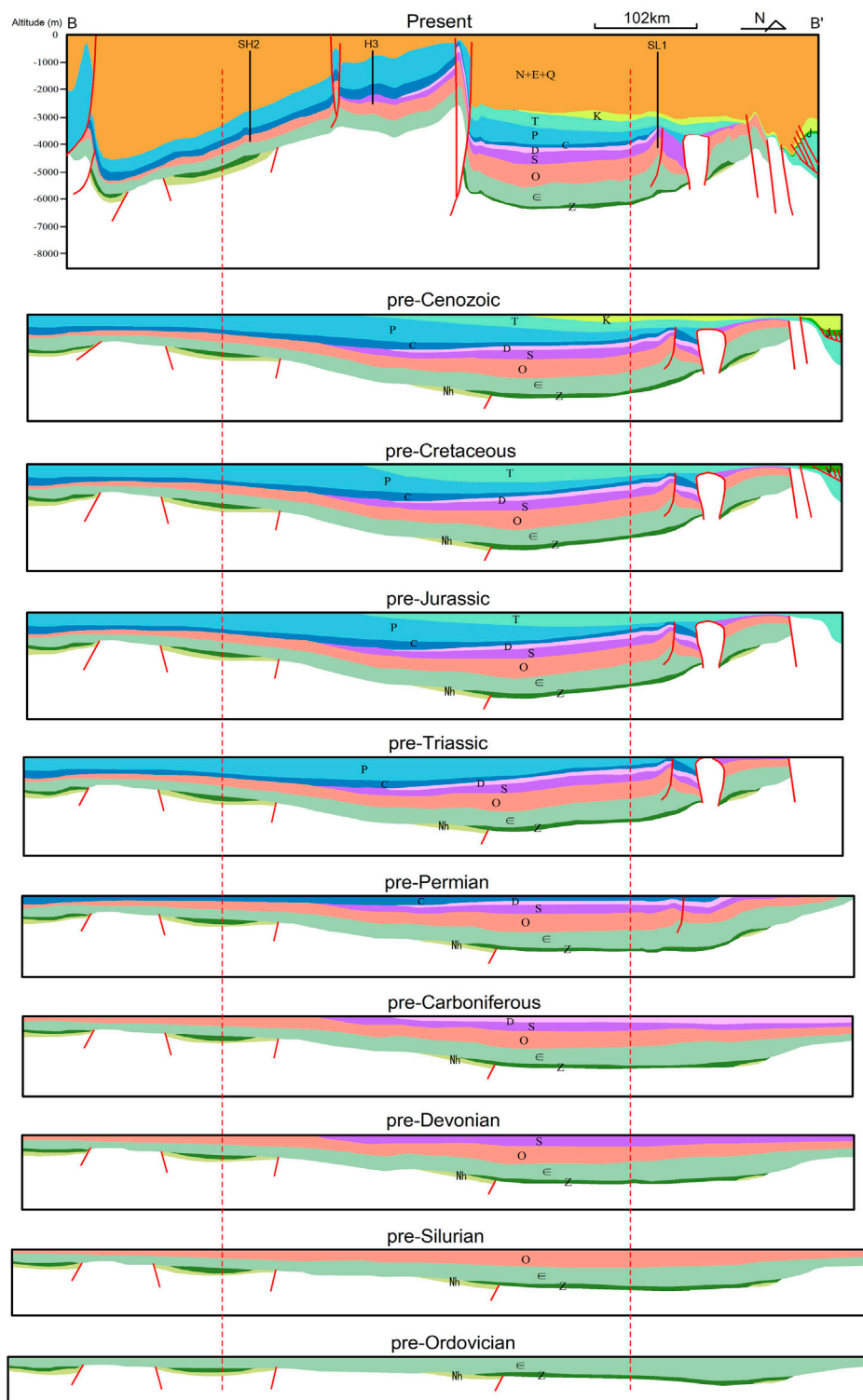


FIGURE 5

Recovered balanced cross-section of BB'. The location of this seismic section is shown in Figure 1B. The red dotted lines visually represent the boundary between the margin and the interior of the Tarim Basin.

(1) Proto-type Tarim Basin in late Middle Cambrian

In the Middle Cambrian, the Tarim Basin was mainly controlled by the extensional tectonic environment (Lin et al., 2008; Yun et al., 2014). The South Tianshan Ocean is in a stage of

continuous expansion, with the South Tianshan intercontinental rift developed in the northern margin of the Tarim Basin. Meanwhile, the Kudi Ocean and the North Altyn Ocean, located in the southern margin of the Tarim Basin, reached the maximum range (Figure 6A).

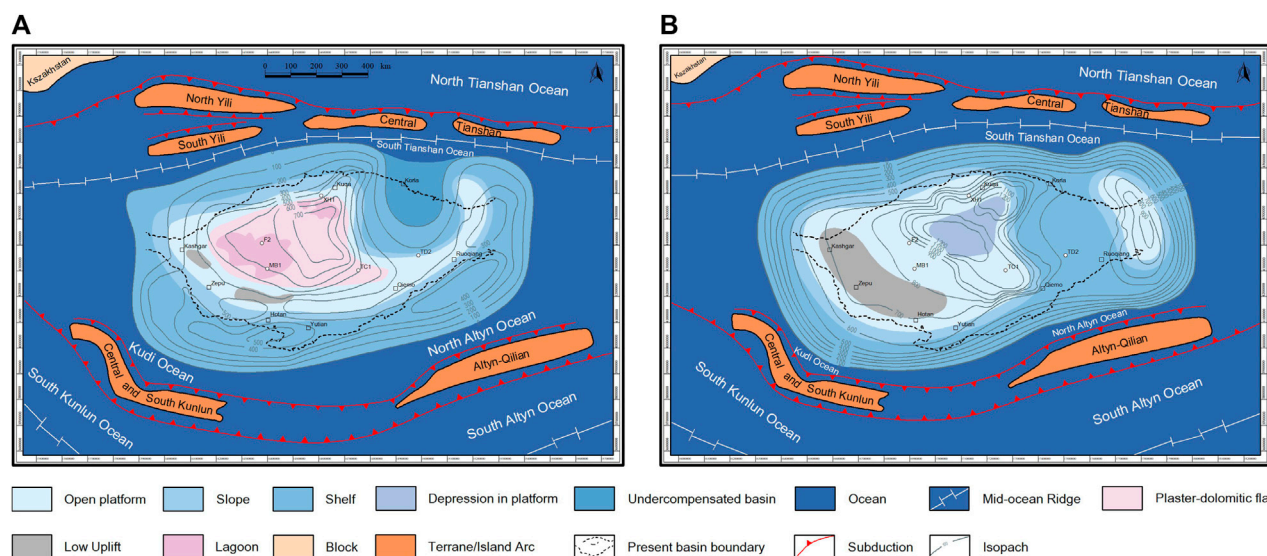


FIGURE 6

Proto-type basin of Tarim and adjacent areas in late Middle Cambrian (A) and late Cambrian (B).

Under the extensional background, the internal uplift-depression pattern of the Tarim Basin changes from north-south differentiation to east-west differentiation, with the embryonic form of “carbonate platform in the west, deep-water basin in the east” appearing (Chen et al., 2015; Li et al., 2015; Gao et al., 2017a). In the western part of the Tarim Basin, the intracratonic basin, characterized by restricted platform sedimentation, widely developed plaster-salt rock facies (Figure 6A), which are good reservoir strata, while the cratonic marginal basin in the eastern part of the Tarim Basin, featured on deep-water deposits, developed siliceous-bearing mudstone (Gao, 2015; Zhang et al., 2015; Wu et al., 2016; Gao et al., 2017a) and has not yet achieved north-south penetration in space (Figure 6A). On the whole, the ramp - evaporate platform - platform margin - slope - deep-water facies model (Chen et al., 2015; Tian et al., 2018) was developed in the Tarim Basin during the middle Cambrian. Passive continental margin basin is developed in both the southern and northern margin of the Tarim Basin, especially the passive continental margin basin in the southwest of the Tarim Basin, where the shelf facies have a wide distribution range, which is beneficial to hydrocarbon generation.

(2) Proto-type Tarim Basin in late Cambrian

In the late Cambrian, as a whole, it inherited the basin pattern of the middle Cambrian (Figure 6B), which was still controlled by the extensional tectonic environment (Lin et al., 2008; Yun et al., 2014). The South Tianshan Ocean, in the northern margin of the Tarim Basin, continued to expand, while the Kudi Ocean and Allyn Ocean in the southern margin of the Tarim Basin were getting narrow (Figure 6B).

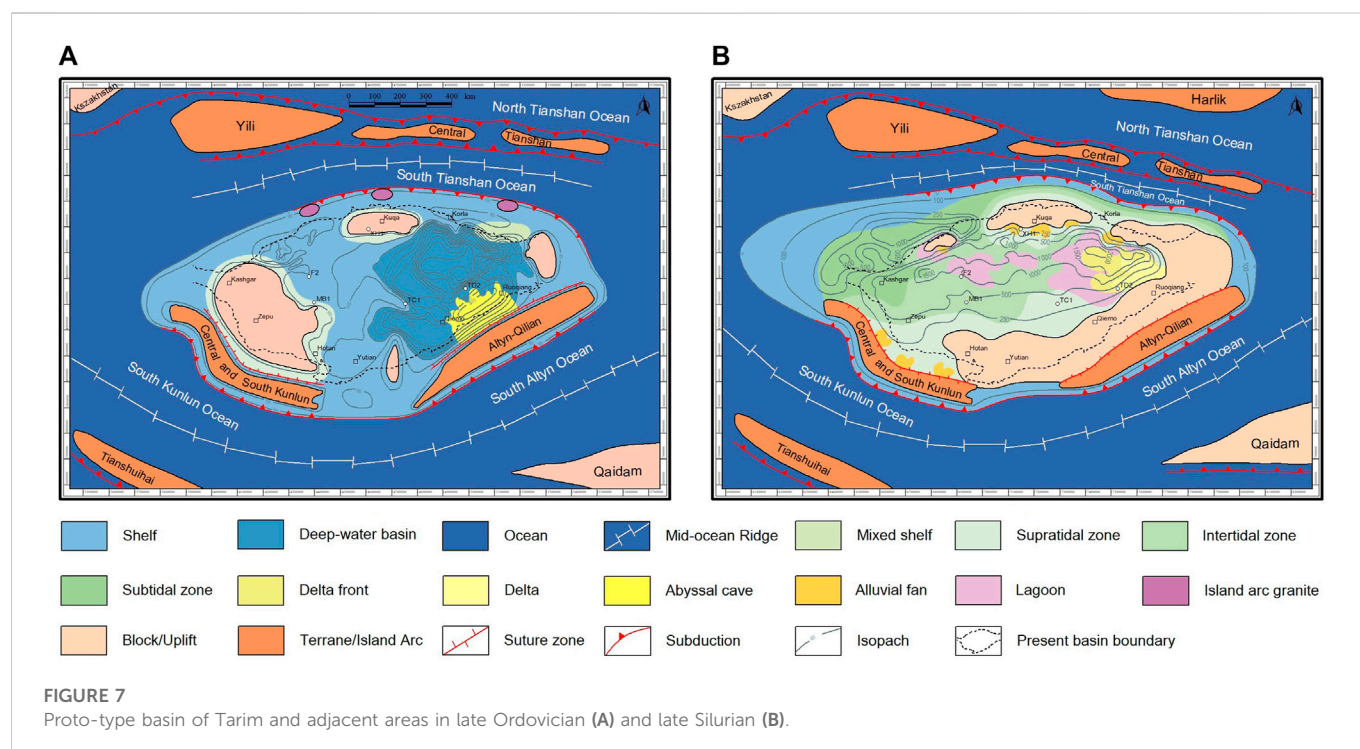
At the end of the late Cambrian, the cratonic marginal basin in the eastern part of the Tarim Basin achieved north-south penetration in space, and the paleogeographic pattern “east-west differentiation” was completely formed (Gao et al., 2012; Gao et al., 2017a). The platform formation developed in the west, dominated by open-platform

deposition, while in the east it was dominated by deep-water basin facies deposition (Figure 6B, Zhang et al., 2015; Wu et al., 2016; Gao et al., 2017a). As a whole, the restricted platform—semi-restricted platform—open platform—platform margin—slope—deep-water facies model (Chen et al., 2015) was developed in the Tarim Basin during the late Cambrian. Compared with the early Middle Cambrian (Figure 6A), the main change in the late Cambrian is the disappearance of evaporate platform facies, transforming to semi-restricted and restricted platform, which indicates that the relative sea level of the late Cambrian gradually rose and the water body deepened slowly, with the plaster-salt rock facies vanishing (Figure 6B). Passive continental margin basins still developed in the southern and northern margin of the Tarim Basin, the former becoming wider and the latter narrowing due to the subduction of the Kudi Ocean and the North Allyn Ocean.

(3) Proto-type Tarim Basin in late Ordovician

In the middle-late Ordovician, the subduction of the Kudi Ocean and the North Allyn Ocean led to the transformation of the tectonic environment from extension to compression in the southern margin of the Tarim Basin (Lin et al., 2008; Yun et al., 2014; Li et al., 2015; Zhang L. N. et al., 2019; Wu et al., 2021). At the end of the Ordovician, the South Tianshan Ocean reached the maximum, then subducted northward to the Central Tianshan and Yili terranes and southward to the Tarim block (Figure 7A, Lin et al., 2012; Jiang et al., 2014).

In the Ordovician, under the influence of the subduction of the Kudi Ocean and the North Allyn Ocean, the uplift-depression pattern of the Tarim Basin changed from east-west differentiation to north-south differentiation (Figure 7A, Lin et al., 2012; Yun et al., 2014; Gao et al., 2016; Gao et al., 2017b), and the peripheral uplift of the Tarim Basin was obvious, especially in the southwest of the Tarim Basin, with the depocenter of the basin migrating to the Manjiaer Depression and the Tabei Uplift surfaced for the first time (Figure 7A). The



intracratonic basin developed in the middle of the Tarim Basin, and the back-arc foreland basin (Figure 7A) developed in the southeast and southwest margin of the Tarim Basin, which gradually disappeared under the injection of abundant provenances at the end of Ordovician (Gao et al., 2017b).

(4) Proto-type Tarim Basin in late Silurian

The continuous collision of the Central and South Kunlun and Allyn-Qilian terraces with the Tarim block during the Silurian period resulted in a strong compression of the Tarim Basin, with the South Kunlun Ocean, the South Altyn Ocean, and the South Tianshan Ocean continuing to subduct (Figure 7B, Xu et al., 2011; Li et al., 2015; Wu et al., 2021).

During the Silurian, uplifts developed in the south, north, and east of the Tarim Basin, with depression in the middle (Figure 7B, Lin et al., 2011; Lin et al., 2012; He et al., 2013; Zheng et al., 2014). Topographically, the Tarim Basin is high in the south and low in the north, developing intracratonic depression in the central basin, which developed mainly from the eastern and southeastern margins of the Tarim Basin (Figure 7B, Jia et al., 2006; Lin et al., 2011). The shallow sea in the west of the Tarim Basin is open, and the east is blocked with the transgression mainly coming from the north and northwest (Jia et al., 2006; Lin et al., 2011; Li et al., 2015), and the lithofacies paleogeographic pattern of shelf - subtidal - intertidal - supratidal facies is developed from northwest to southeast (Figure 7B, Wu et al., 2020). The back-arc foreland basins in the southeastern and southwestern margin of the Tarim Basin have been extinct, and the Tanan Uplift developed under the background of extrusion.

4.3 Reconstruction of early Paleozoic tectono-paleogeography around the Tarim basin

In the middle Cambrian, the North Altyn Ocean, in the southeast margin of the Tarim block, and the Kudi Ocean, in the southwest margin, began to subduct southward, and the Central and South Kunlun and Allyn-Qilian terrane began to approach the Tarim block (Figure 8A, Gao et al., 2017a; Mou et al., 2018). The South Tianshan Ocean on the northern margin of the Tarim Basin continued to expand, the Yili and Central Tianshan terranes were far away from the Tarim Basin, while the North Tianshan Ocean continued to subduct southward beneath the Yili and Central Tianshan terranes (Figure 8A). It should be noted that the Yili terrane was an arc-basin system, which was divided into North and South Yili, until the end of the Ordovician (Figure 8A, B, Figure 9A, Wang et al., 2012; Wang et al., 2014a; Wang et al., 2014b; Huang et al., 2021). At the end of the middle Cambrian, the Arabian and Indian blocks had not yet been separated from the Gondwana supercontinent, all in a shallow sea environment, dominated by carbonate deposits (Li et al., 2013; Rao et al., 2016), while the Kazakhstan block was free outside the Gondwana, but also developed shallow marine deposits (Shen et al., 2016; Zhang G. Y. et al., 2019).

During the Cambrian period, the Tarim block and surrounding blocks were still controlled by the extensional tectonic environment (Lin et al., 2008; Yun et al., 2014). The North Altyn Ocean and the Kudi Ocean continued to subduct southward, thus the North Altyn Ocean and the Kudi Ocean further narrowed, with the Central and South Kunlun and Allyn-Qilian terrane closer to the Tarim block (Figure 8B). From a more macro perspective, the Paleo-Asian Ocean and the Proto-Tethys Ocean were also subducting towards the Tarim block (Figure 8B, Zhao et al., 2018). At the end of the Cambrian, driven

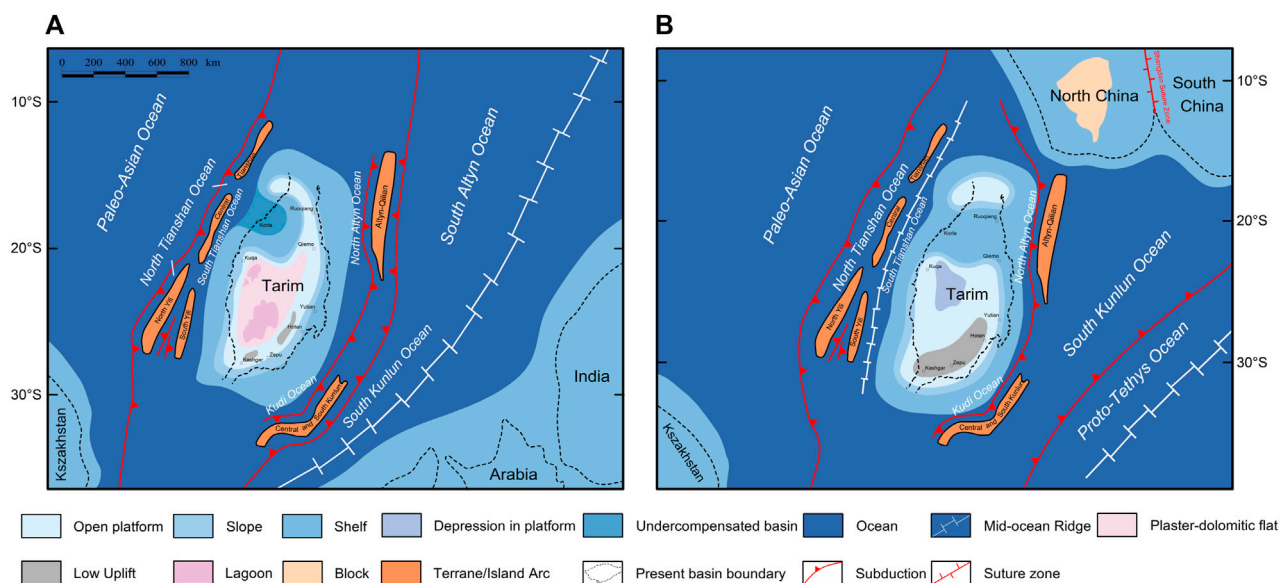


FIGURE 8

Tectono-paleogeography of Tarim and adjacent areas in late Middle Cambrian (A) and late Cambrian (B).

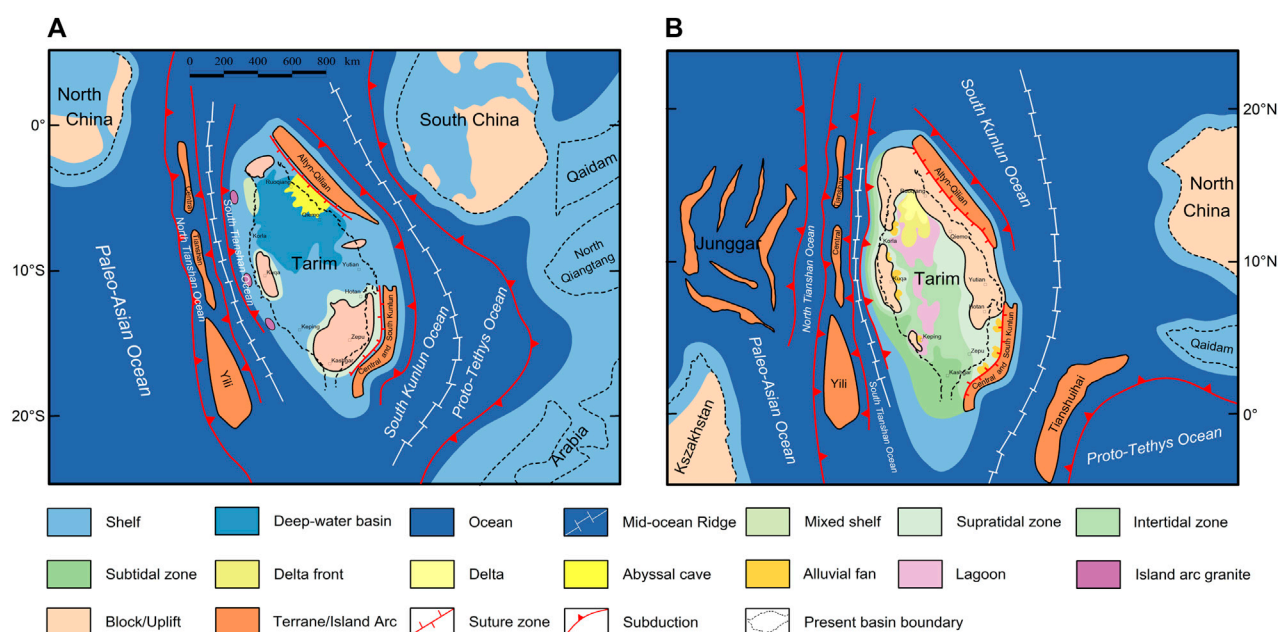


FIGURE 9

Tectono-paleogeography of Tarim and adjacent areas in late Ordovician (A) and late Silurian (B).

by the subduction of the Shangdan Ocean, the North China block collided with the South China block, which formed the Shangdan suture zone and developed uplifts in the interior of the North and South China blocks (Chen and Liu, 2011; Li and Jiang, 2013; Lin et al., 2016), with shallow marine deposits in the periphery (Hu et al., 2022; Zhang G. Y. et al., 2019; Zhang et al., 2019).

In the Ordovician, except for the Gondwana Supercontinent, all the other landmasses drifted northward, and the Tarim, South China,

and North China blocks also drifted to low latitudes (Figure 9A, Huang et al., 2018; Zhao et al., 2018). The South China and North China blocks separated again, and the latter drifted westward relative to the Tarim block, accompanied by clockwise rotation (Figure 9A, Huang et al., 2018; Zhao et al., 2018). The Tarim block and its surrounding areas are under compression environment, and part of the South and North China blocks have developed large-scale uplifts, other areas developing shallow marine deposits with the Qaidam

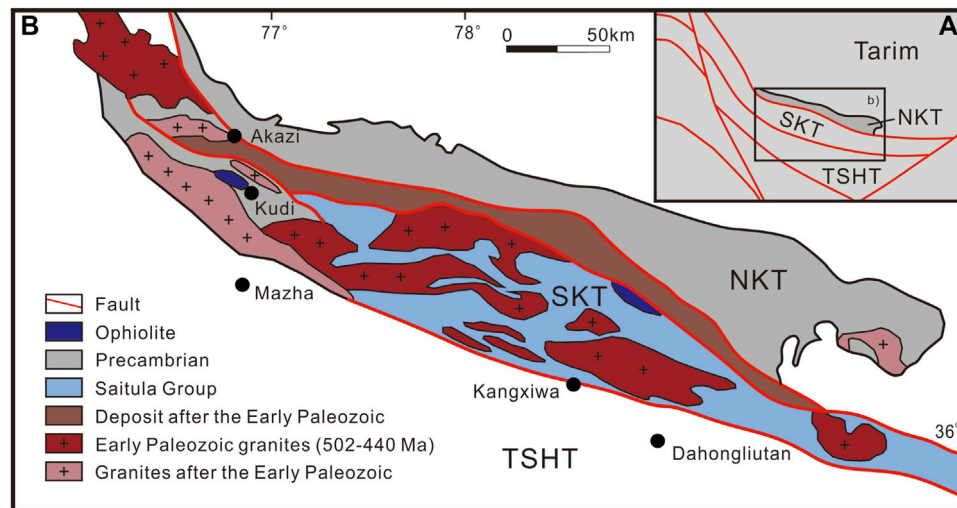


FIGURE 10

Location (A) and tectonic framework (B) of the West Kunlun orogenic belt and its adjacent areas (NKT: The North Kunlun terrane, which is a part of the Tarim block; SKT: The South Kunlun terrane, which can correspond to the Central and South Kunlun terrane in early Paleozoic; TSHT: The Tianshuihai terrane) (modified after Zhang L. N. et al., 2019).

terrane, North Qiangtang terrane, and the northwestern margin of the Arabian Plate, located on the margin of the Gondwana (Figure 9A, Feng et al., 2004; Li et al., 2013; Chen et al., 2015; Zhou et al., 2017; Zhang G. Y. et al., 2019). Until the end of the Ordovician, the middle Caledonian movement led to the closure of the Kudi Ocean and the North Altyn Ocean (Figure 9A, Lin et al., 2008; Yun et al., 2014; Li et al., 2015; Zhang L. N. et al., 2019; Wu et al., 2021). The Central and South Kunlun and Altyn-Qilian terranes collided with the Tarim block, while the Tianshuihai-Bayanhar terrane and Qaidam block approached the Tarim block (Mou et al., 2018; Zhang L. N. et al., 2019). At the same time, the South Tianshan Ocean began to subduct southward beneath the Tarim block and northward beneath the Yili and Central Tianshan terranes (Figure 9A, Zhou et al., 2004; Wang et al., 2009; Ge et al., 2012; Lin et al., 2012; Jiang et al., 2014).

During the Silurian period, the position of the three blocks in China was relatively discrete, and the North China block was uplifted into a denudation area (Figure 9B), which was the same as the Kazakhstan, Arabian and Indian plates, while the South China block developed shallow marine deposits as a whole, which was located on the eastern side of the North China block (Huang et al., 2018; Zhao et al., 2018; Zhang G. Y. et al., 2019). The Tarim block is relatively isolated, and the shallow marine deposits are mainly developed in the northwest of the Tarim block (present location, Figure 7B, Figure 9B, Lin et al., 2011; Lin et al., 2012; He et al., 2013; Zheng et al., 2014; Li et al., 2015). The Qaidam terrane between the Tarim and North China terranes also develops shallow marine deposits (Figure 9B, Zhang G. Y. et al., 2019). At the end of the Silurian, the Central and South Kunlun and Altyn-Qilian terranes completely merged with the Tarim block, forming a larger Tanan uplift, and the South Kunlun Ocean and the South Altyn Ocean continued to submerge northward, with the Tianshuihai-Bayanhar terrane and Qaidam block closer to the Tarim block (Figure 9B, Xu et al., 2011; Li et al., 2015; Wu et al., 2021). It should be noted that in the north of the Tarim block (present location) and the east of the

Kazakhstan plate, the Junggar arc group has not been collaged to form the Junggar terrane (Figure 9B, Xiao et al., 2010; Carmichael et al., 2019).

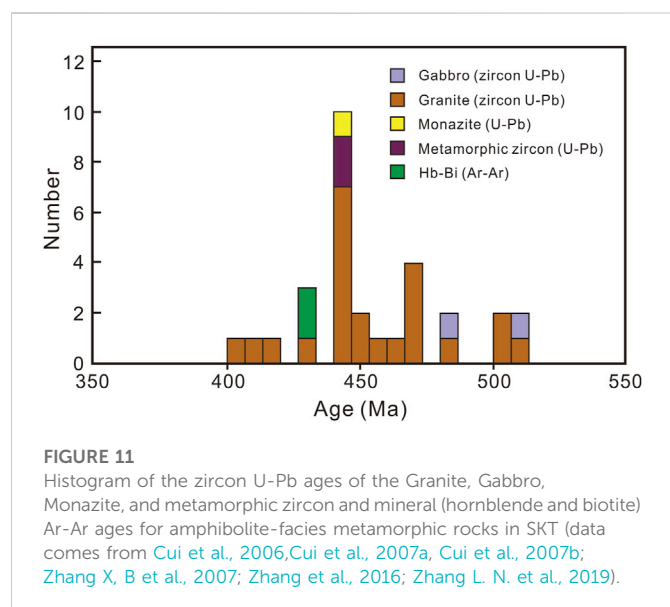
5 Discussion

In the early Paleozoic, the periphery of the Tarim Basin was greatly changed, especially the appearance, expansion, and closure of the Kudi Ocean and North Altyn Ocean on the southern margin, transforming the tectonic environment of the Tarim Basin from extension to extrusion, which changed the scope and nature of the proto-type basin. To determine the peripheral background of the Tarim Basin in the early Paleozoic, the focus is on when the peripheral oceans of the Tarim Basin were opened and closed, and when the surrounding terranes collided.

5.1 The expansion and closure of the Kudi Ocean

The Kudi ophiolite exposed in the West Kunlun orogenic belt is evidence of the existence of the early Paleozoic Kudi Ocean between the Tarim Basin and the Central and South Kunlun terrane in the southwest margin of the Tarim Basin (Zhang L. N. et al., 2019).

Through the spatial relationship between ophiolite and granite in the same period, the subduction direction of the Kudi Ocean can be judged, and then the nature of the southwest peripheral basin of the Tarim Basin can be determined (Zhang L. N. et al., 2019). The residual ophiolite in the northern margin of the Saitula Group and the granite developed on SKT in the early Paleozoic (Figure 10) indicate that the Kudi Ocean subducted southward to the Central and South Kunlun terrane (Figures 8, 10), thus the passive continental margin basin develops at the southwest margin of



the Tarim Basin, which is a good place for the development of hydrocarbon resources.

The age of the gabbro in the Kudi ophiolite is concentrated between 510 and 525 Ma (Xiao et al., 2003; Zhang et al., 2004; Fang et al., 2010), indicating that the Kudi Ocean was in the stage of oceanic expansion in the early-middle Cambrian. The Tiekelike Formation of the NKT contains a mass of middle-late Ordovician granodiorite (Matte et al., 1996), showing that the NKT is the collisional orogenic belt in the middle-late Ordovician.

The zircon U-Pb ages of the granite, monazite, and metamorphic zircons, and the Ar-Ar ages for hornblende and biotite in the amphibolite-facies metamorphic rocks in SKT are concentrated in 450–440 Ma (Figure 11, Cui et al., 2006, Cui et al., 2007a, Cui et al., 2007b; Zhang X B et al., 2007; Zhang et al., 2016; Zhang et al., 2019b), which means that the collision period of the

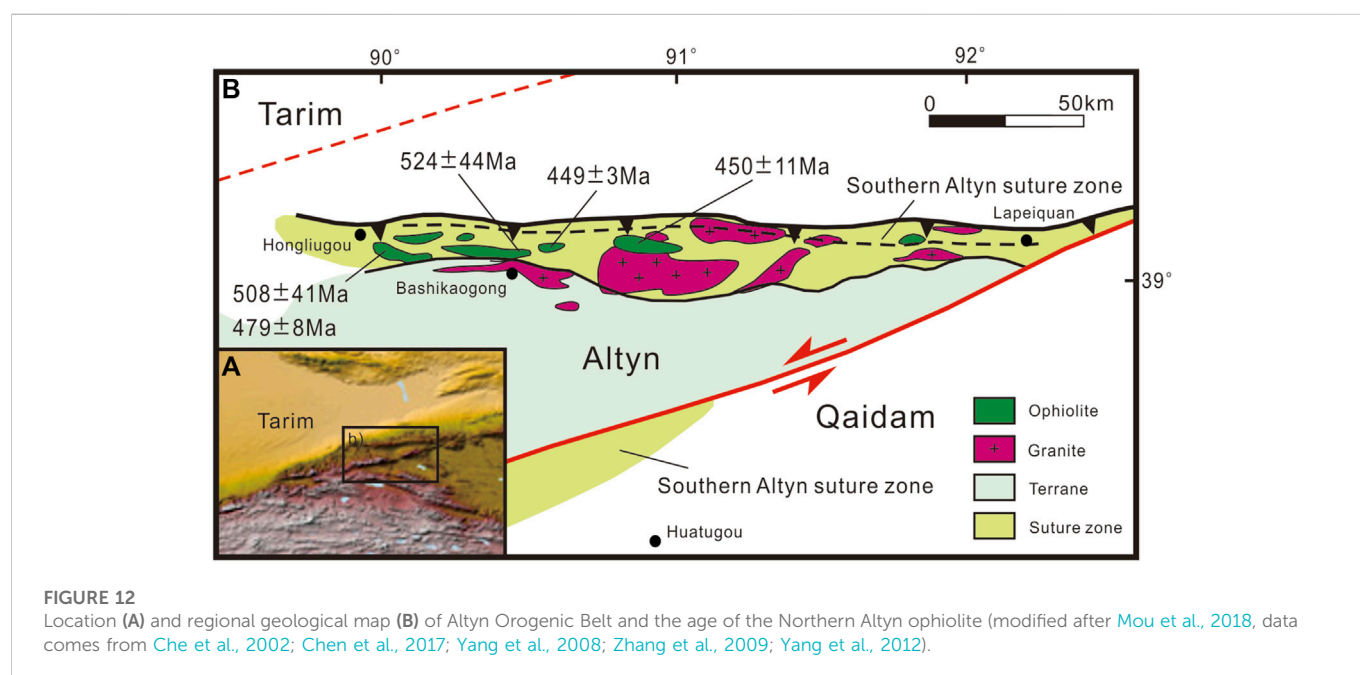
SKT is 450–440 Ma, that is, in the late Ordovician, the Central and South Kunlun terrane collage up and the Kudi Ocean closed (Figure 9A, Zhang L. N. et al., 2019).

5.2 The expansion and closure of the North Altyn Ocean

The Hongliugou-Lapaiquan ophiolite in the Northern Altyn suture zone is evidence of the existence of the North Altyn Ocean (Mou et al., 2018), which is located in the southeastern margin of the Tarim Basin and between the Tarim Basin and the Altyn-Qilian terrane in the early Paleozoic. There are two areas of concentrated ophiolites in the Altyn orogenic belt, called the Hongliugou-Lapaiquan ophiolite belt and the Apa-Mangya ophiolite belt, corresponding to the Northern Altyn suture zone and the Southern Altyn suture zone, respectively, and the Altyn-Qilian terrane is sandwiched between two suture zones (Figure 12, Sobel and Araud, 1999; Xu et al., 1999; Meng et al., 2010).

The formation age of the Northern Altyn metamorphic rocks in Hongliugou is concentrated in the Middle-late Cambrian (Mou et al., 2018), indicating that the North Altyn Ocean began to subduct in the Middle-late Cambrian, and the age of the Northern Altyn ophiolite is concentrated in 524–449 Ma (Figure 12, Che et al., 2002; Chen et al., 2015; Yang et al., 2008; Zhang et al., 2009; Yang et al., 2012), indicating that the closure of the North Altyn Ocean should not be earlier than 449 Ma. In addition, in Hongliugou and other places, there are granites formed in the subduction environment in the late Cambrian-late Ordovician (500–443 Ma) (Chen et al., 2003; Kang et al., 2011) and granites representing syn-collision and post-collision setting in the Ordovician-late Silurian (474–419 Ma) (Wu et al., 2005, 2007; Yang et al., 2012).

Based on the geochemical study of the intermediate-acid volcanic rocks in the Altyn orogenic belt, it is found that the granites, from south to north, have the characteristic of the transition from I-type granite to S-type granite, indicating that the North Altyn Ocean



subducted to the Altyn-Qilian terrane in the early Paleozoic (Figure 8, Li et al., 2013).

5.3 Two-direction subduction of the South Tianshan Ocean

At the beginning of the early Paleozoic, the Tarim block was separated from the Rodinia supercontinent. The continental rift basalts were developed in the Lower Cambrian of the Kuruketage, Keping, and South Tianshan areas (Jia, 1997; Li et al., 2006), representing the extensional movement on the northern margin of the Tarim block in the Cambrian and the emergence of the South Tianshan Ocean between the Central Tianshan terranes and the Tarim block. Until the early Carboniferous period, there were still new oceanic crusts formed in the South Tianshan Ocean (Jiang et al., 2014).

According to the traditional view, the northward subduction of the South Tianshan Ocean lasted from the late Ordovician to the late Carboniferous, while the northern margin of the Tarim Basin was always a passive continental margin environment, thus continuously developing thick layers of Paleozoic sediments (Zhou et al., 2004; He et al., 2007; Li et al., 2010; Wang et al., 2011). However, in recent years, several medium-acidic intrusive rocks have been discovered near the northern margin of the Tarim Basin, and the U-Pb zircon ages of these medium-acidic intrusive rocks are concentrated in the late Ordovician-early Silurian, indicating the southward subduction of the South Tianshan Ocean at the same time (Figure 9A, Wang et al., 2009; Ge et al., 2012; Lin et al., 2012; Jiang et al., 2014). In other words, the northern margin of the Tarim Basin has changed from passive continental margin to active continental margin at the end of the Ordovician period (Figure 9A).

6 Conclusion

- (1) Due to the influence of the Pamir Salient, the shortening of the Tarim Basin gradually decreases from west to east, and the Cenozoic shortening rate accounts for the largest proportion of the total shortening rate in the western margin of the Tarim Basin. The shortening amount of the Tarim Basin is mainly reflected in the margin of the Tarim Basin, and the impact on the interior of the Tarim Basin can be ignored.
- (2) In the Cambrian, the Tarim Basin was mainly controlled by the extensional tectonic environment, with the sedimentary framework of “carbonate platform in the west, deep-water basin in the east”. During the middle-late Ordovician, the subduction of the Kudi Ocean and the North Altyn Ocean led

to the transformation of the tectonic environment from extension to compression in the southern margin of the Tarim Basin, thus the uplift-depression pattern of the Tarim Basin changed from east-west differentiation to north-south differentiation.

- (3) The North Altyn Ocean and the Kudi Ocean began to subduct southward beneath the Central and South Kunlun and Altyn-Qilian terranes in the middle Cambrian. Until the end of the Ordovician, under the influence of the middle Caledonian movement, the two oceans closed, and the Central and South Kunlun and Altyn-Qilian terranes collided with the Tarim block, which greatly changed the uplift-depression pattern, basin properties, and sedimentary facies distribution of the Tarim Basin.

Data availability statement

The original contributions presented in the study are included in the article/Supplementary Material, further inquiries can be directed to the corresponding author.

Author contributions

ZZ did most of the job in this article, including literature review, balanced cross-section recovery, manuscript writing, drawing of maps and so on; SH and CL generously offered the main data used in this article, HC, JX, XL, and LW contributed to the reconstruction of early Paleozoic proto-type Tarim Basin; HZ helped a lot in reconstructing global plates distribution.

Conflict of interest

SH and CL were employed by Tarim Oilfield Company.

The remaining authors declare that the research was conducted in the absence of any commercial or financial relationships that could be construed as a potential conflict of interest.

Publisher's note

All claims expressed in this article are solely those of the authors and do not necessarily represent those of their affiliated organizations, or those of the publisher, the editors and the reviewers. Any product that may be evaluated in this article, or claim that may be made by its manufacturer, is not guaranteed or endorsed by the publisher.

References

- Cao, W. C., Zahirovic, S., Flament, N., Williams, S., Golonka, J., and Müller, R. D. (2017). Improving global paleogeography since the late Paleozoic using paleobiology. *Biogeosciences* 14, 5425–5439. doi:10.5194/bg-14-5425-2017
- Carmichael, S. K., Waters, J. A., Königshof, P., Suttner, T. J., and Kido, E. (2019). Paleogeography and paleoenvironments of the late devonian kellerwasser event: A review of its sedimentological and geochemical expression. *Glob. Planet. Change* 183, 102984. doi:10.1016/j.gloplacha.2019.102984
- Che, Z. C., Liu, L., and Luo, J. H. (2002). *Regional tectonics of China and its adjacent regions*. Beijing: Science Press, 07–369. (in Chinese).
- Chen, D. L., and Liu, L. (2011). New data on the chronology of eclogite and associated rock from Guanpo Area, North Qinling orogeny and its constraint on nature of North Qinling HP-UHP eclogite terrane. *Earth Sci. Front.* 18, 158–169. (in Chinese with English abstract).
- Chen, H. D., Hou, M. C., Chen, A. Q., Shi, Z. Q., Xing, F. C., Huang, K. K., et al. (2017). Research progress and key scientific problems of palaeogeography in China. *Acta Sedimentol. Sin.* (05), 888–901. (in Chinese). doi:10.14027/j.cnki.cjxb.2017.05.003
- Chen, X. H., Gehrels, G., Wang, X. F., Yang, X. F., Yang, F., and Chen, Z. L. (2003). Discussion on the formation age and tectonic environment of granite in the northern

- margin of Altyn Mountain. *Bull. Mineralogy, Petrology Geochem.* 22 (4), 294–298. (in Chinese). doi:10.3969/j.issn.1007-2802.2003.04.002
- Chen, X. H., Wang, X. F., and Li, Z. H. (1996). Arenigian chitinozoan biostratigraphy and paleobiogeography in South China. *Geol. Rev.* 42 (3), 200–208. (in Chinese). doi:10.3321/j.issn:0371-5736.1996.03.002
- Chen, X. W., Mou, C. L., Zhou, K. K., Kang, J. W., Wang, Q. Y., Ge, X. Y., et al. (2015). Lithofacies and palaeogeography of ordovician in north China. *Sediment. Geol. Tethyan Geol.* 35 (04), 1–11. (in Chinese).
- Chen, Y. Q., Yan, W., Han, C. W., Yang, P. F., and Li, Z. (2015). Redefinition on structural paleogeography and lithofacies paleogeography framework from cambrian to early ordovician in the Tarim Basin: A new approach based on seismic stratigraphy evidence. *Nat. Gas. Geosci.* 26 (10), 1831–1843. (in Chinese). doi:10.11764/j.issn.1672-1926.2015.10.1831
- Cocks, L. R. M., and Torsvik, T. H. (2002). Earth geography from 500 to 400 million years ago: A faunal and palaeomagnetic review. *J. Geol. Soc.* 159, 631–644. doi:10.1144/0016-764901-118
- Cui, J. T., Bian, X. W., and Wang, G. B. (2006). Geological composition and evolution of the West Kunlun. *Geol. Shaanxi* 24, 1–11. doi:10.1016/j.gsf.2018.05.006
- Cui, J. T., Wang, J. C., Bian, X. W., Luo, Q. Z., Zhu, H. P., Wang, M. C., et al. (2007a). Zircon SHRIMP U-Pb dating of the dongbake gneissic tonalite in the northern kangxiwa, West Kunlun. *Geol. Bull. China* 26, 726–729. (in Chinese with English abstract). doi:10.3969/j.issn.1671-2552.2007.06.014
- Cui, J. T., Wang, J. C., Bian, X. W., Zhu, H. P., Luo, Q. Z., Yang, K. J., et al. (2007b). Zircon SHRIMP U-Pb dating of early Paleozoic granite in the Mengguobao-Pushou area on the northern side of the Kangxiwa, West Kunlun. *Geol. Bull. China* 26, 710–719. (in Chinese with English abstract). doi:10.3969/j.issn.1671-2552.2007.06.012
- Dong, Y. P., He, D. F., Sun, S. S., Liu, X. M., Zhou, X. H., Zhang, F. F., et al. (2018). Subduction and accretionary tectonics of the East Kunlun Orogen, Western segment of the central China orogenic system. *Earth-Science Rev.* 186, 231–261. doi:10.1016/j.earscirev.2017.12.006
- Duan, J. Y., and Ge, X. H. (2005). Stratigraphic and paleobiogeographic affinities between different tectonic units in northwestern China-With a discussion of the tectonic framework of northwestern China. *Geol. Bull. China* 24 (6), 558–563. (in Chinese with English abstract). doi:10.3969/j.issn.1671-2552.2005.06.013
- Duan, J. Y., and Ge, X. H. (1992). Tarim-Yangzi and its paleogeographic pattern. *J. Changchun Univ. Earth Sci.* 22 (3), 260–268. (in Chinese).
- Fang, A. M., Li, J. L., and Chu, Z. Y. (2010). Sm-Nd isochron age of basic volcanic rocks in Kudi ophiolite, West Kunlun. *Chin. J. Geol.* 45 (01), 113–121. (in Chinese). doi:10.3969/j.issn.0563-5020.2010.01.011
- Fang, D. J., Jin, G. H., Jiang, L. P., Wang, P. Y., and Wang, Z. L. (1996). Paleozoic paleomagnetic results and the tectonic significance of Tarim Plate. *Chin. J. Geophys.* 39 (4), 522–532. (in Chinese with English abstract). doi:10.3321/j.issn:0001-5733.1996.04.010
- Feng, Z. Z., Peng, Y. M., Jin, Z. K., and Bao, Z. D. (2004). Lithofacies palaeogeography of the late ordovician in China. *J. Palaeogeogr.* 02, 127–139. (in Chinese with English abstract). doi:10.3969/j.issn.1671-1505.2004.02.001
- Gao, H. H., He, D. F., Tong, X. G., Wen, Z. X., Wang, Z. M., and He, J. Y. (2016). Tectonic-depositional environment and proto-type basins during the depositional period of middle ordovician yijianfang formation in Tarim Basin. *J. Palaeogeogr.* 18 (06), 986–1001. (in Chinese with English abstract). doi:10.7605/gdxb.2016.06.075
- Gao, H. H., He, D. F., Tong, X. G., Wen, Z. X., and Wang, Z. M. (2017a). Tectonic-depositional environment and proto-type basin evolution of the cambrian in the Tarim Basin. *Geoscience* 31 (01), 102–118. (in Chinese with English abstract). doi:10.3969/j.issn.1000-8527.2017.01.009
- Gao, H. H., He, D. F., Tong, X. G., Wen, Z. X., Wang, Z. M., and Zhang, Y. Q. (2017b). Tectonic-depositional environment and proto-type basins evolution of the Tarim Basin in the late ordovician. *Earth Sci. Front.* 24 (05), 350–367. (in Chinese with English abstract). doi:10.13745/j.esf.yx.2016-10-3
- Gao, H. H. (2015). Tectonic-depositional setting and proto-type basin evolution of the Cambrian and Ordovician in Tarim area. *China University of Geosciences.* 52, 164.
- Gao, Z. Q., and Fan, T. L. (2015). Carbonate platform-margin architecture and its influence on Cambrian-Ordovician reef-shoal development, Tarim Basin, NW China. *Mar. Petroleum Geol.* 68, 291–306. doi:10.1016/j.marpetgeo.2015.08.033
- Gao, Z. Q., Fan, T. L., Yang, W. H., and Wang, X. (2012). Structure characteristics and evolution of the eopaleozoic carbonate platform in Tarim Basin. *J. Jilin Univ. (Earth Sci. Ed.)* 42 (03), 657–665. (in Chinese with English abstract). doi:10.13278/j.cnki.jjuese.2012.03.004
- Ge, R. F., Zhu, W. B., Wu, H. L., Zheng, B. H., Zhu, X. Q., and He, J. W. (2012). The paleozoic northern margin of the Tarim craton: Passive or active. *Lithos* 142, 1–15. doi:10.1016/j.lithos.2012.02.010
- He, B., Jiao, C., Xu, Z., Cai, Z., Zhang, J., Liu, S., et al. (2016). The paleotectonic and paleogeography reconstructions of the Tarim Basin and its adjacent areas (NW China) during the late Early and Middle Paleozoic. *Gondwana Res.* 30, 191–206. doi:10.1016/j.gr.2015.09.011
- He, B. Z., Jiao, C. L., Xu, Z. Q., Cai, Z. H., Liu, S. L., Zhang, J. X., et al. (2015). Distribution and migration of the phanerozoic palaeo-uplifts in the Tarim Basin, NW China. *Earth Sci. Front.* 22 (3), 277–289. (in Chinese with English abstract). doi:10.13745/j.esf.2015.03.024
- He, B. Z., Jiao, C. L., Xu, Z. Q., Liu, S. L., Cai, Z. H., Li, H. B., et al. (2013). Unconformity structural architecture and tectonic paleo-geographic environment: A case of the middle caledonion on the northern margin of Tibet Plateau and Tarim Basin. *Acta Petrol. Sin.* 29 (6), 2184–2198. (in Chinese with English abstract).
- He, D. F., Jia, C. Z., Li, D. S., Zhang, C. J., Meng, Q. R., and Shi, X. (2005). Formation and evolution of polycyclic superimposed Tarim Basin. *Oil & Gas Geol.* 26 (1), 64–77. (in Chinese with English abstract). doi:10.3321/j.issn:0253-9985.2005.01.010
- He, D. F., Li, D. S., and WangLiuChen, C. S. S. F. J. J. (2020). Status, thinking, and methodology of studying on the mobile tectono-palaeogeography. *J. Palaeogeogr.* 22 (01), 1–28. (in Chinese with English abstract). doi:10.7605/gdxb.2020.01.001
- He, D. F., Zhou, X. Y., Zhang, C. J., and Yang, X. F. (2007). Type and evolution of Ordovician proto-type basin in Tarim. *Chin. Sci. Bull.* 52, 126–135. (in Chinese). doi:10.3321/j.issn:0023-074x.2007.z1.015
- Hou, G. T., Santosh, M., Qian, X. L., Lister, G. S., and Li, J. H. (2008). Configuration of the Late Paleoproterozoic supercontinent Columbia: Insights from radiating mafic dyke swarms. *Gondwana Res.* 14 (3), 395–409. doi:10.1016/j.gr.2008.01.010
- Hou, M. C., Chen, A. Q., Ogg, J. G., Ogg, G. M., Huang, K. K., Xing, F. C., et al. (2019). China paleogeography: Current status and future challenges. *Earth-Science Rev.* 189, 177–193. doi:10.1016/j.earscirev.2018.04.004
- Hou, Z. S., Fan, J. X., Zhang, L. N., and Shen, S. Z. (2020). Construction method and comparison of global paleogeographic reconstruction models and associated knowledge discovery. *Geol. J. China Univ.* 26 (01), 86–99. (in Chinese with English abstract). doi:10.16108/j.issn1006-7493.2019105
- Huang, B. C., Piper, J. D. A., Sun, L. S., and Zhao, Q. (2019). New paleomagnetic results for Ordovician and Silurian rocks of the Tarim Block, Northwest China, and their paleogeographic implications. *Tectonophysics* 755, 91–108. doi:10.1016/j.tecto.2019.02.010
- Huang, B. C., Piper, J. D. A., and Zhu, R. X. (2009). Paleomagnetic constraints on neotectonic deformation in the Kashi depression of the Western Tarim Basin, NW China. *Int. J. Earth Sci.* 98 (6), 1469–1488. doi:10.1007/s00531-008-0401-5
- Huang, B. C., Yan, Y. G., Piper, J. D. A., Zhang, D. H., Yi, Z. Y., Yu, S., et al. (2018). Paleomagnetic constraints on the paleogeography of the east asian blocks during late paleozoic and early mesozoic times. *Earth-Science Rev.* 186, 8–36. doi:10.1016/j.earscirev.2018.02.004
- Huang, B. C., Zhou, T. X., and Zhu, R. X. (2008). Discussions on Phanerozoic evolution and formation of continental China, based on paleomagnetic studies. *Earth Sci. Front.* 15 (3), 348–359. (in Chinese with English abstract). doi:10.3321/j.issn:1005-2321.2008.03.031
- Huang, B. C., Zhu, R. X., Otofujii, Y., and Yang, Z. Y. (2000). Discussion on the Palaeogeographic location of the main blocks in China in the early Paleozoic. *Chin. Sci. Bull.* (04), 337–345. (in Chinese). doi:10.3321/j.issn:0023-074X.2000.04.001
- Huang, H. M., Li, P. F., Hu, W. W., and Ling, J. Q. (2021). Early paleozoic collage of the Yili block, west tianshan: Constraints from U-Pb geochronology and Hf isotopes of clastic zircons. *Geotect. Metallogenia* 45 (04), 786–804. (in Chinese). doi:10.16539/j.ddgzyckx.2021.04.007
- Ji, H. L., He, Z. B., Qin, M. K., Wei, S. Y., Cao, J. H., and Yang, F. (2020). Sedimentary characteristics of lower cretaceous mangshigou formation in hegang sag, sanjiang basin, heilongjiang province. *Geol. Rev.* 66 (01), 52–68. (in Chinese).
- Jia, C. Z. (2004). *Plate tectonics and continental dynamics, Tarim Basin*. Beijing: Petroleum Industry Press, 1–202. (in Chinese).
- Jia, C. Z. (1997). *Structural characteristics and hydrocarbon in Tarim Basin*. China. Beijing: Petroleum Industry Press, 1–438. (in Chinese).
- Jia, J. H., Zhang, B. M., Zhu, S. H., Zhu, Y. C., and Li, Z. Y. (2006). Stratigraphy, sedimentary characteristics, and lithofacies palaeogeography of the Silurian in Tarim Basin. *J. Palaeogeogr.* 08 (03), 339–352. (in Chinese with English abstract).
- Jiang, T., Gao, J., Klemd, R., Qian, Q., Zhang, X., Xiong, X. M., et al. (2014). Paleozoic ophiolitic mélanges from the South Tianshan Orogen, NW China: Geological, geochemical and geochronological implications for the geodynamic setting. *Tectonophysics* 612–613, 106–127. doi:10.1016/j.tecto.2013.11.038
- Jiang, Z. X. (2010). *Sedimentology*. Beijing: Petroleum Industry Press, 1–507. (in Chinese).
- Johnson, M. R. W. (2002). Shortening budgets and the role of continental subduction during the India-Asia collision. *Earth-Science Rev.* 59, 101–123. doi:10.1016/S0012-8252(02)00071-5
- Kang, L., Liu, L., Cao, Y. T., Wang, C., Yang, W. Q., and Zhu, X. H. (2011). Geochemistry, zircon LA-ICP-MS U-Pb ages and Hf isotopes of Hongliugou moyite from north Altyn Tagh tectonic belt. *Geol. Bull. China* 30 (7), 1066–1076. (in Chinese with English abstract). doi:10.3969/j.issn.1671-2552.2011.07.009
- Laborde, A., Barrier, L., Simoes, M., Li, H., Coudroy, T., Van Der Woerd, J., et al. (2019). Cenozoic deformation of the Tarim Basin and surrounding ranges (xinjiang, China): A regional overview. *Earth-Science Rev.* 197, 102891. doi:10.1016/j.earscirev.2019.102891
- Li, J. H., and Jiang, H. F. (2013). *Global paleo-plate reconstruction, lithofacies Palaeogeography and paleoenvironment atlas*. Beijing: Geology Press, 1–127. (in Chinese).
- Li, J. H., Wang, H. H., Li, W. B., and Zhou, X. B. (2014). Discussion on global tectonics evolution from plate reconstruction in Phanerozoic. *Acta Pet. Sin.* 35 (2), 207–218. (in Chinese with English abstract). doi:10.7623/syxb201402001
- Li, J. H., Zhou, X. B., Li, W. B., Wang, H. H., Liu, Z. L., Zhang, H. T., et al. (2015). Preliminary reconstruction of tectonic paleogeography of Tarim Basin and its

- adjacent areas from Cambrian to Triassic, NW China. *Geol. Rev.* 61 (6), 1225–1234. (in Chinese).
- Li, J. Z., Zheng, M., Guo, Q. L., and Wang, S. J. (2019). *The fourth evaluation of hydrocarbon resources*. Beijing: Petroleum Industry Press, 1–385. (in Chinese).
- Li, Q. M., Wu, G. H., Pang, X. Q., Pan, W. Q., Luo, C. S., Wang, C. L., et al. (2010). Hydrocarbon accumulation conditions of ordovician carbonate in Tarim Basin. *Acta Geol. Sin. - Engl. Ed.* 84 (5), 1180–1194. doi:10.1111/j.1755-6724.2010.00289.x
- Li, S. B., Chen, B. L., Chen, Z. L., Hao, R. X., Zhou, Y. G., and Han, F. B. (2013). Petrogeochemical characteristics and tectonic setting of early Paleozoic intermediate-acid volcanic lava in Karadawan area, the northern margin of Altyn. *Geol. Rev.* 59 (3), 423–436. (in Chinese). doi:10.3969/j.issn.0371-5736.2013.03.003
- Li, S. Z., Zhao, S. J., LiuCao, X. H., Yu, S., Li, X. Y., Somerville, I., et al. (2017). Closure of the Proto-Tethys Ocean and early paleozoic amalgamation of microcontinental blocks in east asia. *Earth-Science Rev.* 186, 37–75. doi:10.1016/j.earscirev.2017.01.011
- Li, X. M., Xia, L. Q., Xia, Z. C., Xu, X. Y., Ma, Z. P., and Wang, L. S. (2006). Geochemical characteristics and petrogenesis of Neoproterozoic-Early Cambrian volcanic rocks in Tianshan area. *Acta Petrologica Mineralogica* (05), 412–422. (in Chinese with English abstract). doi:10.3969/j.issn.1000-6524.2006.05.005
- Li, X. P., Zhang, L. F., Wilde, S. A., Song, B., and Liu, X. M. (2010). Zircon from rodingite in the Western Tianshan serpentinite complex: Mineral chemistry and U-Pb ages define nature and timing of rodingitization. *Lithos* 118, 17–34. doi:10.1016/j.lithos.2010.03.009
- Li, Y. P., McWilliams, M., Sharps, R., Cox, A., Li, Y. A., Li, Q., et al. (1990). A Devonian paleomagnetic pole from red beds of the Tarim Block, China. *J. Geophys. Res.* 95 (B12), 19185–19198. doi:10.1029/JB095iB12p19185
- Li, Z. X., Bogdanova, S. V., Collins, A. S., Davidson, A., Waele, B. D., Ernst, R. E., et al. (2008). Assembly, configuration, and break-up history of Rodinia: A synthesis. *Precambrian Res.* 160 (1–2), 179–210. doi:10.1016/j.precamres.2007.04.021
- Lin, C. S., Li, S. T., Liu, J. Y., Qian, Y. X., Luo, H., Chen, J. Q., et al. (2011). Tectonic framework and paleogeographic evolution of the Tarim Basin during the Paleozoic major evolutionary stages. *Acta Petrol. Sin.* 27 (1), 210–218. (in Chinese with English abstract).
- Lin, C. S., Yang, H. J., Liu, J. Y., Cai, Z. Z., Peng, L., Yang, X. F., et al. (2008). Paleohigh geomorphology and paleogeographic framework and their controls on the formation and distribution of stratigraphic traps in the Tarim Basin. *Oil Gas Geol.* 29 (2), 189–197. (in Chinese with English abstract). doi:10.3321/j.issn:0253-9985.2008.02.006
- Lin, C. S., Yang, H. J., Liu, J. Y., Rui, Z. F., Cai, Z. Z., and Zhu, Y. F. (2012). Distribution and erosion of the Paleozoic tectonic unconformities in the Tarim Basin, Northwest China: Significance for the evolution of paleo-uplifts and tectonic geography during deformation. *J. Asian Earth Sci.* 46, 1–19. doi:10.1016/j.jseas.2011.10.004
- Liu, C. Y., Wang, J. Q., Zhao, X. C., Huang, L., Zhang, D. D., Zhao, J. F., et al. (2020). The proto-type basin and its nomenclatures and research. *Petroleum Geol. Exp.* 42 (05), 720–727. (in Chinese with English abstract). doi:10.11781/sysydz202005720
- Liu, L., Liao, X. Y., Wang, Y. W., Wang, C., Santosh, M., Yang, M., et al. (2016). Early paleozoic tectonic evolution of the North qinling orogenic belt in central China: Insights on continental deep subduction and multiphase exhumation. *Earth-Science Rev.* 159, 58–81. doi:10.1016/j.earscirev.2016.05.005
- Liu, L., Liao, X. Y., Zhang, C. L., Chen, D. L., Gong, X. K., and Kang, L. (2013). Multi-metamorphic timings of HP-UHP rocks in the North Qinling and their geological implications. *Acta Petrol. Sin.* 29, 1634–1656. (in Chinese with English abstract).
- Lou, Q. Q., Xiao, A. C., Zhong, N. C., and Wu, L. (2016). A method of proto-type restoration of large depressions with terrestrial sediments: A case study from the cenozoic Qaidam basin. *Acta Petrol. Sin.* 32 (03), 892–902. (in Chinese).
- Maruyama, S., Sawaki, Y., Ebisuzaki, T., Ikoma, M., Omori, S., and Komabayashi, T. (2014). Initiation of leaking Earth: An ultimate trigger of the Cambrian explosion. *Gondwana Res.* 25 (3), 910–944. doi:10.1016/j.jgr.2013.03.012
- Matte, P., Tapponnier, P., Arnaud, N., Bourjot, L., Avouac, J. P., Vidal, P., et al. (1996). Tectonics of western tibet, between the Tarim and the indus. *Elsevier* 142 (3–4), 311–330. doi:10.1016/0012-821x(96)00086-6
- Matthews, K. J., Maloney, K. T., Zahirovic, S., Williams, S. E., Seton, M., and Müller, R. D. (2016). Global plate boundary evolution and kinematics since the late Paleozoic. *Glob. Planet. Change* 146, 226–250. doi:10.1016/j.gloplacha.2016.10.002
- Meng, F. C., Zhang, J. X., Yu, S. X., and Chen, S. Y. (2010). Early paleozoic pillow basalt in hongliuquan, North Altyn, and its geotectonic significance. *Acta Geol. Sin.* 84 (7), 981–990. (in Chinese).
- Mou, D. L., Li, S. Z., Wang, Q., Li, X. Y., Wang, P. C., Yu, S. X., et al. (2018). The early paleozoic orocline in the southeastern Tarim Basin. *Acta Petrol. Sin.* 34 (12), 3739–3757. (in Chinese with English abstract).
- Nie, S. Y. (1991). Paleoclimatic and paleomagnetic constraints on the Paleozoic reconstructions of south China, north China, and Tarim. *Tectonophysics* 196 (3/4), 279–308. doi:10.1016/0040-1951(91)90327-o
- Rao, Y., Yu, S., Huang, X. W., and Chen, C. (2016). Hydrocarbon distribution regularity and main controlling factors analysis of Paleozoic reservoirs in Middle East. *Glob. Geol.* 35 (04), 1041–1051. (in Chinese with English abstract). doi:10.3969/j.issn.1004-5589.2016.04.014
- Shao, L. Y., Wang, X. T., Li, Y. N., and Liu, B. Q. (2019). Review on palaeogeographic reconstruction of deep-time source-to-sink systems. *J. Palaeogeogr.* 21 (01), 67–81. doi:10.7605/gdxb.2019.01.004
- Shen, P., Pan, H. D., Seitmuratova, E., Yuan, F., and Jakupova, S. (2016). A Cambrian intra-oceanic subduction system in the Bozshakol area, Kazakhstan. *Lithos* 224–225, 61–77. doi:10.1016/j.lithos.2015.02.025
- Sobel, E. R., and Araud, N. (1999). A possible middle paleozoic suture in the Altyn Tagh, NW China. *Tectonics* 18 (1), 64–74. doi:10.1029/1998tc900023
- Steinberger, B., Sutherland, R., and O'Connell, R. J. (2004). Prediction of Emperor-Hawaii seamount locations from a revised model of global plate motion and mantle flow. *Nature* 430, 167–173. doi:10.1038/nature02660
- Sun, L. S., and Huang, B. C. (2009). New paleomagnetic result for Ordovician rocks from the Tarim Block, Northwest China and its tectonic implications. *Chin. J. Geophys.* (07), 1836–1848. (in Chinese with English abstract). doi:10.3969/j.issn.0001-5733.2009.07.018
- Tian, J., Wang, Q. H., Yang, H. J., and Li, Y. (2021). Petroleum exploration history and enlightenment in Tarim Basin. *Xinjiang Pet. Geol.* 42 (03), 272–282. (in Chinese with English abstract). doi:10.7657/XJPG20210303
- Tian, L., Cui, H. F., Liu, J., Zhang, N. C., and Shi, X. X. (2018). Early-middle cambrian paleogeography and depositional evolution of Tarim Basin. *Oil Gas Geol.* 39 (05), 1011–1021. (in Chinese with English abstract). doi:10.11743/ogg20180515
- Tong, X. G., and He, D. F. (2021). *Principles and methods of hydrocarbon exploration*. Beijing: Petroleum Industry Press, 1–257.
- Torsvik, T. H., and Cocks, L. R. M. (2004). Earth geography from 400 to 250 Ma: A palaeomagnetic, faunal and facies review. *J. Geol. Soc.* 161, 555–572. doi:10.1144/0016-764903-098
- Torsvik, T. H., and Cocks, L. R. M. (2013). Gondwana from top to base in space and time. *Gondwana Res.* 24 (3–4), 999–1030. doi:10.1016/j.gr.2013.06.012
- Torsvik, T. H., and Cocks, L. R. M. (2019). The integration of palaeomagnetism, the geological record and mantle tomography in the location of ancient continents. *Geol. Mag.* 156, 242–260. doi:10.1017/s001675681700098x
- Torsvik, T. H., Steinberger, B., Ashwal, L. D., Doubrovine, P. V., and Trønnes, R. G. (2016). Earth evolution and dynamics-a tribute to Kevin Burke. *Can. J. Earth Sci.* 53, 1073–1087. doi:10.1139/cjes-2015-0228
- Van der Voo, R. (1993). *Paleomagnetism of atlantic, Tethys, and lapetus oceans*. Cambridge: Cambridge University Press, 1–411.
- Van der Voo, R. (1990). The reliability of paleomagnetic data. *Tectonophysics* 184, 1–9. doi:10.1016/0040-1951(90)90116-P
- Wang, B., Jahn, B. M., Shu, L. S., Li, K. S., Chung, S. L., and Liu, D. Y. (2012). Middle-late ordovician arc-type plutonism in the NW Chinese tianshan: Implication for the accretion of the Kazakhstan continent in central asia. *J. Asian Earth Sci.* 49, 40–53. doi:10.1016/j.jseas.2011.11.005
- Wang, B., Liu, H. S., Shu, L. S., Jahn, B. M., Chung, S. L., Zhai, Y. Z., et al. (2014a). Early Neoproterozoic crustal evolution in northern Yili Block: Insights from migmatite, orthogneiss, and leucogranite of the Wenquan metamorphic complex in the NW Chinese Tianshan. *Precambrian Res.* 242, 58–81. doi:10.1016/j.precamres.2013.12.006
- Wang, B., Shu, L. S., Faure, M., Jahn, B. M., Cluzel, D., Charvet, J., et al. (2011). Paleozoic tectonics of the southern Chinese Tianshan: Insights from structural, chronological and geochemical studies of the Heiyingshan ophiolitic mélange (NW China). *Tectonophysics* 497, 85–104. doi:10.1016/j.tecto.2010.11.004
- Wang, B., Shu, L. S., Liu, H. S., Gong, H. J., Ma, Y. Z., Mu, L. X., et al. (2014b). First evidence for ca. 780 Ma intra-plate magmatism and its implications for Neoproterozoic rifting of the North Yili Block and tectonic origin of the continental blocks in SW of Central Asia. *Precambrian Res.* 254, 258–272. doi:10.1016/j.precamres.2014.09.005
- Wang, C., Luo, J. H., Che, Z. C., Liu, L., and Zhang, J. Y. (2009). Geochemical characteristics and zircon LA-ICP-MS dating of the oxidaban granite in xinjiang: Implications for the subduction process of the paleozoic Ocean in southwestern tianshan. *Acta Geol. Sin.* 83 (2), 272–283. (in Chinese). doi:10.3321/j.issn:0001-5717.2009.02.012
- Wang, C. S., and Lin, C. S. (2021). Development status and trend of sedimentology in China in recent ten years. *Bull. Mineralogy, Petrology Geochem.* 40 (06), 1217. (in Chinese with English abstract). doi:10.19658/j.issn.1007-2802.2021.40.096
- Wang, C. S., Zheng, H. R., Ran, B., Liu, B. P., Li, X. H., Li, Y. L., et al. (2010). Practice and reflection on reconstruction of active paleogeography: A case study in the qinghai-tibet Tethys. *Acta Sedimentologica Sin.* (05), 849–860. (in Chinese). doi:10.14027/j.cnki.cjxb.2010.05.002
- Wang, P., Zhao, G., Han, Y., Liu, Q., Yao, J., and Yu, S. (2021). Position of the Tarim craton in Gondwana: Constraints from neoproterozoic to early paleozoic strata in south Tarim, NW China. *Tectonophysics* 803, 228741. doi:10.1016/j.tecto.2021.228741
- Wang, T., Zheng, M. L., Ren, H. J., Li, T., Wu, H. S., Wang, X. L., et al. (2021). New understandings of stratigraphic division and correlation of Jiamuhe Formation and natural gas exploration target in Mahu Sag and its periphery, Junggar Basin. *China Pet. Explor.* 26 (04), 99–112. (in Chinese with English abstract). doi:10.3969/j.issn.1672-7703.2021.04.008
- Wen, B., Evans, D. A. D., and Li, Y. X. (2017). Neoproterozoic paleogeography of the Tarim Block: An extended or alternative “missing-link” model for Rodinia? *Earth Planet. Sci. Lett.* 458, 92–106. doi:10.1016/j.epsl.2016.10.030
- Wu, C. L., Yang, J. S., Yao, S. Z., Zeng, L. S., Chen, Y. S., Li, H. B., et al. (2005). Characteristics of the granitoid complex and its zircon SHRIMP dating at the south margin

- of the Bashikaogong Basin, North Altyn, NW China. *Acta Petrol. Sin.* 21 (3), 846–858. (in Chinese with English abstract). doi:10.3321/j.issn:1000-0569.2005.03.024
- Wu, C. L., Yao, S. Z., Zeng, L. S., Yang, J. S., Wooden, J. L., Chen, Y. S., et al. (2007). Characteristics and SHRIMP U-Pb zircon dating of the Bashikaogong-Smilbrak granitic complex in the northern Altyn. *Sci. China (Series D Earth Sci.* 37 (1), 10–26. (in Chinese).
- Wu, G. H., Chen, X., Ma, B. S., Chen, Y. Q., Tian, W. Z., Huang, S. Y., et al. (2021). The tectonic environments of the late neoproterozoic-early paleozoic and its tectono-sedimentary response in the Tarim Basin. *Acta Petrol. Sin.* 37 (08), 2431–2441. (in Chinese with English abstract). doi:10.18654/1000-0569/2021.08.11
- Wu, G. H., Deng, W., Huang, S. Y., Zheng, D. M., and Pan, W. Q. (2020). Tectonic-paleogeographic evolution of the Tarim Basin. *Chin. J. Geol.* 55 (02), 305–321. (in Chinese). doi:10.12017/dzlx.2020.020
- Wu, G. H., Pang, X. Q., Li, Q. M., and Yang, H. J. (2016). *Structural characteristics in intracratonic carbonate rocks and its implication for oil/gas accumulation: A case study in the Tarim Basin*. China. Beijing: Science Press, 1–344. (in Chinese).
- Wu, L., Guan, S. W., Zhang, S. C., Yang, H. J., Jin, J. Q., Zhang, X. D., et al. (2018). Neoproterozoic stratigraphic framework of the Tarim Craton in NW China: Implications for rift evolution. *J. Asian Earth Sci.* 158, 240–252. doi:10.1016/j.jseas.2018.03.003
- Xiao, W. J., Huang, B. C., Han, C. M., Sun, S., and Li, J. L. (2010). A review of the Western part of the alts: A key to understanding the architecture of accretionary orogens. *Gondwana Res.* 18 (2), 253–273. doi:10.1016/j.gr.2010.01.007
- Xiao, W. J., Windley, B. F., Yuan, C., Sun, M., Han, C. M., Lin, S. F., et al. (2009). Paleozoic multiple subduction-accretion processes of the Southern Altaids. *Am. J. Sci.* 309, 221–270. doi:10.2475/03.2009.02
- Xiao, X. C., Wang, J., Su, L., and Song, S. G. (2003). A further discussion of the Kudi ophiolite, west Kunlun, and its tectonic significance. *Geol. Bull. China* 22 (10), 745–750. (in Chinese). doi:10.3969/j.issn.1671-2552.2003.10.001
- Xiu, Q. Y., Yu, H. F., Liu, Y. S., Lu, S. N., Mao, D. B., Li, H. M., et al. (2007). Characteristics and SHRIMP U-Pb zircon dating of the pillow basalt in the northern Altyn. *Acta Geol. Sin.* 81 (6), 787–794. (in Chinese). doi:10.3321/j.issn:0001-5717.2007.06.006
- Xu, B., Xiao, S. H., Zou, H. B., Chen, Y., Li, Z. X., Song, B., et al. (2008). SHRIMP zircon U-Pb age constraints on Neoproterozoic Qurqatagh diamictites in NW China. *Precambrian Res.* 168 (3–4), 247–258. doi:10.1016/j.precamres.2008.10.008
- Xu, Z. Q., Li, S. T., Zhang, J. X., Yang, J. S., He, B. Z., Li, H. B., et al. (2011). Paleo-Asian and Tethyan tectonic systems with docking the Tarim block. *Acta Petrol. Sin.* 27 (1), 1–22. (in Chinese with English abstract).
- Xu, Z. Q., Yang, J. S., Zhang, J. X., Jiang, M., Li, H. B., and Cui, J. W. (1999). Comparison of tectonic units on both sides of Altyn fault and lithospheric shear mechanism. *Acta Geol. Sin.* 73 (3), 193–205. (in Chinese). doi:10.3321/j.issn:0001-5717.1999.03.001
- Yang, J. S., Shi, R. D., Wu, C. L., Su, D. C., Chen, S. Y., Wang, X. B., et al. (2008). Petrology and SHRIMP age of the Hongliugou ophiolite at Milan, north Altyn, at the northern margin of the Tibetan plateau. *Acta Petrol. Sin.* 24 (7), 1567–1584. (in Chinese with English abstract).
- Yang, Z. J., Ma, D. H., Wang, Z. X., and Xiao, W. F. (2012). SHRIMP U-Pb zircon dating of gabbro from the Binggou ophiolite mélange in the northern Altyn, and geological implication. *Acta Petrol. Sin.* 28 (7), 2269–2276. (in Chinese with English abstract).
- Yang, Z. Y., Sun, Z. M., Yang, T. S., and Pei, J. L. (2004). A long connection (750–380 Ma) between south China and Australia: Paleomagnetic constraints. *Earth Planet. Sci. Lett.* 220, 423–434. doi:10.1016/S0012-821X(04)00053-6
- Yu, H. B., Qi, J. F., Yang, X. Z., Sun, T., Liu, Q. X., and Cao, S. J. (2016). Analysis of mesozoic proto-type basin in kuga depression, Tarim Basin. *Xinjiang Pet. Geol.* 37 (06), 644–653+666. (in Chinese with English abstract). doi:10.7657/XJPG20160604
- Yun, J. B., Jin, Z. J., and Xie, G. J. (2014). Distribution of major hydrocarbon source rocks in the lower paleozoic, Tarim Basin. *Oil Gas Geol.* 35 (06), 827–838. (in Chinese with English abstract). doi:10.11743/ogg201406010
- Zhang, C. L., Lu, S. N., Yu, H. F., and Ye, H. M. (2007). Tectonic evolution of western orogenic belt: Evidences from zircon SHRIMP and LA-ICP-MS U-Pb ages. *Sci. China, (Series D)* 50, 1–12.
- Zhang, C. L., Yu, H. F., Shen, J. L., Dong, J. G., Yie, H. M., and Guo, K. Y. (2004). Zircon SHRIMP age determination of the giant-crystal gabbro and basalt in K(u)da, west Kunlun: Dismembering of the Kudi ophiolite. *Geol. Rev.* 50 (6), 639–643. doi:10.16509/j.georeview.2004.06.013
- Zhang, C. L., Zou, H. Bo., YeTao, X., and ChenYan, X. (2019). Tectonic evolution of the West Kunlun orogenic belt along the northern margin of the Tibetan plateau: Implications for the assembly of the Tarim terrane to Gondwana. *Geosci. Front.* 10 (03), 973–988. doi:10.1016/j.gsf.2018.05.006
- Zhang, G. Y., Liu, W., Zhang, L., Yu, B. S., Li, H. H., Zhang, B. M., et al. (2015). Cambrian-Ordovician prototypic basin, paleogeography, and petroleum of Tarim Craton. *Earth Sci. Front.* 22 (3), 269–276. (in Chinese with English abstract). doi:10.13745/j.esf.2015.03.023
- Zhang, G. Y., Tong, X. G., Xin, R. C., Wen, Z. X., Ma, F., Huang, T. F., et al. (2019a). Evolution of lithofacies and paleogeography and hydrocarbon distribution worldwide (I). *Petroleum Explor. Dev.* 46 (04), 664–686. doi:10.1016/S1876-3804(19)60225-9
- Zhang, L. N., Fan, J. X., and Chen, Q. (2019b). Deep-time paleogeographic reconstruction based on database: Taking the South China T. Approximatus biozone (early ordovician) as an example. *Acta Geol. Sin. Engl. Ed.* 93 (S1), 76–79. doi:10.1111/1755-6724.14251
- Zhang, X. B., Zhang, S. N., Zhao, X. K., He, J. J., Li, K., Dai, H. S., et al. (2007). Calculation of denudation thickness of superimposed basin by seism stratigraphic comprehensive method: A case study from the akekule uplift in Tarim Basin. *Xinjiang Pet. Geol.* (03), 366–368. (in Chinese). doi:10.3969/j.issn.1001-3873.2007.03.030
- Zhang, Y., Niu, Y. L., Hu, Y., Liu, J. J., Ye, L., Kong, J. J., et al. (2016). The syncollisional granitoid magmatism and continental crust growth in the West Kunlun Orogen, China: evidence from geochronology and geochemistry of the Arkarz pluton. *Lithos* 245, 191–204. doi:10.1016/j.lithos.2015.05.007
- Zhang, Z. C., Guo, Z. J., and Song, B. (2009). SHRIMP zircon dating of gabbro from the ophiolite mélange in the northern Altyn Tagh and its geological implications. *Acta Petrol. Sin.* 25 (3), 568–576. (in Chinese with English abstract).
- Zhao, G. C., Wang, Y. J., Huang, B. C., Dong, Y. P., Li, S. Z., Zhang, G. W., et al. (2018). Geological reconstructions of the east asian blocks: From the breakup of Rodinia to the assembly of pangea. *Earth-Science Rev.* 186, 262–286. doi:10.1016/j.earscirev.2018.10.003
- Zheng, M. L., Wang, Y., Jin, Z. J., Li, J. Z., Zhang, Z. P., Jiang, H. S., et al. (2014). Superimposition, evolution, and petroleum accumulation of Tarim Basin. *Oil Gas Geol.* 35 (06), 925–934. (in Chinese with English abstract). doi:10.11743/ogg20140619
- Zheng, X. J., Du, Y. S., Zhu, X. M., Liu, Z. J., Hu, B., Wu, S. H., et al. (2021). The main progresses of Chinese paleogeography in the past decade. *Bull. Mineralogy, Petrology Geochem.* 40 (01), 94–114+4. (in Chinese with English abstract). doi:10.19658/j.issn.1007-2802.2020.39.089
- Zhou, D. W., Su, L., Jian, P., Wang, R. S., Liu, X. M., Lu, G. X., et al. (2004). SHRIMP zircon U-Pb age and tectonic significance of high-pressure granulite in Yushugou ophiolite terrane, South Tianshan. *Acta Petrol. Sin.* 49 (14), 1411–1413. (in Chinese). doi:10.3321/j.issn:0023-074X.2004.14.013
- Zhou, K. K., Mou, C. L., Ge, X. Y., Liang, W., Chen, X. W., Wang, Q. Y., et al. (2017). The reflection of the new lithofacies palaeogeographic mapping on the major geological problems in south China: The evolution of "the South China unified plate" in the late early paleozoic. *Acta Sedimentol. Sin.* 35 (03), 449–459. (in Chinese). doi:10.14027/j.cnki.cjxb.2017.03.003
- Zhu, R. X., Yang, Z. Y., Wu, H. N., Ma, X. H., Huang, B. C., Meng, Z. F., et al. (1998). Paleomagnetic constrains on the tectonic history of the major blocks of China since the Phanerozoic. *Sci. China (Series D Earth Sci.* 41, 1–19.



OPEN ACCESS

EDITED BY

Jianwei Feng,
China University of Petroleum, China

REVIEWED BY

Vincenzo Tripodi,
Research Institute for Hydrogeological
Protection (CNR), Italy
Hao Yu,
Southwest Petroleum University, China
Kaizong Xia,
Institute of Rock and Soil Mechanics
(CAS), China

*CORRESPONDENCE

Kai Zhang,
✉ reservoirs@163.com

SPECIALTY SECTION

This article was submitted to Structural
Geology and Tectonics,
a section of the journal
Frontiers in Earth Science

RECEIVED 23 July 2022

ACCEPTED 01 February 2023

PUBLISHED 22 February 2023

CITATION

Wang Z, Zhang K, Wu Q, Zhou H, Yu S and
Li Y (2023), Structural evolution
characteristics and genesis of buried hill
faults in the Chengdao–Zhuanghai area.
Front. Earth Sci. 11:1001489.
doi: 10.3389/feart.2023.1001489

COPYRIGHT

© 2023 Wang, Zhang, Wu, Zhou, Yu and
Li. This is an open-access article
distributed under the terms of the
[Creative Commons Attribution License
\(CC BY\)](https://creativecommons.org/licenses/by/4.0/). The use, distribution or
reproduction in other forums is
permitted, provided the original author(s)
and the copyright owner(s) are credited
and that the original publication in this
journal is cited, in accordance with
accepted academic practice. No use,
distribution or reproduction is permitted
which does not comply with these terms.

Structural evolution characteristics and genesis of buried hill faults in the Chengdao–Zhuanghai area

Zhiwei Wang^{1,2}, Kai Zhang^{1*}, Qunhu Wu², Hongke Zhou²,
Shina Yu² and Yang Li²

¹School of Petroleum Engineering, China University of Petroleum, Qingdao, China, ²Haiyang Oil
Production Plant, Shengli Oilfield Company, Sinopec, Dongying, China

The buried hills in the Chengdao–Zhuanghai area are rich in oil and gas resources, and their structures exhibit complex styles with unique evolutionary characteristics. Based on the most recent exploration progress in this region, the structural characteristics and active parameters of the buried hill faults in this region were quantitatively analyzed using the balanced section technique. In addition, the structural evolution process of the study area was reproduced by combining the structural-physical simulation experiment. Its spatio-temporal evolution characteristics and genesis mechanisms were also systematically investigated. As observed, the study area developed three basic sets of fault systems: the NW-trending extensional strike-slip fault, the NNE-trending left-handed compression–torsion fault, and the near-EW-trending extensional fault. The study area was further segmented into six buried hills: West Row Hill, Middle Row Hill, East Row Hill, Zhuanghai Buried Hill, Zhuangxi Buried Hill, and Changdi Buried Hill. The inner fault of the NW-trending Buried Hill is a strike-slip extensional fault that formed under the influence of the right-lateral strike-slip activity of the NW-trending Chengbei Fault from the Late Jurassic to the Early Cretaceous. In particular, the NNE-trending fault was a left-handed compression–torsion fault that formed under the left-handed strike-slip activity and regional compression stress field of the Tanlu fault zone. The near-EW fault was closely related to the near-SN extension stress field in the Late Cretaceous. Since the late Triassic, the study area has experienced six evolution stages, namely, overall uplift erosion (T_3), overall coating deposition (J_{1+2}), fault segmentation (J_3-K_1), extrusion uplift differentiation (K_2), middle buried hill differentiation E), and overall stable subsidence (N–Q). Its tectonic evolution was primarily controlled by the significant variations in the tectonic stress field in the study area as well as its adjacent areas since the late Triassic, which were controlled by the tectonic stress field.

KEYWORDS

buried hill, fault structure, the balanced section, evolution characteristics, Chengdao–Zhuanghai area

1 Introduction

In recent years, deep-buried hill reservoirs have served as the major field of oil and gas exploration in China, with the Chengdao–Zhuanghai area a key region for these activities in the Jiyang Depression. Affected by the superposition of the Indosinian, Yanshan, Himalayan, and other multistage tectonic movements and the strike-slip activities of the Tanlu fault zone, the buried hill features differ in diverse structural styles, and the trend of hydrocarbon accumulation in these buried hills is complex and variable. Thus far, several scholars have studied the fault system of the typical complex oil and gas accumulation area in the Bohai Sea. They have reported that the NW and NE faults in the area exhibit strike-slip characteristics and conjugate shear characteristics (Xie, 2011; Xie et al., 2021). In particular, two sets of deep and shallow fault systems developed in the Bodong Low Uplift–Bodong Sag, wherein the shallow layer mainly resided in the EW direction and displayed an *en-échélon* arrangement. In addition, typical NE- and NW-trending faults formed in the Chengdao Low Uplift. The traditional perspective states that the two groups of faults were synchronous faults (Li et al., 2014; Shi, 2021; Xin et al., 2021), but this was not completely consistent with the actual drilling results; moreover, corresponding empirical research is still lacking in this respect. Thus, typically buried hill reservoirs developed in the Chengdao–Zhuanghai area, and their formation process, enrichment regularity, and major controlling factors are all closely associated with the development of the fault system.

Considering the Mesozoic and Paleozoic fault structures in the Chengdao–Zhuanghai area as the research object and using the latest exploration data in the study area based on balanced section technology, this study quantitatively analyzes the fault structure characteristics and active parameters in the Chengdao–Zhuanghai area. Combined with the structural physical simulation experiment, we restored the key structural evolution process in the study area and clarified its control on the development of the buried hills. Accordingly, we further explored the mechanisms of regional dynamics. The two methods corroborated each other, and the spatiotemporal characteristics and genesis of the buried hill faults in the Chengdao–Zhuanghai area have been systematically studied to obtain a series of new concepts. This study aims to add to the theory of Mesozoic basin formation in the Bohai Bay Basin and provide references for deep oil and gas exploration and future development.

2 Regional geological background

The Chengdao–Zhuanghai area, located in the southeast of the Jiyang Depression, is a secondary structural unit of the Bohai Bay oil and gas basin. It is separated from the Ludong Uplift by the middle section of the Tanlu Fault to the east and is adjacent to the Huanghua Sag and Bozhong Sag by the Chengning Uplift to the west and Boonan Uplift to the north, and the Luxi Uplift by the Qiguang Fault to the south and Linqing Sag to the southwest. The study region is located at the intersection of the Bozhong Sag, Jiyang Depression, and Chengning Uplift—with a northwest trend that includes two secondary tectonic units, the Chengbei Low Uplift (southeast) and Bonan Low Uplift (west). In particular, three

typically inherited boundary basement faults developed in this area, namely, the NW-trending Chengbei Fault, the NE-trending Chengbei 30 West Fault, and the NEE-trending Chengbei 30 South Fault (Figure 1).

From bottom to top, the study area includes the Archaeozoic Taishan Group (Art), Cambrian (Є), Ordovician (O), Carboniferous (C), Permian (P), Middle-Lower Jurassic (J_{1+2}), Upper Jurassic–Lower Cretaceous (J_3+K_1). Affected by the multistage tectonic movement, the remaining Mesozoic and Paleozoic strata in the study area are non-uniformly distributed. The top surface of the Paleozoic is covered by Lower-Middle Jurassic. The local area of the No. 5 Pile Fault and the southern region of the middle row hill in Chengdao have been seriously eroded, resulting in a Mesozoic boundary that is directly covered by Archaeozoic strata. The northern region of the Middle Row Hill is locally higher and seriously denuded, and the Dongying Formation directly covers the Paleozoic strata. The superposition relationship of the Cenozoic boundary's bottom surface is complex, influenced by varying strata denudation in the late Cretaceous and varying fault activity in the early Cenozoic. The stratigraphic structure characteristics of the buried hills in the study area have been determined by the distribution characteristics of the Mesozoic and Paleozoic residual strata, in addition to the superposition relationship at the key strata interface.

3 Characteristics of the buried hill faults in the Chengdao–Zhuanghai area

Based on the drilling and logging data in the study area, the seismic data have been analyzed in detail through the combination of well and seismic data. As observed, six buried hills sequentially developed in the Chengdao–Zhuanghai area from north to south and west to east, including the Chengdao West-Row Hill, Chengdao Middle-Row Hill, Chengdao East-Row Hill, Zhuanghai Buried Hill, Zhuangxi Buried Hill, and Changdi Buried Hill. Simultaneously, the study reports that the fracture forms the predominant tectonic deformation pattern in the Chengdao–Zhuanghai area, in addition to multiple dominant development directions, primarily in the NW, NNE (NE), and near-EW directions (Figure 2), and that it controls a series of NW, NNE, and near-EW buried hill interior fractures. Overall, the pattern resembles a “north-sub-south convergence” network.

3.1 Plane distribution characteristics of the fracture system

Affected by regional and local stress field variations across different periods, the fracture system in the study region has been essentially controlled by extension, extrusion, and slip. Therefore, the fault systems of various layers varied significantly with complex, diverse characteristics, exhibiting a prominent multiperiod tectonic-superposition effect (Zhang M., 2006; Jiu et al., 2013). In addition, the fault system of the lower strata (Mesozoic and Paleozoic) in the study area displayed distinct multi-directionality, with faults of various directions and properties intersecting each other to form a north–south convergence network

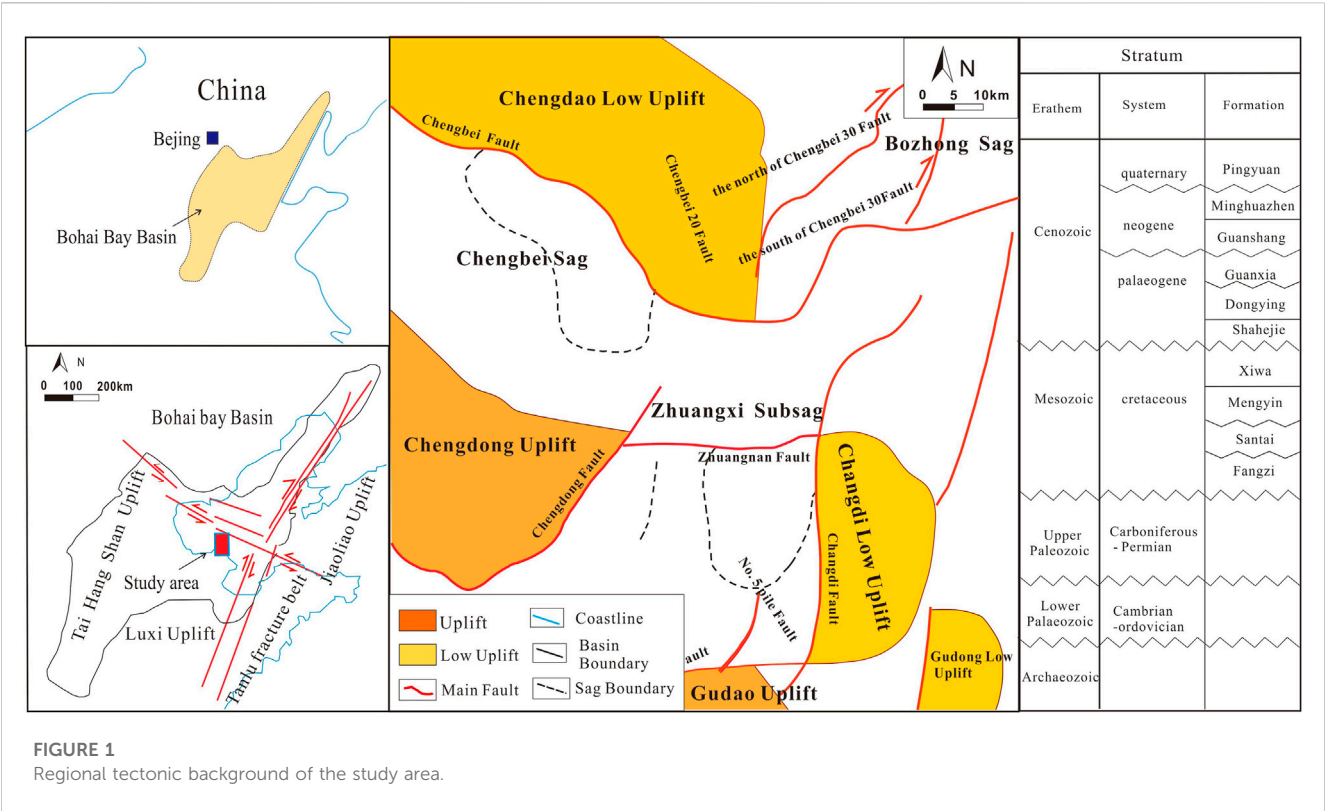


FIGURE 1 Regional tectonic background of the study area.

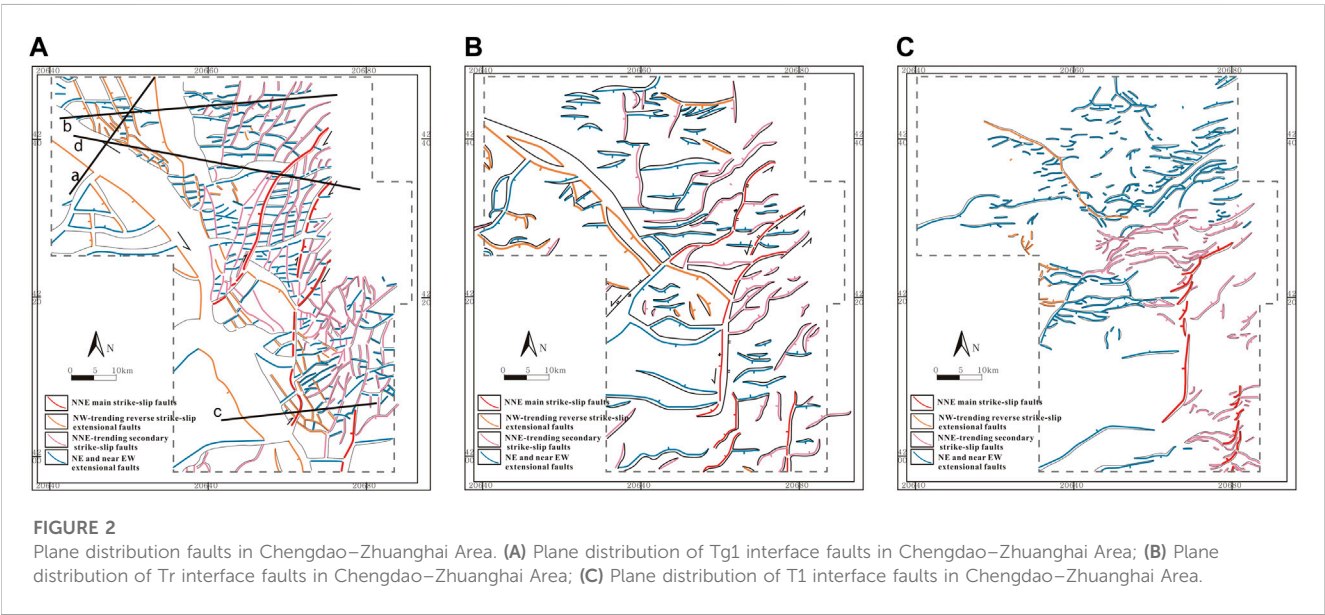


FIGURE 2 Plane distribution faults in Chengdao–Zhuanghai Area. (A) Plane distribution of Tg1 interface faults in Chengdao–Zhuanghai Area; (B) Plane distribution of Tr interface faults in Chengdao–Zhuanghai Area; (C) Plane distribution of T1 interface faults in Chengdao–Zhuanghai Area.

tectonic pattern. Among them, large-scale NW-trending fractures existed with numerous interior fractures, primarily along the NNE-trending and near-EW-trending directions in the area intersected by the Middle Row Hill, East Row Hill, Zhuanghai Buried Hill, and Changdi Buried Hill. In contrast, in the area of West-Row Hill and Zhuangxi Buried Hill (Figure 2A) (Zhang X., 2006; Li, 2008; Yang, 2008; Mao et al., 2019), the NW-trending and near-EW-trending

inner fractures dominated. In the middle strata (Palaeogene), the NW-trending No. 5 Pile Fault and Chengbei 20 Fault gradually disappeared, and the No. 5 Pile Fault was reconstructed by the NNE-trending Changdi Fault. Although the NW-trending Chengbei Fault continued to move, the horizontal fault distance decreased significantly. All the interior faults disappeared, and numerous NNE strike-slip faults, NE-trending, and EW-trending

TABLE 1 Characteristics of the fracture system profile development in the Chengdao–Zhuanghai Area.

Type of fracture profile	Fault	Characteristics of fracture system profile
NW-trending fractures	Chengbei Fault	Chengbei Fault is the southern boundary fault of the Chengbei low uplift, which is the depression-controlling fault of the Chengbei Sag and the mountain-controlling fault of the Chengdao West Row mountain. The fault is inclined toward SW, and the shovel-shaped main section cuts deeper. The lower Paleozoic exhibits a thin bottom, and the upper portion of the fault can be combined with the secondary faults to form a “Y”-shaped, flower-like combination of the structural styles on the section
	Chengbei 20 Fault	The Chengbei 20 Fault is the mountain-controlling fault of Middle Row Hill. The fault is inclined toward SW and displays a shovel-type normal fault from north to south, with a gradually decreasing scale. The upper plate of the fault exhibited a thin bottom and was clearly thinner than the lower plate on the section
	No. 5 Pile Fault	The deep NW-trending structure of the No. 5 Pile fault was evident, whereas the shallow layer ceased the activity and gradually intersected the NNE-trending Changdi Fault from north to south. The profile is a shovel-type normal fault that does not cut through the bottom interface of the Cenozoic. The Lower Paleozoic displayed a thin or bald bottom because of the cutting and reconstruction of the Changdi fault
NNE-trending fractures	Changdi Fault	The Changdi Fault is the mountain-controlling fault of the Changdi Buried Hill, with a vertical fault plane at the section inclined toward NW, which was combined with secondary faults to form a multistage “Y”-shaped, flower-like structure in the shallow portion that cut the No. 5 Pile Fault in its deep portion. The local regions exhibited certain pressure–torsion properties, and the east side of the strata bending arch formed a forced anticline
	North and south of Chengbei 30 Faults	The north and south Chengbei 30 Faults are the mountain-controlling faults of the East Row Hill. The two faults on the section tend in opposite directions with a steep principal section. The shallow part and the secondary fault formed a flower-like, multistage “Y” combination. The north of the Chengbei 30 Fault became inactive during the Guantao Formation, whereas the south of the Chengbei 30 Fault disappeared during the Minghuazhen Formation
	Chengdong Fault	The Chengdong Fault is a major control fault in the Gubei Sag. In the profile, the North–South Fault was positive by inversion and exhibited a certain strike-slip effect. Zhuanggu 29 Fault was formed at the junction of the northernmost Chengbei Fault, and the compression–torsion effect was the strongest. In its entirety, the Chengdong Fault was characterized by normal plate- or shovel-type faults, strong shallow strike-slip action, and multilevel “Y” shape combination with secondary faults
NW-trending fractures	Chengbei 304 South Fault	The Chengbei 304 South Fault is the boundary fault between the Chengdao East Row Hill and the Zhuanghai Buried Hill. The deep layer was clear and continuous, and the shallow layer was composed of multiple parallel faults inclined toward the south with a shovel-type principal section. The upper and multiple secondary faults formed a multilevel “Y”-shaped combination with certain strike-slip properties
	South of Zhuanghai 104 Fault	The Zhuanghai 104 Fault is the controlling fault of the Zhuanghai Buried Hill, which is inclined southward with a shovel-type principal section and poses a strong control effect on the Palaeogene. The pre-Palaeogene system was cut and reformed. The upper and secondary faults merged to form the “Y”-shaped, flower-like combination with other structural styles
	Zhuangnan Fault	The Zhuangnan Fault is the mountain-controlling fault of the Zhuangxi Buried Hill, inclined southward with a shovel-type principal section. The upper and secondary faults were combined into a multilevel “Y”-shaped combination

extensional faults developed, with secondary faults increasing in the EW and NE-trending (Figure 2B) (Ma, 2018).

Due to the dominant effect of the strike-slip features, the overall number of fractures increased significantly in the upper strata (Neogene), and the primary fractures were discontinuous in all directions. More specifically, the NNE-trending fractures were composed of NEE-trending faults along the NNE-trending lateral rows, and the number of secondary faults in the west decreased, with the strike-slip effect becoming weaker (Figure 2C) (Wang et al., 2004).

3.2 Profile development characteristics of the fracture system

In the dominant fault systems of the study area, the NW trending faults are typically represented by the Chengbei Fault,

Chengbei 20 Fault, and No. 5 Pile Fault; the NNE (NE) trending faults are represented by the Chengbei 30 North Fault, Chengbei 30 South Fault, Changdi Fault, and Chengdong Fault; and the near EW trending faults are represented by the Chengbei 304 South Fault, Zhuanghai 104 South Fault, and Zhuangnan Fault. Combined with extensive geophysical data, we studied the development characteristics of the fault system in detail (Table 1; Figure 3).

3.3 Control effects of the main fault system on the buried hill

The main fault system in the study area is crucial for controlling the development and evolution of the buried hills. Among them, the C–P and C–O strata in the upper wall of the NW-trending Chengbei Fault, Chengbei 20 Fault, and No. 5 Pile Fault displayed a prominent “bare bottom” or “thin bottom”, indicating that they underwent

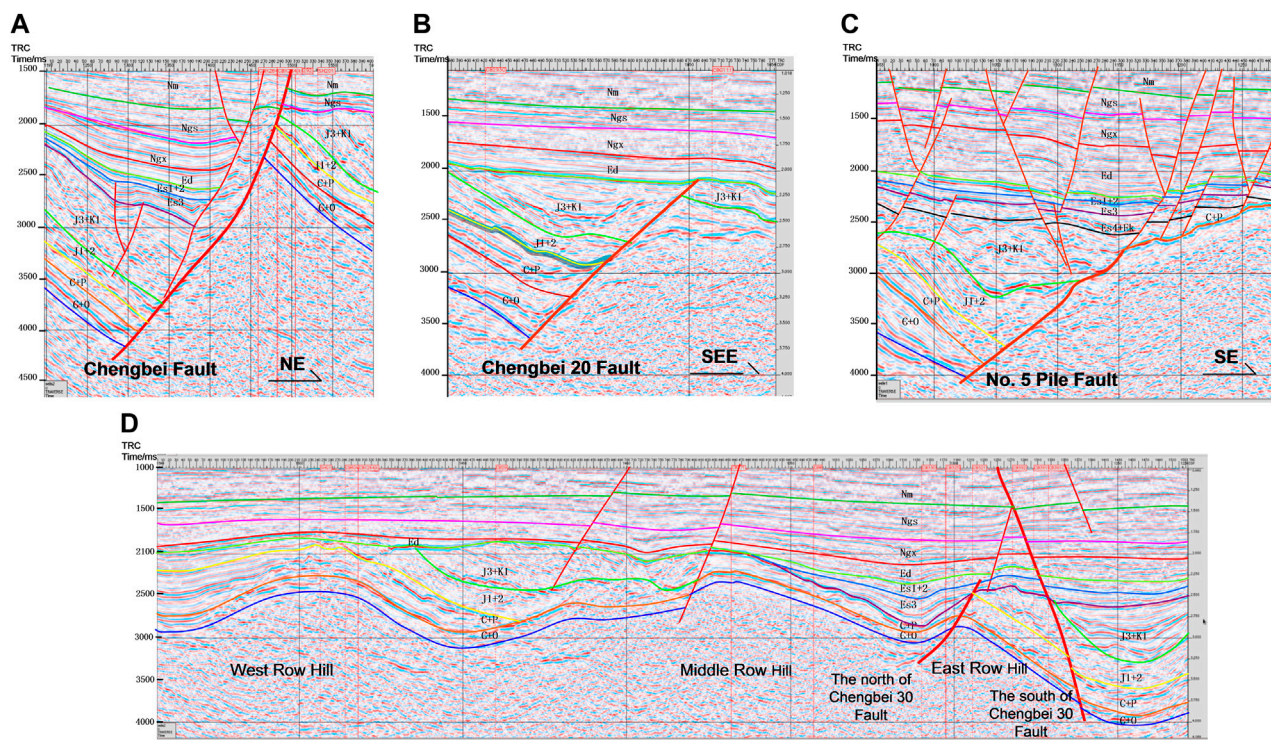


FIGURE 3

Control effect of major fault systems on buried hills. (A) Control effect of Chengbei Fault on buried hills; (B) Control effect of Chengbei 20 Fault on buried hills; (C) Control effect of No.5 Pile Fault on buried hills; (D) Control effect of Chengbei 30 Fault systems on buried hills and the distribution of buried hills.

compressional thrust in the late Triassic, resulting in strong erosion in the upper Paleozoic. During the late Jurassic to early Cretaceous, the fault occurrence caused a structural inversion from “reverse fault” to “normal fault” (Figures 3A–C), thereby shaping the NW-trending buried hill system in the area.

During this time, the NNE (NE)-trending fault started to experience sinistral tension and torsion from J_3 to K_1 , and subsequently experienced compression and right-lateral tension and torsion, such that the NW-trending buried hill system was segmented into three sections: the north section and the south section, primarily controlled by the NW-trending fault and the middle section, predominantly controlled by the NNE-trending fault. Influenced by the conversion effect of the pre-existing NW-oriented Chengbei-Pile 5 fault, the combination of the NNE-oriented Chengbei 30 north and south fractures formed the NNE-trending Chengdong and NNE-trending Changdi faults, which created a graben that segmented the mountain system in the study area into the north, middle, and south sections. In addition, under the influence of the right-lateral strike-slip of the Palaeogene Tanlu Fault, the nearly north–south tectonic stress field was derived in the study area, which controlled the tensile activity of the nearly EW-trending fault and formed shovel-type normal faults such as the Zhuangnan Fault, Zhuanghai 104 South Fault, and Chengbei 304 South Fault. These faults segmented the middle portion of the NNE-trending extension buried hill formed by the Mesozoic cutting into the buried hill bodies such as the East Row Hill, Zhuanghai Buried Hill, and Zhuangxi Buried Hill (Hu, 1997;

Dai and Meng, 2000; Chen and Zhang, 2002; Hou et al., 2005; Li et al., 2010).

4 Structural evolution characteristics of the buried hill faults in the Chengdao–Zhuanghai area

4.1 Analysis of fault activity of the buried hill in the Chengdao–Zhuanghai area

The activity characteristics of the faults can reflect the expansion and compression of the study area. The balanced section technique is a vital tool for studying fault activity characteristics, and its basic principle is that the stratigraphic length is always retained during deformation (Guo et al., 2012; Wei et al., 2018). The geological section of the tectonic evolution stage can be restored by layer-by-layer stripping to clarify the fault activity and evolution characteristics in each period. Under the constraint of multiple wells such as Chengbei 30 and Chengbei 304, the horizon was initially tracked using the time-domain data of the seismic profile. The tracked seismic horizon primarily included Nm, Ngs, Ngx, Es1+2, Es3, Ed, Es, J3+K1, J1+2, C+P, and C+O, among others. The second phase involves the interpretation of the fault and the depiction of the geometry of the buried hill. The third stage involves the conversion of the time-domain data into depth-domain data, to then study the evolution of the balanced profile.

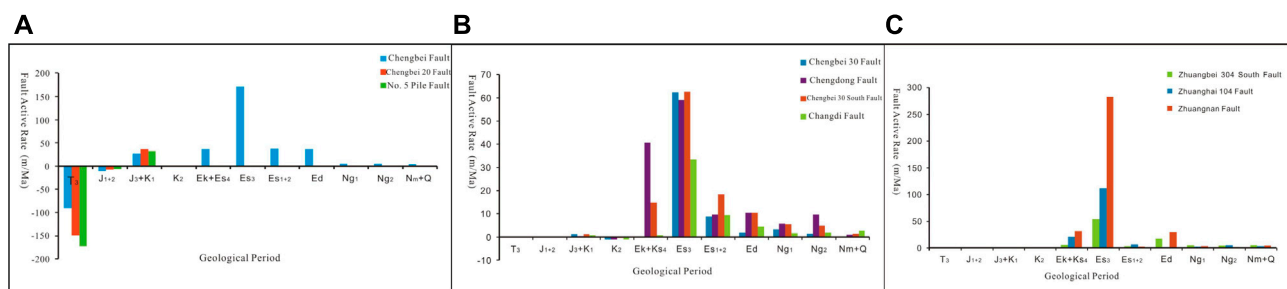


FIGURE 4

Column diagram of the fracture activity rate in the study area. (A) Extension rate of the NW direction survey line; (B) Extension rate of the NNE direction survey line; (C) Extension rate of the EW direction survey line.

Typical survey lines in the study area were intercepted, and the structural equilibrium evolution profiles were obtained using the equilibrium profile technique after seismic layer tracking, fault interpretation, and time-depth conversion. In the study area, the NE–SW, NWW–SEE, and near–SN sections were back-stripped on a layer-by-layer basis, and the amount of extension in each period was calculated and plotted as a histogram (Figure 4). These fault growth indices were used to characterize the influence of faults on the thickness distribution of the residual strata, in addition to the control of faults on the development of depressions and lake basins. The results revealed that the formation of the NW faults initiated in the late Triassic and displayed strongly active reverse-faulting properties, with “thin bottom” or “bald bottom” phenomena in the upper Paleozoic. Compared with the Late Triassic, the faults continued to thrust, but the intensity was low, and the activity rate was significantly reduced in the early-middle Jurassic. In the late Jurassic to early Cretaceous, the faults were tectonically reversed—from negative inversion of reverse fault to extensional normal fault—whereas in the Late Cretaceous, the faults were almost inactive, and only the Chengbei Fault remained continuously active in the Cenozoic. The intensity of the fault activity progressed from strong to weak to relatively strong to strong from Es_3 – Es_2 – Es_1 – Ed – Ng – Nm . In contrast, the activity of the Chengbei 20 Fault and No. 5 Pile Fault ceased after entering the Cenozoic (Figure 4A). As depicted in Figure 4A, during the Triassic Period thrust, the Chengbei Fault, Chengbei 20 Fault, and No. 5 Pile Fault created an uplift and denudation of the upper and lower Palaeozoic strata in the three regions, including the thinning or loss of the strata. Between the Jurassic and the Shasi periods, these three faults exhibited less activity and gradually transformed into normal faults. Overall, the strongest fault activity occurred during the Shahejie Formation, which was the boundary fault of Chengbei Sag, Chengbei 20 West Sag, and Gubei Sag. This controlled the formation of the faulted lake basin and deposited a thick layer of shale that acted as the area’s primary source of rock. The activity rate of the fault decreased as it moved from the Es_2 to the Pingyuan Formation.

Compared with the NW-trending faults, the NNE-trending faults became active at a later time and started to move in the late Jurassic to early Cretaceous with weaker activity. In the late Cretaceous, they underwent EW compression and exhibited specific compression–torsion properties. In the Cenozoic

(E_k – Es_4), except for the north Chengbei 30 Fault, which was inactive, the remaining faults were reactivated and started to control deposition. During Es_3 , each fault was strongly active, including the north of Chengbei 30, which peaked with an activity rate of up to 65 m/Ma. Thereafter, it gradually decreased and tended to extinguish (Figure 4B). The EW-trending key fault was formed during the latest stage and started to be active in the Cenozoic, cutting and reforming the pre-Palaeogene, in the Kongdian Formation–Sha4 layer had minimal activity, and the activity rate attained its peak in the Sha3 layer—150 m/Ma. The Kongdian Formation–Sha4 layer had minimal activity, and the activity rate attained its peak in the Sha3 layer—150 m/Ma. Following that, it tended to decline, only slightly picked up during the Ed period, and gradually weakened and stopped (Figure 4C). As can be seen in Figures 4B,C, the NNE and EW trending faults were primarily active during the Shahejie Formation period. Additionally, the high fault-activity rate under tension controlled the formation of the faulted lake basin. For instance, the Zhuanghai 104 South Fault controlled the formation of the Zhuangxi Depression.

4.2 Structural evolution characteristics of the buried hill faults in the Chengdao–Zhuanghai area

To further clarify the tectonic evolution characteristics of the buried hill faults in the Chengdao–Zhuanghai area, three lines were selected to restore the balanced section (Figures 5A–C). In accordance with the conservation principle for the section area and layer length, the balanced section was restored using the back-stripping method. The influence of denudation and deformation were considered in the process of restoring the balanced profile. The principle of constant thickness was applied to the denudation on a layer-by-layer basis in regions experiencing no structural inversion and compression deformation. The curved strata were leveled in the areas where compression formed folds. For the denuded areas, the thickness was restored by referring to the non-denuded areas. Based on the geometric relationship, 2d MOVE software was used to conduct a time-depth conversion of the seismic interpretation profile, conduct structural restoration processing for various structural components, repeat experiments, and obtain a reasonable structural evolution profile. The extension rate of each

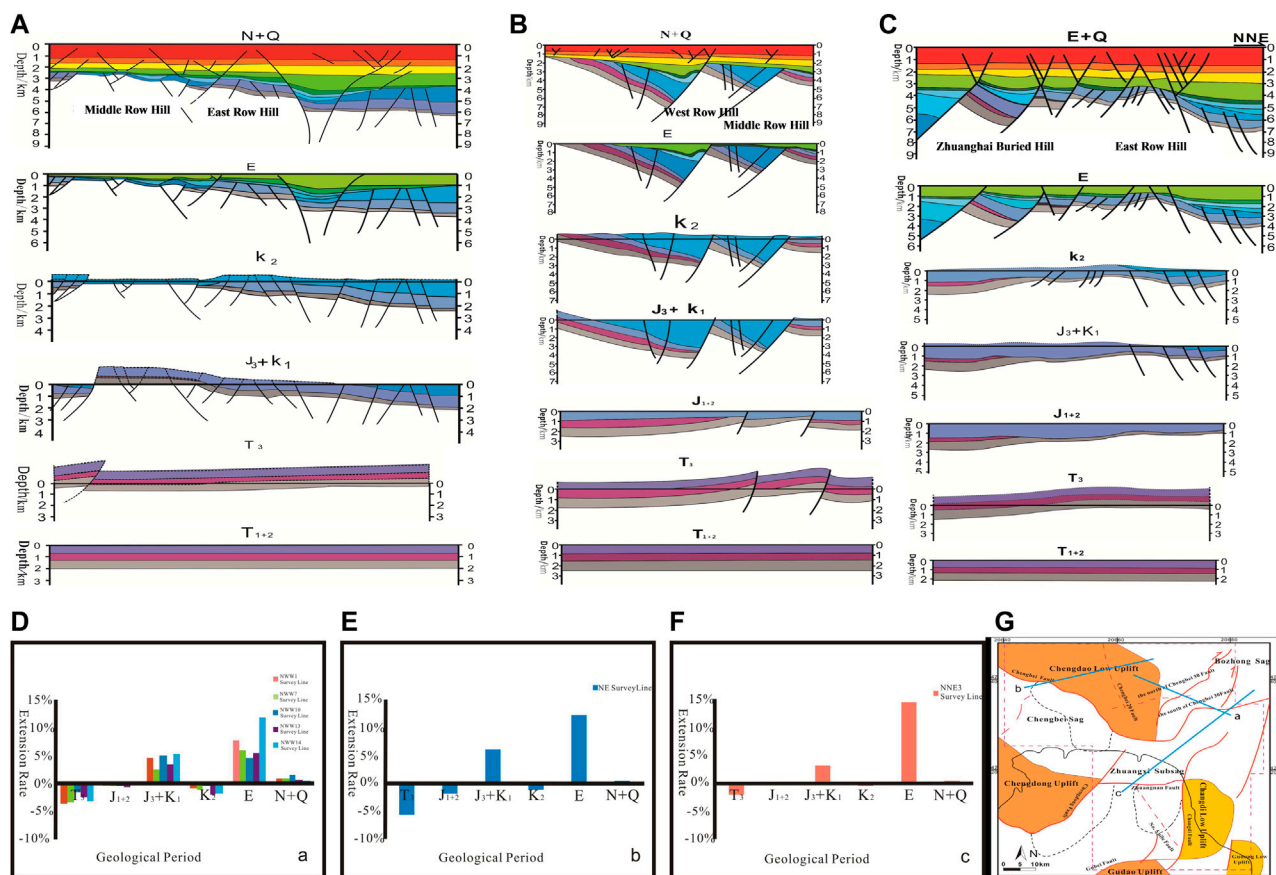


FIGURE 5

Restoration of equilibrium profile and comparison of stretching rate along various directions of the study area (A) Section map of the NWW direction survey line; (B) Section map of NE direction survey line; (C) Section map of the NNE direction survey line; (D) Extension rate of the NWW direction survey line; (E) Extension rate of the NE direction survey line; (F) Extension rate of the NNE direction survey line; (G) Section location.

survey line was calculated accordingly. Combined with the comprehensive analysis of the geometric characteristics, the kinematic characteristics and tectonic evolution history profile were obtained with a new understanding of the buried hill structure in the study area.

The results of the balance section demonstrated that the Chengdao-Zhuanghai area was experienced multiple stages of uplift and erosion, the extrusion and extension displayed evident stages (Figures 5D–G). In the late Triassic, the study area was controlled by a NE-trending compressive stress field, which formed a series of NW-trending thrust faults, with the evident shortening of the NE-trending survey lines. In the Early-Middle Jurassic, the study area experienced weak extrusion in the NE-SW direction, and the survey lines in all directions were somewhat shortened, with NE-trending survey lines being more pronounced in this process. In the late Jurassic to early Cretaceous, the entire study area entered the stage of fault depression, which was primarily controlled by the NE-SW-trending extensional stress field. In addition, the NW fault reversed and controlled the deposition, with a strong NE-trending line extension. By the late Cretaceous, the study area had been uplifted and eroded by a near-EW directional extrusion. By the late Cretaceous, the study area was influenced by the near-

EW directional extrusion that uplifted and denuded the entire study area. More importantly, this denudation was relatively intense in the NNE directional fault compression and torsion activity area, and the NNE directional measurement line exhibited a large extension rate. In the Neoproterozoic-Quaternary period, the entire research area entered a depressional stage, which slowed tectonic activity and gave each direction a low extension rate.

5 Discussion on the origin of the buried hill fault structure in the Chengdao-Zhuanghai area

5.1 Structural physics simulation experiments

To further establish the evolution process of the buried hill fault structure in the Chengdao-Zhuanghai area and explore its genetic

mechanism, we used the structural physical simulation experiment for forward modeling. The structural physical simulation experiment uses the similarity principle to reproduce the natural tectonic deformation process in a short time and on a small scale (Hu et al., 2020; Zhang et al., 2022).

The study area experienced multistage extension and compression in the Mesozoic, with strong NE–SW compression in the late Triassic–early and middle Jurassic, strong NE–SW extension in the late Jurassic–early Cretaceous, and EW compression in the late Cretaceous (Zhang et al., 2017; Jing, 2020). The faults in the studied area experienced a transformation from negative inversion to positive inversion during their development and evolution (Liu et al., 2019). The structural physical simulation experiment aims to reconstruct and restore the two stages of structural inversion experienced in the study area to provide an essential basis for the genesis of buried hill faults.

The structural physics simulation experiment was completed in two stages. During the T_3 – J_3 + K_1 period, the faults in the study area experienced strong to weak compression to tensile negative inversion. In the K_2 period, the faults experienced a positive inversion of tension to compression. Here, only the two experimental groups that fit the data the best were selected for analysis.

5.1.1 Materials for the experiments

Yellow quartz sand with 80–100 mesh and blue quartz sand with 40–60 mesh sand was chosen as the experimental materials. According to the distribution of strata and lithology, the T_3 – J_3 + K_1 period's primary strata were the Fangzi Formation 7400 m, Santai Formation 350 m, Mengyin and Qingshan Formation 250 m, and its main lithology was medium and fine sandstone. In order to represent the medium and fine sandstones, 40–60 and 80–100 mesh sand were used, respectively. The early sedimentary strata were stratified with 80–100 mesh blue quartz sand, and the later sedimentary strata were stratified using 80–100 mesh bright yellow and green quartz sand. In accordance with the similarity principle, the strata thickness in the T_3 – J_3 + K_1 period was set at 3.5 cm, and that in the K_2 period was set at 4.5 cm. Based on the perspective of stratum thickness, T_3 – J_3 + K_1 was Fangzi Formation~400m, Santai Formation~350m, Mengyin and Qingshan Formation~250m thick, and K_2 was approximately 285 m thick, with a thickness ratio of 1000:285=3.5:1. Therefore, the stratum thickness in the T_3 – J_3 + K_1 period was set at 3.5 cm, the total stratum thickness in the K_2 period was set at 4.5 cm, and the stratum thickness in the K_2 period was 1 cm.

5.1.2 Substrate conditions and experimental model

To represent the T_3 – J_3 + K_1 period, rubber skin and canvas were placed at the bottom of the sandbox. After splicing these two layers, the two ends were fixed on the driving units to reflect the different properties of the substrate. During the experiment, moving the driving units to either side caused the displacement to propagate upward and deform the sand body (Figure 6A). For the K_2 period, an elastic cloth and a polystyrene simulation basin were positioned at the bottom of the sandbox. Both ends of the elastic fabric were fastened to the driving unit to achieve the transfer displacement to the upper sand body (Figure 6B).

5.1.3 Experimental process and results analysis

The tectonic physics simulation experiment for the time span T_3 – J_3 + K_1 lasted 63 min. At the initial stage, the left drive unit was extruded at a speed of 0.5 mm/s. At 18 min, the No. 1 Fault was generated after altering the basement properties, and the fault property corresponded to a reverse fault. The cross-section was flat, inclined on the SW, small dip angle, and continuous development. At 25 min, the left and right driving units were set to two-way tension: the tensile speed of the right drive unit was 0.4 mm/s, and the extensional displacement reached up to 0.8 mm/s. At 42 min, the extension displacement reached 2.7 cm. The smaller No. 2 and No. 3 faults were generated on the upper plate of the No. 1 Fault, both of which were positive faults inclined toward NE, during the early stage when the No. 1 Fault was structurally reversed under the influence of tensile stress, and the reverse fault was reversed from negative to positive. After conducting the simulation experiment for 49 min, fault No. 4, similar to Fault No.3, was formed in the forward direction of the No. 3 Fault. Upon running the experiment for 63 min, Fault No. 5, a positive fault that was consistent with fault No. 4, was generated in the forward direction of Fault No. 4. The upper plate of Fault No. 1 displayed a forward normal-fault layer combination (Figure 7A). The experimental results revealed that the NE–SW directional stress-field transformation in the study area initially extruded before being subjected to tension, which caused the tectonic negative reversal of the previously developed reverse faults. This finding is consistent with the general negative reversal of the NW directional faults in the T_3 – J_3 + K_1 period throughout the Jiyang Depression.

For the K_2 period, the duration of the tectonic physics simulation experiment was 92 min. In the initial stage of the experiment, the model was biaxially stretched. The speed of the left and right drive units was 0.08 and 0.1 mm/s, respectively. After conducting the experiment for 15 min, the No. 1 Fault - a normal fault inclined toward SE - was generated along the polystyrene foam. As the tensile displacement increased, the No. 2 Fault was produced in the upper plate of the No. 1 Fault at 32 min. A typical graben structural style was produced by the fault, which was of the normal type, inclined toward NW and forming a common descending plate with No. 1 Fault. With the continuous extension, more small-scale normal faults were generated in the fault block, including the No. 3 Fault. The fault scale continued to increase with the extension displacement. The final displacement of the tension stage was 6 cm, and the vertical fault spacing of the large boundary fault was 1 cm. After continuing the experiment for 41 min, the ensuing sedimentary strata were placed in accordance with the aforementioned experimental model. Combined with the non-uniform deformation of the previous strata, the subsequent strata were reasonably settled. The velocities of both the left and right driving units were set at –0.1 mm/s, respectively. This ensured the simultaneous extrusion of both sides of the sandbox to ensure the transformation of the stress-field properties of the model from extension to extrusion. After performing the simulation experiment for 67 min, a slight extrusion, uplift and, contraction occurred in the formation. As the extrusion displacement reached 1.9 cm, the descending plate of the first fault gradually transformed into the ascending plate, and the normal fault layer progressively

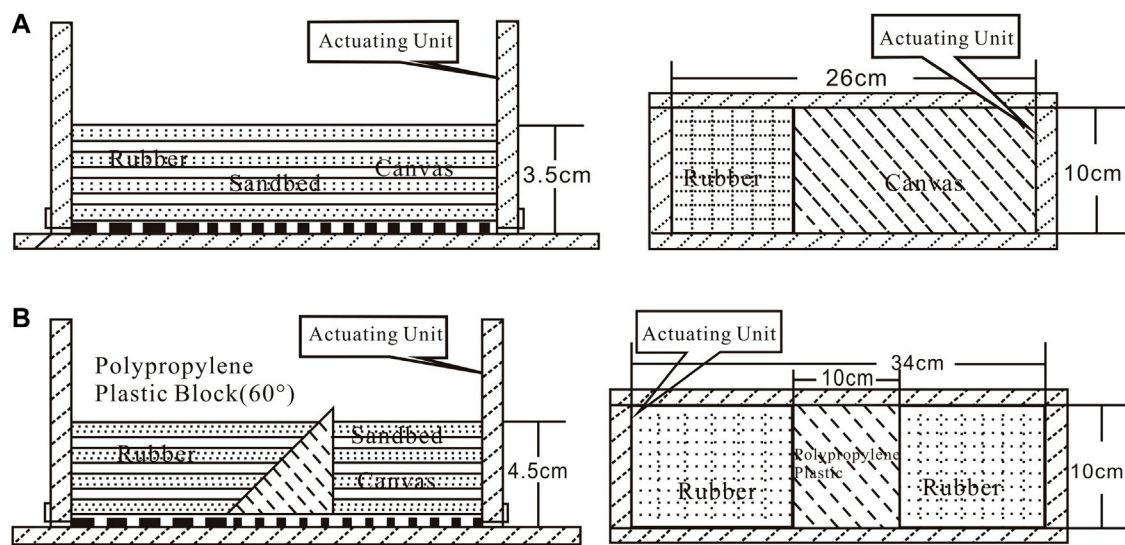


FIGURE 6

Basament conditions and experimental model of structural physical simulation experiment in the study area (A) Results of the tectonic physical simulation experiment for the T3-J3+K1 period (B) Results of the tectonic physical simulation experiment for the K2 period.

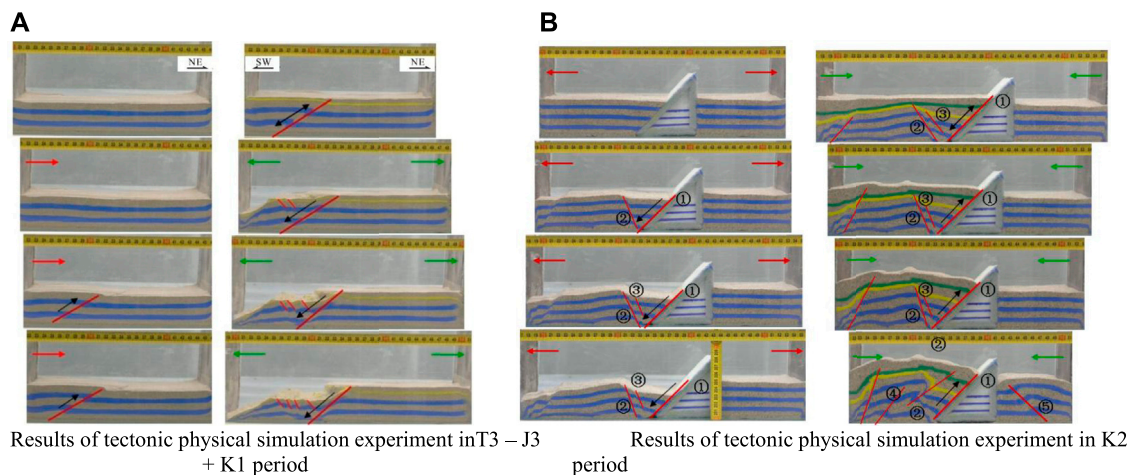


FIGURE 7

Results of the structural physics simulation experiment section in the study area. (A) Results of tectonic physical simulation experiment in T3-J3+K1 period; (B) Results of tectonic physical simulation experiment in K2 period.

transformed into the reverse fault with structure reversal (Figure 7B).

As extrusion displacement increased further, the inversion degree of the No. 1 Fault strengthened, and a series of new reverse faults were eventually generated. As a result, both the number and size of faults gradually increased. The lower plate of the No. 1 Fault generated new faults, but both their scale and number were small. The experiment ended after 92 min. Based on the comparison of multiple sets of simulation experiments, the early fracture system was found to be susceptible to reversal, which is

consistent with the direction lines of the tensile and compressive stresses before and after reversal. If the direction of the tensile and extrusion stresses before and after inversion coincided with the section tendency, the early fracture system was vulnerable to reversal. Before and after the inversion, the directions of the tensile and extrusion stresses were the opposite of the section tendency, and a significant amount of friction resistance produced a new thrust fracture system. The experimental results revealed that in the study area, the stress-field transformation of the NW-SE trending initially exhibited tension and later displayed

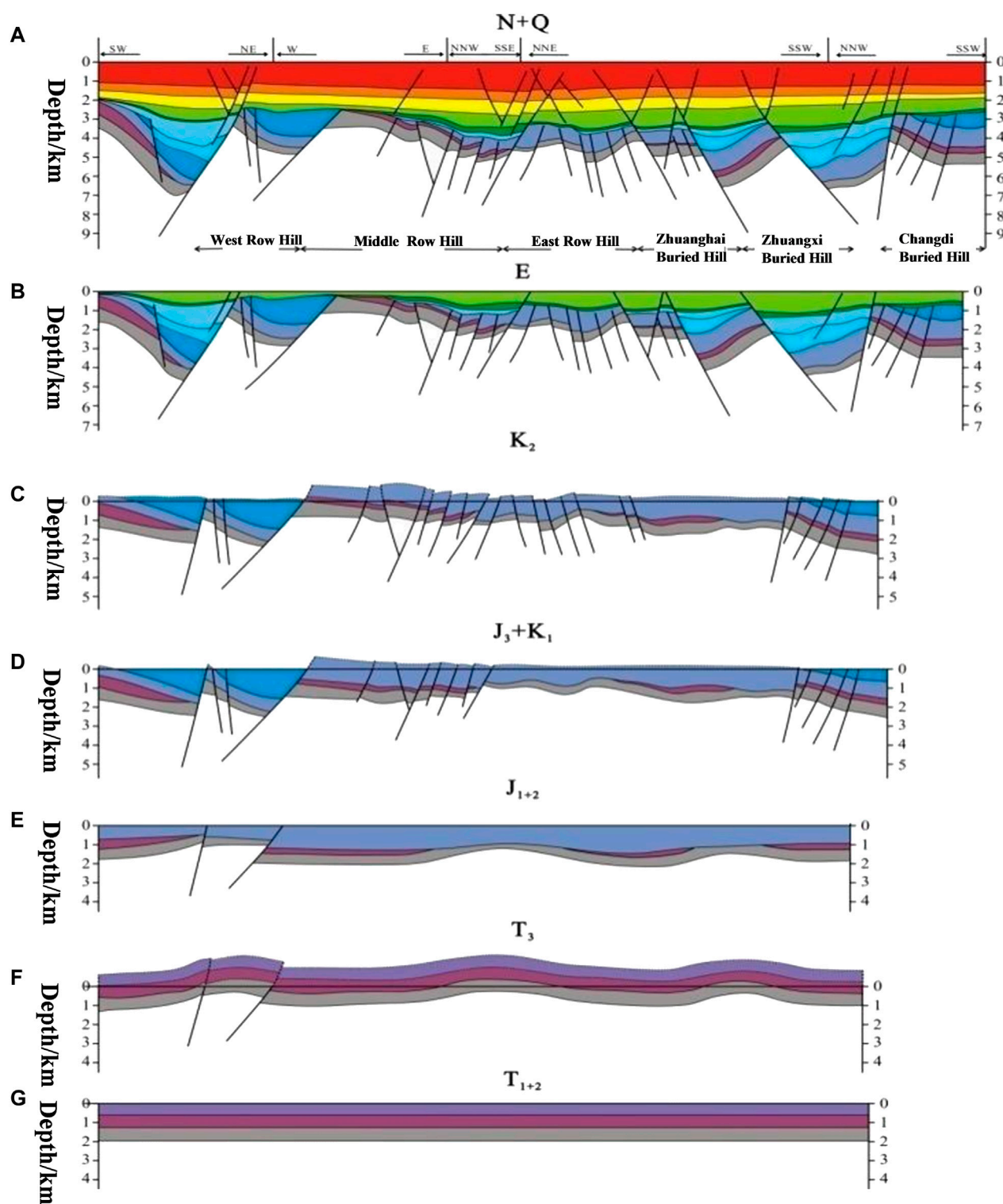


FIGURE 8

Typical structural balanced sections in the study area (refer to Figure 1 for details of section location). (A) Stratigraphic distribution in N+Q period; (B) Stratigraphic distribution in E period; (C) Stratigraphic distribution in K_2 period; (D) Stratigraphic distribution in J_3+K_1 period; (E) Stratigraphic distribution in J_{1+2} period; (F) Stratigraphic distribution in T_3 period; (G) Stratigraphic distribution in T_{1+2} period.

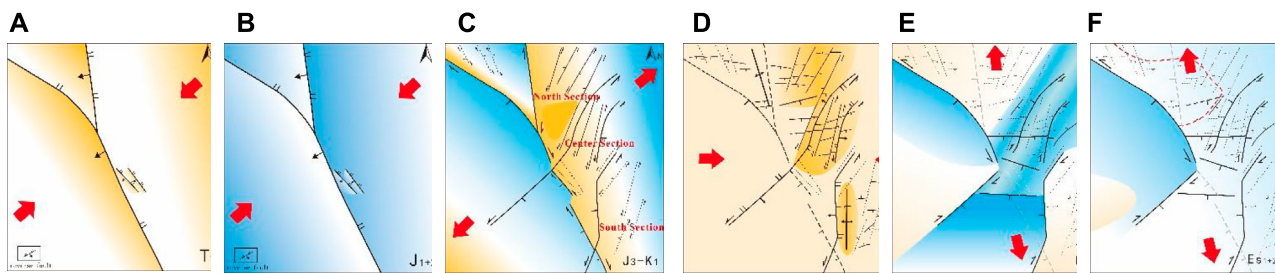


FIGURE 9

T3-E genetic model and structural framework changes in the study area. (A) genetic model and structural framework in T_3 period; (B) genetic model and structural framework in J_{1+2} period; (C) genetic model and structural framework in J_3+K_1 period; (D) genetic model and structural framework in K_2 period; (E) genetic model and structural framework in Es_3 period; (F) genetic model and structural framework in Es_{1+2} -Ed period.

extrusion, which caused structural positive inversion in the earlier-formed normal faults. This result is consistent with the general positive inversion of the NE-trending faults in the K_2 period of the Jiyang Depression.

5.2 Causes of the buried hill fault structure in the study area

Based on the interpretation of the discussed seismic profile and structural physical simulation experiment analysis, combined with the data sourced from previous studies, the formation of the buried hill fault structure in the Chengdao-Zhuanghai area is closely related to the significant transformation of the tectonic stress field in the study area and those adjacent to it since the late Triassic.

5.2.1 Overall uplift and erosion (Indosinian T_3)

The Yangtze plate converged and collided with the North China plate in the late stages of the Indo-Chinese movement (He, 2001), having a substantial impact on the tectonic pattern of the studied area (Qi, 2004). Controlled by the compressional collision between the North China plate and the Yangtze plate, the Jiyang depression is a regional stress field in the near-NNE of the compression system, which is in a state of uplift and erosion. Depletion of the Middle-Lower Triassic (Figures 8A,B) results in the development of a number of NW-NWW fold and thrust faults (Figure 9A). During this time, the Tanlu fracture belt did not affect the tectonic evolution of the Jiyang Depression. In particular, a series of NW-trending thrust faults were developed in the stress field of the Chengdao-Zhuanghai area, thereby forming an NW-trending thrust mountain-system tectonic pattern. Among these, the large-scale Chengbei-Wuhaozhuang fault zone exhibited significant activity that reached up to 120 m/Ma. Influenced by the regional compressive stress and NW-trending reverse fault activity, the overall uplift of the study area underwent erosion, and the peak of denudation was found in the upper plate of the NW-trending fault that was severely eroded near the fault side. The Upper Paleozoic and Lower Paleozoic were extensively or completely eroded, with prominent thin or bare-bottom phenomena. During this period,

only the NW-trending faults developed in the Chengdao-Zhuanghai area, and the inner fault of the buried hill had not yet formed.

5.2.2 Overall filling deposits (Yanshanian J_{1+2})

During the early Yanshanian movement, the collision and extrusion between the Yangtze plate and the North China plate gradually weakened, and the influence of the western Pacific plate activity on the study area gradually increased. Eastern China began the transition between the Paleo-Asian and the Pacific tectonic stages (Zhou, 2006; Dong et al., 2007; Zhang et al., 2007).

A set of fluvial-lacustrine coal-bearing strata were deposited in the Jiyang Depression over a protracted period of inland depressional subsidence, and they bear cap-type and NW-trending belt distribution characteristics. At this point, the Chengdao-Zhuanghai area had inherited the structural pattern of the late Triassic, and the overall depression deposition was still influenced by the NE-SW compressive stress field. However, the intensity of the activity was significantly lower in comparison with that of the Late Triassic, and the average activity rate was only -8 m/Ma. The area with a higher terrain exhibited less deposition, and that with a lower topography displayed a thicker deposition. The buried hills formed in the Late Triassic experienced the first burial (Figure 8C; 9B).

5.2.3 Fault segmentation (J_3 - K_1 , Mid-Yanshanian)

In the late Jurassic-early Cretaceous, the Yangtze plate and Siberia plate activities were replaced by the Pacific plate activity, which emerged as the primary control factor of the tectonic evolution in North China. This resulted in the formation of the Pacific tectonic domain. The NNW-trending subduction of the Pacific plate created a strong left-lateral strike-slip of the NNE-trending Tanlu Fault zone, which yielded a compressive-torsional tectonic stress field in eastern China. Simultaneously, the lithosphere in eastern China emerged strongly thinned, accompanied by mantle plume activity and asthenosphere uplift. Under the superposition of these two forces, eastern China entered a stage of large-scale rift development and thick strata deposition, accompanied by strong volcanic activity.

The research area was strongly affected by the left-lateral strike-slip of the Tanlu Fault zone. The NW-trending Chengbei

No. 5 Pile Fault exhibited a negative inversion that altered the original compressional thrust into an extensional fault. The strong fault activity and the average activity rates were approximately 30 m/Ma. The NW-trending buried hill system was initially formed when the bottom wall of the NW-trending fault was uplifted. The new NNE-trending left-lateral strike-slip fault occurred in the study area, whereas the right-lateral strike-slip activity occurred in the early NW-trending fault. The strike-slip activities of the NW-trending Chengbei–No. 5 Pile Fault and the NNE-trending Chengbei 30 North–Chengdong Fault in the late Cretaceous generated regional conjugate pressurization between the two faults. In addition, numerous NNE-trending compressive–torsional strike-slip faults were formed within the Middle Row Hill and East Row Hill owing to the influence of the compressive–torsional tectonic stress-field throughout eastern China. A small amount of strike-slip extensional faults was formed under the strike-slip activities in the west row of the fault between the NW-trending Chengbei Fault and the NNW-trending Chengbei 20 Fault. As of this moment, a series of strike-slip faults similar to those in the Tanlu Fault zone have been determined in the study area, cutting the NW-trending buried hill system. This occurrence complicated the NW-trending mountain system and segmented it into the north, middle, and south sections (Figure 8D; 9C).

5.2.4 Extrusion uplift differentiation (late Yanshanian K₂)

In the late Cretaceous, the Pacific Plate transformed into a low-velocity northward movement, resulting in the retreat of trenches and plates. The trench retreat vector shifted southward, and the east of the North China Craton appeared to be stretched along the near-SN direction. During this stage, the near-EW extrusion formed the near-SN thrust structure, and the entire area was uplifted and eroded (Zhang and Dong, 2008). Partially formed in the late Jurassic–early Cretaceous NNE strike-slip faults (distributed in Middle Row Hill, East Row Hill, and Zhuanghai Buried Hill) by compressive and torsional activities, a series of new near-EW-trending secondary normal faults were also formed. Among them, the fault activity of Chengbei 8 was strong and lowered the southern part of the Middle Row Hill in the high region of the late Jurassic–early Cretaceous with relatively moderate denudation. In their entirety, the NNE and near-EW faults were further complicated. The near-EW compressional structure enhanced the NNE-trending mountains (Figure 8E, Figure 9D).

5.2.5 Mid-subduction differentiation (early himalayan period E)

The sedimentary period of the Kongdian Formation-Sha 4 member represents the transition period between the Yanshan movement and the Himalayan movement. At this stage, the subduction direction of the Pacific plate persisted in the NNW direction, and the Tanlu Fault zone inherited the Yanshan movement mode, which corresponded to the left-lateral strike-slip (Li et al., 2019). The NW-trending Chengbei Fault inherited this activity and maintained its strength, whereas the NW-trending Chengbei 20 Fault and No. 5 Pile Fault started to diminish. The NNE-trending Chengbei 30 South Fault, the Chengdong Fault, and

the Changdi Fault started to resurface. In the vicinity of the EW-trending Chengbei 304 South Fault, the Zhuanghai 104 South Fault, and the Zhuangnan fault formed and started to move, thereby regulating certain depositions. Only a small portion of the Zhuanghai and Zhuangxi Buried Hills started to receive deposition during this time, and other buried hills were still undergoing exposure and erosion (Figure 8F, Figures 9E–F).

A regional tectonic movement known as the Jiyang event, which was an essential tectonic movement in the development of the Jiyang Depression (Zhu & Xu, 2019) occurred in the Sha3 layer. During the Cenozoic, the Pacific plate and Indian Ocean plate surrounding Eurasia underwent major kinematic adjustments. The movement direction of the Pacific plate varied from NNW to NWW, which was positively subducted beneath Eurasia. The collision of the Indian subcontinent with the Eurasian plate was eventually completed at the end of the Middle-Eocene. As a result, the Tanlu Fault rotated from left to right, resulting in the formation in the area of an NW-trending extensional stress field. The NE- and EW-trending faults in the study area became strongly active and developed as the Cenozoic basin-controlling faults in the study area (Feng J et al., 2017; Du et al., 2020). Owing to the coupling of the strong activities of the Chengbei 304 South Fault, Zhuanghai 104 South Fault, and Zhuangnan Fault, the Zhuanghai and Zhuangxi Buried Hills were completely covered. The eastern mountain is still topographically controlled by terrain, some areas are subject to sedimentation, and other areas are still exposed to the water surface and being eroded (Figure 9E).

In the Sha 2 and Sha 1 layers, the overall stress field characteristics of the study area were similar to those of the Sha 3 Formation. However, the relative strengths of the right-handed shear stress and horizontal tensile stress started to change, which weakened the tensile stress and gradually increased the shear stress. Even if the entire fault system exhibited inheritance, the active strength started to weaken. Although the activity rates of the NNE-trending and near EW-trending primary faults in the study area were significantly lower than those of Sha 3, numerous secondary NNE-trending and near EW-trending faults continued to exist. Among these faults, the transformation of NNE-trending faults onto the structural pattern was more evident. During this period, East Row Hill and Changdi Buried Hill were completely interred, and Middle Row Hill was partially buried. During the sedimentary period of the Dongying Formation, the structural pattern inherited the sedimentary period of the Sha 2 and Sha 1 layers, with a dominant NEE-oriented fault activity. The number of NNE-trending right-lateral strike-slip faults (or extensional strike-slip faults) and derived NEE-trending secondary faults increased drastically. In the local regions, the primary faults started being discontinuous, and the strike-slip effect became more pronounced (Figure 9F).

5.2.6 Overall stable subsidence (late himalayan N + Q)

The entire Chengdao–Zhuanghai area entered the subsidence stage in the Neogene, during which the fault activity in all directions decreased significantly and the primary faults in all directions became intermittent. Consequently, a series of *en-échelon* secondary faults developed along the direction of the primary fault, and the influence of strike-slip movement gradually

increased from west to east. Compared with the previous period, the fault activity rate was considerably reduced. The buried hills in the study area remained deeply buried (Figure 8G). The section location is presented in Figure 1.

In conclusion, the thrusting activity of the NW-trending faults in the late Triassic and the tectonic inversion of the late Jurassic to early Cretaceous shaped the NW-trending Buried Hill system in the research area. The left-lateral strike-slip fault of the Tanlu Fault zone yielded the NNE-trending synclinal strike-slip fault, which divided the NW-trending mountain system and segmented it into three sections: north, middle, and south. The core of the buried hill is further complicated by the EW-trending extensional faults that developed in the late Cretaceous, and the NNE- and NW-trending strike-slip faults that formed in the late Jurassic to early Cretaceous. Until the Palaeogene, the Tanlu Fault fluctuated from left-handed activity to right-handed activity, and near-EW-trending normal faults were observed in the study area, which transformed the middle part of the mountain system into a buried hill with a near-EW-trending distribution. After the sedimentary period of the Dongying Formation, the overall subsidence received the deposition that formed the current structural pattern of the buried hill.

6 Relationship between faults and oil distribution in the buried hills

Chengbei, Shanan, Bozhong, Huanghekou, Gubei, and other oil-generating depressions are distributed throughout the buried hills in the Chengdao-Zhuanghai area, with adequate oil and gas supply and suitable oil source conditions. The Chengbei Fault, the Changdi Fault, and the Chengbei 20 Fault are the three main NW trending faults. In particular, the Chengbei and Changdi faults have been active for a long time and can be used as channels for oil and gas migration. The stratum dip traverses in the opposite direction from the fault dip. As the oil and gas migration cannot easily fill the buried hill, the oil and gas reservoir in the buried hill is small, whereas the upper Guantao Formation and Dongying Formation are large. The Chengbei Fault, along which the oil and gas are partially filled, forms the west boundary fault of the Chengdao Buried Hill. Similarly, the Changdi Fault forms the west boundary fault of the Changdi Buried Hill, with oil and gas migrating upward along the Changdi Fault along the Gubei Sag in the west, and with some of this migration occurring southward along the structural beam of the Changdi Low Uplift in the northeast. Furthermore, the Changdi Fault regulates the oil-bearing boundary of the Changdi Buried Hill. Owing to the shallow burial in this area, the buried oil and gas pool is small. Specifically, the Chengbei 20 Fault forms the west boundary of the Zhongpai Mountain in the Chengdao Buried Hill. The oil source in the Chengbei Zhongpai Mountain originates in the northern Shanan Depression and moves south along the structural beam. Therefore, the Chengbei 20 Fault controls the oil-bearing property of the Zhongpai Mountain, and the oil and gas are primarily distributed along the structurally high regions of the Zhongpai Mountain.

Overall, the presence of multiple NE-trending faults has created three main structural beams that control the oil and gas migration

channels, forming the distribution characteristics of oil and gas enrichment in the structural beams.

The NEE-trending faults can be segmented into small faults and boundary large faults, where small faults complicate the distribution of oil and gas. These faults exhibit various sealing properties depending on the fault-filling cementation and dissolution. In principle, the degree of sealing controls both the height and distribution of oil and gas. Oil- and gas-bearing properties are identified by the well-sealed fault's rising wall. The lower collapsing wall is devoid of the oil and gas injection that created the oil difference in the buried hill fault block. Primarily, the main faults include the Chengbei 304 South Fault, the Zhuanghai 104 South Fault, and the Zhuangnan Fault, all of which are Nandiao reverse faults. The Chengbei 304 and Zhuanghai 104 South Faults contained the formation of the buried hill reservoir and hindered the oil and gas migration from several similar channels in the northeast. This generated the most abundant distribution of oil and gas north of the Chengbei 304 South Fault, followed by the Zhuanghai 104 South Fault. The Zhuangnan Fault blocked the oil and gas that formed in the Chengbei Sag and Zhuangxi Sag and controlled the south boundary of Zhuangxi Buried Hill.

7 Discussion and conclusion

Fault structure is the most important controlling factor for buried hill reservoirs in the Chengdao-Zhuanghai area. The inner fault of the NW-trending buried hill in this area is similar to the strike-slip extensional fault formed by the right-lateral strike-slip movement of the NW-trending Chengbei Fault in the late Jurassic-early Cretaceous eras. More specifically, the NNE-trending fault is a left-handed compression-torsion fault that developed under the left-handed strike-slip activity and the regional compression stress field of the Tanlu Fault zone. Furthermore, the near-EW fault is closely associated with the near-SN extension stress field in the late Cretaceous.

The current research provided the following insights.

1. NW-trending faults govern the formation of "mountains": faults have undergone the stable craton, compression thrust, denudation and leveling, and structural inversion stages. The NW-trending fault was formed by the compressional thrust in the late Triassic. After that, it experienced a tectonic inversion process that ranged from a thrust to a normal fault in the Mesozoic. In the Cenozoic, the Chengbei Fault was inherited and developed, whereas the Chengbei 20 Fault disappeared.
2. The cutting of an NNE (NE)-trending fault into an NW trending "mountain system" segmented the mountain system in the study area into three sections: north, middle, and south. The NNE (NE) trending fault was formed in the J3-K1 period, which experienced a transformation from J3 to K1 left-handed to K2 compressional torsional to E right-handed tensional torsion. The section formed a flower-like and multistage Y-shaped combination due to its relative steepness. Owing to the transformation from the NW to the Chengbei No. 5 Pile Fault, the Chengbei 30 North and Chengbei 30 South Fault groups formed horsts, and the

Chengdong and Changdi faults generated grabens. The strata on both sides of the Changdi Fault bent violently and were compressed in the Late Cretaceous, creating forced folds.

3. The EW-trending fault cut the NNE-trending zone to form the Dongpaishan, Zhuanghai, and Zhuangxi Buried Hill “mountains”, wherein most EW-trending faults were Cenozoic active faults. The peak activity occurred in Es3, which is a typical shovel-type normal fault. The EW-trending fault separated the Dongpaishan, Zhuanghai, and Zhuangxi Buried Hills from the middle section of the buried hills in the study area.
4. The superposition effect of the multiple faults resulted in the complexity and diversity of the “mountain” structures.
5. The oil and gas reservoirs currently discovered were primarily concentrated in the Lower Paleozoic. The Ordovician served as the primary reservoir, and the pores, caves, and fractures that developed along the top surface of the Ordovician carbonate rock created the primary reservoir spaces (Kong and Lin, 2000; Li et al., 2004; Li et al., 2000; Feng et al., 2019; Du, et al., 2022).

In total, five types of traps were developed in the lower Paleozoic, including fault block traps, fault nose traps, residual hill traps, unconformity traps, and compression twist-fold traps, with fault block traps having the greatest density and the most extensive distribution.

6. The formation of buried hill reservoirs was determined based on the effective hydrocarbon source rocks, reservoirs, migration pathways, traps, preservation conditions, and their spatiotemporal configuration in the Chengdao–Zhuanghai area (Yang et al., 2001; Qiu et al., 2010). In the study area, the buried hill reservoirs were the most abundant in the NW and NNE fault conjugate locations (Feng et al., 2021). The oil sources for Zhongpaishan, Dongpaishan, and other buried hill reservoirs were found in the east and north Shan'an Sags as well as Bozhong Sags, which exhibited the characteristics of migration and accumulation along the parallel fault in the far source.
7. The oil source of the northwest Chengbei and Changdi faults primarily originated on the downthrow side of the faults, and the oil and gas migration occurred upward along the faults. Therefore, the favorable reservoir inside the buried hill matched the direction of oil and gas exploration. In the Chengbei 20 fault, oil and gas mainly originated from the unconformity surface of the buried hill to the north. As a result, the fault block parallel to the direction of the oil and gas migration represents the path of future exploration and development. The NE-trending fault controlled the shape and distribution of the top surface of the buried hill, thereby forming three structural beams. Numerous fault blocks were created as a result of the NE-trending fault and the NNE-trending fault cutting each other. Overall, the buried hill fault block along the lower portion of the structural beam indicated the direction of oil and gas exploration.

In conclusion, the systematic understanding of the fault structure characteristics and genetic mechanism, which confirms the impact of multiple sets of unconformity and various faults in the area on the migration and accumulation of oil and gas in buried hills, allows for further exploration of the differential oil and gas migration and accumulation characteristics

in different buried hills. As such, this finding highlights the favorable direction of exploration. Furthermore, fault sealing under the influence of multiple parameters can be quantitatively evaluated to provide a systematic, comprehensive fault-sealing prediction method with great scientific value.

Data availability statement

The original contributions presented in the study are included in the article/Supplementary Material, further inquiries can be directed to the corresponding author.

Author contributions

ZW, KZ, and QW contributed to conception and design of the study. HZ organized the database and experiment. SY, YL performed the statistical analysis. ZW, KZ, and QW wrote the first draft of the manuscript. SY and YL wrote sections of the manuscript. All authors contributed to manuscript revision, read, and approved the submitted version.

Funding

The work throughout the conception, design, and publication of this Research Topic was supported by the National Natural Science Foundation of China (42072234).

Acknowledgments

We would like to thank all the reviewers and authors for their contributions to this Research Topic. We also thank the entire team at Frontiers in Earth Science for their dedicated effort in guiding the revision and detailed editing of the papers on the Research Topic.

Conflict of interest

ZW, QW, HZ, SY, and YL were employed by Haiyang Oil Production Plant, Shengli Oilfield Company, Sinopec.

The remaining author declares that the research was conducted in the absence of any commercial or financial relationships that could be construed as a potential conflict of interest.

Publisher's note

All claims expressed in this article are solely those of the authors and do not necessarily represent those of their affiliated organizations, or those of the publisher, the editors and the reviewers. Any product that may be evaluated in this article, or claim that may be made by its manufacturer, is not guaranteed or endorsed by the publisher.

References

- Chen, G., and Zhang, S. (2002). Discussion on the exploration of low buried hills between Chengdao and Zhuangxi areas. *Pet. Exp. Geol.* 24 (4), 306–310. doi:10.3969/j.issn.1001-6112.2002.04.004
- Dai, J., and Meng, Z. (2000). Finite strain study on paleozoic structures in Chengdao region. *J. Geomechanics* 6 (1), 77–83. doi:10.3969/j.issn.1006-6616.2000.01.010
- Dong, S., Zhang, Y., Long, C., Yang, Z., Ji, Q., Wang, T., et al. (2007). Jurassic tectonic revolution in China and new interpretation of the Yanshan Movement. *Acta Geol. Sin.* 81 (11), 1449–1460. doi:10.3321/j.issn:1000-9515.2008.02.012
- Du, H., Feng, J., Xu, S., Shang, S., and Li, C. (2022). Quantitative characterization of volcanic expansion fractures based on thermodynamic coupling analysis. *Geoenergy Sci. Eng.* 221, 211387. doi:10.1016/j.geoen.2022.211387
- Du, H., Xu, S., Feng, J., Ren, Q., Wang, Z., and Xu, K. (2020). Digital outcrop representation for karst fracture-cave reservoir. *J. China Univ. Petroleum (Edition Nat. Sci.)* 44 (5), 1–9. doi:10.3969/j.issn.1673-5005.2020.05.001
- Feng, J., Qu, J., Wan, H., and Ren, Q. (2021). Quantitative prediction of multiperiod fracture distributions in the cambrian-ordovician buried hill within the futai oilfield, Jiyang depression, east China. *J. Struct. Geol.* 148, 104359. doi:10.1016/j.jsg.2021.104359
- Feng, J., Sun, Z., Wang, Y., and She, J. (2019). Study on stress sensitivity of ordovician fractures in hetianhe gas field, tarim basin. *Geol. J. China Univ.* 25 (2), 276–286. doi:10.16108/j.issn1006-7493.2018059
- Feng, J., Wang, Z., and Shang, L. (2017). Genetic mechanisms of superimposed fault systems in block 3 of nanpu SagBohai Bay Basin. *OIL&GAS Geol.* 38 (6), 1032–1042. doi:10.11743/ogg20170603
- Guo, F., Hou, S., Liu, R., Xia, B., Yuan, Y., and Wan, Z. (2012). Balanced cross-section for restoration of structural evolution in a foreland thrust belt: Taking the northwestern margin of junggar basin for example. *Mar. Geol. Front.* 28 (12), 46–51. doi:10.16028/j.1009-2722.2012.12.005
- He, B. (2001). On dynamics of the Bohai Bay complex faulted basin. *Pet. Geol. Exp.* 23 (1), 27–31. doi:10.3969/j.issn.1001-6112.2001.01.005
- Hou, F., Li, S., Wang, J., Yu, J., Lv, H., and Xu, S. (2005). Buried hill fault in Zhuanghai area of Jiyang depression. *Mar. Geol. Quater. Geol.* 25 (3), 69–74. doi:10.16562/j.cnki.0256-1492.2005.03.010
- Hu, Q., Dong, D., Yang, J., Gao, L., Kong, X., Yang, G., et al. (2020). Geostructural analysis and physical simulation for the 4th block of the central Junggar Basin. *Sci. Technol. Eng.* 20 (10), 3898–3907. doi:10.3969/j.issn.1671-1815.2020.10.015
- Hu, W. (1997). The types of forward and inversion structures and their research methods. *Daqing Pet. Geol. Dev.* 16 (2), 6–9. doi:10.19597/j.issn.1000-3754.1997.02.002
- Jing, A. (2020). Characteristics and control of faults on reservoir of Lower Paleozoic buried hill in Chengdao area, Jiyang depression. *Sci. Technol. Engin.* 20 (15), 6011–6017. doi:10.3969/j.issn.1671-1815.2020.15.018
- Jiu, K., Ding, W., Huang, W., You, S., Zhang, Y., and Zeng, W. (2013). Simulation of paleotectonic stress fields within Paleogene shale reservoirs and prediction of favorable zones for fracture development within the Zhanhua Depression, Bohai Bay Basin, east China. *J. Pet. Sci. Eng.* 110, 119–131. doi:10.1016/j.petrol.2013.09.002
- Kong, F., and Lin, H. (2000). Characteristics of buried hill reservoirs in Chengdao area. *J. Chengdu Inst. Technol.* 27 (2), 116–122. doi:10.3969/j.issn.1671-9727.2000.02.002
- Li, L., and Dai, J. (2000). Numerical simulation of tectonic stress field and fracture distribution of Mesozoic and Paleozoic erathem in Chengdao area. *J. UnivPet. China (Ed. Nat. Sci.)* 24 (1), 6–9. doi:10.3321/j.issn:1000-5870.2000.01.002
- Li, P., Zhang, S., Wang, Y., and Ma, L. (2004). Study on the Genesis and reservoir formation of diversified buried hills in fault basin taking Jiyang Depression as an example. *J. Pet.* 25 (3), 29–31. doi:10.3321/j.issn:0253-2697.2004.03.005
- Li, S., Xianzhi, C., Guangzeng, W., Zhaoxia, J., Wang, P., Gang, W., et al. (2019). Meso-Cenozoic tectonic evolution and plate reconstruction of the Pacific Plate. *J. Geomech.* 25 (5), 642–677. doi:10.10290/j.issn.1006-6616.2019.25.05.060
- Li, W., Wu, Z., and Zhao, W. (2010). Yanshanian tectonic characteristics and basin transformation in Bohai Bay basin area. *Prog. Geophys.* 25 (6), 2068–2077. doi:10.3969/j.issn.1004-2903.2010.06.024
- Li, Y. (2008). Hydrocarbon enrichment regularity and exploration of buried hill in Bohai Bay Basin. *J. Mar. Geol. Dyn.* 24 (3), 1–7. doi:10.3969/j.issn.1009-2722.2008.03.001
- Li, Z., Dong, S., and Qu, H. (2014). Sedimentary evidences of jurassic orogenic process and key time limit on the northern margin of North China craton. *J. Jilin University: Earth Sci. Ed.* 5, 1553–1574. doi:10.13278/j.cnki.jjuese.201405113
- Liu, Y., and Wu, Z. (2019). Cenozoic fault system and tectonic framework of Chengbei Sag and its adjacent areas, Bohai Bay Basin. *Geotect. Metallogenia* 43 (6), 1133–1143. doi:10.11817/j.issn.1672-7207.2022.03.029
- Ma, L., Wang, Y., Jing, A., Yang, G., Wu, Y., and Zhao, M. (2018). Palaeogene structural style and its reservoir control in the beach area of Jiyang Depression. *Oil Gas. Geol. Recov.* 25 (1), 1–5. doi:10.13673/j.cnki.cn37-1359/te.2018.01.001
- Mao, L., Tian, J., Wang, L., Zhang, C., Zhang, W., Tian, R., et al. (2019). Initiation and origin of dextral deformation at mid-eocene in the Western Bohai Bay Basin, east China. *J. Asian Earth Sci.* 185, 104031. doi:10.1016/j.jseas.2019.104031
- Qi, J. (2004). Two tectonic systems in the Cenozoic Bohai Bay basin and their genetic interpretation. *Geol. China* 31 (1), 15–22. doi:10.3969/j.issn.1000-3657.2004.01.002
- Qiu, Y., Wand, Y., and Liu, W. (2010). Study on internal structure and migration in fault zones. *Pet. Geol. Recov. Eff.* 17 (4), 1–3. doi:10.3969/j.issn.1009-9603.2010.04.001
- Shi, X. (2021). Study on characteristics and sealing of buried hill faults in Chengdao area, Jiyang Depression. *Complex Hydrocarb. Reserv.* 14 (3), 1–7. doi:10.16181/j.cnki.fzyqc.2021.03.001
- Wang, Y., Wang, Y., and Zhao, X. (2004). The influence of tectonic evolution of Jiyang Depression on the formation of fault block buried hill and hydrocarbon reservoir. *Mineral. Rock* 24 (2), 73–77. doi:10.19719/j.cnki.1001-6872.2004.02.015
- Wei, Z., Zhang, L., Shuai, Q., Yi, H., Qian, X., Lei, Z., et al. (2018). Application of balanced cross section technique to the study of tectonic evolution of Western Taiwan Strait Basin. *Mar. Geol. Quater. Geol.* 38 (5), 193–201. doi:10.16562/j.cnki.0256-1492.2018.05.019
- Xie, Z. K. (2011). Sequence boundaries and regularities in the oil-gas distribution of the low swelling slope belt in the continental rift basin. *Min. Sci. Technol. (China)* 21 (3), 419–425. doi:10.1016/j.mstc.2011.05.011
- Xie, Z., Wang, Z., Ming, Y., Wang, M., Zhang, Z., Yang, B., et al. (2021). Cenozoic fault system in the southern East Chengdao low rise of Bohai Sea area and its control on oil and gas distribution. *Earth Sci. Front.* 28 (5), 413–420. doi:10.13745/j.esf.sf.2021.1.62
- Xin, Y., Liu, H., Ma, L., and Tian, W. (2021). The controlling factors of oil and gas differential accumulation in Chengdao buried hill. *Geol. Rev.* 67 (S1), 235–236. doi:10.16509/j.georeview.2019.s1.087
- Yang, F., Zhou, Z., and Liao, Y. (2001). Hydrocarbon migration and accumulation system analysis for Chengdao complicated oilfield. *J. Tongji Univ. Nat. Sci. Ed.* 29 (07), 838–844. doi:10.3321/j.issn:0253-374X.2001.07.016
- Yang, M. (2008). Comparative analysis of buried hill diversity and reservoir forming elements in Bohai Bay Basin. *Pet. Nat. Gas. Geol.* 29 (5), 621–631. doi:10.3321/j.issn:0253-9985.2008.05.011
- Zhang, G., Huang, J., Lu, X., Wang, Z., and Shi, Z. (2022). Ordovician limestone boundary structural factor analysis in Qipanjiang Minefield. *Zhuozishan Coal. based Tect. Phys. Simul. Exp.* 34 (2), 10–18. doi:10.3969/j.issn.1674-1803.2022.02.03
- Zhang, M., Fu, J., and Yin, X. (2006). Characteristics of strike slip and compression structures in Zhuanghai area. *Oil Gas. Geol. Recov. Fact.* 13 (02), 5–8. doi:10.3969/j.issn.1009-9603.2006.02.002
- Zhang, X., Wu, Z., Zhou, X., Niu, C., Li, W., Ren, J., et al. (2017). Cenozoic tectonic characteristics and evolution of the southern Bohai sea. *Geotect. Metallogenia* 41 (1), 50–60. doi:10.16539/j.ddgzyckx.2017.01.004
- Zhang, X. (2006). Structural style of pre-Tertiary buried hill in Zhuanghai area of Jiyang depression. *Oil Gas. Geol. Recov.* 13 (4), 12–14. doi:10.3969/j.issn.1009-9603.2006.04.004
- Zhang, Y., and Dong, S. (2008). Mesozoic tectonic evolution history of the Tan—Lu fault zone, China: Advances and new understanding. *Geol. Bull. China* 27 (9), 1371–1390. doi:10.3969/j.issn.1671-2552.2008.09.002
- Zhang, Y., Dong, S., Zhao, Y., and Zhang, T. (2007). Jurassic tectonics of North China: A synthetic view. *Acta Geol. Sin.* 81 (11), 1462–1480. doi:10.3321/j.issn:1000-9515.2008.02.010
- Zhou, X. (2006). Major transformation and thinning of subcontinental lithosphere beneath eastern China in the cenozoic—mesozoic: Review and prospect. *Earth Sci. Front.* 2 (13), 50–64. doi:10.3321/j.issn:1005-2321.2006.02.004
- Zhu, R., and Xu, Y. (2019). The subduction of the west Pacific plate and the destruction of the North China Craton. *Sci. China Earth Sci.* 62, 1340–1350. doi:10.1007/s11430-018-9356-y



OPEN ACCESS

EDITED BY

Shuping Chen,
China University of Petroleum, China

REVIEWED BY

Jingshou Liu,
China University of Geosciences Wuhan,
China

Li Wei,
China University of Petroleum, China

*CORRESPONDENCE

Lunyan Wei,
✉ weilunyan@pku.edu.cn

SPECIALTY SECTION

This article was submitted to
Structural Geology and Tectonics,
a section of the journal
Frontiers in Earth Science

RECEIVED 10 November 2022

ACCEPTED 08 February 2023

PUBLISHED 23 February 2023

CITATION

Wei L, Huang S, Luo C, Duan Y, Xia J,
Zhong Z, Li X and Chang H (2023),
Reconstruction of the proto-type basin
and tectono-paleogeographical evolution of
Tarim in the Cenozoic.
Front. Earth Sci. 11:1095002.
doi: 10.3389/feart.2023.1095002

COPYRIGHT

© 2023 Wei, Huang, Luo, Duan, Xia,
Zhong, Li and Chang. This is an open-
access article distributed under the terms
of the [Creative Commons Attribution
License \(CC BY\)](#). The use, distribution or
reproduction in other forums is
permitted, provided the original author(s)
and the copyright owner(s) are credited
and that the original publication in this
journal is cited, in accordance with
accepted academic practice. No use,
distribution or reproduction is permitted
which does not comply with these terms.

Reconstruction of the proto-type basin and tectono-paleogeographical evolution of Tarim in the Cenozoic

Lunyan Wei^{1*}, Shaoying Huang², Caiming Luo², Yunjiang Duan²,
Jinkai Xia¹, Ziqi Zhong¹, Xiang Li¹ and Haining Chang¹

¹The Key Laboratory of Orogenic Belts and Crustal Evolution, Ministry of Education, School of Earth and Space Sciences, Peking University, Beijing, China, ²Institute of Petroleum Exploration and Development, Tarim Oilfield Company, Korla, China

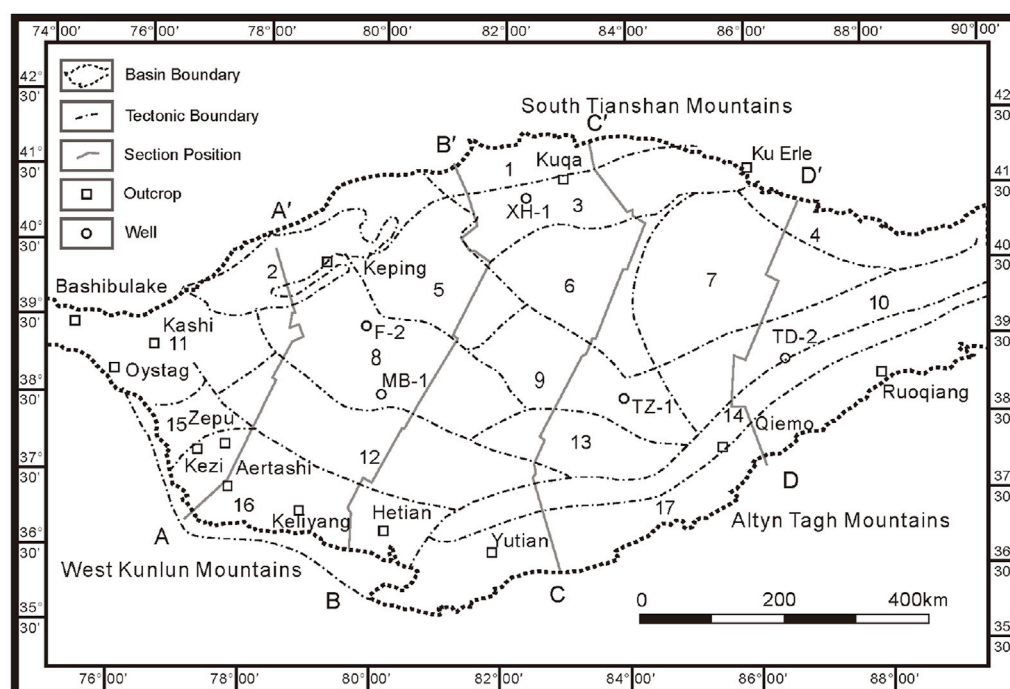
The Tarim Basin is the largest sedimentary basin in China, and it has experienced a complex tectonic evolutionary history. Reconstruction of the proto-type basin and tectono-paleogeography is helpful to understand the different stages of evolution of the sedimentary basin and basin-mountain relationship. It is significant to combine the basin with the regional tectonic background to discuss the process of basin-mountain coupling and the tectonic evolution of the peripheral orogenic belts. With a reliable residual thickness map and lithofacies map of the Tarim Basin in the Cenozoic, based on the amount of shortening we quantified from previous works and 81 balanced cross-sections, we restored the original range and compiled the proto-type basin map of Tarim Basin. From a compilation of previous studies on the lithofacies of peripheral blocks, the tectono-paleogeography of the Tarim Basin in Cenozoic has been reconstructed. The Indian Plate collided with the Eurasian continent at ~45–40 Ma. The remote effect of the collision led to the resurrection and reactivation of the Kunlun and Tianshan Mountains. The Southwest Tarim and Kuqa rejuvenated foreland basins separately developed along the north front of the Kunlun Mountains and the south front of the Tianshan Mountains. The tectonic evolution process of the Tarim Basin in the Cenozoic was divided into two stages: 1) in the Paleogene, the Neo-Tethys Ocean retreated stepwise westward from the Southwest of the Tarim Basin, and the sedimentary lithofacies of the Southwest Tarim Depression were bay lagoon facies and lake facies; 2) the Neo-Tethys Ocean retreat finally occurred in the Tarim Basin during the Late Oligocene to Early Miocene, and it became an almost closed terrestrial basin, with the deposition of fluvial facies and lacustrine facies. The Cenozoic tectono-paleogeography of the Tarim Basin is closely related to the closure of the Neo-Tethys Ocean and the reactivation of the Kunlun and Tianshan Mountains.

KEYWORDS

Tarim Basin, Cenozoic, proto-type basin, tectono-paleogeographic evolution, basin-mountain

1 Introduction

The Tarim Basin is the largest intracratonic basin in China and covers an area of 560,000 km². Source rocks for oil and gas were deposited widely in the Tarim Basin during different geological periods, including the Paleogene, and excellent oil and gas can usually be found in its marine rocks. The Tarim Basin is a natural laboratory with unique geological and geomorphological units, and can be divided into seventeen



1-Kuqa Depression; 2-Kepingtage Faulted-uplift; 3-Tabei Uplift; 4-Kongquehe Slope; 5-Awati Depression; 6-Shuntuoguole Uplift; 7-Manjiaer Depression; 8-Bachu Uplift; 9-Tazhong Uplift; 10-Guchengxu Uplift; 11-Kashi Depression; 12-Maigaiti Slope; 13-Tangguzibas Depression; 14-Tanan Uplift; 15-Shache Bulge; 16-Yecheng Depression; 17-Southeast Depression

FIGURE 1

Schematic structural map of the Tarim Basin (modified after He et al., 2016; Laborde et al., 2019).

tectonic units in the Cenozoic (Dong et al., 2016; He et al., 2016) (Figure 1). Geographically bounded by the Western Kunlun Mountains, the Altyn Tagh mountain belt, and the Tianshan Mountains, the Tarim Basin has experienced a complicated tectonic history (Allen et al., 1993; Zhang et al., 2011; He et al., 2016; Laborde et al., 2019) (Figure 1).

In the early Cenozoic, the India-Asia collision caused large-scale intra-continental deformations (Liu et al., 2009; Fang et al., 2020). Under the far-field effect of the collision, a prominent tectonic salient formed on the Pamir plateau and the Pamir Salient experienced some northward translation (Lin et al., 2019; Li Y. P. et al., 2020). A major reactivation of the Western Kunlun Range occurred during the Cenozoic in response to the India-Asia collision (Tapponnier and Molnar, 1977; Laborde et al., 2019). A major reactivation of the Tian Shan also occurred during the Cenozoic in response to the India-Asia collision and this reactivation seems to have been initiated in the Oligocene with subsequent Miocene accelerations, which is supported by evidence including sediment provenance and growth strata (Izquierdo-Llavall et al., 2018; Li et al., 2019). The Altyn Tagh Range was also reactivated during the Cenozoic due to the India-Asia collision and this reactivation seems to have been initiated in the Eocene with subsequent Oligocene to Miocene accelerations (Cheng et al., 2015; Zhao et al., 2016). The maximum principal stress

direction in different areas of the Tarim Basin is diverse. In the north of the Tarim Basin, the maximum principal stress direction is mainly N-S and NNW-SSE (Huang et al., 2013). In the southwest, the maximum principal stress direction is mainly NE-SW; and in the southeast, the maximum principal stress direction is mainly NW-SE (Wang et al., 2007).

A schematic structural map and seismic cross-sections was constructed to document the Cenozoic deformation through the Tarim area (Figures 1, 2). In the Cenozoic, the Tarim Basin was in a stage of strong compression, and the continuous collision around the Tarim Block accommodated a large amount of Cenozoic compressive deformation (Li et al., 2007; Laborde et al., 2019). Ancient orogens around the Tarim Basin were rejuvenated, and a thick (up to ~10 km) and continuous Cenozoic sedimentary series, mainly supplied by the erosion of the surrounding mountain ranges (Wei et al., 2000; Jia, 2009; He et al., 2013), formed the rejuvenated foreland basin in Kuqa and Southwest Tarim (Laborde et al., 2019) and the complex fault system in Bachu Uplift (Ning et al., 2021; Zhang et al., 2021) (Figure 2). In the case of the Western Kunlun and Southwestern Tian Shan compressive systems, these foothills mainly formed the Basin-Mountain system at the edge of the Tarim Basin (Figure 2). Wide (from ~50 to ~150 km) and long (100 s of km) uplifts, such as the Bachu uplift, are visible to the west of the basin (Figure 2).

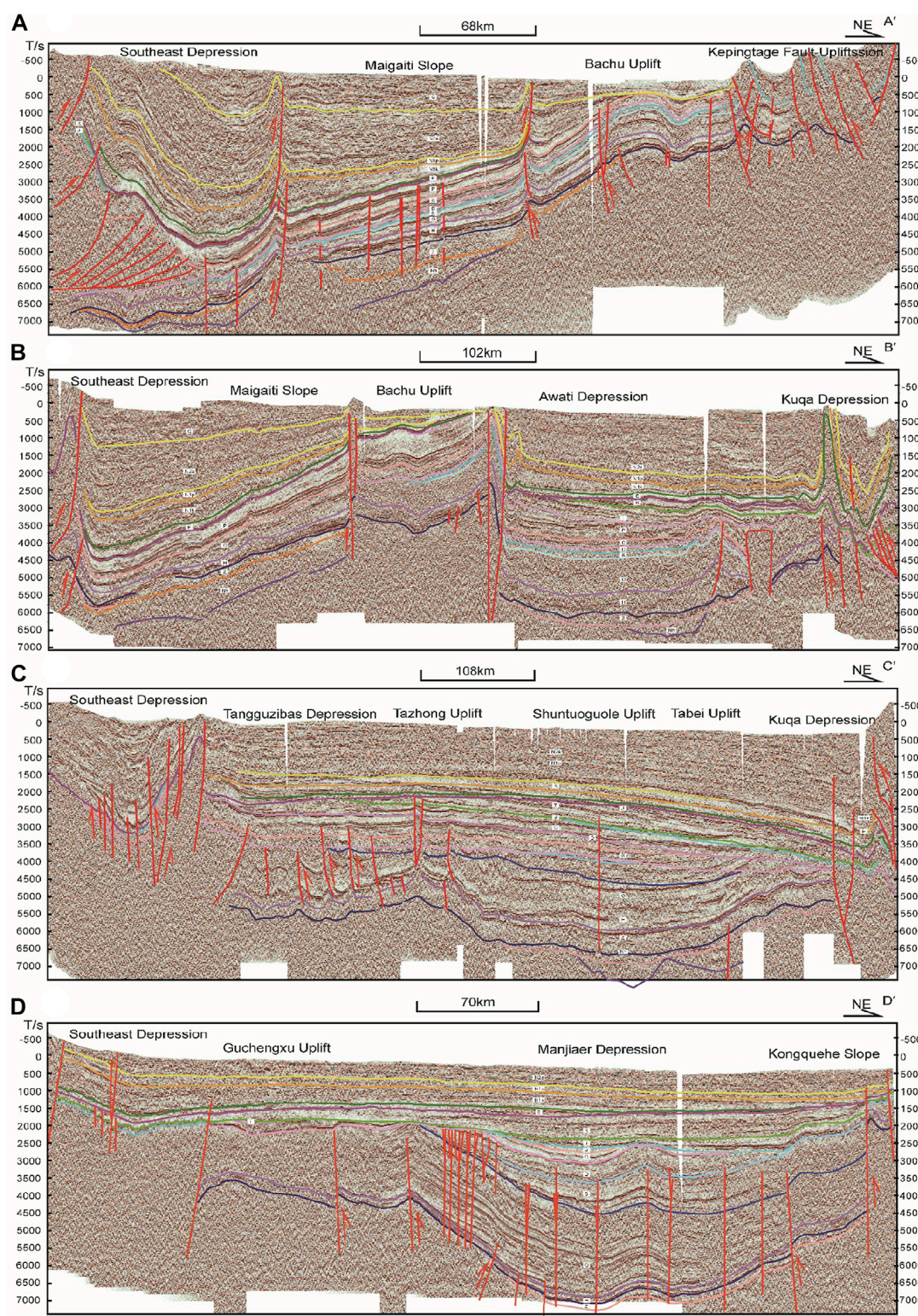


FIGURE 2

Four seismic cross-sections of the Tarim Basin (see Figure 1 for locations).

The far-field effect caused the reactivation of the Paleozoic and Mesozoic tectonic belts, changing the sea-land configuration in eastern Asia (Tapponnier et al., 1981; Wang et al., 2014; Lin

et al., 2019; Li Y. P. et al., 2020). The Neo-Tethys Ocean retreated from Western Tarim in response to a combination of eustatic sea-level lowering, plate tectonics, and the autocyclic

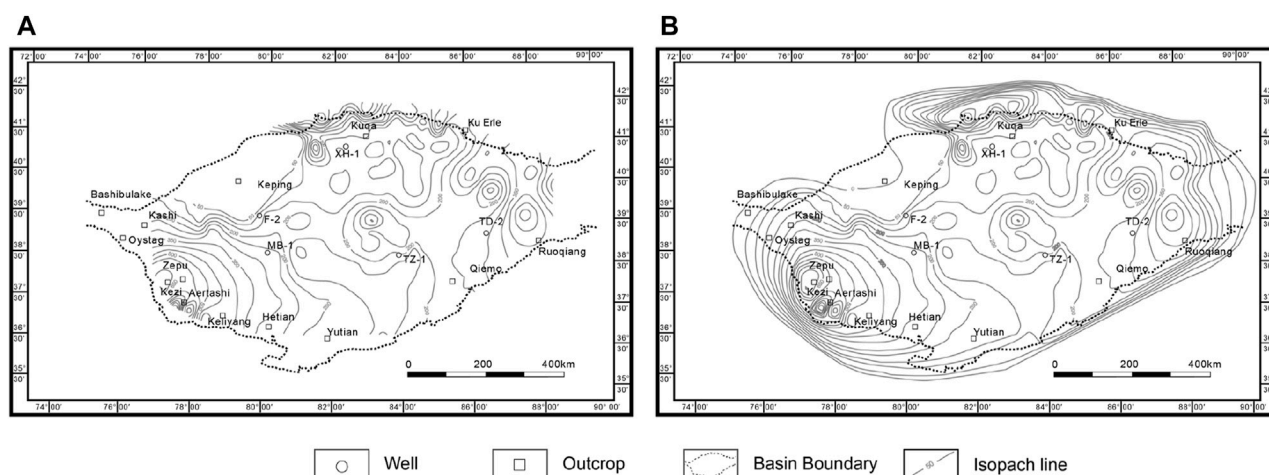


FIGURE 3

Schematic diagrams showing the steps of restoring the original thickness map, taking the late Paleogene restoration as an example. **(A)**: The residual thickness map of residual basin; **(B)** the pre-shortening original thickness map of the residual basin; thickness map contours show the depth (m) of the Upper Eocene to Oligocene in the Tarim Basin.

sedimentary infilling of the basin (Bosboom et al., 2011; Bosboom et al., 2014). At least five different seawater transgression-regression cycles occurred and the sea retreated from different parts of the Tarim Basin (Sun and Jiang, 2013; Bosboom et al., 2014; Sun et al., 2016a). The last regression marking the Tarim Basin generated a huge transformation from marine facies to terrestrial facies.

As a result of the collision of the Indian Plate and the Eurasian continent, the Tarim Block has different types of sedimentary facies from different stages of the Cenozoic. There are two issues to be addressed in this study: the tectono-paleogeographic evolution of the Tarim Basin and the tectonic interrelationships between the basin and the orogenic belts during the different stages. There are some studies that have mapped the lithofacies paleogeography of the Tarim Basin; however, several studies considered the whole basin and its periphery, and few compiled the proto-type basin by considering the India-Asia collision and the huge shortening of the basin. In this study, we restored the proto-type basin of the Tarim Basin and reconstructed the Tectono-paleogeographic evolution around the Tarim Basin in the Cenozoic, analyzing the changes of the paleo-geographical environment and Cenozoic deformation of the Tarim Basin and its periphery. When and how the retreat of the Neo-Tethys Ocean occurred were specially considered to reconstruct the proto-type basin and tectono-paleogeography of the Tarim Basin and its periphery.

2 Methodology and database

Guided by three steps of map compilation, we reconstructed the proto-type basin and tectono-paleogeography of the Tarim Basin and its periphery in the Cenozoic.

First, we restored the original thickness map (Figure 3). Based on the analysis of wells and outcrops in the

whole basin, the lithofacies-paleographic maps in the range of the present basin were reliable. If there were border facies in the basin, they could be used to help delineate the scope of the basin. If there were none, to recover the denudation area, it was necessary to reconstruct the original thickness map based on the Cenozoic residual thickness map with thickness trend analysis (Figure 3). For an intracratonic basin, the thickness line needed to be concentric and closed. While for the foreland basin, the thickness line needed to be asymmetrical and the distance of each thickness line outside the basin at one-half of the inside. Therefore, the scope of the foreland basin was relatively narrow, and the terrane was near the Tarim Block.

Second, we restored the range of the proto-type basin, which meant restoring it to what it was before shortening or extension. The balanced cross-section method (Lou et al., 2016; Laborde et al., 2019) is one of the most practical ways to obtain the proto-type basin boundary. Based on previous balanced sections (Laborde et al., 2019), 71 balanced sections provided by Tarim Oilfield, and 10 balanced sections restored by us (Figure 4), we quantified the shortening and reconstructed the boundary of the pre-shortening proto-type basin.

Third, we restored the tectonic configuration of the Tarim Block and its adjacent plates during the development of the proto-type basin. After clarifying the sedimentation and deformation of the Tarim Basin, it was essential to clarify the peripheral margin of the Tarim Basin and the tectonic relationship between the Tarim Basin and its surrounding plates. To compile the proto-type basin maps and the tectono-paleogeographic maps, it was essential to figure out the answers to some questions: 1) the lithofacies distribution of the Tarim Basin in the Paleogene and Neogene (Guan and Guan, 2002; Shao et al., 2006; Yue et al., 2017; Ma CM. et al., 2020); 2) the paleogeographic distribution in its adjacent plates (Wang, et al., 2019; Ma T. et al., 2020; Song et al., 2022); 3) the sea retreat process of Neo-Tethys and its effect on the Tarim Basin (Bosboom et al., 2011; Bosboom, 2013; Sun and Jiang, 2013; Bosboom et al., 2014; Sun et al., 2016b; Li Q. et al., 2020; Sun et al., 2021).

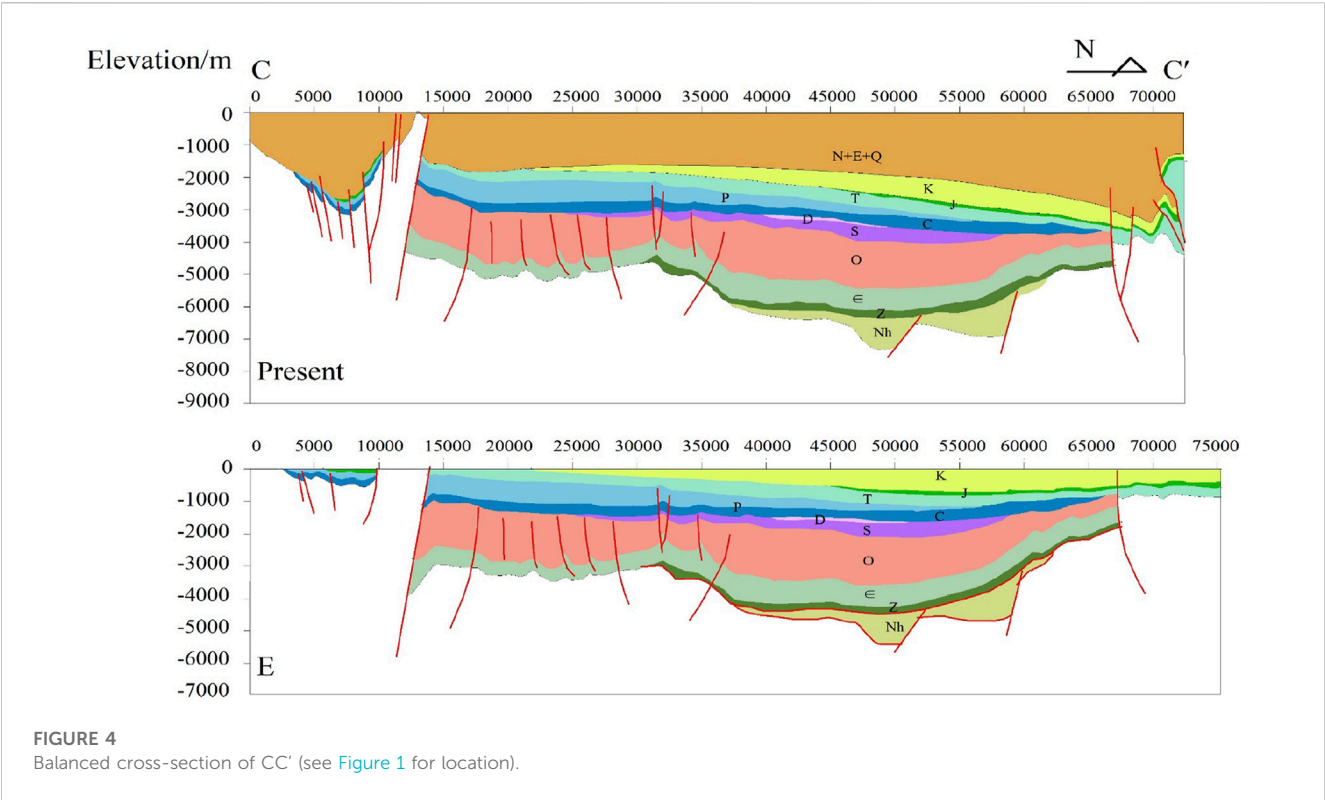


TABLE 1 Cenozoic stratum in the Tarim Basin (Ding et al., 1993; 2011; Guo, 1994; Jia et al., 2004; Shao et al., 2006; Li et al., 2017).

Strata		Southwest Tarim		North Tarim		Southeast Tarim
Quaternary	Lower Pleistocene	Xiyu		Xiyu		Xiyu
Neogene	Pliocene	Atushi		Kuche		Kuche
	Miocene	Wuqia	Pakabulake	Kangcun		Kangcun
			Anjuan	Jidike		Jidike
			Keziluoyi	Suweiyi		Suweiyi
Paleogene	Oligocene	Kashi	Bashibulake	Kulugeliemu	Awate	Kulugeliemu
	Eocene		Zhuoyoulegansu		Xiaokuzibai	
			Wulagen			
			Kalatar			
			Gaijitage			
			Qimugen			
	Paleocene		Aertashi			
		Tuyiluoke			Talak	

Based on previously published data (Laborde et al., 2019) and our new data, we obtained the proto-type basin maps and the tectono-paleogeographic maps in the Cenozoic. It is noteworthy that the biggest difference between the proto-type basin map and the tectono-paleogeographic map is the latter includes larger geographical range, which provides more information with the tectonic configuration of the Tarim Basin and its adjacent plates.

3 Analysis

Before compiling proto-type basin maps, we clarified three issues: firstly, the division of the evolution stages in the Cenozoic; secondly, the marine sedimentation problem of the Tarim Basin in the Cenozoic; and thirdly, the quantified shortening amount of the Tarim Basin.

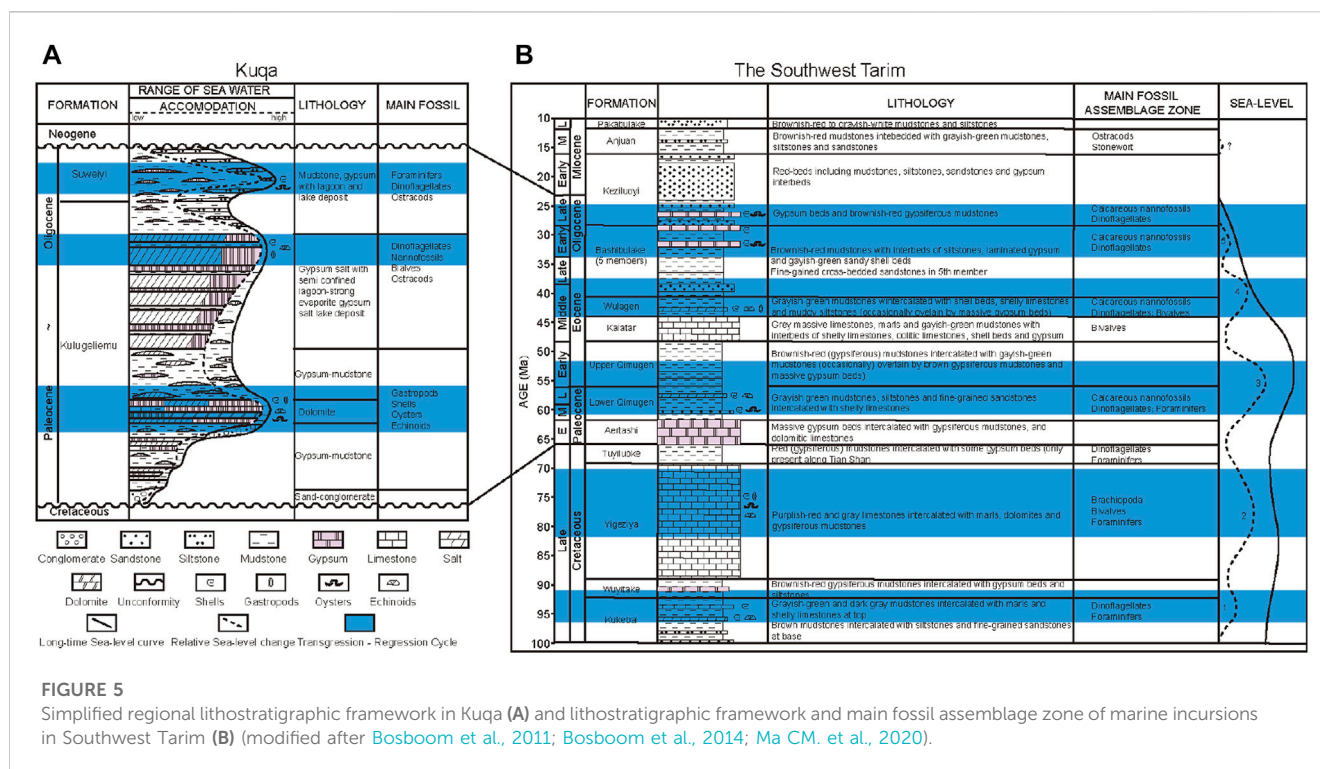


FIGURE 5

Simplified regional lithostratigraphic framework in Kuqa (A) and lithostratigraphic framework and main fossil assemblage zone of marine incursions in Southwest Tarim (B) (modified after Bosboom et al., 2011; Bosboom et al., 2014; Ma CM. et al., 2020).

3.1 Division of the evolution stages in the Cenozoic

The strata of the Cenozoic Tarim Basin were mainly exposed around the basin, and most of the basin was covered by desert. According to the sedimentary characteristics of Cenozoic strata in the basin, the Tarim Basin could be divided into three regions: Southwest Tarim, North Tarim, and Southeast Tarim (Table 1). Although there were different division schemes for Cenozoic stratigraphic subdivision in this area, in this study, the evolution stages in the Cenozoic were based on the stratigraphic subdivision unified as follows (Table 1).

In Southwest Tarim, the Paleogene strata included the Bashibulake Formation, Zhuoyoulegansu Formation, Wulagen Formation, Kalatar Formation, Gajitage Formation, Qimugen Formation, and Aertashi Formation in the Kashi Group; the Neogene strata included the Pakabulake Formation, Anjuan Formation, Keziluoyi Formation in the Wuqia Group and the Atushi Formation (Table 1). In North Tarim, the Paleogene strata included the Awate Formation, Xiaokuzibai Formation, and Talak Formation in the Kulugeliemu Group; the Neogene strata included the Kuche Formation, Kangcun Formation, Jidike Formation, and Suweiyi Formation (Table 1). In Southeast Tarim, the Paleogene strata included the Kulugeliemu Group; the Neogene strata included the Kuche Formation, Kangcun Formation, Jidike Formation, and Suweiyi Formation (Table 1).

Since the Paleogene, the tectonic compression caused the uplift of the surrounding mountains around the Tarim Basin, while the basin itself was relatively stable (Wang et al., 2014;

Laborde et al., 2019; Li Y. P. et al., 2020). During the Neogene, with the uplift of the Qinghai - Tibet Plateau, there are long-term growth and erosion in the mountain ranges and caused progressive thrusting over the Tarim basin (Jolivet et al., 2010; Wang et al., 2014; Laborde et al., 2019). Since the Quaternary, the Tarim Basin was surrounded by high mountains, progressively soil drying and forming China's largest inland water system and the largest desert.

3.2 Marine sedimentation problem of the Tarim Basin in the Cenozoic

According to the long-term eustatic trend of the Tarim Basin, there were at least five episodes of marine incursion in the Tarim Basin from the Cretaceous to the Paleogene (Figure 5), which are supported by Cretaceous-Paleogene sedimentary records (Bosboom et al., 2011; Bosboom, 2013; Bosboom et al., 2014; Li et al., 2017; Zhang et al., 2018). There are reliable pieces of evidence to restrict the time of the fourth and fifth incursions and the sea retreat to the Cenozoic (Bosboom et al., 2011; Bosboom et al., 2014; Zhang et al., 2018) (Figure 5).

The palaeomagnetic chronology and paleoenvironmental records of Cenozoic sections indicate that the fourth sea retreat from Aertashi occurred at ~41 Ma (Bosboom et al., 2014). Research on marine-terrestrial sediments at Oytay in the Early Cenozoic also suggests that the sea retreat from the Tarim Basin may have been diachronous (Sun and Jiang, 2013). The sea retreat from Oytay occurred in the Early Eocene at ~47 Ma and from Keliyang at ~45 Ma (Sun and Jiang, 2013; Sun et al., 2016a); the ~45 Ma peak in detrital zircon U/Pb was considered as an indication of a new sedimentary source (Wang et al., 2021).

Pieces of evidence, including the palaeomagnetic chronology and paleoenvironmental records, also restricted the fifth sea retreat occurring from Kuqa, Kezi, and Bashibulake to ~37 Ma and ~33–25 Ma (Bosboom et al., 2014) (Figure 5). In the Pamir-Tianshan convergence zone, the successions changed from marine deposits in the lower, continental clay, fine sand in the middle, and molasse in the upper part, recording the climate changes and evolution of the sea retreat (Wang et al., 2014). Small-scale sea incursions still occurred when the Neo-Tethys Ocean retreat occupied the Tarim Basin, which is supported by the sulfur isotope of gypsums or anhydrites in Kuqa ($\delta^{34}\text{S}$ from 11.6‰ to 15.9‰ in the Middle Paleocene, from 12.7‰ to 15.9‰ in the Late Eocene) (Zhang et al., 2013). Particle size analysis of the Suweiyi Formation sediments of the Southwest Tarim Depression indicated the sand was similar to near-shore sedimentary environments including lagoons and shallow lake facies (Tang et al., 2014). The lakes in the Jidike Formation were generally broad and shallow, and the lake shoreline was in response to both climate change and tectonic activities (Ma CM. et al., 2020).

Marine and lagoon deposits with fossils were recognized from southwest to the north, which was more than a thousand of kilometers by the outcrop and wells of the Miocene formations of the northern Tarim Basin (Guo et al., 2002). There were thin gypsum interbeds of marine strata in the Late Oligocene Suweiyi Formation in the Kuqa and Late Oligocene Keziluoyi Formation reserved in Southwest Tarim (Guo et al., 2002; Ma T. et al., 2020) (Figure 5). These fossils, including Foraminifer, Dinoflagellates, Ostracods, and Calcareous nannofossils, would seem to suggest that the range of seawater influence in the Early Miocene included two main areas, Kuqa and Southwest Tarim (Figure 5B). The high saline concentration of saltwater deposits with Foraminifer and Ostracods identified in Kuqa and Southwest Tarim showed that two lagoon bays in the western Tarim Basin were linked to the residual sea in the Late Oligocene or even until the early Miocene (Guo et al., 2002). However, from the Late Miocene to the Pliocene, the marine or lagoon environments vanished completely, and lake and freshwater deposits with Stonewort were common in the Tarim Basin (Guo et al., 2002) (Figure 5B).

The final time of the retreat of the Neo-Tethys Ocean from the Tarim Basin remains controversial. Some believe it was in the Early Oligocene (Bosboom et al., 2011; Sun and Jiang, 2013; Sun et al., 2016b), while others believe it occurred in the Late Miocene (Guo et al., 2002). Re-evaluating the fossil evidence and sedimentary facies (Figure 5), it was concluded that the final sea retreat occurred at 37–25 Ma, and the lagoon environments in the southwest and northwest of the Tarim Basin linked to the Neo-Tethys Ocean during the Late Oligocene. Taken together, these studies supported the notion that, as suggested by the presence of marine fossils and gypsum deposits, stepwise and diachronous sea retreat from the southwestern and northwestern margins of the Tarim Basin occurred in the late Oligocene—early Miocene.

3.3 Shortening amount of the Tarim Basin

The tectonic configuration of the Tarim Basin and its adjacent plates played an important role in the

reconstruction of the proto-type basin because the compressive component of Cenozoic deformation controlled the basin (Wei et al., 2000; Li et al., 2007; Li Y. P. et al., 2020), with up to ~66.7% of compressive deformation accommodated in the Cenozoic orogeny (Laborde et al., 2019). Previous studies have explored the quantified compressive component (Li et al., 2007; Laborde et al., 2019). A regional-scale balanced cross-section constructed on Southwest Tarim—Kuqa including foreland fold-thrust showed a 64% shortening rate for Southwest Tarim and 30.6% for Kuqa (Li et al., 2007). Detailed analysis and examination found that most of the Cenozoic compressive deformation (from ~94% to 100%) was concentrated in the mountains along the basin margins, which meant it was negligible (up to ~6%) within the Tarim Basin (Laborde et al., 2019). Therefore, it was of great importance to restore the original thickness isopaches and determine the pre-shortening tectonic configuration of the Tarim Basin.

We calculated the shortening amount of every cross-section and quantified them into four representative profiles: AA', BB', CC', and DD' (Table 2) (Figure 1). According to the quantified data, we enlarged the range of the pre-shortening original thickness map and considered the zero-thickness line as the boundary of the pre-shortening proto-type basin.

4 Reconstruction of the proto-type Tarim Basin

Due to the uplift of the mountains around the Tarim Basin in the context of the India-Asian collision, the Tarim Basin gradually became a closed continental sedimentary basin (Wang et al., 2014; Lin et al., 2019; Li Y. P. et al., 2020). The paleogeography of the Tarim Basin in the Cenozoic was also related to the evolution of the Neo-Tethys Ocean (Shao et al., 2006; Li et al., 2017; Zhang et al., 2018). The Paleogene strata in the Tarim Basin were bay lagoons and shore-shallow lake facies, and the Neogene strata were flood plain-salt lakes and fluvial-alluvial fan facies (Zhuang et al., 2002; Shao et al., 2006; Li et al., 2017; Yue et al., 2017; Wu et al., 2020). This study also mapped the proto-type basin in the Late Eocene to better understand the tectono-paleogeography evolution in the Cenozoic.

4.1 In the Late Eocene

The landform pattern of the Tarim Basin in the Paleocene was mainly characterized by uplift in the center with depressions in the north and south (Shao et al., 2006). A short-term invasion of seawater occurred in the Kuqa Depression and Southwest Tarim Depression from the Paleocene to the Late Eocene (Guo et al., 2002; Li et al., 2017; Zhang et al., 2018; Lin et al., 2019) (Figure 6), where there were marine sediments from tens to hundreds of meters thick deposited in fluvial-deltaic and shallow-water lacustrine settings (Shao et al., 2006).

The degree of seawater influence was decreasing in the Late Eocene due to the small-scale, stepwise Neo-Tethys Ocean retreat (Shao et al., 2006). When seawater came from the west, sabkha or the

TABLE 2 Shortening estimates across the Tarim Basin and its periphery.

Mountains			Shortening (km)		
			1	2	3
			Cenozoic (Laborde et al., 2019)	Paleogene	Neogene
N Tibet	W Kunlun	Transect A (A)	32	20.64	10.55
		Transect B (B)	35	(20)	(10)
		Altn Tagh	0.9		
		Transect D (D)	0.3		
S Tianshan	SW Tianshan	Transect A (A')	36	(12.6)	(11)
		Transect B(B')	4	12.00	9.13
		Transect C (C')	22	13.33	12.51
		SE Tianshan	0		

Note: Shortening in brackets are speculated.

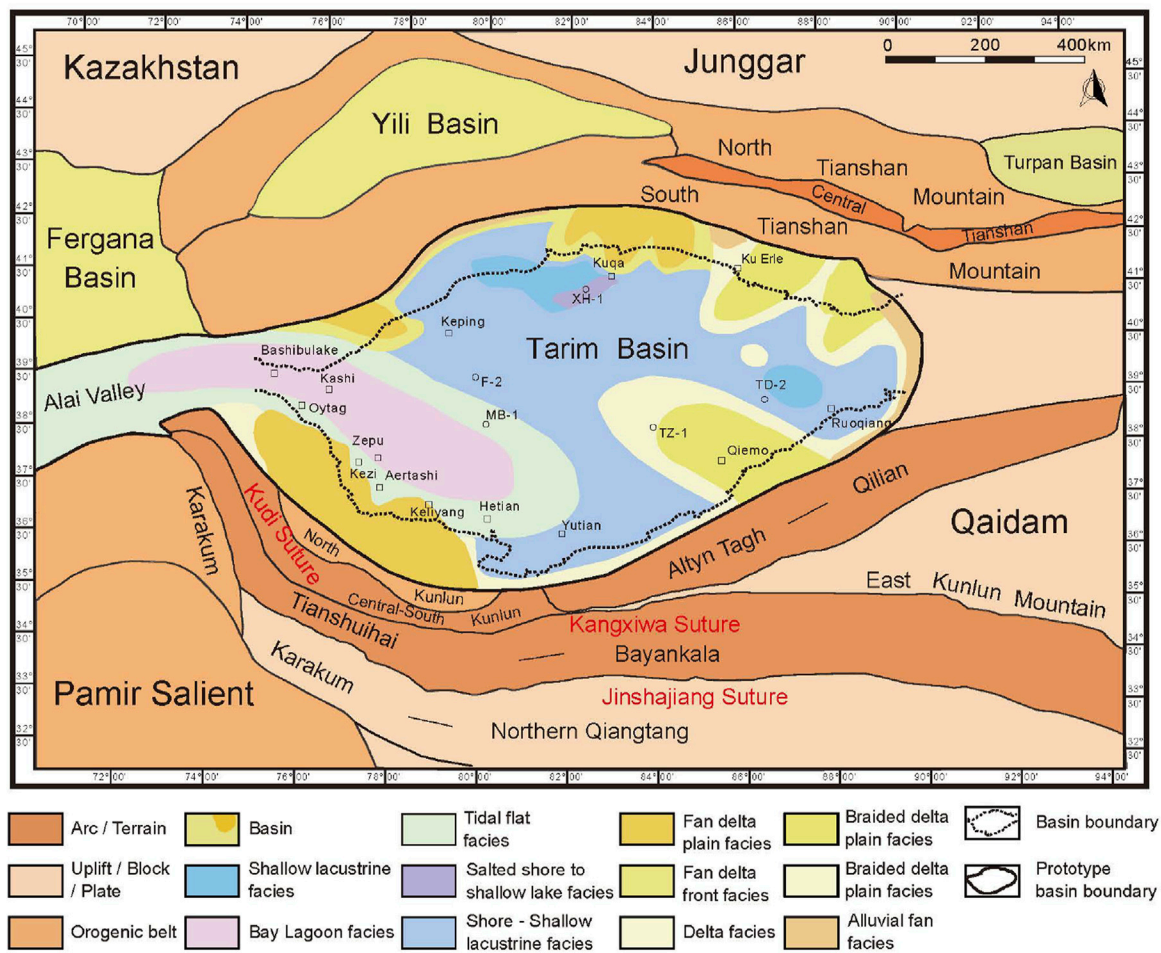


FIGURE 6
The Tarim proto-type basin and its periphery in the Late Eocene.

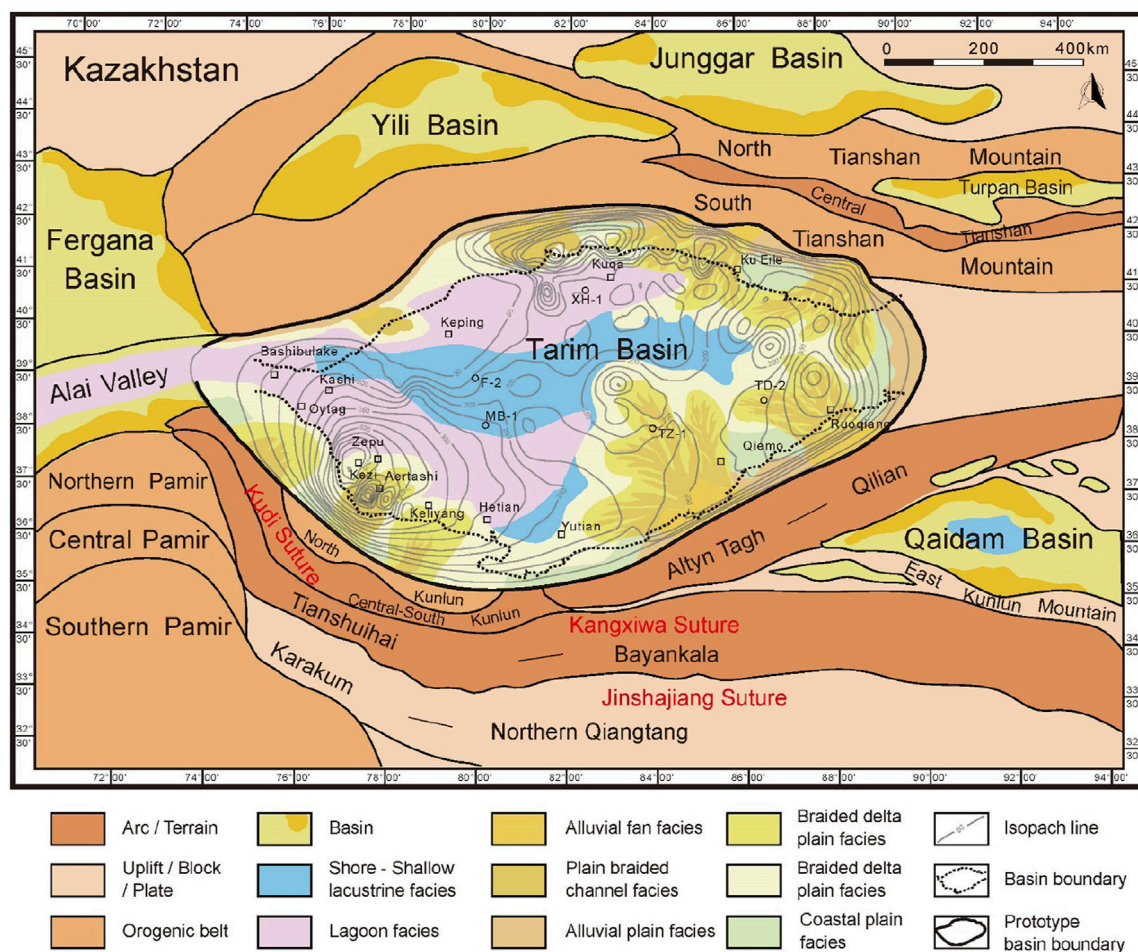


FIGURE 7

The Tarim proto-type basin and its periphery in the Late Oligocene. Thickness map contours show the depth (m) of the upper Eocene to Oligocene in the Tarim Basin.

open platform type of depositional environment was the most important sedimentary facies (Yue et al., 2017). Turning to the period of sea retreat, the basin fill was mainly composed of several typical facies, representing: bay lagoon facies and tidal facies dominated by carbonates and gypsum in the southwestern part; shore-shallow lacustrine facies dominated by sandstone, mudstone, carbonates, and gypsum in the northern part; and fluvial fan facies and fan delta facies dominated by conglomerate, sandstone, and siltstone along the basin margin (Shao et al., 2006; Li et al., 2013) (Figure 6).

The deformation and northward indentation of the Pamir Salient could have played an important role in controlling the lithofacies and sedimentary facies in the Tarim Basin. The provenance of the Cretaceous-Oligocene strata of the Southwest Tarim Depression was mainly from the Central Pamir (Sun et al., 2016a; Wang et al., 2021) (Figure 6), and the deposition center was near the West Kunlun Mountains (Shao et al., 2006). Regarding the Kuqa Depression, the provenance was mainly from the South Tianshan Mountains (He et al., 2004; Shao et al., 2006) (Figure 6), with the deposition center moving southward gradually (He et al., 2004).

4.2 In the Late Paleogene

The India-Asian collision had a remote effect on structural deformation and tectonic activity (Li et al., 2007; Jia, 2009; Laborde et al., 2019). For example, the West Kunlun reactivation was initiated in the Eocene with subsequent Oligocene to Miocene accelerations (Figures 2A, B), the Southwestern Tianshan thrust wedge was formed above a decollement level (Figures 2A–C), and the Altyn Tagh strike-slip wedge was formed above a deep decollement level (Figures 2C, D).

In order to reconstruct the proto-type basin map of the Tarim Basin and its adjacent plates, we considered the structures activated during the Cenozoic and quantified the compressive component of this deformation. To the west, about 12.5 km of crustal shortening were accommodated in the Kuqa Depression, while to the east, about 20 km of crustal shortening were accommodated in the Southwest Tarim Depression (Table 2). Then we enlarged the range of the pre-shortening proto-type basin and combined the overall tectonic background. Separating the South Tianshan Mountains and the Pamir Salient was the intervening Alai Valley. The

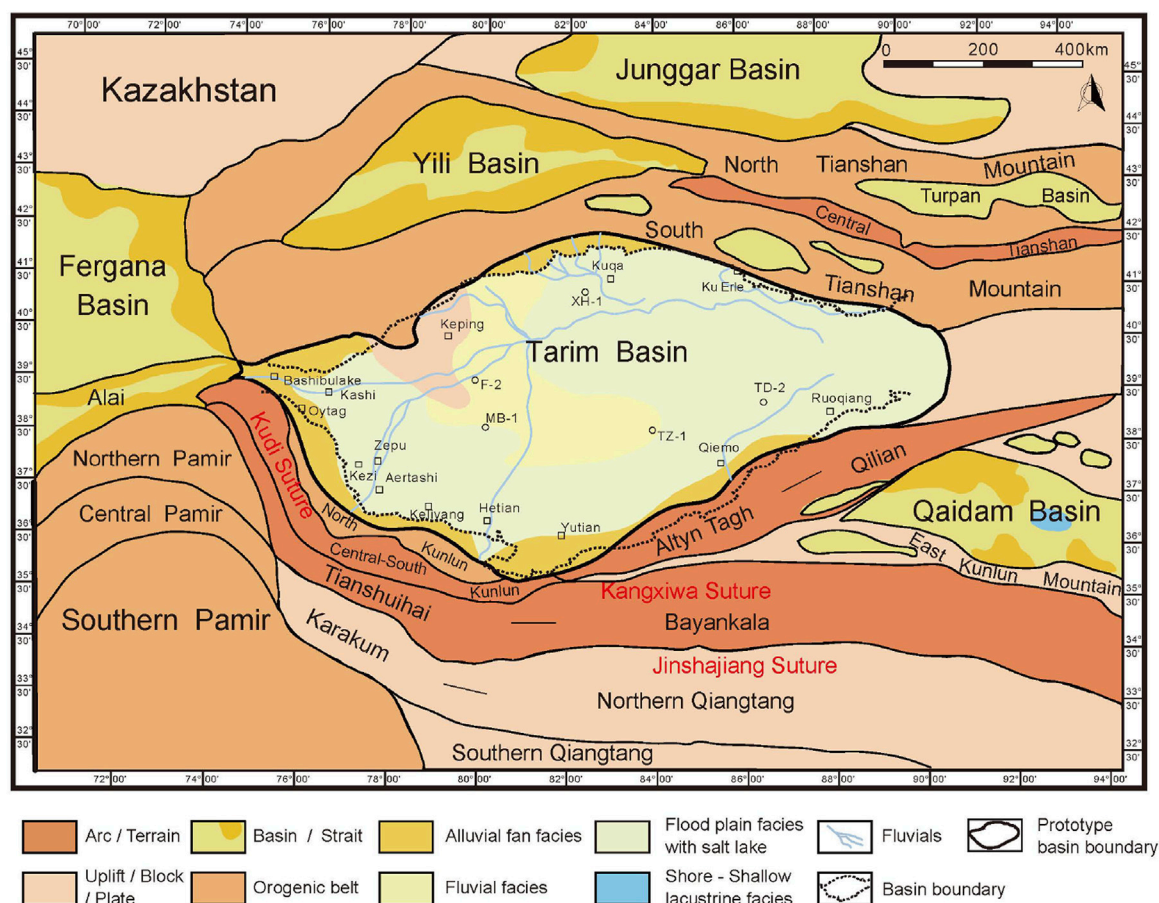


FIGURE 8

The Tarim proto-type basin and its periphery in the Late Neogene.

history of the Pamir Salient has been argued but data from new studies in the geology of Northern Pamir suggest that subsequent Cenozoic northward translation of the Pamir was interpreted to be only ~50 km and no more than ~80–100 km (Li Y. P. et al., 2020), establishing a greater degree of accuracy on the compressive component we quantified.

During the Late Eocene to Oligocene, the western part of the Tarim Basin contained an open marine, lagoon environment, with a continental environment in the eastern part (Zhang et al., 2022) (Figure 7). Eight sedimentary facies were divided in the study area, including lagoon facies, lacustrine facies, plain braided channel facies, braided delta facies, braided delta plain facies, alluvial plain facies, and alluvial fan facies, showing that the characteristics of spatial distribution in this area were from marine to continental (Figure 7). The Southwest Tarim Depression and Kuqa Depression could be identified as major deposition centers, where the maximum sediment deposition were both over eight-hundred-meters thick (He et al., 2004; Shao et al., 2006; Zhang et al., 2022). In Kuqa, the Suweiyi Formation was mainly composed of mudstones, siltstones, sandstones, and gypsum interbeds with nannofossils (Figure 5). In Southwest Tarim, mudstones with interbedded

siltstones and laminated gypsum with nannofossils occurred in the Bashibulake Formation (Figure 5), which is evidence of the depositional environment of a lagoon.

However, whether the lagoon facies developed its range in the Late Oligocene is controversial. Based on the latest lithofacies-paleogeographic map of the Tarim Basin in the Suweiyi Formation provided by Tarim Oilfield, and combined with the analysis of the Neo-Tethys Ocean retreat (Figure 5), the outside seawater was linked to the western Tarim Basin via the Alai Valley, and the range of seawater influence in the Late Oligocene included two main areas, north to Kuqa and south to Southwest Tarim (Figure 7). In Kuqa, gypsum interbeds of marine strata and marine fossils developed in the Suweiyi Formation and Jidike Formation, which provides some support that lagoon facies developed in the Late Oligocene or even early Miocene. It could be concluded that the range of lagoon facies in the Late Oligocene was larger than the Late Eocene (Figures 6, 7). In the eastern part of the Tarim Basin, a continental sedimentary system existed from the basin margins to the center, from alluvial fan to braided river delta plain and braided river delta front (Shao et al., 2006; Zhang et al., 2022) (Figure 7).

4.3 In the Late Neogene

During the Neogene, the lasting tectonic compression caused the mountains surrounding the Tarim Basin to uplift and the basin closed, and the compressive component of the Neogene deformation could also be quantified. To the west, about 11 km of crustal shortening were accommodated in the Kuqa Depression, while to the east, about 10 km of crustal shortening were accommodated in the Southwest Tarim Depression (Table 2). Then we restored the range of the pre-shortening proto-type basin and combined the overall tectonic background. Compared with the Late Paleogene, the mountains, such as the Tianshan Mountains and West Kunlun Mountains, were reactivated by the ongoing structure deformation and tectonic activity (Figures 7, 8). A northward indentation of the Pamir Salient in the Cenozoic, causing a lower amount of shortening documented along the Alai Valley, and the basins, such as the Tarim Basin and the Qaidam Basin, were considered to have undergone continuous aridification.

Compared with the proto-type basin map of the Tarim Basin and its adjacent plates in the Late Eocene and Late Oligocene, the depositional environment of the Tarim Basin significantly changed in the Oligocene–Miocene: marine facies disappeared, and continental sedimentation patterns formed (Figures 6–8). The sea retreated from the whole Tarim Basin in the Late Neocene, and the Tarim Basin gradually graded to a closed inland environment (Figure 8). The Tarim Basin contained terrestrial depositional environments, such as alluvial fan groups, deltas, and flood plain facies with salt lakes (Figure 8). There were large thick molasse units near the deposition center in the Southwest Tarim Depression and Kuqa Depression, while toward the Bachu Uplift the thickness decreased gradually (Wu et al., 2020).

In the Neogene, it was still active on the south edge of the Tianshan mountain, the deformation was influencing the northern edge of the Tarim Basin (Jolivet et al., 2010). The deposition center of the Kuqa Depression gradually moved north to south and the thickness of the sediment increased (He et al., 2004). Several tectonic stages occurred in the Pamir-Tianshan convergence zone in the Cenozoic, and alluvial deposits dominated the sequences from the early Miocene (Wang et al., 2014) (Figure 8). The reactivation event of the Bachu Uplift could be linked to the India-Asian collision, where there were thrust fault systems may related to a deep decollement within the basement below the Tarim Block (Laborde et al., 2019) (Figures 2A, B).

Based on the lithofacies-paleogeographic map of the proto-type basin and our calculations of the quantified shortening (Table 2), and combined with the regional tectonic configuration, the Tarim proto-type basin and its periphery in the Late Eocene (Figure 6), Late Oligocene (Figure 7), and Late Neogene (Figure 8) was obtained. When comparing the proto-type basin and its periphery in the Late Eocene (Figure 6) and in Late Oligocene (Figure 7), the biggest difference that could be seen was that the range of seawater influence became larger and the range of lagoon facies increased from the Southwest Tarim Depression to the Kuqa Depression (Figure 7). This variation indicated that there was still an intermittent connection between the Tarim Basin and the Neo-Tethys Ocean that occurred separately during the third, fourth, and fifth transgression-regression events in the Paleogene (Figure 5), as well as the final sea retreat which occurred at

25–30 Ma in the Late Oligocene (Figure 5) or even the early Miocene.

5 Reconstruction of the tectono-paleogeography around the Tarim Basin

To obtain the tectono-paleogeographic map around the Tarim Basin in the Cenozoic, more studies were considered, such as the configuration of the plates around the Tarim Block in Asia, the lithofacies and paleogeography of basins in the adjacent plates, especially in the central Asian plates (Wang et al., 2019; Zhang et al., 2019; Ma T. et al., 2020; Song et al., 2022), and the proto-type basin map of the Tarim Basin and its periphery in the Cenozoic we compiled (Figures 7, 8).

5.1 Continued subduction of the Indian ocean in the Late Paleogene

In the long-term paleo-geographical evolution in the Cenozoic, as the global sea levels fell, the Neo-Tethys Ocean retreat gradually occurred from the Junggar Basin and the Tarim Basin, and the Fergana Basin and the Alai Valley in southern Kyrgyzstan, and the Afghan-Tajik Basin (Bosboom et al., 2011; Carrapa et al., 2015; Li et al., 2017; Li Q. et al., 2020). In the Paleogene, the Neo-Tethys Ocean entered the western Tarim Basin via the present-day Alai Valley (Bosboom et al., 2011; Zhang et al., 2013; Bosboom et al., 2014) (Figure 9). The sea retreated westward in at least five transgressions in the west of the Tarim Basin during the Cretaceous-Cenozoic (Bosboom et al., 2011; Bosboom, 2013; Zhang et al., 2013; Bosboom et al., 2014), where tidal flat and lagoon facies associations were extended and carbonate reservoirs and mudstone covers were formed (Shao et al., 2006; Yue et al., 2017). The sedimentary lithofacies were reflected by the Neo-Tethys Ocean seawater, and developed lagoon facies in the Alai Valley and shore-shallow lacustrine facies in the east of the Tarim Basin (Guan and Guan, 2002; Guo et al., 2002; Ma CM. et al., 2020) (Figure 5).

For many decades, the time of the India-Asia continental collision has been debated. But it is accepted that the final collision was completed at ~45–40 Ma, followed by continued post-collisional convergence to the present (Xia et al., 2009; Bouilhol et al., 2013; Todrani et al., 2022). The Tibetan Plateau is still experiencing deformation (Liu et al., 2009), distributing a lot of Cenozoic basin groups (Song et al., 2022) (Figure 9). The northeastern margin of the Tibetan Plateau, which includes the North Qiangtang terrane and the South Qiangtang terrane as well as the Kunlun Mountains and the Qaidam Basin, continues to deform in response to the ongoing India-Asia collision (Liu et al., 2009; Fang et al., 2020). As a huge intermontane basin, the Qaidam Basin was dominated by lacustrine facies during the Oligocene (Wu et al., 2020) (Figure 9).

The tectonic evolution of the Pamir Salient in the Cenozoic has played an important role in controlling the shift from marine to continental sedimentation in the Tarim and Tajik Basins (Bosboom

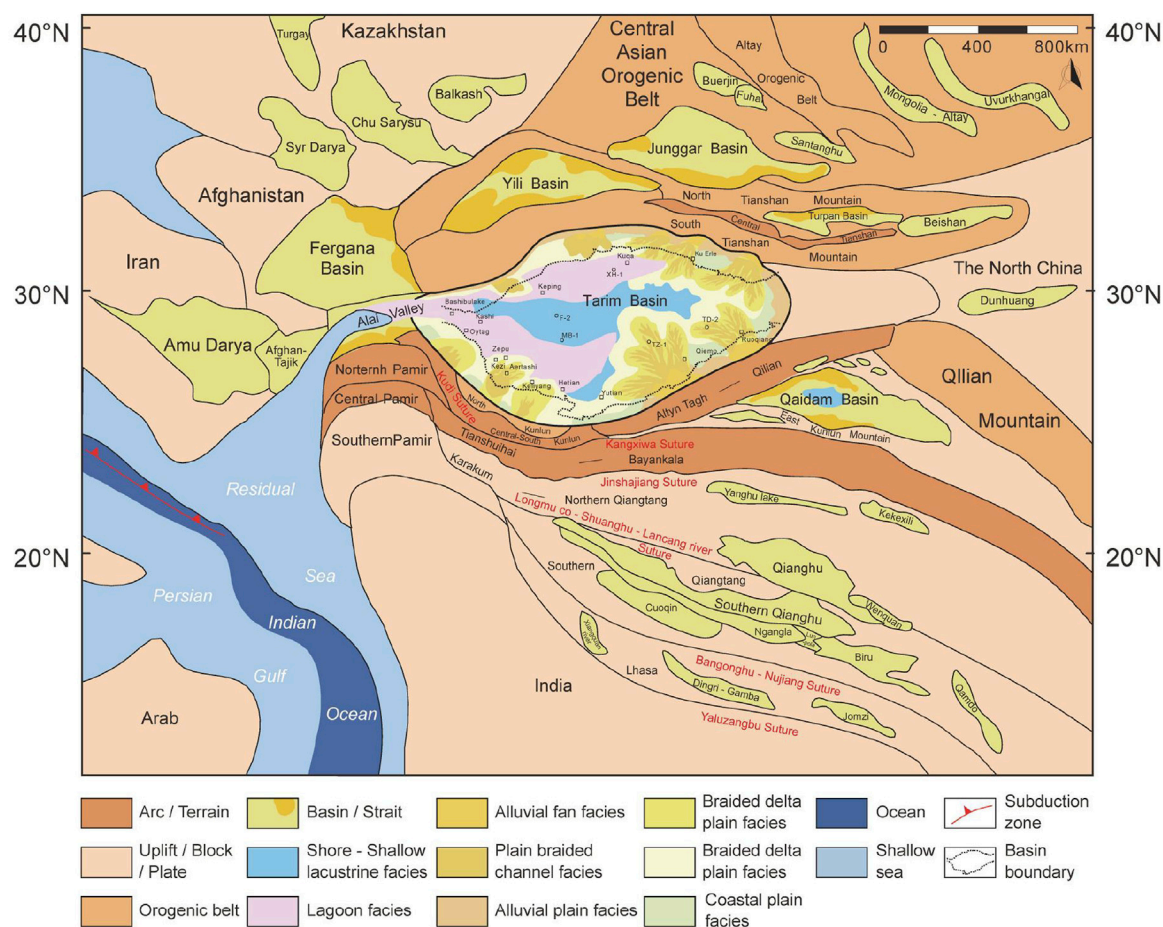


FIGURE 9

Tectono-paleogeography map around the Tarim Basin in the late paleogene.

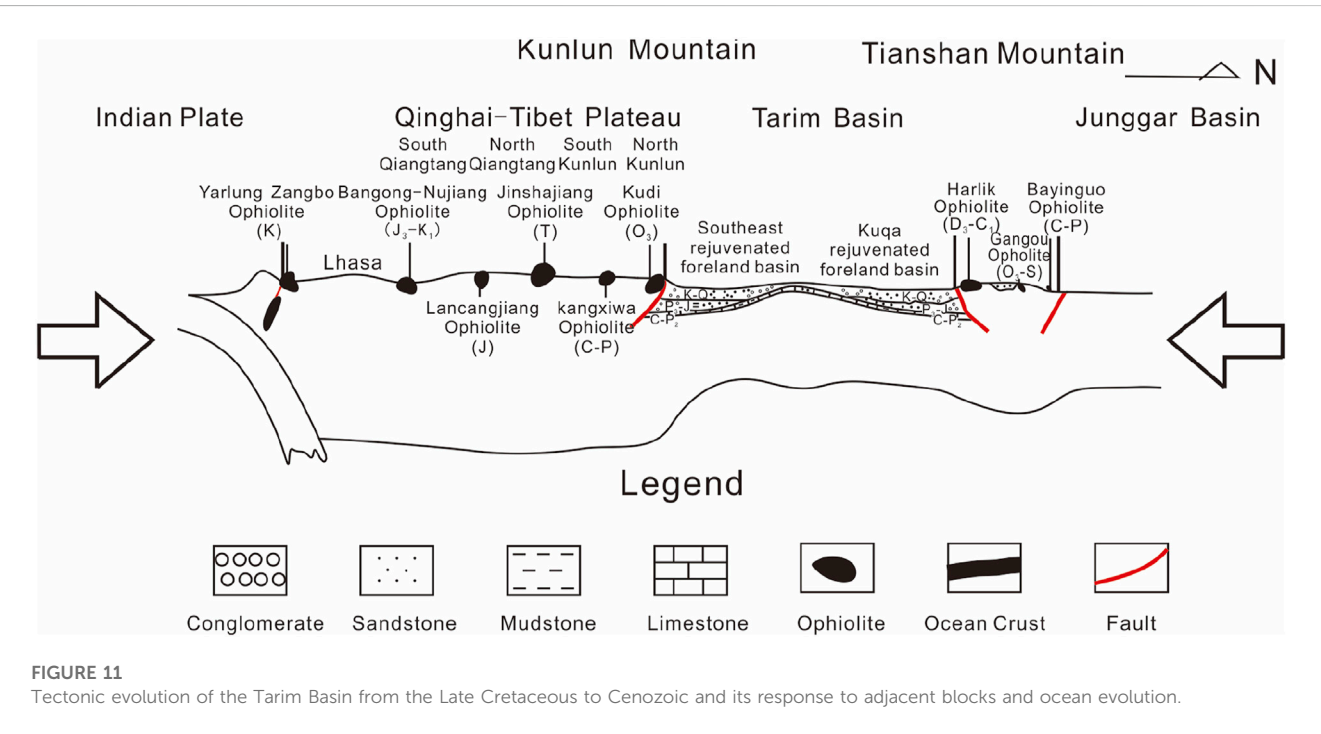
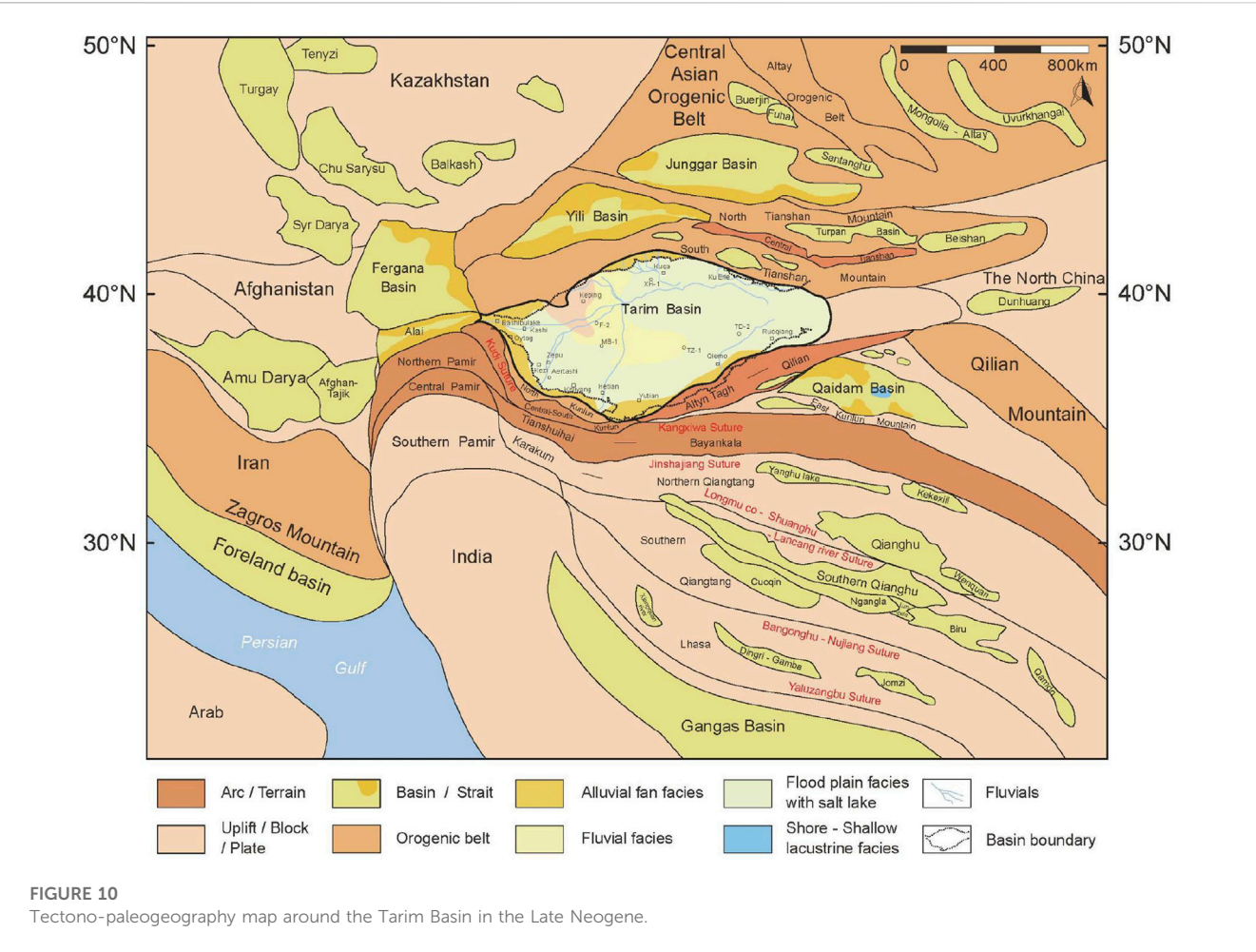
et al., 2011; Sun and Jiang, 2013; Carrapa et al., 2015; Sun et al., 2016b). There were also basin groups distributed in Central Asia that experienced Paleozoic–Cenozoic sedimentary evolution including, for example, the Fergana Basin, Afghanistan-Tajik Basin, and Turgay Basin in the west, and the Junggar Basin and Santanghu Basin in the east (Figure 9) (Wang et al., 2019; Ma T. et al., 2020). Several intermontane basins, such as the Yili basin and the Turpan basin, were preserved within the interior of the Tianshan Mountains (Figure 9) (Jolivet et al., 2010). In the west of the tectono-paleogeography map around the Tarim Basin in the Late Paleogene, a remnant Neo-Tethys Ocean branched via Alai Valley into a remnant marine embayment, causing the lagoon facies to develop in the Southwest Tarim Depression and Kuqa Depression in the northern Tarim Basin (Figure 9).

5.2 Basin-mountain system developed in the Late Neogene

The continental collision between the Arabian and Eurasian plates following the subduction of the Neo-Tethys Ocean beneath Eurasia resulted in a complex deformation across the Zagros Mountains (Figure 10). There was permanent

closure of the northwestern segment of the Tethyan Seaway by 12.8 Ma in the Early-Middle Miocene (Homke et al., 2004; Pirouz et al., 2015; Sun et al., 2021). Both the complex mountain building deformation across the Zagros Mountains and the further northward indentation of the Pamir Salient resulted in the closure of the Alai Valley and a complete sea retreat from the Tarim Basin (Figure 10). The sea retreat was the one of the most significant events during the Late Oligocene–Early Miocene, causing the biggest differences in the southwest of the Tarim Basin (Figures 9, 10).

As the India-Asia continental collision is still ongoing, the Pamir Salient is still experiencing deformation. Intraplate orogeny occurred in the Kunlun Mountains and Tianshan Mountains due to the strong remote effect in the Miocene. In the mountains surrounding the Tarim Basin, mainly at the front of the Western Kunlun Mountains and Southwestern Tianshan Mountains, a significant fraction of the deformation was accommodated by new-formed structures during the Cenozoic (Li et al., 2007; Laborde et al., 2019). Accordingly, the margins of the Tarim Basin, mainly in the Southwest Tarim Depression and the Kuqa Depression, corresponded to the basin-mountain system and became rejuvenated foreland basins due to the intense regional



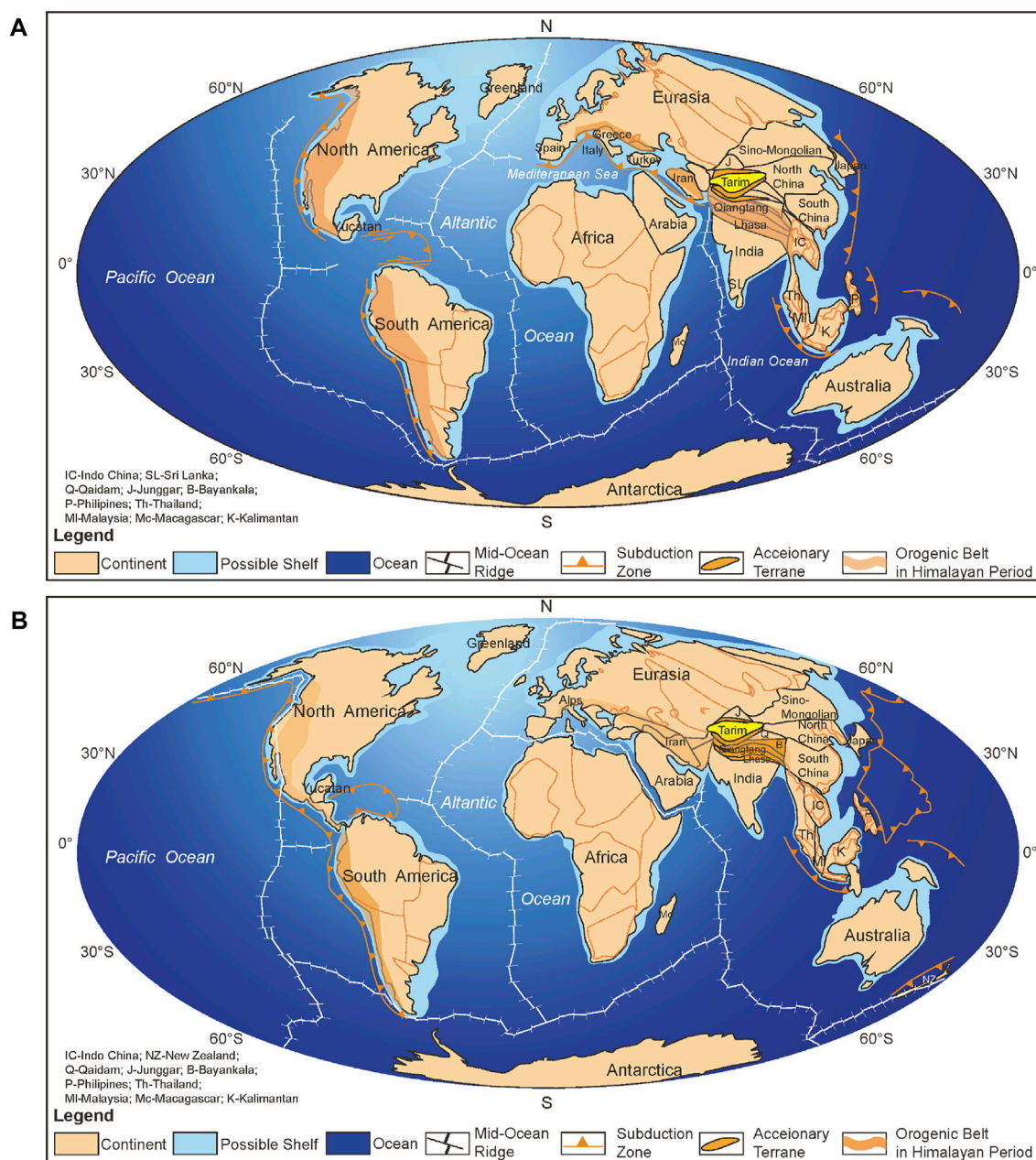


FIGURE 12
Global plate reconstruction in the late Paleogene (A) and Late Neogene (B) (modified after Scotese, 2004).

compression (Wei et al., 2000; Wang et al., 2020) (Figures 10, 11).

The present-day topography of the Tarim Basin and its surrounding mountains and adjacent blocks is considered to be related to the ongoing India-Asia collision (Figures 9–11). In the Cenozoic, the Western Kunlun Mountains and the South Tianshan Mountains were rejuvenated, and the Southwest Tarim Depression and Kuqa Depression formed rejuvenated foreland basins (Figure 11). Associated with these compressive structures, the Bachu Uplift also corresponded to the rejuvenated Western Kunlun Mountains, forming steep bounding thrusts, in particular deep fault systems (Zheng et al., 2014; Laborde et al., 2019) (Figures 2A, B).

6 The Tarim Block in global plate tectonics and its evolution history in the Cenozoic

The Tarim Block occupies an important position in Central Asia and the tectonic configuration around the Tarim Block has been evolving in the Cenozoic. Based on studies by previously published papers about the Tarim Block in global plate tectonics and the regional geological background in the Cenozoic (Scotese, 2004; Ma CM. et al., 2020; Wang, et al., 2020; Song et al., 2022), we combined our newly compiled proto-type basin maps (Figures 6–8) and tectono-paleogeography maps (Figures 9, 10) to modify the

global plate reconstruction in the Late Paleogene (Figure 12A) and Late Neogene (Figure 12B). In our study, the Tarim Block was considered important and its response to adjacent blocks and ocean evolution were highlighted.

To the south of the Tarim Block, some terranes and blocks continue to deform, including the Tianshuihai, North Qiangtang, South Qiangtang, and Lhasa blocks, in response to the ongoing India-Asia collision (Figure 12). Since the collisions of the Lhasa Block and the India Plate with the Asian Plate in the Late Cretaceous, the mountains surrounding the Tarim Basin have rapidly uplifted, with a large amount of compressive deformation at the basin edges (Li et al., 2007; Jia, 2009; Laborde et al., 2019). To the north of the Tarim Block, the North and the South Tianshan Mountains were reactivated, and fold-and-thrust belts localized the topographic front of the mountain range (Jolivet et al., 2010; Jolivet et al., 2013; Laborde et al., 2019). The basins that formed on the Central Asian Orogenic Belt were small-sized continental basin groups (Song et al., 2022). To the Northwest of the Tarim Block, there were also some basin groups formed on the Kazakhstan Block, including the Syr Darya, Turgay, Chu-Sarysu, and Balkhash Basin (Wang et al., 2019; Ma T. et al., 2020).

Besides the long-lasting plate collision, global climate change was another key on the paleogeography and tectonic evolution of the Tarim Block and its adjacent blocks. As the global sea levels fell, the Neo-Tethys Ocean gradually retreated from Asian Plate in the Cenozoic (Sun and Jiang, 2013; Carrapa et al., 2015; Sun et al., 2016a; Li et al., 2020; Sun et al., 2021). The Tarim Basin has a paleogeographical evolution characterized by a long-term stepwise Neo-Tethys sea retreat punctuated by short-term shallow-marine incursions (Bosboom et al., 2011; Bosboom, 2013; Bosboom et al., 2014). The last incursion extended to the southwest and the north of the Tarim Basin with its marine deposits and fossil assemblages, and the sea retreated at ~37–25 Ma (Figure 12).

7 Conclusion

1. Several localized tectonic activities around the Tarim Basin occurred due to the ongoing India-Asia collision in the Cenozoic, causing tectono-paleogeography changes in the basin.

References

- Allen, M. B., Windley, B. F., and Zhang, C. (1993). Palaeozoic collisional tectonics and magmatism of the Chinese Tien Shan, central Asia. *Tectonophysics* 220 (1–4), 89–115. doi:10.1016/0040-1951(93)90225-9
- Bosboom, R. E., Dupont-Nivet, G., Grothe, A., Brinkhuis, H., Villa, G., Mandic, O., et al. (2014). Timing, cause and impact of the late Eocene stepwise sea retreat from the Tarim Basin (west China). *Palaeogeogr. Palaeoclimatol. Palaeoecol.* 403 (2), 101–118. doi:10.1016/j.palaeo.2014.03.035
- Bosboom, R. E., Dupont-Nivet, G., Houben, A., Brinkhuis, H., Villa, G., Mandic, O., et al. (2011). Late Eocene sea retreat from the Tarim Basin (west China) and concomitant Asian paleoenvironmental change. *Palaeogeogr. Palaeoclimatol. Palaeoecol.* 299 (3–4), 385–398. doi:10.1016/j.palaeo.2010.11.019
- Bosboom, R. E. (2013). *Palaeogeography of the central asian proto-paratethys sea in the Eocene* [D] (Utrecht: Ph.D. thesis).
- Bouilhol, P., Jagoutz, O., Hanchar, J. M., and Dudas, F. O. (2013). Dating the India-Eurasia collision through arc magmatic records. *Earth Planet. Sci. Lett.* 366, 163–175. doi:10.1016/j.epsl.2013.01.023
- Carrapa, B., Decelles, P. G., Wang, X., Clementz, M. T., Mancin, N., Stoica, M., et al. (2015). Tectono-climatic implications of Eocene Paratethys regression in the Tajik basin of central Asia. *Earth Planet. Sci. Lett.* 424, 168–178. doi:10.1016/j.epsl.2015.05.034
- Cheng, F., Guo, Z. J., Jenkins, H. S., Fu, S. T., and Cheng, X. (2015). Initial rupture and displacement on the Altyn Tagh fault, northern Tibetan plateau: Constraints based on residual mesozoic to cenozoic strata in the Western Qaidam Basin. *Geosphere* 11, 921–942. doi:10.1130/GES01070.1
- Ding, X. Z., Lin, C. S., Liu, J. Y., Han, K. Y., Pang, J. F., and Pang, W. H. (2011). The sequence stratigraphic response to the basin-orogene coupling process of Cretaceous-Neogene in Tarim Basin, China. *Earth Sci. Front.* 18 (4), 144–157. (in Chinese with English abstract).
- Ding, X. Z., Liu, X., Wu, S. Z., Fu, D. R., Yao, J. X., Wu, S. Z., et al. (1993). Discussion on the Cretaceous-Paleogene dimensity features and environments of Kuzigongsu area, Western Tarim basin. *Xinjiang Geol.* 11 (3), 179–193. (in Chinese with English abstract).
2. As the Neo-Tethys Ocean retreat finally occurred in the Tarim Basin during the Late Oligocene - Early Miocene, the proto-type basin of the Tarim Basin evolved from lagoon facies in the west and terrestrial facies in the east in the Paleogene to the evolution of terrestrial depositional environments in the Neogene.
3. By quantifying the compressive component of the Cenozoic deformation, it could be seen that the main part of the deformation was accommodated by the reactivated basin-mountain system, mainly in the edges of the Tarim Basin and surrounding ranges.

Data availability statement

The original contributions presented in the study are included in the article/supplementary material, further inquiries can be directed to the corresponding author.

Author contributions

LW did the main work and wrote the paper; SH, CL and YD provided the data; JX, ZZ, XL, and HC contributed to the map-compiling. All authors read and approved the final manuscript.

Conflict of interest

SH, CL, and YD were employed by Tarim Oilfield Company. The remaining authors declare that the research was conducted in the absence of any commercial or financial relationships that could be construed as a potential conflict of interest.

Publisher's note

All claims expressed in this article are solely those of the authors and do not necessarily represent those of their affiliated organizations, or those of the publisher, the editors and the reviewers. Any product that may be evaluated in this article, or claim that may be made by its manufacturer, is not guaranteed or endorsed by the publisher.

- Dong, S. L., Li, Z., and Jiang, L. (2016). The early Paleozoic sedimentary–tectonic evolution of the circum-Mangar areas, Tarim block, NW China: Constraints from integrated detrital records. *Tectonophysics* 682, 17–34. doi:10.1016/j.tecto.2016.05.047
- Fang, X. M., Dupont-Nivet, G., Wang, C. S., Song, C. H., Meng, Q. Q., Zhang, W. L., et al. (2020). Revised chronology of central tibet uplift (lunpola basin). *Sci. Adv.* 6 (50), eaba7298. doi:10.1126/sciadv.aba7298
- Guan, S. Z., and Guan, S. Q. (2002). Stratigraphic age and depositional environment of Jidike Formation in Kuche basin of xinjiang [J]. *Geol. Chemical Minerals* (01), 1–6+22. (in Chinese with English abstract). doi:10.3969/j.issn.1006-5296.2002.01.001
- Guo, X. P., Ding, X. Z., He, X. X., Li, H. M., Su, X., and Peng, Y. (2002). New progress in the study of marine transgression events and marine strata of the meso-cenozoic in the Tarim Basin. *Acta Geol. Sin.* (03), 299–307. (in Chinese with English abstract). doi:10.3321/j.issn:0001-5717.2002.03.002
- Guo, X. P. (1994). The stratigraphic division of the marine Paleocene in the Western Tarim basin [J]. *Geol. Review* 40 (4), 322–329. (in Chinese with English abstract). doi:10.3321/j.issn:0371-5736.1994.04.005
- He, B. Z., Jiao, C. L., Xu, Z. Q., Cai, Z. H., Zhang, J. X., Liu, S. L., et al. (2016). The paleotectonic and paleogeography reconstructions of the Tarim Basin and its adjacent areas (NW China) during the late Early and Middle Paleozoic. *Gondwana Res.* 30, 191–206. doi:10.1016/j.gr.2015.09.011
- He, D. F., Li, D. S., He, J. Y., and Wu, X. Z. (2013). Comparison in petroleum geology between Kuqa depression and Southwest depression significance. *Acta Geosci. Sin.* 34 (02), 201–218. (in Chinese with English abstract). doi:10.7623/syxb201302001
- He, G. Y., Lu, H. F., Yang, S. F., and Li, S. X. (2004). Subsiding features of the mesozoic and cenozoic Kuqa basin, northwestern China. *J. Zhejiang Univ.* (01), 110–113+120. (in Chinese with English abstract). doi:10.3321/j.issn:1008-9497.2004.01.024
- Homke, S., Verges, J., Garcés, M., Emami, H., and Karpuz, R. (2004). Magnetostratigraphy of miocene–pliocene Zagros foreland deposits in the front of the push-e kush arc (lurestan province, Iran). *Earth Planet. Sci. Lett.* 225, 397–410. doi:10.1016/j.epsl.2004.07.002
- Huang, Y. P., Jiang, Z. L., Li, J. R., Wang, B. Q., and Man, L. (2013). Analysis of tectonic stress direction of Tarim basin during neotectonic period. *Petroleum Geol. Recovery Effic.* 20 (3), 5–9. (in Chinese with English abstract). doi:10.3969/j.issn.1009-9603.2013.03.002
- Izquierdo-Llavall, E., Roca, E., Xie, H. W., Pla, O., Munoz, J. A., Rowan, M. G., et al. (2018). Influence of overlapping décollements, syntectonic sedimentation, and structural inheritance in the evolution of a contractional system: The central Kuqa fold-and-thrust belt (tian Shan mountains, NW China). *Tectonics* 37, 2608–2632. doi:10.1029/2017TC004928
- Jia, C. Z., Zhang, S. B., and Wu, S. Z. (2004). *Stratigraphy of the Tarim Basin and adjacent areas*. Beijing: Science Press, 1–1063. (upper and lower volumes) [M]. (in Chinese with English abstract).
- Jia, C. Z. (2009). The structures of Basin and range system around the Tibetan plateau and the distribution of oil and gas in the Tarim Basin [J]. *Geotect. Metallogenia* 33 (01), 1–9. (in Chinese with English abstract). doi:10.3969/j.issn.1001-1552.2009.01.001
- Jolivet, M., Dominguez, S., Charreau, J., Chen, Y., Li, Y. A., and Wang, Q. C. (2010). Mesozoic and Cenozoic tectonic history of the central Chinese Tian Shan: Reactivated tectonic structures and active deformation. *Tectonics* 29, TC6019.
- Jolivet, M., Heilbronn, G., Robin, C., Barrier, L., Bourquin, S., Guo, Z. J., et al. (2013). Reconstructing the late palaeozoic – mesozoic topographic evolution of the Chinese tian Shan: Available data and remaining uncertainties. *Adv. Geosciences* 37, 7–18. doi:10.5194/adgeo-37-7-2013
- Laborde, A., Barrier, L., Simoes, M., Li, H., Coudroy, T., Van der Woerd, J., et al. (2019). Cenozoic deformation of the Tarim Basin and surrounding ranges (xinjiang, China): A regional overview. *Earth-science Rev.* 197, 102891. doi:10.1016/j.earscirev.2019.102891
- Li, B. L., Jia, C. Z., Pang, L. Q., Guan, S. W., Yang, G., Shi, X., et al. (2007). The spatial distribution of the foreland thrust tectonic deformation in the circum-Tibetan plateau Basin and range system [J]. *Acta Geol. Sin.* (09), 1200–1207. (in Chinese with English abstract). doi:10.3321/j.issn:0001-5717.2007.09.005
- Li, C., Wang, S. L., and Wang, L. S. (2019). Tectonostratigraphic history of the southern Tian Shan, Western China, from seismic reflection profiling. *J. Asian Earth Sci.* 172, 101–114. doi:10.1016/j.jseae.2018.08.017
- Li, J. F., Zhao, Y., Pei, J. L., Liu, F., Zhou, Z. Z., Gao, H. L., et al. (2017). Cenozoic marine sedimentation problem of the Tarim Basin [J]. *J. Geomechanics* 23 (01), 141–149. (in Chinese with English abstract). doi:10.3969/j.issn.1006-6616.2017.01.010
- Li, Q., Li, L., Zhang, Y. Y., and Guo, Z. J. (2020). Oligocene incursion of the paratethys seawater to the Junggar Basin, NW China: Insight from multiple isotopic analysis of carbonate. *Sci. Rep.* 10 (1), 6601. doi:10.1038/s41598-020-63609-0
- Li, X., Zhong, D. K., Li, Y., Lei, G. L., Yang, X. Z., Wu, Q. K., et al. (2013). Sedimentary characteristics and evolution of the Neogene and quaternary in Kuqa depression of Tarim Basin [J]. *J. Palaeogeogr.* 15 (02), 169–180. (in Chinese with English abstract). doi:10.7605/gdxb.2013.02.016
- Li, Y. P., Robinson, A. C., Gadoev, M., and Oimuhammadzoda, I. (2020). Was the Pamir salient built along a Late Paleozoic embayment on the southern Asian margin? *Earth Planet. Sci. Lett.* 550, 116554. doi:10.1016/j.epsl.2020.116554
- Lin, X., Cheng, X. R., Feng, Y. F., and Peng, B. F. (2019). A review on regressive time in southwest Tarim Basin and its forming mechanism. *Mar. Geol. Quat. Geol.* 39 (03), 84–93. (in Chinese with English abstract). doi:10.16562/j.cnki.0256-1492.2018060301
- Liu, C. Y., Zhao, H. G., Zhang, C., and Wang, J. Q. (2009). The important turning period of evolution in the Tibet-Himalaya tectonic domain. *Earth Sci. Front.* 16 (04), 1–12. (in Chinese with English abstract). doi:10.3321/j.issn:1005-2321.2009.04.001
- Lou, Q. Q., Xiao, A. C., Zhong, N. C., and Wu, L. (2016). A method of prototype restoration of large depressions with terrestrial sediments: A case study from the cenozoic Qaidam Basin. *Acta Petrol. Sin.* 32 (03), 892–902. (in Chinese with English abstract).
- Ma, C. M., Li, J. H., Cao, Z. L., Liu, L. X., and Wang, M. N. (2020). Lithofacies palaeogeographic reconstruction and evolution of the Carboniferous-Permian basin group in Central Asia. *Acta Petrol. Sin.* 36 (11), 3510–3522. (in Chinese with English abstract). doi:10.18654/1000-0569/2020.11.16
- Ma, T., Ma, Q., Wang, Z. Y., Yuan, C., Hu, J. F., and Wang, H. (2020). Sequence stratigraphic framework and sedimentary evolution of Paleogene prototype sedimentary basin in Kuqa Depression. *Chin. J. Geol.* 55 (02), 369–381. (in Chinese with English abstract). doi:10.12017/dzxx.2020.024
- Ning, F., Yun, J. B., Li, J. J., Song, H. M., and Zhao, L. D. (2021). Structural characteristics and exploration prospects of the southwestern margin of Bachu Uplift, Tarim Basin [J]. *Oil Gas Geol.* 42 (02), 299–308. doi:10.11743/ogg20210204
- Pirouz, M., Simpson, G., and Chiaradia, M. (2015). Constraint on foreland basin migration in the Zagros mountain belt using Sr isotope stratigraphy. *Basin Res.* 27, 714–728. doi:10.1111/bre.12097
- Scotese, C. R. (2004). A continental drift flipbook. *J. Geol.* 112 (06), 729–741. doi:10.1086/424867
- Shao, L. Y., He, Z. P., Gu, J. Y., Liu, W. L., Jia, J. H., Liu, Y. F., et al. (2006). Lithofacies palaeogeography of the Paleogene in Tarim Basin [J]. *J. Palaeogeogr.* 03, 353–364. (in Chinese with English abstract). doi:10.3969/j.issn.1671-1505.2006.03.008
- Song, B. W., Zhang, K. X., Xu, Y. D., Ji, J. L., Luo, M. S., Han, F., et al. (2022). Neogene Tectonic-stratigraphic realms and sedimentary sequence in China. *Earth Sci.* 47 (04), 1143–1161. (in Chinese with English abstract). doi:10.3799/dqxx.2021.072
- Sun, J. M., and Jiang, M. S. (2013). Eocene seawater retreat from the southwest Tarim Basin and implications for early Cenozoic tectonic evolution in the Pamir Plateau. *Tectonophysics* 588, 27–38. doi:10.1016/j.tecto.2012.11.031
- Sun, J. M., Morteza, S., Nahid, A., Cao, M. M., Zhang, Z. L., Tian, S. C., et al. (2021). Permanent closure of the Tethyan Seaway in the northwestern Iranian Plateau driven by cyclic sea-level fluctuations in the late Middle Miocene. *Palaeogeogr. Palaeoclimatol. Palaeoecol.* 564, 110172. doi:10.1016/j.palaeo.2020.110172
- Sun, J. M., Windley, B. F., Zhang, Z. L., Fu, B. H., and Li, S. H. (2016a). Diachronous seawater retreat from the southwestern margin of the Tarim Basin in the late Eocene. *J. Asian Earth Sci.* 116, 222–231. doi:10.1016/j.jseae.2015.11.020
- Sun, J. M., Xiao, W. J., Windley, B. F., Ji, W. Q., Fu, B. H., Wang, J. G., et al. (2016b). Provenance change of sediment input in the northeastern foreland of Pamir related to collision of the Indian Plate with the Kohistan-Ladakh arc at around 47 Ma. *Tectonics* 35 (2), 315–338. doi:10.1002/2015TC003974
- Tang, X. D., Tuo, X. S., Mi, D. J., and Qin, H. F. (2014). Research on provenance and sedimentary environment of Suweiyi formation of Bashentamu area, Southwest Tian Shan mountainous region, Xinjiang [J]. *Contributions Geol. Mineral Resour. Res.* 29 (04), 579–586. (in Chinese with English abstract). doi:10.6053/j.issn.1001-1412.2014.04.016
- Tapponnier, P., Mattauer, M., Proust, F., and Cassaigneau, C. (1981). Mesozoic ophiolites, sutures, and large-scale tectonic movements in Afghanistan. *Earth Planet. Sci. Lett.* 52 (2), 355–371. doi:10.1016/0012-821X(81)90189-8
- Tapponnier, P., and Molnar, P. (1977). Active faulting and tectonics in China. *J. Geophysical Res.* 82, 2905–2930. doi:10.1029/JB082i020p02905
- Todrani, A., Speranza, F., D'Agostino, N., and Zhang, B. (2022). Post-50 Ma evolution of India-Asia collision zone from paleomagnetic and GPS data: Greater India indentation to eastward Tibet flow. *Geophys. Res. Lett.* 49, e2021GL09662.
- Wang, B. Q., Wang, Q. H., Han, L. J., Han, J., and Wang, L. G. (2007). Segmentation characteristics and dynamic mechanism of the che'erchen fault in the southeast Tarim basin. *Oil Gas Geol.* (06), 755–761. (in Chinese with English abstract). doi:10.3321/j.issn:0253-9985.2007.06.008
- Wang, P., Liu, D. L., Li, H. B., Chevalier, M. L., Wang, Y. D., Pan, J. W., et al. (2021). Sedimentary provenance changes constrain the Eocene initial uplift of the central Pamir, NW Tibetan plateau. *Front. Earth Sci.* 9, 741194. doi:10.3389/feart.2021.741194
- Wang, S. H., Zheng, J. Z., Gao, S. Q., Wang, Y. K., Zhang, M. J., Zhou, T. W., et al. (2019). “The play characteristic and exploration potential in sedimentary basins in central Asia.” in *Proceedings of the international field exploration and development conference* (Singapore: Springer Singapore), 3487–3494. doi:10.1007/978-981-15-2485-1_321

- Wang, T. F., Jin, Z. K., Shi, Z. W., Dai, X. C., and Cheng, R. H. (2020). Phanerozoic plate history and structural evolution of the Tarim Basin, northwestern China. *Int. Geol. Rev.* 62 (12), 1555–1569. doi:10.1080/00206814.2019.1661038
- Wang, X., Sun, D. H., Chen, F. H., Wang, F., Li, B. F., Popov, S. V., et al. (2014). Cenozoic paleo-environmental evolution of the Pamir–Tien Shan convergence zone. *J. Asian earth Sci.* 80, 84–100. doi:10.1016/j.jseas.2013.10.027
- Wei, G. Q., Jia, C. Z., Shi, Y. S., Lu, H. F., and Wang, L. S. (2000). Tectonic characteristics and petroleum prospects of cenozoic compound rejuvenated foreland basins in Tarim. *Acta Geol. Sin.* (02), 123–133. (in Chinese with English abstract). doi:10.3321/j.issn:0001-5717.2000.02.004
- Wu, G. H., Deng, W., Huang, S. Y., Zheng, D. M., and Pan, W. Q. (2020). Tectonic-paleogeographic evolution in the Tarim Basin. *Chin. J. Geol.* 55 (02), 305–321. (in Chinese with English abstract). doi:10.12017/dzks.2020.020
- Xia, L. Q., Ma, Z. P., Li, X. M., Xia, Z. C., and Xu, X. Y. (2009). Paleocene-early Eocene (65–40Ma) volcanic rocks in Tibetan plateau: The products of syn-collisional volcanism. *Northwest. Geol.* 42 (03), 1–25. (in Chinese with English abstract). doi:10.3969/j.issn.1009-6248.2009.03.001
- Yue, Y., Xu, Q. Q., Fu, H., and Xi, D. P. (2017). Reservoir-cap rock assemblage and sedimentary characteristics of Cretaceous-Paleogene in southwest Tarim Basin. *Petroleum Geol. Exp.* 39 (03), 318–326. (in Chinese with English abstract). doi:10.11781/sydz201703318
- Zhang, G. Y., Tong, X. G., Xin, R. C., Wen, Z. X., Ma, F., Huang, T. F., et al. (2019). Evolution of lithofacies and paleogeography and hydrocarbon distribution worldwide (II). *Petroleum Explor. Dev.* 46 (5), 896–918. doi:10.1016/S1876-3804(19)60248-X
- Zhang, H., Liu, C. L., Cao, Y. T., Sun, H. W., and Wang, L. C. (2013). A tentative discussion on the time and the way of marine regression from Tarim bay during the cenozoic. *Acta Geosci. Sin.* 34 (05), 577–584. (in Chinese with English abstract). doi:10.3975/cagsb.2013.05.08
- Zhang, J. Y., Xing, F. C., Krijgsman, W., Zhang, C., Wei, W., Chen, L., et al. (2022). Palaeogeographic reconstructions of the eocene-oligocene Tarim Basin (NW China): Sedimentary response to late Eocene sea retreat. *Palaeogeogr. Palaeoclimatol. Palaeoecol.* 587, 110796. doi:10.1016/j.palaeo.2021.110796
- Zhang, S. J., Hu, X. M., Han, Z., Li, J., and Garzanti, E. (2018). Climatic and tectonic controls on Cretaceous-Palaeogene sea-level changes recorded in the Tarim epicontinental sea. *Palaeogeogr. Palaeoclimatol. Palaeoecol.* 501, 92–110. doi:10.1016/j.palaeo.2018.04.008
- Zhang, Y., Zheng, M. L., Chen, J. J., Deng, M. Z., Tian, F. L., Zhang, W. K., et al. (2021). Geometrical and kinematical characteristics of the mazartag fault zone in Bachu uplift, Tarim Basin. *Oil Gas Geol.* 42 (02), 325–337. (in Chinese with English abstract). doi:10.11743/ogg20210206
- Zhang, Y., Zwingmann, H., Liu, K., and Luo, X. (2011). Hydrocarbon charge history of the Silurian bituminous sandstone reservoirs in the Tazhong uplift, Tarim Basin, China. *AAPG Bull.* 95 (3), 395–412. doi:10.1306/08241009208
- Zhao, H. F., Wei, Y. Y., Shen, Y., Xiao, A. C., Mao, L. G., Wang, L. Q., et al. (2016). Cenozoic tilting history of the south slope of the Altyn Tagh as revealed by seismic profiling: Implications for the kinematics of the Altyn Tagh fault bounding the northern margin of the Tibetan Plateau. *Geosphere* 12, 884–899. doi:10.1130/GES01269.1
- Zheng, M. L., Wang, Y., Jin, Z. J., Li, J. C., Zhang, Z. P., Jiang, H. S., et al. (2014). Superimposition, evolution and petroleum accumulation of Tarim Basin. *Oil Gas Geol.* 35 (06), 925–934. (in Chinese with English abstract). doi:10.11743/ogg20140619
- Zhuang, X. J., Xiao, L. X., and Yang, J. (2002). Sedimentary facies in southwestern region of Tarim Basin. *Xinjiang Geol.*, 78–82. (in Chinese with English abstract). doi:10.3969/j.issn.1000-8845.2002.z1.014



OPEN ACCESS

EDITED BY

Yuan Neng,
China University of Petroleum Beijing,
China

REVIEWED BY

Jinning Zhang,
China University of Petroleum Beijing,
China
Yonghe Sun,
Chongqing University of Science and
Technology, China
Shiguo Wu,
Institute of Deep-Sea Science and
Engineering (CAS), China

*CORRESPONDENCE

Fusheng Yu,
✉ fushengyu@cup.edu.cn

SPECIALTY SECTION

This article was submitted to Structural
Geology and Tectonics,
a section of the journal
Frontiers in Earth Science

RECEIVED 21 November 2022

ACCEPTED 09 March 2023

PUBLISHED 20 March 2023

CITATION

Guo B, Yu F and Li H (2023), Structural
evolution and mechanism of multi-phase
rift basins: A case study of the Panyu 4 Sag
in the Zhu I Depression, Pearl River Mouth
Basin, South China Sea.
Front. Earth Sci. 11:1103827.
doi: 10.3389/feart.2023.1103827

COPYRIGHT

© 2023 Guo, Yu and Li. This is an open-
access article distributed under the terms
of the [Creative Commons Attribution
License \(CC BY\)](https://creativecommons.org/licenses/by/4.0/). The use, distribution or
reproduction in other forums is
permitted, provided the original author(s)
and the copyright owner(s) are credited
and that the original publication in this
journal is cited, in accordance with
accepted academic practice. No use,
distribution or reproduction is permitted
which does not comply with these terms.

Structural evolution and mechanism of multi-phase rift basins: A case study of the Panyu 4 Sag in the Zhu I Depression, Pearl River Mouth Basin, South China Sea

Bowei Guo^{1,2}, Fusheng Yu^{1,2*} and Hui Li^{1,2}

¹College of Geosciences, China University of Petroleum (Beijing), Beijing, China, ²State Key Laboratory of Petroleum Resources and Prospecting, China University of Petroleum (Beijing), Beijing, China

The study of changes in normal fault systems during different rift stages is important to understand the genesis and evolution of multi-phase rift basins, such as the Panyu 4 Sag in the Zhu I Depression. Using 2D and 3D seismic data and analogue modelling, the Zhu I Depression was characterized as a series of half-grabens bounded by NE-NEE-trending normal faults, it was found to have undergone two phases of the extension during the Paleogene. The Zhu I Depression exhibited four fault sets with different strikes, including NNE, NE-NEE, EW, and NWW. The main controlling faults were NE-trending and EW-trending with high activity rates during Rift Phase 1 and Rift Phase 2, respectively. The average azimuths of the dominant strikes for type Ia, type Ib, and type II faults were 75°, 85°, and 90°, which revealed that the minimum principal stress (σ_3) directions during the rift phases 1 and 2 of the Zhu I Depression were SSE (~165°) and near-EW (~180°), respectively. Two phases of structural-sedimentary evolution, with different directions and analogue modelling results, illustrated that the Panyu 4 Sag was formed as a superimposed basin under multi-phase anisotropic extension. The structural evolution of the Panyu 4 Sag since the Paleogene was mainly controlled by the combined effects of the Pacific, Eurasian, and Indian plates. Since the orientation of subduction of the Pacific plate changed from NNW to NWW, the stress field shifted from NW-SE-trending tension to S-N-trending tension, causing the superimposition of late near-E-W-oriented structural pattern on the early NE-oriented structural pattern.

KEYWORDS

structural evolution, analogue modelling, multi-phase rift basins, Panyu 4 Sag, Zhu I Depression, Pearl River Mouth Basin

1 Introduction

The evolution of rift basins can be generally divided into the syn-rift subsidence stage, which is controlled by faults, and the post-rift thermal subsidence stage (McKenzie, 1978; Ziegler and Cloetingh, 2004). The syn-rift subsidence stage of rift basins is usually a multi-level and multi-phase stage (Ravnas and Steel, 1998; Morley et al., 2004; Henstra et al., 2015; Deng et al., 2017). Many rift basins have developed through multi-phase extension

comprising two or more rift phases, which are separated by a period of tectonic quiescence (Deng et al., 2017). Such as the North Sea Basin (Whipp et al., 2014), the Songkhla Basin, Thailand (Morley et al., 2004), the East African Rift Valley (Korme et al., 2004), the Dampier Basin, Australia (Frankowicz and McClay, 2010), the Bohai Bay Basin (Zhu et al., 2014), the Sichuan Basin (Ma et al., 2022), the Pearl River Mouth Basin (Ge et al., 2017) and the Jiangnan Basin (Huang and Hinnov, 2014), China, etc. Multi-phase rifts, which respond to plate or regional tectonic events, are the main controlling factor in the formation of regional multi-cycle sedimentary sequences (McKenzie, 1978; Morley et al., 2004). The extension direction of rift basins usually changes during different rift periods. The fault geometries and kinematics are produced by multiple trends and various interaction styles within these basins (Ma et al., 2020).

The Pearl River Mouth Basin (PRMB) is located at the northern continental margin of the South China Sea (SCS) and is a rift basin that developed on top of the Mesozoic fold basement (Yu, 1990; Zhou et al., 1995; Wu et al., 2001; Chen, 2003; Zhu et al., 2008; Xie et al., 2014). The PRMB has undergone a complex evolutionary process owing to the combined effects of the Indian, Eurasian, and Pacific plates (Zhong et al., 2014). The collision between Eurasia and India and the subduction of the Pacific under the Eurasian plates during the Mesozoic era led to the development of a series of pre-existing structures, which laid the foundation for the formation and development of the basin. The Zhu I Depression is an important hydrocarbon-rich unit within the PRMB. The structural evolution of the basin controls hydrocarbon accumulation and reflects the evolution of the SCS (Pigott and Ru, 1994; Zhou et al., 1995; Yao et al., 2005; Shi, 2013; Liu et al., 2019).

The dynamics and evolution of the PRMB are still debated due to the combined influences of the Pacific, Indian, and Eurasian plates during the Cenozoic era. Regarding the dynamics, some scholars consider it to be a rift basin that was controlled by a series of NE-NEE-trending and EW-trending faults (Zhong et al., 2014). However, other researchers consider it to be a pull-apart basin, whose initial formation phase was controlled by strike-slip and pull-apart motions (Cheng et al., 2012; Suo et al., 2014). In terms of its evolution, the PRMB demonstrates obvious characteristics of three-phase rifting (Jiao et al., 1997; Lv et al., 2012; Neng et al., 2013; Wu et al., 2014). However, consensus about the age of each rift stage is lacking, with the representative views being as follows. Some authors proposed that the PRMB mainly underwent the first rifting stage from the Paleocene to the middle Eocene, the second rifting stage from the late Eocene to the early Oligocene, and the third rifting stage during the late Oligocene. Neng et al. (2013) proposed that the PRMB underwent three main stages of rifting evolution. These included the initial rifting stage from the Paleocene to the early Eocene, the early rifting stage during the middle Eocene, and the thermal rifting stage from the late Eocene to the late Oligocene. On the other hand, Wu et al. (2014) suggested a slightly different framework for the rifting evolution of the basin. They identified three stages as well, but with some variation in their timing and nomenclature. These stages included the first rifting stage from the Paleocene to the early Eocene, the second rifting stage during the middle Eocene, and the third rifting stage from the late Eocene to the early Oligocene. These views suggested that the PRMB experienced multi-phase rifting from the Eocene to the early Oligocene.

To improve our understanding of the evolution of the PRMB, we conducted seismic interpretation and analogue modelling to elucidate the structural evolution process of the Zhu I Depression in this work, taking the Panyu 4 Sag in the Zhu I Depression as an example. Firstly, we described the geological background of the studied area based on existing literature. Secondly, we studied the distribution and evolution of faults and sedimentation according to seismic interpretation and structural-sedimentary features of different units of the Wenchang Formation. Thirdly, we carried out analogue modelling to illustrate the formation of two-phase rifting to better constrain the evolution of the internal sub-structural units of the Panyu 4 Sag. Finally, a model for the formation of the Panyu 4 Sag was proposed to elucidate the structural evolution of the Zhu I Depression.

2 Geological setting

The PRMB is a rift basin that formed from the Mesozoic to the Cenozoic eras. The basin is bounded by a series of NE-NEE trending faults (Chen and Pei, 1993; Robinson et al., 1998; Franke et al., 2014; Jiang et al., 2015; Guo et al., 2022). The pre-existing NEE-trending uplifts and faults divide the basin into the present structural framework of three uplift zones and two depression zones (Li, 1993; Chen et al., 2003; Shi et al., 2012; Zhong et al., 2014; Figure 1A), which are the Northern Uplifted Belt, the Northern Depression Zone (including Zhu I Depression and Zhu III Depression), the Central Uplifted Belt (including Shenhu Uplift, Panyu Uplift, and Dongsha Uplift), the Southern Depression Zone (consisting of Zhu II Depression and Chaoshan Depression), and the Southern Uplifted Belt (Li, 1994; Robinson et al., 1998; Chen, 2000; Zhang et al., 2004; Sun et al., 2010; Leyla et al., 2015).

Five typical unconformities relating to the seismic surfaces represented the Shenhu, the First episode of Zhuqiong, and the Second episode of Zhuqiong, Nanhai, and Dongsha events, respectively. (Zhong et al., 2014; Ge et al., 2017; Figure 1A). The Shenhu (undeveloped in the study area), Wenchang (E_{2w}), and Enping (E_{2en}) formations were developed in the syn-rift stage which was affected by the Shenhu, First episode of Zhuqiong and Second episode of Zhuqiong tectonic events (Figure 1D).

The Zhu I Depression is a sub-unit on the northern side of the PRMB. It has a NE-SW orientation and covers an area of approximately 38,000 km², with the Central Uplift Belt to its south, the Zhu III Depression to its west, and the Northern Uplift Belt to its north (Figure 1A). The Zhu I Depression can divide into five sags, namely, Enping Sag, Xijiang Sag, Huizhou Sag, Lufeng Sag, and Hanjiang Sag from west to east, with four low uplifts - Enxi, Huixi, Huilu, and Haifeng low uplifts, separating them from each other (Zhong et al., 2014). The Zhu I Depression underwent only two rift phases from the middle Eocene to the early Oligocene since the Shenhu event did not occur in this area (Ding et al., 2015). These two rift phases resulted in the creation of the Wenchang and Enping Formations. Therefore, two rift phases were named after “Rift Phase 1 (RP1)” and “Rift Phase 2 (RP2)”, respectively (Ma et al., 2020; Figure 1D).

The Xijiang south Sag (Panyu 4 Sag), which has similar structure and evolution characteristics to the Zhu I Depression, is a sub-unit on the south-central side of the Zhu

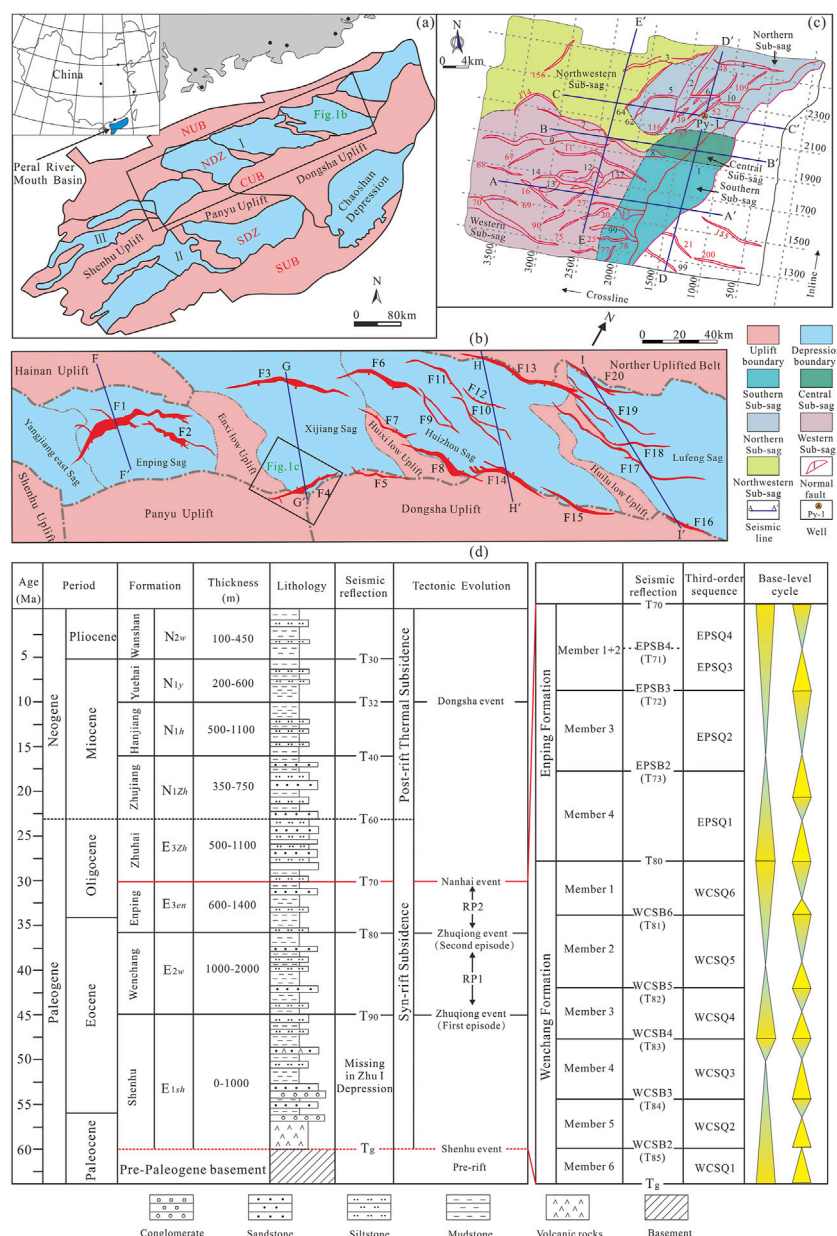


FIGURE 1

(A) Location and structural units of the Pearl River Mouth Basin, South China Sea, NUB - Northern Uplift Belt, NDZ - Northern Depression Zone, CUB - Central Uplift Belt, SDZ - Southern Depression Zone, SUB - Southern Uplift Belt, I - Zhu I Depression, II - Zhu II Depression, III - Zhu III Depression (Liu et al., 2019); (B) The structural units and major faults of the top of the basement in the Zhu I Depression (Hu, 2019); (C) The structural units and major faults of the Panyu 4 Sag; (D) Tectonostratigraphic evolution of the Pearl River Mouth Basin (modified after Chen and Zhang, 1991; Zhang et al., 2003; Zhu et al., 2008).

I Depression (Figure 1C). The tectonic location and multi-phase structural evolution have resulted in complex internal structure, and the unit has undergone multi-phase erosion. To the east of the boundary faults, the sequence was terminated by the overlying interface on the west side during the early stage. To the north of the boundary faults, the sequence was terminated by the overlying interface on the south side during the late stage. The Panyu 4 Sag could be subdivided into five secondary negative structural units, namely, Northern, Central, Southern, Western, and Northwestern Sub-sags (Figures 1C, 5). Therefore, the study

of the Panyu 4 Sag could well reflect the internal structure and evolution characteristics of the Zhu I Depression.

3 Data and methodology

3.1 Date

Two-dimensional (2D) and three-dimensional (3D) seismic data were utilized to describe the geometries and kinematics of

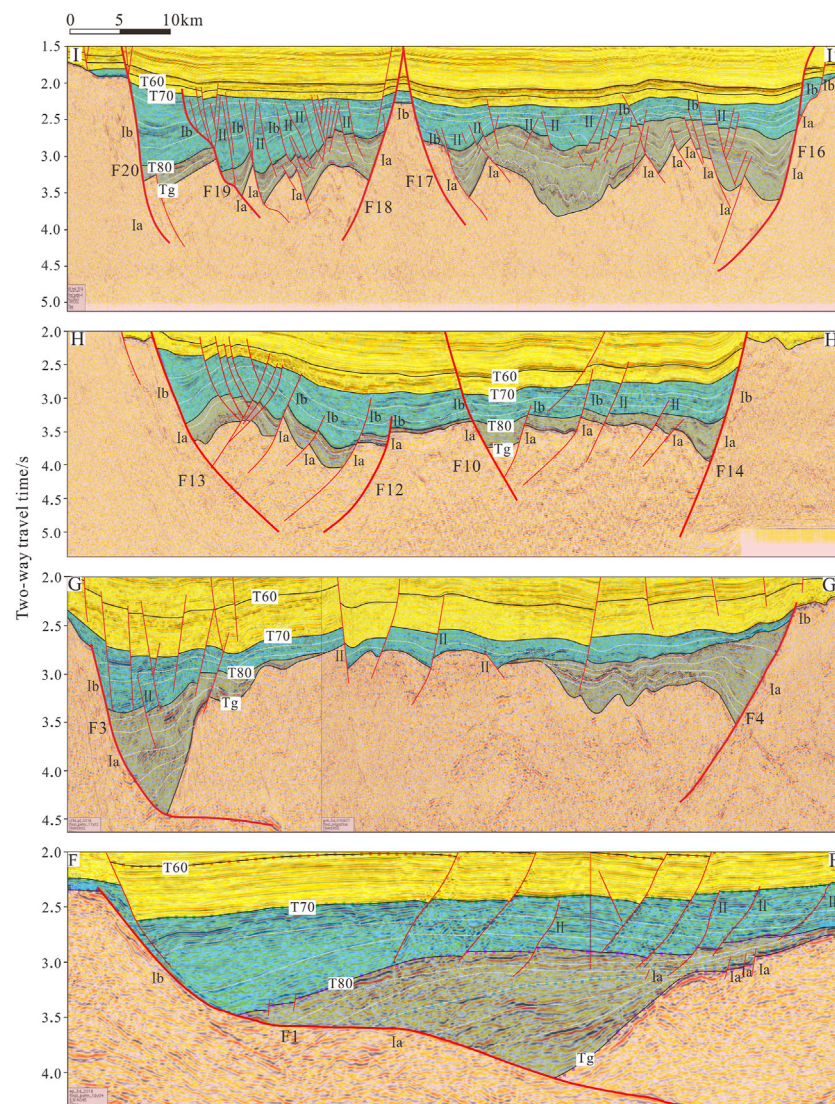


FIGURE 2

Typical seismic profiles of fault system in the Zhu I Depression (for section locations, see Figure 1B).

rift-related faults, including boundary faults and secondary faults. The seismic data, provided by Shenzhen Company of CNOOC, had high dominant frequency and consisted of two parts. The first part was the seismic data of the entire Zhu I Depression (Figure 1B; Figure 2, 3), which was used to explain the geometries of faults and the transformation of the stress field during different rift periods. The second part was the local data volume of the Panyu 4 Sag, which was used to analyze the fault evolution during different periods. Seismic data interpretation and fault throw curves were conducted along the fault strike in the main fault zone of the Panyu 4 Sag.

3.2 Methodology

In this work, several regional unconformities (Tg, T80 and T70) were identified based on the strata terminations and seismic reflections, separating the pre-rift, RP1, and RP2 periods. In

addition, combining drill well data, some unconformity surfaces (T85, T84, T83, T82, T81 from bottom to top) were identified within the RP1 in the Panyu 4 Sag. These unconformity surfaces, together with regional unconformity surfaces (Tg and T80), divided the Wenchang Formation into six members (Members six to one from bottom to top (Figure 8A) in the Eocene rift period. Interpreted horizons were demarcated by synthetic seismograms, which were consistent with stratigraphy, and had the same names (Figure 1D).

Different types of faults were identified based on seismic data, including twenty major faults (F1-F20) representing the boundary faults or interior major faults of the RP1 and RP2 periods in the whole Zhu I Depression (The RP1 and the RP2; Figures 1B, 2, 3). The relationship between different types of faults was analyzed by interpreting four NW-SE sections crossing the Zhu I Depression (Figure 2). Additionally, three NWW-SEE and two NNE-SSW sections crossing the Panyu 4 Sag were analyzed to illustrate the

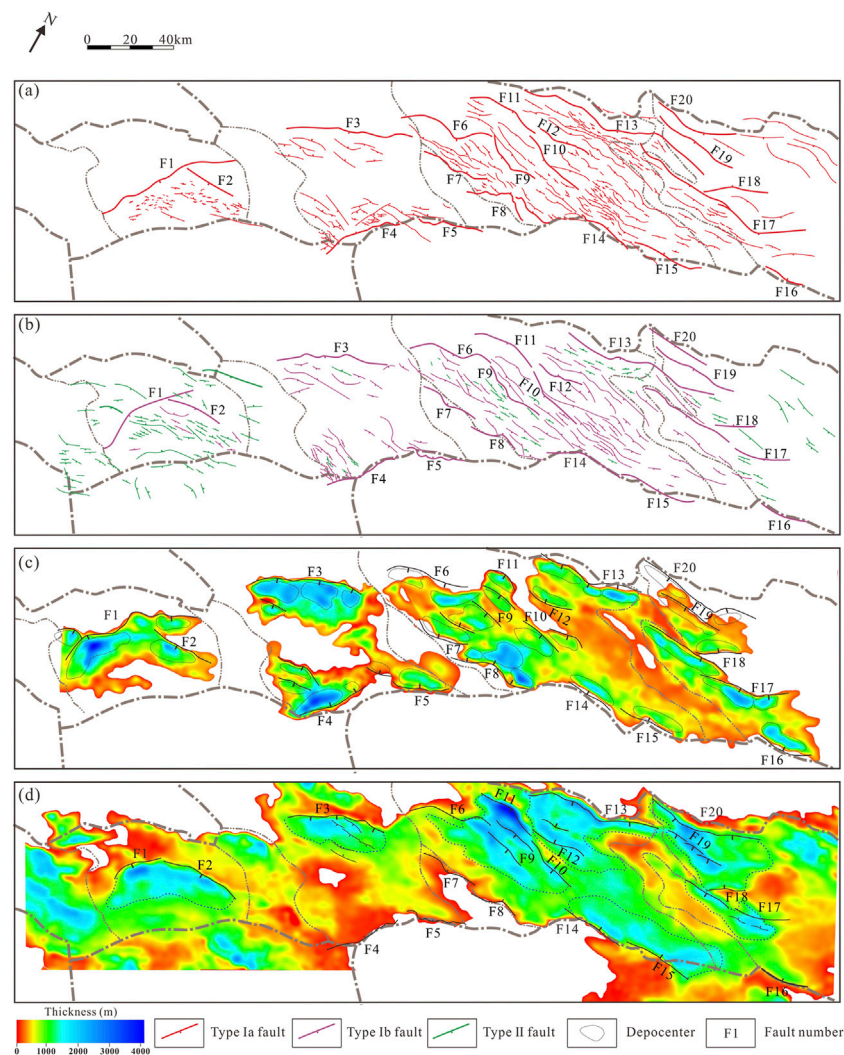


FIGURE 3

(A) The distribution of faults during the RP1; (B) The distribution of faults during the RP2; (C) The sedimentary thickness during the RP1; (D) The sedimentary thickness during the RP2.

structural units and evolution of faults in two different rifting directions (Figure 5).

The seismic profiles of the Panyu 4 Sag, PY-1 drilling data, and logging data were used to interpret, calibrate and close thickness of six members of the Wenchang Formation (Figures 8B–F) in Panyu 4 Sag were calculated by using seismic interpretation and extrapolation of structural trends (Figure 8). Crossline and inline were extrapolated and closed with an accuracy of 1 km × 1 km on the workstation. Based on these analyses, the prototype basin was established (Figure 10).

The tectonic subsidence history of the Panyu 4 Sag was recognized using the back-stripping analysis (balanced cross section) technique. A seismic line was chosen as a representative profile to demonstrate the basin structure and stratigraphic variations within the sag (Figure 9).

Based on the distribution of faults and local stress field during different stages in Panyu 4 Sag of the Zhu I Depression, one analogue

model was set up to simulate the structural evolution. The sandbox model measured 57 cm long and 60 cm wide and was driven by one motor at the left side of the model and one plastic sheet measuring 30 cm × 17 cm × 1 mm (Figure 11A). A thin elastic rubber sheet (thickness of 1 mm) was placed at the bottom of the model and fixed on two sidewalls from the left and right sides to initiate extension from the left side. One plastic plate (The size shown in plastic plate 1 of Figure 11A) was placed on the rubber sheet close to the right side to simulate the local granite located on the hanging wall of the Fp1 in the basement. Another plastic plate (Plastic plate 2 in Figure 11A) measuring 30 cm × 15 cm × 5 cm was placed on the steel plate close to the left side to represent the basement granite which was located on the hanging wall of the faults Fp7, Fp8 and Fp64 in the basement. During extension stages 1–3, the left mobile sidewall was made to pull out at a rate of 0.25 mm/min. One layer of loose sand (total thickness of 6.2 cm) was sieved at the bottom of the model to simulate the metamorphic sedimentary layer (Table 1a; Figure 11B). The deformation of the model surface was covered by

TABLE 1 Kinematics and scaling parameters of models presented in this study.

a) Kinematics of models presented in this study					
Deformation phase (#)	Extensional stage 1		Extensional stage 2		Total thickness (cm)
	Extension direction	Total extension amount (cm)	Extension direction	Total extension amount (cm)	
1	NW-SE	1.5			6.2
2 ¹	NW-SE	3			6.5
2 ²	NW-SE	6.5			6.5
2 ³	NW-SE	12			6.5
3 ¹	NW-SE	12.5			7
3 ²	NW-SE	15			7
4 ¹			N-S	1	7.3
4 ²			N-S	2	7.3
5	Subsidence stage after erosion				7.9
b) Scaling parameters of the model					
Scaling Parameter		Model	Nature		Model/Nature ratio
Length, <i>l</i> (m)		0.01	1,000		1.0×10^{-5}
Density (sand) ρ (kg m ⁻³)		~1,450	~2,700		0.54
Gravity acceleration, <i>g</i> (m s ⁻²)		9.81	9.81		1
Stress, σ (Pa) $\sigma^* = \rho^* g^* l^*$					$\sim 0.54 \times 10^{-6}$
Grain shape		Well-rounded	-		-
Grain size (mm)		0.20	-		-
Friction angle		~36	~40		0.9
internal friction μ		0.73	0.84		0.86
cohesion (τ_0) (Pa)		100-140	10^7		$1.0\text{-}1.4 \times 10^{-5}$

an additional layer of white sand (thickness of 0.3 cm) to represent Member 6 after 1.5 cm bulk extension from the left side. The left motor continued to move until the total extension reached 12.0 cm, then a 0.5-cm-thick white sand layer was sieved on the depressed area of the deformation model to represent the deposition of Members 5 and 4. The left motor was stopped after 15.0 cm of total extension, and a 0.3-cm-thick white sand layer was sieved on the model surface to represent the deposition of Members 3 and 2. Eventually, three layers of white sand (total thickness of 1.1 cm) were sieved uniformly on the surface of the first layer of sand to represent the deposition of the Wenchang Formation (E_2w). Following the subsidence, the model was pulled by the plastic sheet at a rate of 0.2 mm/min to simulate the second extension stage. The model was driven by the plastic sheet to continue the second extension stage simulation until 2.0 cm of total displacement reached.

Finally, we obtained a structural evolution model of the Zhu I Depression (Figures 13, 14). The seismic interpretation was performed using Geo-frame software; data statistics and sandbox model reconstruction were performed using Petrel software. All statistical graphics were acquired through Shuanghu software.

4 Fault systems of the Zhu I depression

4.1 Distribution of faults

The study area comprised four fault sets with different strikes, including NNE, NE-NEE, EW, and NWW directions. Most of these faults were syn-rift faults during the Paleogene, and some post-rift faults formed during the Neogene. Based on the control exerted by the faults on the internal structural units of the depression, the Paleogene syn-rift faults in the Zhu I Depression could be divided into the main controlling boundary faults and the accommodation faults within the depression. The main controlling boundary faults controlled the formation and development of the depression, and had an important influence on the deposition process in the Paleogene. Approximately twenty such faults could be identified in the Zhu I Depression, including two faults (F1-F2) in the Enping Sag, three faults (F3-F5) in the Xijiang Sag, ten faults (F6-F15) in the Huizhou Sag, and five faults (F16-F20) in the Lufeng Sag. These faults were mainly distributed in the northern and southern parts of the depression zone and in the margins of low uplifts inside the depression, and they mostly cut into the basement, with a large fault throw (more than 1,000 m in Tg reflection layer), long extension distance (more than 30 km), and strong sedimentation controlling effects (sedimentation thickness of Wenchang and Enping Formations is more than 500 m). Most of the fault surfaces were listric, and a few of them had planar and ramp-flat surfaces. In terms of the dip angle of the faults, the western boundary faults of the depression (Enping Sag and Xijiang Sag) were mainly low-angle normal faults with dips ranging from 17° to 36°, while the eastern boundary faults of the depression (Huizhou Sag and Lufeng Sag) were mainly high-angle normal faults, except for the fault F6. The dip angles of the faults were generally greater than 40°. Accommodation faults

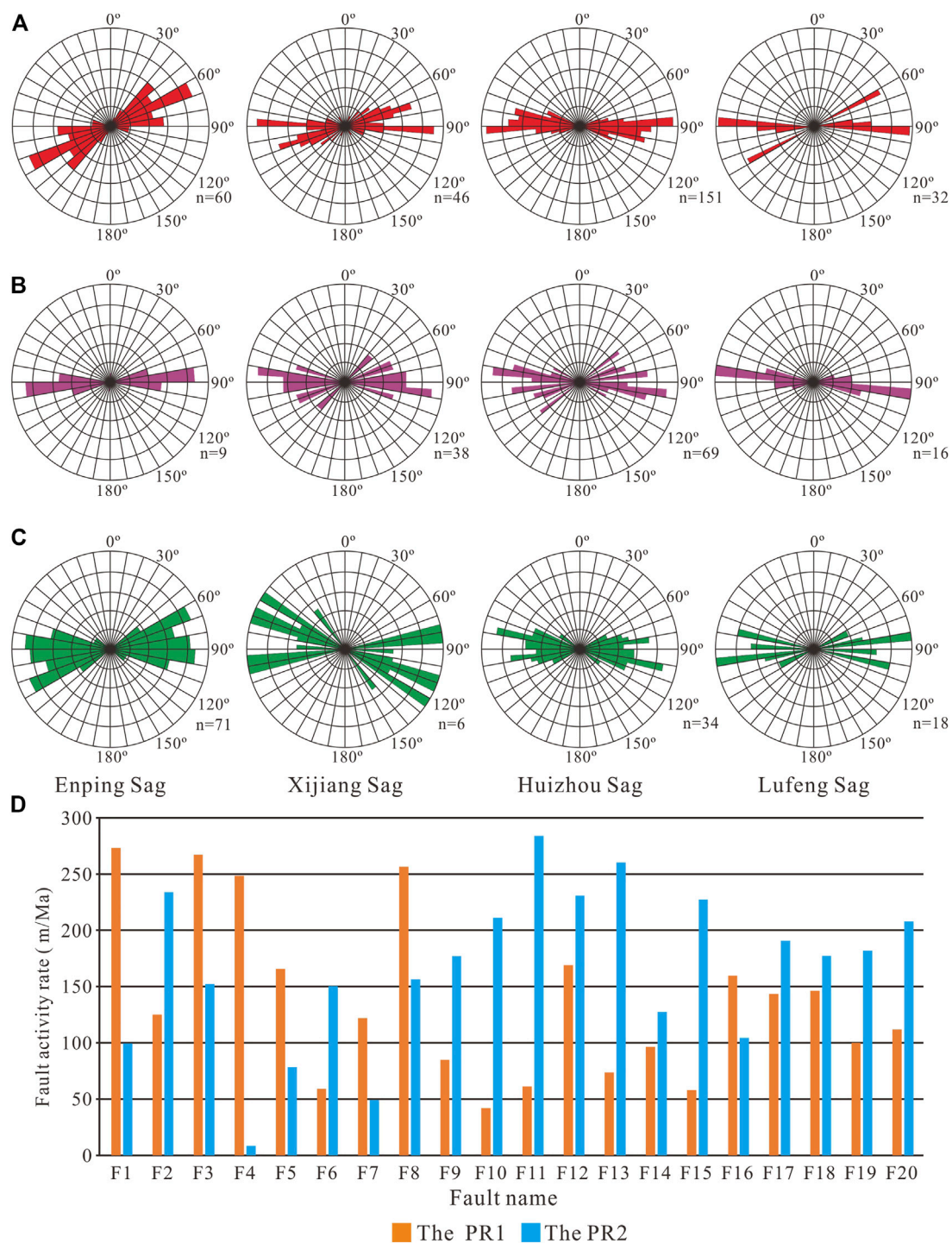
were mainly formed by displacement adjustment during the activity of the main controlling boundary faults and had a controlling effect on the development of sub-sags, secondary structural belts, and local structures. They were characterized by a short extension (less than 20 km), small fault throw, and steep dip angles (above 45°) during the early deformation stage. On dip-oriented profiles, these faults cut into the basement and ceased in the Neogene, being overlain by nearly horizontal strata.

4.2 Evolution of faults

During the rift stage, most faults were active until the early Oligocene (Below the T70 unconformity interface), and some of the faults continued to be active until the Quaternary. Based on the period during which the faults were active, the rifting structural layers could be divided into the RP1 and RP2 fault structural layers by the T80 unconformity interface. Most newly generated faults during the RP1 cut downward to the basement and upward to the Enping Formation, some faults cut downward to the basement and ceased in the Wenchang Formation, and a few faults only developed within the Wenchang Formation. Most of the faults in the RP2 were inherited faults from the RP1, some newly generated faults in the RP2 cut the Wenchang and Enping formations, some faults cut into the basement, and a few faults only developed within the Enping Formation.

The large number of normal faults developed during the early rifting stage formed the pre-existing weak surface for the development of the late faults, which had an important influence on the development of the late faults. Under the same stress state, it is much easier for pre-existing faults to re-activate along the weak zone than for the new faults with the same attitude to be generated (Morley et al., 2004; Tong et al., 2014). Whether the early normal faults inherit activity in the late rifting stage depends on many factors, such as the tectonic strength, the extensional direction, and the magnitude of the intersection angle between the stress direction and the strike of the pre-existing faults during the late rifting stage. New faults with direct expression of the stress field in the geological body were not influenced by earlier pre-existing faults, and their characteristics best reflect the tectonic dynamics (Morley et al., 2004). Therefore, to study the kinetic characteristics of the RP1 and the RP2, it is necessary to separately investigate the inheritance and neogenesis of faults during the two rifting phases. Based on the development of inherited faults, the active faults in the two rifting stages are divided into three types: Type Ia faults are those that fault began to develop during the RP1. Type Ib faults are inherited Type Ia faults that continued to develop during the RP2; Type II faults are those that began to develop during the RP2 (Figures 2, 3).

The characteristics of fault activity and the spreading of syn-sedimentary faults in different periods can fully reflect the evolutionary characteristics of the fault system. The fault activity could be characterized quantitatively by the throw between the hanging wall and footwall and the fault activity rate (Xu et al., 2010). Analysis of the activity of the main

**FIGURE 4**

(A) The strike rose diagram of type Ia faults; (B) The strike rose diagram of type Ib faults; (C) The strike rose diagram of type II faults; (D) The fault activity rate of main faults during the RP1 and the RP2.

boundary faults (F1-F20) in the study area revealed obvious differences in the activity of different strike faults in each period in the study area. The NE-NEE-trending faults exhibited strongest activity during the RP1, and the intensity of activity along other faults followed the order NNE > NE-NEE > NWW > EW. The maximum fault activity rate of F1,

F3, and F4 exceeded 250 m/Ma. A series of depocenters was formed along the strikes of these faults, controlling the development of sedimentary strata. The fault activity rates of the Huizhou and Lufeng Sags were relatively low, ranging from 50 to 200 m/Ma (Figure 4D). There were multiple groups of fault strikes, which jointly controlled the development of the

sags, forming a deposition unit with a wide area. The fault activity decreased significantly but was still strong. A large number of EW-trending and NW-trending faults developed within the depression in the RP2. The intensity of fault activity was EW > NWW > NE-NEE > NNE. At this time, strong fault activity was mainly concentrated in the eastern part of the northern margin of the depression, where the fault activity rate of the F11 and F13 exceeded 250 m/Ma, while that of other faults mainly ranged from 100 to 200 m/Ma (Figure 4D). NE-NNE-trending faults stopped developing in the late RP2 and were replaced by new faults in the later period. During this period, the depositional range of the Zhu I Depression was expanded, but the depocenter was reduced to one. As a result, the thickness of the Enping Formation was thinner compared to that of the Wenchang Formation (Figures 3C,D).

The fault strike statistics provided valuable information for analyzing the stress field during fault formation. The dominant strike average azimuths of type Ia, type Ib, and type II faults were 75°, 85°, and 90° (Figures 4A–C), which revealed that the minimum principal stress (σ_3) directions in the RP1 and RP2 of the Zhu I Depression changed from the SSE (~165°) to near-EW (~180°). Moreover, the direction of the minimum principal stress in different sags from west to east within the Zhu I Depression changed to a certain extent (Zhou et al., 1995), possibly due to the existence of structural weak surfaces, which resulted in the formation of regional stresses that acted on different local structural deformation zones and led to stress re-orientation (Corti et al., 2013; Philippon et al., 2015). The change in the direction of minimum principal stress could also have been related to clockwise rotation during the dragging of the ancient SCS plate (Liu et al., 2018).

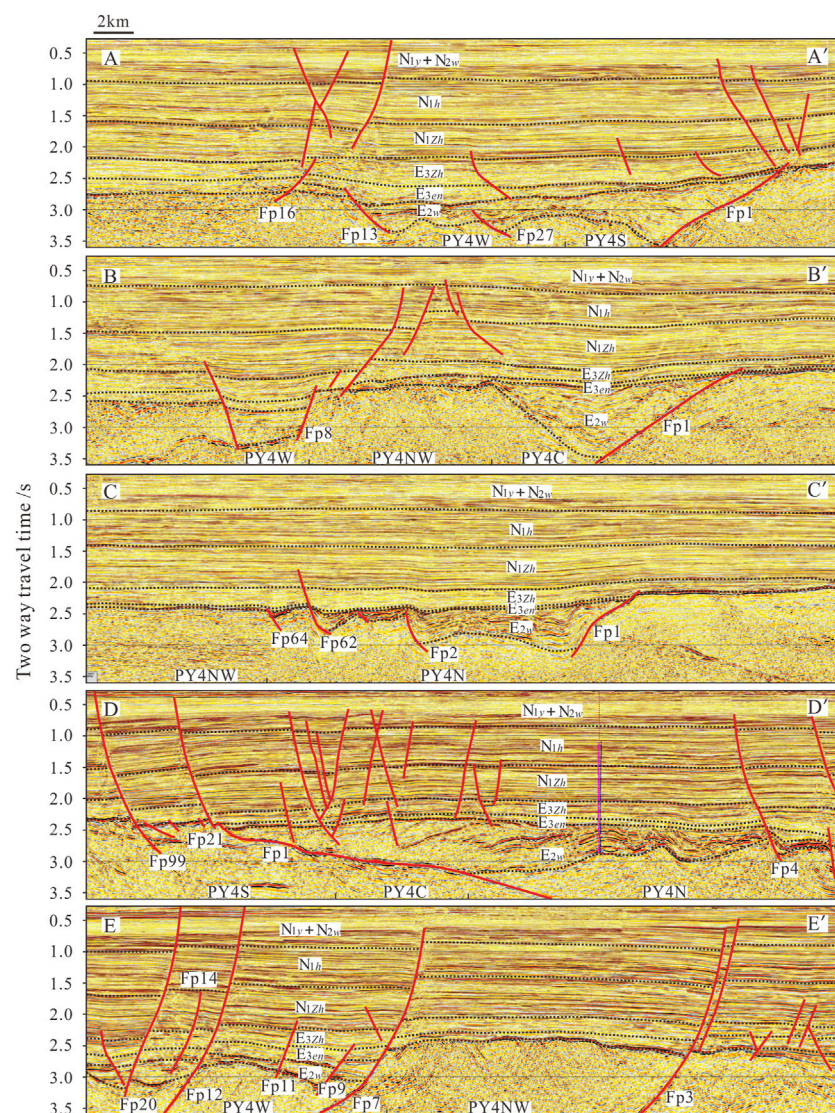


FIGURE 5

Seismic profiles of the Panyu 4 Sag (for section locations, see Figure 1C). AA', BB', CC', DD', EE' - Seismic line; PY4S - Southern sub-sag; PY4N - Northern sub-sag; PY4C - Central sub-sag; PY4W - Western sub-sag; PY4NW - Northwestern sub-sag; E2w - Wenchang Formation of Eocene; E3en - Enping Formation of later Eocene and early Oligocene; E3zh - Zhuhai Formation of Oligocene; N1zh, N1h, N1v, respectively, denote the Zhujiang, Hanjiang, Yuehai Formations of Miocene; N2w - Wanshan Formation of Pliocene.

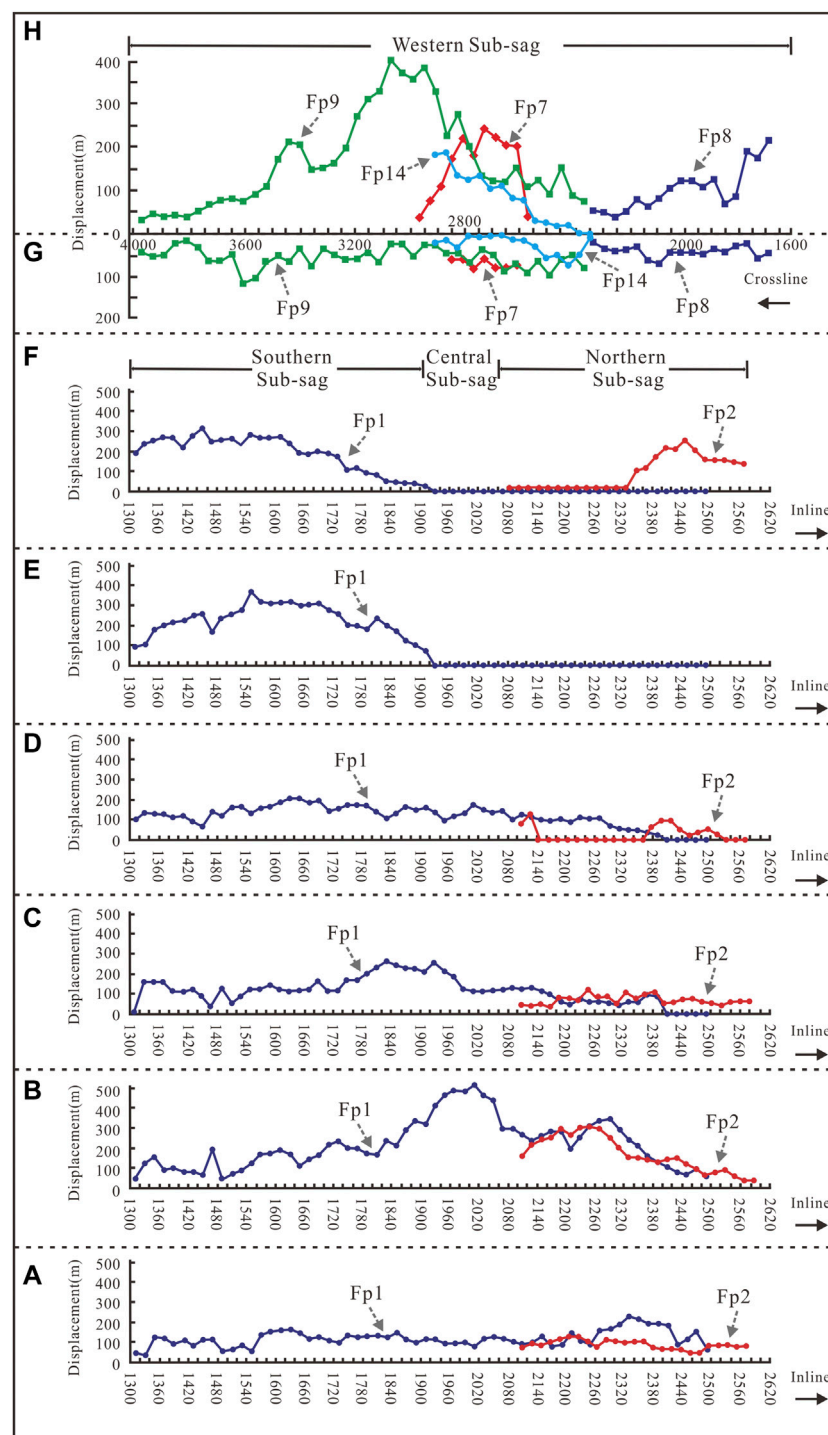


FIGURE 6

The Displacement-distance curves of main controlling faults (Fp1, Fp2, Fp7, Fp8, Fp9, Fp14) in the Panyu 4 Sag. The Displacement-distance curves of Fp1 and Fp2 during the RP1 (A–E) and RP2 (F); The Displacement-distance curves of Fp7, Fp8, Fp9 and Fp14 during the RP1 (G) and RP2 (H).

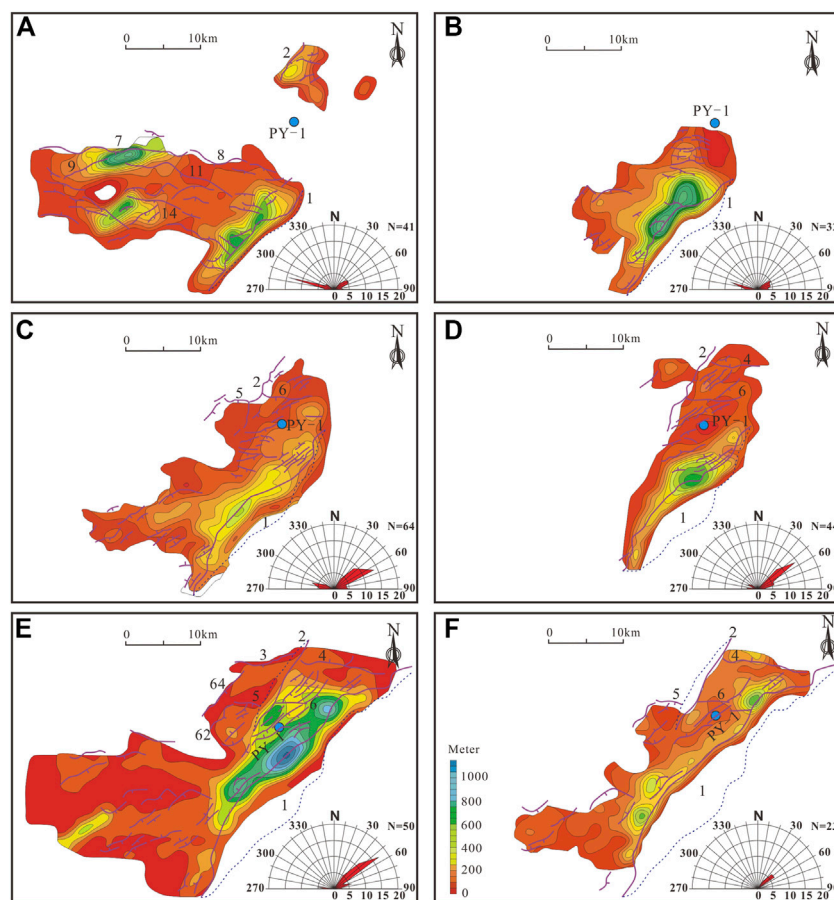


FIGURE 7

The comparison of syn-sedimentary faults, strike rose diagram of faults and sedimentary thickness distribution from Member 1 to Member 6 [from (A–F)] of Wenchang Formation.

5 Structural-sedimentary evolution of the Panyu 4 Sag

5.1 Structural units of the Panyu 4 Sag

The five sub-sags of Panyu 4 Sag exhibited some differences. Northern Sub-sag consisted of a full-graben with faults dipping to the east and west (Figures 1C, 5). Owing to changes in the intensity of activity of the main controlling faults on the eastern and western sides, the structural characteristics of Northern Sub-sag demonstrated variations during different periods. During the deposition of Member 6, Fp1 (F4) on the eastern side was more active than Fp2 on the western side (Figure 6A), resulting in thicker sedimentary strata on the eastern side and thinner sedimentary strata on the western side. During the deposition of Members 5 and, Fp1 and Fp2 exhibited the same intensity of activity (Figures 6B,C), forming a graben and a series of secondary half-graben assemblages, which developed in the footwall of Fp2. During the deposition of Member 3 to 1, the high intensity of activity of Fp2 resulted in thinner sedimentary strata on the eastern side and thicker sedimentary strata on the western side (Figures 6D–F).

The sedimentation of Central Sub-sag, which was continuously controlled by Fp1 on the eastern side, formed the central part of the

main sag with features of a half-graben. The eastern side was bounded by a fault. On the western side, the sequence was terminated by the overlying interface (Figures 1C, 5).

NW-SE-trending extension during the deposition of Members 6 to 2 caused the formation of Southern Sub-sag, which featured a half-graben with a boundary fault on the east side (Figures 1C, 5). The portion of the eastern steeply sloping area with the maximum sedimentary thickness was located close to the hanging wall of Fp1. Owing to the near-S-N-oriented extension during the deposition of Member 1, Fp1 inherited the original active condition under the oblique extension, forming an inherited half-graben. The near-E-W-trending faults cut the Wenchang and Enping Formations on the seismic profile, but these faults had no obvious controlling effect on deposition.

Before the deposition of Member 1, Western sub-sag was a sloping landform. Most of the strata from Members 6 to 2 were thinning or missing (Figures 1C, 5). However, it formed a half-graben with a boundary on the northern side during the deposition of Member 1.

Northwestern Sub-sag was derived from the eastern extension of the Xijiang Middle-Low Uplift (Figures 1C, 5). The Wenchang Formation was missing from the profile. A few faults began to develop during the deposition of the Enping Formation.

5.2 Fault system of the Panyu 4 Sag

The fault systems could be divided into early and late extensional fault systems based on the principle of combination and matching of fault phases in the Panyu 4 Sag. The early fault system referred to faults that developed during the deposition of Members 6 to 2, whereas the late fault system mainly referred to faults that formed during the deposition of Member 1.

The early fault system was dominated by NE-trending faults (40–60°), followed by a few near-EW-trending and NEE-trending faults (Figure 7). The NE-trending faults were cut by the near-EW-trending faults, which were transverse accommodation faults, and the NEE-trending faults developed and aligned diagonally during the deposition of Members 3 and 2 (Figures 7B,C). The fault system in this period was mainly a combination of normal faults formed under the action of NW-SE-oriented extensional stress. The NEE-trending normal faults formed during the deposition of Member 2 (Figure 7B), possibly during the period when the stress field began to shift from the NW-SE direction to the NNW-SSE direction. They developed in the near-S-N-trending crossline and exhibited steep dip angles, short extents, and features indicating that they were newly developed. The near-EW-trending transverse accommodation faults (Fp4, Fp5, Fp6, and Fp10) had a controlling effect on the deposition of Members 6 to 4 (Figures 7D–F).

The late fault system was dominated by NWW-trending faults (280–290°) that developed from the deposition of Member 1 of the Wenchang Formation to the Enping Formation (Figure 7A), with a few NE-trending faults (50–70°). The NWW-trending faults were arranged in parallel belts, and the faults in the same belt were distributed in a segmented pattern, while the NE-trending faults were arranged in an arc-shaped series and were cut by the NWW-trending faults. This phase of the fault system was a combination of tensor faults formed under near-S-N-oriented extensional stresses. The NWW-trending faults were formed in the direction of vertical tension and exhibited steeply dipping slab-like surfaces; they continued to be active after the deposition of the Wenchang Formation. The NE-trending faults were inherited faults with tensional and torsional features that were based on pre-existing faults. The NE-trending main boundary faults, such as Fp1 and Fp2, exhibited large extents. The NWW-trending sag-controlled faults, such as Fp7, Fp8, Fp9, Fp11, and Fp14, had large extents (Figures 6G,H), whereas the curved NE-trending faults had small extents.

5.3 Thickness distribution of Wenchang Formation

Six members of the Wenchang Formation could be identified in the Panyu 4 Sag. (Zhu et al., 2014; Ge et al., 2019), and the following features of each member were noted (Figure 7).

Member 6 had a relatively small distribution area, which was narrow along the NE direction with a maximum thickness of 450 m; it was confined to the main sag (Northern, Central, and Southern Sub-sags). There was a small amount of sediment on the slope on the southeastern side (Figure 7F). The distribution area of Member 5 was the largest in Wenchang Formation, with the overall strike oriented in the NE-SW direction. In addition to the main sag, it was found on the slope, with a maximum thickness of

1,100 m (Figure 7E). The distribution area of Member 4 was smaller than that of Members 6 and 5. It exhibited a NE orientation and was confined to the northeastern part of the main sag; the maximum thickness of Member 4 was 500 m (Figure 7D). A gradual reduction in the distribution area was observed from Member 4 to Member 2, reflecting the gradual shrinkage of the basin; the maximum thicknesses of Members 3 and 2 were 400 m and 650 m, respectively (Figures 7B,C). The distribution area of Member 1 was larger than those of Members 3 and 2; it covered the entire western slope area, and the strike of the thickness contour exhibited a shift to a near-EW orientation, which reflected the characteristics of basin regeneration. The maximum thickness was 700 m (Figure 7A).

There were three relatively independent depocenters in Member 6. The thickness and distribution area of the depocenters in the north were slightly larger than those in the south. From Members 5 to 2, three independent depocenters gradually evolved into a unified depocenter and migrated from north to south. The axis of the depocenter was oriented NE, parallel to the main controlling boundary fault on the eastern side, indicating that the intensity of activity of the controlling boundary fault gradually increased from north to south. The depocenter on the southwest slope was oriented NEE, whereas that in the main sag on the eastern side was oriented NE, which reflected the coexistence of inheritance and regeneration.

5.4 Eroded thickness recovery

The eroded thickness contours of Member 1 were distributed throughout the region, but the scale of the erosion and the strike of the contours varied. In Western Sub-sag, the eroded thickness was less than 100 m, and the contour line was oriented EW. The erosion of the T_{80} interface on Member 1 could not be observed clearly. Furthermore, the structural trend extrapolation method was not very reliable for the calculation of the eroded thickness, and only a small amount of estimation was possible, so the actual eroded thickness was of little significance. The NE-trending eroded thickness contours in Northern, Central, and Southern Sub-sags showed an anticlinal structure in the seismic profile, so the eroded thickness was relatively reliable, and the maximum value was approximately 260 m, which was equivalent to the thickness of the core of the anticline (Figure 8B). The eroded thickness contours of Member 2 were only distributed on the southern side of Northern Sub-sag and southwestern side of Southern Sub-sag. The area with the greatest eroded thickness was the same as that of Member 1, and the maximum eroded thickness was 200 m (Figure 8C). The eroded thickness contours of Member 3 were only distributed in Northern Sub-sag, and the eroded area of E_2w_3 was smaller than that of Member 2. The area with the largest amount of erosion was the same as that of Member 2, and the maximum amount of erosion was 120 m (Figure 8D). The part of the northeast side that extended slightly northward was the result of the erosion of the T_{81} unconformity. The eroded thickness of Members 3 to 1, whose maximum eroded thickness was located at the same position with the total thickness being less than 600 m, was mainly caused by the T_{80} unconformity. The eroded thickness contours of Member 4 were distributed in narrow strips in Northern, Central, and Southern Sub-sags, but the causes of erosion varied (Figure 8E). The T_{83} unconformity was the main cause of the eroded thickness of Member 4 in Southern and

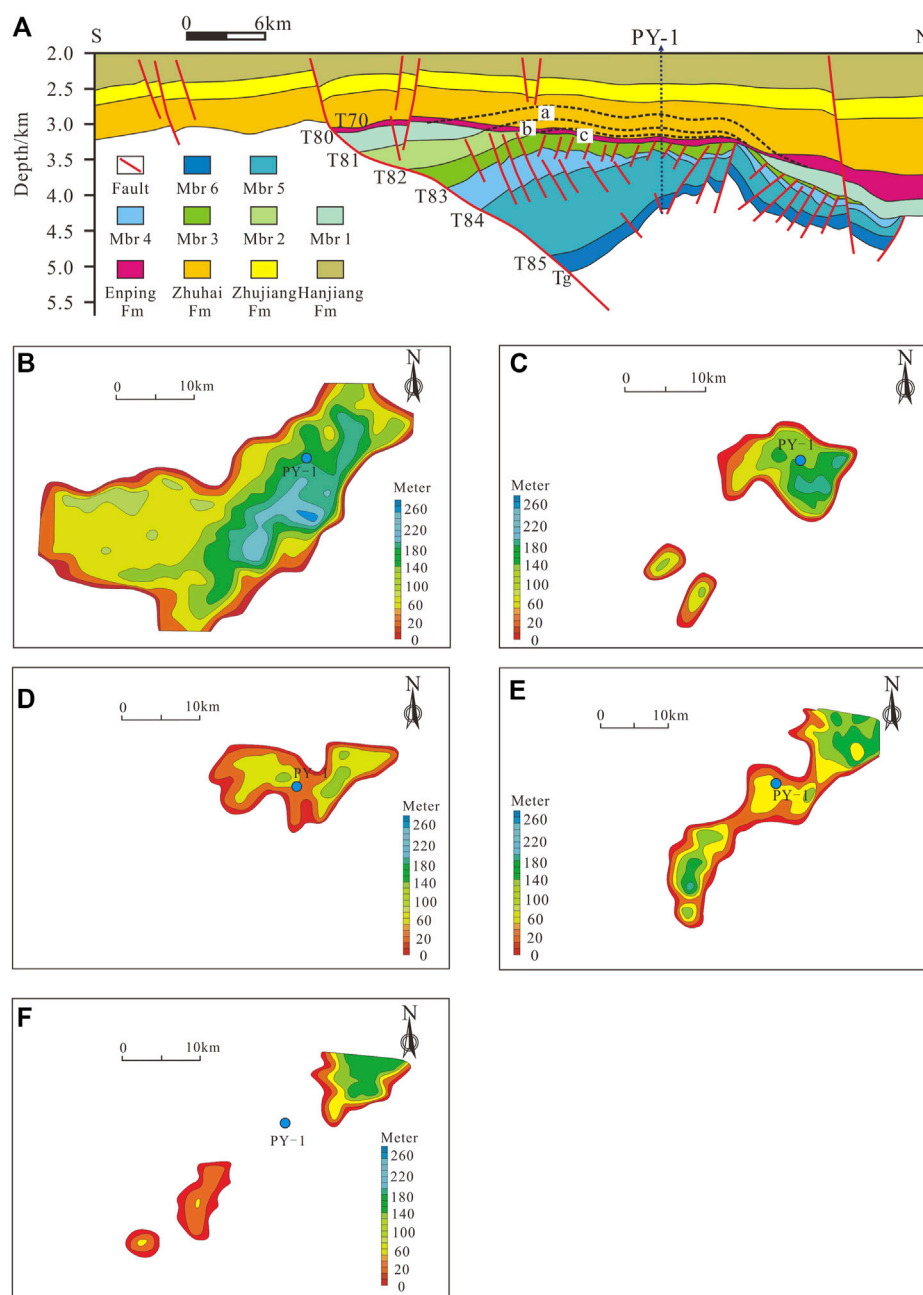


FIGURE 8

(A) The principle of structural trend extrapolation to restore erosion amount. (A) Eroded thickness of Member 1; (B) Eroded thickness of Member 2; (C) Eroded thickness of Member 3; Mbr - Member, Fm - Formation. The eroded thickness recovery from Member 1 to Member 5 [from (B–F)] in Panyu 4 Sag.

Central Sub-sags. The erosion was pronounced at the zone of transition between the slope and depression; the maximum thickness was close to 200 m, and the contour trend was oriented NE. In Northern Sub-sag, the eroded thickness contours were oriented EW. The maximum erosion was 180 m and the point thereof was close to the main boundary fault on the eastern side; it formed due to the erosion of the T_{80} unconformity. In contrast, the eroded thickness was significantly reduced (less than 100 m) on the western side and was caused by the erosion of the T_{81} unconformity, indicating that the intensity of erosion of T_{80} was greater than that of T_{81} . The distribution of eroded thickness

contours for Member 5 was limited, and only a small amount of erosion was distributed in Southern and Northern Sub-sags (Figure 8F). The maximum amount of erosion in Northern Sub-sag was approximately 180 m, and the location of the area of maximum erosion was the same as that for Member 4; it was caused by erosion of the T_{80} unconformity. The maximum eroded thickness of Member 4 was the same as that of Member 5, and both were caused by erosion of the T_{80} unconformity; the total eroded thickness was approximately 360 m. The eroded thickness at this position of Member 1 was 140 m, so the total eroded thickness of the Wenchang Formation at the same position from

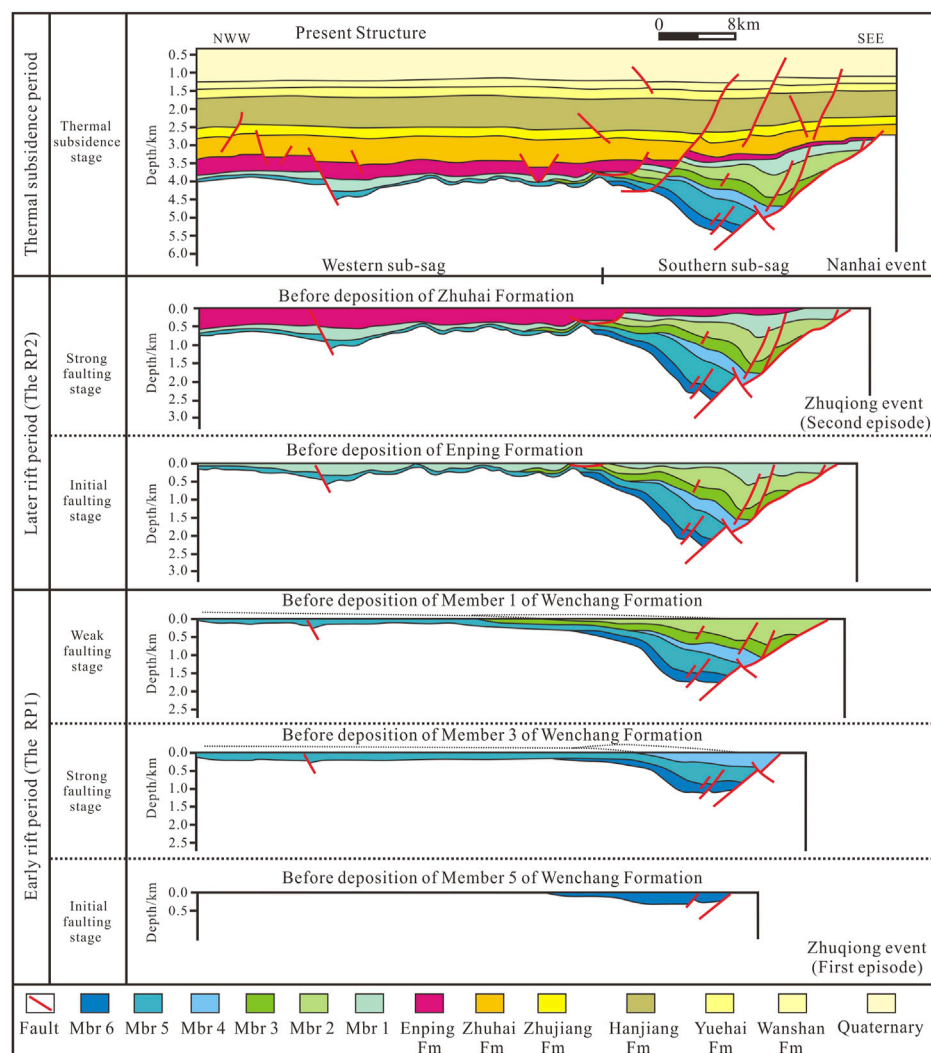


FIGURE 9
Structural evolution profile of Panyu 4 Sag. Mbr - Member, Fm - Formation.

Members 5 to 1 was 500 m. The area with a large amount of erosion was located in the developed part of the anticline, which was a rolling anticline formed in the hanging wall of Fp1 during the period of strong extension. During the formation of the T_{80} unconformity, the fold amplitude increased due to the tectonic uplift of the Zhuqiong event, so it suffered the strongest erosion.

5.5 Evolution of the Panyu 4 Sag

The structural evolution of the Panyu 4 Sag in the Cenozoic could be divided into three periods (six stages), namely, the early rift period, late rift period, and thermal subsidence period (Li, 1989; Zhu et al., 2008; Chen and Zhang, 1991; Zhang et al., 2003; Figures 9, 10). The evolution of the Panyu 4 Sag could be divided into three stages from the deposition of Members 6 to 2, which were the initial faulting stage (IFS), the strong faulting stage (SFS), and the weak faulting stage (WFS, Figure 9).

5.5.1 Early rift period

The IFS referred to the deposition of Member 6. It was equivalent to the beginning of the first episode of the Zhuqiong event, which caused the PRMB to enter a strong rifting phase (the middle Eocene, Figures 9, 10F). The sedimentary filling was mainly composed of coarse clastic rocks formed in rivers, alluvial fans, fan deltas, and similar environments (Jiang et al., 2015). The faults controlling deposition were mainly the NE-trending faults, which developed under an NW-SE tensile stress regime, along with a small number of accommodation faults. Fp1 and small-scale transfer normal faults mainly developed in Southern and Central Sub-sags. In addition, Southern and Central Sub-sags were controlled by faults along the east-west boundary. There were also EW-trending lateral accommodation faults and a few NEE-trending transfer faults in Northern Sub-sag. The intensity of activity of the sag-controlling faults was high in the east and low in the west; it was high in the north and south and low in the central region.

During the process of structural evolution, the boundary of Northern Sub-sag was controlled by Fp1 in the east and Fp2 in the

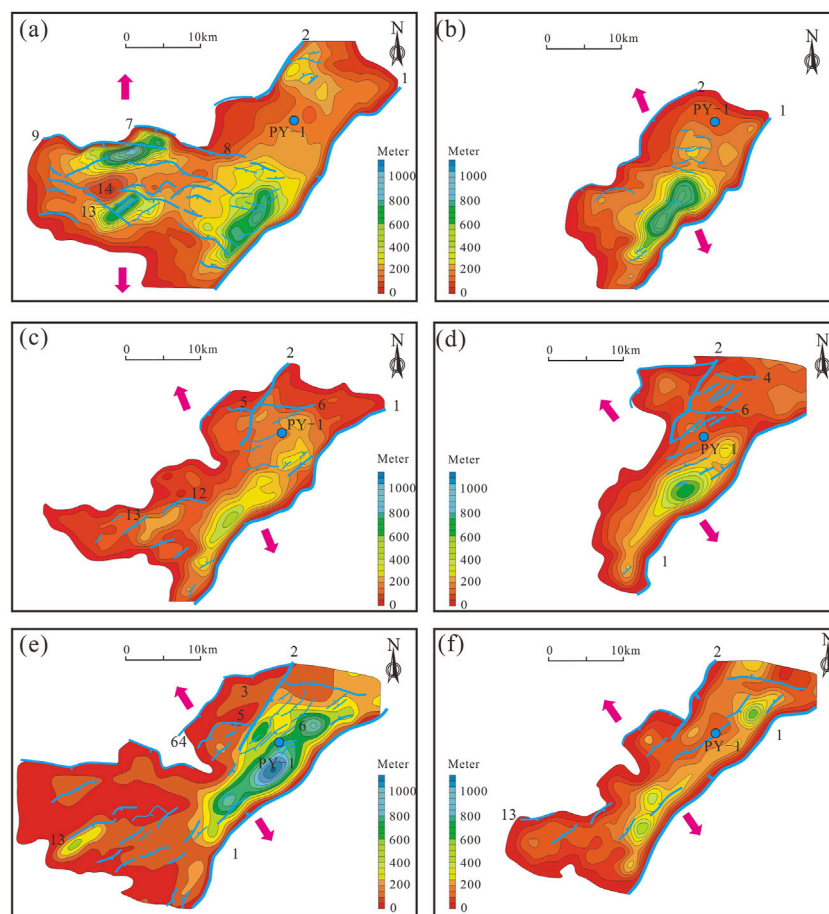


FIGURE 10

The superimposition of original sediment thickness and syn-sedimentary faults from Member 1 to Member 6 [from (A–F)] in Panyu 4 Sag.

west. Because the intensity of activity of Fp1 was greater than that of Fp2, the sedimentary thickness was thick in the east and thin in the west. The depocenter was close to Fp1 on the east side, with a maximum thickness of 450 m. The boundary of Central Sub-sag was controlled by Fp1 on the eastern side, and by two small faults developed on the western side, forming a horst-graben interphase structure. Due to the low intensity of fault activity, the deposited strata were distributed in a plate-shaped area with a thickness of less than 200 m. The Southern Sub-sag was bounded by Fp1 on the east side, forming a half-graben. The distribution area was limited to the main sag, with no deposition on the western gentle slope. Three small depocenters, resembling a string of beads, were located near the main boundary fault on the east side; the maximum thicknesses were 250 m, 400 m, and 330 m. Northwestern Sub-sag was a sub-uplift during this period; it originated from the eastern extension of the Xijiang Middle-Low Uplift. It gradually transitioned from Central Sub-sag and was separated from Northern Sub-sag by faults. Western Sub-sag was a secondary structural unit that gradually transferred from Southern Sub-sag. During this period, it was a gently sloping landform and was in a state of erosion, and no residual strata were present.

The SFS referred to the deposition of Members 5 and 4 (Figures 9, 10d–e). It was equivalent to a period of intense activity during the

first episode of the Zhuqiong event. The area of the sag distribution increased significantly. Faults were mainly planar, listric, and ramp-flat faults, with various combinations of step and domino styles. EW-trending and NEE-trending accommodation faults were widely developed; the structural trend was mainly oriented NE.

Northern Sub-sag exhibited a graben structure with double faults in the east and west. With the increase in the intensity of activity of Fp2, many domino accommodation faults developed on its hanging wall, and two new faults (Fp3 and Fp64) developed on the footwall, forming a half-graben. The distribution area of Members 5 and 4 was significantly larger than that of Member 6, and a new depocenter was developed near Fp2, with a maximum thickness of approximately 500 m. The Central Sub-sag was a half-graben controlled by Fp1 on the east side. The increase in intense activity of Fp1 on the eastern side gave rise to multiple stepped accommodation faults on the hanging wall and caused the development of small listric normal faults on the slope, forming a half-graben. Compared to Member 6, the thickness of Member 5 increased; it was thick in the east and thin in the west, with a maximum thickness of approximately 1,100 m. The thickness of Member 4 was reduced to approximately 300 m, indicating that the intensity of activity of the sag-controlling faults reduced. Southern Sub-sag appeared as a single half-graben, and the intensity of fault

activity at the eastern boundary as well as the thickness of deposits increased significantly. In Southern Sub-sag, the eastern side was bounded by a fault. On the western side, the sequence was terminated by the overlying interface. The distribution area of Members 5 and 4 extended across the entire western slope and was significantly larger than that of Member 6. The depocenter was close to the main boundary fault on the eastern side, with a maximum thickness of 700 m. Northwestern Sub-sag did not receive sediment input. Western sub-sag, which gradually transferred to Southern Sub-sag, was a gentle slope with a small amount of deposition.

The WFS referred to the deposition of Members 3 and 2 (Figures 9, 10b-c). Because structural activity diminished, the subsidence of the basin slowed down, the area of deposition decreased, and the thickness of sediments reduced. In addition to the continuous activity of the sag-controlling boundary faults, a series of small-scale NEE-trending en echelon normal faults developed in the southern part of Northern Sub-sag, which appeared as a stepped combination in the section. The fault activity in Northern Sub-sag weakened, and the deposition area reduced and was limited to the hanging wall of Fp2. The thickness of deposition was significantly reduced, with a maximum thickness of less than 350 m. The intensity of fault activity in Central Sub-sag reduced, but there were some stepped faults trending opposite to the main fault trend. The deposition area reduced, and the thickness of the deposition was approximately 300 m. The intensity of fault activity in Southern Sub-sag reduced, and the deposition area decreased and disappeared on the western gentle slope; the maximum thickness of deposition was close to 400 m. The upper part of Member 4 in the transitional part of the slope and sag was eroded. Northwestern Sub-sag did not receive sediment input, and Western Sub-sag was in the form of a gentle slope with no stratigraphic deposition.

5.5.2 Late rift period

The late rift period started from the deposition of Member 1 in the Panyu 4 Sag and continued until the end of the deposition of the Enping Formation (the late Eocene to the early Oligocene). Based on the deformation style and the distribution characteristics of the local unconformity, it was divided into two stages, namely, an IFS and an SFS (Figure 9).

The IFS referred to the deposition of Member 1 (Figures 9, 10A). It was equivalent to the period of sediment deposition between the two reflection interfaces (T_{80} and T_{81}) on the seismic profiles. The area of deposition increased significantly. Except for Northwestern Sub-sag, the sediments of Member 1 were distributed in other secondary structural units. The seismic reflection was characterized by continuous weak reflection, and the sediments were mainly fluvial deposits. Except for the inherited activities of the NE-trending main controlling boundary faults, the newly developed sag-controlling faults and their associated faults in Western Sub-sag were NWW-trending, forming a half-graben controlled by faults on the north side or a combination of stepped faults. The direction of the fault strike in this period changed from its NE orientation during the early rifting period to the NWW orientation, and the regional stress field changed from NW-SE-trending extension to near-SN-trending extension. This was a significant period of structural transformation in the Panyu 4 Sag with the orientation of the T_{81} unconformity coinciding with

that of T_{80} . Moreover, there was no obvious erosion between T_{81} and T_{80} in the sag, and Member 1 exhibited a large residual thickness. Therefore, it was believed that the T_{81} unconformity in the Panyu 4 Sag might be the product of the beginning of the second episode of the Zhuqiong event, which led to the second rifting of the PRMB and the formation of near-E-W-trending faults.

During the structural evolution, the pre-existing NE-trending boundary faults within the Panyu 4 Sag underwent tensional and torsional activity, and they controlled the deposition of Member 1. In Northern Sub-sag, a small amount of Member 1 sediment was deposited in the upper part of Fp1 and Fp2. At this time, the activity of Fp2 was slightly more intense than that of Fp1, which formed an asymmetrical graben combination that was thicker in the west and thinner in the east, with the thickest part (approximately 300 m) located in the upper part of Fp2. In Central Sub-sag, a small amount of Member 1 was deposited, with a thickness of less than 200 m. The top of Member 2 in Southern Sub-sag suffered a small amount of erosion, and multiple independent depocenters developed in the sag and on the slope, with a maximum thickness of 600 m within the Panyu 4 Sag. Northwestern Sub-sag did not receive sediment input. Western Sub-sag was transformed into a near-SN-oriented extension during this period due to the tectonic stress field, forming a half graben-type assemblage that could be characterized as a “northern fault beside southern stratigraphic overlap”, with faults Fp7, Fp8, Fp9, and Fp14 controlling the boundaries of the half-graben. Furthermore, the early NE-trending faults Fp12 and Fp13 inherited the late activity trends, spreading in a NEE-oriented arc; they were cut by Fp14 and controlled the deposition of Members 6 and 5. Two depocenters, 800 m and 550 m thick, developed in the footwall of Fp7 and Fp14, respectively.

The SFS referred to the deposition of the Enping Formation, which corresponded to the period of stratigraphic deposition between the two reflection layers T_{80} and T_{70} on the seismic profile (Figure 9). The depositional area extended across the entire region, and the sediments changed to fine clastic sediments formed in a lacustrine marsh environment. The depositional thickness was mainly controlled by the near-EW-trending faults; the depositional thickness was thick in the west and thin in the east, and thick in the south, and thin in the north. Compared with Member 1, the distribution area and depositional thickness increased significantly, the intensity of the activity of the sag-controlling fault increased, and erosion associated with the T_{80} angular unconformity peaked. Thus, this stage belonged to the stage of strong fault subsidence, which was equivalent to the period of strong activity during the second episode of the Zhuqiong event.

The intensity of activity of the near-EW-trending fault Fp3 in Northern Sub-sag increased during this period, forming a boundary fault that controlled the deposition of the Enping Formation. The east was bounded by a fault. On the west side, the sequence was terminated by the overlying interface. Member 2 and Member 1 in Central Sub-sag suffered erosion. The T_{80} interface in Southern Sub-sag had obvious truncation and erosion. The near-EW-trending faults Fp11 and Fp67 had a controlling effect on sedimentation, whereas the intensity of activity of Fp1 on the eastern side was low and it had little control over sedimentation. This was manifested as a structural pattern of thick deposits in the west and thin deposits in

the east on the EW-trending section. Northwestern Sub-sag received sediment input during this period and the deposits accumulated on the pre-Cenozoic basement, forming an angular unconformity. Due to the lack of pre-existing basement faults, new faults did not develop, neither under the effects of late extension nor those of strike-slip.

5.5.3 Thermal subsidence period

The thermal subsidence period was equivalent to the deposition period of the Zhuhai Formation to Hanjiang Formation (the late Oligocene to the middle Miocene), which consisted of fine sandstones, siltstones, mudstones, and other fine clastic rocks of coastal-neritic facies; the depositional thickness was evenly distributed. As a result of the Nanhai event, which was a strong tectonic activity associated with the expansion of the SCS with a long duration, the PRMB entered the stage of passive continental margin subsidence (Figure 9). The intensity of tectonic activity was low, and the faults were mainly high-angle near-EW-trending strike-slip faults, which had no obvious controlling effect on sedimentation, but had a reforming effect on the pre-existing faults during the early and late rift periods.

6 Analogue simulation of the evolution of the Panyu 4 Sag

6.1 Model scaling

The model presented here was scaled to the Panyu 4 Sag geometrically, kinematically, and dynamically. The geometric similarity was fulfilled using a thickness ratio of approximately 1.0×10^{-5} , where 1 cm of loose quartz sand in the model simulated 1.0 km of sediments in nature. Dry quartz sand has an average angle of internal friction of 36° , a cohesive strength (1.05 kPa), and deforms according to Navier-Coulomb failure, making it a favorable material for simulating the brittle deformation of sediments in the upper crust (McClay, 1990). The grain shape of quartz sand is well-rounded and grain size is about 0.2 mm (see sand properties in Table 1b).

The kinematic similarity was approached by simulating a sequence of events in the model that closely followed the interpreted evolution history of Panyu 4 Sag. Therefore, based on our interpretation of the seismic data, along with the tectonostratigraphic relations of different sedimentary formations, a five-stage evolution was proposed and mimicked in the model.

The dynamic similarity was fulfilled by simulating the physical properties of the sedimentary units of Panyu 4 Sag with appropriate modelling materials. In this regard, the intrinsic material properties, such as the cohesion (τ_0) and coefficient of internal friction (μ), in the models and nature need to be approximated (Koyi and Kenneth, 1993; Koyi, 1997). The angle of the internal friction of rocks in the upper crust (<10 km) was averaged as 40° (Brace and Kohlstedt, 1980), thereby resulting in a coefficient of internal friction (μ) of 0.84. The angle of internal friction of the uncompacted loose sand used in the model was 36° , resulting in a coefficient of internal friction of 0.73 (Koyi and Vendeville, 2003; Yu and Koyi, 2016; 2017), which is considerably close to that of the rocks in the upper crust. Meanwhile,

cohesion (τ_0) was scaled by the equality between the non-dimensional shear strength in the models and in nature.

$$\left(\frac{\rho g l}{\tau_0}\right)_m = \left(\frac{\rho g l}{\tau_0}\right)_n \quad (1)$$

where ρ is the density, l is the length, g is the acceleration due to gravity, and subscripts m and n , respectively, denote the model and nature. The non-dimensionalised ratio was calculated for the model and for the nature by using the shear strength of sedimentary rocks ranging from 1 to 10 MPa (Hoshino, 1972). For clastic sediments, the shear strength and density were 10 MPa and $2,550 \text{ kg m}^{-3}$, respectively (Yu and Koyi, 2016). The cohesion of the loose sand was approximately 100–140 Pa (Yu and Koyi, 2016) and its density was $1,550 \text{ kg m}^{-3}$ (Table 1b). These characteristics resulted in non-dimensional shear strengths (Eq. 1) of 11–15 for the model and 25 for the nature. These two ratios, which are within the same order of magnitude, suggest that our models approximated the dynamic similarity with their prototypes.

Following the scaling procedure (Ramberg, 1981; Weijermas and Harro, 1986), the scaling stress (σ^*) is given by the following equation:

$$\sigma^* = \frac{\sigma_{\text{mod}}}{\sigma_{\text{nat}}} = \rho^* g^* l^* = \frac{\rho_{\text{mod}} g_{\text{mod}} l_{\text{mod}}}{\rho_{\text{nat}} g_{\text{nat}} l_{\text{nat}}} \quad (2)$$

The calculated σ^* equals to $\sim 0.54 \times 10^{-6}$, and all the scaling parameters used in our models are reported in Table 1b.

6.2 Modeling results

During the initial phase of first extension deformation in the model, after 1.5 cm of total extension, NE-trending normal faults (f1, f2, f3, and f4) first developed in the area near the edges of plastic plates 1 and 2, forming two grabens (Figure 11Ca). When the total extension amount increased to 12 cm, two new secondary faults f5 and f6 respectively formed in front of faults f1 and f2 (Figures 11Cb–d). With the total extension amount increasing to 15 cm, several new secondary normal faults, such as f7 and f8 formed in front of f1 and f6, respectively. f6 and f7 formed a narrow graben. Meanwhile, f5, along with other secondary normal faults (f6, f7, and f8) developed in the hanging wall of major fault f1 (Figures 11Ce–f). In the second extension stage, the extension direction shifted clockwise from NW–SE to near N–S. During the first phase of this stage, after 1 cm of total extension, two new E–W trending normal faults (f9 and f10) were generated, forming an asymmetrical graben (Figure 11Cg). When the total extension amount increased to 2 cm, several new normal faults (f11, f12, and f13) developed, forming a duplex graben that was separated from previous asymmetrical graben by a horst (Figure 11Ch).

The main boundary normal fault f1 was preserved in the right part of the cross section in the model and broke through the white sand layers 2 and 3. It developed along the boundary of the pre-existing plastic block in the basement and was sealed by white sand layer 4 (Figure 12). Another boundary normal fault f2 generated during the extension and was preserved in the middle part of the cross section, sealed by gray sand layer 5.

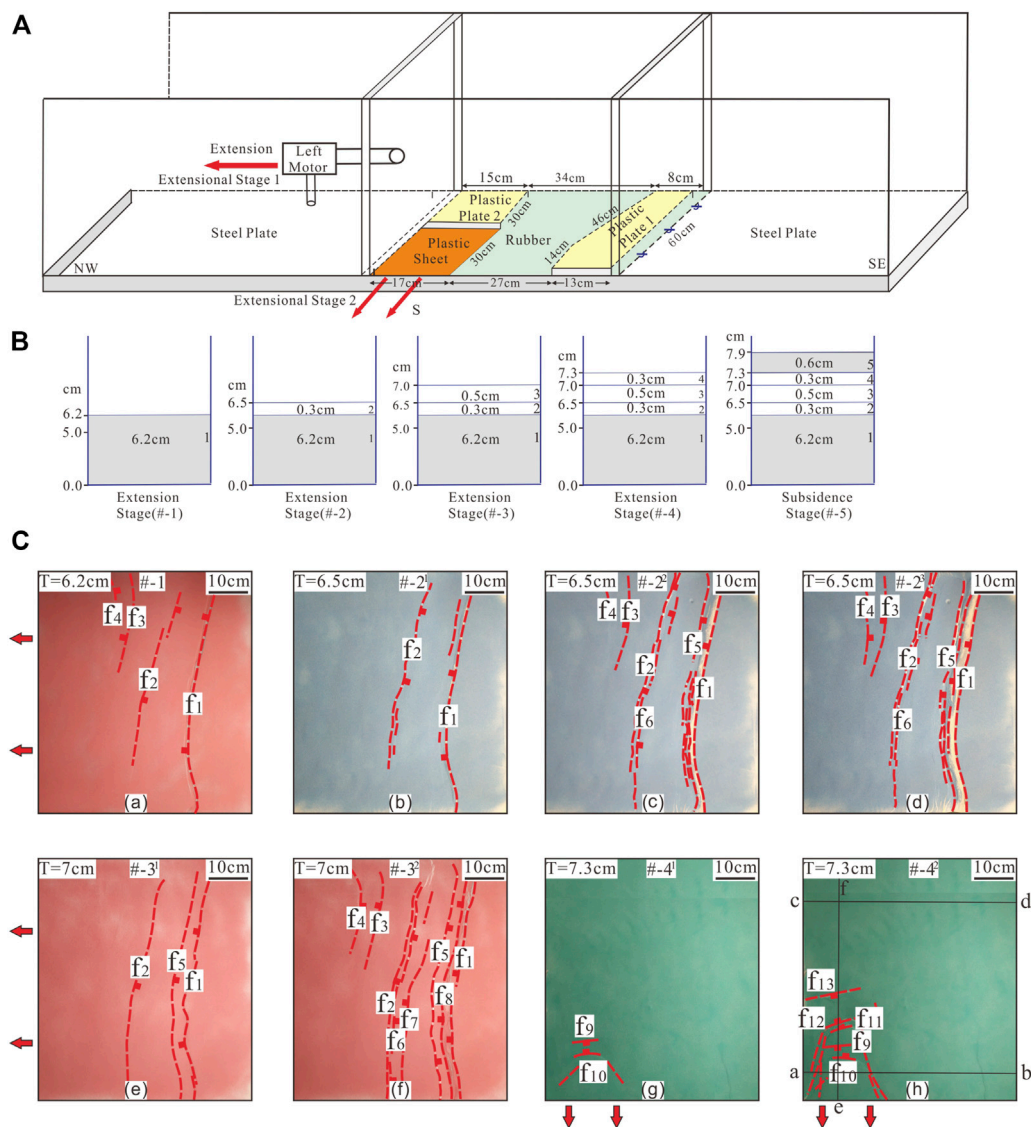


FIGURE 11

(A) Model setup showing a 3D view of the deformation rig and its components for modeling the evolution of the Panyu 4 Sag from the middle Eocene to the Oligocene; (B) The sketch to shows the filling process of the model at different stages. The red solid arrows represent the stress direction in the extension stages; (C) Top view (photographs and line drawings) of different stages of the model showing the evolution of the Panyu 4 Sag from the extension stage 1 (a-f) to the extension stage 2 (g-h). T denotes the total thickness of the sand layers; # denotes the deformation phase of the simulation process; the fault label numbers represent the order of the faults developed in the experiment.

Boundary faults f1 and f2 formed a graben where several synthetic and antithetic secondary normal faults (such as f5, f6, f7, and f8) developed. These faults broke through white sand layers 2, 3, and 4, and were sealed by gray sand layer 5. These boundary and secondary faults formed some secondary narrow grabens. In the left part of the cross section, two additional boundary faults f3 and f4 comprised a graben. The EW-trending normal faults (f9, f10, f11, f12, and f13) were preserved in the left bottom part of the cross section in the model and broke through gray sand layer 5. These faults formed two grabens and one horst. Several secondary normal faults generated between the boundary faults f11 and f13.

6.3 Comparison between modelling results and nature

The model exhibited a structural evolution similar to that of Panyu 4 Sag. During the early extension stage, faults f1 and f2 controlled the deformation in the model (Figures 11Ca–b). The depocenter was in strip shape, corresponding to the beaded shape of the Northern, Central, and Southern sub-sags in Panyu 4 Sag (Figure 1C; Figure 10F). With increasing extension amount, the scale of the major faults continued to increase, and numerous accommodation faults developed simultaneously. However, the overall structural evolution was mainly controlled by several major faults (Figure 10B–e; Figures 11Cc–f). In the

late extension stage, as the stress field transformed and the strike of the faults also changed accordingly. The model generated multiple nearly parallel sub-sag-controlling faults (such as f9 and f10), which formed a half-graben sub-sag (Figures 11Cg–h). This development was similar to that of the Western Sub-sag in the Panyu 4 Sag (Figure 1C; Figure Fig10A). At this point, the overall structure of the sag had formed, and it entered the thermal subsidence stage, which had little influence on the structure of the Panyu 4 Sag. The modelling results of the second extension stage were then compared with the structural map based on the bottom reflections of the Eocene in Panyu 4 Sag. The map view of model results showed similarities in the distribution and configuration of the second-order structure units to those developed on the bottom reflection of the Paleogene in Panyu 4 Sag (Figure 12). The boundary faults Fp1, Fp2, and Fp64 of Northern, Central and Southern Sub-sags exhibited similar trends and dips to faults f1, f2, and f4 developed in the experiment conducted at 15 cm extension during the first extension phase. The boundary faults Fp7 and Fp8 of Western Sub-sag were

comparable to fault f13 observed in the experiment conducted at the 2 cm extension during the second extension phase.

7 Discussion

7.1 Formation mechanism of the RP1

The structural evolution of the Panyu 4 Sag in the Zhu I Depression since the Paleogene was mainly affected by the combined action of the NNW- or NW-trending subduction in the western Pacific tectonic domain, the northward subduction and collision in the western part of the Tethys tectonic domain (India), and the NNW-trending subduction and collision in the eastern domain (Australia) (Lee and Hwang, 1993; Northrup et al., 1995; Ge et al., 2017; Liu et al., 2019; Ma et al., 2020; Guo et al., 2022). During the deposition of Members 6 to 2 in the early Eocene, the

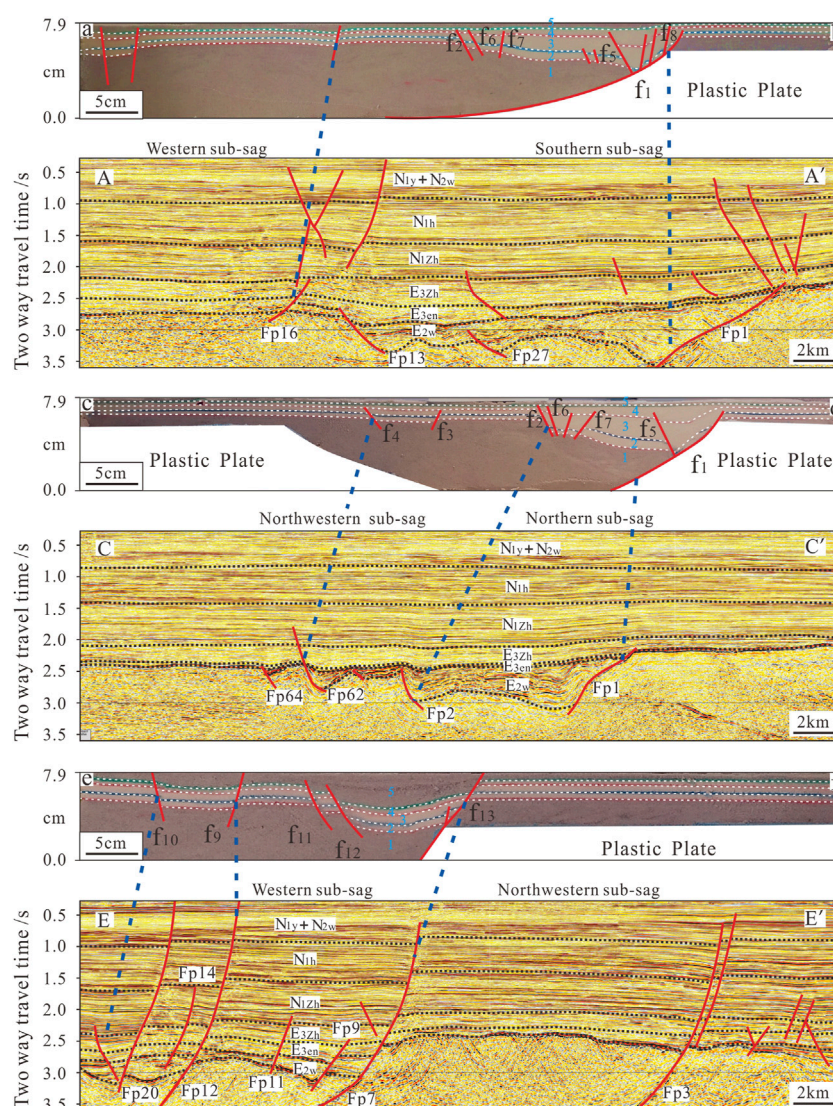


FIGURE 12

Comparison between modeling results and interpretation of seismic sections across the Panyu 4 Sag. Photograph and line drawing of a cross section in Model (for the location, see Figure 11Ch); interpreted seismic sections across the Panyu 4 Sag (for the location, see Figure 1C).

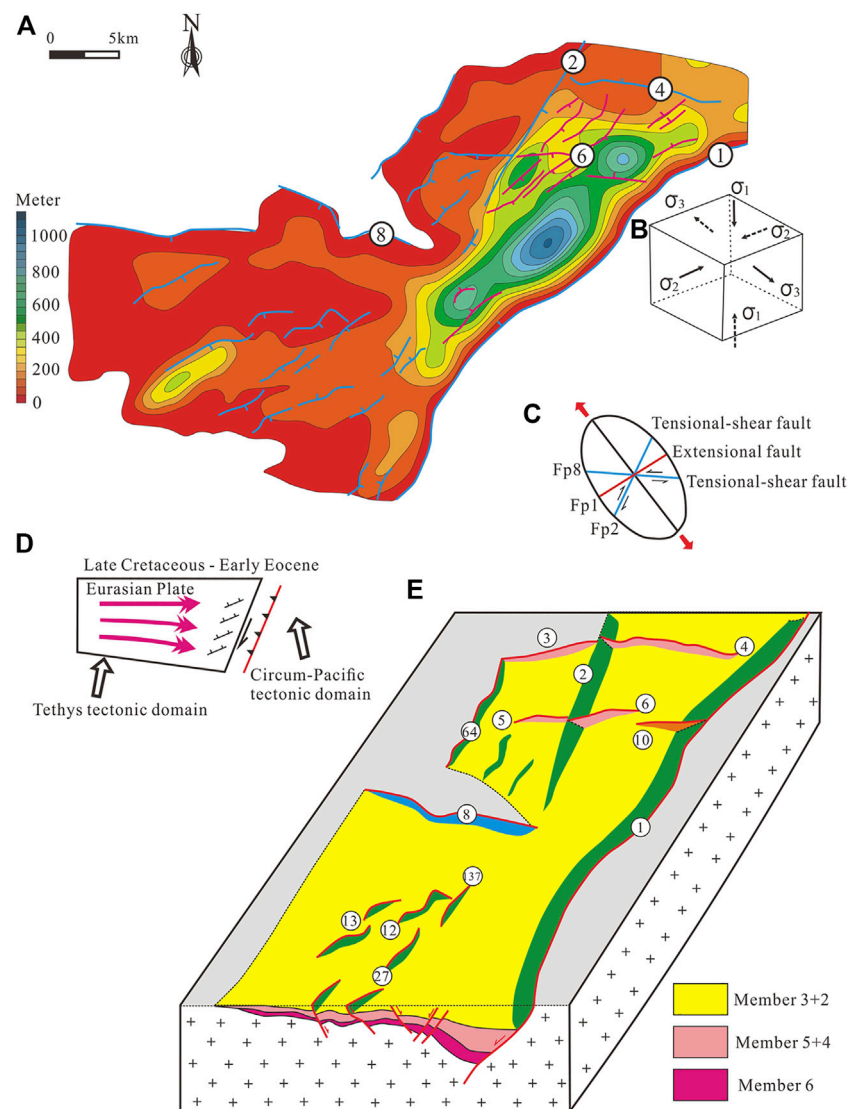


FIGURE 13

(A) The prototype basin of Member 5 in Wenchang Formation; (B) Three-dimensional stress state of principal stress in the middle Eocene of Paleogene; (C) Strain ellipse under the direction of NW-SN; (D) Movement status of Eurasian Plate, Tethys tectonic domain and Circum-Pacific tectonic domain; (E) Formation model stereogram.

Indian plate drifted northward at a high speed, and the northern Pacific oceanic crust subducted under Eurasia. The Australian plate slowly drifted northward, away from the Eurasian plate (Northrup et al., 1995). The rate of convergence of the Pacific and Eurasian plates gradually decreased, and the western Pacific subduction zone retreated seaward. The East Asian continental margin underwent a considerable transformation from the left-handed compression system to the right-lateral extension system (Zhou et al., 2006; Shu et al., 2006; Dong et al., 2008; Zhang et al., 2009; Li et al., 2017; Zhou et al., 2022; Figure 13D). The main dynamic factors were the compression caused by the NE-oriented subduction of the Indian plate and the tension caused by the subduction and roll-back of the Pacific Plate. Under the action of NE-SW-oriented compressive stress (σ_2) and NW-SE-oriented tensile stress (σ_3) (Figure 13B), the Panyu 4 Sag in the Zhu I Depression began to enter the RP1.

For the Zhu I Depression, the NW-SE extensional stress field acted on the thickened crust with the weak lithosphere. This stress field showed homogeneous extension and a wide deformation range, and exhibited a wide rift extension pattern (Buck, 1991; Liu et al., 2018; Zhou et al., 2022), forming a group of fault basins with half grabens or narrow grabens as structural units. Each half graben was isolated from others and strongly divided (Figures 3A,C), and internal block rotation was obvious (Figure 2). In addition to the northern rift zone of the PRMB, the northern SCS and the South China Continent also developed the same period of late Cretaceous to early and middle Eocene rift basin groups such as the Beibu Gulf Basin, Nanxiong Basin, and Sanshui Basin (Hu, 2019).

The RP1 was the weakest period of Pacific Plate subduction (Engelbreton et al., 1985; Pang et al., 2007). It was controlled by the

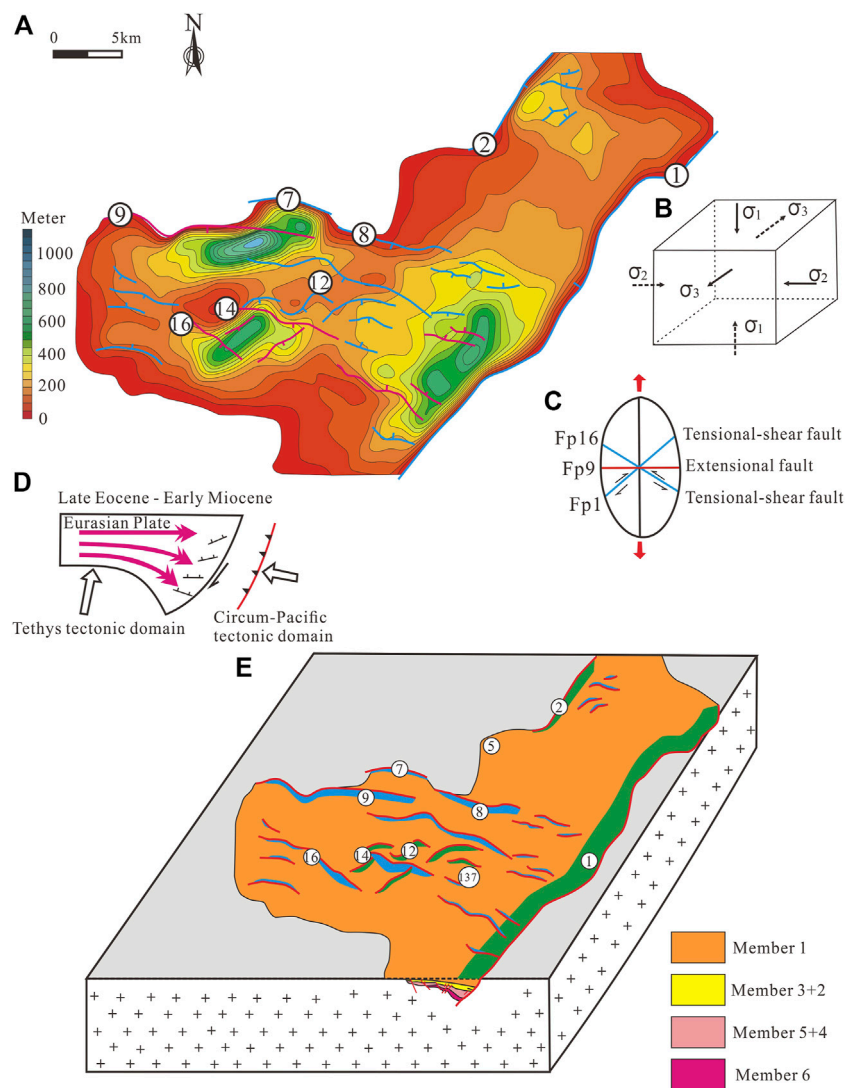


FIGURE 14

(A) The prototype basin of Member 1 in Wenchang Formation; (B) Three-dimensional stress state of principal stress in the late Eocene of Paleogene; (C) Strain ellipse under the direction of N-S; (D) Movement status of Eurasian Plate, Tethys tectonic domain and Circum-Pacific tectonic domain; (E) Formation model stereogram.

NW-SE regional extensional dynamic background and was dominated by NE-, NEE-, and near-EW-trending basin-controlling faults. Moreover, NWW-trending faults were developed. The intensity of fault activity was the strongest in the NE-trending faults, followed in decreasing order by the NEE-trending faults, the near EW-trending faults, and the NWW-trending faults. The developmental characteristics of basin-controlling faults in the four sags were distinctly different (Figures 1B, 3A, 4a-c). The Enping Sag was mainly controlled by NE- and near-EW-trending faults with high activity rates, such as F1 with an activity rate of up to 270 m/Ma (Figure 4D); The Xijiang Sag was dominated by NE- and NEE-trending faults with an activity rate of approximately 260 m/Ma (Figure 4D), while NWW- and near-EW-trending faults were mainly accommodation faults with relatively low activity rates. However, the Huizhou and Lufeng Sags were dominated by near-EW- and NWW-trending faults with an en

echelon distribution in the plane and a tension-torsional feature. Compared to the Enping and Xijiang Sags, the intensity of fault activity was relatively lower, with most of the fault activity rates being less than 150 m/Ma (Figure 4D).

With regard to the developmental characteristics of faults in the study area during the RP1, there were obvious differences in the local extensional directions from west to east. The basin-controlling faults in the western Enping and Xijiang Sags were predominantly NE- and NEE-trending, reflecting a NW-SE direction of local extension, which was consistent with the direction of the regional stress field. However, the eastern Huizhou and Lufeng Sags were dominated by near-EW boundary faults, with a near-N-S direction of local extension (Figures 3, 4). The west-to-east extensional direction was observed to be deflected clockwise, which may have been related to the southeastward flow of the mantle during this period. The Indian plate rapidly moved northwestward and

entered into a period of “soft collision” with the Eurasian plate (Zhang, 2012). This collision resulted in the southeastward flow of mantle in eastern Asia, and the direction of mantle flow changed due to the blockage of the eastern Pacific plate. As a result, the extension direction shifted clockwise from west to east.

Under the same stress state, the strike and scale of the pre-existing structural line of the basement had a controlling effect on the sedimentary axis of the caprock in the basin (Figure 13A). Strong extensional activity occurred when the strike of the pre-existing large-scale structure was nearly perpendicular to the direction of tensile stress (nearly parallel to the direction of compressive stress). Such activity resulted in the genesis of boundary faults that controlled the depression, such as fault Fp1. When the strike of the pre-existing large-scale structure and the tensile stress field intersected at a large angle, tensile and torsional activity would occur. Such activity also exerted a certain degree of control over the sag *via* faults, such as faults Fp2 and Fp8 (Figure 13C).

During the deposition of Members 6 to 2, the Panyu 4 Sag in the Zhu I Depression was formed mainly under the action of controlling factors such as NW-SE-oriented tensile stress (σ_3) and NE-trending pre-existing structures. Under the influence of NW-SE oriented extension, the activity of the pre-existing faults (such as Fp1) was initiated; this activity was relatively strong, and these pre-existing faults formed boundary faults on the southeast and northwest sides of the depression. The pre-existing fault Fp2 exhibited right-lateral tension and torsional activity, and it controlled deposition. However, the intensity of activity of Fp2 was lower than that of Fp1. Fp8 exhibited left-lateral strike-slip activity, which also weakly controlled deposition. While the main fault was active, a tensile fault was formed that was nearly perpendicular to the tensile stress direction; this tensile fault was parallel to or intersected the main fault at a slight angle. Simultaneously, near-EW-trending accommodation faults developed, such as faults Fp4 and Fp6 (Figure 13E).

7.2 Formation mechanism of the RP2

During the late Eocene to the early Oligocene (the deposition period of Member 1 to Enping Formation), the Indian Plate collided with and squeezed the Eurasian Plate, resulting in large-scale slippage between the intraplate blocks (Tapponnier et al., 1982; 1986; Ding et al., 2020; Zhang et al., 2021; Guo et al., 2022; Li et al., 2022). The orientation of subduction of the Pacific Plate changed from NNW to NWW, and its convergence with the Eurasian Plate increased (Li and Li, 2007; Shi and Li, 2012; Yao et al., 2011; Hall, 2012; Morley, 2012; Ye et al., 2020; Wang et al., 2021; Li et al., 2022; Figure 14D). This type of dynamical background formed a near-EW-trending compression and a near-SN-trending tension stress system of the Panyu 4 Sag in the Zhu I Depression, resulting in a transition of the tectonic framework from a NE orientation to a near EW orientation, thereby entering the RP2.

The lithospheric structure of the northern rift zone during the RP2 showed a normal, continental margin lithospheric structure that thinned from land (north) to sea (south) (Zhong et al., 2014). Accompanied by crustal thinning and thickening of the lithospheric mantle (Wu et al., 2001), the strength of the lithosphere increased,

and extension shifted from a wide rift to a narrow rift pattern under the near N-S tensile stress field (Buck, 1991). Furthermore, the extensional deformation changed from homogeneous to concentrated and migrated southward (crustal thinning site), and the rifting was concentrated in the present-day northern continental margin of the SCS. The northern rift zone exhibited a thinning crustal structure, and the rifting was concentrated. The lithospheric extensional kinematics showed a necking pattern, which led to a weak block rotation during extension (Figure 2). Moreover, the early independent and highly segmented half grabens or narrow grabens were interconnected and underwent expansion, and the basin range was significantly increased (Figure 3D). At the same time, under the action of the near N-S tensional stress field, the Zhu I Depression was located at the northern boundary of the stretching action, and the inherited development and strong activity of the earlier margin basin-controlling faults at the northern margin was attributed to the fact that they were pre-existing weak zones with more concentrated stress. As a whole, the fault activity expanded northward and the depocenter migrated northward.

Against the background of near-N-S extension, the fault system underwent transformation. The dominant extension direction was no longer oriented NW-SE, and the activity of the NE- and NEE-trending basin-controlling faults was weakened. The NWW- and near-EW-trending faults, which were previously less active, matched better with the near-N-S extension direction; their activity was enhanced, and they became the main controlling faults. Differences in the prior main basin-controlling faults led to different fault transformation processes in different regions (Figures 3, 4). The activity of the NE-trending F1 in the early stage of the Enping Sag was weakened, and the northeast section died out, whereas the southwest section was inherited and developed, but the activity rate decreased to below 100 m/Ma. The activity of the near-EW-trending F2 increased significantly, reaching about 230 m/Ma, and F2 became the main controlling fault (Figures 3B, 4D). The faults of the Xijiang Sag were primarily inherited, but the activity of the NE-trending F4 and the NEE-trending F3 and F5 tended to weaken during the early development phase, and the rate of fault activity decreased to 10 m/Ma, 150 m/Ma, and 70 m/Ma, respectively, with F3 on the northern boundary being more active than F4 and F5 on the southern boundary. In addition, a series of new near EW-trending faults were emerging in the northern uplift belt (Figures 3B, 4D). The Huizhou and the Lufeng Sags, which were preceded by near EW-trending faults, matched better with the N-S extensional direction, and the intensity of activity was significantly enhanced. The strike of the main basin-controlling faults did not change significantly, but the intensity of fault activity changed alternately. For example, in the western part of Huizhou Sag, the activity rate of the north-south boundary faults changed significantly in an alternate fashion, and the basin morphology showed a reverse wedge superposition. The activity rate of F7 and F8 at the southern boundary, which was more active in the early stage, was significantly lower than 160 m/Ma, whereas the activity rate of F11 at the northern boundary was significantly enhanced and reached 280 m/Ma (Figures 3B, 4D).

Pre-existing structural factors had inherited control effects on deposition. The near-EW-trending pre-existing faults became active and controlled the deposition. Under the action of near-SN-oriented tensile stress, the pre-existing NE-trending faults (such as Fp1 and Fp2) exhibited tensile and torsional activities with increased strengths. Furthermore, the thickness of the depocenter increased (Figures 14A,C).

During deposition of the RP2, the Panyu 4 Sag in the Zhu I Depression was formed mainly under the action of controlling factors such as S-N-oriented tensile stress (σ_3) and pre-existing structures (Figure 14B). Under the action of S-N-oriented extensional stress, the near-EW- and NE-trending pre-existing faults had inherited activities, forming boundary faults that controlled the depression. The centers of depression were independent of each other and were separated by uplifts. In addition to the main boundary faults, there were near-EW-trending small normal faults, and NE- and NW-trending tension-torsion faults. Some areas (such as Northwestern Sub-sag) exhibited a lack of pre-existing basement faults, so there were only a few inherited faults in the caprock, and only a few small-scale new-generation faults were formed (Figure 14E).

7.3 Implications for structural signatures in the Zhu I depression and other rift basins

Henstra and Whipp et al. (Whipp et al., 2014; Henstra et al., 2015) proposed that the boundary faults formed during the early rift period (RP1) were likely to reactivate and evolve into basin-controlling faults during the later rift period (RP2), even when there was a slight change in the direction of the stress field. In this paper, we proposed a multi-phase rift structural evolution model based on a study of the Panyu 4 Sag in the Zhu I Depression, which suggested the existence of multi-phase rift basins where the direction of extensional stress was deflected; the small faults during the early rift period gradually grew and became connected and finally evolved into a mature boundary fault system, while the boundary faults during the RP2 grew and were resurrected rapidly. These resurrected boundary faults were often large pre-existing faults with near-perpendicular new stress field directions. It could be inferred that these boundary faults were not part of the stress concentration zone during the RP1, although they might have formed the weak zone of the pre-existing basement. They began to rupture under the NW-SE directional extensional stress during the RP1 and were preferentially selected for resurrection during the N-S directional extension and the displacement rapidly reached the maximum. The evolutionary history of the two-phase rift in the study area indicated that fault activity dominated the systematic variability in basin structure and stratigraphic thickness. Firstly, in the IFS of the RP2, EW-trending faults (such as F11, F19, and F20) joined and rapidly expanded into coherent basin-controlling faults, and each fault controlled a unified and large depocenter, exhibiting a “large lake and deep basin” environment (Figure 3D). Secondly, in the IFS of the RP2, the NE-trending basin-controlling faults (such as F1, F3, F4, and F16) were not

dominant. Thus, the fault activity was weak, and the depocenters were not obvious, showing gentle topography and exhibiting the characteristics of a “large lake and shallow basin” environment (Figure 3D).

In summary, the structural-sedimentary characteristics of the RP2 formed a sharp contrast with those of the RP1: 1) the faults in the IFS of the RP1 were segmentally active with relatively small displacements, and the lake basin was characterized as a “shallow basin”. However, the large faults in the IFS of the RP2 were rapidly growing and penetrating, with large displacements and strong activities, and the lake basin was rapidly becoming a “deep basin”. 2) the depocenters of the IFS of the RP1 were small and scattered, whereas the depocenters of the IFS of the RP2 were large and uniform. In the multi-phase rift basin with deflection of the extensional stress direction (Figures 3C, 7), the RP2 was often characterized by rapid growth and resurrection of specific boundary faults. The pre-existing faults, which were approximately perpendicular to the direction of the new stress field, were preferentially active, and the displacement reached the maximum rapidly (Figures 3C, 7). The tectonic subsidence was weak in the areas controlled by inactive faults. The above understanding had important theoretical value for the evolution analysis of the PRMB and other multi-phase rift basins.

8 Conclusion

Based on our interpretation of the seismic data and the results of scaled analogue models, the following conclusions were drawn regarding the evolution and mechanism of the Panyu 4 Sag in the Zhu I Depression, PRMB.

- (1) The Zhu I Depression comprised four fault sets with different strikes, including NNE, NE-NEE, EW, and NWW directions. Most of these faults were syn-rift faults that formed during the Paleogene, whereas others were post-rift faults that formed during the Neogene. The average azimuths of the dominant strike for type Ia, type Ib, and type II faults were 75°, 85°, and 90°, respectively. These indicated that the minimum principal stress (σ_3) directions in the Zhu I Depression during the RP1 and RP2 were SSE (~165°) and near-EW (~180°), respectively.
- (2) The Panyu 4 Sag in the Zhu I Depression undergone three cycles of structural evolution—an early rift period (during the middle Eocene), a late rift period (from the late Eocene to the early Oligocene), and a thermal subsidence period (from the late Oligocene to the middle Miocene).
- (3) During the IFS of the RP1, three small and isolated depocenters developed controlled by Fp1 and Fp2. A uniform depocenter formed and migrated from north to south along Fp1 during the SFS and the WFS of the RP1. During the PR2, controlled by Fp7, Fp8, Fp9, and Fp14, several new EW-trending depocenters formed. Analogue modelling of the two phases of anisotropic extension revealed a high degree of correspondence with the natural geological conditions, revealing the evolution process of the Panyu 4 Sag. The structural-sedimentary evolution and

analogue modelling results indicated that the Panyu 4 Sag in the Zhu I Depression was formed as a superimposed basin under multi-phase anisotropic extension.

- (4) The structural evolution of the Panyu 4 Sag in the Zhu I Depression since the Paleogene was mainly controlled by the combined effect of the Pacific, Eurasian, and Indian Plates. Since the orientation of subduction of the Pacific Plate changed from NNW to NWW, the stress field mainly shifted from NW-SE-trending tension to S-N-trending tension, which caused the superposition of the late near-E-W-oriented structural pattern on the early NE-oriented structural pattern.

Data availability statement

The original contributions presented in the study are included in the article, further inquiries can be directed to the corresponding author.

Author contributions

BG, FY, and HL contributed to conception and design of the study. HL organized the database. BG performed the statistical analysis. BG and FY design and conducted experiments. BG wrote the first draft of the manuscript. FY and HL wrote sections of the manuscript. All authors contributed to manuscript revision, read, and approved the submitted version.

References

- Brace, W. F., and Kohlstedt, D. L. (1980). Limits on lithospheric stress imposed by laboratory experiments. *J. Geophys. Res. Solid Earth* 85 (B11), 6248–6252. doi:10.1029/jb085ib11p06248
- Buck, W. R. (1991). Modes of continental lithospheric extension. *J. Geophys. Res.* 96 (B12), 20161–20178. doi:10.1029/91jb01485
- Chen, C. M. (2003). *Formation condition of tertiary oil/gas reservoirs in Pearl River Mouth basin (east)*. Beijing: Science Press.
- Chen, C. M. (2000). Petroleum geology and conditions for hydrocarbon accumulation in the eastern Pearl River Mouth basin. *China Offshore Oil Gas* 14, 73–82. (in Chinese with English abstract).
- Chen, S., and Pei, C. (1993). Geology and geochemistry of source rocks of the eastern Pearl River Mouth basin, south China sea. *J. Southeast Asian Earth Sci.* 8, 393–406. doi:10.1016/0743-9547(93)90041-m
- Chen, S., Zhang, M., and Zhang, J. (1991). Study on oil and gas generation and exploration in eastern Pearl River Mouth Basin. *Oil Gas Geol.* 12, 95–106. (in Chinese with English Abstract).
- Cheng, S. X., Li, S. Z., Suo, Y. H., Liu, X., Yu, S., Dai, L. M., et al. (2012). Cenozoic tectonics and dynamics of basin groups of the northern South China Sea. *Mar. Geol. Quat. Geol.* 32, 79–93. (in Chinese with English abstract). doi:10.3724/sp.j.1140.2012.06079
- Corti, G., Philippon, M., Sani, F., Keir, D., and Kidane, T. (2013). Re-Orientation of the extension direction and pure extensional faulting at oblique rift margins: Comparison between the main Ethiopian rift and laboratory experiments. *Terra nova*. 25 (5), 396–404. doi:10.1111/ter.12049
- Deng, C., Fossen, H., Gawthorpe, R. L., Rotevatn, A., and Fazlikhani, H. (2017). Influence of fault reactivation during multiphase rifting: The oseberg area, northern North Sea rift. *Mar. Petroleum Geol.* 86, 1252–1272. doi:10.1016/j.marpetgeo.2017.07.025
- Ding, L., Guo, G., Hao, J., Wang, S., Zhu, W., and Liao, Z. (2015). Characteristics of Paleogene source rocks of Wenchang Formation and hydrocarbon potential in Xijiang sag, Zhu I depression. *China Offshore Oil Gas* 27, 21–26. (in Chinese with English abstract).
- Ding, W. W., Sun, Z., Mohn, G., Nirrengarten, M., Tugend, J., Manatschal, G., et al. (2020). Lateral evolution of the rift-to-drift transition in the South China Sea: Evidence from multi-channel seismic data and IODP Expeditions 367&368 drilling results. *Earth Planet. Sci. Lett.* 531, 115932–116014. doi:10.1016/j.epsl.2019.115932
- Dong, S. W., Zhang, Y. Q., Chen, X. H., Long, C. X., Wang, T., Yang, Z. Y., et al. (2008). The formation and deformational characteristics of East Asia multi-direction convergent tectonic system in Late Jurassic. *Acta Geosci. Sin.* 29 (3), 306–317. (in Chinese with English abstract).
- Engebretson, D. C., Cox, A., and Gordon, R. G. (1985). Relative motions between oceanic and continental plates in the pacific basin. *Geol. Soc. Am. Special Pap.* 206 (9), 1–60.
- Franko, D., Savva, D., Pubellier, M., Steuer, S., Mouly, B., Auxietre, J., et al. (2014). The final rifting evolution in the South China Sea. *Mar. Petroleum Geol.* 58, 704–720. doi:10.1016/j.marpetgeo.2013.11.020
- Frankowicz, E., and McClay, K. (2010). Extensional fault segmentation and linkages, Bonaparte Basin, outer North west shelf, Australia. *AAPG Bull.* 94, 977–1010. doi:10.1306/01051009120
- Ge, J. W., Zhu, X. M., Yu, F. S., Brian, G. J., and Wang, T. (2019). Controls of faulting on synrift infill patterns in the Eocene PY4 sag, Pearl River Mouth basin, south China sea. *Aust. J. Earth Sci.* 66 (1), 111–132. doi:10.1080/08120099.2018.1512524
- Ge, J. W., Zhu, X. M., Zhang, X. T., Jones, B. G., Yu, F. S., Niu, Z. C., et al. (2017). Tectono-stratigraphic evolution and hydrocarbon exploration in the Eocene southern Lufeng depression, Pearl River Mouth basin, south China sea. *Aust. J. Earth Sci.* 64, 931–956. doi:10.1080/08120099.2017.1370613
- Guo, B. W., Yu, F. S., Li, H. B., Li, H., Yu, S., and Wu, Z. (2022). Semi-quantitative analysis on reservoir-controlling structural elements of lower Wenchang Formation in southwestern Huizhou sag, Pearl River Mouth basin. *China Offshore Oil Gas* 34 (6), 34–43.
- Guo, B. W., Yu, F. S., Wang, Y. F., Li, H., Li, H. B., and Wu, Z. (2022). Quantitative prediction of palaeo-uplift reservoir control and favorable reservoir formation zones in Lufeng Depression. *Adv. Geo-Energy Res.* 6 (5), 426–437. doi:10.46690/ager.2022.05.07

Funding

This study was supported by the research project of CNOOC (Shenzhen) (No. SCKY-2020-SZ-21).

Acknowledgments

We gratefully acknowledge the Shenzhen Branch of the China National Offshore Oil Corporation for providing data used in this study and permission to publish the results.

Conflict of interest

The authors declare that the research was conducted in the absence of any commercial or financial relationships that could be construed as a potential conflict of interest.

The reviewer JZ declared a shared affiliation with the author(s) to the handling editor at the time of review.

Publisher's note

All claims expressed in this article are solely those of the authors and do not necessarily represent those of their affiliated organizations, or those of the publisher, the editors and the reviewers. Any product that may be evaluated in this article, or claim that may be made by its manufacturer, is not guaranteed or endorsed by the publisher.

- Hall, R. (2012). Late jurassic–cenozoic reconstructions of the Indonesian region and the Indian ocean. *Tectonophysics* 570, 1–41. doi:10.1016/j.tecto.2012.04.021
- Henstra, G. A., Rotevatn, A., Gawthorpe, R. L., and Ravnås, R. (2015). Evolution of a major segmented normal fault during multiphase rifting: The origin of plan-view zigzag geometry. *J. Struct. Geol.* 74, 45–63. doi:10.1016/j.jsg.2015.02.005
- Hoshino, K. (1972). Mechanical properties of Japanese tertiary sedimentary rocks under high confining pressures. *Geol. Survey Jpn. Rep.*
- Hu, Y. (2019). basin structure and genetic evolution of the Zhu depression, during the cenozoic, Pearl River Mouth Basin, south China. *Geol. J. China Univ.* 25 (01), 81–92. (in Chinese with English Abstract).
- Huang, C. J., and Hinnov, L. (2014). Evolution of an eocene–oligocene saline lake depositional system and its controlling factors, Jiangnan Basin, China. *J. Earth Sci.* 25 (06), 959–976. doi:10.1007/s12583-014-0499-2
- Jiang, H., Pang, X., Shi, H., Liu, L., Bai, J., and Zou, S. (2015). Effects of fault activities on hydrocarbon migration and accumulation in the Zhu I depression, Pearl River Mouth basin, south China sea. *Aust. J. Earth Sci.* 62, 775–788.
- Jiao, Y. Q., Li, S. T., Xie, X. N., and Ren, J. Y. (1997). Manifestation of multistage episodic rifting — take western Pearl River Mouth basin and its peripheral area as an example. *Petroleum Geol. Exp.* (03), 222–227. (in Chinese with English Abstract).
- Korme, T., Acocella, V., and Abebe, B. (2004). The role of pre-existing structures in the origin, propagation and architecture of faults in the Main Ethiopian Rift. *Gondwana Res.* 7, 467–479. doi:10.1016/s1342-937x(05)70798-x
- Koyi, H. A., and Vendeville, B. C. (2003). The effect of décollement dip on geometry and kinematics of model accretionary wedges. *J. Struct. Geol.* 25 (9), 1445–1450. doi:10.1016/s0191-8141(02)00202-x
- Koyi, H. (1997). Analogue modelling: From a qualitative to a quantitative technique—A historical outline. *J. Petroleum Geol.* 20 (2), 223–238. doi:10.1111/j.1747-5457.1997.tb00774.x
- Koyi, H., and Kenneth, P. (1993). Influence of basement faults on the development of salt structures in the Danish basin. *Mar. Petroleum Geol.* 10 (2), 82–94. doi:10.1016/0264-8172(93)90015-k
- Lee, M. J., and Hwang, Y. J. (1993). *Tectonic evolution and structural styles of the East shetland basin*. London, United Kingdom: Geological Society of London, 1137–1149.
- Leyla, B., Ren, J., Zhang, J., and Lei, C. (2015). En echelon faults and basin structure in Huizhou sag, south China sea: Implications for the tectonics of the SE Asia. *J. Earth Sci.* 26 (5), 690–699. doi:10.1007/s12583-015-0588-x
- Li, G., Mei, L. F., Pang, X., Zheng, J. Y., Ye, Q., and Hao, S. H. (2022). Magmatism within the northern margin of the South China Sea during the post-rift stage: An overview, and new insights into the geodynamics. *Earth-Science Rev.* 225, 103917–103925. doi:10.1016/j.earscirev.2022.103917
- Li, H., Yu, F. S., Wang, M., Wang, Y. F., and Liu, Y. L. (2022). Quantitative prediction of structural fractures in the Paleocene lower Wenchang formation reservoir of the Lufeng Depression. *Adv. Geo-Energy Res.* 6 (5), 375–387. doi:10.46690/ager.2022.05.03
- Li, P. L. (1993). Cenozoic tectonic movement in the Pearl River Mouth basin. *China Offshore Oil Gas Geol.* 7 (6), 11–17. (in Chinese with English abstract).
- Li, P. L. (1989). Tectonic structures and evolution of the Pearl River Mouth basin. *China Offshore Oil Gas Geol.* 3, 11–18. (in Chinese with English abstract).
- Li, P. (1994). Structural features and oil-gas accumulation in Pearl River Mouth basin. *Guangdong Geol.* 9 (4), 21–28. (in Chinese with English Abstract).
- Li, S. Z., Zang, Y. B., Wang, P. C., Suo, Y. H., Li, X. Y., Liu, X., et al. (2017). Mesozoic tectonic transition in South China and initiation of Palaeo-Pacific subduction. *Earth Sci. Front.* 24 (4), 213–225. (in Chinese with English abstract).
- Li, Z. H., and Li, X. H. (2007). Formation of the 1300-km-wide intracontinental orogen and postorogenic magmatic province in mesozoic south China: A flat-slab subduction model. *Geology* 35 (2), 179–182. doi:10.1130/g23193a.1
- Liu, H. L., Mei, L. F., Shi, H. S., Shu, Y., Tian, W., and Ye, Q. (2018). Rift style controlled by basement attribute and regional stress in Zhu I depression. *Pearl River Mouth Basin Ear. Sci.*, 117. (in Chinese with English abstract).
- Liu, Y. Q., Wu, Z. P., and Cheng, Y. J. (2019). Spatial and temporal difference of Paleogene rift structure and its controlling factors in the northern south China sea: A case study of Pearl River Mouth basin. *J. China Univ. Min. Technol.* 48 (2), 367–376. (in Chinese with English Abstract).
- Lv, B. F., Yin, Z. X., Cai, Z. X., and Wan, Z. F. (2012). Cenozoic tectonic evolution sequence in northern south China sea and its oil/gas significance. *Acta Geol. Sin.* 86 (08), 1249–1261. (in Chinese with English Abstract).
- Ma, B. S., Qi, J. F., Chen, W. C., and Zhao, M. (2020). Fault interaction and evolution during two-phase rifting in the Xijiang sag, Pearl River Mouth basin, northern south China sea. *Geol. J.* 55 (2), 1128–1147. doi:10.1002/gj.3474
- Ma, K., Wen, L., Zhang, B. J., Li, Y., Zhong, J. Y., Wang, Y. L., et al. (2022). Segmented evolution of Deyang-Anyue erosion rift trough in Sichuan Basin and its significance for oil and gas exploration, SW China. *Petroleum Explor. Dev.* 49 (02), 313–326. doi:10.1016/s1876-3804(22)60026-0
- McClay, K. R. (1990). Deformation mechanics in analogue models of extensional fault systems. *Geol. Soc. Lond. Spec. Publ.* 54 (1), 445–453. doi:10.1144/gsl.sp.1990.054.01.40
- McKenzie, D. (1978). Some remarks on the development of sedimentary basins. *Earth Planet. Sci. Lett.* 40 (1), 25–32. doi:10.1016/0012-821x(78)90071-7
- Morley, C. K., Haranya, C., Phoosongsee, W., Pongwapee, S., Kornsawan, A., and Wonganan, N. (2004). Activation of rift oblique and Rift parallel pre-existing fabrics during extension and their effect on deformation style: Examples from the rifts of Thailand. *J. Struct. Geol.* 26, 1803–1829. doi:10.1016/j.jsg.2004.02.014
- Morley, C. K. (2012). Late cretaceous–early palaeogene tectonic development of SE Asia. *Earth-Science Rev.* 115 (1–2), 37–75. doi:10.1016/j.earscirev.2012.08.002
- Neng, Y., Wu, J. F., Qi, J. F., Zhang, G. C., He, Y., and Chen, W. C. (2013). Three structural layers and its evolution of cenozoic basins in deep water area of northern margin south China sea. *Acta Geol. Sin.* 87 (03), 403–414+13. (in Chinese with English Abstract).
- Northrup, C. J., Royden, L. H., and Burchfiel, B. C. (1995). Motion of the Pacific plate relative to Eurasia and its potential relation to Cenozoic extension along the eastern margin of Eurasia. *Geology* 23 (8), 719–722. doi:10.1130/0091-7613(1995)023<0719: motppr>2.3.co;2
- Pang, X., Chen, C. M., and Peng, D. J. (2007). *The pearl river deep-water fan system & Petroleum in south China sea*. Beijing: Science Press, 49–50.
- Philippon, M., Willingshofer, E., Sokoutis, D., Corti, G., Sani, F., Bonini, M., et al. (2015). Slip re-orientation in oblique rifts. *Geology* 43 (2), 147–150. doi:10.1130/g36208.1
- Pigott, J. D., and Ru, K. (1994). Basin superposition on the northern margin of the South China Sea. *Tectonophysics* 235, 27–50. doi:10.1016/0040-1951(94)90015-9
- Ramberg, H. (1981). *Gravity, deformation and earth's crust*. San Diego: Academic.
- Ravnas, R., and Steel, R. J. (1998). Architecture of marine rift basin successions. *AAPG Bull.* 82, 110–146.
- Robinson, C., Elrod, W., and Bissadak, K. (1998). Petroleum generation, migration, and entrapment in the Zhu I depression, Pearl River Mouth basin, south China sea. *Int. J. Coal Geol.* 37, 155–178. doi:10.1016/s0166-5162(98)00023-8
- Shi, H. S., and Li, C. F. (2012). Mesozoic and early Cenozoic tectonic convergence-to-rifting transition prior to opening of the South China Sea. *Int. Geol. Rev.* 54 (15), 1801–1828. doi:10.1080/00206814.2012.677136
- Shi, H. S. (2013). On heterogeneous distribution and differential enrichment by zones of hydrocarbon resources: A case in Zhu I depression. Pearl River Mouth basin. *China Offshore Oil Gas* 25, 1–576. (in Chinese with English Abstract).
- Shu, L. S., Zhou, X. M., Deng, P., and Yu, X. Q. (2006). Principal geological features of Nanling tectonic belt, South China. *Geol. Rev.* 52 (2), 251–265. (in Chinese with English Abstract).
- Sun, Z., Zhou, D., Sun, L., Chen, C., Pang, X., Jiang, J., et al. (2010). Dynamic analysis on rifting stage of Pearl River Mouth basin through analogue modeling. *J. Earth Sci.* 21 (4), 439–454. doi:10.1007/s12583-010-0106-0
- Suo, Y., Li, S., Yu, S., Somerville, I. D., Liu, X., Zhao, S., et al. (2014). Cenozoic tectonic jumping and implications for hydrocarbon accumulation in basins in the East Asia Continental Margin. *J. Asian Earth Sci.* 88, 28–40. doi:10.1016/j.jseas.2014.02.019
- Tapponnier, P., Peltzer, G., and Armijo, R. (1986). On the mechanics of the collision between India and Asia. *Geol. Soc. Lond. Special Publ.* 19 (1), 113–157. doi:10.1144/gsl.sp.1986.019.01.07
- Tapponnier, P., Peltzer, G., Le dain, A. Y., Armim, R., and Cobbold, P. (1982). Propagating extrusion tectonics in Asia: New insights from simple experiments with plasticine. *Geology* 10, 611–616. doi:10.1130/0091-7613(1982)10<611:petian>2.0.co;2
- Tong, H. M., Koyi, H., Huang, S., and Zhao, H. T. (2014). The effect of multiple pre-existing weaknesses on formation and evolution of faults in extended sandbox models. *Tectonophysics* 626, 197–212. doi:10.1016/j.tecto.2014.04.046
- Wang, P. C., Li, S. Z., Suo, Y. H., Guo, L. L., Santosh, M., Li, X. Y., et al. (2021). Structural and kinematic analysis of cenozoic rift basins in south China sea: A synthesis. *Earth-Science Rev.* 216, 103522–103529. doi:10.1016/j.earscirev.2021.103522
- Weijermars, R., and Harro, S. (1986). Scaling of Newtonian and non-Newtonian fluid dynamics without inertia for quantitative modelling of rock flow due to gravity (including the concept of rheological similarity). *Phys. Earth Planet. Interiors* 43 (4), 316–330. doi:10.1016/0031-9201(86)90021-x
- Whipp, P. S., Jackson, A. L., Gawthorpe, R. L., Dreyer, T., and Quinn, D. (2014). Normal fault array evolution above a reactivated rift fabric: A subsurface example from the northern horda platform, Norwegian North Sea. *Basin Res.* 26 (4), 523–549. doi:10.1111/bre.12050
- Wu, S., Zhou, D., and Qiu, X. (2001). Tectonic setting of the northern margin of south China sea. *Geol. J. China Univ.* 7 (4), 419–427. (in Chinese with English Abstract).
- Wu, X. J., P. X., He, M., Shen, J., and Yan, C. Z. (2014). Structural style and dynamical mechanism during rifting in the passive-continental-margin basins, the northern South China Sea. *China Offshore Oil Gas* 26 (03), 43–50. (in Chinese with English Abstract).
- Xie, H., Zhou, D., Li, Y., Pang, X., Li, P., Chen, G., et al. (2014). Cenozoic tectonic subsidence in deep-water sags in the Pearl River Mouth basin, northern south China sea. *Tectonophysics* 615–616, 182–198. doi:10.1016/j.tecto.2014.01.010

- Xu, M. C., Gao, J. H., Rong, L. X., Wang, G. K., and Wang, X. J. (2010). Seismic analysis of the active character of the Taihang Mountain piedmont fault. *Appl. Geophys* 7, 392–398. doi:10.1007/s11770-010-0265-x
- Yao, B. C., Ling, W., and Wu, N. Y. (2005). Cenozoic tectonic evolution and the 3D structure of the lithosphere of the South China sea. *Geol. Bull. China* 24 (1), 1–8. (in Chinese with English Abstract).
- Yao, B. C., Zhang, L., Wei, Z. Q., Yi, H., Lin, Z., Wan, L., et al. (2011). The Mesozoic tectonic characteristics and sedimentary basins in the eastern margin of South China. *Mar. Geol. Quat. Geol.* 31 (3), 47–60. (in Chinese with English Abstract). doi:10.3724/sp.j.1140.2011.03047
- Ye, Q., Mei, L. F., Shi, H. S., Du, J. Y., Deng, P., Shu, Y., et al. (2020). The influence of pre-existing basement faults on the Cenozoic structure and evolution of the proximal domain, northern south China sea rifted margin. *Tect.* 39 (3), 1–18. doi:10.1029/2019tc005845
- Yu, F. S., and Koyi, Hemin. (2016). Cenozoic tectonic model of the Bohai Bay Basin in China. *Geol. Mag.* 153 (5-6), 866–886. doi:10.1017/s0016756816000492
- Yu, F. S., and Koyi, Hemin. (2017). Theoretical and experimental estimation of geometric relationship of non-parallel conjugate normal faults. *Tectonophysics* 703, 85–97. doi:10.1016/j.tecto.2017.03.009
- Yu, H. (1990). The Pearl River Mouth basin: a rift basin and its geodynamic relationship with the southeastern eurasian margin. *Tectonophysics* 183, 177–186. doi:10.1016/0040-1951(90)90415-5
- Zhang, C., Li, S., Yang, J., Yang, S., and Wang, J. (2004). Petroleum migration and mixing in the Pearl River Mouth basin, south China sea. *Mar. Petroleum Geol.* 21, 215–224. doi:10.1016/j.marpetgeo.2003.11.010
- Zhang, C. M., Sun, Z., Manatschal, G., Pang, X., Li, S. Z., Sauter, D., et al. (2021). Ocean-continent transition architecture and breakup mechanism at the mid-northern South China Sea. *Earth-Science Rev.* 217, 103620–103718. doi:10.1016/j.earscirev.2021.103620
- Zhang, L. (2012). *Tectonic evolution of the South China sea and a numerical modeling*. Beijing, China: University of Chinese Academy of Sciences (Institute of Oceanology, 15–20).
- Zhang, S., Liang, D., Gong, Z., Wu, K., Lie, M., Song, F., et al. (2003). Geochemistry of petroleum systems in the eastern Pearl River Mouth basin: Evidence for mixed oils. *Org. Geo-chemistry* 34, 971–991. doi:10.1016/s0146-6380(03)00034-2
- Zhang, X. B., Xu, X. B., Dong, J., and Shu, L. S. (2009). Deformation record of the change from Indosinian collision related tectonic system to Yanshanian subduction related tectonic system in South China during the Early Mesozoic. *Earth Sci. Front.* 16 (1), 234–247. (in Chinese with English Abstract).
- Zhong, Z. H., Shi, H. S., Zhu, M., Pang, X., He, M., and Zhao, Z. X. (2014). A discussion on the tectonic-stratigraphic framework and its origin mechanism in Pearl River Mouth basin. *China Offshore Oil Gas* 26 (5), 20–29. (in Chinese with English Abstract).
- Zhou, D., Ru, K., and Chen, H. (1995). Kinematics of cenozoic extension on the South China sea continental margin and its implications for the tectonic evolution of the region. *Tectonophysics* 251 (1), 161–177. doi:10.1016/0040-1951(95)00018-6
- Zhou, J., Li, S. Z., Suo, Y. H., Zhang, L., Du, X. D., Cao, X. Z., et al. 2022. NE-Trending transtensional faulting in the Pearl River Mouth basin of the northern south China sea margin. *Gondwana Res.*, 1–16. doi:10.1016/j.gr.2022.02.016
- Zhou, X. M., Sun, T., Shen, W. Z., Shu, L., and Niu, Y. (2006). Petrogenesis of mesozoic granitoids and volcanic rocks in south China: A response to tectonic evolution. *Episodes* 29 (1), 26–33. doi:10.18814/epiugs/2006/v29i1/004
- Zhu, H. T., Yang, X. H., Liu, K. Y., and Zhou, X. (2014). Seismic-based sediment provenance analysis in continental lacustrine rift basins: An example from the Bohai Bay Basin, China. *AAPG Bull.* 98 (10), 1995–2018. doi:10.1306/05081412159
- Zhu, W., Zhang, G., and Gao, L. (2008). Geological characteristics and exploration objectives of hydrocarbons in the northern continental margin basin of South China Sea. *Acta Pet. Sin.* 29 (1), 1–9. (in Chinese with English Abstract).
- Zhu, X. M., Huang, H. D., Dai, Y. D., Zhu, S. F., Tao, W. F., and Liu, C. G. (2014). Study on depositional system and sequence framework of Wenchang Formation in Panyu 4 depression of the Pearl River Mouth basin. *Lithol. Reserv.* 26, 1–8. (in Chinese with English Abstract).
- Ziegler, P. A., and Cloetingh, S. (2004). Dynamic processes controlling evolution of rifted basins. *Earth-Science Rev.* 64 (1), 1–50. doi:10.1016/s0012-8252(03)00041-2



OPEN ACCESS

EDITED BY

Yuan Neng,
China University of Petroleum Beijing,
China

REVIEWED BY

Fusheng Yu,
China University of Petroleum, China
Eun Young Lee,
University of Vienna, Austria

*CORRESPONDENCE

Xiang Li,
✉ lixiang@stu.pku.edu.cn

RECEIVED 11 December 2022

ACCEPTED 12 April 2023

PUBLISHED 07 July 2023

CITATION

Li X, Chang H, Huang S, Luo C, Duan Y,
Zhang H, Xia J, Zhong Z and Wei L (2023),
Reconstruction of the proto-type basin
and tectono-paleogeography of Tarim
Block in the Mesozoic.
Front. Earth Sci. 11:1121428.
doi: 10.3389/feart.2023.1121428

COPYRIGHT

© 2023 Li, Chang, Huang, Luo, Duan,
Zhang, Xia, Zhong and Wei. This is an
open-access article distributed under the
terms of the [Creative Commons
Attribution License \(CC BY\)](https://creativecommons.org/licenses/by/4.0/). The use,
distribution or reproduction in other
forums is permitted, provided the original
author(s) and the copyright owner(s) are
credited and that the original publication
in this journal is cited, in accordance with
accepted academic practice. No use,
distribution or reproduction is permitted
which does not comply with these terms.

Reconstruction of the proto-type basin and tectono-paleogeography of Tarim Block in the Mesozoic

Xiang Li^{1*}, Haining Chang¹, Shaoying Huang², Caiming Luo²,
Yunjiang Duan², Hao Zhang¹, Jinkai Xia¹, Ziqi Zhong¹ and
Lunyan Wei¹

¹The Key Laboratory of Orogenic Belts and Crustal Evolution, Ministry of Education, School of Earth and Space Sciences, Peking University, Beijing, China, ²Institute of Petroleum Exploration and Development, Tarim Oilfield Company, Korla, China

The reconstruction of the proto-type basin and tectono-paleogeography of the Tarim Basin during the Mesozoic is crucial for hydrocarbon exploration, particularly for identifying hydrocarbon source rocks. This study reconstructs the position, thickness, and distribution of the original stratigraphy, the shortening amount by structural deformation, and the distribution of sedimentary facies in each Mesozoic period using paleomagnetic data, residual stratigraphy data, seismic profiles, and lithofacies distribution. During the Triassic period, a syn-collision thrust fault structure formed in the southern Tarim Block due to the successive collision of the Tianshuihai-Bayankara terrane, North Qiangtang terrane, and South Qiangtang terrane with the Tarim Block. The sedimentary strata mainly distributed in the Northern Depression and Kuqa Depression, and their sedimentary centers continuously moved northward. In the Early-Middle Jurassic, faulted basins representing post-collision extensional structures developed on the margins of the Tarim Block. In the Late Jurassic, the Tarim Block was compressed, and the faulted basin transformed into a depression downwarped basin with red coarse clastic sediments due to the collision of the Amdo-Dongkacuo microcontinent with the Tarim Block. In the late Early Cretaceous, the collision between the Lhasa Block and the Tarim Block caused the entire uplift of the Tarim Block, which stopped accepting deposition except for the deposition of marine facies in the southwestern Tarim Basin influenced by a large-scale transgression event. The complex evolution of the Paleo-Tethys and Neo-Tethys Oceans during the Mesozoic significantly influenced the sediment distribution and structural features of the Tarim Basin.

KEYWORDS

Tarim Basin, proto-type basin, tectono-paleogeography, Mesozoic, basin evolution

1 Introduction

The Tarim Basin, located in western China, is a large superimposed basin that underwent multiple phases of tectonic deformation from the late Neoproterozoic to Cenozoic (Figure 1; Li et al., 1996). The basin's architecture is complex and characterized by the development of a series of large-scale paleo-uplifts and tectonic non-conformities because of the drastic variation in disintegrations and collisions with the surrounding terranes in different periods. The deformation phase indicated by the extensive angular non-conformity has resulted in significant changes in the tectonic geomorphology and geography of the basin. Petroleum

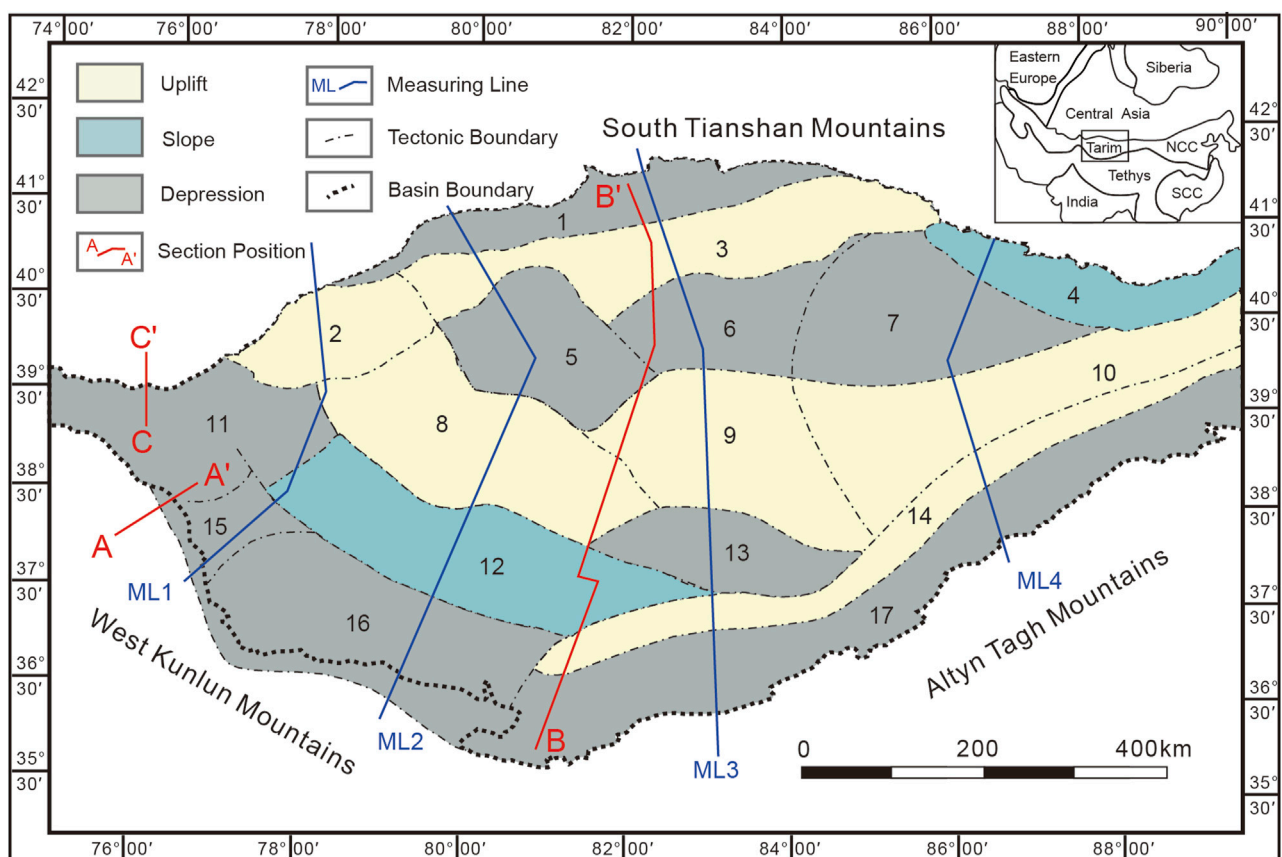


FIGURE 1

Tectonic framework of the Tarim Basin (modified after [He et al., 2016](#); [Laborde et al., 2019](#)) 1–Kuqa Depression, 2–Kepingtage Faulted-uplift, 3–Tabei Uplift, 4–Kongquehe Slope, 5–Awati Depression, 6–Shuntuoguole Low Uplift, 7–Manjiaer Depression, 8–Bachu Uplift, 9–Tazhong Uplift, 10–Guchengxu Uplift, 11–Kashi Depression, 12–Maigaiti Slope, 13–Tangguzibas Depression, 14–Tanar Uplift, 15–Shache Bulge, 16–Yecheng Depression, 17–Southeast Depression.

exploration in the basin has shown that most of the hydrocarbon accumulation was closely related to development of the proto-type and tectono-paleogeography. Thus, research on the evolution of proto-type and tectono-paleogeography of the Tarim Basin has greatly intensified over the past 2 decades ([Jia and Wei, 1997](#); [Jin and Wang, 2004](#); [He et al., 2007](#); [Gao et al., 2017](#); [Wang et al., 2017](#); [Lei et al., 2020](#); [Wu et al., 2020](#); [Wei et al., 2021](#); [Xia et al., 2023](#); [Zhong et al., 2023](#)).

The Tarim basins we see today are the result of multiple tectonic cycles and various types of tectonic activity. Over time, the nature of these basins has changed and they have undergone different transformations. To better understand these changes, researchers use proto-type basin reconstruction which involves analyzing the current basin fill and tectonic background to uncover the original basin and analyze the effects of its transformation. Tectono-paleogeography is a field of research that examines the formation, development, and evolution of basins, and how tectonic activity affects sedimentary facies. This is achieved through the reconstruction of basins, orogenic belts, and global paleocontinents. Several studies have utilized proto-type basin and tectono-paleogeography reconstruction to gain insight into the Tarim basins ([Feng et al., 2004](#); [He et al., 2013](#); [Chen et al., 2013](#);

[Chen et al., 2015](#)). Systematic analysis from the proto-type basin and tectono-paleogeography development perspective is crucial for hydrocarbon exploration due to the significant role played by reconstruction techniques in identifying the types and locations of organic rock facies belts in the basin, as well as understanding the paleo-ecological environment and sedimentary rock facies. The analysis of the tectonic setting, the proto-type and tectono-paleogeography in the Tarim Basin is of theoretical importance and exploration value to understanding of formation and development of the Tarim Basin and prediction of the favorable reservoir rock belts and play fairways ([He et al., 2007](#); [Wu et al., 2021](#)).

The Mesozoic Tarim Basin was an intracontinental basin surrounded by orogenic belts and mostly developed terrigenous clastic deposits ([He et al., 2005](#)). The closure of the Paleo-Tethys Ocean and the opening-closing of the Neo-Tethys Ocean in the southern Tarim Basin had a powerful influence on the basin ([Wang et al., 2010](#); [Xu et al., 2011](#)). The frequent tectonic events of the Mesozoic formed several unconformities and the denudation destroyed the original basin structure. The Mesozoic is a key time in the tectonic evolution history of the Tethysides. For the Tethysides, the oceanic crust subduction, the oceanic basins closing,

and some collision events occurred in the Paleo-Tethyan realm during the Mesozoic, and the Neo-Tethys was opened and spreading in Mesozoic (Mattern and Schneider, 2000; Xiao et al., 2015; Wu et al., 2020). The impact of Mesozoic tectonic events on the sedimentary and evolutionary history of the basin remains poorly understood due to the challenges of obtaining geological information from the basin's interior, which is covered by desert. Denudation and thrust resulting from tectonic events caused damage to the Mesozoic prototype basins, leading to ongoing debates about the nature and evolution of these basins. For example, questions remain about whether a basin containing sediments existed in the southwest Tarim Basin during the Early–Middle Triassic (He et al., 2005; Zheng et al., 2014; He et al., 2016), and whether the Triassic Kuqa depression and the Late Jurassic southwest Tarim Basin represent a downwarped basin or a foreland basin (Liu et al., 2000; Jia et al., 2003; Yang et al., 2019; Li et al., 2022).

This paper presents a comprehensive analysis of the Tarim Basin's nature and evolution, using a range of methods such as paleomagnetic, petrological, stratigraphic thickness data, and seismic profiles. Through this research, the Mesozoic proto-type basin and tectono-paleogeography of the Tarim Block have been reconstructed, shedding new light on the geological history of the region. Additionally, the study examines the impact of tectonic events on the Tarim Basin, providing insights into the factors that have shaped the basin's structure and geological characteristics over time. Overall, the findings presented in this paper contribute to a better understanding of the Tarim Basin and its complex geological history, offering valuable information for further research and exploration.

2 Database and methods

2.1 Database

For the reconstruction of the Mesozoic proto-type basin and tectono-paleogeography in the Tarim Basin, we collected the residual stratigraphic thickness data, outcrops data, wells data, and 81 seismic sections of the Tarim Basin in each period of the Mesozoic mainly from the Tarim Oilfield. The timing of the north-south collision between two terranes can be determined by the overlap of their paleolatitudes or the change of their convergence rate. For the location reconstruction, this paper mainly collected Mesozoic paleomagnetic data from various terranes around the Tarim Basin (Mcfadden et al., 1988; Li et al., 1988; Zhang et al., 1989; Li, 1990; Fang et al., 1991; Chen et al., 1992; Li et al., 1995; Fang et al., 1997; Meng et al., 1998; Fang et al., 2001; Shen et al., 2005; Gilder et al., 2003; Wang, 2004; Gilder et al., 2008; Song et al., 2012; Song et al., 2015; Ma et al., 2020; Hu et al., 2022; Wei et al., 2022).

2.2 Methods

There are three principles we need to obey when reconstructing the proto-type basin maps. Firstly, reconstruct its location, which means figuring out the paleogeographic position. Secondly, reconstruct the isopach maps of proto-type basins and the

distribution of sedimentary lithofacies. Finally, reconstruct the original range of the proto-type basin by calculating the extension or shortening amount. Detailed procedures are explained below.

1 The paleolatitude of the blocks can be obtained from paleomagnetic data compared with paleopoles, but the paleolongitude is uncertain (Hou et al., 2008). The igneous rocks representing subduction and collision and oceanic magnetic anomaly bands can determine the relationship between the terranes and whether the oceans closed or spreading. We can build a global plate distribution map based on these paleolatitudes and the relationship between the plates. In this paper we emphasize that two reliability criteria must be satisfied for inclusion in the assessment namely: 24 or more samples yielding a 95% confidence limit (A_{95}) of $<16^\circ$ and $Q \geq 4$ (An internationally-recognized reliability index for paleomagnetic data, Van der Voo, 1990).

2 At present, the erosional thickness of major unconformities is quantitatively calculated by such means as vitrinite reflectance, paleopore analysis, and sonic well log data based on borehole information (Magara, 1976; Henry and Natalya, 1996; Liu et al., 2000). However, it is usually difficult to use only these data to map the distribution of an unconformity or its erosion amount in plane owing to limitations of the available borehole data (Lin et al., 2011). Therefore, this paper reconstructed the thickness and extent of denuded stratigraphy in different basins according to the trend surface of formation thickness, based on the residual stratigraphy information of Tarim Oilfield. In this study, we estimated the erosion thicknesses of the unconformities by analyzing the geometry of the eroded strata beneath the unconformity surfaces, as depicted in seismic profiles that have been calibrated with borehole data (Lin et al., 2012). Then, the sedimentary facies were supplemented on the extent of the original basin inferred from the existing sedimentary facies.

3 The extension or shortening amount is measured from the 81 balanced cross-sections which can eliminate the effects of structure and deformation. The amount of shortening and extension of each period can be got by comparing the length of that period with the length of the next period, combining the shortening amount from Laborde et al. (2019) since the Cenozoic. The reconstruction of the final original stratigraphic spreading is carried out according to these shortening amounts from 81 profiles averaged in eight directions (M1N, M1S, M2N, M2S, M3N, M3S, M4N, M4S). Since the deformation mainly exists at the edge of the Tarim Basin, the shortening is mainly distributed in the northern and southern margins (Table 1).

To determine the characteristics of the Kuqa Basin and the southwestern Tarim Basin, we reconstructed their distribution and deformation. Initially, we gathered information on the residual thickness and distribution of each basin in the Tarim Block. Next, we reconstructed the denuded stratigraphy of the basin perimeter using the trend surface of formation thickness method (Wu et al., 2019). To complete the reconstruction of the proto-type basin extent, we supplemented the denuded strata with sedimentary facies according to sedimentary facies distribution (Chen, 1995; Jia, 2009; Liu et al., 2012; Yu et al., 2016). Finally, to eliminate the impact

TABLE 1 The Mesozoic and Cenozoic shortening amount of the Tarim Basin (km).

Distribution of the shortening amount	Cenozoic	Cretaceous	Jurassic	Triassic
Northern margin of ML1	36	0	0	0
Southern margin of ML1	32	1.4	−0.8	2.2
Northern margin of ML2	21	0.2	−0.4	0.4
Southern margin of ML2	35	0	0	4
Northern margin of ML3	22	0.4	−0.8	0.7
Southern margin of ML3	0.9	3	−1	9.3
Northern margin of ML4	0	0	0	0
Southern margin of ML4	0.3	2	−0.7	6.1

of deformation on basin distribution, we calculated shortening or extension (Table 1) based on the balanced cross-sections (81 seismic sections) and previously published data (Chen et al., 2009; Laborde et al., 2019; Wang et al., 2020). As a result, Mesozoic proto-type basin maps were drawn based on the above reconstructions of the proto-type basin of the Tarim Basin.

3 Tarim Block in the global plate tectonics and its evolution

3.1 The position and orientation of Tarim Block in the Mesozoic

The Tarim Basin is a large composite and superimposed sedimentary basin developed on the crystal basement of pre-Cryogenian continental crust, whilst a large Meso–Cenozoic composite inland basin is developed on a Paleozoic platform (Zhou et al., 2001; Jia et al., 2004; He et al., 2005). The Mesozoic sediments in the Tarim Basin are mainly continental clastic rocks, primarily distributed in the Kuqa Depression, North Depression, Southwest Depression and Southeast Depression. Only the Southwest Depression developed shallow marine carbonate deposits in the late Cretaceous Tarim Basin. The main paleomagnetic data are acquired from sedimentary strata in the margins of the Kuqa and southwestern Tarim Depression due to the lack of magmatic activity in the Tarim Basin during the Mesozoic and the large area of the basin covered by the Taklamakan Desert (Li et al., 1988; McFadden et al., 1988; Zhang et al., 1989; Li, 1990; Fang et al., 1991; Chen et al., 1992; Li et al., 1995; Fang et al., 1997; Meng et al., 1998; Fang et al., 2001; Gilder et al., 2003; Wang, 2004; Shen et al., 2005; Gilder et al., 2008). The only exception has been reported from a Middle Jurassic alkali gabbro and basalt in the Tuoyun Basin of southwestern Tarim (Li et al., 1995; Meng et al., 1998; Wang, 2004; Gilder et al., 2008). The characteristic remanent magnetization here has dual polarity and consistent tilt-corrected inclinations between the gabbro and sandstone specimens of the Triassic and Jurassic seem to rule out significant inclination shallowing in the sediments. The relative rotation of the individual mean C3–T1 and J3–E1 poles has been Gilder reported between Tarim and Eurasia, which is $9.4^\circ + 6.4^\circ$ clockwise (Gilder et al., 2003). The paleomagnetic poles from Early Cretaceous redbeds in the Kuqa and southwestern

Tarim show a $\sim 10^\circ$ – 15° inclination shallowing compared with coeval observations from volcanic rocks from the Tuoyun Basin in southwestern Tarim. No sizeable extensional structure is found in the north margin of Tarim Basin, and there is block limitation in the south margin of Tarim Basin. Therefore, it is the inclination shallowing of the redbeds, not the result of the massive southward movement of the Tarim Block. The pole remained at intermediate to present high latitudes throughout the Permian to the Mesozoic interval with Permian to Jurassic paleopoles identifying little or no apparent polar wander (APW) (Huang et al., 2018). Paleomagnetic data and apparent pole-shift curves show that the Tarim Block was between $\sim 35^\circ$ and 45° N during the whole Mesozoic with quasi-stationary position and direction (Gilder et al., 2008).

3.2 Relationship between the Tarim Block and the surrounding massif in the pre-Mesozoic

Numerous lines of evidence from paleomagnetic, petrological, geochronological, and paleontological studies indicate that the North Qiangtang terrane (NQT), South Qiangtang terrane (SQT), Lhasa terrane (LT), India plate, and Indochina block underwent convergence, and the Tethys Ocean gradually closed during the Permian period. Zhao et al. (2018) synthesized the most recent data and geologic evidence that place critical constraints on the closure history of the oceanic domains (Liu et al., 2015; Liu et al., 2016; Liu et al., 2017; Eizenhöfer and Zhao, 2018; Han and Zhao, 2018; Liu et al., 2018), proposed the shear closure of the paleo-Asian Ocean from west to east at 310–245 Ma, leading to the collision of Tarim Block with the Kazakhstan–Yili Central Tianshan Block at 310–285 Ma, Alex block (plus Central Qilian and Qaidam) with the Mongolia Terrane and Siberia plate at 280–265 Ma, and North China block with the Mongolia Terrane and Siberia plate at 260–245 Ma (Zhao et al., 2018). Comparison of the equal-area plot diagrams for paleopoles from the East Asia blocks/terrains in the Permian to Early Triassic interval shows most blocks/terrains in the Central Asian Orogenic Belt (CAOB) and surrounding blocks are concentrated within a narrow palaeolatitudinal band around $\sim 35^\circ$ N (Figure 2) implying that closure of the Paleo-Asian Ocean (PAO) and amalgamation of the CAOB were completed prior to the Early Triassic and that the majority of the CAOB was a quasi-rigid

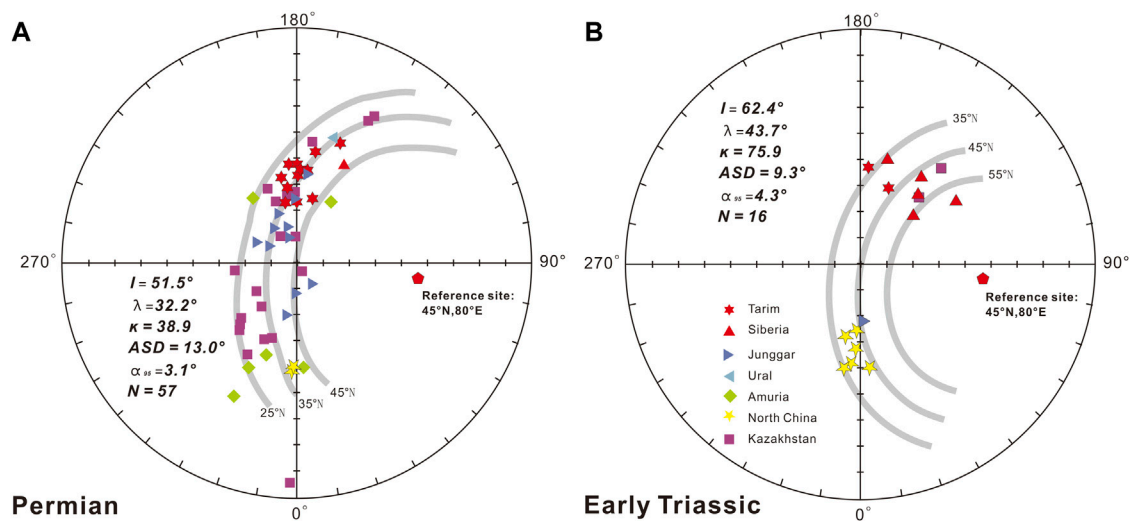


FIGURE 2
Equal-area projections showing paleomagnetic comparisons within the Permian to Early Triassic paleomagnetic poles from the CAOB and adjacent Siberia, North China and Tarim cratons (modified from Huang et al., 2018). (A) Permian, (B) Early Triassic.

assemblage from the end of the Permian (Huang et al., 2018). The fragmentary tetrapod bones collected from the Lower Triassic Ehuobulak Group of Kuqa Depression indicate that the Tarim Block collaged with Eurasia at least in the Early Triassic. Terrestrial tetrapod fossils from the East Asian blocks (North China, South China, Tarim, Alex-Hexi-Qilian, Indochina) suggest that these blocks were already connected in the Early Triassic, allowing non-marine tetrapods to migrate between the blocks (Liu et al., 2020). These suggest that massifs (Kazakhstan-Yili Central Tianshan, Junggar, Alex, Qaidam, South China, North China, Mongolia Terrane and other East Asian blocks) in the northern and eastern Tarim collaged as part of the Eurasian continent and that the ancient Asian Ocean was closed in Central Asia before the early Triassic.

3.3 Relationship between the Tarim Block and the surrounding massif in the Mesozoic

The formation and rapid northward movement of the Cimmerian continent in the south of the Tarim Block in the early Permian to Late Triassic involved the opening and closing of Tethyan oceans and the rifting, drifting and collision of multiple continental blocks. Two significant paleomagnetic poles from sandstones of the SQT and the NQT show paleolatitudes of 27°N and 27.8°N, respectively, and indicate that the NQT was already collaged with the Tarim Block at ~220 Ma (Song et al., 2012). Song et al. (2015) reported the first volcanic-based paleomagnetic results from Triassic rocks of the Qiangtang block that appeared to average secular variation well enough to yield a reliable paleolatitude estimate. Combined with the published paleomagnetic data of the Qiangtang block, the latitude of the NQT in the Late Triassic was calculated to be $31.7 \pm 3.0^\circ\text{N}$ (Song et al., 2015). The first Paleozoic paleomagnetic data from the basalt of SQT indicate that it was located at a latitude of $22.3 \pm 5.8^\circ\text{S}$ during the middle Permian and drifted rapidly

northward with the Cimmerian blocks in early Permian to Late Triassic time. According to a simple interpolation between the paleolatitude determined from the paleomagnetism of the NQT and its surrounding blocks/terrane the early Permian to Late Triassic, the NQT collaged with Laurasia and SQT in the late Triassic (Figure 3; Wei et al., 2022).

Based on comparing these paleomagnetic evidence, this paper proposed that the NQT drifted ~50° northward rapidly during the Permian and Triassic and was collocated with Laurasia but not yet with SQT (4° difference) at ~220 Ma. The pillow basalt (~223 Ma) erupted underwater, the gabbro (~220 Ma) composed of normal mid-ocean ridge (N-MORB) fraction, the Nadi Kangri basalt (~220 Ma) formed in a continental rift setting and the peraluminous S-type granite (~222 Ma) associated with the subduction collision indicate that the Paleo-Tethys Ocean was still subducting and colliding with SQT which not yet collaged with Laurasia (Li et al., 2006; Wang et al., 2007; Fu et al., 2010; Zhang et al., 2014; Li et al., 2015). The muscovite peraluminous granite (~214 Ma) formed through magmatic underplating delamination represents SQT and NQT have been collaged at 214 Ma (Li et al., 2015). As a result of the above paleomagnetic, geochronologic, and petrological evidence, this paper proposes that the SQT and NQT terranes successively collided in Laurasia rather than merging into the NQT first and then SQT colliding in Laurasia.

Li et al. (2016) compiled existing data published mainly in Chinese literature and provided a new, high-quality, well-dated paleomagnetic pole from the ca. 180 Ma Sangri Group volcanic rocks of the LT that yields a paleolatitude of $3.7^\circ\text{S} \pm 3.4^\circ$ (Li et al., 2016). This new pole confirms a trend in the data that suggest that Lhasa drifted away from Gondwana in the Late Triassic instead of Permian as widely perceived (Xu et al., 2011; Song et al., 2015; Li et al., 2016; Li et al., 2022). This drift history is constrained by geological and paleomagnetic evidence. The Lhasa terrane was located adjacent to northern Gondwana in late Triassic time, with rifting starting around 235 Ma (Zheng et al., 2018), and

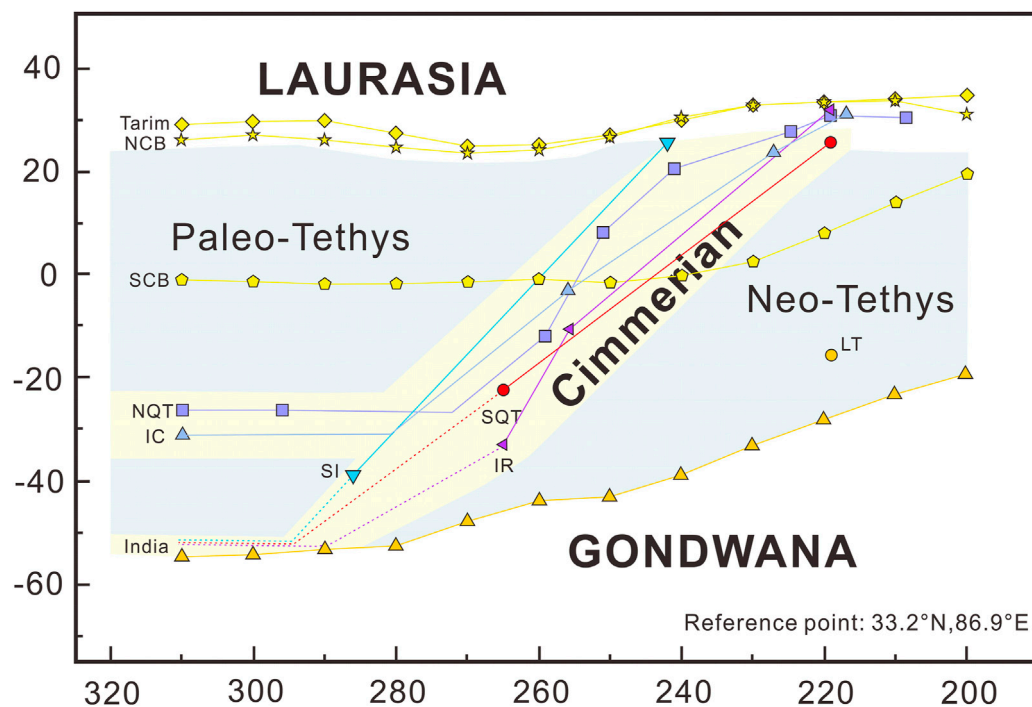


FIGURE 3
Paleolatitude evolution of the SQT and its surrounding blocks during the early Permian to Late Triassic (modified from [Wei et al., 2022](#)).

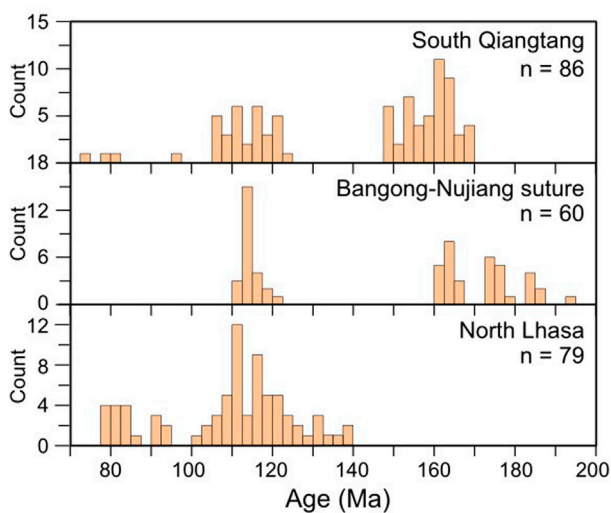


FIGURE 4
Histograms of the ages of Jurassic–Cretaceous magmatic rocks in South Qiangtang, Bangong–Nujiang suture zone, and North Lhasa ([Hu et al., 2022](#)).

northward drift occurring mostly after ~215 Ma ([Li et al., 2016](#)). The Amdo–Dongkacuo microcontinent between NQT and LT began to collide with SQT at 166–163 Ma according to the unconformity of the Dongqiao Formation with the ophiolite ([Ma et al., 2020](#)) and alluvial fan deposits sourced from the Amdo basement ([Li et al., 2019](#)), resulting in the closure of the Dongqiao–Amdo oceanic

seaway. Paleomagnetic data from the western segment of the LT indicate a paleolatitude of $20.6 \pm 5.0^\circ\text{N}$ at ~132–106 Ma suggesting that the LT had already collided with Eurasia by this time ([Chen et al., 2012](#)). The large number of igneous rocks showing subduction, collision, and crustal thickening is concentrated in two ages, ~110–130 Ma and ~150–170 Ma, also indicating two collisions associated with Amdo–Dongkacuo (AD) microcontinent and LT ([Figure 4](#); [Hu et al., 2022](#)).

This paper concludes that the position of the Tarim Basin remained unchanged during the Mesozoic except for a slight rotation and that the NQT, SQT, AD, LT collided successively on the southern margin of the Tarim, based on the above paleomagnetic, petrological, geochronological, stratigraphic, and paleontological data. Therefore, the global plates distribution map centered on Tarim in the Mesozoic (~220 Ma, ~160 Ma, ~120 Ma; [Figure 5](#)) was drawn on the basis of these insights, and the other plate locations were mainly referred to the data in [Huang et al. \(2018\)](#); [Zhao et al. \(2018\)](#).

4 Reconstruction of the proto-type basin

There are two major controversies related to the nature of each depression in the Tarim Basin during the Mesozoic. The first is whether a foreland basin existed during the Triassic in the southwestern Tarim, and the second is whether the Kuqa Basin was a depression or a rejuvenated foreland basin during the Triassic. In the southwestern Tarim, [He et al. \(2013\)](#) suggested that the southwestern Tarim region suffered denudation due to intense uplift influenced by the closure of the Paleo-Tethys Ocean and locally

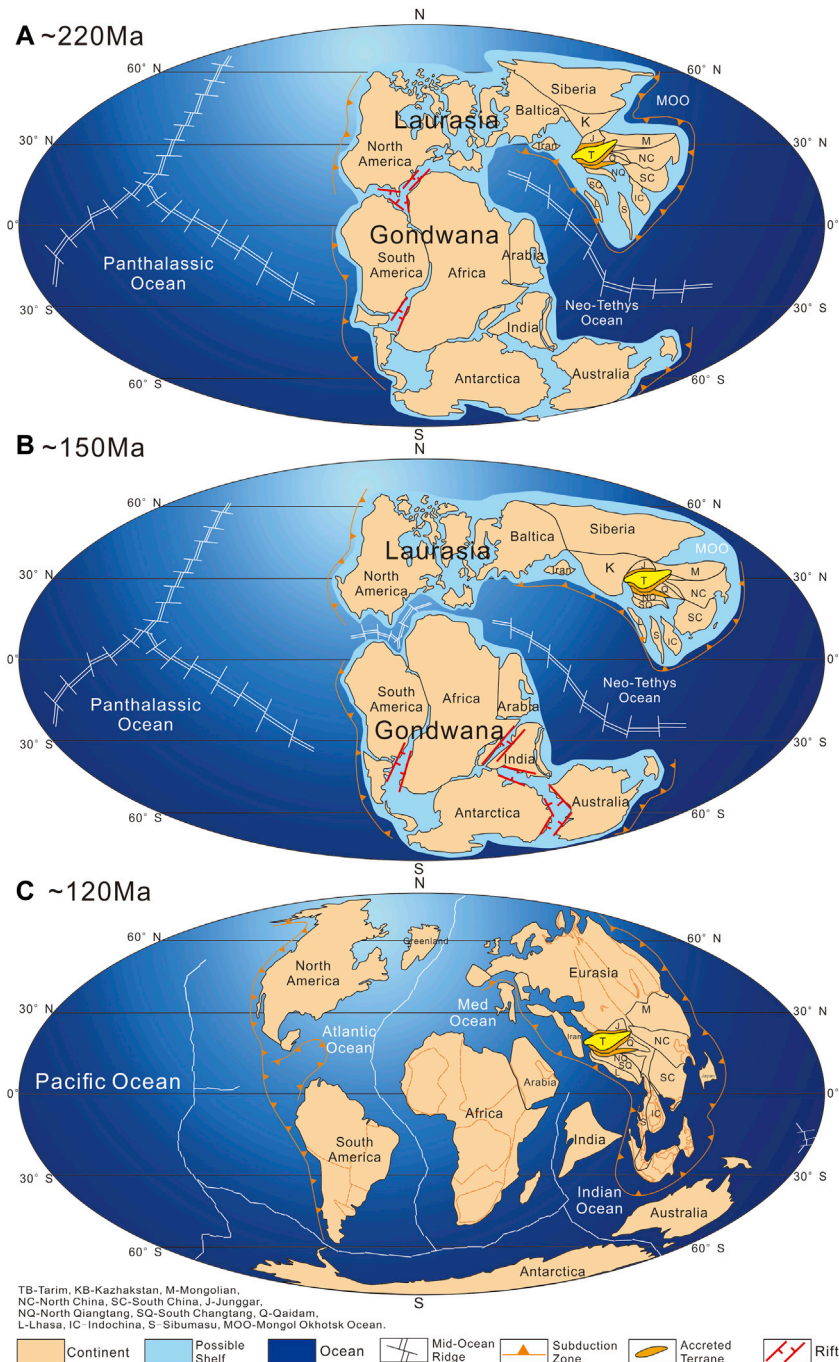


FIGURE 5

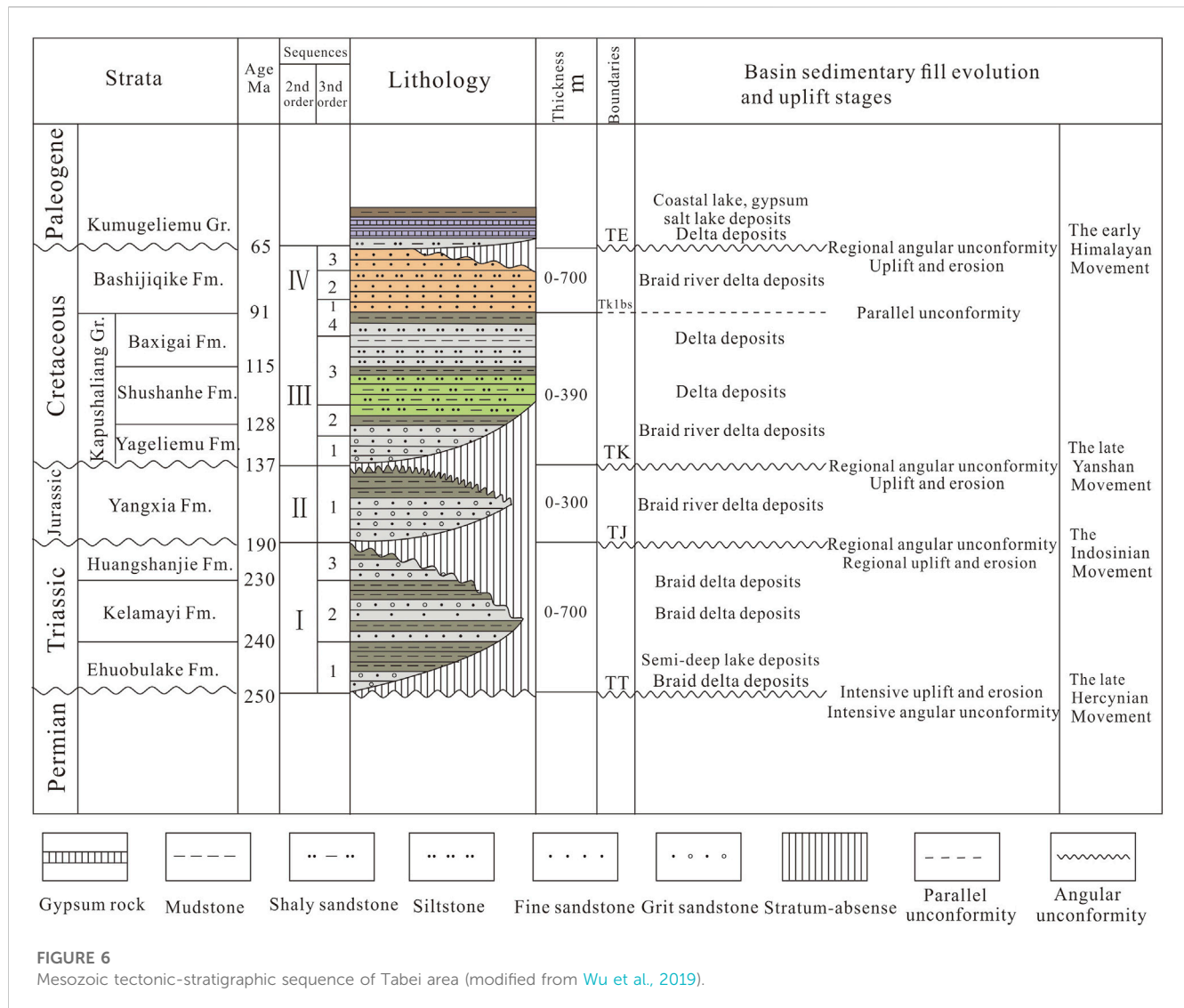
Reconstruction of global plates distribution in the Mesozoic (modified from Huang et al., 2018; Wei et al., 2022). (A) 220 Ma, (B) 150 Ma, (C) 120 Ma.

developed mountain basin (He et al., 2013). Zheng et al. (2014) concluded that downwarped basins should have existed in the southwestern Tarim area in the Triassic by reconstructing the proto-type basin. However, the intense uplift destroyed the sedimentary basins in the Late Triassic (Zheng et al., 2014). In the Kuqa area, Liu et al. (2000); Jia et al. (2003) considered that the Kuqa Basin belongs to the foreland basin in front of the South Tianshan folded orogenic belt in the Triassic. Qu et al., 2004; Li et al., 2017 consider the Kuqa Basin as a regional downwarped basin above

the northern margin uplift of the Late Paleozoic Tarim Block in the Triassic period.

4.1 Triassic

The Triassic stratigraphy in the Tarim Basin is mainly located in the Kuqa Basin, Tabei and Tazhong areas, and is dominated by alluvial fan-braided river delta-flood plain-lake



facies (Figure 6; Jia et al., 2013; Wei et al., 2021). The Triassic stratigraphy (0–300 m thickness) is widely distributed in an east-west strip throughout the Kuqa Basin. The depocenter of the basin formed by the combined area of Tabei and Tazhong is in the Awati depression. Based on thickness trends, the stratigraphic thickness of the Triassic denudation may locally reach 500 m, with the original boundary line typically 2–4 km and up to 10 km from the current stratigraphic boundary line of the remnant. The width of the denuded Triassic area is 30–40 km in the northern Kuqa Basin, and the denuded thickness is 0–2,400 m (Yu et al., 2016). The balanced cross-sections can be seen that the main Triassic deformation occurred in the southwestern Tarim Basin (~3 km) and the southeastern Tarim (~7 km).

In the southwestern Tarim Basin, few Triassic strata are remained, only the Duwa site (Figure 9A) developed the Lower Triassic Wuzunsayi Formation of 200–300 m thick river-lake facies sandstone and dark mudstone in the Triassic. The Wuzunsayi Formation is conformably overlying the Upper Permian Duwa Formation with synchronous deformation and

unconformably overlain by the Jurassic-Cretaceous strata conformity, which was parallel unconformity (Yang, 1994). The Late Triassic thrust structures were also revealed by seismic interpretation (Li et al., 2017). On the seismic sections, the Late Triassic thrusts cut through the Paleozoic and stop at the bottom of the Jurassic-Cretaceous (Figure 7), and the deformations in the Jurassic-Cretaceous are similar to the overlying the Cenozoic both not involved in the Late Triassic thrusting. These may be critical evidence for developing a small basin at the Duwa of the southwestern Tarim Basin in the Early Triassic but were destroyed by thrust faults in the Late Triassic.

In the Kuqa Basin, both the remnant stratigraphy and the reconstructed primary stratigraphy show that the depocenter moved toward the orogenic zone and that the thickness thinned gradually from the depocenter to the orogenic zone. However, the depocenter of the foreland basin commonly moves toward the foreland and gradually thins from the orogenic belt to the basin. The Triassic strata are overlain on top of the South Tianshan orogenic wedge and show a progressive change in sedimentary facies and sequence structure with the overlying Jurassic strata.

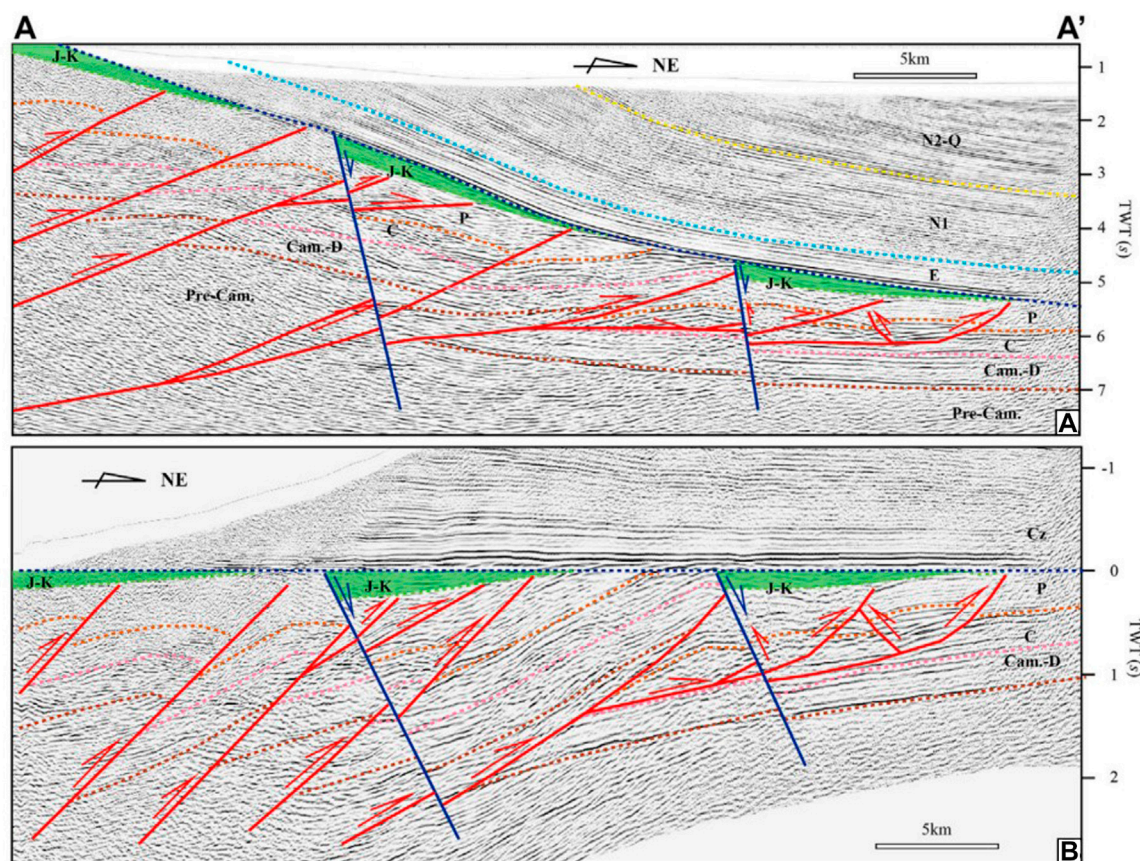


FIGURE 7
Two-dimensional seismic section A-A' in piedmont of W. Kunlun (A) and flattened its Paleogene bottom (B) (Li et al., 2017).

As a result, the Kuqa Basin is more like a downwarped basin superimposed on the transition zone between the South Tianshan orogenic belt and the Tarim Craton. The balanced cross-sections of B-B' (Figure 8) and Qi et al. (2022) also show that the Triassic basin did not develop large-scale thrust faults, and even normal faults may exist. Thus, the Kuqa Basin is a downwarped basin developed on top of the Late Paleozoic thrust-fold wedge or even a faulted basin in the Triassic.

The reconstruction of the Triassic proto-type basin in the Tarim Basin indicates that the Kuqa Basin and the Tazhong Basin are downwarped basins controlled by crustal isostasy (Figure 9A). There was also a local downwarped basin in the southern Tarim Basin in the Early Triassic, which was destroyed by thrust faults in the Late Triassic.

4.2 Jurassic and Cretaceous

There are three main controversial types of Jurassic faulted basins in the southwestern Tarim: the pull-apart basin associated with the Fergana-Kashgar-Yecheng strike-slip fault (Sobel, 1999), the large half-graben faulted basin between Tarim Block and West Kunlun orogenic belt (Zhang et al., 2000), and small horst-graben structure after the collision orogeny (Li et al., 2017). To address this

issue, we reconstructed the Jurassic and Cretaceous proto-type basins of the Tarim Block in the same way as above and obtained Figures 9B, C.

Jurassic formations in the Tarim Block are mainly found in the Kuqa Basin, the southwestern Tarim Basin, the southeastern Tarim Basin and the eastern Tarim Basin. The continental clastic rocks of alluvial fan-braided river delta-flood plain-lake facies are developed under the control of normal faults in the Kuqa Basin, the southwestern Tarim Basin, and the southeastern Tarim Basin. The maximum thickness of Jurassic strata in each basin is ~1,000–2,000 m, and it gradually thins from the fault to the basin (Wei et al., 2022). The depocenter of the basin gradually moved toward the orogeny. Deformation in the Late Jurassic led to uplift and denudation, resulting in the formation of a regional unconformity with a general denudation thickness of 0–250 m in the interior of the basin and a maximum denudation thickness of 500 m. However, the denudation thickness is up to 2,000 m, and the denudation distance is up to 40 km in the northern margin of the Kuqa basin (Yu et al., 2016). Jurassic basins are predominantly unshortened and developed faulted basins in regional extensional settings.

The Late Jurassic is a transitional phase from the stable stage of fault subsidence to the initial stage of depression. The underlying faulted basin combines with the overlying downwarped basin to form a basin with a binary structure from observation of the seismic

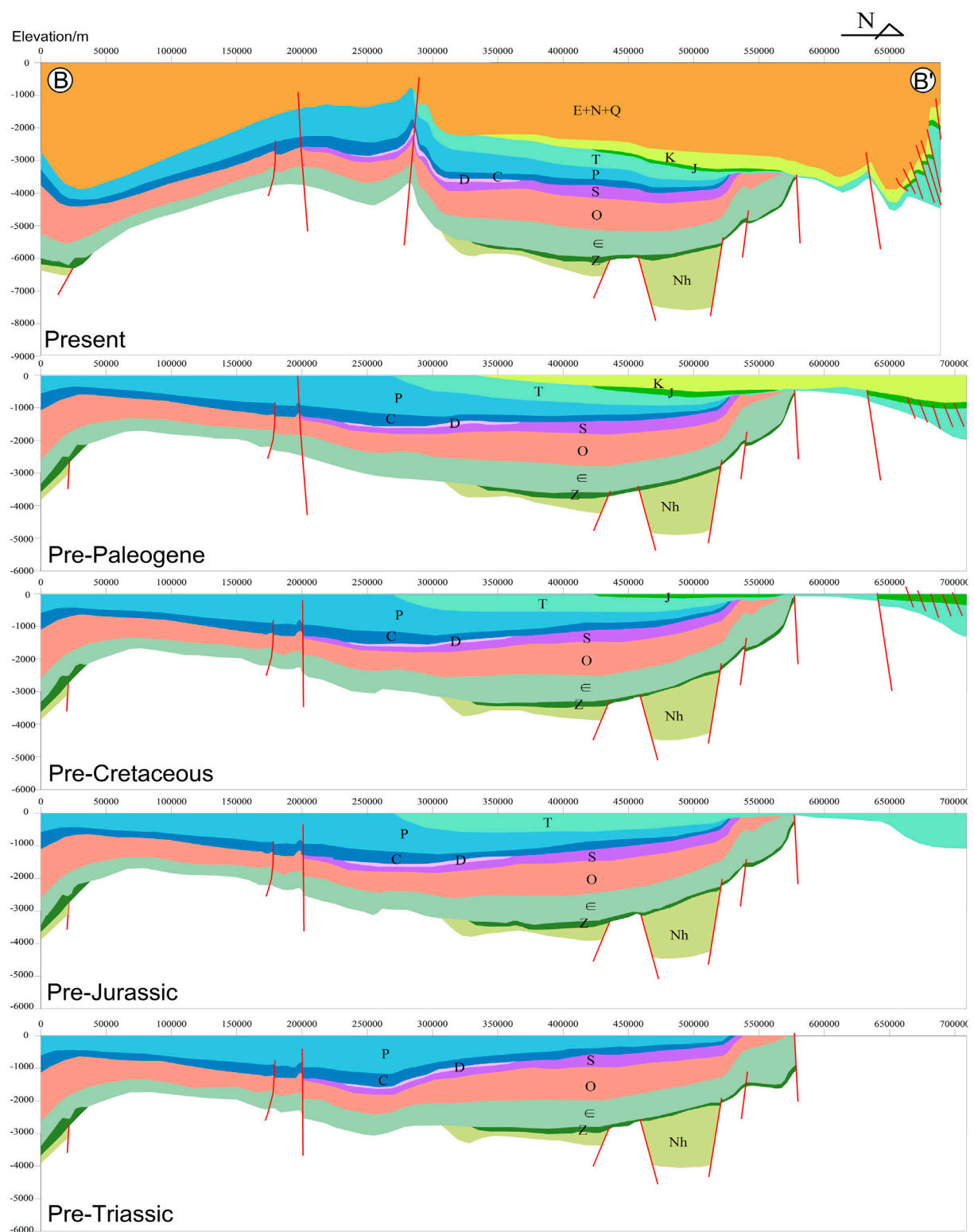
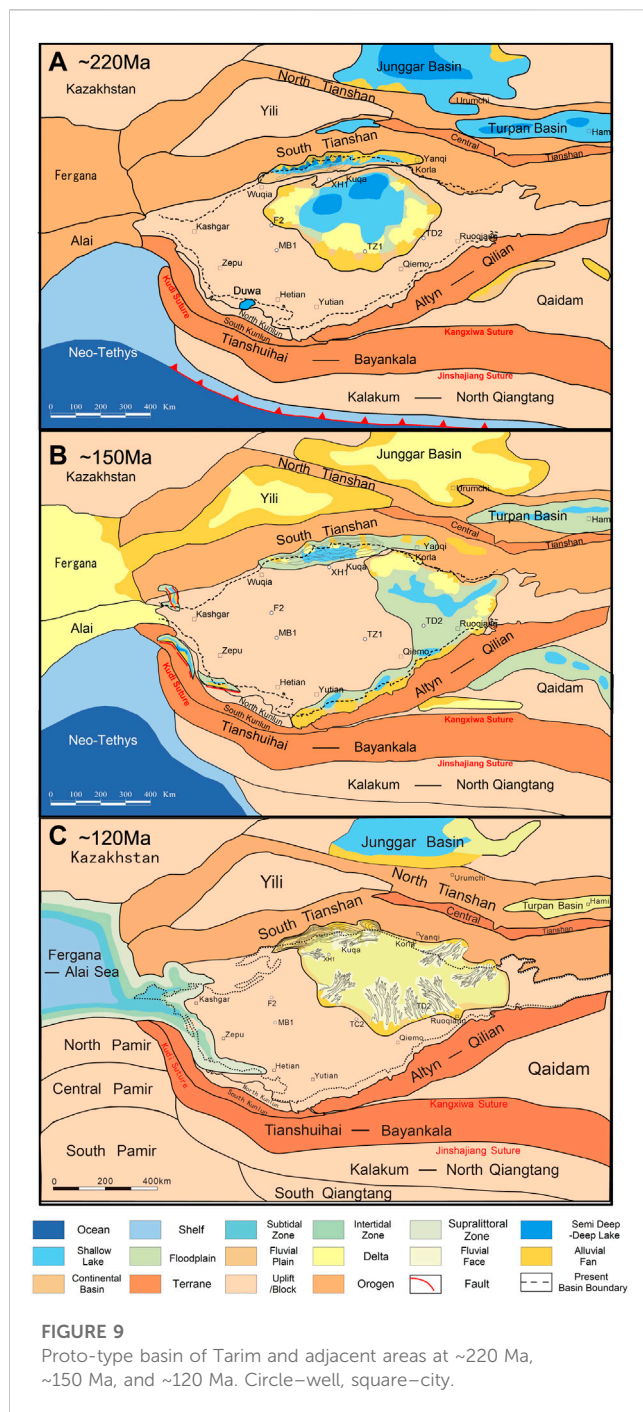


FIGURE 8

The balanced cross-section of B-B' section. Abbreviations: Nh–Nanhua system (Cryogenian system), Z–Sinian system (Ediacaran system), ε–Cambrian system; O–Ordovician system; S–Silurian system; D–Devonian system; C–Carboniferous system; P–Permian system; T–Triassic system; J–Jurassic system; K–Cretaceous system; E–Paleogene system; N–Neogene system; Q–Quaternary system.



section in Jurassic (Figure 10). An approximately 60 km-wide Triassic fold-and-thrust belt along the southwestern margin of Tarim Basin is unconformably overlain by a Jurassic–Cretaceous sedimentary sequence along a regional angular unconformity in the southwestern Tarim Basin. The Lower–Middle Jurassic strata consists mainly of an upward-fining sequence ranging from terrestrial conglomerates to turbidite deposits, representing the products of an initial rift stage. Contrast to the pioneering phase, the sequence of Late Jurassic through Early Cretaceous were characterized by several cycles of coarse clastic deposits with large-scale cross laminations that suggest a fluvial to braided

delta setting (Wu et al., 2021). These basins were not unified as one but existed in the graben-horst structure. These Jurassic basins are distributed along the Karakorum premontane faults and cannot be extended to the Ferghana Fault as no contemporaneous Jurassic clastic deposits exist between the Karakorum and the Western Tianshan. Therefore, based on reconstructions of proto-type basins, the southwest Tarim Basin was a faulted basin with small horst-graben structure after the collision of orogeny during the Jurassic.

The Early Cretaceous strata are mainly distributed in the southwestern Tarim Basin and the Central Basin consisting of Kuqa, Tazhong, Tadong, Tanan, and southeastern Tarim, and deposit red coarse clastic terrestrial deposits of alluvial fan-braided river delta-flood plain-fluvial faces. Compared to the Late Jurassic strata, the Cretaceous strata are thinner in thickness and slower in deposition rate but are similar in depositional and structural characteristics without being controlled by faults (Li et al., 2017; Wu et al., 2021). The crustal shortening did not alter significantly in most areas, except for the southeastern Tarim, where a shortening of 2–3 km occurred, resulting in a substantial uplift that reduced the area of the southeast Tarim Basin by approximately half in the Early Cretaceous. The Central Tarim Basin is an intracratonic depression basin according to these sedimentary features. During the Late Cretaceous, the Tarim Basin was denuded due to general uplift, resulting in practically no sedimentary record for the entire basin, except for the southwest Tarim Basin. The late Early Cretaceous in the northeastern part of the eastern Tethys witnessed a large-scale transgression event that resulted in the formation of the trumpet-shaped bay in the western Tarim Basin (Xi et al., 2020). Finally, the basin is dominated by repeated deposition of multiple mudstone-carbonate assemblages in the Late Cretaceous (Bosboom et al., 2014), indicating that the sedimentary environment is mainly controlled by multiple transgression-regressive cycles rather than intense tectonic activities (Zhang et al., 2018). The inconspicuous shortening of the crust and the inactive thrust faults indicate that southwest Tarim Basin was a downwarped basin throughout the Cretaceous.

The Jurassic and Cretaceous proto-type basin reconstructions (Figures 9B, C) show that the Jurassic was a fault-basin period and began a transition to a downwarped basin in the Late Jurassic. The early Cretaceous basins were deposited and sequenced in a similar manner to those of the Late Jurassic. However, unlike the Late Cretaceous Tarim Basin, which experienced uplift and ceased deposition (Jia et al., 2003; Jin et al., 2008), except for the southwest region where there was the development of marine sedimentation due to multiple transgression-regression cycles.

5 Reconstruction of tectono-paleogeography around the Tarim Basin

The study of tectono-paleogeography focuses on tectonic patterns and paleogeographic features. The basin types and global tectonic events control the paleogeographic distribution, basin subsidence rates, depositional systems and evolution of proto-type basin. The Tarim Basin has entered the stage of continental basin development since the Mesozoic and mainly developed

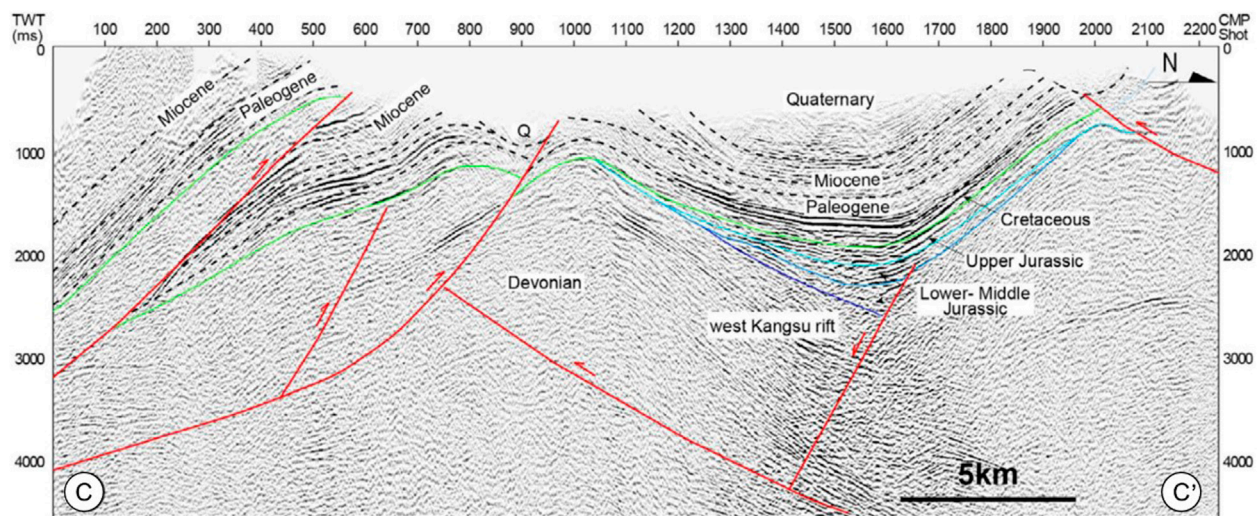


FIGURE 10
Interpretation of the seismic profile C-C' in the southwestern Tarim Basin (Wu et al., 2021).

terrestrial clastic rocks (He et al., 2005). The closure of the Paleo-Tethys Ocean and the opening-closing of the Neo-Tethys Ocean in the southern Tarim Basin heavily influenced the Tarim Basin, including changes its uplift-depression pattern and unconformity development (Wang et al., 2010; Xu et al., 2011). In order to clarify the influence of global tectonic events on the Mesozoic paleogeography of the Tarim Basin, this paper analyses the Mesozoic geotectonic events on the periphery of the Tarim Basin and reconstructs the Mesozoic tectono-paleogeography of the Tarim Basin in a comprehensive view.

5.1 Tectono-paleogeography around the Tarim Basin in the Late Triassic period

The Paleo-Tethys Ocean had begun to northward subduction since the Carboniferous in the southern Tarim and eventually closed in the Late Triassic in response to the accretion of the Tianshuihai-Bayankara terrane, NQT and SQT with the Tarim Block (Jolivet et al., 2001; Xiao et al., 2002; Xiao et al., 2003; Liu et al., 2015; Song et al., 2015; Ma et al., 2020; Wei et al., 2022). The intense compressional collision caused an uplift in the southern Tarim Basin, transforming the Permian foreland into an uplift (He et al., 2015). This collision also formed the thrust fault structure from the West Kunlun orogenic belt and the Altyn orogenic belt toward the basin in the southern margin of the Tarim Basin, as well as the back thrust structure from the basin to the orogenic belt in the Maigaiti slope (Li et al., 2017). Uplift and thrust of the basin caused the Early-Middle Triassic strata in Bachu, Tanggu and Tadong areas to be denuded to the Central basin and formed a sizeable regional unconformity. Alluvial fan-braided river delta-flood plain-lake facies were mainly developed in the central basin, and the depocenter was located in the Tabei area and moved northward continuously during the Triassic period (Liu et al., 2012). At this time, Kuqa Basin, as a downwarped basin superimposed on the

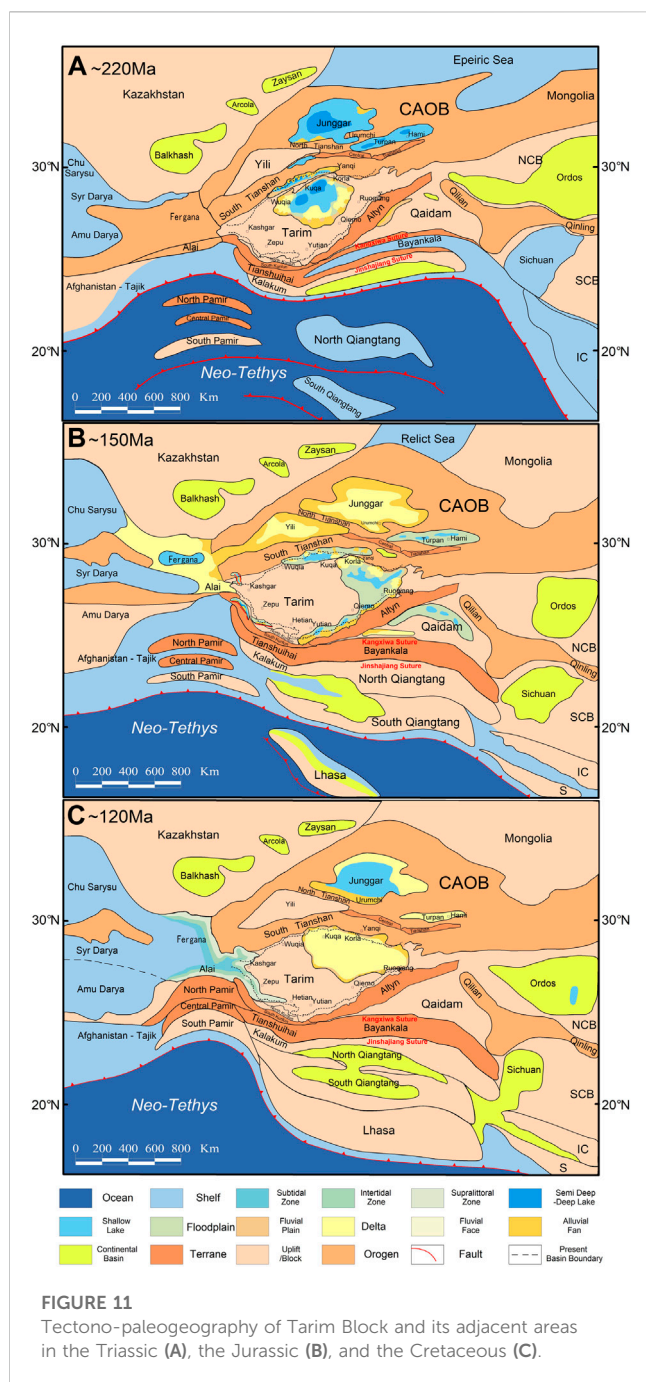
transitional zone between the northern margin uplift of the Tarim Craton and the Late Paleozoic southern Tianshan orogenic wedge, was not evidently affected by the collision (Figure 11A).

5.2 Tectono-paleogeography around the Tarim Basin in the Late Jurassic period

The Tethys region was in an expanding setting as the New Tethys Ocean spread during the Early to Middle Jurassic. The Triassic uplift transformed into depressions in the southern Tarim Basin under the extensional background, and a series of narrow and deep faulted basins with coal-bearing strata composed of sand-mudstone intercalated with coal seams at the margin of the Tarim Basin (Figure 11B). The Amdo-Dongkacuo microcontinent collided with the southern margin of Tarim during the Late Jurassic period, which caused the Tarim Basin to be influenced by compressional stresses (Ma et al., 2020). The normal fault ceased to be active and the graben basin began to transform into a downwarped basin. Red coarse-grained clastic rocks were deposited throughout the basin during the Late Jurassic, and alluvial fans suddenly appeared in the southeastern Tarim.

5.3 Tectono-paleogeography around the Tarim Basin in the late Early Cretaceous period

The collision of the Amdo-Dongkacuo microcontinent with the Tarim Block in the Late Jurassic represents the beginning of the collision of the paleo Lasa terranes with Eurasia. The northward subduction of the Meso-Tethys during the Early Cretaceous and the continued collision of microcontinents created continuous compressional stress on the Tarim Basin. The southeastern Tarim began to uplift and no longer received



deposition, and the Kuqa Basin and the Central Basin have combined into a whole with red coarse clastic deposits (Figure 11C). The collision of the Lhasa Block with the Tarim Block formed an enormous compressional stress during the Late Early Cretaceous that caused the entire Tarim Basin to uplift and no longer accept sedimentation. The widespread transgression of the Tethys Ocean resulted in seawater influx from the western openings of the Tarim Basin into the southwestern Tarim Basin.

It began to receive a deposition of multiple mudstone-carbonate assemblages (~110 Ma).

6 Conclusion

1 The North Qiangtang Terrane and the South Qiangtang Terrane collided with the Tarim Block successively during ~220 Ma to 215 Ma, rather than merging into a single block before colliding in the late Triassic. This collision led to a large uplift in the southern Tarim Basin resulting in denudation of strata. Therefore, a large number of alluvial fans appeared in the southern margin of the sedimentary basin and the depositional center moved northward.

2 Faulted basins combined to form a large floodplain developed in the Early–Middle Jurassic extensional setting in the margins of the Tarim Basin. In the Late Jurassic, the Tarim Block was compressed to some extent and the faulted basin started to transform into a downwarped basin with red coarse clastic sediments as a result of the Amdo-Dongkacuo microcontinent collision with Tarim Block at ~160 Ma.

3 During the early Cretaceous period, the Tarim Basin was characterized by a downwarped basin inherited from the late Jurassic period. Around 120 Ma ago, the Lhasa Block collided with the Tarim Block, causing the Tarim Basin to experience uplift and denudation. Additionally, the southwestern region of the Tarim Basin underwent transgression from the Neo-Tethys Ocean, leading to the deposition of marine sediments.

Author contributions

XL did the main analysis, writing and editing. HC participated in the analysis and mapping of this paper. SH, CL, and YD provided extensive geological data and guidance. HZ, ZZ, JX, and LW have provided information from other eras as well as image making.

Conflict of interest

Authors SH, CL, and YD were employed by the company Tarim Oilfield Company.

The remaining authors declare that the research was conducted in the absence of any commercial or financial relationships that could be construed as a potential conflict of interest.

Publisher's note

All claims expressed in this article are solely those of the authors and do not necessarily represent those of their affiliated organizations, or those of the publisher, the editors and the reviewers. Any product that may be evaluated in this article, or claim that may be made by its manufacturer, is not guaranteed or endorsed by the publisher.

References

- Bosboom, R., Dupont-Nivet, G., Grothe, A., Brinkhuis, H., Villa, G., Mandic, O., et al. (2014). Linking Tarim Basin sea retreat (west China) and Asian aridification in the late Eocene. *Basin Res.* 26 (5), 621–640. doi:10.1111/bre.12054
- Chen, H. L., Luo, J. C., Guo, Q. Y., Liao, L., Cheng, X. G., Yang, S. F., et al. (2009). Deformation history and tectonic evolution of southeastern Tarim Basin in mesozoic and cenozoic. *Geotect. Metallogenia* 33 (1), 38–45.
- Chen, R. L. (1995). Once more discussion on the middle jurassic marine-flooding event deposition of the Tarim Basin. *Exp. Pet. Geol.* 17 (4), 311–315.
- Chen, R., Shen, Y. P., and Zhang, C. C. (2015). The Meso-Cenozoic tectono-paleogeographic characteristics and evolution of Caribbean Plate margins. *J. Paleogeogr.* 17 (1), 63–81. doi:10.7605/gdxb.2015.01.006
- Chen, S. J., Zhao, Z. M., Ji, W. H., Li, R. S., Liu, R. L., and Zha, X. F. (2013). The characteristic of tectonic-lithofacies paleogeography during Early-Middle Permian in the west Kunlun and adjacent areas. *Chin. J. Geol.* 48 (4), 1015–1032. doi:10.3969/j.issn.0563-5020.2013.04.005
- Chen, W. W., Yang, T. S., Zhang, S. H., Yang, Z. Y., Li, H. Y., Wu, H. C., et al. (2012). Paleomagnetic results from the early cretaceous zenong Group volcanic rocks, cuoqin, tibet, and their paleogeographic implications. *Gondwana Res.* 22 (2), 461–469. doi:10.1016/j.gr.2011.07.019
- Chen, Y., Cogne, J. P., and Courtillot, V. (1992). New cretaceous paleomagnetic Poles from the Tarim Basin, northwestern China. *Earth Planet. Sci. Lett.* 114 (1), 17–38. doi:10.1016/0012-821x(92)90149-P
- Eizenhöfer, P. R., and Zhao, G. (2018). Solonker suture in East Asia and its bearing on the final closure of the eastern segment of the palaeo-asian ocean. *Earth-Science Rev.* 186, 153–172. doi:10.1016/j.earscirev.2017.09.010
- Fang, D. J., Chen, H. L., Wang, P. Y., and Tan, X. D. (1997). Paleomagnetic study and its tectonic significance for Tarim basin in Mesozoic. *Acta Geophys. Sin.* 40, 47–55.
- Fang, D., Jin, G., Chen, H., Guo, Y., Wang, Z., Yin, S., et al. (1991). Preliminary approach to Late Paleozoic-Mesozoic geomagnetism and tectonic evolution in north margin of Tarim plate. *Res. Petroleum Geol. North. Tarim Basin China* 2, 96–104.
- Fang, D. J., Shen, Z. Y., Ying, S. H., and Tan, X. D. (2001). Early cretaceous paleomagnetic results from the kuche depression, Tarim block and the cause of their inclination shallowing. *Chin. J. Geophys.* 44 (1), 68–78. doi:10.1002/cjg2.117
- Feng, Z. Z., Peng, Y. M., Jin, Z. K., and Bao, Z. D. (2004). Lithofacies palaeogeography of the late ordovician in China. *J. Paleogeogr.* 6 (2), 128–139.
- Fu, X. G., Wang, J., Tan, F. W., Chen, M., and Chen, W. B. (2010). The Late Triassic rift-related volcanic rocks from eastern Qiangtang, northern Tibet (China): Age and tectonic implications. *Gondwana Res.* 17 (1), 135–144. doi:10.1016/j.gr.2009.04.010
- Gao, H. H., He, D. F., Tong, X. Y., Wen, Z. X., and Wang, Z. M. (2017). “Tectonic-depositional environment and proto-type basins evolution of the late ordovician in the Tarim Basin,” in *Egu general assembly conference abstracts* (Vienna, Austria: EGU), 11218.
- Gilder, S. A., Gomez, J., Chen, Y., and Cogne, J. P. (2008). A new paleogeographic configuration of the eurasian landmass resolves a paleomagnetic paradox of the Tarim Basin (China): A paleomagnetic paradox. *Tectonics* 27 (1), 2155. doi:10.1029/2007tc002155
- Gilder, S., Chen, Y., Cogné, J. P., Tan, X., Courtillot, V., Sun, D., et al. (2003). Paleomagnetism of Upper Jurassic to Lower Cretaceous volcanic and sedimentary rocks from the Western Tarim Basin and implications for inclination shallowing and absolute dating of the M-0 (ISEA?) chron. *Earth Planet. Sci. Lett.* 206 (3–4), 587–600. doi:10.1016/s0012-821x(02)01074-9
- Han, Y. G., and Zhao, G. C. (2018). Final amalgamation of the tianshan and junggar orogenic collage in the southwestern central asian orogenic belt: Constraints on the closure of the paleo-Asian ocean. *Earth-Science Rev.* 186, 129–152. doi:10.1016/j.earscirev.2017.09.012
- He, B. Z., Jiao, C. L., Xu, Z. Q., Liu, S. L., Cai, Z. H., Li, H. B., et al. (2013a). Unconformity structural architecture and tectonic paleo-geographic environment: A case of the middle caledonion on the northern margin of tibet plateau and Tarim Basin. *Acta Petrol. Sin.* 29 (6), 2184–2198.
- He, B. Z., Jiao, C. L., Xu, Z. Q., Cai, Z. H., Zhang, J. X., Liu, S. L., et al. (2016a). The paleotectonic and paleogeography reconstructions of the Tarim Basin and its adjacent areas (NW China) during the late Early and Middle Paleozoic. *Gondwana Res.* 30, 191–206. doi:10.1016/j.gr.2015.09.011
- He, B. Z., Jiao, C. L., and Xu, Z. Q. (2015). Distribution and migration of the phanerozoic palaeo-uplifts in the Tarim Basin, NW. China. *Earth Sci. Front.* 22 (3), 277–289. doi:10.13745/j.esf.2015.03.024
- He, D. F., Zhou, X., Zhang, C. J., and Yang, X. F. (2007). Tectonic types and evolution of Ordovician proto-type basins in the Tarim region. *Chin. Sci. Bull.* 52 (1), 164–177. doi:10.1007/s11434-007-6010-z
- He, D. F., Jia, C. Z., Zhou, X. Y., Shi, X., Wang, Z. M., Pi, X. J., et al. (2005). Control principles of structures and tectonics over hydrocarbon accumulation and distribution in multi-stage superimposed basins. *ACTA PET. SIN.* 26 (3), 1–9.
- He, D. F., Li, D. S., He, J. Y., and Wu, X. Z. (2013b). Comparison in petroleum geology between Kuga depression and Southwest depression in Tarim Basin and its exploration significance. *Acta Pet. Sin.* 34 (2), 201–218. doi:10.7623/syxb201302001
- He, J., Wang, Y., Liu, S. L., and He, D. F. (2016b). Characteristics of fault structure and its control on hydrocarbon accumulation in the eastern part of southwestern Tarim Basin. *Petroleum Geol. Exp.* 38 (3), 326–332. doi:10.11781/sysydz20160332
- Henry, P., and Natalya, A. (1996). Analysis of sonic well logs applied to erosion estimates in the Bighorn basin, Wyoming. *AAPG Bull.* 80 (5), 630–646.
- Hou, G. T., Santosh, M., Qian, X. L., Ister, G. S., and Li, J. H. (2008). Configuration of the Late Paleoproterozoic supercontinent Columbia: Insights from radiating mafic dyke swarms. *Gondwana Res.* 14 (3), 395–409. doi:10.1016/j.gr.2008.01.010
- Hu, X. M., Ma, A. L., Xue, W. W., Garzanti, E., Cao, Y., Li, S. M., et al. (2022). Exploring a lost Ocean in the Tibetan plateau: Birth, growth, and demise of the bangong-nuijiang ocean. *Earth-Science Rev.* 229, 104031. doi:10.1016/j.earscirev.2022.104031
- Huang, B. C., Yan, Y. G., Piper, J. D. A., Zhang, D. H., Yi, Z. Y., Yu, S., et al. (2018). Paleomagnetic constraints on the paleogeography of the East Asian blocks during late paleozoic and early mesozoic times. *Earth-Science Rev.* 186, 8–36. doi:10.1016/j.earscirev.2018.02.004
- Jia, C., and Wei, G. (1997). *Tectonic characteristics and petroleum, Tarim basin*. Beijing: China. Petrol. Ind. Press.
- Jia, C. Z., Chen, H. L., Yang, S. F., Lu, H. F., and Zhou, Y. Z. (2003). Late Cretaceous uplifting process and its geological response in Kuqa Depression. *ACTA Pet. Sin.* 24 (3), 1–5.
- Jia, C., Zhang, S., and Wu, S. (2004). *Stratigraphy of the Tarim Basin and adjacent areas*. (Beijing: Springer, 1–450).
- Jia, C. Z., Li, B. L., Lei, Y. L., and Chen, Z. X. (2013). The structure of Circum-Tibetan Plateau Basin-Range System and the large gas provinces. *Sci. China Earth Sci.* 43 (10), 1853–1863. doi:10.1007/s11430-013-4649-7
- Jia, J. H. (2009). Sedimentary characteristics and paleogeography of the early cretaceous in Tarim Basin. *J. Paleogeogr.* 11 (2), 167–176.
- Jin, Z. J., and Wang, Q. C. (2004). Recent developments in study of the typical superimposed basins and petroleum accumulation in China: Exemplified by the Tarim Basin. *Sci. China Ser. D-Earth Sci.* 47, 1–15. doi:10.1360/04zd0020
- Jin, Z. J., Yang, M., Lu, X. X., Sun, D. S., Tang, X., Peng, G. X., et al. (2008). The tectonics and petroleum system of the Qulitagh fold and thrust belt, northern Tarim basin, NW China. *Mar. Petroleum Geol.* 25 (8), 767–777. doi:10.1016/j.marpetgeo.2008.01.011
- Jolivet, M., Brunel, M., Seward, D., Xu, Z., Yang, J., Roger, F., et al. (2001). Mesozoic and cenozoic tectonics of the northern edge of the Tibetan plateau: Fission-track constraints. *Tectonophysics* 343 (1–2), 111–134. doi:10.1016/S0040-1951(01)00196-2
- Laborde, A., Barrier, L., Simoes, M., Li, H., Coudroy, T., Van der Woerd, J., et al. (2019). Cenozoic deformation of the Tarim Basin and surrounding ranges (xinjiang, China): A regional overview. *Earth-Science Rev.* 197, 102891. doi:10.1016/j.earscirev.2019.102891
- Lei, T., Zhang, H. Q., Jun, L., Zhang, N. C., and Shi, X. Q. (2020). Distribution of Nanhua-Sinian rifts and proto-type basin evolution in southwestern Tarim Basin, NW China. *Petroleum Explor. Dev.* 47 (6), 1206–1217. doi:10.1016/S1876-3804(20)60130-1
- Li, C., Zhai, Q. G., Dong, Y. S., and Huang, X. P. (2006). Discovery of eclogite in central Qiangtang, qinghai-tibet plateau and its significance. *Chin. Sci. Bull.* 51 (1), 70–74.
- Li, D., Liang, D., Jia, C., Wang, G., Wu, Q., and He, D. (1996). Hydrocarbon accumulations in the Tarim basin, China. *Aapg Bull.* 80 (10), 1587–1603.
- Li, J. C., Zhao, Z. B., Zheng, Y. L., Yuan, G. L., Liang, X., Wang, G. H., et al. (2015). The magmatite evidences in southern Qiangtang for paleo-Tethys ocean subducting collision: Gangtang-co granites in Rongma, Tibet. *Acta Petrol. Sin.* 31 (7), 2078–2088.
- Li, S., Yin, C. Q., Guilmette, C., Ding, L., and Zhang, J. (2019). Birth and demise of the bangong-nuijiang tethyan ocean: A review from the gerze area of central tibet. *Earth-Science Rev.* 198, 102907. doi:10.1016/j.earscirev.2019.102907
- Li, Y. A., Li, Q., Zhang, H., Sun, D. J., Cao, Y. D., and Wu, S. Z. (1995). Palaeomagnetic study of tarim and its adjacent area as well as the formation and evolution of Tarim Basin. *Xinjiang Geol.* 13 (4), 293–316.
- Li, Y. (1990). An apparent polar wander path from the Tarim Block, China. *Tectonophysics* 181 (1–4), 31–41. doi:10.1016/0040-1951(90)90007-u
- Li, Y., Qi, J. F., Shi, J., Sun, T., Xu, Z. P., Yu, H. B., et al. (2017). Microwave-assisted synthesis of imidazo[4,5-f] [1,10]phenanthroline derivatives as apoptosis inducers in chemotherapy by stabilizing bcl-2 G-quadruplex DNA. *Geotect. Metallogenia* 41 (5), 829–842. doi:10.3390/molecules22050829
- Li, Y., Wen, L., Yang, X., Li, C., Zhang, L., Wang, B., et al. (2022). Mesozoic collision-related structures in the southern Tarim Basin, W. China: Implications for the paleo-tethys closing process. *Front. Earth Sci.* 9, 792049. doi:10.3389/feart.2021.792049
- Li, Y., Zhang, Z., McWilliams, M., Sharps, R., Zhai, Y., Li, Y., et al. (1988). Mesozoic paleomagnetic results of the Tarim craton: Tertiary relative motion between China and Siberia? *Geophys. Res. Lett.* 15 (3), 217–220. doi:10.1029/gl015i003p00217
- Li, Z. Y., Ding, L., Lippert, P. C., Song, P. P., Yue, Y. H., and van Hinsbergen, D. J. J. (2016). Paleomagnetic constraints on the mesozoic drift of the Lhasa terrane (tibet) from Gondwana to Eurasia. *Geology* 44 (9), 727–730. doi:10.1130/G38030.1
- Lin, C., Li, S., Liu, J., Qian, Y., Luo, H., Chen, J., et al. (2011). Tectonic framework and paleogeographic evolution of the Tarim basin during the Paleozoic major evolutionary stages. *Acta Petrol. Sin.* 27 (1), 210–218.

- Lin, C. S., Yang, H. J., Liu, J. Y., Rui, Z. F., Cai, Z. Z., and Zhu, Y. F. (2012). Distribution and erosion of the Paleozoic tectonic unconformities in the Tarim Basin, Northwest China: Significance for the evolution of paleo-uplifts and tectonic geography during deformation. *J. Asian Earth Sci.* 46, 1–19. doi:10.1016/j.jseas.2011.10.004
- Liu, J., Lin, C., and Jiang, L. (2000a). A quantitative model of compaction trend using sonic well logs: Applied to erosion amount estimation in the xihu depression, east China sea. *Petroleum Sci.* 4, 41–48.
- Liu, J., Yi, J., and Chen, J. Y. (2020). Constraining assembly time of some blocks on eastern margin of Pangea using Permo-Triassic non-marine tetrapod records. *Earth-Science Rev.* 207, 103215. doi:10.1016/j.earscirev.2020.103215
- Liu, L., Zhang, J. F., Cao, Y. T., Green, H. W., Yang, W. Q., Xu, H. J., et al. (2018). Evidence of former stishovite in UHP eclogite from the South Altyn tagh, Western China. *Earth Planet. Sci. Lett.* 484, 353–362. doi:10.1016/j.epsl.2017.12.023
- Liu, Q., Zhao, G. C., Han, Y. G., Eizenhofer, P. R., Zhu, Y. L., Hou, W. Z., et al. (2017). Timing of the final closure of the paleo-Asian Ocean in the alxa terrane: Constraints from geochronology and geochemistry of late carboniferous to permian gabbros and diorites. *Lithos* 274, 19–30. doi:10.1016/j.lithos.2016.12.029
- Liu, Q., Zhao, G. C., Sun, M., Eizenhofer, P. R., Han, Y. G., Hou, W. Z., et al. (2015). Ages and tectonic implications of neoproterozoic ortho- and paragneisses in the beishan orogenic belt, China. *Precambrian Res.* 266, 551–578. doi:10.1016/j.precamres.2015.05.022
- Liu, Q., Zhao, G. C., Sun, M., Han, Y. G., Eizenhofer, P. R., Hou, W. Z., et al. (2016). Early paleozoic subduction processes of the paleo-Asian ocean: Insights from geochronology and geochemistry of paleozoic plutons in the alxa terrane. *Lithos* 262, 546–560. doi:10.1016/j.lithos.2016.07.041
- Liu, Y. L., Hu, X. F., Wang, D. X., Zhao, Y., Zhang, Q., and Wen, L. (2012). Characteristics of triassic lithofacies palaeogeography in Tarim Basin. *Fault-Block Oil Gas Field* 19 (6), 696–700. doi:10.6056/dkqyt201206004
- Liu, Z. H., Lu, H. F., Li, X. J., Jia, C. Z., Lei, G. L., Chen, C. M., et al. (2000b). Tectonic evolution of kuqa rejuvenated foreland basin. *Sci. Geol. Sin.* 35 (4), 482–492.
- Ma, A. L., Hu, X. M., Kapp, P., BouDagher-Fadel, M., and Lai, W. (2020). Pre-oxfordian (>163 Ma) ophiolite obduction in central tibet. *Geophys. Res. Lett.* 47 (10), e2019GL086650. doi:10.1029/2019gl086650
- Magara, K. (1976). Thickness of removed sedimentary-rocks, paleopore pressure, and paleotemperature, southwestern part of western Canada basin. *Aapg Bulletin-American Assoc. Petroleum Geol.* 60 (4), 554–565.
- Mattern, F., and Schneider, W. (2000). Suturing of the proto- and paleo-tethys oceans in the Western Kunlun (xinjiang, China). *J. Asian Earth Sci.* 18 (6), 637–650. doi:10.1016/S1367-9120(00)00011-0
- Mcfadden, P. L., Ma, X. H., McElhinny, M. W., and Zhang, Z. K. (1988). Permo-triassic magnetostratigraphy in China - northern Tarim. *Earth Planet. Sci. Lett.* 87 (1–2), 152–160. doi:10.1016/0012-821x(88)90071-4
- Meng, Z., Deng, Y., Ding, Z., Zheng, Y., Li, Y. a., and Sun, D. (1998). New paleomagnetic results from Ceno-Mesozoic volcanic rocks along southern rim of the Tarim Basin, China. *Sci. China Ser. D Earth Sci.* 41 (2), 91–104. doi:10.1007/bf02984517
- Qi, J., Li, Y., Xu, Z., Yang, S., and Sun, T. (2022). A structural interpretation model and restoration of the mesozoic proto-basin for the Kuqa depression, Tarim Basin. *Acta Geol. Sin.* 97, 207–225. doi:10.1111/1755-6724.14963
- Qu, G. S., Zhang, N., Liu, J., Li, Y. G., and Li, Y. F. (2004). Structural deformation mechanism of Meso-Cenozoic basement and cover in the north Tarim uplift-Kuqa depression. *Geol. Bull. China* 23 (2), 113–119.
- Shen, Z., Chen, H., Fang, D., Ding, J., Zhang, S., Huang, Z., et al. (2005). Paleomagnetic results of the Cretaceous marine sediments in Tongyuluke, southwest Tarim. *Sci. China Ser. D Earth Sci.* 48 (3), 406–416. doi:10.1360/03yd0378
- Sobel, E. R. (1999). Basin analysis of the jurassic-lower cretaceous southwest Tarim basin, northwest China. *Geol. Soc. Am. Bull.* 111 (5), 709–724. doi:10.1130/0016-7606(1999)111<0709:baotjl>2.3.co;2
- Song, C., Wang, J., Fu, X., Feng, X., Chen, M., and He, L. (2012). Late Triassic paleomagnetic data from the Qiangtang terrane of Tibetan Plateau and their tectonic significances. *J. Jilin Univ.* 42 (2), 526–535.
- Song, P. P., Ding, L., Li, Z. Y., Lippert, P. C., Yang, T. S., Zhao, X. X., et al. (2015). Late triassic paleolatitude of the Qiangtang block: Implications for the closure of the Paleo-Tethys Ocean. *Earth Planet. Sci. Lett.* 424, 69–83. doi:10.1016/j.epsl.2015.05.020
- Van der Voo, R. (1990). Phanerozoic paleomagnetic poles from Europe and North America and comparisons with continental reconstructions. *Rev. Geophys.* 28 (2), 167–206. doi:10.1029/RG028i002p0167
- Wang, C. S., Zheng, H. R., Ran, B., Liu, B. P., Li, X. H., Li, Y. L., et al. (2010). On paleogeographic reconstruction: An example for application in Tibetan Tethys. *Acta Sedimentol. Sin.* 28 (5), 849–860.
- Wang, Q., Li, S. Z., Zhao, S. J., Mu, D. L., Guo, R. H., and Somerville, Ian. (2017). Early paleozoic Tarim orocline: Insights from paleogeography and tectonic evolution in the Tarim Basin. *Geol. J.* 53 (12), 436–448. doi:10.1002/gj.2985
- Wang, T., Jin, Z., Shi, Z., Dai, X., and Cheng, R. (2020). Phanerozoic plate history and structural evolution of the Tarim Basin, northwestern China. *Int. Geol. Rev.* 62 (12), 1555–1569. doi:10.1080/00206814.2019.1661038
- Wang, Y. C. (2004). Paleomagnetic result of the cretaceous-cenozoic basalts from the Tuoyun Basin, southwestern tianshan of China and its tectonic implications. *Chin. Sci. Bull.* 49, 1288–1295.
- Wang, Y. S., Qu, Y. G., Sun, Z. G., Zheng, C. Z., Xie, H. Y., and Lu, Z. L. (2007). Characteristics and tectonic setting of volcanic rocks of the Late Triassic Nongbai Formation at the northern margin of south Qiangtang block, northern Tibet, China. *Geol. Bull. China* 26 (6), 682–691.
- Wei, B. T., Cheng, X., Domeier, M., Jiang, N., Wu, Y. Y., Zhang, W. J., et al. (2022). Placing another piece of the tethyan puzzle: The first paleozoic paleomagnetic data from the South Qiangtang block and its paleogeographic implications. *Tectonics* 41 (10), e2022TC007355. doi:10.1029/2022tc007355
- Wei, G. Q., Zhu, Y. J., Zheng, J. F., Yu, G., Ni, X. F., Yan, L., et al. (2021). Tectonic-lithofacies paleogeography, large-scale source-reservoir distribution and exploration zones of Cambrian subsalt formation, Tarim Basin, NW China. *Petroleum Explor. Dev.* 48 (6), 1289–1303. doi:10.1016/S1876-3804(21)60287-2
- Wu, G. H., Deng, W., Huang, S. Y., Zheng, D. M., and Pan, W. Q. (2020). Tectonic-paleogeographic evolution in the Tarim Basin. *Chin. J. Geol.* 55 (2), 305–321. doi:10.12107/dzxx.2020.020
- Wu, G., Lin, C., Yang, H., Liu, J., Liu, Y., Li, H., et al. (2019). Major unconformities in the mesozoic sedimentary sequences in the kuqa-tabei region, Tarim Basin, NW China. *J. Asian Earth Sci.* 183, 103957. doi:10.1016/j.jseas.2019.103957
- Wu, H. X., Cheng, X. G., Chen, H. L., Chen, C., Dilek, Y., Shi, J., et al. (2021). Tectonic switch from triassic contraction to jurassic-cretaceous extension in the western Tarim Basin, northwest China: New insights into the evolution of the paleo-tethyan orogenic belt. *Front. Earth Sci.* 9, 636383. doi:10.3389/feart.2021.636383
- Xi, D., Tang, Z., Wang, X., Qin, Z., Cao, W., Jiang, T., et al. (2020). The Cretaceous-Paleogene marine stratigraphic framework that records significant geological events in the Western Tarim Basin. *Earth Sci. Front.* 27 (6), 165.
- Xia, J. K., Zhong, Z. Q., Huang, S. Y., Luo, C. M., Lou, H., Chang, H. N., et al. (2023). The proto-type basin and tectono-paleogeographic evolution of the Tarim basin in the Late Paleozoic. *Front. Earth Sci.* 11, 1097101. doi:10.3389/feart.2023.1097101
- Xiao, W. J., Han, F. L., Windley, B. F., Yuan, C., Zhou, H., and Li, J. L. (2003). Multiple accretionary orogenesis and episodic growth of continents: Insights from the Western Kunlun Range, central Asia. *Int. Geol. Rev.* 45 (4), 303–328. doi:10.2747/0020-6814.45.4.303
- Xiao, W. J., Windley, B. F., Hao, J., and Li, J. L. (2002). Arc-ophiolite obduction in the western Kunlun range (China): Implications for the paleozoic evolution of central Asia. *J. Geol. Soc.* 159 (5), 517–528. doi:10.1144/0016-764901-093
- Xiao, W. J., Windley, B. F., Sun, S., Li, J. L., Huang, B. C., Han, C. M., et al. (2015). A tale of amalgamation of three permo-triassic collage systems in central Asia: Oroclines, sutures, and terminal accretion. *Annu. Rev. Earth Planet. Sci.* 43 (43), 477–507. doi:10.1146/annurev-earth-060614-105254
- Xu, Z. Q., Li, S. T., Zhang, J. X., Yang, J. S., He, B. Z., Li, H. B., et al. (2011). Paleo-asian and tethyan tectonic systems with docking the Tarim block[J]. *Acta Petrol. Sin.* 27 (1), 1–22.
- Yang, K. (1994). The formation and evolution of the Western Kunlun continental margin. *Geol. Rev.* 40 (1), 9–18.
- Yang, P. X., Tian, J. C., and Zhang, X. (2019). Study of characteristics of Triassic sedimentary facies and depositional model in the northern Shunbei region, Tarim basin. *Mineralogy Petrology* 39 (4), 86–96. doi:10.19719/j.cnki.1001-6872.2019.04.10
- Yu, H. B., Qi, J. F., Yang, X. Z., Liu, Q. Y., Cao, S. J., Fan, S., et al. (2016). The mesozoic tectonic paleogeographic analysis in Kuqa depression of Tarim Basin. *Geol. J. China Univ.* 22 (4), 657–669. doi:10.16108/j.issn1006-7494.2016021
- Zhang, C. S., Xiao, A. C., Li, J. Y., and Shi, D. (2000). Depositional feature of jurassic fault BASIN IN southwest Tarim depression. *J. Mineral Pet.* 20 (3), 41–45. doi:10.19719/j.cnki.1001-6872.2000.03.008
- Zhang, S. J., Hu, X. M., Han, Z., Li, J., and Garzanti, E. (2018). Climatic and tectonic controls on Cretaceous-Paleogene sea-level changes recorded in the Tarim epicontinental sea. *Palaeogeogr. Palaeoclimatol. Palaeoecol.* 501, 92–110. doi:10.1016/j.palaeo.2018.04.008
- Zhang, X. Z., Dong, Y. S., Li, C., Xie, C. M., Wang, M., Deng, M. R., et al. (2014). A record of complex histories from oceanic lithosphere subduction to continental subduction and collision: Constraints on geochemistry of eclogite and blueschist in Central Qiangtang, Tibetan Plateau. *Acta Petrol. Sin.* 30 (10), 2821–2834.
- Zhang, Z. K., Li, Y. A., and Li, Q. (1989). Jurassic and cretaceous paleomagnetism of the Tarim block. *Seismol. Geol.* 11 (3), 9–16.
- Zhao, G. C., Wang, Y. J., Huang, B. C., Dong, Y. P., Li, S. Z., Zhang, G. W., et al. (2018). Geological reconstructions of the East Asian blocks: From the breakup of rodnia to the assembly of pangea. *Earth-Science Rev.* 186, 262–286. doi:10.1016/j.earscirev.2018.10.003
- Zheng, M. L., Wang, Y., Jin, Z. J., Li, J. C., Zhang, Z. P., Jiang, H. S., et al. (2014). Superimposition, evolution and petroleum accumulation of Tarim Basin. *Oil Gas Geol.* 35 (6), 925–934. doi:10.11743/ogg20140619
- Zhong, Z. Q., Xia, J. K., Huang, S. Y., Luo, C. M., Chang, H. N., Li, X., et al. (2023). Reconstruction of proto-type basin and tectono-paleogeography of Tarim Block in early Paleozoic. *Front. Earth Sci.* 11, 1101360. doi:10.3389/feart.2023.1101360
- Zhou, Z., Zhao, Z., and Hu, Z. (2001). *Stratigraphy of the Tarim Basin*. Beijing: Sci. Press, 1–359.



OPEN ACCESS

EDITED BY

Wenlong Ding,
China University of Geosciences, China

REVIEWED BY

Gang Rao,
Southwest Petroleum University, China
Yangwen Pei,
China University of Petroleum, Huadong,
China

*CORRESPONDENCE

Zhuxin Chen,
✉ chenzhuxin@petrochina.com.cn

RECEIVED 09 February 2023

ACCEPTED 26 June 2023

PUBLISHED 17 July 2023

CITATION

Zhai Y, Chen Z, Zhang Y, Su N, Wang L,
Ren R and Yang G (2023), A new
superimposed model of the Tongnanba
anticline in northeastern Sichuan and its
exploration implications.
Front. Earth Sci. 11:1162586.
doi: 10.3389/feart.2023.1162586

COPYRIGHT

© 2023 Zhai, Chen, Zhang, Su, Wang, Ren
and Yang. This is an open-access article
distributed under the terms of the
[Creative Commons Attribution License](#)
(CC BY). The use, distribution or
reproduction in other forums is
permitted, provided the original author(s)
and the copyright owner(s) are credited
and that the original publication in this
journal is cited, in accordance with
accepted academic practice. No use,
distribution or reproduction is permitted
which does not comply with these terms.

A new superimposed model of the Tongnanba anticline in northeastern Sichuan and its exploration implications

Yonghe Zhai, Zhuxin Chen*, Yuqing Zhang, Nan Su, Lining Wang,
Rong Ren and Geng Yang

Research Institute of Petroleum Exploration and Development, PetroChina, Beijing, China

Understanding the structural style, kinematic process, and timing of superimposed structures worldwide is often difficult due to complex structure deformation process. Fortunately, the newly acquired high-quality seismic reflection data and geological observations covering the Tongnanba anticline provide an excellent chance to characterize such structures. Here, we used geological and seismic data from the Tongnanba region to evaluate the structural style and deformation sequence of Tongnanba anticline. In this regard, we propose a new model of the northeastern Sichuan Basin, which are different from the model that deep structures formed earlier than shallow structures demonstrated by previous studies, and we also discussed the implications of this new model for the deep oil and gas exploration. Compressed by Micangshan and Dabashan thrust belts and controlled by three detachment layers, the Tongnanba anticline shows a complex multi-stage, multi-directional, and multi-level superimposed structure. There were three deformation layers vertically, leading to the multi-level detachment thrust structure style. Specifically, the upper and middle deformation layers were mainly controlled by South Dabashan thrust belt in the early stage, forming long-distance detachment thrust structure extended in the NW-SE direction. A series of pop-up structures propagated toward the upper and middle detachment layers. On the other hand, the lower deformation layer was primarily controlled by the Micangshan thrust belt in the late stage, forming complex basement faults extended in the NE-SW direction, which was consistent with Trishear fault-propagation fold. Along the basement detachment developed multiple branch slopes spread from northeast to southwest. The middle and upper deformation layers was transformed by the basement faults, thus forming the complex superimposed structure of north-south zonation and east-west segmentation at present. It was such complex superimposed structure that control the process of hydrocarbon accumulation and adjustment in each deformation layer, and the deep-ultra-deep ancient oil and gas reservoirs may be worth of exploring.

KEYWORDS

superimposed structure, multi-detachments, Micangshan, Dabashan, Sichuan basin

Introduction

There are large number of superimposed structures develop orogenic belts and continental crustal deformation areas. Multiple phases compression causes the deformation formed in the early stage being modified by the deformation formed lately (Kusky and Loring, 2001; Saha, 2002; Dario et al., 2010; Shah et al., 2013; Deng et al., 2015;

Zhang et al., 2019; Hou et al., 2020). For instance, in the core zones of the Alpi Apuane metamorphic complex in the northwest Tuscany Italy, the switch from the crustal scale contractional regime to the extensional one has been documented (Molli et al., 2022). Two phases of deformation of Paleozoic accretion of the orogenic belt are reported based on the analysis of folds on the northern margin of the North China Craton (Hou et al., 2020). Zhang (2019) report that NE-near EW trending fold superimposed NW-NNE trending fold in the Jianchi area of western Dabashan according to field investigation and identification.

However, the study of these superimposed structures pay attention to outcrop- and regional-scale, which ascertain the fold interference patterns which are influenced by two phases of orthogonal or oblique deformation. Therefore, a series of interference patterns are proposed for the single-layer superimposed folds (Ramsay, 1962, 1967; Ghosh et al., 1992; Grasemann, 2004). Otherwise, a series of numerical simulation and physical simulation experiments are fully used in the study of superimposed structures (Deng et al., 2016; Long et al., 2021; Ma et al., 2023).

Unlike most superimposed structures investigated currently, there are always multi-level folds superimposed vertically in front of the foreland thrust belt. And been subjected to Mesozoic-Cenozoic multi-phase, multi-directional compression, the superimposed structures are different with the conventional one. This makes us not only understand the superimposed structure in single-layer or in planar, but also comprehend it vertically.

This article chooses Tongnanba anticline as the research object to discuss the structural styles and evolution process of multi-phase, multi-directional and multi-level superimposed structure. The Tongnanba anticline is intersection zone in the fronts of the Dabashan and Micangshan fold thrust belts. Decades have been spent studying the structural style, evolutionary processes (Wu et al., 2006; Hu et al., 2012; Shi et al., 2012; Dong et al., 2013; Wen et al., 2013; Chen, 2015; Chen et al., 2016; Li et al., 2015) and oil and gas exploration (Jin et al., 2012; Li et al., 2016; Jiang et al., 2020) of the Tongnanba anticline and peripheral thrust belt. It is commonly believed that the Tongnanba anticline was compressed by Micangshan in the early stage to form the NE-SW striking deep thrust fold deformation and experienced the Dabashan overthrusting to form the NW-SE striking compressive thrust deformation in the middle and upper parts in the late stage (Dong et al., 2006; Wu et al., 2006; Jiang et al., 2008; Li et al., 2008; Xu et al., 2009; Zhang et al., 2010; Zhang et al., 2011; Li et al., 2013; Wang et al., 2013; Chen et al., 2015; Chen et al., 2016). And a multi-detachment deformation system is formed under the control of multiple sets of detachment layers, which incorporate a classic incorporate a classic decoupled deformation model. But the regional seismic profile indicates that different tectonic deformation layers exhibit local coupling, which contradicts the notion that early deformation occurs in the lower deformation layer and late in the upper and middle deformation layers. Therefore, it is necessary to redefine the structure style and deformation sequence.

In this study, the structural style was discussed by a series of region seismic profiles in different directions. Based on seismic profile interpretation results, a new tectonic evolution process of the study area is restored. Finally, we discussed the adjustment and modification of hydrocarbon by the new tectonic evolution process.

Geologic setting

The Tongnanba anticline, located in northeastern part of the Sichuan Basin, is a major part of Micangshan-Hannan Uplift and the Southern Dabashan arc thrust belt, with a general trend of NE to NNE (Figure 1). It experienced an orogenic collision between the Yangtze Plate and the North China Plate and uplift of the eastern margin of the Qinghai-Tibet Plateau since the late Triassic, forming a series of underground structures with northeast and northwest trends (He et al., 2011; Jia et al., 2013). From Cretaceous-Cenozoic, exhumation formed the relief at present. It composed two stratigraphic units on a Precambrian crystalline base: 1) Marine sedimentary sequences from the Sinian to Middle Triassic formed in the Marine Craton rift basin to the craton depression basin; and 2) terrestrial sedimentary sequences from the Late Triassic to the Neogene developed in the continental depression basin to foreland basin (He et al., 2011; Huang et al., 2021). The absence of an angular unconformity and the development of multiple parallel unconformities in the region are notable. Due to intense denudation, the strata exposed on the surface are mainly Jurassic and Lower Cretaceous (Figure 2).

The Micangshan and Southern Dabashan FTB

The Micangshan FTB is connected and intersected with several structural belts, including the Sichuan Basin, the Songpan-Ganzi orogenic belt, the Longmenshan FTB and the south Dabashan FTB. It comprises Mesoproterozoic metamorphic rocks, with Paleozoic and Mesozoic sedimentary rocks surrounding it. Micangshan FTB underwent multiple phases of tectonic movement, forming a complex structural system (Wu et al., 2011; Sun et al., 2011). Two rapid uplift events occurred in Micangshan uplift, respectively during the Early Jurassic-Early Cretaceous and Late Miocene to present, which are related to the collision of the Yangzian-North China and Indo-Eurasian plate (Li et al., 2010; Zhang et al., 2022).

Located at the northern margin of the Yangtze Craton, the Southern Dabashan FTB is a curved tectonic belt in the southern Qinling orogen formed by the Late Triassic collision of the Qinling microplate and the Yangtze plate. Due to the Late Triassic collision and structural superposition during the Late Jurassic to Early Cretaceous, it experienced foreland folding and thrusting (Dong et al., 2006; Zhang et al., 2011). The Southern Dabashan FTB is mainly characterized by the multi-detachment structures. Governed by the Lower Triassic Jialingjiang Formation and Cambrian detachment layers, the multi-level and multi-stage detachment deformation are formed (Li et al., 2017; Huang et al., 2021).

Detachment layers in the Tongnanba anticline

Gypsum rock, mud, and shale demonstrate the characteristics of plastic flow upon subjection to compression deformation, which is easily transformed into a detachment layer. Other rock strata, such as limestone and dolomite, are primarily distinguished by their brittle fracture. Multiple detachment layers are recognized in the study area, including the pre-Sinian basement detachment layer, the Silurian mudstone detachment layer and the Triassic Jialingjiang-Leikoupo

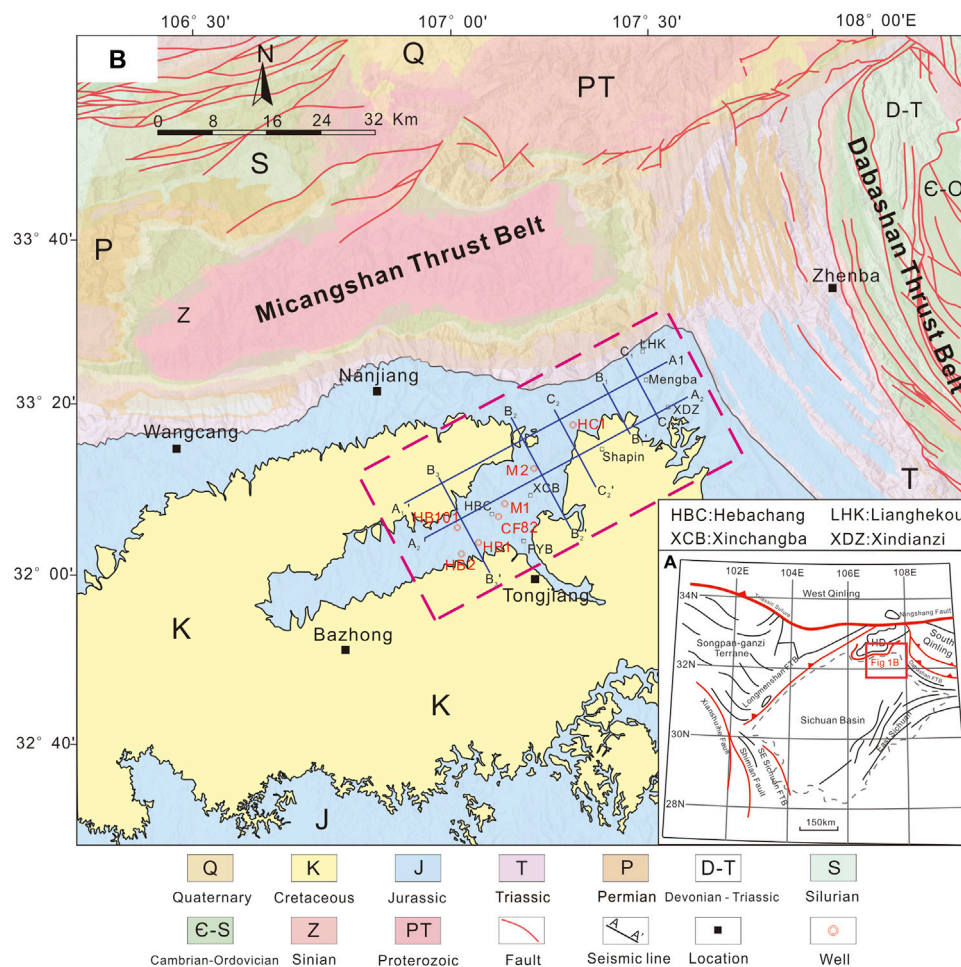


FIGURE 1

(A) A simplified structure map of the North China plate, the South China plate, the Qinling Mountains orogenic belt and the location of the study area (modified from Chen et al., 2016). HD, Hannan uplift; SD, Shennongjia uplift. (B) A simplified geologic map of Tongnanba anticline and its adjacent thrust belts.

Formation gypsum detachment layer (Jin et al., 2006; Zheng et al., 2013). The gypsum detachment layer in the Leikoupo Formation has a chaotic seismic event feature, thickens locally under strong extrusion, according to the high-quality seismic profile (Figure 3). It is buried between 4,500 and 5,500 m deep. The Silurian detachment layer shows weak and discontinuous seismic reflection, with no obvious thickness change. Its depth is 6,000–6,500 m. The depth of the pre-Sinian basement detachment layer is currently controversial. Local detachment layers are not discussed in detail here. According to the analysis of the detachment layer in the study area presented above, three structural deformation layers (upper, middle, and lower) are formed in the upper portion of the pre-Sinian basement detachment layer, exhibiting inconsistent deformation in different deformation layers.

Data and methods

Comprehensive seismic data on the Tongnanba region form the basis for studying its structural geometric features in this paper. This

study employs twenty NE-SW trending and twenty-eight NW-SE trending time-migrated 2D seismic profiles. The approximate depths are converted based on an average velocity of 4,000 m per second. Although this time-depth conversion method is simple compared to the reality, the vertical stretching and compression do not affect our analysis of structure style in the study region.

We primarily employed fault-related fold, balanced section restoration technique, and forward modeling analysis to characterize the Tongnanba anticline's superimposed deformation pattern, evolution process, and spatial structure characteristics. To constrain the underground structural model while interpreting seismic reflection profiles, we projected 1:200,000 regional geological mapping results onto seismic profiles. Two NE-SW 2D seismic profiles and five NW-SE 2D seismic profiles are chosen as examples for this explanation. Otherwise, the Trace710 seismic profile was constructed to investigate the evolution process and variations in shortening. Its tectonic strike is perpendicular to Micangshan FTB and parallel to Dabashan FTB, containing the maximum structural

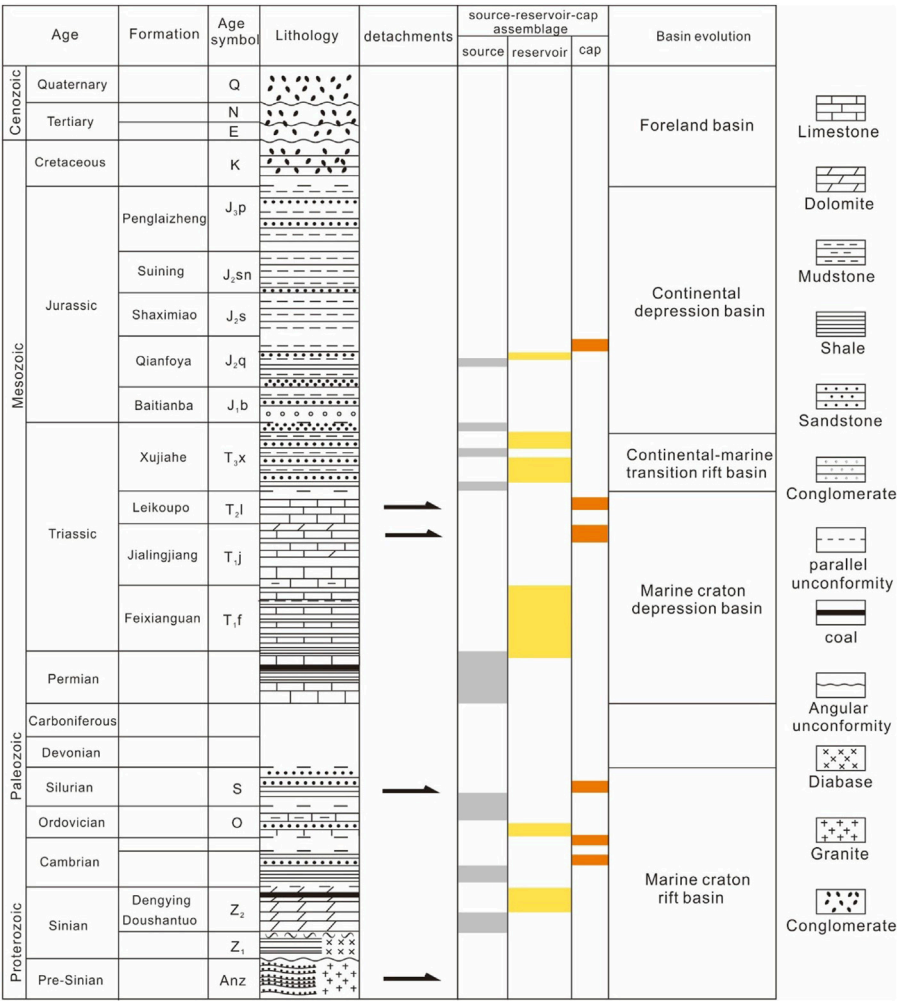


FIGURE 2
A simplified stratigraphic column of the Tongnanba anticline, indicating multistage tectonic activities (modified from [Chen et al., 2016](#)).

features. Finally, the relationship between regional geological structure, evolution processes, and petroleum is discussed. We divided the characteristics of source-reservoir-cap assemblages into those of the upper, middle, and lower tectonic deformation layers by investigating the characteristics of source-reservoir-cap assemblages of different tectonic deformation layers.

Structural geometry of the Tongnanba anticline

The regional seismic profiles' structural analysis clarifies the structural characteristics of the piedmont area of South Dabashan and Micangshan FTB, respectively. In this paper, use two NE-SW and five NW-SE 2D seismic profiles are interpreted explain the typical tectonic features of the southern Dabashan and Micangshan front regions, with the location of the seismic profile is shown in [Figure 1](#). The interpreted results explains that the Tongnanba anticline belt is characterized by the NW-trend long-distance detachment thrust deformation of the upper and middle deformation layers, and NE-

SW trending deep basement fold structural deformation of the lower structural deformation layer, which is evidence of the prominent vertically stratified multi-detachment thrust deformation pattern of the Tongnanba anticline ([Figure 4](#)).

Structural analysis of NE-SW directed seismic profiles

Three deformation layers are displayed from bottom to top in the NE-SW seismic profiles: 1) The chaotic reflection with depths greater than 8 km, representing the Precambrian crystalline basement; 2) the strong continuous reflection with depths approximately 8–4 km, representing the Cambrian-Permian; and 3) the shallow, weak continuous reflection with depths approximately 4 km, representing the Triassic-Cretaceous ([Figures 4A, 5A](#)).

NE-SW directed seismic profiles reflect the detachment thrust deformation in the upper and middle deformation layers. On the whole, the deformation distribution is wide,

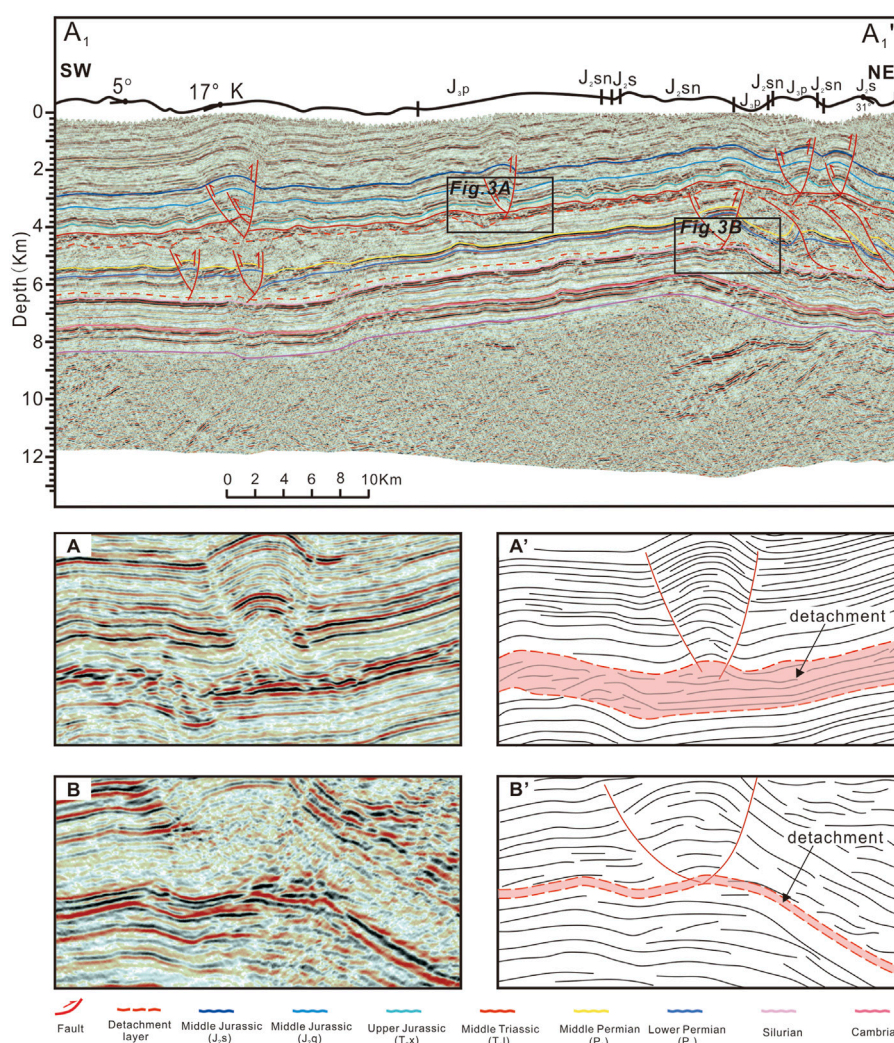


FIGURE 3

Seismic reflection characteristics of the detachment layer. (A) NE-SW regional seismic profile Hctrace710. (B) Enlarged area of seismic profile shown the Lower Triassic (Leikoupo Formation) detachment layer. (C) Line-drawing of Figure 3B. (D) Enlarged area of seismic profile shown the Lower Silurian detachment layer. (E) Line-drawing of Figure 3D.

but the fault displacement is small. Because of differences in the shorting strength, different styles of structures are exposed from South Dabashan to the Sichuan Basin. In the upper deformation layer, it is revealed that multiple small folds and pop-up structures developed along the upper detachment layer on both limbs, showing the unequal distance distribution of structures. There are large-scale detachment structures near the Huangcaogou and HBC area, forming the subsidiary anticline with large amplitude (Figures 4B, 5B). Also, it can be seen that multiple NE-dipping thrust faults distributed in the Shapin area and numbers of pop-up structures near the South Dabashan. Closed to the Southern Dabashan FTB, the structural deformation becomes complicated and the upper detachment layer gradually uplift. In addition, salt accumulation occurs in the upper detachment layer, resulting in the thickening of the detachment layer in the local place (Figures 4A, B).

Because of the strong thrusting, different types of structures are developed in the middle deformation layers. Like the upper deformation layers, thin-skinned thrust fold structures distributed on the two limbs of the anticline, and the position of deformation is the same as the upper deformation layers locally. Deformation close to the South Dabashan is characterized by an imbricate thrust structure, which involved the Sinian, Lower Paleozoic, and Permian and a small portion of Triassic units. Continuous imbricate structure resulted in obvious thickening of strata (Figures 4B, 5B). There are also several thrust fault and back thrust fault appear near the region of Hebchang, with the strata in the upper deformation uplifting locally.

The deformation in the lower structure deformation layer is controlled by Micangshan FTB, which form the SE-directing thrust faults. Therefore, in the NE-SW seismic profiles, these SE-directing faults are showed as several branch fault flats

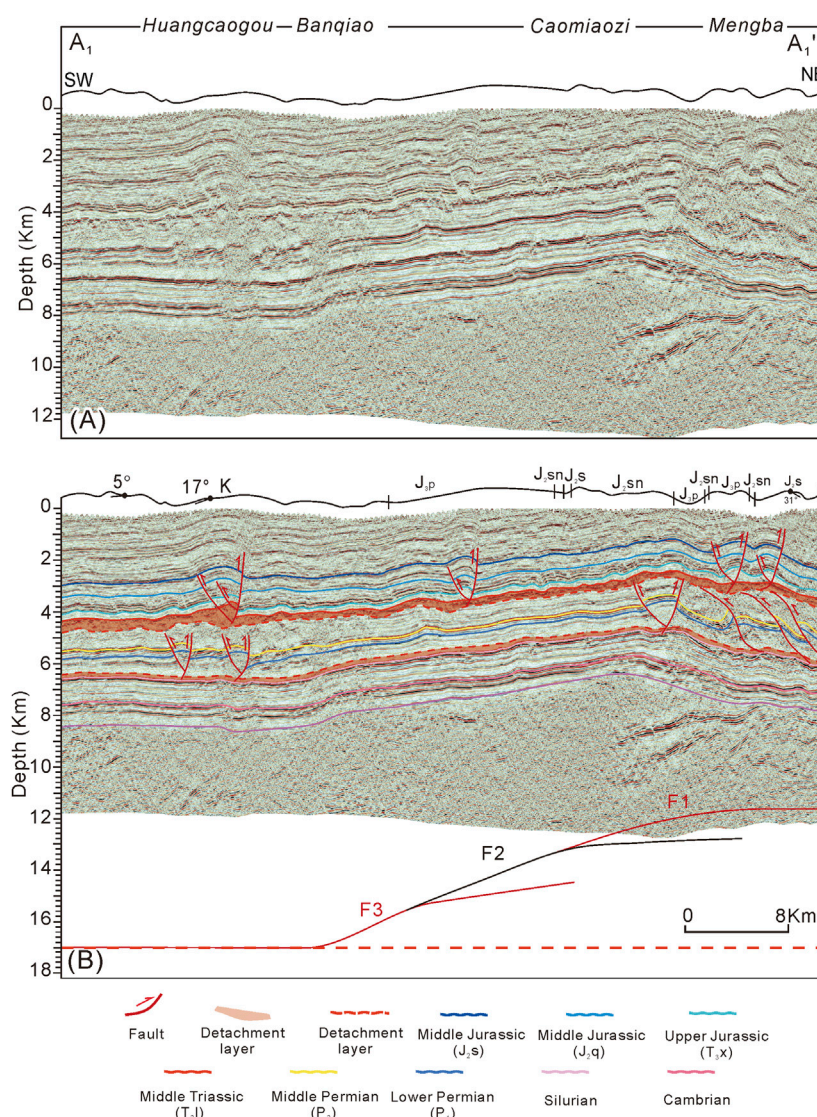


FIGURE 4

NE-SW seismic profile (A₁-A₁') in the Tongnanba anticline shown the structure of Dabashan thrust system. (A, B) Seismic profile and its interpretation result for (A₁-A₁'). The basement faults are distributed in SE-directing, which are flat in the NE-SW striking section.

superimposed one by one. And there are different fault flats in different seismic profiles.

Structural analysis of NW-SE directed seismic profiles

NW-SE seismic profiles reflect the deformation formed by Micangshan FTB, with the basement anticline of the Tongnanba area (Figures 6, 7). There are also three parts to the reflections, but unlike the NE-SW profile, there is no discernible dislocation of the reflection axis in the shallow layers. On the contrary, obvious reflection axis deformation occurs in the middle and deep layers, which reveals the basement fold structure and its control over the upper strata. The seismic profile also reveals that the shallow, middle, and deep structure deformation layers exhibit partially synchronous deformation in the

NW-SE direction, indicating that the deep structure deformation time is later than that of the middle and shallow long-distance detachment thrust structural layers.

Generally, from NW to SE, the Tongnanba anticline is a broad anticline whose shape changes from monocline to asymmetric anticline from northeast to southwest, and it can be seen that there are two types of basement anticlines arise in the study area (Figures 6, 7). One is single basement anticline controlled by one basement fault (Figure 6). According to 2D move-forward modeling, it is inferred in this paper that the pre-Sinian basement detachment layer has a significant burial depth about 17 km and maybe a weak layer in the middle-lower crust. From SW to NE, the anticline transited from broad gentle anticline to monocline. The basement fault disappeared downward into the lower detachment, and terminated in the upper detachment layer locally, showing that the middle structure deformation layer is severed by basement faults

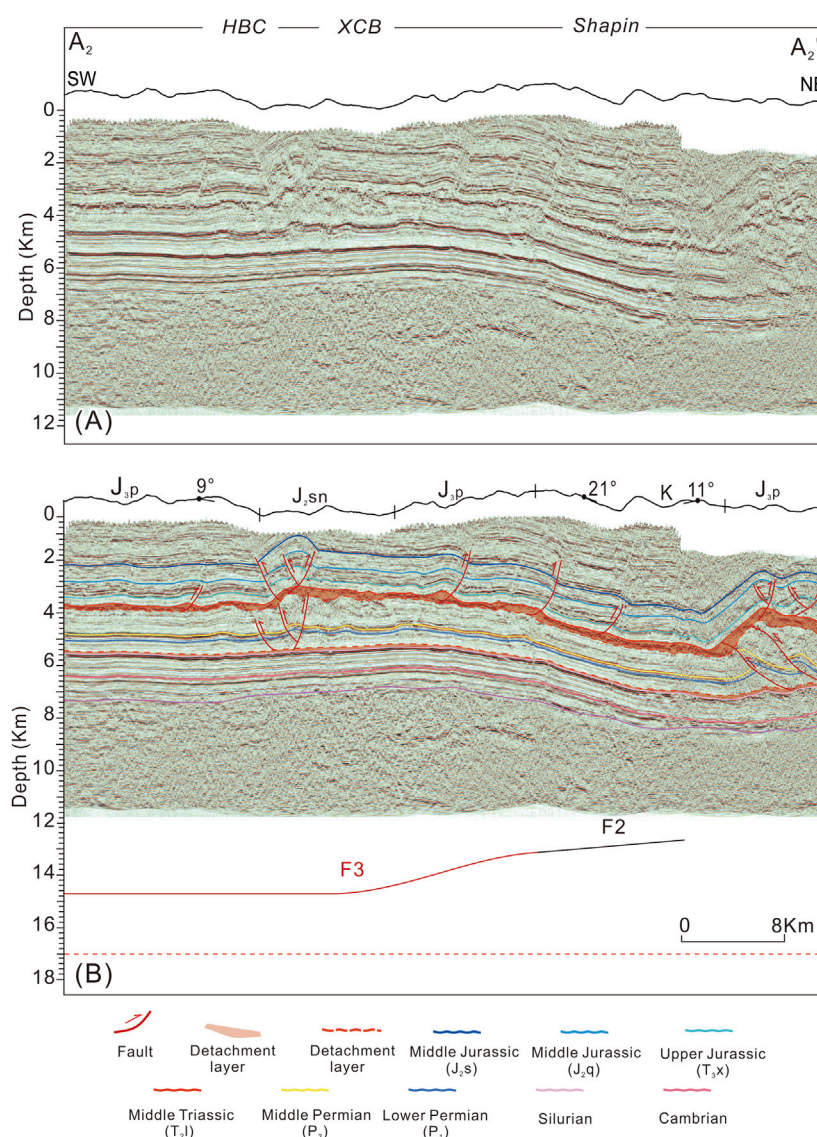


FIGURE 5

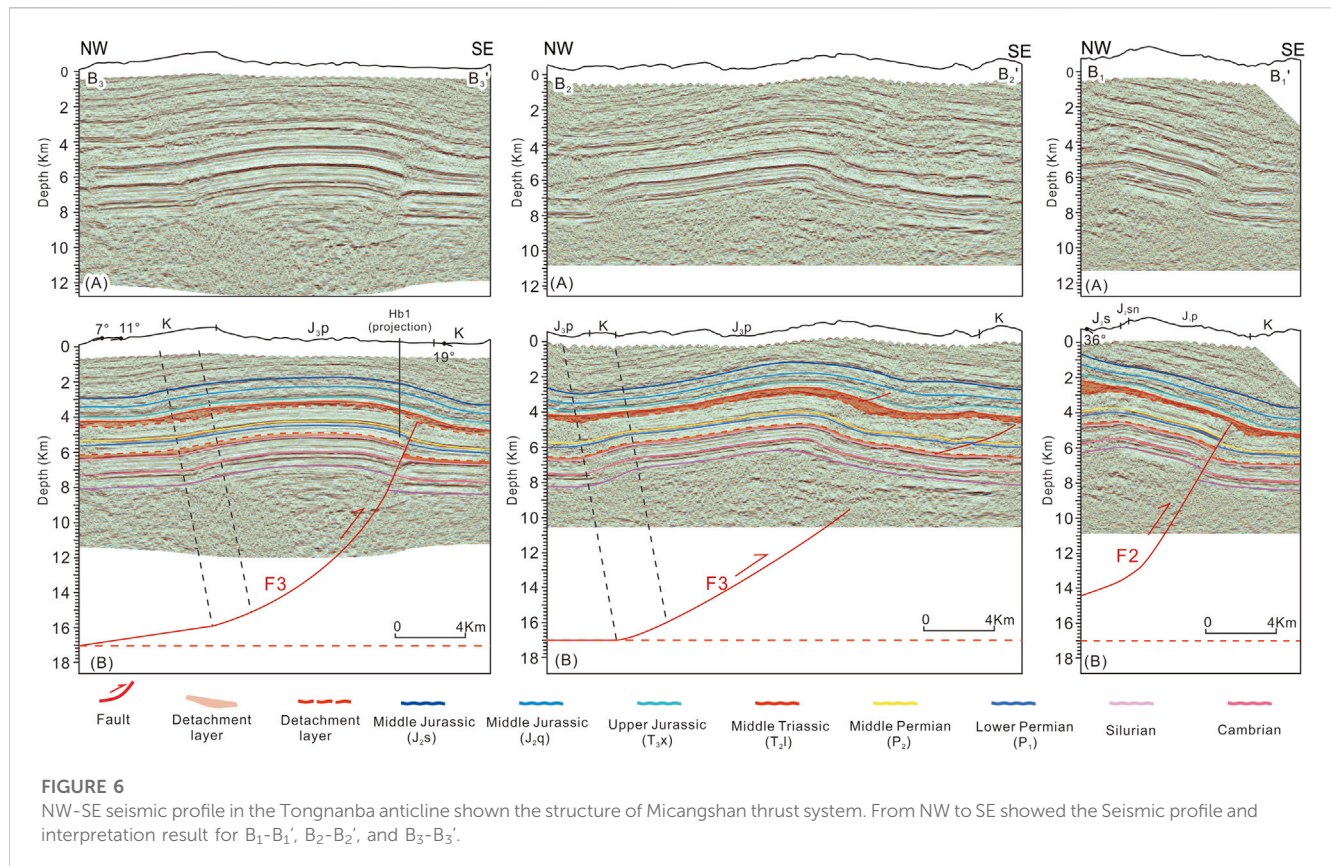
NE-SW seismic profile (A_2-A_2') in the Tongnanba anticline shown the structure of Dabashan thrust system. (A, B) Seismic profile and its interpretation result for (A_2-A_2'). The basement fault is distributed in SE-directing, which are flat in the NE-SW striking section.

(Figure 6 B_1-B_1' , B_3-B_3'). It is worth noting that the fault displacement decreases gradually from Sinian to the upper detachment layer. In specific profiles, the basement fault does not cut through the upper strata, and SE-dipping faults appeared in the middle and upper deformation layers, representing the NW-strike faults from Dabashan FTB which cause the stratum to thicken. Under the adjustment of the upper detachment layer, the upper deformation layer has no noticeable thrust faults, and the strata in the upper deformation layer is relatively continuous and complete. Moreover, due to compression, the upper detachment layer thickens close to the Micangshan.

Another one is double basement anticline controlled by two basement faults (Figure 7). Like the anticline which is controlled by one basement fault, the upper detachment layer thickens because of compression from Micangshan FTB. And near south Dabashan, a

series of NW-strike thrust faults cause the middle deformation layer to thicken (Figure 7 C_1-C_{1b}). However, the difference is that the lower and middle deformation layer are double anticlines, while the upper tectonic deformation is simple anticlines, which illustrate that in the vertical it is decoupled locally. According to the planar distribution of the NW-SE seismic profiles, it can be seen that the single basement anticline and the complex basement anticline appear alternately, which represented the transitional location of two basement faults.

According to the seismic profile interpretation and balanced cross-section restoration, it is confirmed that the basement faults in the lower structure deformation layer conforms to the Trishear fault-propagation fold model (Suppe J and Medwedeff D A, 1984; Erslev, 1991; Allinendinger R W, 1998). It is known that the Trishear fault-propagation fold model has the characteristics that the shape of



the anticline is asymmetric, whose front wing is narrow and the rear wing is wide. Besides, the fold becomes more and more tightly closed with the increase of depth and the deformation cannot be transmitted forward. The fault displacement gradually increases from bottom to top. In this paper, the NW-SE seismic profiles have the same feature. Firstly, the seismic profile shows asymmetric anticline in Figures 6, 7, with the front limb being steeper than the back limb. The dip angle of the front limb decreasing gradually from bottom to top (Figure 7). Otherwise, the fault displacement gradually decreases from Sinian to the lower Triassic. Furthermore, there is no discernible deformation propagated towards the basin, indicating that the basement deformation the basement deformation from Micangshan FTB is no longer transmitting forward. All the above proved that the basement faults are consistent with the Trishear fault-propagation fold model.

Characteristics of fault distribution

To comprehend the fault distribution and geometric style of the Tongnanba anticline systematically and comprehensively, we analyze the planar fault distribution characteristics of the different structure deformation layers using regional seismic profiles (Figure 8).

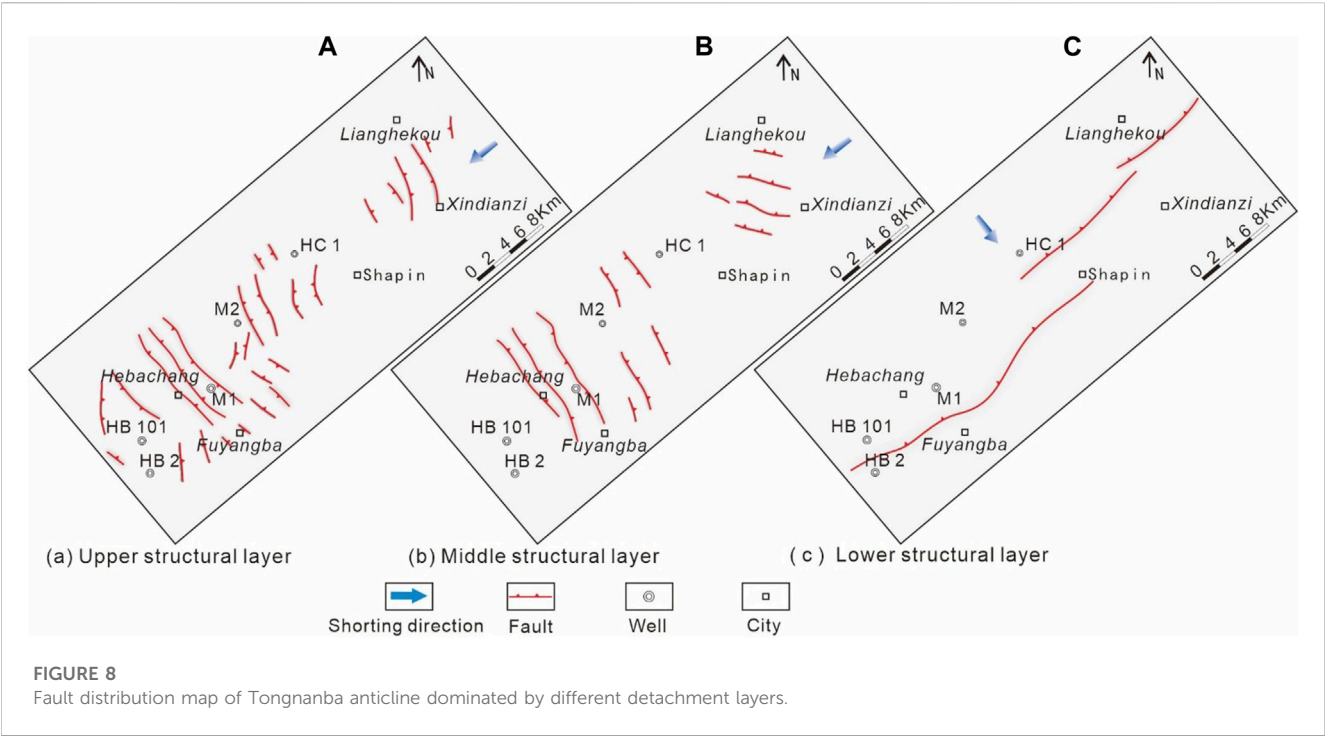
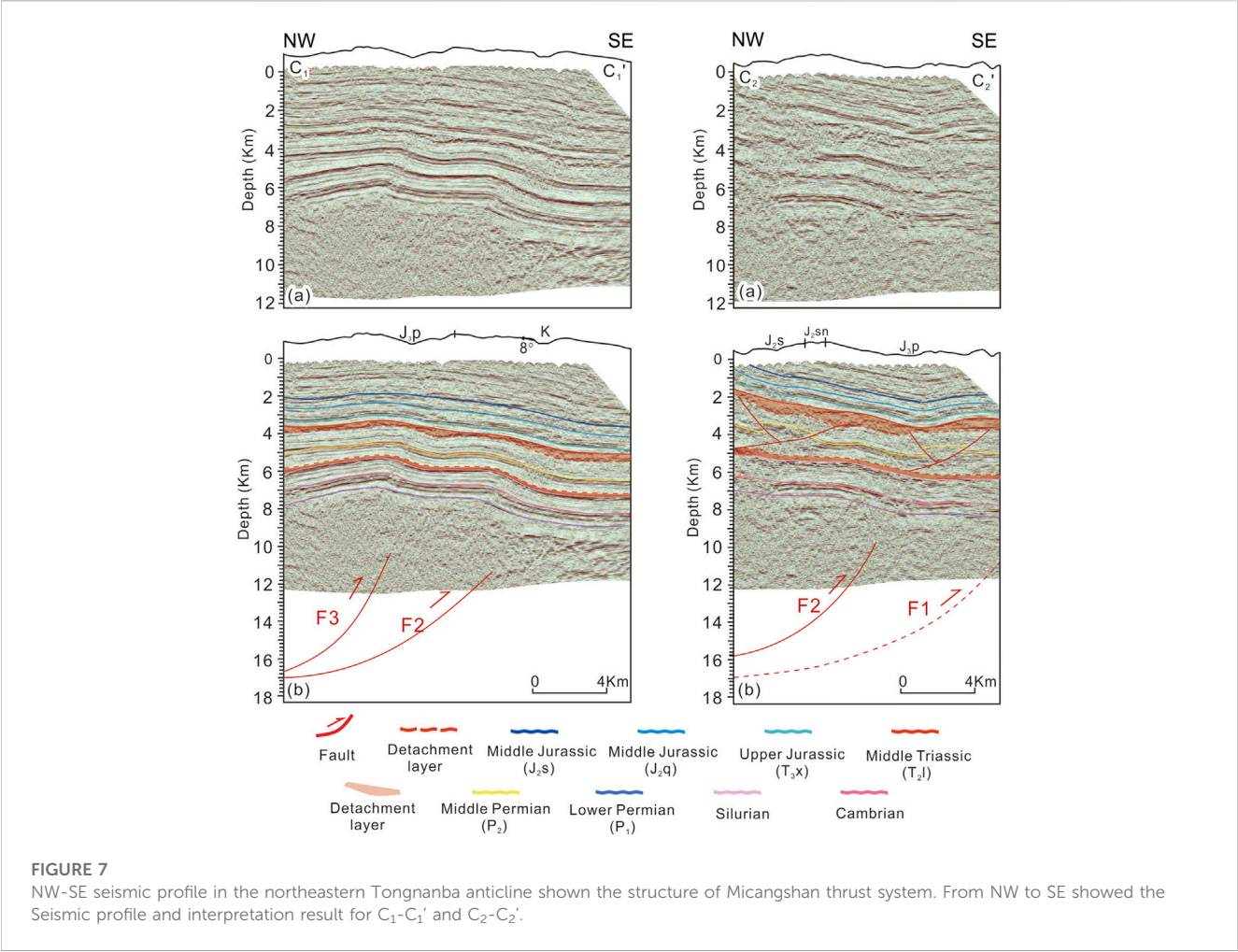
In the upper structure deformation layer, under the compression of South Dabashan, it forms a series of NW-SE and NS striking pop-up structures which were primarily formed in Fuyangba and Xindianzi area. Near the Hebachang area develop three groups of NW-trending thrust and back-thrust faults, and faults with slight displacement dominate the

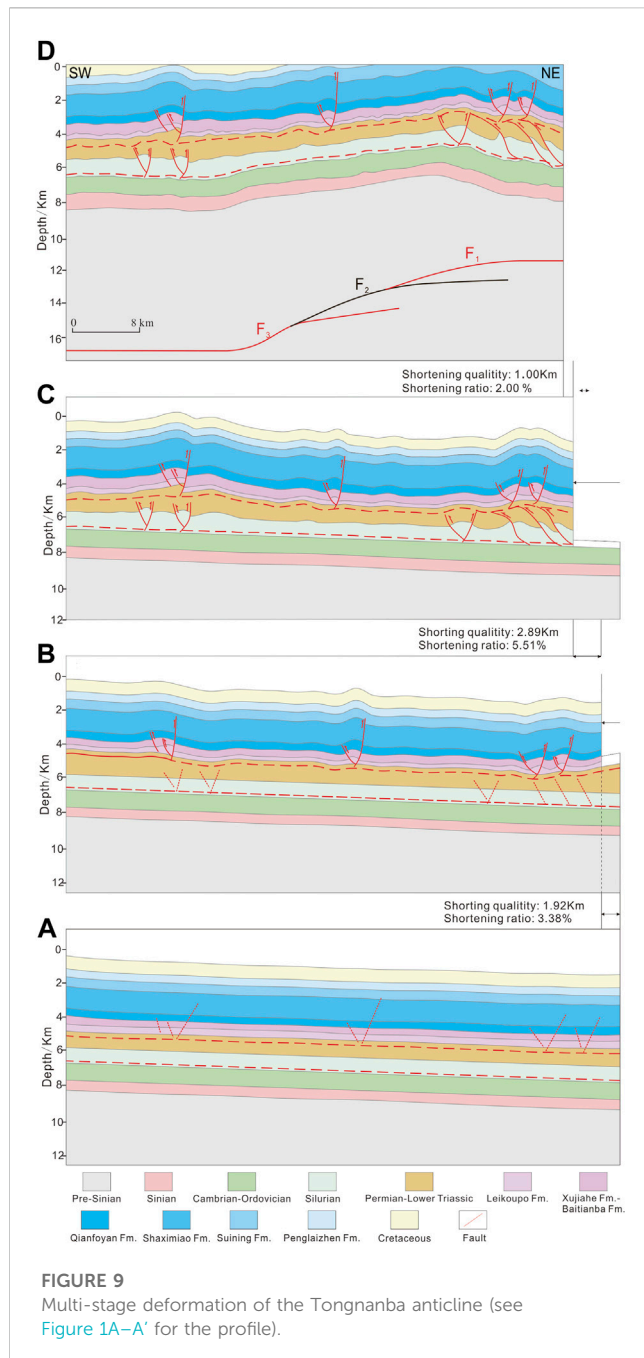
Fuyangba. On the southern side of the Well M-2 forms two near-NS faults. Multiple large-displacement faults distribute near Xindianzi and Lianghekou area, illustrating the intense compression in the vicinity of the Southern Dabashan (Figure 8A).

The middle structure deformation layer, also under the compression from South Dabashan, develops a series of NW and near-EW trending fault groups. Compared to the upper structure deformation layer, no faults have formed near the well HB-101 and HB-2, indicating that the compression from South Dabashan has yet to be transmitted here. In the Hebachang region, there are three groups of NW-trending thrust and back-thrust faults whose positions corresponded to those of the upper structure deformation layer. Fuyangba area is devoid of small faults, whereas in the Xindianzi and Lianghekou area exhibit near-EW imbricate structures which structural strike consistent with the western section of the Dabashan FTB (Figure 8B).

Compared to the upper and middle structure deformation layers, the lower structure deformation layer has the opposite fault distribution direction. A group of NE-trending thrust faults form a pattern of lateral spread. The F1 fault has the smallest distribution range, which terminates north of Lianghekou. Fault F2 extends northeast from HC-1, while Fault F3 extends northeast to the Shaping region. These faults are stacked on top of one another in a piggyback fashion (Figure 8C), which controlled the structure of the lower structural deformation layer.

Under the compression along the South Dabashan and Micangshan, the planar distribution of faults reveals that faults of different stages have diverse distribution characteristics. The faults in the upper and middle structural deformation layers parallel or obliquely intersect the structural trend of South Dabashan, resulting in groups of





thrust and back-thrust faults of varying scales. The NE-SW striking faults in the lower structural deformation layer are nearly parallel or oblique to the trend of the Micangshan thrust belt. These faults traversed the entire Tongnanba anticline, forming a structural combination of NW and NE striking faults stacked vertically.

Restoration of tectonic evolution

The complex deformation of the Tongnanba anticline can be attributed to the multistage regional tectonic activities. This article, the NW-SE seismic profile is restored under the analysis of structure deformation in the Tongnanba anticline for clarifying the structure deformation process of different

stages in the Tongnanba region. Different stages of the compression generated by the Micangshan and South Dabashan FTB were transmitted to the Tongnanba region, resulting in the multi-detachment thrust structure (Figure 9).

This article suggested that the upper and middle structure deformation layers formed earlier than the lower structure deformation layer, which means that the deformation from South Dabashan FTB is earlier than Micangshan FTB. Firstly, it is evident that three structure deformation layers are coupled locally in the NE-SW and NW-SE seismic profiles, which have consistent axes in some seismic profiles. Otherwise, Sandbox simulation experiment indicates that the structure trace of shallow deformation if the paleo-uplift was formed first (Marshak, 2004; Long et al., 2021). And we believe that the middle and shallow structures could not spread forward across the paleo-uplift. In addition, there is no significant regional unconformity in the stratigraphic sequences, which may imply that the development of the anticline is in the late stage. Therefore, the deformation from south Dabashan FTB is early than Micangshan FTB.

In the early stage, a series of thrust and back-thrust faults were formed during the early stage that South Dabashan produced NW-SE compression (Figure 9B). The deformation traveled long distances along the upper detachment layer. Several imbricate thrust structures develop near the front of South Dabashan during the middle stage (Figure 9C). And there are a series of thrust and back-thrust faults occur far from South Dabashan. The upper structure deformation layer is further folded due to the substantial folding deformation of the middle structure deformation layer. In the late stage, under the compression of Micangshan FTB, three forward thrust fault were formed which were characterized by laterally-arranged piggyback thrust structures. In the meantime, these faults modified the deformation which is generated earlier (Figure 9D).

According to the above analysis, the Tongnanba anticline is subjected to two long-distance detachment thrust formations above the Silurian mudstone detachment layer, producing near-EW and NW-SE striking faults in the shallow and middle structure deformation layers. Subsequently, basement structure produced by Micangshan FTB modified the upper deformation. These tectonic processes combine to form the Tongnanba anticline's multi-level superimposed structure.

Discussion

A new model explains the superimposed structure

The lateral extension-superposition model of the deep basement detachment thrust structure

We use 2D MOVE for the forward modeling of basement faults to verify the validity of the model of the basement fault structure. In the model, the dip angle of the faults is 20.5°, the trishear angle is 80°, and the fault propagation slip ratio is 1 (Figure 10).

As depicted in Figure 10, the fault F1 developed in the basement, with its lower endpoint in the pre-Sinian detachment layer and its upper endpoint in the basement (Figure 10A). When the displacement is transmitted along F1, the rear limb bends and slides along the fault, forming a broad anticline. At this time, the displacement of the fault is the distance between the inactive axial plane and the active axial plane

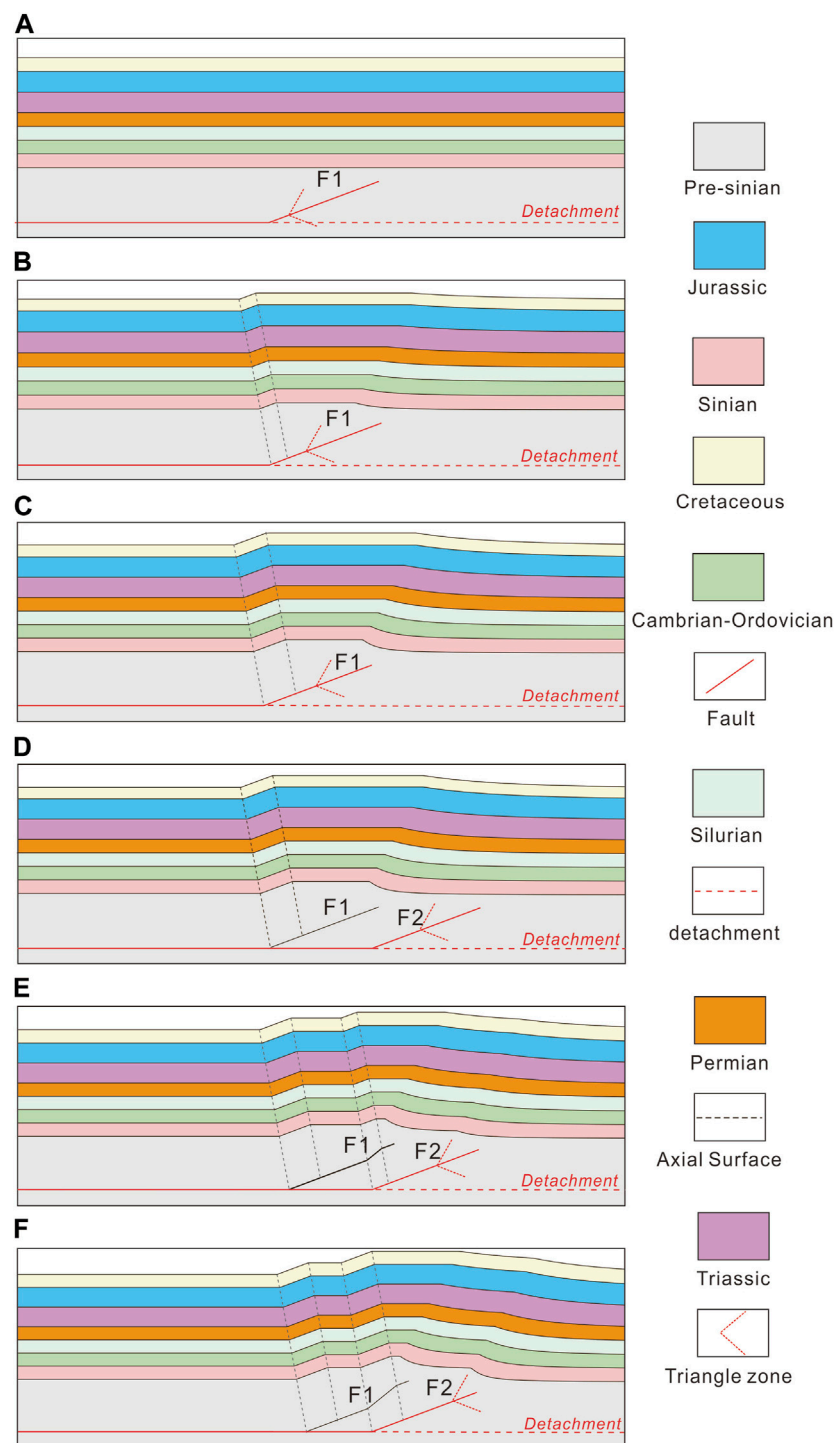


FIGURE 10

Sequential model of the growth Tongnanba anticline controlled by lower detachment. F1: dip angle is 20.5° , trishear angle is 80° , propagation/slip ratio is 1; F2: dip angle is 20.5° , trishear angle is 80° , propagation/slip ratio is 1.

projected onto Fault F1 (Figure 10B). The anticline core contracted when the displacement was increased, and the high point of the anticline roes at the same time (Figure 10C). This model resembles the single anticline in the Tongnanba region.

When the fault F2 is created along the basement detachment layer in the front limb direction of a previously formed anticline, it

manifested two forward thrust faults, with fault F2 controlling the deformation and generating new displacement along the fault F2. And the fault F1 deformed passively in response to the fault F2 (Figure 10D). The anticline formed previously was altered and reflected the double anticline with one anticline high point (Figure 10E). With the displacement increasing, the folds become more tightly closed. This

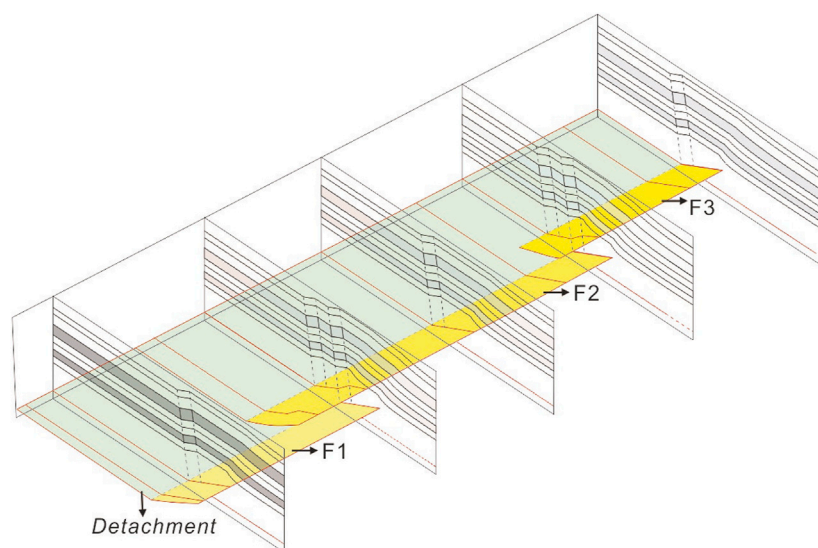


FIGURE 11
Distribution pattern of the basement fault.

model is consistent with the double anticline of the Tongnanba anticline, which is controlled by two branch faults.

Based on the analysis and forward modeling, we established the basement fault spatial distribution of Tongnanba anticline (Figure 11). It is clear that three faults, developed from NE to SW, result in the broad anticline. While two faults which is stacking between the fault slopes displays a double anticline. Under the influence of basement faults, it is showing that the Tongnanba anticline has a complex geological structure, which is segmented from NE to SW.

Implications for oil and gas explorations

Complex segmentation is developed in the Tongnanba anticline due to the multi-detachment superimposed structure. The structural segmentation and tectonic evolution are closely related to hydrocarbon accumulation. Consequently, it is necessary to analyses the hydrocarbon accumulation in the vertical and horizontal direction (Figure 12).

In the upper structure deformation layer, the shallow Triassic Xujiahe Formation, such as the continental 2nd and 4th Members, are the focus of shallow exploration. The source rocks are the 3rd and 5th Members of the Xujiahe Formation, and the regional caprock is the upper mudstone. Consequently, the advantageous source-reservoir-cap combination is formed (Du et al., 2019; Jiang et al., 2020). In the Late Jurassic, the source rock reached the peak of hydrocarbon generation (Wang et al., 2014) (Figure 12). During the Late Cretaceous, intense compression is produced from South Dabashan, resulting in crude oil and natural gas generation. Thus, structural hydrocarbon reservoir is formed, in which the shallow structural traps is corresponded with the oil and gas generation of the source rocks. Otherwise, faults in the upper structure deformation layer enhance the physical properties of the reservoir and connect the source rocks and reservoir effectively. Therefore, the reconstruction of shallow layers from late basement faults may alter or destroy previously formed oil and gas reservoirs.

In the middle structure deformation layer, it develops the gas reservoirs of the granular beach facies in the 3rd Member of the Lower Triassic Feixianguan Formation and the reef-beach facies of the Upper Permian Changxing Formation. Permian Wujiaping Formation and Dalong Formation are primarily source rocks. In addition, older source rocks like Silurian may also contribute to the middle trap. The Jialingjiang Formation's gypsum rocks serve as a high-quality regional caprock (Lan et al., 2019; Wang and Ji, 2020). During the Early to Middle Jurassic, oil production peaked in the Permian source rocks. The paleo-lithologic reservoirs may be taken shape in the Feixianguan Formation and Changxing Formation On the premise that no paleo-structures existed at the time. In the Late Jurassic, the crude oil cracked to produced gas, leading to paleo-gas reservoir (Zhang et al., 2013; Liu et al., 2019). The structural trap of the middle structure deformation layer was formed after the Late Cretaceous because of Dabashan compression, which corresponded to the stage of thermal cracking and gas generation in crude oil. There is some possibility that structural-lithologic or structural hydrocarbon reservoirs are existed. Besides, these hydrocarbon reservoirs are difficult to be modified by the basement faults in the late stage. So special consideration must be given to these reservoirs during exploring the middle layers.

Dengying Formation in the Sinian is the exploration focus in the lower structure deformation layer, which consists primarily of alga-rich microbial dolomite. The source rocks consist of mudstone and shale from the Qiongzhusi Formation and Doushantuo Formation, with Silurian mudstone serving as the regional caprock (Jia et al., 2015; Lan et al., 2019; Guo et al., 2020; Guo et al., 2020). During the Late Silurian, with the burial depths increasing, the source rocks of the Qiongzhusi Formation and Sinian began producing oil, but the paleo-reservoir was initially formed during the Middle Permian (Liu et al., 2021). It may migrate laterally into the platform margin at the higher elevation to form lithologic reservoirs under the condition of no significant paleo-structures. In the Late Triassic, the crude oil in the Sinian paleo-reservoirs cracked into gas and paleo-gas reservoirs

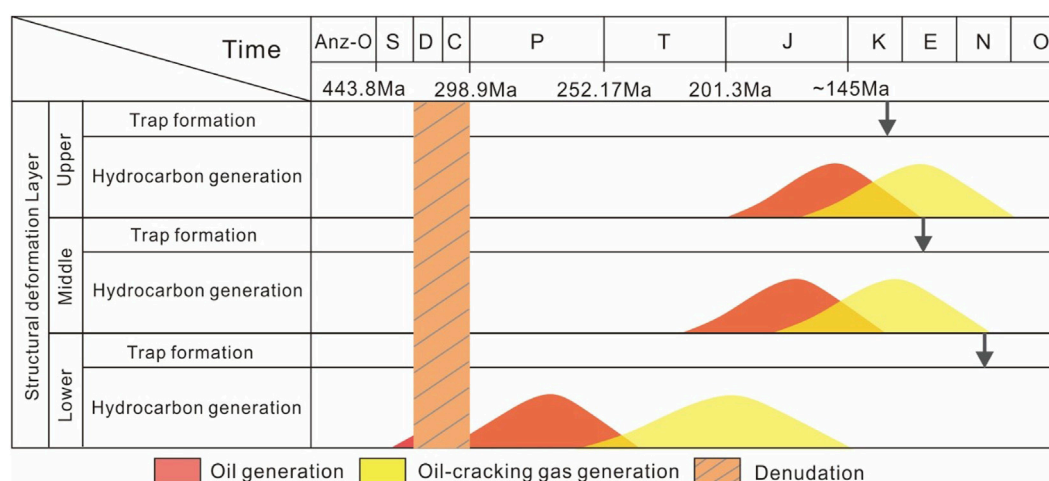


FIGURE 12

The relationship between hydrocarbon generation and structural trap formation of multilayer source rocks in Tongnanba Anticline.

were formed because of the increased formation temperature (Liu et al., 2021) (Figure 12). The crude oil completed the oil-cracking process before the Jurassic and the basement deformation occurred after oil-cracking process, which means that no structural traps is matched with the hydrocarbon. Therefore, early-formed paleolithic reservoirs in deep layers may be the key to oil and gas exploration.

Conclusion

- (1) Due to the multi-stage uplift tectonic events of Micangshan and South Dabashan, the Tongnanba anticline is primarily controlled by three sets of detachment layers: the pre-Sinian basement, Silurian mudstone, and Lower Triassic gypsum salt rock to form a complex multistage, multi-directional and multi-level superimposed structure. As a result, the Tongnanba anticline is vertically stratified and differentiated.
- (2) The NW-SE striking long-distance detachment thrust structures develop in the upper and middle structural deformation layers of the Tongnanba anticline because of the early stage thrusting of South Dabashan, which forms a series of thrust and imbricate thrust structures. In the late stage, the Micangshan uplift produces three basement faults in the lower structure deformation layer that are laterally arranged in a piggyback fashion. The early-formed deformation is reconstructed by basement faults. Consequently, the Tongnanba anticline is segmented and planarly differentiated.
- (3) The Tongnanba anticline has hydrocarbon accumulation that is vertically stratified and laterally segmented. The formation of shallow gas reservoirs corresponds well with the emergence of structural traps. Nevertheless, the formation of deep oil and gas reservoirs temporally mismatches the formation of structural traps, making a complex process of reservoir formation. The exploration may be given to pay attention to early paleo-oil and gas reservoirs.

Data availability statement

The original contributions presented in the study are included in the article/Supplementary Material, further inquiries can be directed to the corresponding authors.

Author contributions

CZ and ZY come up with this research topic, completed the seismic interpretations and then wrote the manuscript. ZY put forward a lot of valuable comments for the figures and the manuscript. RR, WL, SN, and YG provided important advice. All authors contributed to the article and approved the submitted version.

Funding

The authors declare that this study received funding from PetroChina Science and Technology Project (Grants No. 2021DJ0301, 2023ZZ0202). The funder was not involved in the study design, collection, analysis, interpretation of data, the writing of this article, or the decision to submit it for publication. This research was financially supported by the National Natural Science Foundation of China (Grant No. U22B6002).

Acknowledgments

We express our gratitude to Denegfa He, Guanshen Liu, Fanglei Tian and others for technical support.

Conflict of interest

Authors YZ, ZC, YZ, NS, LW, RR, and GY were employed by PetroChina.

Publisher's note

All claims expressed in this article are solely those of the authors and do not necessarily represent those of their affiliated

organizations, or those of the publisher, the editors and the reviewers. Any product that may be evaluated in this article, or claim that may be made by its manufacturer, is not guaranteed or endorsed by the publisher.

References

- Allinender, R. W. (1998). Inverse and forward numerical modeling of trishear fault-propagation folds. *Tectonics* 17 (4), 640–656. doi:10.1029/98tc01907
- Chen, L., He, D., Wen, Z., Mei, Q., and Li, Y. (2016). The geometry, kinematics of Tongnanba anticline and its structural model. *Chin. J. Geol.* 51 (2), 384–401. doi:10.12017/dzcx.2016.004
- Chen, L. (2015). *Structural geometric, kinematic features and three-dimensional restoration of Tongnanba anticline*. (Beijing): China University of Geosciences.
- Dario, C., Claudio, M., and Mossimo, Z. (2010). Contractional deformation and Neogene tectonic evolution of the pergola-melandro valley area (southern apennines). *GeoActa (Bologna)* 9, 1e19.
- Deng, H., and Koyi, H. A. (2015). Mega arrowhead interference patterns in the central part of the Yanshan orogenic belt, North China. *J. Struct. Geol.* 80, 25–37. doi:10.1016/j.jsg.2015.06.004
- Deng, H., Koyi, H. A., and Nilfouroushan, F. (2016). Superimposed folding and thrusting by two phases of mutually orthogonal or oblique shortening in analogue models[J]. *J. Struct. Geol.* 83, 28–45. doi:10.1016/j.jsg.2015.08.005
- Dong, S., Gao, R., Yin, A., Guo, T., Zhang, Y., Hu, J., et al. (2013). What drove continued continent-continent convergence after ocean closure? Insights from high-resolution seismic-reflection profiling across the daba Shan in central China. *Geology* 41 (6), 671–674. doi:10.1130/g34161.1
- Dong, S., Hu, J., Shi, W., Zhang, Z., and Liu, G. (2006). Jurassic superposed folding and jurassic foreland in the daba mountain, central China. *Acta Geosci. Sin.* 27 (05), 403–410.
- Du, H., Wang, W., Shi, Z., Tan, J., Cao, H., and Yin, X. (2019). Geochemical characteristics and source of natural gas of the upper triassic xuiiaye Formation in malubei area, northeastern Sichuan Basin. *Oil Gas Geol.* 40 (01), 34–40. doi:10.11743/ogg20190104
- Erslev, E. A. (1991). Trishear fault-propagation folding. *Geology* 19 (6), 617–620. doi:10.1130/0091-7613(1991)019<0617:tfpf>2.3.co;2
- Ghosh, S. K., Mandal, N., Khan, D., and Deb, S. (1992). Modes of superposed buckling in single layers controlled by initial tightness of early folds. *J. Struct. Geol.* 14 (4), 381–394. doi:10.1016/0191-8141(92)90100-b
- Grasemann, B., Wiesmayr, G., Draganits, E., and Füsseis, F. (2004). *Classification of re-fold structures*, 119–125.
- Guo, T., He, X., Zeng, P., Gao, Y., Zhang, P., and He, G. (2020a). Geological characteristics and beneficial development scheme of shale gas reservoirs in complex tectonic regions: A case study of Wufeng-longmaxi formations in Sichuan Basin and its periphery. *Acta Pet. Sin.* 41 (12), 1490–1500. doi:10.7623/syxb202012004
- Guo, X., Hu, D., Huang, R., Duan, J., Jiang, Z., and Zhu, X. (2020b). Feature of paleo-oil pools in the Sinian Dengying formation, northeastern Sichuan Basin, and its significance to exploration. *Oil Gas Geol.* 41 (04), 673–683. doi:10.11743/ogg20200402
- He, D., Li, D., Zhang, G., Zhao, L., Fan, C., Lu, R., et al. (2011). Formation and evolution of multi-cycle superposed Sichuan Basin, China. *Chin. J. Geol.* 46 (03), 589–606.
- Hou, L., Zhang, C., Lin, Y., Li, C., Huang, Y., and Dong, T. (2020). From oblique arc-continent collision to orthogonal plate subduction in the southeastern central Asia Orogenic Belt during Paleozoic: Evidence from superimposed folds at the northern margin of the north China Craton. *J. Asian Earth Sci.* 200, 104499–109120. doi:10.1016/j.jseas.2020.104499
- Hu, J., Chen, H., Qu, H., Wu, G., Yang, J., and Zhang, Q. (2012). Mesozoic deformations of the Dabashan in the southern Qinling orogen, central China. *J. Asian Earth Sci.* 47, 171–184. doi:10.1016/j.jseas.2011.12.015
- Huang, H., Mei, Q., He, D., Lu, R., and Li, Y. (2021). Multi-level detachment deformation of the west segment of the South Dabashan fold-and-thrust belt, South China: Insights from seismic-reflection profiling. *Front. Earth Sci.* 24 (09), 1–17. doi:10.3389/feart.2021.633816
- Jia, C., Li, B., Lei, Y., and Chen, Z. (2013). The structure of Circum-Tibetan Plateau Basin-Range System and the large gas provinces. *Sci. China Earth Sci.* 56, 1853–1863. doi:10.1007/s11430-013-4649-7
- Jia, C., and Pang, X. (2015). Research process and main development directions of deep hydrocarbon geological theories. *Acta Pet. Sin.* 36 (12), 1457–1469. doi:10.7623/syxb201512001
- Jiang, F., Su, P., and Qin, Q. (2008). Discussion of main tectogenetic models in Tongnanba area. *Fault-Block Oil Gas Field* 15 (03), 14–17.
- Jiang, Y., Li, M., Wang, L., Zeng, T., Liu, J., and Li, J. (2020). Controlling effect of faults on tight sandstone natural gas accumulation and enrichment in Tongnanba Area, Northeast Sichuan. *J. China Univ. Petroleum Ed. Nat. Sci.* 44 (05), 19–31. doi:10.3969/j.issn.1673-5005.2020.05.003
- Jin, Z., Wan, G., Cui, Z., Wang, J., Yang, X., and Bai, W. (2012). Key tectonic change epoch and hydrocarbon accumulation periods of continental clastic reservoir in Sichuan Basin. *Fault-Block Oil Gas Field* 19 (03), 273–277.
- Jin, Z., Long, S., Zhou, Y., Wo, Y., Xiao, K., Yang, Z., et al. (2006). A study on the distribution of saline-deposit in southern China. *Oil Gas Geol.* 27 (05), 571–583+593.
- Kusky, T. M., and Loring, D. P. (2001). Structural and U/Pb chronology of superimposed folds, adirondack Mountains: Implications for the tectonic evolution of the grenville province. *J. Geodyn.* 32 (3), 395–418. doi:10.1016/s0264-3707(01)00038-2
- Lan, C., Xu, Z., Ma, X., Hu, C., Chen, H., and Zou, H. (2019). Development and distribution of mound-shoal complex in the Sinian dengying formation, Sichuan Basin and its control on reservoirs. *Acta Pet. Sin.* 40 (09), 1069–1084.
- Li, H. (2016). Accumulation process and pattern of oolitic shoal gas pools in the platform: A case from member 3 of lower triassic Feixianguan Formation in the heba area, northeastern Sichuan Basin. *Petroleum Explor. Dev.* 43 (05), 787–797. doi:10.1016/s1876-3804(16)30094-5
- Li, J., Dong, S., Yin, A., Zhang, Y., and Shi, W. (2015). Mesozoic tectonic evolution of the Daba Shan Thrust Belt in the southern Qinling orogen, central China: Constraints from surface geology and reflection seismology. *Tectonics* 34 (8), 1545–1575. doi:10.1002/2014tc003813
- Li, J., Zhang, Y., Dong, S., Shi, W., and Li, H. (2010). Apatite fission track thermochronologic constraint on Late Mesozoic uplifting of the Fenghuangshan basement uplift. *Chin. J. Geol.* 45 (4), 969–986.
- Li, J., Zhang, Y., Dong, S., and Shi, W. (2013). Structural and geochronological constraints on the mesozoic tectonic evolution of the North dabashan zone, south qinling, central China. *J. Asian Earth Sci.* 64, 99–114. doi:10.1016/j.jseas.2012.12.001
- Li, W., Liu, S., Wang, Y., Qian, T., and Gao, T. (2017). Duplex thrusting in the South Dabashan arcuate belt, central China. *J. Struct. Geol.* 103, 120–136. doi:10.1016/j.jsg.2017.09.007
- Li, Y., Qu, S., Liu, S., and Zhang, H. (2008). Structural characters and mechanism in Micang Shan and southern Daba Shan Mountains front. *Geotect. Metallogenia* 32 (03), 285–292.
- Liu, S., Li, Z., Deng, B., Zhong, Y., Wen, L., Sun, W., et al. (2021). Occurrence morphology of bitumen in Dengying formation deep and ultra-deep carbonate reservoirs of the Sichuan Basin and its indicating significance to oil and gas reservoirs. *Nat. Gas. Ind.* 41 (08), 102–112.
- Liu, Z., Luo, K., Tang, Y., Yang, F., Mei, L., and Shen, C. (2019). Critical tectonic periods and the response of gas accumulation in non-marine tight sandstone reservoir in Yuanba-Tongnanba area, Sichuan Basin. *Earth Sci.* 44 (03), 756–772. doi:10.3799/dqkx.2019.032
- Long, Y., Chen, H., Cheng, X., Deng, H., and Lin, X. (2021). Influence of paleo-uplift on structural deformation of salt-bearing fold-and-thrust belt: Insights from physical modeling. *J. Struct. Geol.* 153 (153-Dec), 104445. doi:10.1016/j.jsg.2021.104445
- Ma, D., Wang, H., Zhang, X., He, D., Fan, R., Wang, Y., et al. (2023). Analogue modeling of structural deformation of Tongnanba Anticline in mesozoic and cenozoic, NE Sichuan Basin. *Earth Sci.* 48 (4), 1307–1320. doi:10.3799/dqkx.2022.423
- Marshak, S. (2005). Salients, recesses, arcs, oroclines, and syntaxes-A review of ideas concerning the formation of map-view curves in fold-thrust belts. *AAPG Mem.* 82 (82), 131–156.
- Molli, G., Koehn, D., Allacorta, L., Danese, L., Zampelli, S., and Zazzeri, M. (2022). Superimposed structures, incremental strain and deformation path from field data to modelling: A case study from the Alpi Apuane metamorphic core complex (NW Tuscany, Italy). *J. Struct. Geol.* 161, 104676. doi:10.1016/j.jsg.2022.104676
- Ramsay, J. G. (1967). *Folding and fracturing of rocks*. New York: McGraw-Hill, 518–534.
- Ramsay, J. G. (1962). Interference patterns produced by the superposition of folds of similar type. *J. Geol.* 60, 466–481. doi:10.1086/626837
- Saha, D. (2002). Multi-stage deformation in the Nallamalai fold belt, Cuddapah Basin, South India - implications for mesoproterozoic tectonism along Southeastern margin of India. *Gondwana Research* 5 (3), 701e719.

- Shah, Z. S., Sayab, M., Aerden, D., and Iqbal, Q. (2013). Formation mechanism and tectonic significance of millipede microstructures in the NW Himalaya. *J. Asian Earth Sci.* 59, 3e13–13. doi:10.1016/j.jseas.2012.05.001
- Shi, W., Zhang, Y., Dong, S., Hu, J., Wiesinger, M., Ratschbacher, L., et al. (2012). Intra-continental dabashan orocline, southwestern qinling, central China. *J. Asian Earth Sci.* 46, 20–38. doi:10.1016/j.jseas.2011.10.005
- Sun, D. (2011). *The structural character and meso-cenozoic evolution of micang mountain structural Zone, Northern Sichuan Basin*. China: Chengdu University of Technology.
- Suppe, J., and Medwedeff, D. A. (1984). *Fault-Propagation folding geological society of America abstracts with programs*, 670.
- Wang, R., Zhang, Y., and Xie, G. (2013). Physical modeling of fold-and-thrust belt evolution and triangle zone development: Dabashan foreland belt (Northeast Sichuan basin, China) as an example. *Acta Geol. Sinica-English Ed.* 87 (01), 59–72. doi:10.1111/1755-6724.12030
- Wang, W., Zhang, X., Liu, R., Luo, H., and Wang, G. (2014). Origin of natural gas in terrestrial reservoirs in Yuanba and Heba regions in northeastern Sichuan Basin, China. *Acta Pet. Sin.* 35 (01), 26–36.
- Wang, W., and Chunhui, J. (2020). Genesis and exploration direction of high-efficiency gas reservoir in the third member of Feixianguan Formation in Tongnanba area. *Petroleum Geol. Recovery Effic.* 27 (03), 39–47.
- Wen, Z., He, D., Fan, C., and Meng, Z. (2013). Geomentry and kinematics model of Donghe geological cross section of Micangshan Mountain and constraint to the intracontinental subduction in the northern Yangtze. *Chin. J. Geol.* 48 (01), 93–108.
- Wu, L., Qian, J., Xiao, A., Shen, Z., Wang, L., Wei, G., et al. (2011). Structural analysis of the Micang Shan basement-involved thrust belt in the Western edge of the Yangtze Block. *Acta Petrol. Sin.* 94 (02), 426–438.
- Wu, S., Ma, Y., Jin, Z., Tang, L., and Li, R. (2006). Tectonic evolution and oil and gas accumulation in the East Micangshan foreland basin, Sichuan. *Petroleum Explor. Dev.* 33 (01), 14–16.
- Xu, H., Liu, S., Qu, G., Li, Y., Sun, G., and Liu, K. (2009). Structural characteristics and formation mechanism in the micangshan foreland, South China. *Acta Geol. Sinica-English Ed.* 83 (01), 81–91. doi:10.1111/j.1755-6724.2009.00010.x
- Zhang, J., Chang, J., Li, W., Fu, X., Yang, L., and He, Y. (2022). Tectono-thermal evolution of the micangshan uplift in thenorthern Sichuan Basin. *Sediment. Geol. Tethyan Geol.*
- Zhang, Q., Chen, Z., Zhao, Y., Zhang, W., and Luo, W. (2013). Relationship between tectonic evolution and hydrocarbon accumulation in the Changxing and Feixianguan Fms in the frontal concealed structural zone of Micangshan Mountain, northeastern Sichuan Basin. *Nat. Gas. Ind.* 33 (05), 24–29. doi:10.3787/J.ISSN.1000-0976.2013.05.004
- Zhang, Y., Dong, S., Li, J., and Shi, W. (2011). Mesozoic multi-directional compressional tectonics and formation-reformation of Sichuan basin. *Geol. China* 38 (02), 233–250.
- Zhang, Y., Shi, W., Li, J., Wang, R., Li, H., Dong, S., et al. (2010). Formation mechanism of the Dabashan foreland arc-shaped structural belt. *Acta Geol. Sin.* 84 (09), 1300–1315.
- Zhang, Z. (2019). Superposed buckle folding at the upper structural levels in Western dabashan: Example from the Jianchi area in zhenba county. *Earth Sci. Front.* 26 (2), 001–015. doi:10.13745/j.esf.sf.2019.3.10
- Zheng, H., Gao, B., Peng, Y., Nie, H., and Yang, F. (2013). Sedimentary evolution and shale gas exploration direction of the Lower Silurian in Middle-Upper Yangtze area. *J. Palaeogeography* 15 (05), 645–656. doi:10.7605/gdxb.2013.05.052



OPEN ACCESS

EDITED BY

Guiting Hou,
Peking University, China

REVIEWED BY

Wei Ju,
China University of Mining and
Technology, China
Jianguo Zhang,
China University of Geosciences, China

*CORRESPONDENCE

Yani Lin,
✉ linyani@cdu.edu.cn

RECEIVED 28 December 2022

ACCEPTED 05 July 2023

PUBLISHED 02 August 2023

CITATION

He C, Lin Y, Zhang T, Ma J, Li Y, Cheng J
and Zhang Y (2023), Study on the
structural characteristics of the
Yangdachengzi oil layer in the Quantou
Formation, ZY block, central depression,
Songliao Basin.
Front. Earth Sci. 11:1132837.
doi: 10.3389/feart.2023.1132837

COPYRIGHT

© 2023 He, Lin, Zhang, Ma, Li, Cheng and
Zhang. This is an open-access article
distributed under the terms of the
[Creative Commons Attribution License
\(CC BY\)](https://creativecommons.org/licenses/by/4.0/). The use, distribution or
reproduction in other forums is
permitted, provided the original author(s)
and the copyright owner(s) are credited
and that the original publication in this
journal is cited, in accordance with
accepted academic practice. No use,
distribution or reproduction is permitted
which does not comply with these terms.

Study on the structural characteristics of the Yangdachengzi oil layer in the Quantou Formation, ZY block, central depression, Songliao Basin

Chunyu He¹, Yani Lin^{1,2*}, Tianze Zhang^{1,3}, Jisheng Ma⁴, Yunfei Li¹,
Jiaju Cheng¹ and Yinde Zhang¹

¹College of Energy, Chengdu University of Technology, Chengdu, China, ²State Key Laboratory of Oil and Gas Reservoir Geology and Exploitation, Chengdu University of Technology, Chengdu, China, ³Research Institute of Petroleum Exploration and Development, Beijing, China, ⁴Oil Production Company of Daqing Oilfield Company Ltd., Daqing, China

The Songliao Basin is a large Mesozoic–Cenozoic continental basin with multiple sedimentary cycles. It has experienced the influence of multidirectional and different structural stresses in the peripheral structural belt, resulting in a complex geological structure. The continental clastic deposits at the depression of the Quantou Formation in the shallow part of the basin, including the Fuyu oil layer and the Yangdachengzi oil layer, are the primary exploration and development target. The structure and faults are the dominant factors controlling the hydrocarbon accumulation in the upper member of the Quantou Formation in the central Songliao Basin. In this study, we finely interpret the three-dimensional structure of the third member of Quantou Formation in the ZY block by the integration of well logging and seismic data and then analyze the stratigraphic distribution and fracture characteristic and the tectonic development history of the Yangdachengzi oil layer. The results show that the Yangdachengzi oil layer is a monoclinic structure from the southeast to northwest. It has four third-level structural units, the Mofantun nose structure, Yumin nose structure, Zhaoyuan nose structure, and Zhaoyuan western nose structure, which form the structure-lithostratigraphic trap zones in the study area, in which a total of 80 traps for the Yangdachengzi oil layer has been identified with the total area of about 58.06 km². Faults are highly developed in the central depression of the Songliao Basin. The ZY block is dominated by the extensional-strike-slip faults. The main fault direction is mostly north–northeast, and the secondary fault direction is mostly north–northwest. The complex tectonic activities determine the formation mechanism and the evolution of faults. The faults in this block can be classified as early-stage, middle-stage, late-stage, and long-term faults. The long-term fault is the major fault type of the five fault bundles, and it acts as the main channel for oil and gas migration. In addition, the reservoir is an above-generation and below-storage model. This study provides evidence for the hydrocarbon accumulation model of the Quantou Formation.

KEYWORDS

Songliao Basin, Quantou Formation, fault characteristics, Yangdachengzi oil layer, structure-lithostratigraphic trap

1 Introduction

Since the discovery of Daqing Oilfield in 1959, the Songliao Basin has become the most important oil- and gas-producing area in China and has made great contributions to the development of China's oil industry. The Songliao Basin is a large continental rift basin developed in the Paleo-Pacific tectonic domain, Mongol-Okhotsk Ocean tectonic domain, and Paleo-Asian Ocean tectonic domain (Hu et al., 2005; Li et al., 2012a; Liu et al., 2020a; Liu et al., 2022b). The rift is the main manifestation of continental extensional structures. Numerous studies focused on the developing mechanism of continental extensional structures (Yang et al., 2019; Zhang and Dong, 2019; Lin and Li, 2021; Xiang et al., 2022; Liu et al., 2023), including the following: 1) Continental rifting is driven by the upwelling of mantle plume; e.g., the Kenya Rift in the East Africa is formed by the upwelling of the Afar mantle plume and Kenya mantle plume (Wilson, 1966; Macgregor, 2015; Pirajno and Santosh, 2015; Ge and Hou, 2018; Yao et al., 2018; Jia et al., 2021). 2) Continental margin extension is caused by subduction slab rollback and subduction zone retreat. For example, the Aegean wide rift basin is caused by the retraction of the African subduction plate under the Mediterranean ridge. When the extension began, large low-angle detachment faults started to develop in the upper crust, and then, in the later stage, high-angle normal faults were developed with the decrease of extension (Gautier et al., 1999; Jolivet and Faccenna, 2000; Chen et al., 2014). 3) The gravitational collapse of the thickened crust drives the extension. For instance, the collapse of post-orogenic extension is responsible for the formation of the large-scale extension basin and range province in western North America. The low-angle normal faults developed in the upper crust received rotational shear deformation in the extensional deformation at first, and then, the high-angle rotating normal faults and tilting fault blocks were developed in the late stage (Eaton, 1982; Rehrig, 1986; Ren and Li, 1998; Chen et al., 2014). 4) The extension can be formed by the stress field in the strike-slip zone, like the Los Angeles Basin and the Sacramento Basin, which are formed by the long-term strike-slip movement and local turning of the San Andres fault zone (Powell and Weldon, 1992). The research on strike-slip faults has gone through more than 100 years. The internationally famous San Andreas Fault is a right-lateral transform fault formed by the NW (northwest) movement of the Pacific plate relative to the North American plate (Reading, 2009; Wesnousky, 2005; Scharer and Streig, 2019). The Tan-Lu strike-slip fault in China, which is similar to the San Andreas Fault, has produced some strike-slip pull-apart basins in the northeastern part of China and has also had a certain impact on the Songliao Basin (Feng et al., 2022).

The Songliao Basin is one of the important rift basins in the Northeast Asian rift system. The driving mechanism has been argued by numerous researchers. It is generally believed that the closure of the Paleo-Asian Ocean, the subduction of the Mongol-Okhotsk Ocean plate, and the subduction of the Paleo-Pacific plate offer the driving force of the Songliao Basin (Huang et al., 2016; Yang et al., 2019; Zhang and Huang, 2019; Feng et al., 2021; Lin and Li, 2021; Dong et al., 2022; Guan et al., 2022; Xiang et al., 2022). The Songliao Basin has experienced four tectonic stages: the basement formation and transformation stage, the rift extension stage, the cooling depression stage, and the tectonic inversion stage (Hou et al., 2004). As the result of repeated extension and strike-slip activities,

multi-stage fault systems can be observed inside the basin: the first-stage faults were developed in the Middle–Late Jurassic period. The basement of the basin was strongly deformed by the large-scale left-lateral strike-slip activities in the northern section of the Tan-Lu fault system and derived NNE, NNW, and near NS trending secondary faults. The second-stage NNE-trending extensional faults were developed during the thermal uplift rifting stage from the Late Jurassic to the Early Cretaceous period. The stress of the basin tectonic system gradually changed from left-lateral compression–torsion to extension, and the faults' trend began to parallel the Paleo-Pacific subduction belt. The third-stage of NNE-trending 'Y'-shaped faults was developed in the subsidence stage from the middle and late Early Cretaceous to the early Late Cretaceous period, and the basin underwent a weak extension. The fourth-stage faults were developed in the Late Cretaceous. The basin was subjected to the compressional stress from the southeast direction and formed a large number of NE-trending compressional faults and NNW-trending tension–torsion faults (Ren et al., 2002; Ge et al., 2009; Li et al., 2014; Huang et al., 2016; Deng et al., 2021; Feng et al., 2021; Jiang et al., 2021; Feng et al., 2022). A study of the Songliao Basin would be challenging because of the complex geodynamic background and unique magmatic activity characteristics.

The Yangdachengzi oil layer is a high-yield oil production unit and one of the key exploration targets in the Songliao Basin (Xi et al., 2015). The faults of the Yangdachengzi oil layer are developed in multiple phases and provide good conditions for oil and gas migration and accumulation. The fault-block, fault-nose, and anticline traps that relate to the tilted Yangdachengzi oil layer are distributed around the fault-concentrated belt. The high density and small scale of the faults cause the strong vertical heterogeneity in the deeply buried Yangdachengzi oil layer (Luo, 2010; Guo, 2019; Mei et al., 2020). The study of the deformation characteristics and evolution patterns of the faults is critically important for understanding the influence of faults on oil and gas migration, yet it has not been fully discussed in the previous research. In this study, by integrating the three-dimensional (3D) seismic, logging, and drilling data in the central depression area of the ZY block of the Songliao Basin, we study the structural style and fault developing characteristics of the Yangdachengzi oil layer in detail. The fracture patterns and characteristics are summarized, and the controlling mechanism of the different stages of faults is demonstrated. The results provide a better understanding of the fault system and its relation with the hydrocarbon distribution. By analyzing the tectonic evolution characteristics of the late Early Cretaceous–early Late Cretaceous in the Songliao Basin, the relationship between tectonic movements and fault-concentrated belts is recognized, which provides a theoretical basis for the control of fault belts on the reservoirs during the deposition of the Quantou Formation in the Songliao Basin.

2 Geological setting

The Songliao Basin lies in the northeast of China. It is geologically located at the intersection of the North China plate, the Pacific plate, and the Siberian plate. The Songliao basin is a typical fault-depression composite structural basin. The basin is

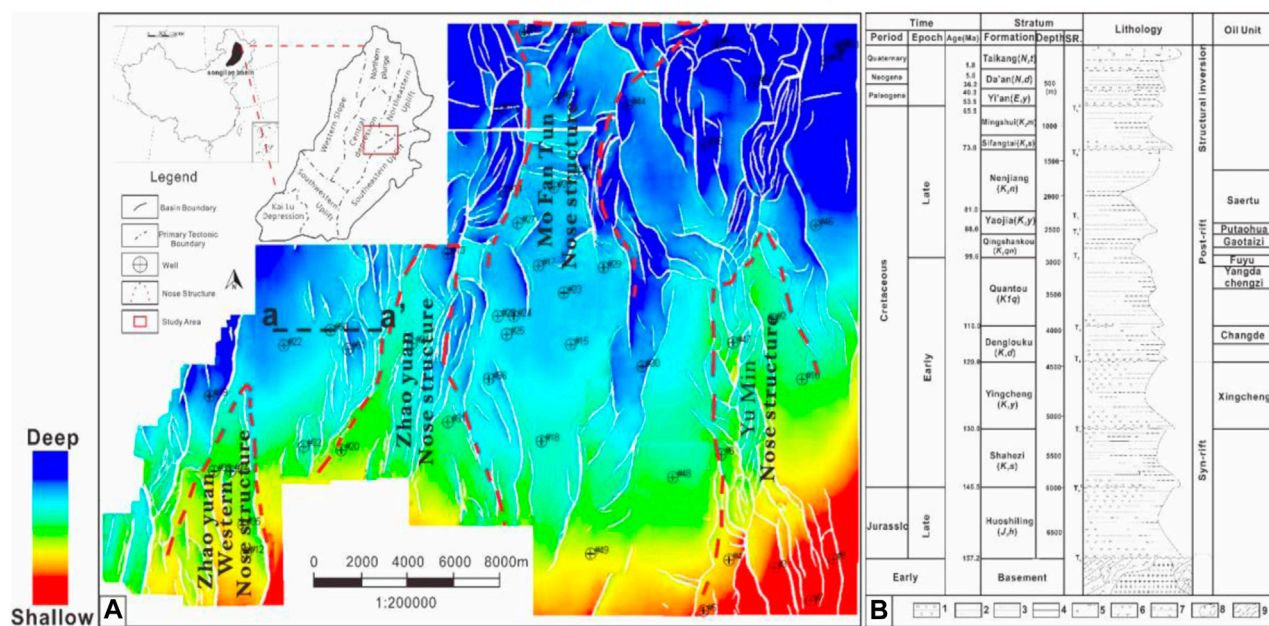


FIGURE 1

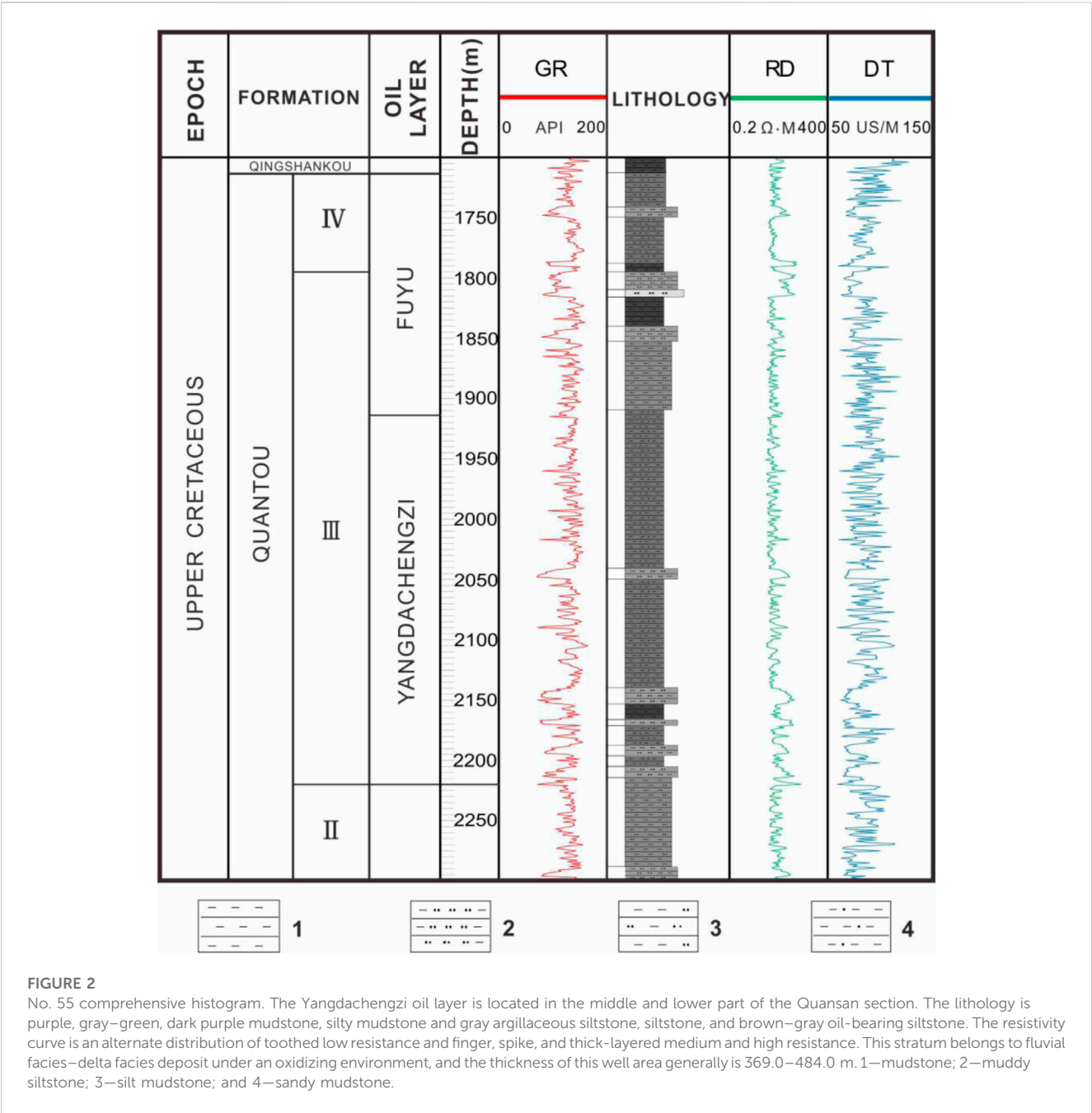
(A) Study location. The Songliao Basin is a large Mesozoic–Cenozoic sedimentary basin in northeast China, spanning Heilongjiang Province, Jilin Province, Liaoning Province, and the Inner Mongolia Autonomous Region. The whole basin can be divided into seven first-order tectonic belts. The red small frame is the location of the work area, which is located on the east side of the central depression. The figure shows the top surface structure of the Yangdachengzi oil layer; the overall strata are low in the NW and high in the SE. The section crossed #50 well is shown in Figure 3: (B) brief stratigraphic histogram of the Songliao Basin (Wang et al., 2007; GE et al., 2010). The Yangdachengzi oil layer is located at the top of the Quantou Formation, with a buried depth of 3,000–3,400 m. It was deposited in the late Early Cretaceous, 100 Ma ago, and the lithology is mainly sandy mudstone. 1—Conglomerate; 2—sandstone; 3—mudstone and shale; 4—coal; 5—loose sediment; 6—volcanic rock; 7—pyroclastic rock; 8—granite; 9—metamorphic rock.

controlled by the regional faults. The western boundary is the Nenjiang–Baicheng Fault and the Greater Khingan Range, the eastern boundary is the Yilan–Yitong Fault and the Zhangguangcai Range, the southern boundary is the Chifeng–Kaiyuan Fault and the Yinshan–Yanshan orogenic belt, and the northern boundary is the Xunke–Tieli Fault and the Lesser Khingan Range. The basin interior is separated by multiple sets of deep faults (Ren et al., 2002; Shan et al., 2009; Lu et al., 2022). The strikes of the main fault zones are north–northeast–southwest–west (NNE–SWW), nearly east–west (EW), and northwest–southeast (NW–SE). The Nenjiang–Baicheng Fault in the western boundary and the Dedu–Da'an fault, Qinggang–Gan'an fault, and Siping–Dehui faults in the interior are all strike-slip faults (Deng et al., 2021). The basin can be further divided into seven first-order tectonic belts—that is, the western slope, northern plunge, central depression, NE uplift, SE uplift, SW uplift, and Kailu depression. The major oil- and gas-producing areas are the Daqing anticline, Qijia–Gulong, Sanzhao, and Changling sags, and the Chaoyanggou terraces developed in the central depression zone (Feng et al., 2010; Xi et al., 2015). The study area covers the eastern part of the central depression and the NW slope of the SE uplift zone (Figure 1A).

The strata can be divided into four main periods based on their tectonic deformation characteristics: the foreland period (Triassic–Jurassic strata), the syn-rift period (Huoshiling Formation–Yingcheng Formation), the post-rift period (Denglouku Formation–Nengjiang Formation), and the

tectonic inversion period (Sifangtai Formation–Taikaang Formation), corresponding to the basement tectonic layer, fault depression layer, depression layer, and inversion tectonic layer, respectively (Figure 1B). Clear regional unconformities can be found between the layers (Feng et al., 2010). Since the Middle Jurassic, the collision and subduction between the Siberian plate, the Sino–Korean plate, and the Paleo-Pacific plate have caused the deep asthenosphere to rise upward, and the crust has continuously thinned and stretched, forming the early structure of the Songliao Basin (Yang et al., 2021).

At the end of the Late Jurassic, the Songliao Basin began to extend and rift and form numerous fault basins with various scales and structural styles. In the early stage of the Late Cretaceous, the cooling effect in the lithosphere caused the uneven sinking of the crust. The basin entered the thermal depression stage (Li et al., 2021). After that, the rift basins unified and formed a large lake basin, and the Quantou Formation started to deposit. During this period, the influence of the basement structure and the extension range decreased and formed normal faults in different scales during the sedimentary period of the Quantou Formation. The strikes of most of these faults were dominated by the north–south (NS) direction, but some areas were dominated by the NNE or NNW direction. The dominant trend often followed the structural trend from the fault depression period, reflecting the control of the deep structure. An individual graben or graben system is indicated by the V-shaped faults or nested V-shaped faults on the seismic section (Sun et al.,



2013a). The depression period holds the largest density of faults, and lesser faults can be found in the inversion period, while the fault depression period contains the least faults. The faults are varied in scale, displacement, and extension range, which revealed the characteristics of multistage activities of the faults (Liu et al., 2017).

The Quantou Formation (*K1q*) that deposited in the large-scale depression lake basin mainly consists of fluvial-lacustrine clastic sediments, which covers almost the entire basin. Several transient transgression events and weak volcanic activity occurred during the deposition of the Quantou Formation, and the intensity of fault activity was greatly reduced (Ge et al., 2010; Fan et al., 2017). The Yangdachengzi oil layer lies in the upper part of the Quantou

Formation (Figure 2). The meandering river deposits of Yangdachengzi oil layer were formed in a humid-arid alternating climate and gentle terrain background with slow subsidence of the basement. The lithology is mainly mudstone, fine sandstone, mudstone-bearing coarse siltstone, mudstone-bearing fine sandstone, coarse siltstone-fine sandstone, fine sandstone-coarse siltstone, and calcium sandstone (Li et al., 2013). The sand body developed in the lower Yangdachengzi oil layer shows a clear reduction of natural gamma ray (GR) value. The middle and upper parts of the Yangdachengzi oil layer are dominated by the thick purplish red mudstone, which host the thin sandstone layers. The GR curve gradually changed upward from a box type to a toothed bell type, indicating an increasing level of river sinuosity.

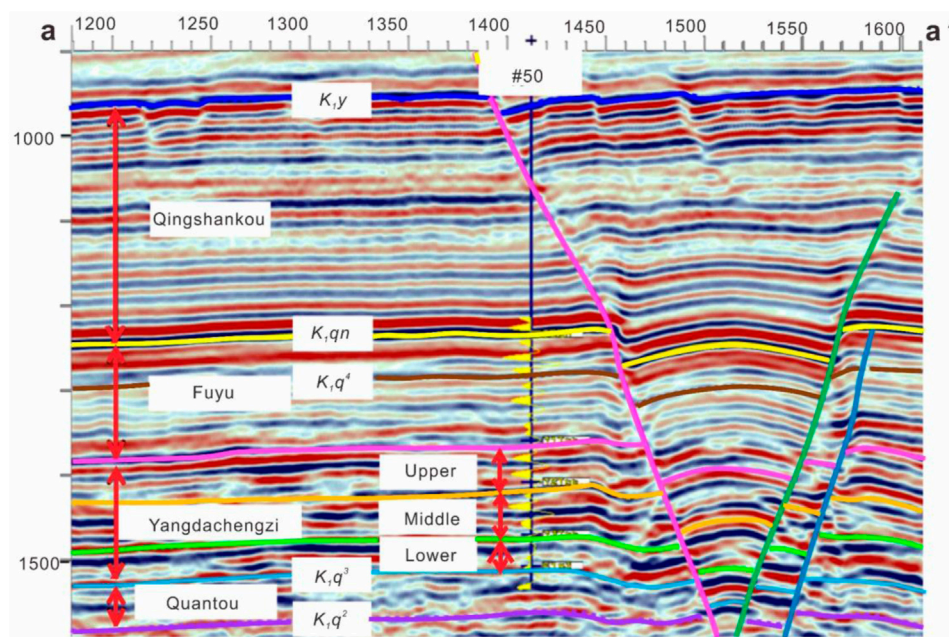


FIGURE 3

Seismic horizon calibration profile of well #50. The seismic reflection interface at the bottom of the Qingshankou Formation has good continuity and strong amplitude, which can be used as a good seismic standard layer. Below it is the Fuyu oil layer and the Yangdachengzi oil layer. The seismic reflection interface is stable and continuous.

The sedimentary environment gradually transitions from a delta deposition to a meandering river deposition.

3 Data and methods

The main purpose of this work is to study the influence of the Yangdachengzi oil layer structure and fracture system on oil and gas migration and accumulation. An integration of 3D seismic data, logging, and drilling data is used. The study area covers the eastern part of the central depression and the NW slope of the SE uplift zone (Figure 1A). It is covered by five 3D seismic working areas with a total coverage of 797 km². These 3D seismic data come from different vintages, and the frequency of seismic data is about 35 Hz. The two-way travel time of seismic data is mainly in the range of 900–1,600 ms. A total of 53 wells encounter the Yangdachengzi oil layer, with 10 wells drilling through.

Based on the evaluation of data, a synthetic seismogram is necessary to generate the identification of seismic horizons. It was also used to correlate the geological data with the well logs' data to justify the seismic trace data. We use the existing drilling data to finely calibrate the seismic geological horizon. Then, starting from the known well points, through the well profile, amplitude change, waveform characteristics, and time difference law, the standard seismic reflection layer is finely compared and tracked to establish a backbone interpretation profile. The bottom of the Qingshankou Formation with stable distribution and easy identification is used as the marker layer, which can guarantee the reliability of the interpretation scheme. Seismic

attributes assisted us to obtain the information obtained from seismic data based on empirical results. The main principle of the coherence attribute technology is to represent the lateral heterogeneity of the formation by the similarity of adjacent seismic traces in the 3D seismic data volume to determine the faults in the formation. Using the coherence attribute technology, horizontal slice technology, and 3D visualization technology, we carried out detailed correlation of the interpreted layers and faults and construction of fault space combination. Through the study of structural characteristics and fault system analysis in the study area, we strengthen our understanding of the Yangdachengzi oil layer and establish an accumulation model.

4 Interpretation and results

4.1 Seismic response characteristics

The top surface of the Yangdachengzi oil layer is about 130 ms below the standard interface of the Fuyu oil layer. The seismic section has the seismic reflection characteristics of medium-high frequency, medium-strong energy, and medium-strong continuous wave peak. The overall lateral waveform is stable and continuous, and the seismic response characteristics of the whole area were relatively uniform. The top surface of the middle Yangdachengzi oil layer is about 190 ms below the standard interface of the Fuyu oil layer. It has the seismic reflection characteristics of medium-high frequency, weak-medium strong energy, and medium-strong continuous wave peak. The lateral waveform is relatively stable,

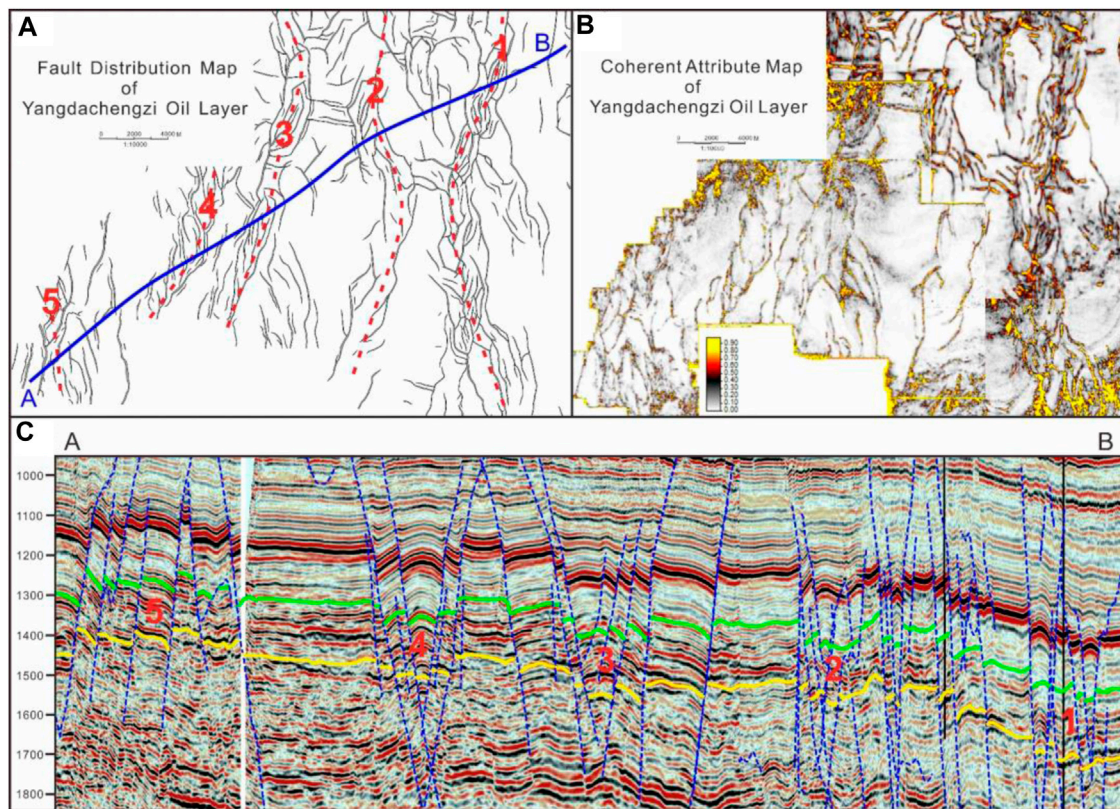


FIGURE 4

(A) Fault distribution map of the Yangdachengzi oil layer in the Zhaoyuan area. The fault is very developed. It is generally divided into five fault zones, with a strike of NNE-NNW. (B) Assistance of coherent attributes in the interpretation of faults. The comparison shows that the fault interpretation is reliable and the fault plane correlation combination is reasonable. (C) Seismic profile of A-B. From SW to NE are the No. 5, No. 4, No. 3, No. 2, and No. 1 fault zones.











continuous, and locally different. The top surface of the lower Yangdachengzi oil layer is about 240 ms below the standard interface of the Fuyu oil layer, which has the seismic reflection characteristics of medium-high frequency, weak-medium strong energy, and medium-strong continuous wave trough. The bottom surface of the Yangdachengzi oil layer is located about 280 ms below the standard interface of the Fuyu oil layer, with medium-high frequency, medium-strong energy, and medium-strong continuous trough reflection. Seismic reflection characteristics are relatively stable laterally and had good continuity (Figure 3).

4.2 Combination characteristics of faults

Faults in the Yangdachengzi oil layer are highly developed. The plane density is large, the distribution is uneven, and it has the characteristics of zoning. With the help of coherent attributes, we identify more than 600 large and small faults in the study area and divide the faults into five fault-concentrated belts with a strike of NNE-NNW (Figure 4). They appear in the nose structure area, which is susceptible to tensile stress and produced a series of concentrated belts parallel or nearly parallel to the long axis of the structure. The faults are mainly located in the depression layer between the Quantou Formation and Qingshankou Formation. In

general, the fault has the following characteristics: 1) The fault is a trans-tensional straight normal fault with an NS strike and a dip angle of 70°. 2) Various style combinations are densely developed to form the fault zones. According to the profile combination characteristics of the faults, the extensional tectonic styles could be classified as graben, horst, fault-step, and Y-shaped types of faults. The density was the largest during the depression period, and the profile shows a combination of V-shaped graben or stepped faults. 3) The faults that ruptured horizons are complex, and the number of faults that developed over the long term was significant. We identified 53 long-term faults in the five fault zones. The fault trough is between 10 and 130 m. The maximum extension length is 13,066 m and generally less than 5,000 m. The overall trend is mainly in the NNW and NNE directions, which shows obvious sinistral characteristics. The fault's surface is curved, which is a typical indicator of a strike-slip fault. 4) The fault density is large in a plane view, and it is nearly parallel, oblique, orthogonal, en echelon, and broom-like (Table 1). In general, the faults are trending SN, and the inner part is separated by flower-like fault belts that formed trap groups. Following the distribution law of fault superposition diagram, the fault system changed little. The fault spread outward from the bottom to the top of the Yangdachengzi oil layer, with a small offset and good inheritance (Figure 4).

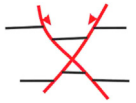
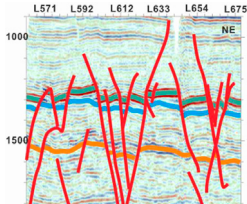


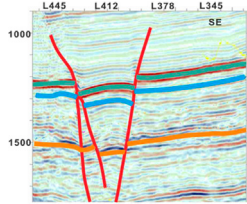


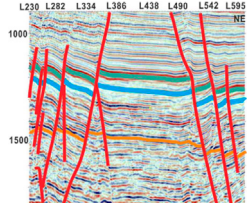


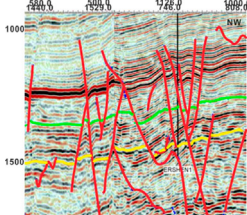

TABLE 1 Fracture space combination classification.

Type	Diagram	Example
Parallel type		
Oblique type		
Orthogonal type		
En echelon type		
Broom type		

4.3 Fault structure style

The extensional tectonic style in the ZY block is not the traditional extension formed under positive stretching or arching, but is an oblique extension with the characteristics of torsion. From the seismic section, the fault combination generally presents a graben–horst combination mode, and the fault style mainly includes graben-type, horst-type, step-like, Y-shaped and X-shaped conjugate, and negative flower-like faults (Table 2). 1) The step-like faults form in a step-like style on the main survey line section. A series of normal faults form a step-like fault zone, and the stratigraphic tendency is the opposite of the fault tendency. 2) The combination of the main fault and reverse inclined secondary fault forms a Y-type fault. The Y-type faults are composed of main faults and secondary small faults, which usually intersect in a Y-shaped pattern, and multiple Y-shaped combinations form a complex Y-shaped pattern. 3) The X-type conjugate faults are formed by a cross combination of two groups of faults in different directions, at different levels, and over different periods, and the acute angle was about 70°. 4) Under the condition of a regional tension–torsion stress field, the

TABLE 2 Classification of fault structural types.

Type	Diagram	Example
X type		
Y type		
Horst		
Graben		
Step-like		
R E N type		
Cauda equina		
Minus flower		

negative flower-like fault accompanies the strike-slip fault, and it spreads upward in the form of a bifurcation from a main fault. Many groups of small faults develop at both ends of the fault, showing graben-like characteristics on the section. There are many grabens and horsts in the study area. For example, in the No. 5 fault belts, the SW side is composed of a series of reverse fault terraces with a tendency toward the SW direction, and the NE side is composed of reverse fault terraces with opposite tendencies that formed horsts between them. In the No. 4 and No. 3 fault belts, reverse fault-steps as well as Y-shaped and X-shaped conjugate faults can be identified, which are combined to form a graben–horst model (Figure 4).

4.4 Plane structural features

In the regional structure, the study area is located in the central depression area and the NW slope area of the SE uplift zone and

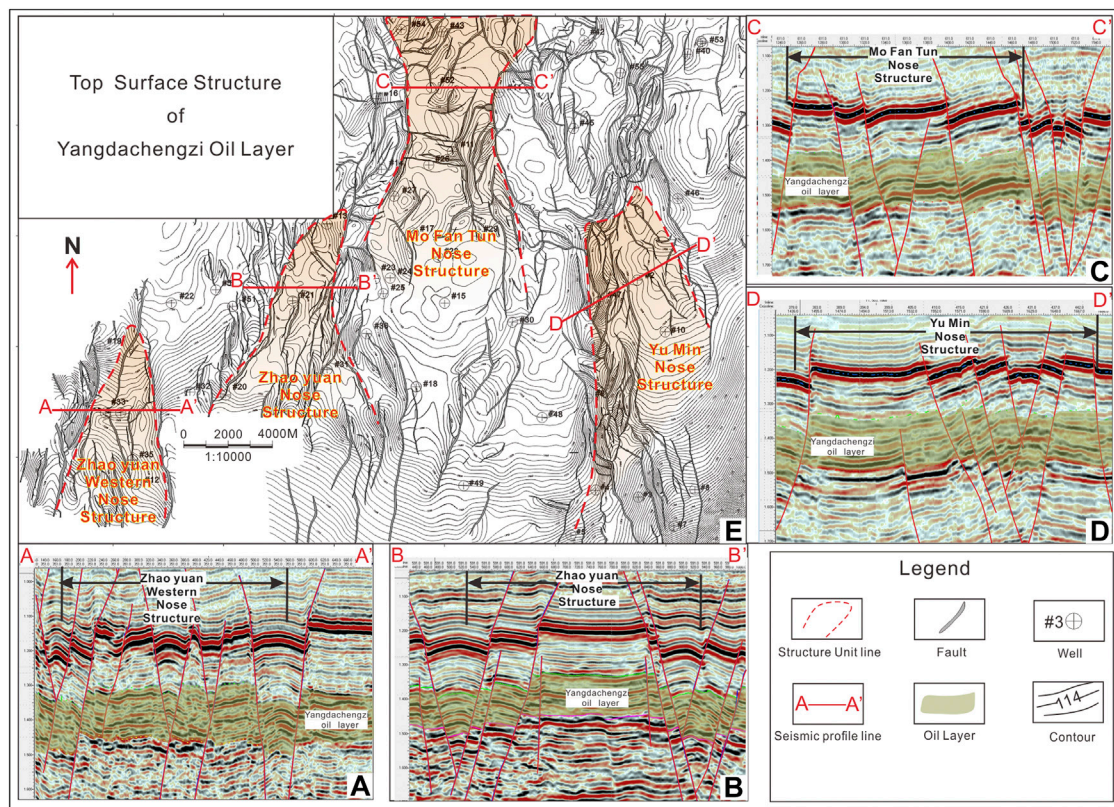


FIGURE 5 (A) The seismic profile of Zhao yuan Western Nose structure. (B) The seismic profile of Zhao yuan Nose structure. (C) The seismic profile of Mo Fan Tun Nose structure. (D) The seismic profile of Yu Min Nose structure. (E) Top structural map of the Yangdachengzi oil layer is a monoclinic structure inclined to the NW. The red dashed line delineate the boundaries of the nose structures.

developed the Zhao yuan nose structure, which inclines to the NW direction. According to the structural map of each layer, the deep and shallow structures of the entire work area are the same. In general, it is a NW-dipping monoclinic structure. The stratum trend is oblique to the near NS fault at a low angle, and the structure is not developed in some areas. The Sanzhao depression in the NW is a long-term developed inherited depression (only a part was in this area), and it is also the sedimentary and subsidence center, which shows a gradual upward trend around this area. The Zhaozhou structure in the east also presents a local depression pattern, and four nose structures are developed in the central uplift belt (Figure 5E): the Mofantun nose structure, the Yumin nose structure, the Zhao yuan nose structure, and the Zhao yuan western nose structure. Among them, the Mofantun structure is located between the two depressions in the east and west, and the fault-nose structure with the long-arm shape in nearly NS trend is developed, and the terrain is relatively gentle (Figure 5C). The NE side of the Yumin nose structure is adjacent to the depression, and the slope of the western side is relatively slow (Figure 5D). The overall trend of the fault-nose structure is NNW; the Zhao yuan nose structure overall trend is NNE, with east and west sides of the fault depression development (Figure 5B). The trend of the Zhao yuan western nose structure is in a NS direction, the terrain is steep, and the fault-nose structure extends northward for a short length (Figure 5A). They were uplifted by the faults to form a graben–horst model.

5 Discussion

5.1 Fault development stage

The developing stage of the faults play a significant role in the formation and evolution of the basin, and it also assists the migration and accumulation of oil and gas. Depending on which strata the fault cuts through, the fault systems in the study area are divided into early-stage fault, middle-stage fault, late-stage fault, and long-term fault (Figure 6). The early-stage faults were extensional faults formed in the rift period of the basin, generally cutting off the Jurassic or Dengloulou Formations. The middle-stage faults were formed in the sedimentary period of Qingshankou Formation in the depression area of the basin, and a large number of small normal faults were produced, which are mainly distributed in the upper part of the Quantou Formation. The fault distance gradually decreases in the shallow layer and mostly disappears in the Yaojia Formation. The late-stage faults were generated from the end of the deposition of the Nenjiang Formation that interrupted the Yaojia Formation. The long-term faults were formed during the fault-depression period of the basin and developed in the later tectonic movement over a long period of time. The long-term faults are identified as the long extension on the plane view and with large fault distance on the vertical seismic profile. The

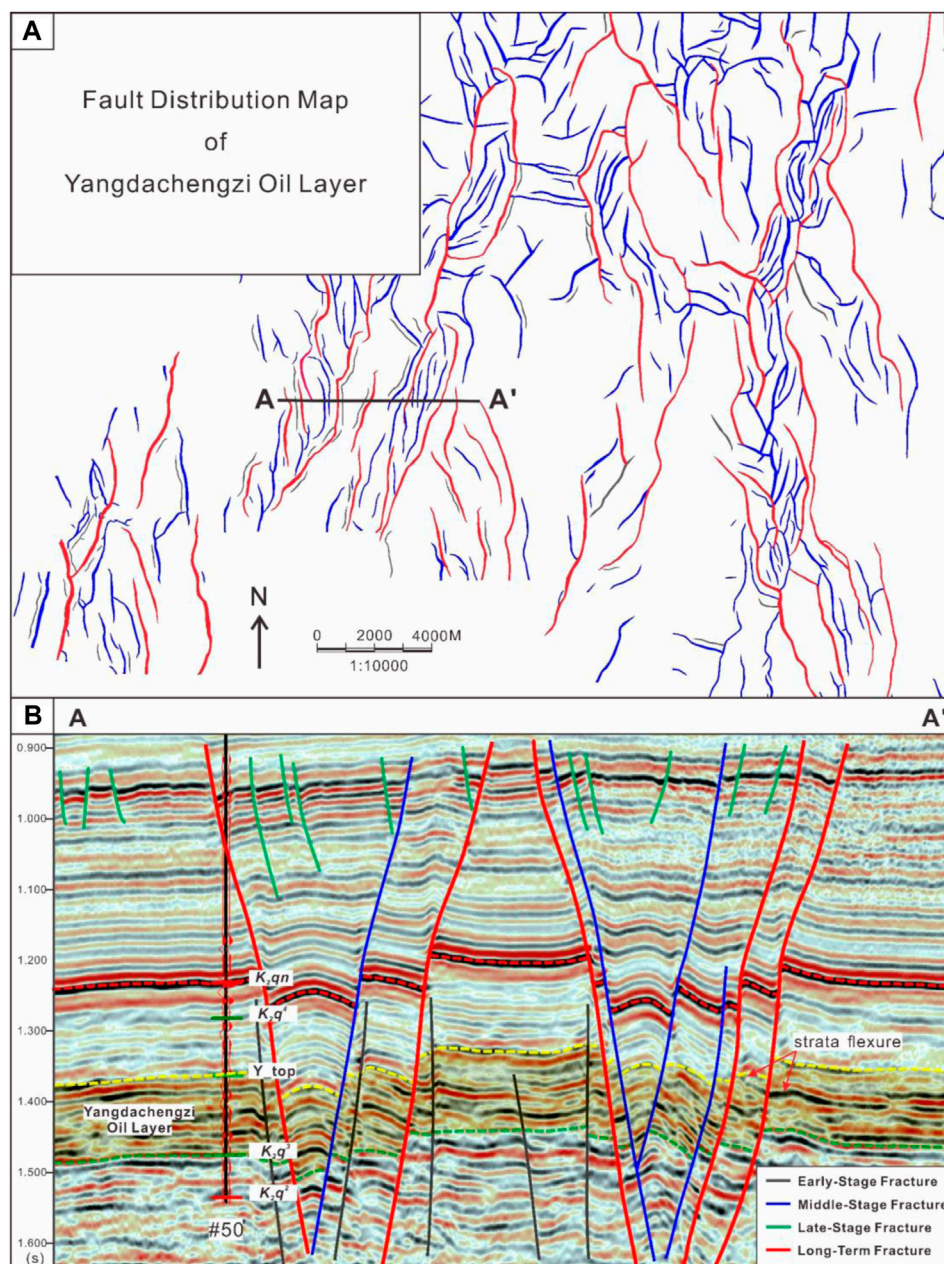


FIGURE 6

(A) Fault distribution map of the Yangdachengzi oil layer. The red is a long-term fault, the blue is a medium-stage fault, and the black is an early-stage fault. (B) Fault seismic profile, with the location (A–A') shown in (A). Obvious flexures along the fault can be observed in the strata near the fault.

upper part of the long-term faults disconnects the Yangdachengzi oil layer, and the following interrupts the Putaohua oil layer at the end of the Yaojia group sedimentary period. The fault distance decreases gradually from deep to shallow. The long-term faults are the main controlling faults which determine the growth of fault belts and act as the main channels for oil and gas migration in this area. In general, the early-stage fault develops in the fault-depression period, the middle-stage fault develops in the depression period, the late-stage fault develops in the

tectonic inversion period, and the long-term fault continues to develop during deposition.

5.2 Formation mechanism and evolution of the fault

As a fault-depression superimposed basin, the Songliao Basin contains a large number of faults. The fault systems of Quantou Formation in the Songliao Basin are formed on the basis of the pre-

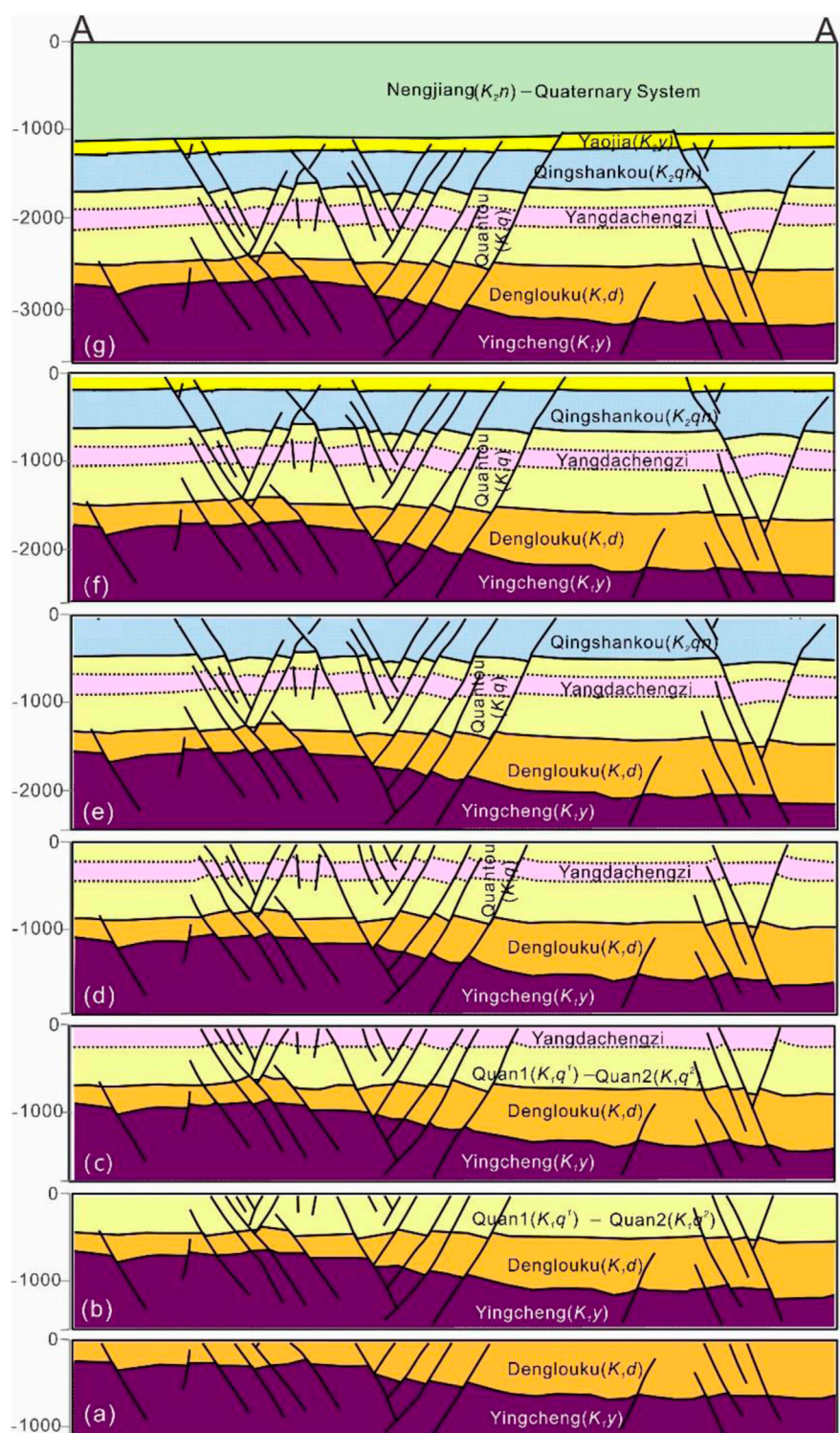


FIGURE 7

Structural development history section of the Yangdachengzi oil layer. The location of the fault (A–A') is shown in Figure 6A. (A–G) Developmental history of the Yingcheng Formation to Nenjiang Formation. The duration of the faults is different. The early-stage faults were active during the deposition of the Yingcheng Formation and Dengloulou Formation, the middle-stage faults were active before the deposition of the Yaojia Formation, and the late-stage faults disconnected the Yaojia Formation. Long-term faults continue to operate in each period and play an important role in oil and gas migration and accumulation.

existing faulted structure, which then experience the tension-twist deformation during the depression stage of the basin, and finally reconstruct during the reversal deformation stage. Therefore,

clarifying the activities of different stages of the Songliao Basin is helpful in revealing the genetic mechanism and evolution of the fault belts of the Yangdachengzi oil layer in the Quantou formation. After

carefully analyzing the fault developing stages and characteristics of stratigraphic distribution, we create a tectonic development history profile (Figure 7). Based on the regional geology and the interpretation results, the analysis of the structure and sedimentary development in this area is as follows:

Figure 7A shows the Yingcheng–Denglouku Formation sedimentary period. During the early stage of the basin development, the joint effect of the closure of the Mongolian–Okhotsk Ocean and the oblique subduction of the Izenagi Plate generated a left-lateral compression and torsion stress, resulting in extensive magmatic activity within the basin (Hou et al., 2010; Yang et al., 2019). Under the NNE trending left-lateral system, a secondary NS compression stress field was generated in the basin basement, resulting in NNE- and NNW-trending fault systems, which had a profound impact on the basin (Ge et al., 2010). After the Late Jurassic, the upwelling of mantle plumes produced thermal domes on Earth's surface, and the geopotential energy of these domes drove the crust to undergo gravity spreading, resulting in NNE-oriented tensile stress. The stress regime of the basin began to transform from left-handed compression and torsion to extension. During the sedimentation period of the Yingcheng Formation, the Songliao Basin developed into a horseshoe-shaped rift basin (Li et al., 2019a; Li et al., 2019b). In the late stage of rifting (Yingcheng Formation sedimentation period), the direction of extension gradually changed from NNE to near EW to ESE, which was related to the WNW–ESE crustal extension and detachment (Yang et al., 2019). During the sedimentation period of the Denglouku Formation, tectonic movement was relatively weak. Because of the weakening of the EW-oriented tensile stress, the basin began to gradually sink regionally, and the basin type transitioned from a rift basin to a depression basin.

Figures 7B–D) show the Quantou Formation sedimentary period. After the deposition of the Denglouku Formation, the basin entered a stage of significant and stable subsidence, and tectonic movement tended to stabilize. The fault activity during the deposition of the Quantou Formation exhibited obvious inheritance and co-deposition characteristics. The fault activity during the deposition of the Quantou Formation can be divided into two stages. The early stage was characterized by a co-deposition normal fault developed at the bottom of the Quantou Formation. Obvious flexures along the fault can be observed in the strata near the fault, and these faults have a characteristic of decreasing vertical displacement from bottom to top (Figure 6B). The early fault activity was strong, and then, it gradually weakened and ceased upward, indicating an inherited activity of a long-existing fault. The late-stage fault developed at the end of the Quantou Formation deposition and is a co-deposition normal fault with extensional and rotational properties under regional differential subsidence (Wang et al., 2022a).

Figures 7E, F) show the Qingshankou Formation sedimentary period. From the late Early Cretaceous to the Late Cretaceous, the distribution range of igneous rocks significantly decreased towards the east and migrated from inland to coastal areas, indicating the eastward drifting of the Eurasian continent and the retreat of the ancient Pacific subduction plate, resulting in continental extension and the formation of weak NW–SE horizontal tension (Zhang et al., 2005; Tang et al., 2018; Fu et al., 2020; Lin and Li, 2021; Xiang et al., 2022). During the sedimentation of the Qingshankou Formation, a

large number of densely distributed fault zones were formed in a belt shape, some of which inherited the pre-existing long-term faults. On the plane, they are closely arranged in parallel, en echelon, and braided patterns. The boundary of the fault belt has a larger fault scale, while the fault scale within the belt is smaller. Typical flower-like structures can be seen on the seismic profile, which has obvious strike-slip characteristics, reflecting the torsion stress state. In addition, there is a “V”-shaped trench system and a “Y”-shaped structural pattern, which cuts off the Quantou Formation. Some of the fault-concentrated belts are not connected to deep faults due to the horizontal detachment of the mudstone layer (Xie and Fu, 2013; Xie et al., 2015). The overall development of the fault-concentrated belt is controlled by the “weak zone” existing during the faulting period, e.g., pre-existing faults, volcanic vents, and uplift zones. The genesis of the fault zone can be divided into three types: 1) strike-slip, where a large-scale strike-slip fault developed in the Sanzhao area named the Xuzhong fault, which became active in the late sedimentation period of the Quantou Group, forming a “braided” fault zone (Li and Li, 2010; Li et al., 2012b). 2) Oblique rifting, where the early north–northwest-oriented basement faults intersect with the near-east–west extensional forces at an angle of approximately 60°, producing oblique tension. 3) Extension, where the NS-oriented faults are formed by the E–W extensional forces. Strike-slip force is prone to forming “braided” fault belts and flower-like fault combinations. Extensional force is prone to forming “parallel belt-shaped” fault zones, as well as “V”-shaped and “y”-shaped fault combinations. Meanwhile, the torsional force is prone to forming “en echelon” fault belts.

Figure 7G shows the Yaojia Formation–Nenjiang Formation sedimentary period. The sedimentation of the Yaojia Formation was during the early stage of basin inversion, where the extensional forces within the basin gradually disappeared, and only small faults developed near the base of the Yaojia Formation, while the long-term faults continued to develop. The subduction of the Pacific plate changed from the northwest to west–northwest direction (Hou et al., 2004), and the basin began to experience compression during the sedimentation of the Yaojia Formation. The compression stress direction was WNW–ESE, causing weak deformation in the fault plane (Gong et al., 2008). The sedimentation period of the Nenjiang Formation was the main period of the transformation of the faults, which experienced the “Nenjiang Movement” and strong compression in the basin (Huang et al., 2014; Liu et al., 2020). However, the tectonic movement did not cause any significant change in the strata or structural pattern, but resulted in a differential uplift within the basin (Chen et al., 2010). During the deposition of the Mingshui Formation, the most intense structural reversal occurred, resulting in a left-hand compressional and rotational deformation of the fault zone, forming the current structural pattern (Sun et al., 2013b).

5.3 Influence of the structure and fault system on oil and gas migration and accumulation

The roles that faults play in hydrocarbon accumulation can be summarized as follows: 1) the migration channels for oil and gas

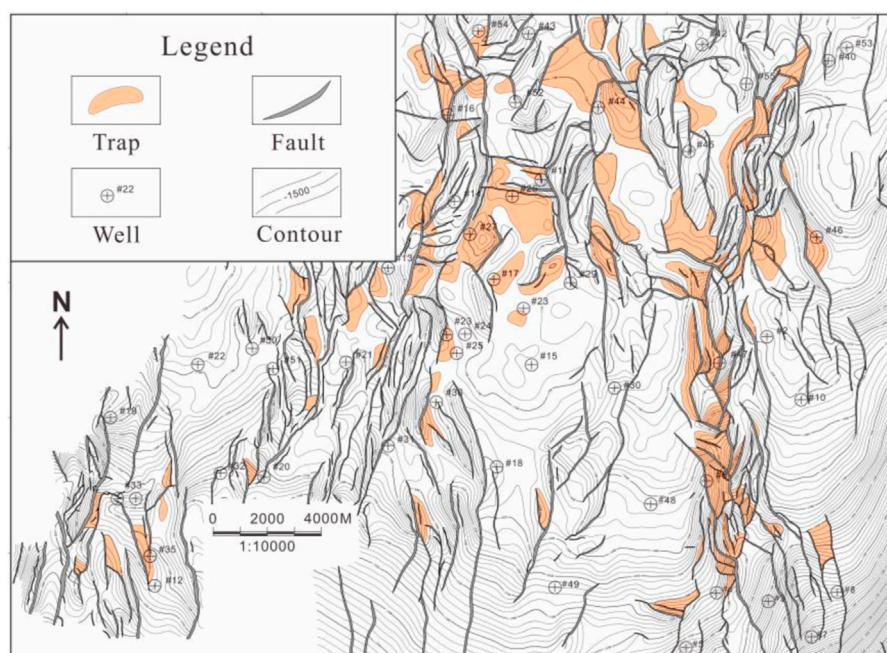


FIGURE 8

Trap distribution map for the top of the Yangdachengzi oil layer. Traps develop along the fault-concentrated belt; the size and number of traps depend on the relationships between faults and strata.

migration, 2) the lateral sealing effect, and 3) the various traps related to faults (Guo, 2010; Liang et al., 2019; Wang et al., 2022b). The Yangdachengzi tight sandstone oil reservoir at the Quantou Formation was accumulated by above-generation and below-storage. The upper Qingshankou Formation was the oil source layer. Due to the difference of the geological structure, the overlying strata of the Qingshankou Formation in the eastern region were mudstone. There were many faults developed in the lower Qingshankou Formation, which can provide a good migration channel for oil and gas to the lower sandstone (Yang, 2022). Based on the geochemical analysis, some of the hydrocarbon in the Yangdachengzi oil layer migrated from the Sanzhao Depression on the NW side of the study area. The Fuyu oil layer on the footwall of the fault was laterally opposed to the source rock of the Qingshankou Formation on the hanging wall, and the oil and gas were directly transported from west to east to the Fuyu and Yangdachengzi oil layer (Sun et al., 2010; Huang et al., 2012; Wang et al., 2020). The distribution of the fault system and the development of sand bodies were the main controlling factors of hydrocarbon lateral migration and accumulation.

The fault-concentrated belt can provide both lateral sealing and vertical conduit system for oil and gas migration in the Songliao Basin. When the banded sand bodies in the river delta system across the fault got concentrated, the sand bodies were blocked by faults in the upward direction, which formed the lithologic-fault traps. When the sand bodies and the faults had the same striking, there was no barrier function in the updip direction and no formation conditions for favorable traps. At this time, the fault belts acted as NS migrating channels, and the oil and gas continued to migrate to the higher part of the structure and gradually accumulated in the traps away from the source

rock (Chen et al., 2011; Mei et al., 2020). Four fault-nose structures were developed along five fault-concentrated belts in the study area, and a total of 80 traps are identified at the top of the Yangdachengzi oil layer, with the total area about 58.06 km² (Figure 8). The trap types are mainly fault-block traps and fault-nose traps. The Yumin nose structure developed at the eastern side of the No. 1 fault concentrated belt, which formed a large number of fault-block traps inside. Because of the high and steep terrain in the southeast part of the study area, these fault-block traps have the characteristics of a small closure area and a high closure height, which are difficult to preserve hydrocarbons. The Mofantun nose structure developed between the No. 2 and No. 3 fault-concentrated belt, which formed several large fault-nose traps due to the flat terrain in the north part of the study area. The Zhaoyuan and Zhanyuan western nose structures developed on the side of the No. 4 and No. 5 fault-concentrated belt. The strata show an NW–SE trending direction, which agrees with the strike of the faults. Therefore, traps developed in these two nose structures are small in size and separated sparsely.

The structural style of the Fuyu and Yangdachengzi oil layers were controlled by horst, antithetic fault terrace, graben, and step-like fault. The degree of hydrocarbon enrichment is diverse in different structure types. The statistical results showed that the success rate of exploration wells with horst, antithetic fault terrace, graben, and step-like fault in the fault-concentrated belt decreased gradually (Chen et al., 2013). When the fault had large displacement, both sides of the horst were blocked by mudstone, forming good accumulation conditions. The height of the oil column increased with the fault displacement distance. The graben structure in the middle of the fault-concentrated belt

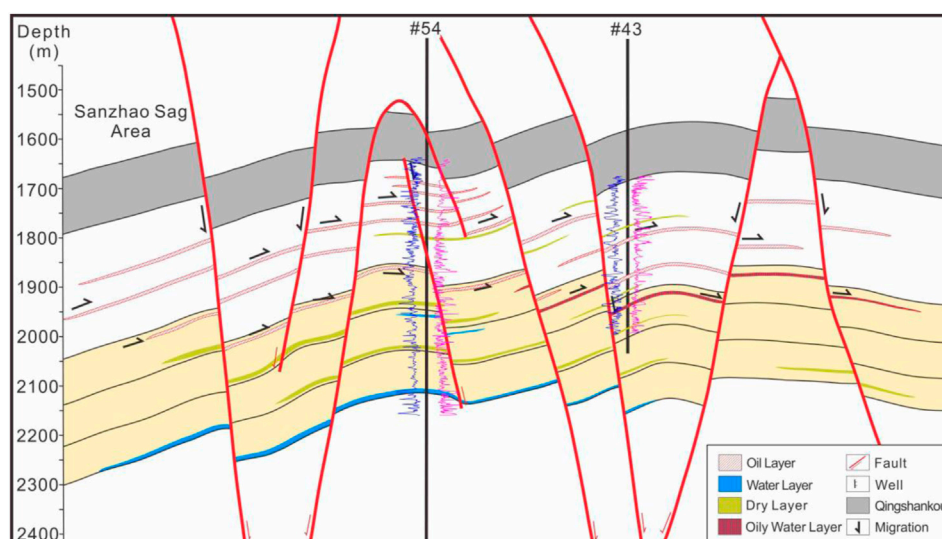


FIGURE 9

Oil–gas migration map. Eastward migration of oil–gas in the Sanzhao area. The oil and gas of the overlying Qingshankou Formation poured downward and accumulated in the Fuyu and Yangdachengzi oil layer (yellow background color) to form lithologic–fault traps. The Yangdachengzi oil layer has less oil, mainly gathered horst and reverse fault terrace parts with many dry and water layers.

has a low terrain, and then, lateral oil and gas can be blocked by the negative topography of the graben, resulting in the reduction of oil column height or completely blocking oil and gas. The horsts and step-like faults on either side of the dense fault zone were the favorable areas for hydrocarbon accumulation in the Yangdachengzi oil layer. As shown in Figure 9, part of the oil and gas migrated from west to east and part of the oil and gas migrated downward. The sand bodies cross the fault plane laterally. Because of the undeveloped induced fractures, the fault footwall had good lateral sealing, which was beneficial to the hydrocarbon accumulation and lithologic–fault trap establishment in the footwall (Luo., 2011). The hydrocarbon in the Fuyu oil layer migrated laterally along the sand body to the vicinity of the fault and continued to migrate downward along the fault to the Yangdachengzi oil layer due to the higher formation pressure in the upper layer. Then, the oil and gas migrated along the sand bodies to the structural high of the Yangdachengzi oil layer.

6 Conclusion

According to the study results, we can draw the following conclusion:

1. The whole study area is a monocline structure striking in the SE–NW direction, with the stratigraphic strike and the nearly NS faults crossed obliquely at low angle. The local structure is undeveloped, and four nose-shaped tectonic units are formed.
2. The faults are highly developed in the study area, and the strikes are mainly in the NS direction. The dense fault zones are formed where fault density is large, and some faults were active in many stages. Five types of fault dense zones are categorized based on vertical characteristics, including step-like, graben, horst, Y-shaped, and X-shaped conjugated faults in herringbone and horsetail styles. In the plane view, the faults can be categorized into near-parallel, oblique, orthogonal, en echelon, and broom types.
3. We divide the fault system into early-stage, middle-stage, late-stage, and long-term fractures. The long-term fractures were formed during the basin rifting period. The basin developed for a long time in the later tectonic movement, featuring characteristics of long extension and large fault displacement distance, and the fault displacement distance gradually decreases from deep to shallow. The long-term fracture is the main controlling fault type and is the main channel for oil and gas migration.
4. The basement faults in the Songliao Basin were developed during the Jurassic period, which controlled the later sedimentary activities. From the end of Jurassic to the early Cretaceous, the basin experienced a fault depression period. In the late Cretaceous, it experienced a depression period. At the end of the Cretaceous, the structure began to reverse. Finally, the structure was finalized, forming a complex fault depression–depression superimposed basin. Clarifying the activities of different stages of the Songliao Basin is helpful in revealing the genetic mechanism and evolution of the fault belts of the Yangdachengzi oil layer in the Quantou formation.
5. Faults can act as channels for oil and gas migration and also provide good lateral sealing. It is conducive for an oil- and gas-shielding reservoir to form a lithology–fault trap. The horst and step-like faults are favorable places for oil and gas accumulation in the Yangdachengzi layer. Four fault-nose structures were developed along five fault-concentrated belts in the study area, and a total of 80 traps are identified at the top of the Yangdachengzi oil layer, with the total area of about 58.06 km².

In conclusion, we discuss the relationship between tectonic movements and fault-concentrated belts, which provides a theoretical basis for the control of fault belts on the reservoirs during the deposition of the Yangdachengzi oil layer in the Quantou Formation in the central depression of the Songliao Basin. However, the microstructures cannot be recognized on the seismic profiles due to the limitations of the resolution for seismic data. In the next plan, we propose discovering the microfractures generated in the Yangdachengzi oil layer combined with advanced identification technology, which can give us a better understanding of crustal stress during the deposition period of the Quantou Formation in the study area.

Data availability statement

The original contributions presented in the study are included in the article/Supplementary Material; further inquiries can be directed to the corresponding author.

Author contributions

Investigation: YaL; formal analysis: CH and YaL; data curation: JC and JM; writing—original draft preparation: CH, YaL, and TZ; writing—review and editing: YZ, CH, and YuL; and project administration: YaL. All authors contributed to the article and approved the submitted version.

References

- Chen, F. W., Lu, S. F., Xu, Y. T., Li, J. J., and Wang, M. (2013). Types and favorable oil accumulation parts of fault dense belts in fuyang formation of Sanzhao depression, Songliao Basin. *Earth Science-Journal China Univ. Geosciences* 6, 1281–1288. doi:10.3799/dqkx.2013.125
- Chen, F. W., Lu, S. F., Xu, Y. T., Wu, Z. Y., and Wei, X. J. (2011). Intensively faulted zones and their controlling on the hydrocarbon migration and accumulation: A case study of the wangfu depression, Songliao basin. *Earth Science-Journal China Univ. Min. Technol.* 40 (2), 235–239.
- Chen, W. J., He, D. F., and Cui, B. L. (2014). Structural style and genetic mechanism of wide rifting. *Adv. Earth Sci.* 29 (3), 344–351. doi:10.11867/j.jssn.1001-8166.2014.03.0344
- Chen, X., Li, Z. Q., Chen, J. L., Li, H. Q., and Zhang, T. (2010). Determination of the reverse period of Songliao Basin, China. *Geol. Bull. China* 29 (2), 305–311. doi:10.3969/j.issn.1671-2552.2010.02.015
- Deng, M., Zuo, Z. X., Qiu, Q., and Bai, F. (2021). Normal fault evolution in lishu fault depression, southern Songliao Basin. *PETROLEUM Geol. Exp.* 43 (2), 288–296. doi:10.11781/sydz202102288
- Dong, Y., Wang, S. M., Yu, Q., Chen, J. S., Yang, H., Ge, W. C., et al. (2022). Late Paleozoic tectonic magmatic evolution history of the northeastern China. *Acta Petrol. Sin.* 38 (8), 2249–2268. doi:10.18654/1000-0569/2022.08.04
- Eaton, G. P. (1982). The Basin and Range Province origin and tectonic significance. *Annu. Rev. s Earth Planet. Sci.* 10, 409–440. doi:10.1146/annurev. ea.10.050182.002205
- Fan, Q., Fan, T. L., Tian, J. J., Sun, M. H., and Li, Sh. (2017). Sequence stratigraphy and sedimentary evolution from the 4th member of Quantou Formation to the 3rd member of Nenjiang Formation in sifangtuozhi area, Songliao Basin. *PETROLEUM Geol. Exp.* 39 (5), 593–602. doi:10.11781/sydz201705593
- Feng, Z. Q., Dong, L., Tong, Y., Feng, Z. H., Zhang, Sh., Wu, G. K., et al. (2021). Impacts of the closure of eastern Mongolia-Okhotsk Ocean on formation and evolution of Songliao Basin. *OIL & Gas. GEOLOGY* 42 (2), 251–264. doi:10.11743/ogg20210201
- Feng, Z. Q., Jia, C. Z., Xie, X. F., Hu, M., Zi-hui, F., and Cross, T. A. (2010). Tectonostratigraphic units and stratigraphic sequences of the nonmarine Songliao basin, northeast China. *Basin Res.* 22 (1), 79–95. doi:10.1111/j.1365-2117.2009.00445.x
- Feng, Z. Q., Li, M., Guo, Y. L., and Liu, G. X. (2022). Genetic analysis of typical strike slip faults and related basins in China. *Earth Sci. Front.* 29 (6), 206–223. doi:10.13745/j.esf.sf.2022.8.6
- Fu, X. F., Shi, H. D., Meng, Q. A., Liu, B., Liang, J. P., He, J. L., et al. (2020). Controlling effects of the structure and deposition on the shale oil enrichment: Taking Formation qn1, in the Central Depression of Songliao Basin as an instance. *Petroleum Geol. Oilfield Dev. Daqing* 39 (3), 56–71. doi:10.19597/j.issn.1000-3754.202005011
- Gautier, P., Brun, J. P., Moriceau, R., Sokoutis, D., Martinod, J., Jolivet, L., et al. (1999). Timing, kinematics and cause of aegean extension: A scenario based on a comparison with simple analogue experiments. *Tectonophysics* 315, 31–72. doi:10.1016/S0040-1951(99)00281-4
- Ge, M., and Hou, G. T. (2018). Geodynamics of the East african rift System~30 Ma ago. A stress field model. *J. Geodyn.* 117, 1–11. doi:10.1016/j.jog.2018.02.004
- Ge, R. F., Zhang, Q. L., Wang, L. S., Xie, G. A., Xu, S. Y., and Chen, J. (2010). Tectonic evolution of Songliao Basin and the prominent tectonic regime transition in eastern China. *Geol. Rev.* 56 (2), 180–195.
- Ge, R. F., Zhang, Q. L., Xu, S. Y., Wang, L. S., Xie, G. A., Chen, J., et al. (2009). Structure evolution and its kinetic setting of Changling fault depression in Songliao basin. *Earth Sci.* 33 (4), 346–358. doi:10.3969/jin1674-3636.2009.04346
- Gong, F. X., Han, Y. H., Lin, G., Li, Z. A., and Liu, L. (2008). Mechanism of early post-rift normal faults in the central Songliao Basin, northeast China. *Earth Sci.* 4, 547–554. doi:10.3321/j.issn:1000-2383.2008.04.012
- Guan, Q. B., Liu, H. H., Liu, Y. J., Li, S. Z., Wang, S. J., Chen, Z. X., et al. (2022). A tectonic transition from closure of the Paleo-Asian Ocean to subduction of the Paleo-Pacific Plate. Insights from early Mesozoic igneous rocks in eastern Jilin Province, NE China. *Gondwana Res.* 102, 332–353. doi:10.1016/j.gr.2020.05.001
- Guo, X. J. (2019). Fracture characteristics and controls on reservoirs in fulongquan fault depression, Songliao Basin. *J. Pet. Geol.* 41 (5), 657–662. doi:10.11781/sydz201905657
- Guo, Y. P. (2010). Study on hydrocarbon accumulation patterns and control factors in fuyang reservoir, chaoyang area. *J. Oil Gas Technol.* 5, 171–175.
- Hou, G. T., Feng, D. C., and Wang, W. M. (2004). Reverse structures and their impacts on hydrocarbon accumulation in Songliao basin. *Oil Gas Geol.* 25 (1), 49–54. doi:10.3321/j.issn:0253-9985.2004.01.009
- Hou, G. T., Wang, Y. X., and Hari, K. R. (2010). The Late Triassic and Late Jurassic stress fields and tectonic transmission of North China craton. *J. Geodyn.* 50, 318–324. doi:10.1016/j.jog.2009.11.007
- Hu, W. S., Lv, B. Q., Zhang, W. J., Mao, zh. G., Leng, J., and Guan, D. Y. (2005). An approach to tectonic evolution and dynamics of the Songliao Basin. *Chin. J. Geol.* 40 (1), 16–31. doi:10.3321/j.issn:0563-5020.2005.01.002

Funding

This research was supported by the Sichuan Science and Technology Program (Grant No. 2022NSFSC0187) and Open Fund (Grant No. PLC20210102) of State Key Laboratory of Oil and Gas Reservoir Geology and Exploitation (Chengdu University of Technology).

Conflict of interest

Author JM was employed by Oil Production Company of Daqing Oilfield Company Ltd.

The remaining authors declare that the research was conducted in the absence of any commercial or financial relationships that could be construed as a potential conflict of interest.

Publisher's note

All claims expressed in this article are solely those of the authors and do not necessarily represent those of their affiliated organizations, or those of the publisher, the editors, and the reviewers. Any product that may be evaluated in this article, or claim that may be made by its manufacturer, is not guaranteed or endorsed by the publisher.

- Huang, Sh. Q., Dong, S. W., Hu, J. M., Shi, W., Chen, X. H., and Liu, Z. Q. (2016). The Formation and tectonic evolution of the mongol-okhotsk belt. *Acta Geol. Sin.* 90 (9), 2192–2205. doi:10.3969/j.issn.0001-5717.2016.09.008
- Huang, W., Wu, H. B., Shi, L. Z., Wang, S. B., and Wang, Z. Z. (2012). Oil and gas source and reservoir characteristic of Fuyu Reservoir of Chaochang area in north Songliao Basin. *J. Central South Univ. Sci. Technol.* 43 (1), 238–248.
- Huang, X., Chen, K. Y., and Deng, Y. H. (2014). Evolved characteristics of fault T2 in south Songliao Basin. *Petroleum Geol. Oilfield Dev. Daqing* 4, 9–15.
- Jia, S., He, D. F., Han, W. M., and Hu, B. (2021). Formation and evolution of the Kenya rift, the eastern branch of the East african rift system. *Acta Geol. Sin.* 95 (4), 1114–1127. doi:10.19762/j.cnki.dizhixuebao.2021035
- Jiang, X. J., Peng, Y. B., Dong, X. J., Li, H. M., and Tu, Y. (2021). The remote role of Mongolia-Okhotsk Ocean: Evidences from the origin of rhyolite porphyry in yangpangou area, the southeast of inner Mongolia. *Earth Sci.* 46, 3057–3073. doi:10.3799/dqkx.2020.335
- Jolivet, L., and Faccenna, C. (2000). Mediterranean extension and the Africa-Eurasia collision. *Tectonics* 19, 1095–1106. doi:10.1029/2000TC900018
- Li, C., Liu, S. F., and Bai, Y. (2014). Differentiation of anomalous cretaceous post-rift subsidence in the southern Songliao Basin. *Geoscience* 28 (6), 1213–1224. doi:10.3969/j.issn.1000-8527.2014.06.012
- Li, H., Hao, J., Song, W. C., Huang, T., Liu, Z., Zhang, Y., et al. (2019a). Formation and evolution of reservoir fractures in Yingcheng Formation of lishu fault depression, Songliao Basin. *Bull. Mineralogy, Petrology Geochem.* 38 (4), 802–809. doi:10.19658/j.issn.1007-2802.2019.38.071
- Li, J. J., Wang, Z. Z., Zhang, Z. H., and Cheng, G. J. (2013). The sedimentary facies of member-3 of Quantou Formation in xinli Oilfield, Songliao Basin. *Xinjiang Pet. Geol.* 34 (5), 534–537.
- Li, S. Q., Chen, F. K., Siebel, W., Wu, J. D., Zhu, X. Y., Shan, X. L., et al. (2012a). Late Mesozoic tectonic evolution of the Songliao basin, NE China. Evidence from detrital zircon ages and Sr–Nd isotopes. *Gondwana Res.* 22, 943–955. doi:10.1016/j.gr.2012.04.002
- Li, X. L., and Li, X. J. (2010). Relationship between the fractal feature of fault T₂ and the hydrocarbon of fuyang reservoir in Sanzhao sag. *Petroleum Geol. Oilfield Dev. Daqing* 29 (4), 13–17.
- Li, Y. Y., Fu, X. F., and Zhang, M. X. (2012b). Fault deformation features and reservoir controlling mechanisms of Xujiawazi fault depression in Songliao basin. *Nat. Gas. Geosci.* 23 (6), 979–988.
- Li, Z. D., Wang, P., Li, L., Li, W., Xu, J. Z., and Liu, Y. K. (2019b). Study of sedimentary characteristic in Dengloulou formation, southern Songliao basin, Northeast China. *Carbonates Evaporites* 34 (3), 1141–1155. doi:10.1007/s13146-018-0468-4
- Li, Z. Q., Chen, J. L., Zou, H., Wang, C., Meng, Q. A., Liu, H. L., et al. (2021). Mesozoic–Cenozoic tectonic evolution and dynamics of the Songliao Basin, NE Asia: Implications for the closure of the paleo-Asian Ocean and mongol-okhotsk Ocean and subduction of the paleo-pacific ocean. *Earth-Science Rev.* 218, 103471. doi:10.1016/j.earscirev.2020.103471
- Liang, J. P., Zhao, B., Chen, J. L., and Niu, W. (2019). Fault systems and their controlling actions on the petroleum distribution in North Songliao Basin. *Petroleum Geol. Oilfield Dev. Daqing* 38 (5), 126–134. doi:10.19597/j.issn.1000-3754.201906064
- Lin, W., and Li, J. Y. (2021). Cretaceous two stage extensional tectonic in eastern Eurasia continent and its geodynamics. *Acta Petrol. Sin.* 37 (8), 2303–2323. doi:10.18654/1000-0569/2021.08.04
- Liu, C. H. Y., Nicotra, E., Shan, X., Y. J., and Ventura, G. (2023). The Cretaceous volcanism of the Songliao Basin: Mantle sources, magma evolution processes and implications for the NE China geodynamics-A review. *Earth-Science Rev.* 237, 104294. doi:10.1016/j.earscirev.2022.104294
- Liu, C. Y., Shan, X. L., Yi, J., Shi, Y. Q., and Ventura, G. (2022a). Volcanism at the end of continental rifting: The Cretaceous syn-rift to post-rift transition in the Songliao Basin (NE China). *Gondwana Res.* 111, 174–188. doi:10.1016/j.jgr.2022.08.005
- Liu, J. Q., Zhang, T., Lv, Y. Y., Zhang, M. D., Sun, T. W., J. G. P., et al. (2017). Controls of intensively faulted zones on hydrocarbon migration and accumulation: An example of Fuyu oil layer in Xingbei area. *Songliao Basin Petroleum Geol. Exp.* 39 (4), 453–460. doi:10.11781/sydz201704453
- Liu, K., Zhang, J. J., Xiao, W. J., Simon, W., and Igor, A. (2020a). A review of magmatism and deformation history along the NE Asian margin from ca 95 to 30 Ma: Transition from the Izanagi to Pacific plate subduction in the early Cenozoic. *Earth-Sci. Rev.* 209, 103317. doi:10.1016/j.earscirev.2020.103317
- Liu, W., Tang, D. Q., Chen, M. Y., Zhang, Y. J., Chen, L., and Li, N. (2022b). Fault structure characteristics and evolution in the Gudian fault depression, southern Songliao Basin. *Fault-Block Oil & Gasfield* 29 (6), 816–823. doi:10.6056/dkyqt202206015
- Liu, Z. H., Song, J., Liu, X. W., Wu, X. M., and Gao, X. (2020b). Discovery of the Cretaceous-Paleogene compressional structure and basin properties of the southern Songliao Basin. *Acta Petrol. Sin.* 36 (8), 2383–2393. doi:10.18654/1000-0569/2020.08.07
- Lu, T. J., Liu, X., Jiang, S., Zhang, L. L., Ning, J., Wang, H. T., et al. (2022). Study on late cretaceous sedimentary evolution and uranium mineralization in southern Songliao Basin. *Uranium Geol.* 38 (4), 607–617. doi:10.3969/j.issn.1000-0658.2022.38.053
- Luo, Q. (2010). Fault systems and characteristics of their controlling reservoir formation in the northeast China. *PETROLEUM Geol. Exp.* 32 (3), 205–210. doi:10.3969/j.issn.1001-6112.2010.03.001
- Macgregor, D. (2015). History of the development of the East african rift system: A series of interpreted maps through time. *J. Afr. Earth Sci.* 101, 232–252. doi:10.1016/j.jafrearsci.2014.09.016
- Mei, X. H., Wu, X. S., Zhao, J. H., Zhang, Q., Liu, J. Y., and Wang, Q. (2020). Types of fault-intensive belts and their control on hydrocarbon accumulation: A case study of Yangdachengzi oil layer in fuxin uplift, Songliao Basin. *Fault-Block Oil Gas Field* 27 (1), 1–6. doi:10.6056/dkyqt202001001
- Pirajno, F., and Santosh, M. (2015). Mantle plumes, supercontinents, intracontinental rifting and mineral systems. *Precambrian Res.* 259, 243–261. doi:10.1016/j.precamres.2014.12.016
- Powell, R. E., and Weldon, R. J. (1992). Evolution of the san Andreas fault. *Annu. Rev. Earth Planet. Sci.* 20 (1), 431–468. doi:10.1146/annurev.ea.20.050192.002243
- Reading, H. G. (2009). Characteristics and recognition of strike-slip fault systems. *Sediment. Oblique-Slip Mob. Zones* 2009, 7–26. doi:10.1002/9781444303735.ch2
- Rehrig, W. A. (1986). Process of regional Tertiary extension in the western Cordillera: insights from the metamorphic core complexes. *Geological Society of America Special Paper* 208, 97–122. doi:10.1130/SPE208-p97
- Ren, J. Y., and Li, S. T. (1998). Comparison between the faulted basin system in northeastern Asia and the extension of The Basin and range province in western North America. *Geol. Sci. Technol. Inf.* 17 (3), 8–12.
- Ren, J. Y., Tamaki, K., Li, S., and Junxia, Z. (2002). Late Mesozoic and Cenozoic rifting and its dynamic setting in Eastern China and adjacent areas. *Tectonophysics* 344, 175–205. doi:10.1016/S0040-1951(01)00271-2
- Scharer, K., and Streig, A. (2019). The san Andreas fault system: Complexities along a major transform fault system and relation to earthquake hazards. *Transform Plate Boundaries Fract. Zones* 2019, 249–269. doi:10.1016/B978-0-12-812064-4.00010-4
- Shan, W., Liu, S. F., and Wu, J. (2009). Tectonic feature and strain pattern of Changling sag on the southern edge of Songliao basin, China. *Geol. Bull. China* 28 (4), 431–438.
- Sun, Y. H., Bai, L., and Fu, X. F. (2013a). Genetic mechanism of T₂ reflector fault dense zones in northern Songliao Basin. *Earth Science-Journal China Univ. Geosciences* 38 (4), 797–806. doi:10.3799/dqkx.2013.078
- Sun, Y. H., Chen, Y. B., Li, X. S., Sun, J. G., and Fu, X. F. (2013b). Evolutionary sequence of faults and the formation of inversion structural belts in the northern Songliao Basin. *Petroleum Explor. Dev.* 40 (3), 296–304. doi:10.1016/S1876-3804(13)60036-1
- Sun, Y., Ma, S. Z., Zhang, D. Z., Zhao, H., Yu, L. M., and Zhang, Y. B. (2010). The analysis of hydrocarbon accumulation characteristics and its main controlling factors in lithologic reservoirs area outside oil source area—example of Fuyu oil layer in the southern fuxin uplift of Songliao Basin. *Geol. Rev.* 55 (5), 693–700. doi:10.16509/j.georeview.2010.04.015
- Tang, J., Xu, W. L., Wang, F., and Ge, W. C. (2018). Subduction history of the paleo-pacific slab beneath Eurasian continent: Mesozoic-paleogene magmatic records in northeast Asia. *Sci. China Earth Sci.* 61, 527–559. doi:10.1007/s11430-017-9174-1
- Wang, P. J., Xie, X. An., Mattern, F., Ren, Y. G., Zhu, D. F., and Sun, X. M. (2007). The cretaceous Songliao Basin: Volcanogenic succession, sedimentary sequence and tectonic evolution, NE China. *Acta Geol. Sinica-English Ed.* 81 (6), 1002–1011. doi:10.1111/j.1755-6724.2007.tb01022.x
- Wang, X. D., Wang, R., Shi, W. Z., Tang, D. Q., Xu, L. T., and Feng, Q. (2022a). Tectonic characteristics and evolution of typical rift basins in eastern China: A case study in the gudian area, Songliao Basin. *Bull. Geol. Sci. Technol.* 41 (3), 85–95. doi:10.19509/j.cnki.dzkq.2022.0089
- Wang, X. Y., Wang, D. H., and Wang, S. L. (2020). Analysis of hydrocarbon accumulation conditions of 4th member of Quantou Formation in yongping Oilfield, southern Songliao Basin. *Glob. Geol.* 39 (2), 388–398. doi:10.3969/j.issn.1004-5589.2020.02.013
- Wang, Y. W., Chen, B. J., Chen, J. L., Cao, W. F., Niu, W., and Jia, Q. (2022b). Roof and floor faults seal of Gulong shale oil reservoir in Songliao Basin and optimization of favorable areas for oil and gas accumulation. *Petroleum Geol. Oilfield Dev. Daqing* 41, 53–67. doi:10.19597/j.issn.1000-3754.202111068
- Wesnowsky, S. G. (2005). The San Andreas and Walker Lane fault systems, Western North America: Transpression, transtension, cumulative slip and the structural evolution of a major transform plate boundary. *J. Struct. Geol.* 27 (8), 1505–1512. doi:10.1016/j.jsg.2005.01.015
- Wilson, J. T. (1966). Did the Atlantic close and then re-open. *Nature* 211, 676–681. doi:10.1038/211676a0
- Xi, K. L., Cao, Y. C., Jens, J., Zhu, R. K., Bj, K., Haile, B. G., et al. (2015). Diagenesis and reservoir quality of the lower cretaceous Quantou Formation tight sandstones in the southern Songliao Basin, China. *Sediment. Geol.* 330, 90–107. doi:10.1016/j.sedgeo.2015.10.007
- Xiang, B. W., Chen, L., Zhang, Q., Wang, Zh. G., and Gao, Ch. (2022). Deformation mechanism of post-orogenic extension and its implications for deep dynamics in the northern dabi orogenic belt. *Geotect. Metallogenia* 46 (5), 867–883. doi:10.16539/j.dgzycxk.2022.05.003
- Xie, Z. H., and Fu, X. F. (2013). The genetic mechanism and accumulation mechanism of “T₂” fault dense zone in Songliao Basin: In Sanzhao depression. *Chin. J. Geol.* 48 (3), 891–907. doi:10.3969/j.issn.0563-5020.2013.03.024

- Xie, Z. H., Luo, J. S., Liu, Z. L., Wei, Z. P., Ye, F., and Wang, Y. X. (2015). Fault Re-active and reservoir-controlling of xujiaweizi Fault depression, Songliao Basin. *Geol. Rev.* 61 (6), 1332–1346. doi:10.16509/j.georeview.2015.06.012
- Yang, M. H. (2022). Determination method of downward hydrocarbon transport period of oil source fault and application in Sanzhao Sag in Songliao Basin. *Petroleum Geol. Oilfield Dev. Daqing*. 41, 51–57. doi:10.19597/j.ISSN.1000-3754.202203031
- Yang, Q., Shi, W., and Hou, G. T. (2019). Late mesozoic extensional detachment structures in eastern China and adjacent areas: Overview and new insight. *Acta Geosci. Sin.* 40 (4), 511–544. doi:10.3975/cagsb.2019.012301
- Yang, X. B., Wang, H. Y., Li, Z. Y., Chao, G., and Wang, X. (2021). Tectonic-sedimentary evolution of a continental rift basin: A case study of the early cretaceous changling and lishu fault depressions, southern Songliao Basin, China. *Mar. Petroleum Geol.* 128, 105068. doi:10.1016/j.marpetgeo.2021.105068
- Yao, H. Z., Chen, K. X., Wang, J. W., Yang, Z. Q., Wei, Y. G., Li, Y. H., et al. (2018). The geochemical criteria of mantle plume origin for Cenozoic volcanism, Eastern African Rift System (EARS). *Geol. Mineral Resour. South China* 34 (1), 10–21. doi:10.3969/j.issn.1007-3701.2018.01.002
- Zhang, J. J., and Huang, T. L. (2019). An overview on continental extensional tectonics. *Earth Sci.* 44 (5), 1705–1715. doi:10.3799/dqkx.2019.009
- Zhang, X. D., Wang, Y., and Li, G. R. (2005). Formation, evolution and earth dynamics of jurassic and cretaceous basins in northern China. *Petroleum Geol. Oilfield Dev. Daqing* 25 (4), 7–9. doi:10.12090/j.issn.1000-3754(2005)05-0013-04
- Zhang, Y. Q., and Dong, S. W. (2019). East asia multi-plate convergence in late mesozoic and the development of continental tectonic systems. *J. Geomechanics* 25 (5), 613–641. doi:10.12090/j.issn.1006-6616.2019.25.05.059

Frontiers in Earth Science

Investigates the processes operating within the major spheres of our planet

Advances our understanding across the earth sciences, providing a theoretical background for better use of our planet's resources and equipping us to face major environmental challenges.

Discover the latest Research Topics

[See more →](#)

Frontiers

Avenue du Tribunal-Fédéral 34
1005 Lausanne, Switzerland
frontiersin.org

Contact us

+41 (0)21 510 17 00
frontiersin.org/about/contact

